

**Characterisation of Hypoglycaemic White Matter
Injury: an electrophysiological, pharmacological and
imaging study in the rodent brain.**

Dr. Christian Zammit

Ph.D. Dissertation

Department of Physiology and Biochemistry
Faculty of Medicine and Surgery
University of Malta

2019

Supervisor: Prof Mario Valentino

Submitted in partial fulfilment of the requirements for the degree of
Doctor of Philosophy



L-Università
ta' Malta

University of Malta Library – Electronic Thesis & Dissertations (ETD) Repository

The copyright of this thesis/dissertation belongs to the author. The author's rights in respect of this work are as defined by the Copyright Act (Chapter 415) of the Laws of Malta or as modified by any successive legislation.

Users may access this full-text thesis/dissertation and can make use of the information contained in accordance with the Copyright Act provided that the author must be properly acknowledged. Further distribution or reproduction in any format is prohibited without the prior permission of the copyright holder.

DECLARATION OF AUTHENTICITY FOR DOCTORAL STUDENTSStudent's I.D. /Code: **7084 G**Student's Name & Surname: **Dr Christian Zammit**Course: **PHB 6000**Title of Dissertation/Thesis: **Characterisation of Hypoglycaemic White Matter Injury: an electrophysiological, pharmacological and imaging study in the rodent brain.****(a) Authenticity of Thesis/Dissertation**

I hereby declare that I am the legitimate author of this Thesis/Dissertation and that it is my original work.

No portion of this work has been submitted in support of an application for another degree or qualification of this or any other university or institution of higher education.

I hold the University of Malta harmless against any third party claims with regard to copyright violation, breach of confidentiality, defamation and any other third party right infringement.

(b) Research Code of Practice and Ethics Review Procedure

I declare that I have abided by the University's Research Ethics Review Procedures.

As a Ph.D. student, as per Regulation 49 of the Doctor of Philosophy Regulations, I accept that my thesis be made publicly available on the University of Malta Institutional Repository.

As a Doctor of Sacred Theology student, as per Regulation 17 of the Doctor of Sacred Theology Regulations, I accept that my thesis be made publicly available on the University of Malta Institutional Repository.

As a Doctor of Music student, as per Regulation 24 of the Doctor of Music Regulations, I accept that my dissertation be made publicly available on the University of Malta Institutional Repository.

As a Professional Doctorate student, as per Regulation 54 of the Professional Doctorate Regulations, I accept that my dissertation be made publicly available on the University of Malta Institutional Repository.

Signature of StudentDr. CHRISTIAN ZAMMIT

Name in Full

05/09/2019

Date

Abstract

Failure of white matter energy metabolism plays a major role in several neurological disorders. Over the years, several studies have focused on mechanisms of neuronal injury and death in the absence of sufficient substrate for oxidative metabolism. In so doing, a gap in the knowledge to central mechanisms of damage that are specific to white matter has been overlooked.

In this study, we used the callosal brain slice from mice as a model of white matter so as to characterise the role of glucose deprivation (GD) and to uncover potential routes of injury for pharmacological intervention. Axonal loss or recovery of function was determined electrophysiologically by monitoring the evoked compound action potential (CAP). This technique was carefully combined with live two-photon microscopy to follow the sequential progression or recovery from injury during pharmacological block of key cellular events. Detailed histological assessment was determined through a combination of confocal, light and electron microscopy techniques.

Results from this study show that 45 min of GD cause delayed structural disruption to YFP-expressing axons, that was preceded by the functional loss in electrical activity as observed by the loss in maintenance of the CAP. We therefore extended this time-window by stimulation of the glycogenolytic pathway through β -adrenergic afferents using clenbuterol. This protection was not mediated by enhanced lactate production as expected, but possibly mediated through the steroid's anti-inflammatory and antioxidative properties. Inhibition of axonal lactate uptake by 4-CIN was associated with severe axonal injury, thus confirming the role of lactate as a central energy substrate for axons. In vivo microdialysis from mouse cerebellar white matter confirmed the continuous uptake of lactate by axons during normal brain physiology.

Excitotoxicity has been shown to play a central role in hypoglycaemic white matter injury. Blocking AMPA/Kainate receptors with NBQX protects both axons and oligodendrocytes after GD as was seen through live-imaging and electron microscopy. Targeting AMPA/Kainate receptors might be a good strategy to preserve the integrity of oligodendrocytes and axons. Combined therapy involving the specific GluN2C/D-containing NMDA receptor antagonist (QNZ-46) and the non-competitive AMPA-specific receptor antagonist (CP-465,022) show excellent preservation of axon integrity and function following GD. Both drugs were able to cross the blood-brain-barrier, were non-toxic, and their presence confirmed through imaging as a result of their intrinsic fluorescence. This, together with the use-dependent features of QNZ-46 makes these drugs ideal candidates for therapeutic intervention in disorders that preferentially affect white matter.

We further show that bath application of callosal axons exposed to micromolar levels of nitric oxide (NO) cause irreversible conduction block. Sequential live imaging of NO using fluorescent dyes during the course of GD shows that its increase preceded the loss in CAP. At the same time, blocking NO release during GD with L-NAME partially protects axons and suggests that this strategy can be a useful therapeutic target. It is to be determined whether QNZ-46 can also mitigate the block in NO by limiting the entry of Ca^+ by way of the use-dependent activity of this drug. The findings from this study suggest a multimodal prophylactic therapy to protect patients that frequently suffer from hypoglycaemia and other forms of excitotoxic insults.

Key words: white matter, glucose deprivation, two-photon microscopy, electron microscopy, compound action potential, lactate, excitotoxicity, nitric oxide, glutamate receptors

Acknowledgements

First and foremost, I would like to express my gratitude to Professor Mario Valentino. I met Mario back in 2010. He supervised my master's degree and he was one of the first to encourage me to continue my studies. I had no background of lab work when I started in his lab. He patiently taught me all the techniques I mastered during these years. The dedication with which he provided me with constant support and guided me throughout these years was outstanding, and without his help and supervision I would never have completed this thesis. I am grateful that after all these years, I no longer repute Mario as simply my supervisor, but I now regard him as a true friend.

I would also like to thank Professor Richard Muscat for his continuous support and guidance throughout the years.

A sincere thanks goes to Mr Robert Zammit and to Dr Jasmine Vella for their technical help and support.

I would also like to express my gratitude to Prof. Robert Fern, from the University of Plymouth, and to Prof Jacques De Keyser from Vrije Universiteit Brussels, for the fruitful collaboration we had over these years which resulted in joint high impact publications as a part of this study.

A special thanks goes to Prof. Godfrey LaFerla, Dean of the Faculty of Medicine and Surgery for the PhD scholarship, which was essential for me to arrive to this stage in my academic career.

I would like to dedicate this thesis to my family. My parents provided me with endless assistance since the early stages of my studies and I cannot thank them enough for their unwavering support. I would also like to thank my sister, and my brother and his wife for always believing in me and backing me up any way they could. A special dedication goes to the most recent addition to our family, our own angel Alessia, who brings out the best in each one of us. Finally, I would also like to dedicate my thesis in loving memory of my uncle, who I am sure would have been really proud of my achievements.

Contents

Abstract	i
Acknowledgements	ii
Contents	iii
List of Figures	viii
List of Tables	xii
List of Abbreviations	xv

1 The pathophysiology and clinical picture of hypoglycaemia

1.1. Incidence and prevalence of hypoglycaemia	2
1.2. General complications associated with hypoglycaemia	5
1.2.1. Cardiovascular	5
1.2.2. Critical care medicine	6
1.2.3. Metabolic	6
1.3. Neurological complications associated with hypoglycaemia	8

2 Characterisation of the structural and functional injury to white matter axons during aglycaemia

2.1. Aims	12
2.2. Literature Review	13
2.2.1. The study of white matter injury	13
2.2.2. The use of YFP-expressing transgenic mice to study white matter	15
2.2.3. Electrophysiology as a useful tool to study axonal injury	17
2.2.4. Clinical evidence that hypoglycaemia is a cause of axonal injury	21
2.2.5. Experimental evidence that glucose deprivation contributes to a loss of function in injured axons	22
2.3. Methodology	24
2.3.1. Dissecting instruments	24
2.3.2. Preparation of cutting solution for the retrieval of callosal slices	25
2.3.3. Preparation of artificial cerebrospinal	26
2.3.4. Optic nerve preparation	27
2.3.5. Brain slice preparation	29
2.3.6. Live imaging under two-photon microscopy	31
2.3.7. Glucose deprivation during live imaging	31
2.3.8. Data analysis	36
2.3.9. Statistical analysis	37
2.3.10. Induction of glucose deprivation in vivo in interphase chambers	38

2.3.11. Immunocytochemistry	41
2.3.12. Assessment of axon and neurofilament morphology	42
2.3.13. Brightfield and electron microscopy for histological analysis and morphometry	42
2.3.14. Preparation of electrodes for electrophysiology and generation of the compound action potential	43
2.3.14.1. Optic nerve electrophysiology	45
2.3.14.2. Callosal brain slice electrophysiology	48
2.3.15. Recording of the compound action potential	52
2.3.16. Data analysis of compound action potential recording	52
2.4. Results	53
2.4.1. Visualisation of axon structure with YFP-expressing callosal slices	54
2.4.2. Progression of injury in YFP-expressing axons	55
2.4.3. Expression of YFP correspond to other common techniques commonly used to study axon integrity	58
2.4.4. Axon survival is dependent upon the duration in glucose deprivation	60
2.4.5. Histopathological hallmarks of axonal injury from glucose deprivation	63
2.4.5.1. Pathological features of axonal injury from glucose deprivation	63
2.4.5.2. Pathological features of oligodendrocyte injury from glucose deprivation	67
2.4.6. Compound action potential recordings from optic nerves and callosal slices during normal physiology and following glucose deprivation	69
2.4.7. Loss of axonal conduction is dependent on the duration of glucose deprivation	72
2.4.8. Loss of axonal conduction is dependent on temperature	74
2.5. Discussion	76
2.5.1. Acute callosal brain slices as the preferred model to study white matter injury	76
2.5.2. YFP-expressing transgenic mice as a model to study axonal injury	78
2.5.3. Glucose deprivation equally injures axons and oligodendrocytes	80
2.5.4. Glucose deprivation is a cause for the delay in structural injury to axons	82
2.5.5. Loss of axonal function precedes the structural injury that is observed after glucose deprivation	83
2.5.6. Heavy myelinated axons are more vulnerable to glucose deprivation than the less-heavily myelinated axons.	84

3 Energy metabolism of white matter during glucose deprivation

3.1. Aims	87
3.2. Literature Review	88
3.2.1. Brain energy metabolism	89
3.2.2. Lactate as a metabolic substrate in the brain	90
3.2.3. Metabolic interactions between astrocytes and neurons	91
3.2.4. Metabolic interactions between astrocytes and axons	94
3.2.5. Metabolic interactions between oligodendrocytes and axons	97
3.3. Methodology	99
3.3.1. In vivo microdialysis in white matter	100
3.3.2. Live imaging to study the role of lactate during glucose deprivation	101
3.3.3. Statistical analysis	102
3.4. Results	103
3.4.1. Analysis of microdialysates after drug administration	103
3.4.2. The block in the uptake of lactate by axons during 30 min of glucose deprivation causes axonal injury	105
3.4.3. β 2-adrenergic stimulation protects axons during 45 min of glucose deprivation	107
3.4.4. The block in the uptake of lactate by axons inhibits the protection of β 2-adrenergic stimulation during 45 min of glucose deprivation	109
3.4.5. β 2-adrenergic stimulation does not alter extracellular lactate and glucose concentration	111
3.5. Discussion	112
3.5.1. The glucose-lactate shuttle in white matter during normal physiology	114
3.5.2. Lactate as a source of energy during glucose deprivation	115
3.5.3. Stimulation of astrocytic β 2-adrenergic receptors protects axons during glucose deprivation	116

4 The central role of excitotoxicity to white mater following glucose deprivation

4.1. Aims	117
4.2. Literature Review	118
4.2.1. Altered ionic flux contribute to axonal injury during glucose deprivation	120
4.2.2. Excitotoxicity contributes to axonal injury during glucose deprivation	121
4.2.3. General mechanisms of excitotoxicity in white matter	125
4.2.4. QNZ-46 blocks GluN2C/D subunits present on NMDA receptors and protects axons and myelin from ischaemic injury	127
4.3. Methodology	133
4.3.1. Pharmacological manipulation of antagonists to AMPA/Kainate receptors before and after glucose deprivation	133
4.3.2. Quantification of axonal injury through electron microscopy	134
4.3.3. The effect of calcium on glucose deprivation	134
4.3.4. Systemic administration of NMDA and AMPA antagonists to block key pathways that participate in white matter injury	135
4.4. Results	137
4.4.1. AMPA/Kainate receptor block protects axons and oligodendrocytes during glucose deprivation	137
4.4.2. Axonal Injury during glucose deprivation is calcium-dependent	141
4.4.3. The preferential localization of QNZ in myelin is key to neuroprotection	144
4.4.4. The combined AMPA and NMDA receptor block protect axons following glucose deprivation	145
4.5. Discussion	
4.5.1. Block of AMPA/Kainate receptors with NBQX protects axons and glia from injury	157
4.5.2. The combined block of GluN2C/D subunits on NMDA receptors and AMPA receptors protects oligodendrocytes and axons following glucose deprivation	159

5	Nitric oxide and aglycaemia induced axonal injury	
5.1.	Aims	156
5.2.	Literature Review	157
5.2.1.	A dual role of nitric oxide in the brain	157
5.2.2.	Production of nitric oxide in the brain	159
5.2.3.	Nitric oxide causes conduction block in axons	160
5.2.4.	Nitric oxide is a cause of white matter injury	161
5.2.5.	Putative role of nitric oxide during glucose deprivation	162
5.3.	Methodology	164
5.3.1.	Application of nitric oxide donor to callosal slices	164
5.3.2.	Detection of nitric oxide in white matter using fluorescent dyes	165
5.3.3.	Quantitative analysis of signal intensity changes from nitric oxide sensitive dyes	168
5.3.4.	Addition of nitric oxide synthase inhibitors to slices exposed to glucose deprivation	170
5.4.	Results	171
5.4.1.	Exposure of callosal axons to donors of nitric oxide cause irreversible conduction block but no structural injury	171
5.4.2.	Nitric oxide is localised in glia, the axoplasm and myelin	174
5.4.3.	Increased levels of nitric oxide during the initial phase of glucose deprivation	179
5.4.4.	The block in nitric oxide attenuates the injury caused to axons following glucose deprivation	183
5.5.	Discussion	
5.5.1.	Incubation of callosal slices with the NO donor DETA NONate, causes irreversible conduction block but no structural injury	186
5.5.2.	Glucose deprivation increases nitric oxide production	188
5.5.3.	Nitric oxide contributes to axonal injury following glucose deprivation	189
6	Conclusion and Future Direction	190
7	References	202
8	Supplementary material	244
9	Publications	250

List of Figures

Chapter 1: The Pathophysiology and Clinical Picture of Hypoglycaemia

Figure 1.1.	Summary of the physiological impact of hypoglycaemia on different body systems	7
Figure 1.2.	Diffusion-weighted MR images and the corresponding apparent	12

Chapter 2: Characterisation of the structural and functional injury to white matter axons during aglycaemia

Figure 2.1.	Ischaemia causes extensive axonal injury as seen by morphologic changes occurring in YFP-labelled axons	16
Figure 2.2.	Diagrammatic representation of the typical hardware required to record compound action potential from the optic nerve	19
Figure 2.3.	A typical recording from the rodent optic nerve	19
Figure 2.4.	Diagrammatic representation of the typical position of the stimulating and recording electrodes on the brain slice	19
Figure 2.5.	A typical recording obtained from the rodent callosal brain	20
Figure 2.6.	The effect of CAP recording following GD in the rodent optic nerve during different time points of the experiment	22
Figure 2.7.	Loss in CAP following GD in the optic nerve	23
Figure 2.8.	Loss in CAP following GD in the callosal brain slice	23
Figure 2.9.	Surgical dissection tools used	24
Figure 2.10.	Step-wise procedure to extract the optic nerve	28
Figure 2.11.	Step-wise procedure to extract the whole brain	30
Figure 2.12.	FV1000 MPE Olympus Multiphoton microscope	31
Figure 2.13.	Integrated setup used for live brain slice imaging	32
Figure 2.14.	Live-imaging set-up	33
Figure 2.15.	Set-up for slice perfusion during live imaging	34
Figure 2.16.	Set-up for the imaging chamber	35
Figure 2.17.	Axonal injury score	36
Figure 2.18.	Various degree of axonal injury with their respective injury score	37
Figure 2.19.	General setup of the Hass-type interphase chambers	39
Figure 2.20.	Control and experimental slices in Hass-type interphase chambers	40
Figure 2.21.	Electrophysiological setup for the optic nerve and the brain slice	43
Figure 2.22.	The Neurolog™ amplifier	44
Figure 2.23.	The stimulus isolator unit	44
Figure 2.24.	Electrophysiology rig used to record CAP from the optic nerve	45

Figure 2.25. Electrodes used for CAP recording from the mouse optic nerve	47
Figure 2.26. Electrophysiology rig used to record CAP from the callosal brain slice	48
Figure 2.27. Electrodes used for CAP recording from the callosal brain slice	50
Figure 2.28. Distribution of the recording and stimulating electrodes for CAP recording from callosal fibres in the brain slice.	51
Figure 2.29. Visualization of axon morphology in transgenic mice (Thy1-YFP line H) with neuron-specific expression	53
Figure 2.30. Coronal brain slice of YFP-H mouse	54
Figure 2.31. Progression of injury in YFP-expressing axons	56
Figure 2.32. Small calibre axons are more vulnerable to injury by GD than the larger calibre axons	57
Figure 2.33. Comparison between YFP-expressing axons and SMI-31 immunostaining	58
Figure 2.34. Brightfield and EM showing normal-appearing axonal ultrastructure including preserved myelin	59
Figure 2.35. Sequential time frames that compare the integrity of axon profiles in slices exposed to variable exposures of GD	61
Figure 2.36. Comparison of axonal injury score between various extents in the duration of GD at different time points	62
Figure 2.37 YFP fluorescence corresponds to other methods that evaluate axon integrity	65
Figure 2.38 Transient GD in brain slices causes ultrastructural disruption of myelinated and unmyelinated axons in the corpus callosum	66
Figure 2.39 Oligodendrocyte pathology following GD	68
Figure 2.40 Typical CAP profiles derived from the optic nerve and callosal slice	70
Figure 2.41 Heavily myelinated axons are more vulnerable to GD	71
Figure 2.42 CAP recording from callosal slices exposed to variable extents in exposure to GD	72
Figure 2.43 Percentage CAP recovery following variable lengths in exposure of GD	73
Figure 2.44 CAP recording from callosal slices exposed to GD maintained at different bath temperatures	74
Figure 2.45 Percentage CAP recovery following 45 min of GD at different temperatures	75
Figure 2.46 Electron microscopy comparing the normal and swollen appearance of a mitochondrion	81
Figure 2.47 Representative trace recordings of the CAP profile from the sciatic nerve, optic nerve, and corpus callosum	85

Chapter 3: Energy metabolism of white matter during aglycaemia

Figure 3.1.	Schematic of the major pathways in the astrocyte-neuron lactate shuttle	92
Figure 3.2.	Proposed metabolic interactions occurring between astrocytes and axons	96
Figure 3.3.	Microdialysate levels of glucose, lactate and glutamate following administration of 4-CIN and TBAO	104
Figure 3.4.	Sequential images of a callosal slice exposed to 30 min of GD in the presence of 4-CIN	105
Figure 3.5.	Injury score of callosal axons exposed to 30 min of GD (+/-) 4-CIN and controls	106
Figure 3.6.	Sequential images of a callosal slice exposed to 45 min of GD in the presence of clenbuterol	107
Figure 3.7.	Injury score of callosal axons exposed to 45 min of GD (+/-) clenbuterol and controls	108
Figure 3.8.	Sequential images of a callosal slice exposed to 45 min of GD in the presence of clenbuterol and 4-CIN	109
Figure 3.9.	Injury score of callosal axons exposed to 45 min of GD (+/-) clenbuterol + 4-CIN and controls	110
Figure 3.10.	Microdialysis levels of glucose, lactate and glutamate following administration of Clenbuterol and ICI-118551	111
Figure 3.11.	Summary of the lactate shuttle and the interconnected glutamate–glutamine cycle between astrocytes and axons	113

Chapter 4: The central role of excitotoxicity to white mater following aglycaemia

Figure 4.1.	Alterations in the Embden-Meyerhof glycolysis and Tricarboxylic Acid Cycle that prevail during hypoglycaemia	119
Figure 4.2.	White matter under normal physiological conditions	122
Figure 4.3.	White matter during ischaemia	123
Figure 4.4.	White matter during aglycaemia	124
Figure 4.5.	Proposed mechanism of oligodendrocyte injury mediated by AMPA/Kainate receptor activation	126
Figure 4.6.	Myelin injury in the adult rat optic nerve is NMDA-receptor-mediated I	128
Figure 4.7.	Myelin injury in the adult rat optic nerve is NMDA-receptor-mediated II	129
Figure 4.8.	QNZ-46 mediated myelin protection in the adult mouse optic nerve	130
Figure 4.9.	Systemic pre-treatment of mice with QNZ-46 protected both grey and white matter from ischaemic injury following MCAO I	131
Figure 4.10.	Systemic pre-treatment of mice with QNZ-46 protected both grey and white matter from ischaemic injury following MCAO I	132
Figure 4.11.	AMPA/KA receptor blockade attenuates axon injury after GD	138

Figure 4.12. NBQX preserves axon structure following GD	139
Figure 4.13. Quantitative assessment of axonal pathology from brain slices by electron microscopy	139
Figure 4.14. AMPA/KA receptor blockade following GD attenuates ultrastructural injury in oligodendrocytes	140
Figure 4.15. Sequential images from a callosal slice exposed to 45 min of GD in a Ca ²⁺ - free environment	141
Figure 4.16. Injury score of callosal axons exposed to 45 min of GD in a calcium-free environment	142
Figure 4.17. CAP recording from callosal slices exposed to 45 min of GD (+/-) Ca ²⁺ and controls	143
Figure 4.18. Percentage CAP recovery of callosal slices exposed to 45 min of GD (+/-) Ca ²⁺ and controls.	143
Figure 4.19. QNZ-46/FM co-staining in brain slice following systemic QNZ-46 injection at 4 hr before sacrifice.	144
Figure 4.20. QNZ-46 and CP-465,022 protect axons following GD	147
Figure 4.21. Addition of QNZ-46 and CP-465,022 attenuates the axonal injury score during the reperfusion	148
Figure 4.22. Combination therapy with QNZ-46 and CP-465,022 maintains electrical excitability during GD I	149
Figure 4.23. Combination therapy with QNZ-46 and CP-465,022 maintains axonal conduction integrity during GD II.	150

Chapter 5: Nitric oxide and aglycaemia induced axonal Injury

Figure 5.1. Potential protective mechanisms of NO during brain injury	157
Figure 5.1. Potential destructive mechanisms of NO during brain injury	158
Figure 5.3. Changes in the fluorescence response in rat hippocampal slices with elevation in NO during GD	163
Figure 5.4. Localisation of the ROI to monitor changes in fluorescence of NO-sensitive dyes during GD	168
Figure 5.5. Dose-dependent conduction block with addition of DETA NONOate	171
Figure 5.6. CAP recording following addition of DETA NONOate	172
Figure 5.7. Live imaging of YFP axons following application of DETA NONOate	172
Figure 5.8. Sequential images of callosal slices during prolonged exposure to DETA NONOate	173
Figure 5.9. Axonal injury score in slices exposed to DETA NONOate for 2 and 3 hrs against control slices held in aCSF	173
Figure 5.10. Brain slice from a CD-1 mouse loaded with 10µM DAF-FM DA or 10µM DAR-4M AM	174
Figure 5.11. Low magnification view of callosal slice from a YFP mouse after incubation in 10µM DAR-4M AM	175
Figure 5.12. High magnification view of callosal slice from a YFP mouse	

	after incubation in 10 μ M DAR-4M AM	176
Figure 5.13.	High magnification view of callosal slice from a CD-1 mouse after incubation in 10 μ M DAF-FM DA	177
Figure 5.14	High magnification view of callosal slice from a CD-1 mouse after incubation in 10 μ M DAF-FM DA supplemented with 10 μ M Nile Red	178
Figure 5.14.	Sequential time frames show a side-by-side comparison of the change in signal intensity over time in DAR-4M AM and DAF-FM DA loaded slices that were perfused for 2 hr in glucose containing aCSF	179
Figure 5.15.	Side-by-side comparison of the percentage change in signal intensity from the start of the recording period in DAR-4M AM and DAF-FM DA pre-treated slices kept for 2 hr in glucose containing aCSF	180
Figure 5.16.	Signal intensity in slice loaded with DAR-4M AM and exposed to 45 min GD and 1 hr reperfusion	181
Figure 5.17.	Side-by-side comparison of the change in signal intensity over time in DAR-4M AM control slices against those slices there were exposed to GD	182
Figure 5.18.	Sequential images of a YFP slice treated with L-NAME and exposed to 45 min of GD followed by 2 hr of reperfusion	183
Figure 5.19.	Axonal injury score in YFP slices exposed to GD (+/-) L-NAME and controls	184
Figure 5.20.	CAP recording from slices exposed to GD (+/-) L-NAME and controls	185
Figure 5.21.	Percentage CAP recovery from slices exposed to GD (+/-) L-NAME and controls	185

Chapter 6: Conclusion

Figure 6.1.	The proposed protective mechanisms mediated by QNZ-46 and CP-465,022 to counteract aglycaemic axonal injury	195
Figure 6.2.	A hypothetical schematic showing how QNZ-46 suppresses NO formation following GD	199

Supplementary material

Figure 8.1.	Representative image showing the site of insertion of the microdialysis probe	244
Figure 8.2.	Sequential images of YFP axons exposed to 30 min GD in DMSO	245
Figure 8.3.	Sequential images of slices exposed to 45 min GD (+/-) and controls	246
Figure 8.4.	Percentage CAP recovery in slices exposed to 45 min GD and controls (+/-) the vehicle	247
Figure 8.5.	Percentage change in signal intensity in slices incubated in DAF-FM DA and exposed to 45 min of GD and controls	251

List of Tables

Chapter 1: The Pathophysiology and Clinical Picture of Hypoglycaemia

Table 1.1. Causes of hypoglycaemia	3
Table 1.2. The common and less common risk factors for hypoglycaemia	4

Chapter 2: Characterisation of the structural and functional injury to white matter axons during aglycaemia

Table 2.1. Surgical dissection tools	24
Table 2.2. Chemical composition of the cutting solution	25
Table 2.3. Chemical composition of the aCSF	26
Table 2.4. Primary and secondary antibodies	41
Table 2.5. Injury score of callosal slices exposed to variable lengths of GD in comparison to controls	60
Table 2.6. Parameters used for recording CAP from corpus callosum in brain slice in comparison to the optic nerve	69

Chapter 3: Energy metabolism of white matter during aglycaemia

Table 3.1. List of drugs used to study the potential role of lactate as an energy substrate during GD	99
Table 3.2. The experimental paradigms employed to study the potential role of astrocytic lactate during GD	101
Table 3.3. Injury score of callosal axons exposed to 30 min of GD (+/-) 4-CIN and controls	106
Table 3.4. Injury score of callosal axons exposed to 45 min of GD (+/-) clenbuterol and controls	108
Table 3.5. Injury score of callosal axons exposed to 45 min of GD (+/-) clenbuterol + 4-CIN and controls	110

Chapter 4: The central role of excitotoxicity to white mater following aglycaemia

Table 4.1. Comparison of the axonal injury scores at different experimental time-points between different experimental protocols	146
Table 4.2. One-way ANOVA followed by Tukey's post hoc test for multiple comparisons between groups	146

Chapter 5: Nitric oxide and aglycaemia induced axonal Injury

Table 5.1. Comparison between the properties of DAF-FM DA and DAR-4M AM	165
Table 5.2. Excitation and emission wavelengths employed for the detection of DAF-FM DA and DAR-4M AM under two-photon microscopy	166

Supplementary material

Table 8.1. Percentage change from start in the signal intensity of DAR-4M AM at different experimental time points	248
Table 8.2. Percentage change from start in the signal intensity of DAF-FM DA at different experimental time points	248

List of Abbreviations

4-CIN	α -Cyano-4-hydroxycinnamic acid
aCSF	artificial cerebrospinal fluid
AMPA	α -amino-3-hydroxy-5-methyl-4-isoxazolepropionic acid
ANLSH	astrocyte-neuron lactate shuttle hypothesis
ATP	adenosine triphosphate
AUC	basal area under the curve
β -APP	β -Amyloid Precursor Protein
BP	band pass
CAP	compound action potential
CNS	central nervous system
coA	coenzyme A
CP-465,022	3-(2-Chlorophenyl)-2-[2-[6-[(diethylamino)methyl]-2-pyridinyl]ethenyl]-6-fluoro-4(3H)-quinazolinone hydrochloride
DAF	diaminofluorescein
DAFCs	diaminoaromatic fluorescent compounds
DAF-FM DA	diaminofluorescein-FM diacetate
DAQ	diaminoanthraquinone
DAR	diaminorhodamine
DAR-4M AM	diaminorhodamine-4M-AM
DETA NONOate	2,2'-(2-Hydroxy-2-nitrosohydrazinylidene)bis-ethanamine
DMSO	dimethyl sulfoxide
EAAT	excitatory amino acid transporter
EGFP	enhanced green fluorescent protein
EM	electron microscopy
eNOS	endothelial NOS
FADH	flavin adenine dinucleotide
FRET	fluorescence resonance energy transfer
GA3P	glyceraldehyde 3-phosphate
GCS	glasgow coma scale
GD	glucose deprivation
GLAST	glutamate aspartate transporter
GLT1	glutamate transporter 1
glucose-6P	glucose-6-phosphate
GLUT	glucose transporter
HbA1c	haemoglobin A1c
HK	hexokinase
ICP	intracranial pressure
IP	intraperitoneal injecting
IR	infra-red
LDH	lactate dehydrogenase
LM	light microscopy
L-NAME	N ^G -Nitro-L-arginine methyl ester
MCTs	monocarboxylate transporters

MK-801	5R, 10S)-(+)-5-methyl-10,11-dihydro-5H-dibenzo[a,d]cyclohepten-5,10-imine
MRI	magnetic resonance imaging
NADH	nicotinamide adenine dinucleotide
NMDA	n-methyl-D-aspartate
nNOS	neuronal NOS
NO	nitric oxide
NOS	nitric oxide synthase
O ²⁻	superoxide
OGD	oxygen and glucose deprivation
OHAs	oral hypoglycaemic agents
ONOO-	peroxynitrite
PBS	phosphate buffer solution
PCP	phencyclidine
PPP	pentose-phosphate shunt pathway
PSD-95	postsynaptic density-95
QNZ-46	4-[6-Methoxy-2-[(1E)-2-(3-nitrophenyl)ethenyl]-4-oxo-3(4H)quinazoliny]]benzoic acid
RNS	reactive nitrogen species
ROI	regions of interest
ROS	reactive oxygen species
RT	room temperature
SNAP	S-Nitroso-N-acetylpenicillamine
SNP	sodium nitroprusside
T1DM	type 1 diabetes mellitus
T2DM	type 2 diabetes mellitus
TBAO	DL- <i>threo</i> -β-Benzyloxyaspartic acid
TBI	traumatic brain injury
TCA	tricarboxylic acid
TRPA1	transient receptor potential A1 channel
VGCC	voltage-gated calcium channels
YFP	yellow fluorescent protein

Chapter 1

The pathophysiology and clinical picture of hypoglycaemia

Hypoglycaemia is a common finding in both daily clinical practice and acute care settings. There are multiple causes of hypoglycaemia and these are predominantly multifactorial. The European Medicines Agency and the American Diabetes Association define hypoglycaemia as “*any abnormally low plasma glucose concentration that exposes the subject to potential harm*” with a proposed threshold plasma glucose value <3.9 mmol/L (<70 mg/dL) (Workgroup on Hypoglycaemia and American Diabetes Association, 2005; European Medicine agency, 2012). Current diabetic guidelines insist to aim at lower levels of Haemoglobin A1c (HbA1c) to limit the complications associated with diabetes. However, this is resulting in more frequent episodes of hypoglycaemia amongst diabetic patients. Acute and recurrent episodes of hypoglycaemia pose a huge burden on the effected individual and society in general. Patients suffering from hypoglycaemia are at risk of cardiological, pulmonary, metabolic and neurological complications and severe hypoglycaemia is often fatal with huge financial burden in terms of direct and indirect medical care (Leese *et al.*, 2003; Lundkvist *et al.*, 2005; Jonsson *et al.*, 2006; Allicar *et al.*, 2000; Holstein *et al.*, 2002).

Hypoglycaemia can be classified as mild, moderate and severe. Mild hypoglycaemia refers to plasma glucose levels between 3.1 – 3.9 mmol/L and is associated with mild autonomic symptoms. Such patients are still aware of their surroundings and can self-reverse the condition by supplementing their sugar intake. Moderate hypoglycaemia refers to plasma glucose levels between 2.2 –3.1 mmol/L and is associated with the activation of the sympathetic nervous system (trembling, palpitations, sweating, anxiety, hunger, nausea and tingling) and a number of neuroglycopenic symptoms (difficulty concentrating, confusion, weakness, drowsiness, vision changes, difficulty speaking, headache, dizziness and tiredness). Patients are still conscious, and therefore able to self-treat. Severe hypoglycaemia refers to plasma glucose level below 1.9 mmol/L. In most cases, such individuals lose consciousness and are unable to self-reverse the situation (Kalra *et al.*, 2013).

1.1 Incidence and prevalence of hypoglycaemia

Patients suffering from type 1 diabetes mellitus (T1DM) treated with insulin are the most likely cohort to suffer from hypoglycaemia (UK Hypoglycaemia Study Group, 2007; Akram *et al.*, 2006; Leese *et al.*, 2003). In fact, such individuals may suffer up to two episodes of hypoglycaemia per week (Cryer *et al.*, 2003). Evidence from several studies suggests that severe hypoglycaemia occurs in 35-42% of T1DM patients and its rate is between 90-130 episodes/100 patient years (Pedersen-Bjergaard *et al.*, 2004; Pramming *et al.*, 1991; ter Braak *et al.*, 2000; Zammitt *et al.*, 2007). This incidence increases in patients with a longer history of diabetes, and who have been on insulin treatment for a long time (UK Hypoglycaemia Study Group, 2007). The current drive to lower the HbA1c level in diabetic patients, albeit having numerous advantages, doubles the risk of severe hypoglycaemia (Control group *et al.*, 2009; ADVANCE control group *et al.*, 2008; Kim *et al.*, 2011).

Type 2 diabetes mellitus (T2DM) patients are prone to develop hypoglycaemia but to a lesser extent. A retrospective questionnaire-based study reported at least one episode of severe hypoglycaemia in 16.5% of T2DM patients with an incidence of 44 episodes/100 patient years (Akram *et al.*, 2006).

Diabetic patients on treatment are at risk of both hyper- and hypo-glycaemia. Factors that increase the risk of developing hypoglycaemia include: infections (Lin *et al.*, 2010), exercise in insulin treated patients (Tsalikian *et al.*, 2005), and alcohol especially in patients on oral hypoglycaemic agents (OHAs) (Huang and Sjöholm, 2008). People on multiple medications are subject to drug interactions that can result in hypoglycaemia (Shorr *et al.*, 1997). Similarly, chronic renal insufficiency, which is common in diabetic patients may result in accumulation of drug metabolites, which in turn can lead to hypoglycaemia (Holstein *et al.*, 2003; Neumiller *et al.*, 2009).

Hypoglycaemia is also a common cause for Emergency Department admissions. Almost 10% of patients presenting with an altered mental state suffer from hypoglycaemia. Around 20% of diabetic patients treated either with insulin or OHAs require Emergency Department assessment and treatment (Diabetes Control and Complications Trial Research Group *et al.*, 1993).

A number of medications other than OHAs have been reported to lower the blood glucose level. Gatifloxacin, quinine and disopyramide may inhibit the pancreatic β -cell adenosine triphosphate (ATP) sensitive potassium channels thus stimulating insulin release (Negishi *et al.*, 2009; Saraya *et al.*, 2004). Quinolones have been reported to increase the level of insulin and c-peptide, resulting in severe hypoglycaemia, especially in patients already on sulphonyureas (Kelesidis and Canseco, 2009, 2010).

Hypoglycaemia is not limited to diabetics. It is an important and common adverse clinical event in a number of other clinical conditions (Agardh and Rosen, 1983; Arky, 1989; Davis and Jones, 1998; Lincoln *et al.*, 1996). Certain malignancies, such as non-islet cell tumours, hepatocellular carcinomas, and haematological malignancies can all present this complication (Sorlini *et al.*, 2010; Lau *et al.*, 2010; Keller *et al.*, 2010; Diaz *et al.*, 2010). Other occurrences associated with increased risk of hypoglycaemia include critically ill patients, patients on mechanical ventilation, and patients on prolonged intensive care stay (Arabi *et al.*, 2009). The most common causes of hypoglycaemia are summarised in Table 1.1.

Cause	Examples
Incorrect Insulin administration	Insulin taken in excess or at the wrong time relative to food intake and/or physical activity; incorrect type of insulin that is administered
Insufficient exogenous carbohydrate	Delayed or missed meals or fasting overnight
Decreased endogenous glucose production	Excess alcohol consumption
Increased utilisation of carbohydrate/depletion of hepatic glycogen stores	Exercise or weight loss
Increased insulin sensitivity	During the night; exercise; weight loss
Delayed gastric emptying	Conditions such as gastroparesis
Decreased insulin clearance	Conditions such as progressive renal failure

Table 1.1. Causes of hypoglycaemia (adapted from Kedia, 2011).

The risk factors for individuals to develop hypoglycaemia are summarised in Table 1.2

Common Risk Factors	<ul style="list-style-type: none"> ▪ Strict glycaemic control ▪ Mismatch of insulin timing, amount, or type of carbohydrate intake ▪ History of severe hypoglycaemia ▪ Sleep/general anaesthesia that place patient in an altered state of consciousness ▪ Duration of diabetes and age ▪ Reduction of oral intake/New non-per oral status ▪ Impaired awareness of hypoglycaemia ▪ Angiotensin-converting enzyme genotype/C-peptide negativity ▪ Critical illness (hepatic, cardiac, and renal failure; sepsis; severe trauma) ▪ Unexpected travel after injection of rapid- or fast-acting insulin
Less common risk factors	<ul style="list-style-type: none"> ▪ Endocrine deficiencies (cortisol, growth hormone, or both) ▪ Non-β-cell tumour ▪ Sudden reduction in corticosteroid dosage ▪ Pathological conditions such as emesis/vomiting ▪ Reduced rate of intravenous dextrose administration ▪ Unexpected interruption of enteral feedings or parenteral nutrition ▪ Drug dispensing error

Table 1.2. The common and less common risk factors for hypoglycaemia (adapted from Kalra *et al.*, 2013).

1.2 General complications associated with hypoglycaemia

1.2.1 Cardiovascular

Patients suffering from an acute coronary syndrome are likely to develop hyperglycaemia, which in turn increases the risk of morbidity and mortality (Falciglia *et al.*, 2009). However, patients who suffer from episodes of hypoglycaemia were reported to have a higher mortality rate following myocardial infarction (Pan *et al.*, 1986). Lowering plasma glucose levels results in activation of the sympathetic nervous system, which in turn increases the cardiac workload. This can be dangerous especially in the elderly who suffer from coronary artery disease, since this can restrict coronary arterial flow resulting in myocardial ischaemia (Sommerfield *et al.*, 2007).

Acute and chronic hypoglycaemia increase the risk of thrombus formation by activating prothrombotic, proinflammatory, and pro-atherogenic mechanisms such as plasminogen activator inhibitor, vascular endothelial growth factor, interleukin-1,6,8, C-reactive protein, tumour necrosis factor α and endothelin (Gogitidze Joy *et al.*, 2010; Razavi Nematollahi *et al.*, 2009; Del Rey *et al.*, 2006). Nocturnal hypoglycaemia has been reported to be associated with prolonged QTC interval and cardiac rate/rhythm disturbances in ambulant patients with T1DM (Feldman-Billard *et al.*, 2010). The prolonged QTC interval can even lead to ventricular tachyarrhythmia which can be fatal (Gill *et al.*, 2009).

Diabetic patients are at risk of sudden cardiac death due to silent myocardial ischaemia, autonomic nervous system dysfunction, abnormal cardiac repolarisation, hypoglycaemia, hypercoagulable state, diabetic cardiomyopathy and impaired respiratory response to hypoxia and hypercapnia (Bergner *et al.*, 2010). Approximately 2 – 4 % of such deaths have been attributed to hypoglycaemia (Laing *et al.*, 1999).

1.2.2 Critical Care Medicine

In critical care medicine, moderate hypoglycaemia is often associated with increased morbidity and mortality. In an intensive treatment setting, tight glycaemic control is mandatory. However, this often leads to episodes of hypoglycaemia in patients not on parenteral nutrition, which leads to a higher risk in mortality in effected individuals (Marik and Preiser, 2010; Ichai and Preiser, 2010).

Pulmonary oedema is a common occurrence in patients under intensive care. Amongst the myriad aetiologies for pulmonary oedema, one also finds severe hypoglycaemia. Hypoglycaemia induces the activation of the sympathetic nervous system, which in turn alters the vascular haemodynamic status of the patient: it disrupts the pulmonary capillary endothelium, thus increasing its permeability, and disrupts the alveolar epithelium (Margulescu *et al.*, 2008; Mishriki *et al.*, 2004; Uchida *et al.*, 2004).

1.2.3 Metabolic

Recurrent episodes of iatrogenic induced hypoglycaemia can lead to hypoglycaemia associated autonomic failure, which affects mostly patients with T1DM (Cryer *et al.*, 2004). This autonomic failure results in a decreased sympathetic response to hypoglycaemia, which in turn reduces the counter-regulatory hormonal responses, and impairs the awareness of hypoglycaemia (Geddes *et al.*, 2008).

Hypoglycaemia can also lead to electrolyte imbalances, namely hyponatraemia, hypokalaemia, hypophosphatemia, and hypomagnesemia (Tofade *et al.*, 2004; Matsumura *et al.*, 2000).

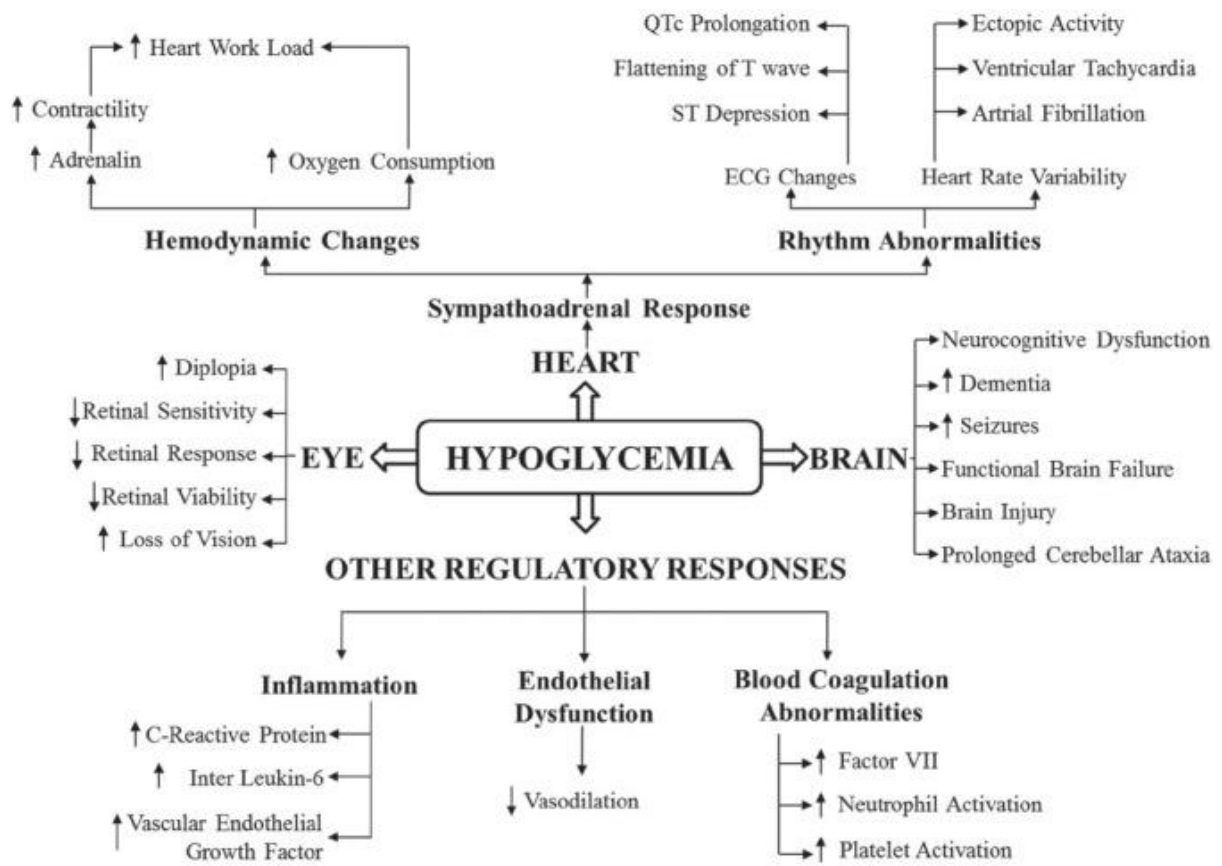


Figure 1.1. Summary of the physiological impact of hypoglycaemia on different body systems (reproduced from Kalra *et al.*, 2013).

1.3 Neurological complications associated with hypoglycaemia

There is substantial evidence that hypoglycaemia alters human behaviour, and recurrent episodes of severe hypoglycaemia may lead to memory loss or impaired cognitive function (Richardson, 1990; Biessels *et al.*, 1994; Hershey *et al.*, 1999). Hypoglycaemia induces a number of diverse neurologic symptoms, which may range from focal neurologic deficits to permanent dysfunction or even death (Böttcher *et al.*, 2005; Finelli 2001; Shirayama *et al.*, 2004). Hypoglycaemia often accompanies profound memory loss, transient motor deficits and a persistent vegetative state and death in 2-4% of cases (Albayram *et al.*, 2006). Both acute hypoglycaemic encephalopathy (Auer, 2004) and recurrent episodes of hypoglycaemia (Hyllienmark, 2005) disrupt the electrocortical activity. Severe hypoglycaemia may aggravate the severity of the neurocognitive dysfunction in patients with diabetes (Chugani, 1998). The elderly are more susceptible to develop hypoglycaemia, and recurrent episodes often leads to instances of increased risk of dementia (Whitmer *et al.*, 2009), functional brain failure (Cryer, 2007) and cerebellar ataxia (Berz and Orlander, 2008).

Severe hypoglycaemia can lead to acute and chronic effects on cognition, with memory function being particularly vulnerable (Hershey *et al.*, 2005; Blasetti *et al.*, 2011). Anterograde amnesia, the inability to form new memories of events, has been reported following severe hypoglycaemia in T1DM (Chalmers *et al.*, 1991; Boeve *et al.*, 1995; Holemans *et al.*, 2001). Anterograde amnesia has also been reported following lesions to the isthmus of the cingulate (Maeshima *et al.*, 2001), suggesting that this region could also play a role in hypoglycaemia-induced memory impairment.

During hypoglycaemia, decreased glucose availability may be associated with altered brain function, including changes in electrical activity, increased cerebral blood flow, increased levels of intracellular Ca^{2+} , and changes in the release of various neurotransmitters, especially glutamate (Uematsu *et al.*, 1989; Nuñez *et al.*, 2000; Ghajar *et al.*, 1982).

Neuroimaging studies of patients with brain damage resulting from hypoglycaemia showed significant alterations, involving both cortical and underlying white matter (Barkovich *et al.*, 1998; Kinnala *et al.*, 1999). Magnetic resonance imaging (MRI) scans administered within hours of severe hypoglycaemia have revealed abnormal signals in the hippocampus

(Chalmers *et al.*, 1991; Boeve *et al.*, 1995; Holemans *et al.*, 2001), thalamus (Cho *et al.*, 2006), basal ganglia (Jung *et al.*, 2005), cortical grey matter (Chalmers *et al.*, 1991; Boeve *et al.*, 1995; Aoki *et al.*, 2004), splenium (Kim *et al.*, 2007; Taguchi *et al.*, 2011), internal capsule (Taguchi *et al.*, 2011), centrum semiovale (Cho *et al.*, 2006) and corona radiata (Aoki *et al.*, 2004). In a particular case study, Kirchoff *et al.*, (2013), reported that hypoglycaemia can be associated with shrinkage in subcortical grey matter volume, with the hippocampus, thalamus and globus pallidus being amongst the brain regions most susceptible to hypoglycaemic injury. The same study also reported that white matter surrounding the ventricles and in posterior brain regions, such as the splenium, isthmus of the cingulate and cerebellum, may also be susceptible to permanent injury from severe hypoglycaemia. Even though most MRI reports on hypoglycaemic coma typically describe lesions involving cerebral cortex, basal ganglia, and hippocampus (Fujioka *et al.*, 1997), Kim and Koh (2007) reported that recurrent hypoglycaemia can also result in acute leukoencephalopathy (Fig 1.2).

Clinical experience and experimental studies show that hypoglycaemia causes damage to both white and grey matter tissue (Auer, 1986; Siesjö, 1988). Widespread neuronal necrosis in grey matter areas and sub cortical white matter was reported in a rat model of insulin-induced hypoglycaemia (Auer *et al.*, 1984). A conspicuous feature of hypoglycaemic brain damage in the rat was the neuronal necrosis typically found in the dentate gyrus. The likelihood vulnerability of this structure is due to the high density of neurons with N-methyl-D-aspartate (NMDA) receptors in the molecular layer and which lie in close proximity (Auer *et al.*, 1985). A similar pattern of necrosis is often seen in human cases of hypoglycaemic brain damage (Auer *et al.*, 1989). In cross-sectional research in adolescents and adults, some studies have not found significant alterations in brain structure associated with severe hypoglycaemia (Ferguson *et al.*, 2003; Kodl *et al.*, 2008). Others have reported reductions in grey matter volume in the left posterior cerebellum (Musen *et al.*, 2006), the thalamus (Northan *et al.*, 2009) and uncus (Musen *et al.*, 2006) bilaterally.

Post-mortem examination in patients who died after a history of hypoglycaemia revealed diffuse, multi-focal distribution of β -APP immunopositive axons with axonal swellings and bulbs scattered throughout the white matter including the brain stem (Graham *et al.*, 2004).

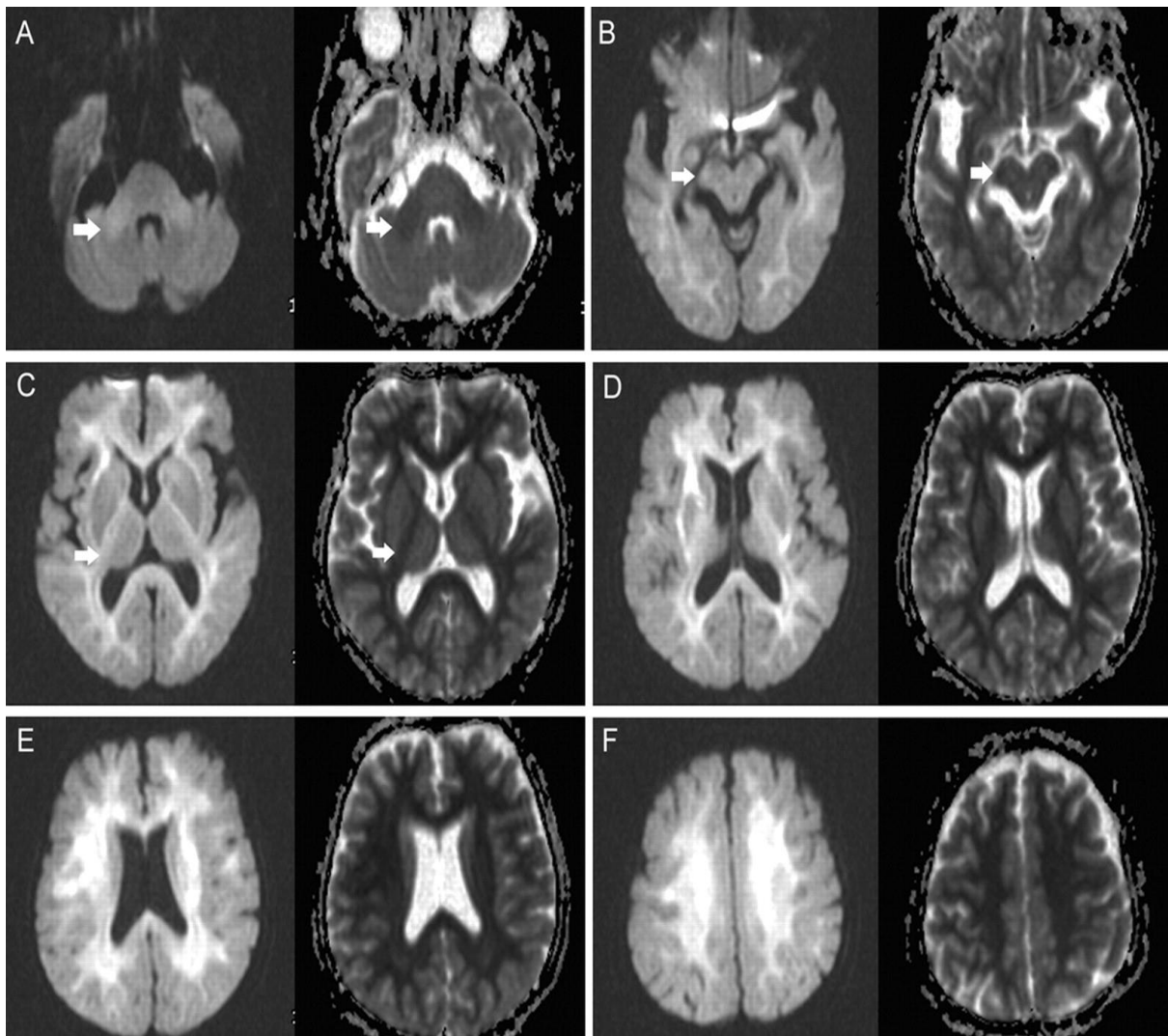


Figure 1.2. Diffusion-weighted MR images and the corresponding apparent diffusion coefficient maps (A through F). Areas of restricted diffusion are evident in the middle cerebellar peduncle (A, white arrows), cerebral peduncle (B, white arrows), and internal capsule (C, white arrows). The periventricular and subcortical white matter are also affected extensively (C through F) (reproduced from Kim and Koh, 2007).

Hypoglycaemia is also important in traumatic brain injury. Recovery following traumatic brain injury is largely based on factors including: the severity of the initial injury, Glasgow Coma Scale (GCS) score, pupillary response, age, and presence of additional physiological derangements. However, secondary insults occur after the initial traumatic event, as is the case with hypoglycaemia. Gupta *et al.*, (2016) reported that hypoglycaemia following traumatic brain injury is an important prognostic factor of outcome. In this study, patients who suffered from episodes of hypoglycaemia following TBI fared poorly on the GCS after examination 3 months post-injury.

Hypoglycaemia induced brain injury is not limited to the adult brain. Neonatal hypoglycaemia is a common complication among preterm infants, small-for-gestational-age infants, and infants of diabetic mothers (Su and Wang, 2012). If improperly treated, infants who had suffered hypoglycaemia may later develop permanent neurological dysfunction, namely neonatal hypoglycaemic encephalopathy (Lou *et al.*, 2010). The latter results in injury to both the cerebral cortex and the subcortical white matter (Anderson *et al.*, 1967; Banker, 1967; Kalimo *et al.*, 1985; Barkovich *et al.*, 1998; Murakmi *et al.*, 1999; Volpe, 2001; Caraballo *et al.*, 2004; Filan *et al.*, 2006; Yalnizoglu *et al.*, 2007). Moreover, persistent or recurrent neonatal hypoglycaemia may lead to other complications, such as: long-term visual disturbance, hearing impairment, cognitive abnormalities, secondary epilepsy, and other disorders of the central nervous system (CNS) (Yue *et al.*, 2006). Children with diabetes who suffered recurrent severe hypoglycaemic episodes were reported to have lower overall cognitive scores than those without a history of severe hypoglycaemia (Åsvold *et al.*, 2010).

Infants suffering from persistent hyperinsulinemic hypoglycaemia develop severe neural damage [Mennni *et al.*, 2001], since it is believed that isolated hypoglycaemia without other any contributing factors enhances hypoxic-ischaemic brain injury [Volpe, 2001]. A similar principle was reported by Dave and his colleagues. They reported that recurrent episodes of hypoglycaemia exacerbated ischaemic injury both in rodent hippocampal slices exposed to oxygen and glucose deprivation (OGD) (Dave *et al.*, 2011a) and in streptozotocin-induced diabetic rats (Dave *et al.*, 2011b).

Chapter 2

Characterisation of the structural and functional injury to white matter axons during glucose deprivation

2.1 Aims

This chapter aims to explore the various experimental methods and approaches to investigate both the structural and functional alterations to white matter secondary to glucose deprivation. The main aims of this chapter are:

- i. To show how the use of YFP-expressing transgenic mice can be a useful tool to monitor and therefore characterise the evolving structural injury occurring in axons under live two-photon microscopy.
- ii. To compare the observed changes in YFP-expressing axons to results obtained from other morphometry, like light and electron microscopy and immunocytochemical labelling of axonal neurofilaments.
- iii. To characterise the histopathological hallmarks of oligodendrocytes injury following GD.
- iv. To establish a reproducible protocol to study axonal conduction and dysfunction in two models of central white matter tracts.
- v. To determine the duration of glucose deprivation that is required to result in irreversible loss of axonal structure and function.

2.2 Literature Review

2.2.1 The study of white matter injury

The two main components of the brain are grey and white matter. Grey matter consists of neuronal cell bodies and glia, whilst white matter is made up of axons and glia. White matter of the mammalian central nervous system (CNS) consists of the afferent and efferent axonal tracts that interconnect cortical and neuronal cell body-containing nuclear areas of the brain and spinal cord. White matter contains no neuronal cell bodies or synapses. It consists of tightly packed glial cells and myelinated and unmyelinated axons; the presence of myelin lends a white appearance to this tissue. White matter regions vary widely regarding the ratio of myelinated to unmyelinated axons; for example, all the axons of the optic nerve are myelinated, but only about 30% of those in the corpus callosum are myelinated. The anatomy and physiology of myelinated axons are highly specialised and unique compared with those of unmyelinated axons. It is not surprising, therefore, that regional differences have been noted in the pathophysiology of white matter injury.

Historically, most of the neuroscientific research has been directed to elucidate the pathophysiology of grey matter injury, as studies had shown that grey matter is much more vulnerable to injury (Marcoux *et al.*, 1982). One of the main reasons is that most of the work was done on rodent models, wherein white matter constitutes only 13% of the total brain volume, when compared to 50% in humans (Zhang and Sejnowski, 2000). However, stroke affect similar proportions of grey and white matter (Goldberg and Ransom, 2003). Conditions such as dementia and difficulties with executive functioning and processing are associated with changes in white matter (Malloy *et al.*, 2007), whilst other pathologies, such as demyelinating and myelinating disorders directly affect white matter tracts.

To study white matter pathology, one must consider that the white matter in the CNS is not just axonal fibres, but a synergistic relationship between axons and glial cells. This represents the main drawback in the use of cell cultures to study white matter injury. With such an approach, the cell-cell 3D-interactions of all the various components are excluded. The three

main models used extensively in the literature to study CNS white matter physiology and pathology that conveniently circumvent this problem include: the optic nerve, the dorsal column preparation and the corpus callosum derived from coronal brain slices.

The optic nerve is a typical CNS white matter tract, made up of axons, astrocytes, oligodendrocytes, NG2 glial cells and microglia (Butt *et al.*, 2004). Its morphology, electrophysiology, and glial differentiation have been well characterised (Butt and Ransom 1993; Raff and Miller 1984). It is also a suitable model to study axon-glial interaction (Ransom and Orkand, 1996). It has been shown that there exists a good homology between the human and rodent subunit expression of the functional glutamate receptors in this preparation (Talos *et al.*, 2006a, b), enabling researchers to relate with accuracy the pattern of injury observed in mice and safely extrapolate these to humans.

The brain slice preparation was pioneered by Henry McIlwain in the 1950s to study the biochemical properties of brain tissue (McIlwain *et al.*, 1951; Yamamoto and McIlwain, 1966; Collingridge, 1995). It is a widely accepted model for investigating the mechanisms underlying neuronal damage because it maintains the *in vivo* anatomical microenvironment without the confounding factors such as the blood–brain barrier and anaesthesia. For this reason, drug penetration and pharmacological testing is very straightforward and permissive. It has been used extensively for immunohistochemistry, electrophysiological studies, and to characterise properties of individual neurons and glial cells (Colbert, 2006; Buskila *et al.*, 2007; Buskila and Amitai, 2007; Khurana and Li, 2013).

The development of appropriate experimental models of white matter injury is therefore essential to understand its progressive nature and to develop novel therapeutics that can ameliorate its devastating clinical consequences.

2.2.2 The use of YFP-expressing mice to study white matter injury

The use of transgenic and knockout technologies makes the mouse brain an ideal candidate to study the cellular and biochemical processes underlying white matter (Emery, 2010). To aid in visualising axon morphology, transgenic mice with neuron-specific expression of the yellow fluorescent protein (YFP), under control of the *thy1* promoter were developed (Feng *et al.*, 2000). The mouse transgenic Line H express YFP in a subset of cortical neurons that project axons across the corpus callosum, thus enabling study of central white matter pathology. YFP is localised in neuronal cytoplasm, and thus intrinsic morphological changes in the axoplasm due to various insults can be visualised in labelled axons by fluorescence microscopy techniques (Brendza *et al.*, 2003; Gillingwater *et al.*, 2002). Importantly, it has been shown that expression of YFP in neurons results in no apparent toxic effects (Feng *et al.*, 2000).

This mouse line has been extensively used in literature to study central white matter pathology both *in vitro* and *in vivo* and the morphological changes that occur have been well characterised. Hypoxic injury was studied on isolated YFP axons (Underhill and Goldberg, 2007). Wallerian degeneration was observed in YFP tibial nerves following sciatic nerve axotomy (Beirowski *et al.*, 2004). Axonal degeneration and regeneration were also studied using YFP-expressing spinal cord axons following traumatic injury (Bareyre *et al.*, 2005; Kerschensteiner *et al.*, 2005; Carter *et al.*, 2008). YFP-expressing callosal axons were used to study traumatic brain injury (Greer *et al.* 2011; Marion *et al.*, 2018), Wallerian degeneration (Beirowski *et al.*, 2004) and ischaemic injury (McCarran and Goldberg, 2007; Alix *et al.*, 2012; Laureys *et al.* 2014; Doyle *et al.*, 2018). McCarran and Goldberg (2007) reported that ischaemia induced injury to YFP-expressing callosal axons is a sensitive marker of injury and is comparable to the loss in classical neurofilament labelling (Fig 2.1). The same authors also developed a scoring injury scale based on a set of progressive structural changes occurring to injured axons and which was adapted in this thesis.

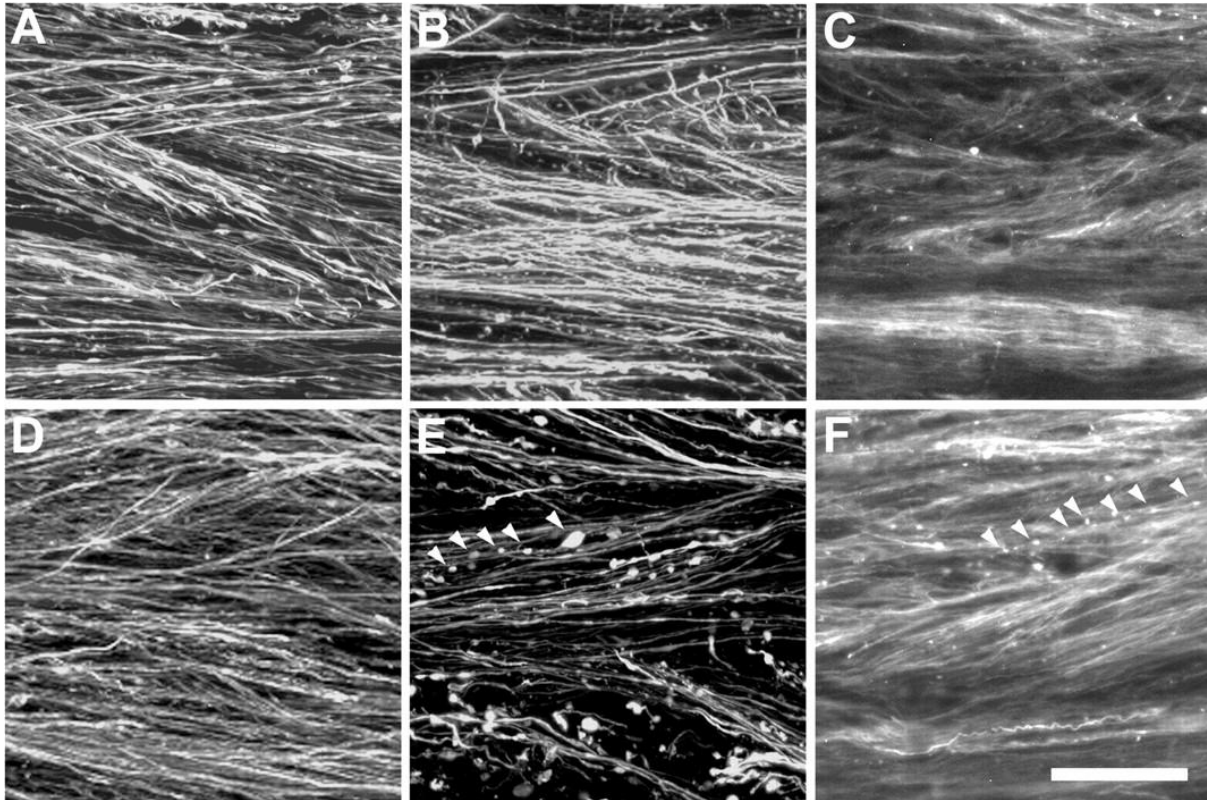


Figure 2.1. Ischaemia causes extensive axonal injury as seen by morphologic changes occurring in YFP-expressing axons. YFP-expressing callosal axons at the start of the experiment (A and B), after 9 hours of perfusion in control slices (D), after 1 hour of OGD followed by 9 hours of reperfusion (E). SMI-31 strongly labels intact callosal axons during normoxia (C), after 1-hour OGD followed by 9 hours of reperfusion (F). Severe axon beading and fragmentation, demarcating injury, are clearly visible in YFP- and SMI-31-labeled axons (arrowheads). Scale bar, 25 μm . (Reproduced from McCarran and Goldberg, 2007)

2.2.3 Electrophysiology as a useful tool to study axonal injury

Electrophysiology is a very important tool to study action potential conduction and speed in white matter tracts. For this reason, it is a very important tool that enables the study of the functional integrity of axons in normal physiology and in disease. This experimental method is based on the principle that electrical activity propagates along intact axonal fibres (Baker *et al.*, 1987; Bostock and Grafe, 1985; Carley and Raymond, 1987; Fulton and Walton, 1986). This process consumes most of the energy required by axons (Ames, 2000) and is therefore affected by disruptions in the supply of energy. Recording the electrophysiological activity of axonal bundles under normal and altered metabolic states, can therefore be used to shed light on how substrate availability affects conduction speed and electrical activity in neurometabolic disorders.

Conduction in isolated nerves is studied by using two electrodes: an electrode to stimulate one end of the nerve, with the other placed at the opposite end that records the evoked change in electrical response. This method of extracellular recording monitors all the axons in the nerve, and the evoked response is called the CAP. According to Stys and colleagues, the CAP is the summation of all the individual action potentials in the axons comprising the nerve bundle (Stys *et al.*, 1991). The larger the number of healthy axonal fibres, the larger is the evoked response. Following an insult, a variable decrease in action potential propagation is expected and this invariably leads to a decrease in CAP. Therefore, monitoring the CAP before, during and after an insult provides a reliable and quantitative measure that corresponds to axonal functional integrity. The mouse optic nerve contains around 24,000 axons (Allen *et al.*, 2006) and during adulthood the optic nerve is fully myelinated (Foster *et al.*, 1982). Although in humans, the optic nerve is regarded to be a peripheral nerve (cranial nerve II), it is actually an extension of the diencephalon, and therefore it is frequently used as a model to study central white matter pathology. To study nerve conduction across the optic nerve, suction electrodes are typically used (Kocsis *et al.*, 1986; Stys *et al.*, 1990; Ransom and Fern, 1997; Stys *et al.*, 1992a, b; Brown *et al.*, 2003; Meakin *et al.*, 2007), and were reviewed in detail by Stys *et al.*, (1990). Briefly, each end of the optic nerve is snugly fit into glass capillaries filled with artificial cerebrospinal fluid (aCSF) after applying suction at the capillary free end. One capillary is connected to a stimulus generator, and the other to an amplifier. Stimulating one end of the nerve causes the impulse to propagate across the optic nerve, to be picked up by the recording electrode.

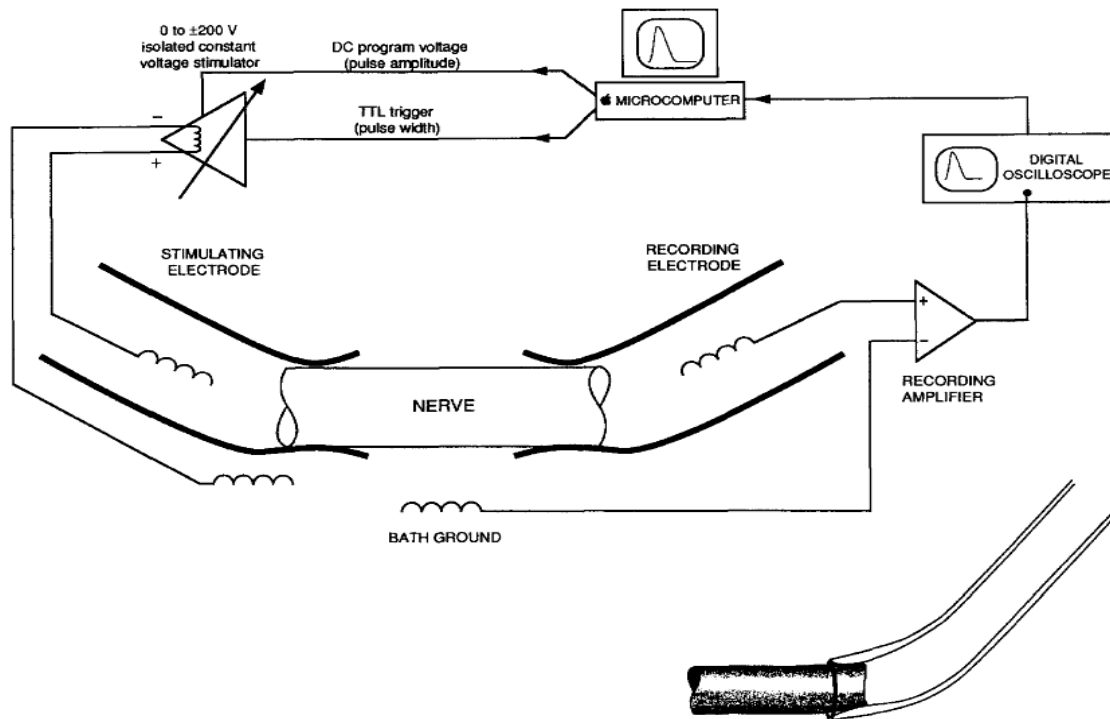


Figure 2.2. Diagrammatic representation of the typical hardware required to record compound action potential from the optic nerve (adapted from Stys *et al.*, 1991).

The CAP generated from the rodent optic nerve typically has three peaks (Fig 2.3). These peaks generally represent axons having variable extents of myelination (Allen *et al.*, 2006; Brown *et al.*, 2003; Fern *et al.*, 1998; Stys *et al.*, 1998; Waxman *et al.*, 1990). The heavily myelinated axons, having the fastest speed of conduction are represented by the first peak, that is closest to the stimulus artefact. The other two peaks represent the groups of intermediate and least myelinated axons respectively.

Coronal brain slices cut at the level of the corpus callosum, provide another alternative model to study the pathophysiology of central white matter injury. Electrodes are inserted above each side of the corpus callosum (Fig 2.4), and the propagation of electrical activity across the axonal bundle that is generated is recorded. Typically, the stimulus is generated using bipolar stimulating electrodes, and the recording microelectrode filled with 2M NaCl (Tekkök and Goldberg, 2001).

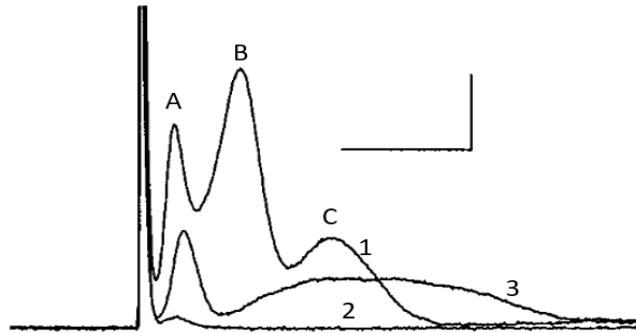


Figure 2.3. A typical recording from the rodent optic nerve. Recording showing the 3 peaks (A, B and C) from axons with different degrees in myelination. Profile 1 represents the recording at the start of the experiment. Profile 2 represents the recording during GD. Profile 3 represents partial recovery of function during the reperfusion phase. Scale: 0.5mV, 1ms (adapted from Wender *et al.*, 2000).

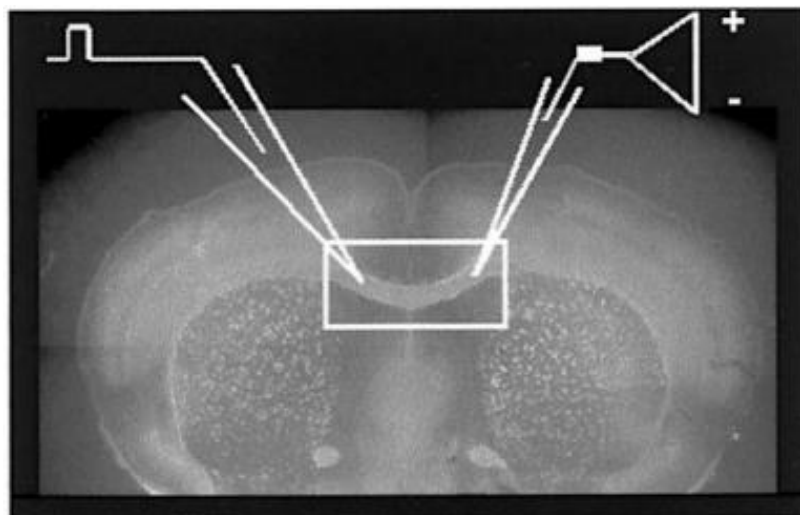


Figure 2.4. Diagrammatic representation of the typical position of the stimulating and recording electrodes on the brain slice (adapted from Tekkök and Goldberg, 2001).

The output obtained from callosal slices typically generates two peaks (Fig 2.5). These two peaks represent axon bundles with different degrees of myelination (and thickness) and therefore different conduction velocities (Reeves *et al.*, 2005; Tekkök and Goldberg 2001; Tekkök *et al.*, 2005a).

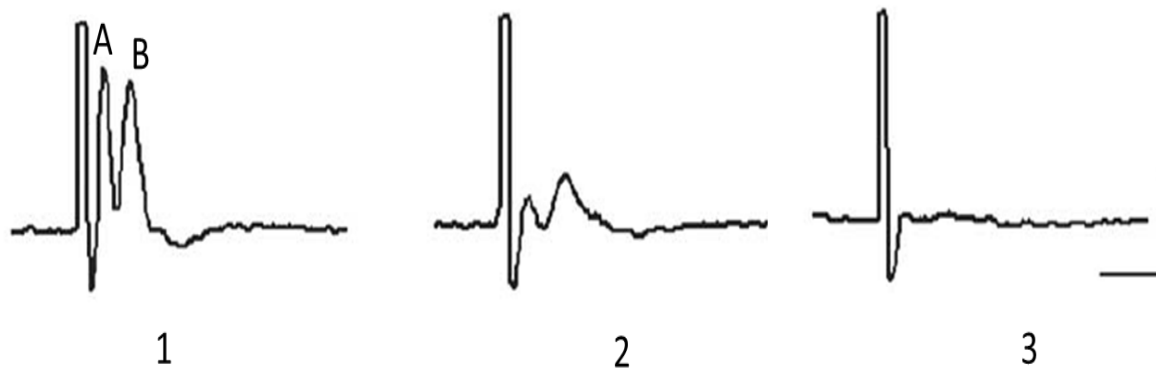


Figure 2.5. A typical recording obtained from the rodent callosal brain slices. The two peaks (A and B) are obtained from axons with variable extent of myelination. Profile 1 represents a typical profile for normal axon conduction. Profile 2 represents the recording of partially recovered axons after ischaemic injury. Profile 3 represents complete loss of function that corresponds to irreversible injury. Scale: 1mV, 1 ms (adapted from Tekkök *et al.*, 2005).

To quantify the degree of axonal injury and recovery, the area under the CAP is quantified and plotted against time (Dong and Hare, 2005). The area under the CAP represents the extent of electrically active axons, since currents generated by individual axons within a fibre tract can summate linearly (Cummins *et al.* 1979; Stys *et al.* 1991). At the onset of the experiment, most axons are electrically active, and therefore the amplitude of the signal is large. Following an injurious insult, electrically active axons are reduced in number, and this follows the decreased CAP amplitude. The extent of recovery of the CAP that accompanies removal of an insult depends on whether the damage that was inflicted was severe enough to induce an irreversible loss in axonal conduction. In mild injuries, a partial recovery of the initial signal would be expected, the amplitude of which depending wholly on the degree of recovered axonal fibres. No signal would be present in the case of extensive injury.

2.2.4 Clinical evidence that hypoglycaemia is a cause of axonal injury

Pathological changes in the brain has mainly been studied on autopsy material from patients who died from insulin-induced coma and from animals exposed to severe hypoglycaemia. In a post-mortem human study of 13 cases wherein coma was attributed to hypoglycaemia (Dolinak *et al.*, 2000), widespread axonal injury was revealed as deposition of β -Amyloid Precursor Protein (β -APP) to the underlying white matter in 11 of the cases. In 6 of the cases investigated, there was no raised intracranial pressure (ICP) or other associated complications that could have contributed or exacerbated axonal injury. MRI studies in two cases of neonatal hypoglycaemia showed cortical and white matter cerebral damage with profound atrophy of these regions in the chronic phase (Traill *et al.*, 1998). Neuroimaging studies of patients with brain injury resulting from neonatal hypoglycaemia showed significant alterations, involving both cortex and underlying white matter, with disproportionate damage of the parietal and occipital lobes (Barkovich *et al.*, 1998; Kinnala *et al.*, 1999). In other studies, neonatal symptomatic hypoglycaemia was suggested to be a cause for the delayed or abnormal myelination in the parieto-occipital and periventricular white matter of full-term infants who later developed neurological handicap (Murakami *et al.*, 1999; Cakmakci *et al.*, 2001). Therefore, the injury that we observed in transgenic mice *in vivo* and *in vitro* complements on existing data from human and animal observations that glucose deprivation is a cause of axonal injury (Dolinak *et al.*, 2000; Auer *et al.*, 1984; Auer and Siesjö, 1993).

2.2.5 Experimental evidence that glucose deprivation contributes to a loss of function in injured axons

Ransom and Fern (1997) reported that a brief exposure of the rat optic nerve to glucose deprivation (GD) did not result in an immediate loss of axonal function. In this study, the CAP started to decline only after 40 min of GD. Slower conducting axons responsible for the second peak showed earlier signs of functional loss than the faster conducting axons. The extent in recovery following reperfusion with glucose containing aCSF was also to a lesser extent than the earlier first peak (Fig. 2.6). The study also reports no significant permanent loss of CAP following 45 min GD, but a complete loss of function after 65 min of GD (Fig. 2.7).

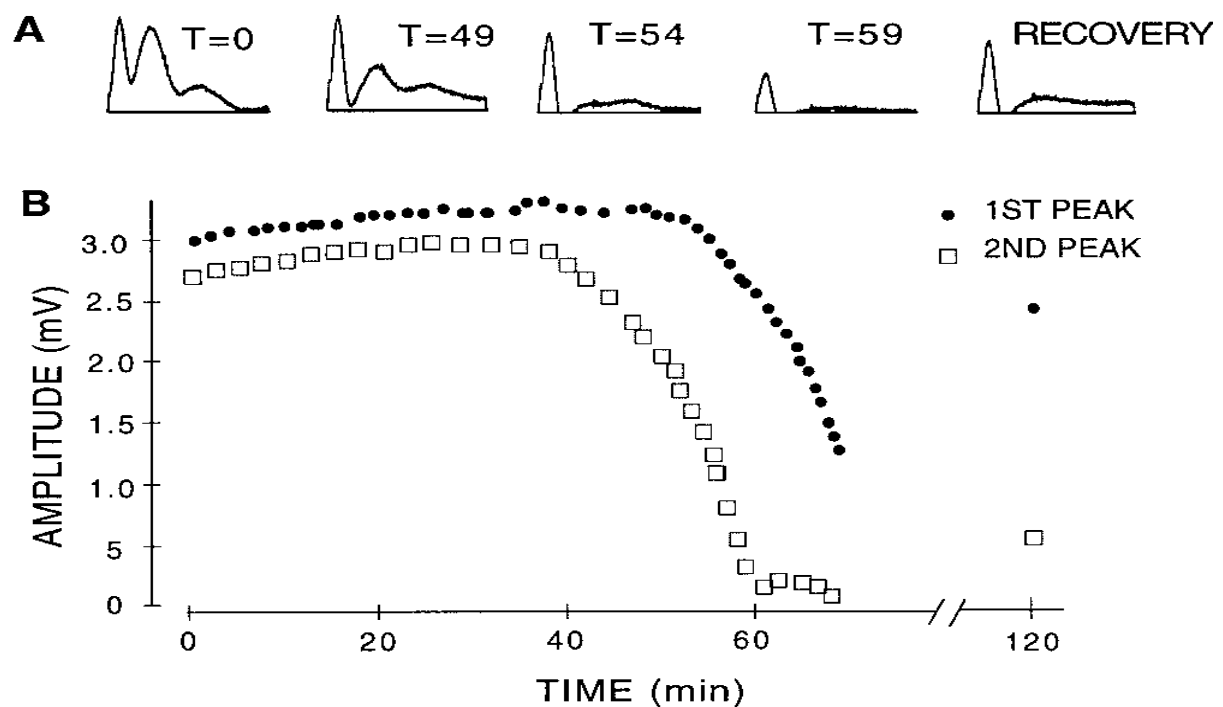


Figure 2.6. The effect of CAP recording following GD in the rodent optic nerve during different time points of the experiment. (B) Plot of CAP of first and second peaks showing an initial preservation in axonal function upon removal of bath glucose. Conduction starts decreasing after 40 min of GD and is lost after 65 min. Slower conducting axons are more susceptible to GD and recovery is poorer than the faster conducting axons (adapted from Ransom and Fern, 1997).

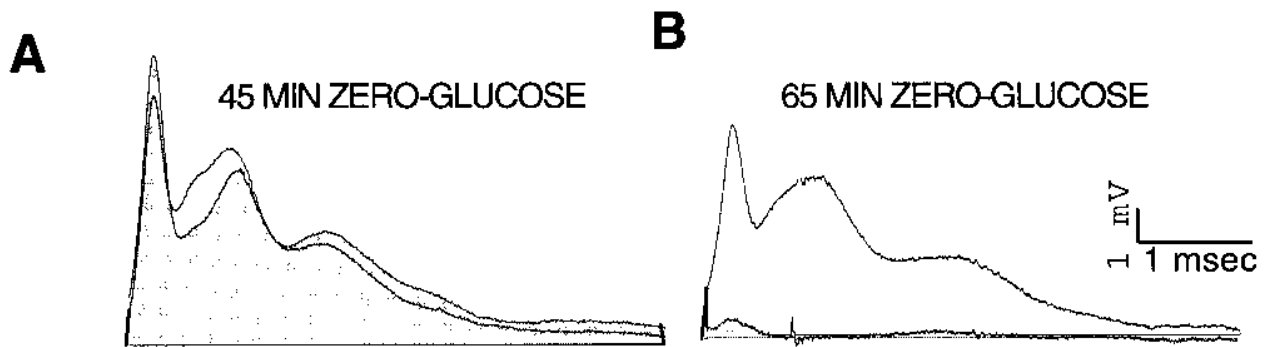


Figure 2.7. Loss in CAP following GD in the optic nerve. (A) Minimal loss of CAP following 45 min of GD. (B) Irreversible loss of CAP following 65 min of GD. (shaded area – GD) (adapted from Ransom and Fern, 1997).

Meyer *et al.* 2018 recently studied the effect of GD on callosal axons present in coronal brain sections. They reported that following the onset of GD, it took 30 min for loss of axonal conduction at room temperature, but only 5 min at 37°C. On reapplying glucose containing aCSF, CAP amplitudes returned to normal just after 5 min in slices at 37°C, and it took 20 mins in slices kept at room temperature (Figure 2.8).

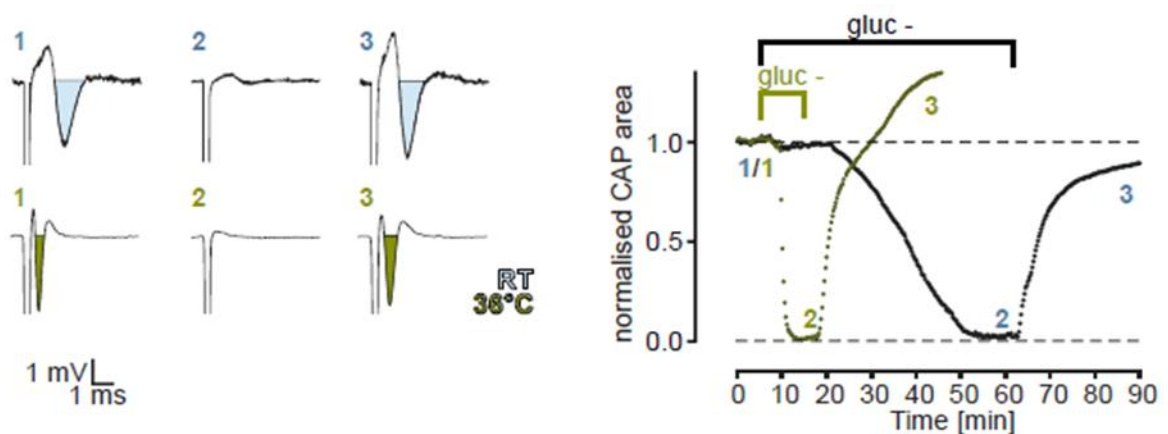


Figure 2.8. Loss in CAP following GD in the callosal brain slice. *Top:* Representative recordings illustrating CAP decline following GD during 55 min (at room temperature – blue) or 10 min (at 36°C - green). The filled area (blue/green) corresponds to the area for CAP calculation. *Plots at the bottom* show sample traces of normalized CAP areas during GD and reperfusion (adapted from Meyer *et al.*, 2018).

2.3 Methodology

2.3.1 Dissecting instruments

Adult male mice aged 12-20 weeks with C57BL6/J genetic background were used for all the experiments. The mice were housed in cages containing paddy husk as bedding material, which was changed on alternate days. Mice were housed in a well-aerated, temperature and humidity-controlled environment and kept at a 12-hour light/dark cycle. They were provided with a constant supply of food and water. Room temperature (RT) was maintained at 23°C and 55% humidity. The dissection of the brain and optic nerve from mice is a simple procedure. The surgical instruments used for the brain and optic nerve retrieval are listed in Table 2.1 and shown in Figure 2.9.

Item	CatLog Number	Company
Straight surgical scissors	91402-14	Fine Science Tools
Hardened Fine Scissors	14090-09	Fine Science Tools
Dissector Scissors - Slim Blades	14081-09	Fine Science Tools
Dumont #7 Forceps	91197-00	Fine Science Tools
Tissue Forceps - 1x2 Teeth	11021-15	Fine Science Tools
Vannas Micro Dissecting Spring Scissors	RS-5619	Roboz Surgical Store

Table 2.1. List of surgical dissection tools.

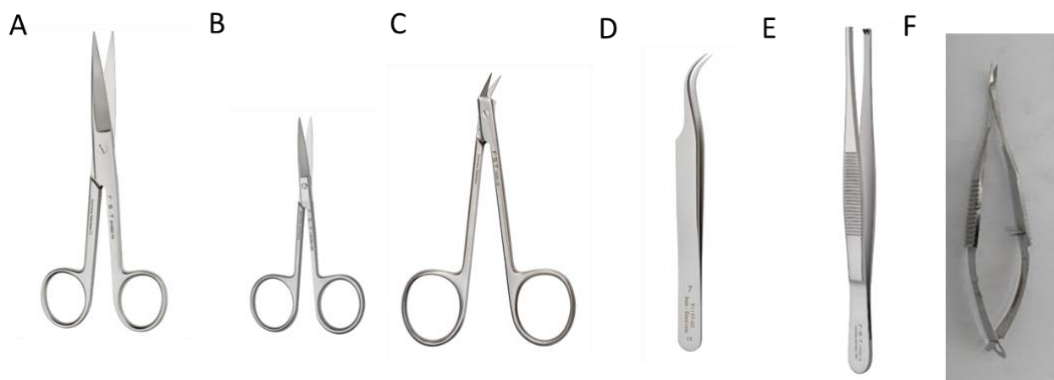


Figure 2.9. Surgical dissection tools used. [A] Straight surgical scissors; [B] Hardened Fine Scissors; [C] Dissector Scissors - Slim Blades; [D] Dumont #7 Forceps; [E] Tissue Forceps - 1x2 Teeth; [F] Vannas Micro Dissecting Spring Scissors

2.3.2 Preparation of cutting solution for the retrieval of callosal slices

To minimise the damage to the brain tissue during dissection and slicing, these procedures were done in a sucrose rich and low calcium aCSF containing NaCl, KCl, NaH₂PO₄, NaHCO₃, MgCl₂ (anhydrous), CaCl₂·2H₂O, glucose, and sucrose. The molarities used (in stock and experimental solutions) are listed in Table 2.2.

	Molecular Weight	Molarity in final solution (mM)	Stock solution preparation	Molarity of stock solution
NaCl	58.4	87	50.8 g in 200 ml	4.35 M
KCl	74.6	2.5	1.86 g in 200 ml	124.75 mM
NaH ₂ PO ₄	138.0	1.25	1.725 g in 200 ml	62.50 mM
NaHCO ₃	84.0	25	21 g in 200 ml	1.25 M
MgCl ₂ (anhydrous)	246.5	2.98	2.84 g in 200 ml	149.14 mM
CaCl ₂ ·2H ₂ O	147.0	0.5	0.735 g in 200 ml	24.99 mM
Glucose	180.16	25	N/A	N/A
Sucrose	342.30	75	N/A	N/A

Table 2.2. Chemical composition of the cutting solution.

The cutting solution was freshly prepared and involved the following steps:

1. 10 ml of NaCl, KCl, NaH₂PO₄, and NaHCO₃, were added to 440 ml of Milli-Q H₂O.
2. 2.25 g of glucose and 12.846 g of sucrose were added to the solution.
3. The solution was then bubbled with 95%O₂/5% CO₂ for 15-30 mins, whilst stirring continuously.
4. 10 ml of MgCl₂ (anhydrous) and CaCl₂·2H₂O were added to the solution and left bubbling with 95%O₂/5%CO₂ for another 10 mins.
5. The pH was finally adjusted to 7.4.
6. The solution was then placed in a -80⁰C freezer for about 45-60 mins, until it formed a slush.
7. The solution was then placed on ice and bubbled with 95%O₂/5% CO₂ for another 15 mins.

2.3.3 Preparation of artificial cerebrospinal fluid

The experimental procedures were all carried out in aCSF containing NaCl, KCl, NaH₂PO₄, NaHCO₃, MgCl₂ (anhydrous), CaCl₂.2H₂O, and glucose. Whenever the experimental protocol required a period of GD, glucose was replaced with sucrose, to maintain the same osmolality. The concentrations used are listed in Table 2.3.

	Molecular Weight	Molarity in final solution (mM)	Stock solution preparation	Molarity of stock solution
NaCl	58.4	126	73.63 g in 100 ml	1.26 M
KCl	74.6	3.49	5.2 g in 200 ml	348.76 mM
NaH ₂ PO ₄	138.0	1.16	3.2 g in 200 ml	115.95 mM
NaHCO ₃	84.0	23.8	20 g in 200ml	1.19 M
MgCl ₂ (anhydrous)	246.5	1.28	2.44 g in 200ml	128.14 mM
CaCl ₂ .2H ₂ O	147.0	2.0	5.8 g in 200ml	197.25 mM

Table 2.3. Chemical composition of the aCSF.

The aCSF was prepared fresh before each experiment, following the subsequent steps:

1. 100 ml of NaCl, 20 ml of NaHCO₃, and 10 ml of KCl and NaH₂PO₄ were added to 840 ml of Milli-Q H₂O.
2. The solution was then bubbled with 95% O₂/5% CO₂ for 15-30 mins, with stirring.
3. 10 ml of MgCl₂ (anhydrous) and CaCl₂.2H₂O were added to the solution and bubbled with 95% O₂/5% CO₂ for a further 10 mins.
4. The pH was adjusted to 7.4.
5. The solution was then divided in two separate beakers, one for glucose-containing aCSF (final molarity of 10mM), and the other for sucrose-containing aCSF (final molarity of 10mM). Sucrose was added to maintain the same osmolality between the two solutions.

From our experience, there are a number of factors that contribute to the viability of the slices. The brain tissue should be handled delicately to reduce physical damage. The preparation time should be short, a prolonged ischaemic period is associated with a fall in intracellular adenosine triphosphate (ATP). Lowering the brain tissue temperature during the preparation is effective in reducing the sensitivity of neurons to ischaemia. In order to reduce the neurotoxicity of the glutamate that may be massively released during slice preparation, we use an aCSF containing 1.28mM magnesium and 1.97 mM calcium for slicing and storage.

2.3.4 Optic nerve preparation

The procedure of the optic nerve preparation can be followed in Fig 2.10. Following induction of generalised inhalation anaesthesia with isoflurane, mice were transferred onto a dissection board, and the head rapidly decapitated using a straight surgical scissors. The body was discarded, and the head was immediately immersed in ice cold water to ensure homeostasis and allow for a clear field of view during the dissection. An incision is made along the sagittal suture (1) with a surgical blade to remove the skin on top of the skull (2). The eyeball is freed from the connective tissues around the orbit with a hardened fine scissors (3), and very gently pulled out. The optic nerve is then cut free from its attachment to the eyeball using the same scissors (4). Great care was taken at this step as one could easily damage the nerve in the process. If the eyeball is extensively pulled out of its socket or with too much vigour, the nerve could be easily stretched and injure with possible transaction from the optic chiasm. On the same lines, if the optic nerve is not freed from the eyeball or from the surrounding connective tissue, at some later stage of dissection when the brain is removed, the optic nerve might fuse to the eyeball resulting in loss of the nerve. Following the above rapid procedure, the head is placed horizontally on the dissecting board, with the dorsum facing upwards. A tissue forceps was applied across the nasal bridge to hold the head in place and an incision was made through the skull along the sagittal suture up to the level of the bregma with dissector scissors (6). This was followed by two diagonal incisions from the medial aspect to each orbit towards the bregma (6). Using a Dumont #7 forceps, the two parietal bones were gently removed to expose the brain (7). At this point, a few drops of oxygenated aCSF were added to prevent drying out of the brain tissue (8). After the brain was exposed, a Dumont #7 forceps was inserted in front of the cerebrum, underneath the olfactory nerves and the brain was gently pulled backwards (9). This movement resulted in both optic nerves being pulled out of the orbit. The brain with both optic nerves still attached at the optic chiasm was then transferred to a petri dish filled with aCSF (with the rostral aspect of the brain facing up) (10). A fine-tipped brush was used to align the optic nerves parallel to each other and the optic chiasm freed from the brain with a Vannas micro dissecting spring scissors (11). The freed nerves (12) were then transferred to an interphase perfusion chamber (Harvard Instruments, UK).

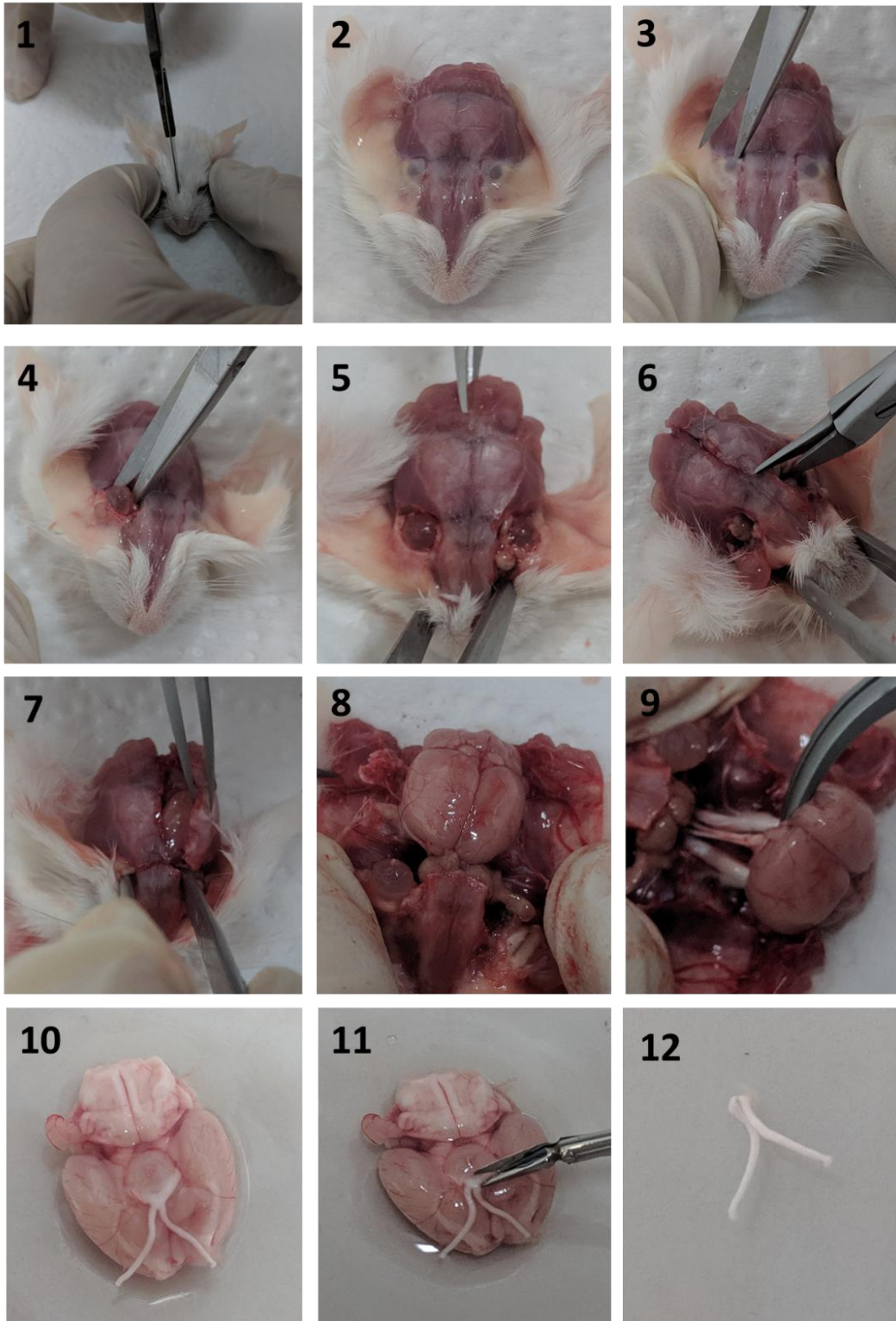


Figure 2.10. Step-wise procedure to extract the optic nerve. Each numbered step is referred to in the text above.

2.3.5 Brain slice preparation

The goal of the brain slice preparation is to obtain a thin section of brain tissue containing the cells of interest and to maintain the slice in a viable (although artificial) condition that is similar to its *in vivo* environment.

The procedure of the optic nerve preparation can be followed in Fig 2.11. Following induction of generalised inhalation anaesthesia with isoflurane, mice were transferred onto a dissection board, and their head rapidly decapitated using a straight surgical scissors. The body was discarded, and the head rapidly immersed in ice cold water to ensure homeostasis and allow for a clear field of view during dissection. The head was then placed with the cranium facing upwards in a dissecting tray filled with chilled cutting solution, which was continuously bubbled with 95% O₂/5% CO₂. An incision was made along the sagittal suture with a surgical blade (1) to remove the skin on top of the skull (2). A tissue forceps was applied across the nasal bridge to hold the head in place, and by means of a dissector scissors, two incision were made (one on each side) diagonally across the frontal bone from the roof of each orbit towards the bregma (3-4). This was followed by another incision along the sagittal suture (5), starting from the posterior aspect of the skull and extending towards the bregma (6). The two parietal bones were gently removed to expose the brain using a Dumont #7 forceps (7). After the brain was exposed (8), a small spatula was inserted (9) beneath the cerebral hemispheres and the brain was gently pulled backwards (10). This movement resulted in freeing the brain from within the skull. The cerebellum was then cut away (11 – dotted line) from cerebral hemispheres using a sharp blade, thus leaving just the two cerebral hemispheres (12).

The cerebral hemispheres were then mounted on the ice-cold platform of a Vibratome 1000 vibroslicer (Technical Products, St. Louis, MO) covered in oxygenated ice-cold cutting solution. Consecutive 400 µm thick coronal slices were cut starting from the anterior end of the hemispheres. From each brain, 8 slices were usually obtained that contained a significant amount of corpus callosum. These slices were then transferred to a holding chamber (Scientific Systems Design) filled with oxygenated aCSF to allow for stabilization for 2 hours at room temperature.

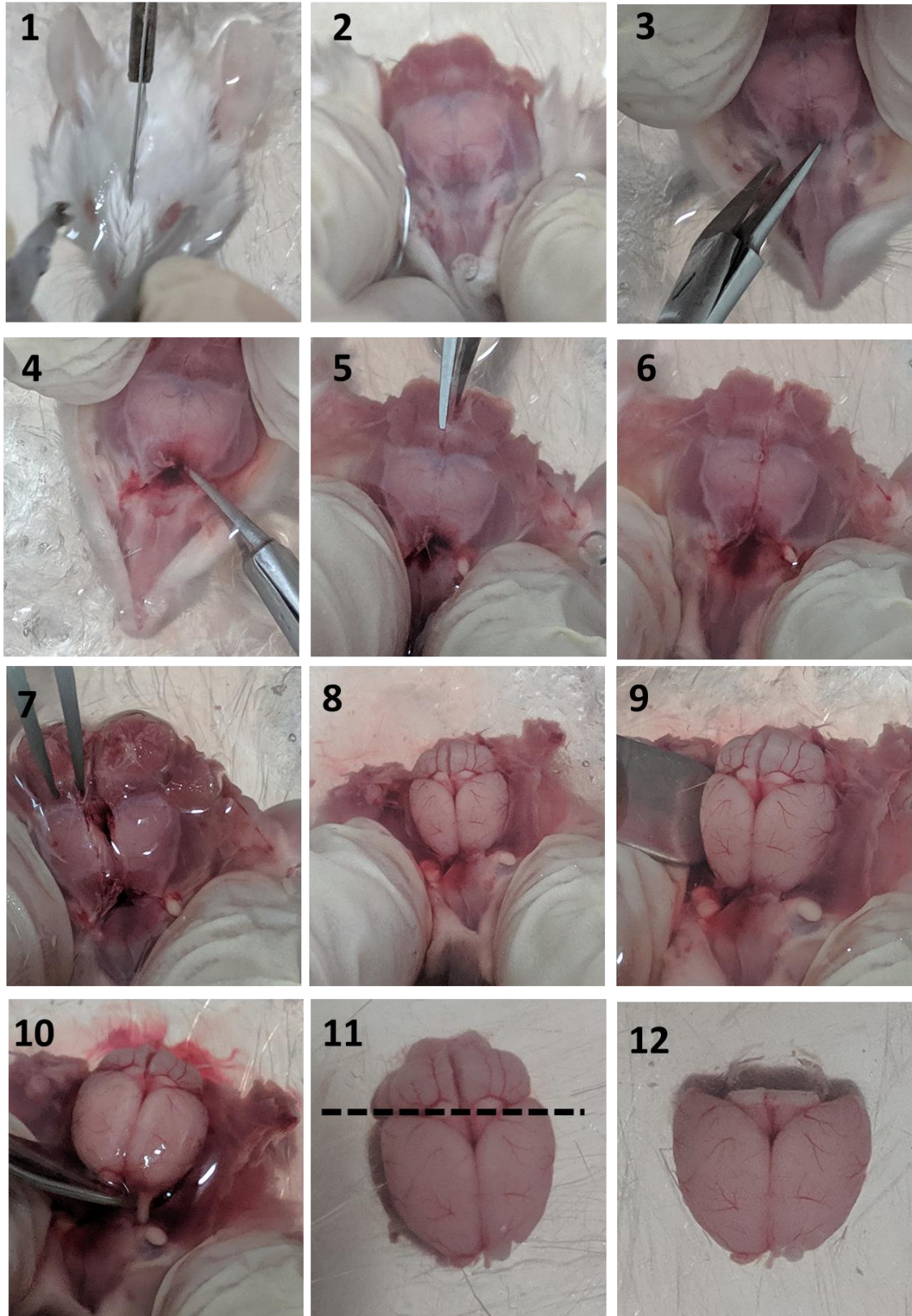


Figure 2.11. Step-wise procedure to extract the whole brain. Numbers 1 – 12 refers to the dissection technique described above.

2.3.6 Live imaging under two-photon microscopy

Live imaging provides exciting opportunities to study dynamic cellular events as they occur in real time. One of the challenges for live imaging is that the live specimen must remain healthy and viable in the imaging setup with considerations such as temperature, pH, gas exchange and light exposure having a major role in the experimental technique. YFP-expressing axons were imaged with a 920 nm laser line (7-10% laser power) using a water-based 25X Olympus XLPLN25xWMP multiphoton apochromatic objective (NA 1.05, WD 2.0, IR-corrected). The multiphoton system housed Keplerian beam expanders with infra-red (IR) introduction light paths to achieve perfect excitation efficiency and highly resolved multiphoton images. A mode-locked MaiTai HP DeepSee IR laser system (Spectra-Physics) with a tuneable Ti: sapphire oscillator (690-1040 nm) was used as the excitation light source (pulse width < 100fs; pulse repetition rate 80Mhz) and controlled through an acousto-optical-modulator to allow for precise changes in laser intensity. The Group Velocity Dispersion was electronically compensated by a prism-coupled pre-chirper and the beam diameter adjusted by a Kepler telescope. The direct detection of emission light (i.e. without a confocal aperture) results in the highest collection efficiency of scattered light as light is 'picked off' before it passes through the scanning system.



Figure 2.12. FV1000 MPE Olympus Multiphoton microscope (Olympus, Tokyo, Japan).

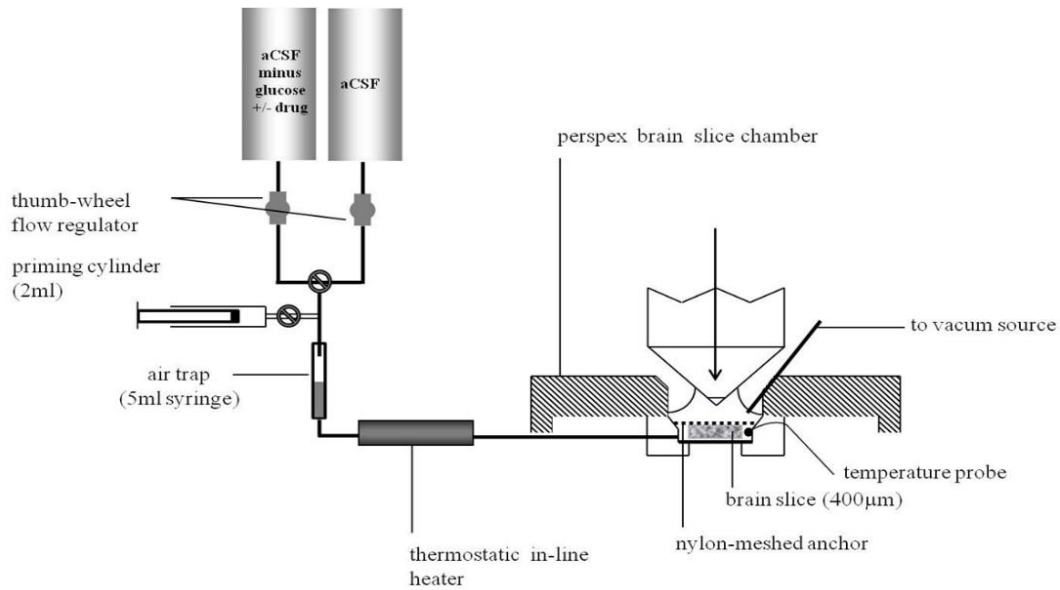


Figure 2.13. Integrated setup used for live brain slice imaging. A gravity-fed system is heated through a thermostatically-regulated in-line heater with feedback control through a temperature sensor. Used perfusate is aspirated from the chamber and transferred into a waste container through a vacuum suction line.

Image acquisition was performed using the Olympus FluoView® V100 software. Single-focal-plane images were collected at 30-min intervals or, more frequently, stacks of five optical sections at an incremental z-step of $1\mu\text{m}$ apart. Subsequently, all z-stacks of images were projected along the z-axis to recreate two-dimensional representations of the three-dimensional structures within the imaged tissue. To ensure full representation of the axons within the field of view, in all z-stacks we set the upper and lower limits so that all axonal profiles were included in the raw imaging data and in their subsequent z projections. Corrective focus changes to keep track of focus drift was necessary during the time-lapse experiment to keep the features within a given image plane. During image acquisition laser power and detector gain and offset settings were adjusted as to minimise background noise for sharper visualisation of axonal profiles. Post-acquisition images were only adjusted for brightness, contrast and background noise by using Imaris software. For brightness and contrast adjustments the depth of pixel intensities that spanned the entire 8-bit range (0–255) was readjusted for display optimisation. The two-photon imaging experiments allowed for the timely acquisition of image frames that followed axonal injury in real-time. These experiments are descriptive in nature and were repeated in triplicate to confirm the reproducibility of the findings and increase statistical power.

2.3.7 Glucose deprivation during live imaging

Immediately after sectioning, slices were transferred to a holding chamber (Scientific Systems Design) where they were left to equilibrate for about 2 hours at room temperature. A brain slice from the holding chamber was transferred to a mini submerged chamber (0.5ml) with a coverglass bottom (Warner Instrument Corporation, Hamden, CT) mounted on an upright FV1000 MPE Olympus Multiphoton microscope (Olympus, Tokyo, Japan) and perfused with oxygenated aCSF at $37.0 \pm 1.0^\circ\text{C}$ at a flow rate of approximately 3 ml/min. Temperature control was maintained using an in-line heater (Warner Instrument Corporation, Hamden, CT) equipped with a feedback thermistor placed in the chamber and the temperature raised gradually over 1 hour. Slices were continually perfused with oxygenated buffer during imaging by means of a peristaltic pump and vacuum aspiration within the imaging chamber. GD was initiated by replacing glucose containing aCSF with no-glucose containing aCSF (replaced by sucrose) for various durations and imaging was continued through 2 hr of reperfusion with substitution to glucose-containing aCSF.

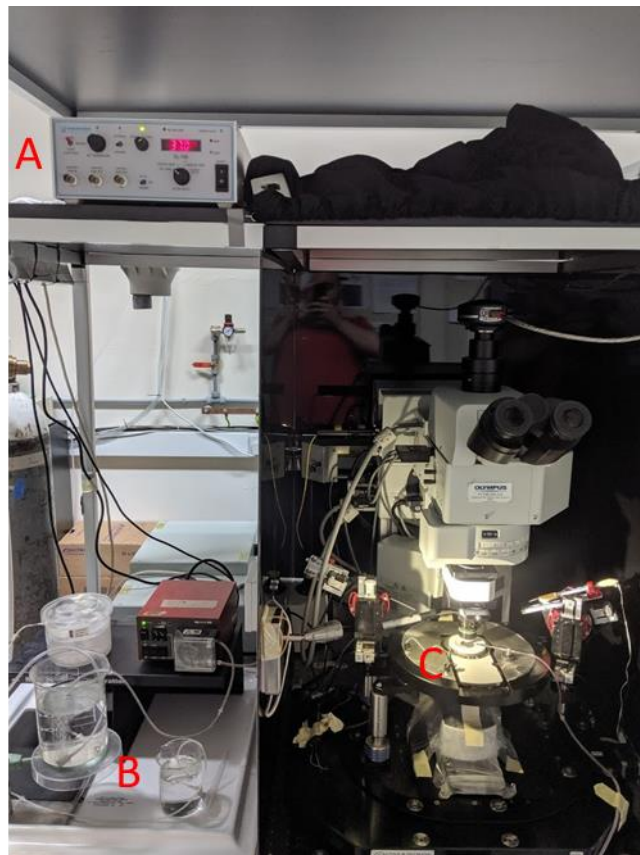


Figure 2.14. Live-imaging set-up. [A] line heater controller. [B] Set-up for slice perfusion. [C] slice under two-photon microscope.

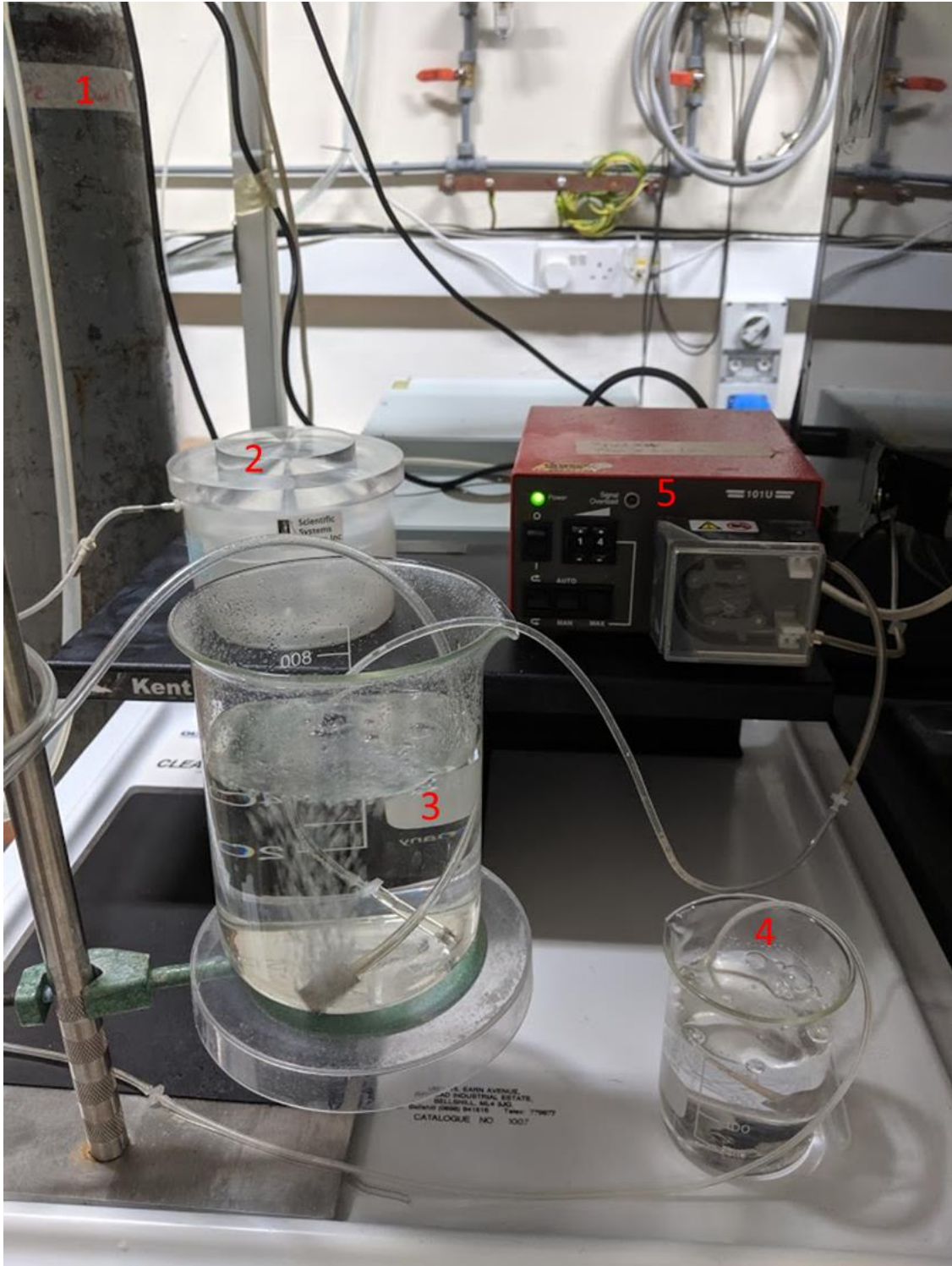


Figure 2.15. Set-up for slice perfusion during live imaging. Slices were left in the holding chamber (2) for 2 hours and then transferred to the imaging chamber. The latter was perfused with glucose containing aCSF (3) continuously bubbled with 95%O₂/5% CO₂ (1) via a peristaltic pump (5). To induce GD, the inlet from the peristaltic pump was transferred from the glucose containing aCSF (3) to the sucrose containing aCSF (4).

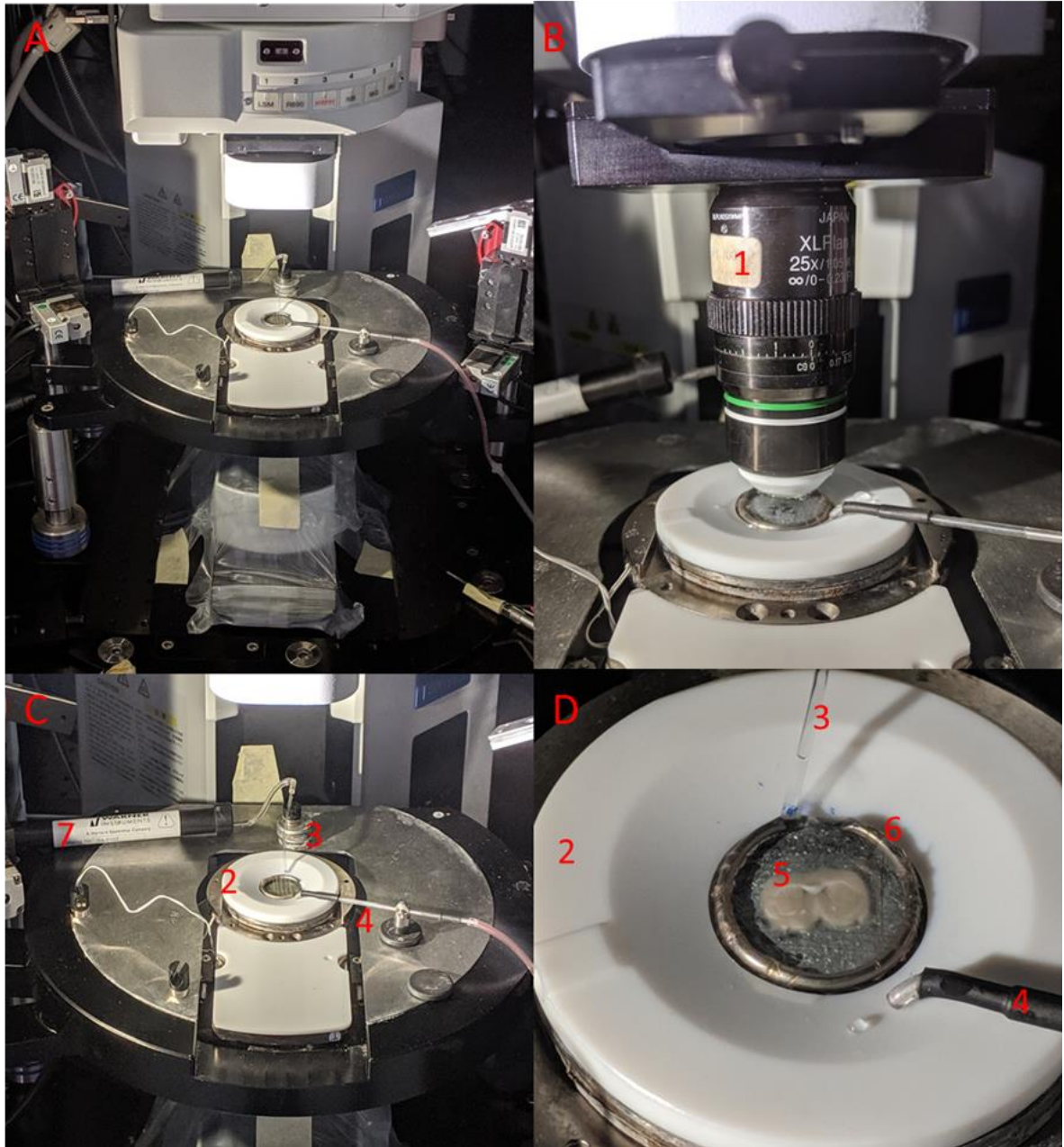


Figure 2.16. Set-up for the imaging chamber. The two-photon microscope stage and the imaging chamber with [A] and without [B] the lens (1). [C-D] Zoomed-in image of the imaging chamber (2). The brain slice was gently placed in the imaging chamber (2) on top of lens paper, and continuously perfused with aCSF via the inlet (3). Before reaching the inlet (3) the aCSF passed through an in-line heater (7) to reach 37°C and was then aspirated from the chamber via a vacuum pump connected to a curved pipette (4). The harp (6) placed on top of the slice prevented it from floating and stabilised it during the live imaging.

2.3.8 Data analysis

Axon damage was quantified by visual scoring. Images were divided into a 5 x 5 grid, and each grid box was scored by a blinded observer for the presence of axon damage using the following system: 0 – no damage; 1 – axon swelling and/or beading; 2 – axon fragmentation (Figure 2.17 and 2.18). The total score for a single section (0–50) was divided by the number of grid boxes to give a mean damage score (0–2). Damage scores from three different experiments were averaged and recorded for each condition.

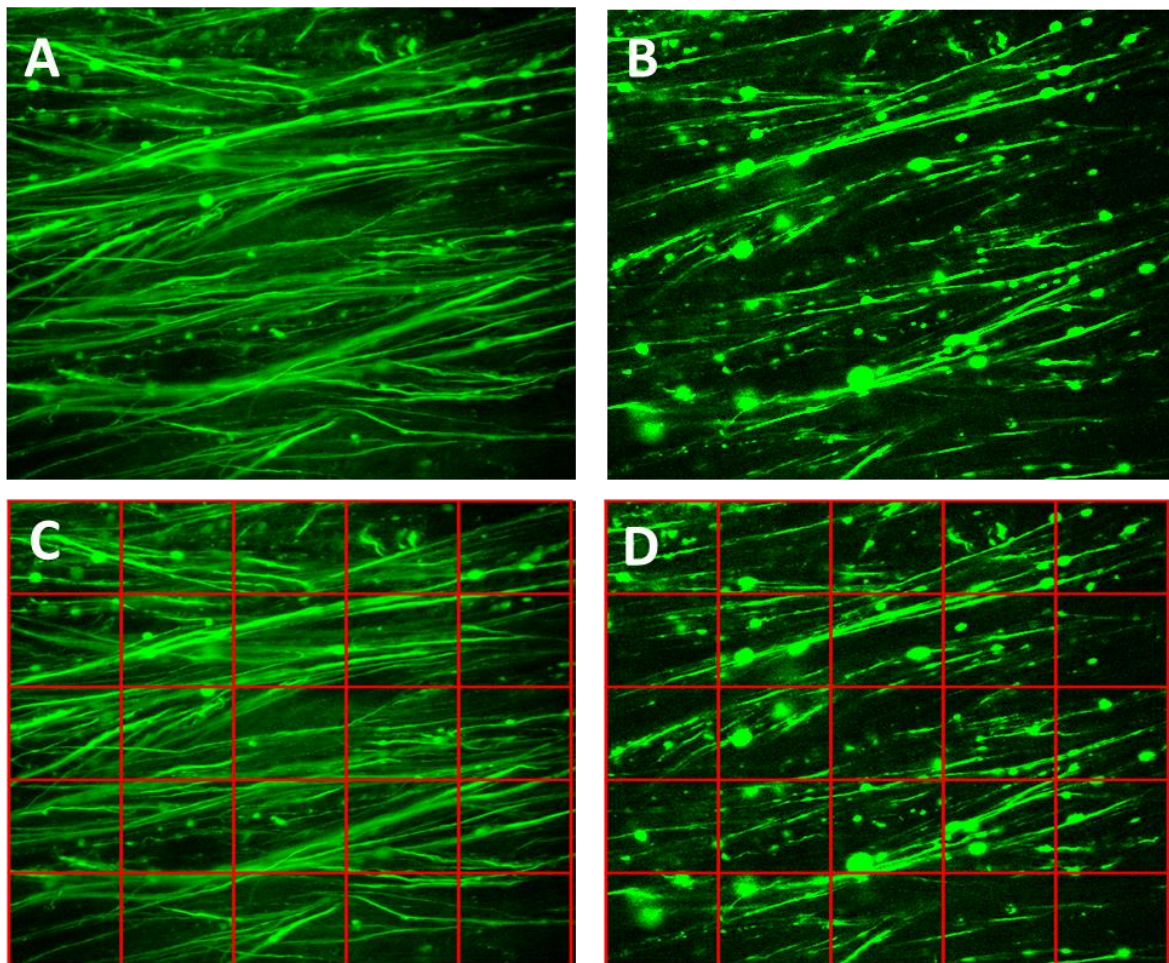


Figure 2.17. Axonal injury score. [A-C] Control slices. [B-D] Injured slices. [C-D] Each image was divided into a 5x5 grid producing 25 sections. Each section was then given a score of 0, 1, or 2 depending on the degree of injury by a blind observer.

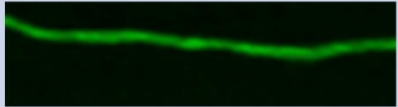

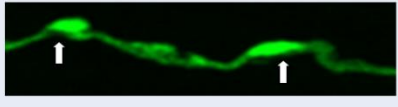

Score	Extent of injury	Example
0	No injury	
1	Axon Swelling	
	Beading	
2	Fragmentation	

Figure 2.18. Various degree of axonal injury with their respective injury score. Linear axons with no signs of injury were given a score of 0. Axons with mild focal swelling and beading were given a score of 1. Fragmented and transected axons were given a score of 2 (adapted from our published data Alix *et al.*, 2012).

To assess the axonal injury score we used an ordinal scale of 0 (no injury), 1 (axonal swelling and beading) and 2 (fragmentation). This was based on previous literature (McCarren and Goldberg, 2007), and we had used it in two of our previously published papers (Alix *et al.*, 2012, Laureys *et al.*, 2014). We acknowledge the fact that although the axonal injury score is an ordinal scale, we had no other means than to represent the axonal injury scores as an interval scale for clearer representation of the results.

2.3.9 Statistical analysis

All data was expressed as means \pm standard deviations. Statistical significance was determined by one-way and two-way ANOVA followed by Tukey's post hoc test for multiple comparisons between groups. Interrater or intrarater reliability was tested using Cohen's kappa, producing a value greater than 0.85.

2.3.10 Induction of glucose deprivation *in vivo* in interphase chamber

Immediately after sectioning, slices were transferred to a Haas-type slice chamber (Harvard Apparatus, South Natick, MA) and allowed to recover at room temperature in oxygenated (95% O₂/5% CO₂) aCSF for 2 hours at a flow rate of 3.0 ml/min. Two Haas-type chambers were used: control vs GD.

Four to five slices were placed in each chamber on lens paper. Slices were then superfused with oxygenated aCSF at 37.0±1.0°C for a further 1 hour. GD was initiated by replacing glucose in normal oxygenated aCSF with 10 mM sucrose for a period of 45 min.

A sample slice from each compartment was sampled immediately after the 45 mins of GD and at 30, 60 and 120 min of reperfusion. Each slice was immediately fixed for 2 hours at RT in fixative composed of 4% paraformaldehyde in phosphate buffer solution (PBS), pH 7.4. Each slice from each condition was carefully cut along the midline under microscopic control and each hemisphere from each condition stored in fixative for light and electron microscopy examination. The other halves from each condition were given a brief rinse in PBS and cryoprotected for < 48 hr in 30% sucrose in PBS in preparation for immunocytochemistry and confocal microscopy.



Figure 2.19. General setup of the Hass-type interphase chambers. 1 - TC-202A Bipolar Temperature Controller (Warner Instruments); 2 – Two-channel peristaltic pump; 3 – Haas-type slice chamber; 4 – aCSF (+/-) glucose; 5 – Ggs regulators.

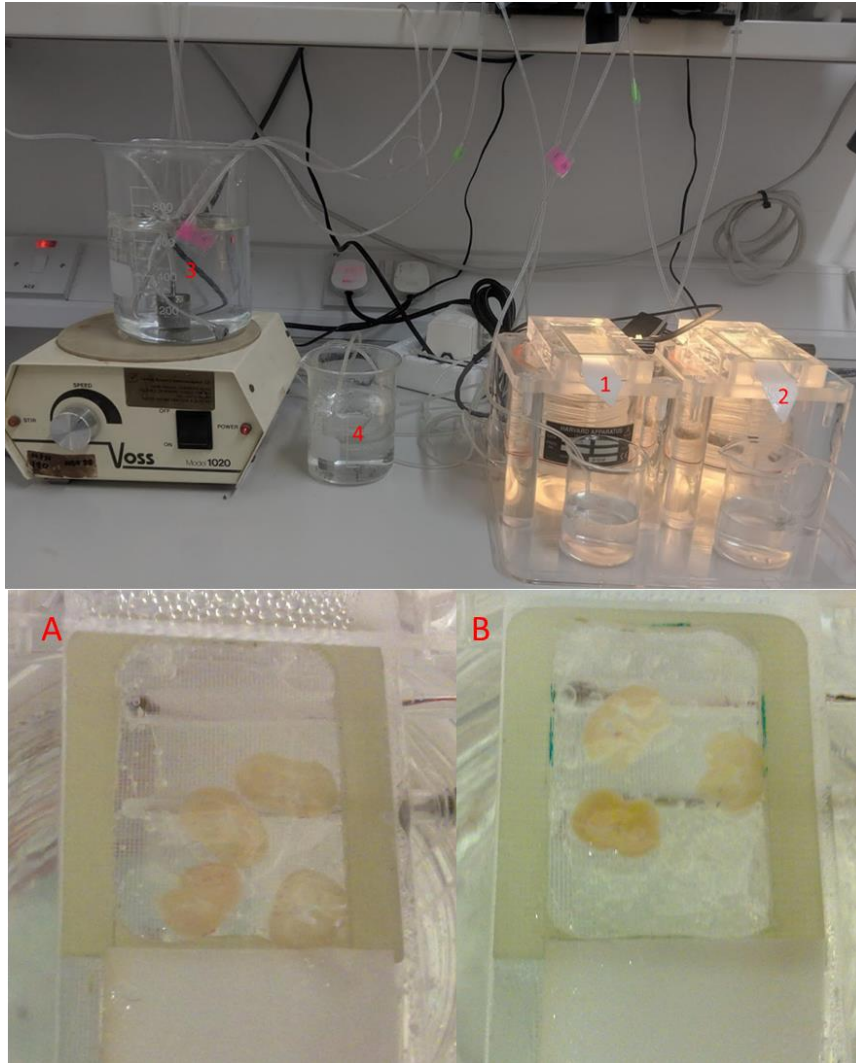


Figure 2.20. Control and experimental slices in Hass-type interphase chambers. After cutting four to five brain slices were placed in each chamber on a lens tissue and allowed to stabilise for about two hours. The slices in chamber (1 – zoomed in A) were continuously perfused with glucose containing aCSF (3). After the stabilisation phase, the slices in chamber (2 – zoomed in B) were exposed to sucrose containing aCSF (4) for 45 min. This was switched back to glucose containing aCSF (3) at the end of the 45 min, and perfusion was continued for a further 2 hr.

2.3.11 Immunocytochemistry

Sixteen micron-thick sections (10-12 / slice) from each 400 µm-thick brain slice were cut by a cryotome and collected onto gelatin-coated slides (Fisher Scientific, Pittsburgh, PA). Sections from the outer 50 µm surfaces were excluded to avoid viewing mechanically damaged tissue on the slice surface. For immunohistochemical analysis, the brain sections were blocked and permeabilised in 40 % normal goat serum (Sigma, St. Louis, MO) and 0.4 % Triton X-100 (Sigma, St. Louis, MO) for 30 min at RT. Sections were labelled for axonal neurofilaments with the monoclonal antibody SMI-31 (Sternberger Monoclonals, Incorporated, Lutherville, MD) against epitopes of phosphorylated NF 200.

Primary antibody was used at a dilution of 1:10,000 in permeabilisation buffer. Sections were incubated in primary antibody for 2-3 hr at RT or overnight at 4°C. Following a thorough wash in PBS, tissue was exposed to secondary antibody, donkey anti-rabbit Cy3 (Jackson ImmunoResearch Laboratories, Inc., West Grove, PA) at a dilution of 1:100 in 2 % normal goat serum for 1 hr at RT. After a final wash in PBS, the sections were treated with Prolong Antifade (Molecular Probes) before they were cover-slipped (Sigma). Slides were kept in the dark at 4°C overnight to assure antifade treatment prior to imaging. For each slice, immunolabelling was examined and quantified from four sections for each experimental condition. In all experiments, the YFP fluorophore was stable and resistant to fading during storage enabling data collection over several months.

	1^o Antibody	2^o Antibody
Type	SMI-31	donkey anti-rabbit Cy3
Dilution	1:10,000	1:100
Duration	2-3 hr at RT/overnight at 4°C	1 hr at RT

Table 2.4. Primary and secondary antibodies.

2.3.12 Assessment of axon and neurofilament morphology

The corpus callosum of each slice was imaged by a BioRad MRC 1024 inverted confocal microscope. Sections were scanned in the z-axis with 488 nm laser line for YFP and 543 nm for Cy3. The sequence of sampling of slices was kept constant. Representative microscopic fields in the middle of the corpus callosum of each brain section were imaged using a 40X (water immersion, N.A 1.2) or 100X (oil immersion, N.A 1.45) objective lens under fixed gain and pinhole settings. Projected images were acquired with Laser Sharp imaging software. Optimal settings were first obtained from slices from perfusion-fixed sections which showed maximum fluorescence intensity.

2.3.13 Brightfield and electron microscopy for histological analysis and morphometry

After overnight fixation (4°C) in 2% paraformaldehyde, 2% glutaraldehyde in 0.1M cacodylate buffer pH 7.4 each halved slice (400µm) from each condition was carefully trimmed (2.0 X 2.0 mm) to contain the genu of the corpus callosum (four sections for each condition). Sections were post-fixed for 1 hr in 1% osmium-1% potassium ferricyanide in 0.1 M cacodylate and en bloc stained with 1% uranyl acetate in maleate buffer, pH 6.0, and flat-embedded in epoxy resin (Ted Pella, Inc., Redding, CA). One micrometre sagittal sections were cut at the level of the septo-striatal region (Bregma around 0.74 mm) from each tissue block and stained with 1% toluidine blue. Sections were screened for evidence of white matter injury under light microscopy.

For electron microscopy (EM), sagittal ultrathin sections (90-100nm) from the epoxy-embedded tissue blocks were cut with a Leica Ultracut UCT ultramicrotome and subsequently counterstained with uranyl acetate and lead citrate. Sections were viewed at 80 kV on a JEOL 100B TEM with digital image capture.

The histological preparation of slides for EM processing and imaging was done at Leicester University, UK. Thereafter, all image analysis was conducted in our laboratory.

2.3.14 Preparation of electrodes for electrophysiology and generation of the compound action potential

For both models, the stimulus was generated via a stimulus isolator unit (Digitimer, U.K). Typically, 25 – 75 μ s long supramaximal pulses were delivered every 30 sec. The evoked signal was amplified with a gain of between 100x-200x and filtered between dc – 5000Hz using NeurologTM amplifier, acquired via 1401 plus data acquisition, and recorded and stored via Signal 1.9 for later analysis.

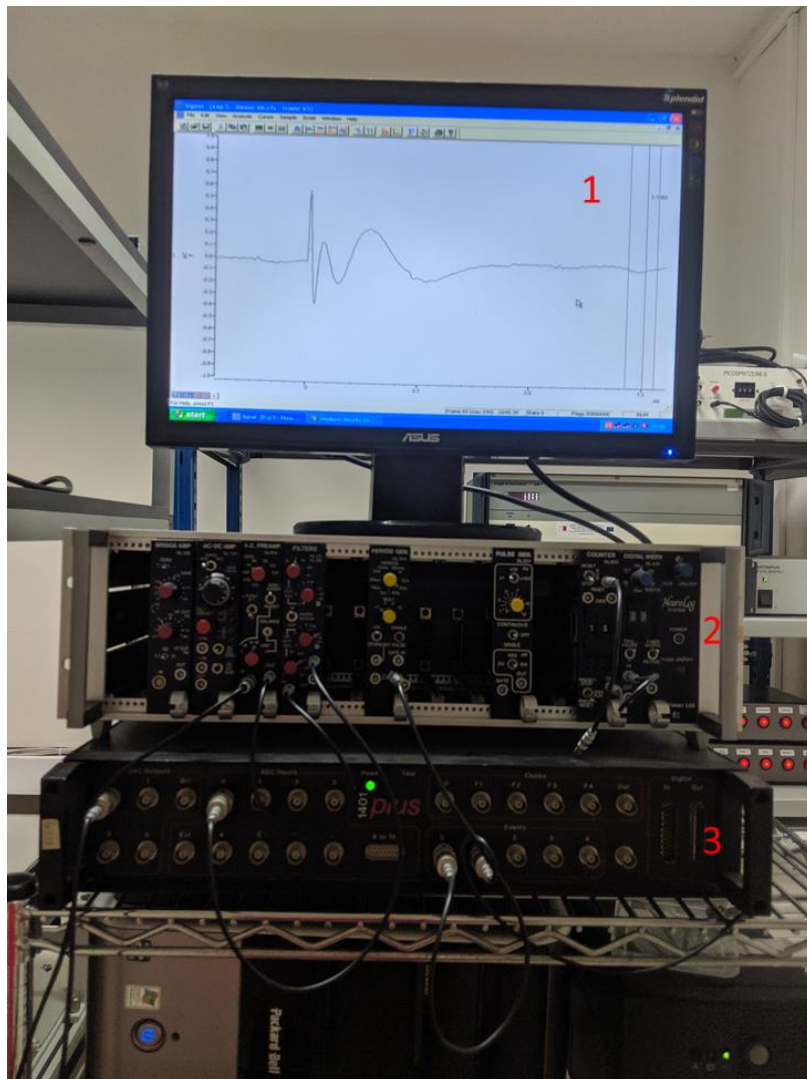


Figure 2.21. Electrophysiology setup for the optic nerve and the brain slice. [1] CAP recorded via Signal 1.9; [2] NeurologTM; 1401 plus data acquisition.

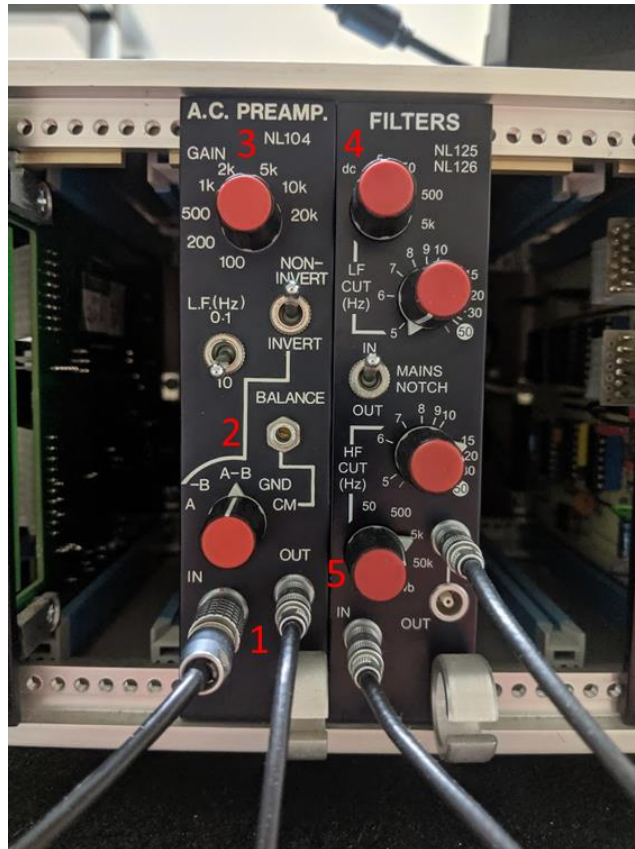


Figure 2.22. The Neurolog™ amplifier. The recording head stage was connected to the amplifier (1). Differential recording was used: signal from input B was deducted from the signal recorded from input A (2). The gain (3) and the low-cut (4) and high-cut (5) filters were kept constant for all the experiments.

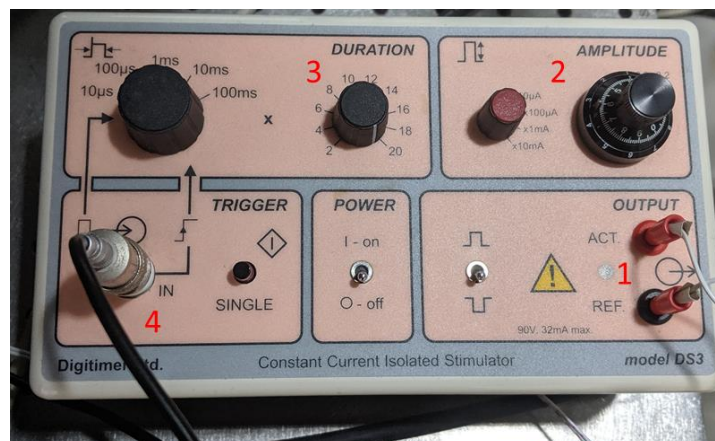


Figure 2.23. The stimulus isolator unit (Digitimer, U.K). The stimulus isolator unit was connected to the stimulating electrode (1). The amplitude (2) and pulse width (3) were gradually increased to optimise the signal-to-noise ratio. The unit was also connected to the 1401 plus data acquisition unit (4) so that a recording is registered every time a stimulus is generated.

2.3.14.1 Optic nerve electrophysiology

The optic nerve preparation is much easier and straightforward than the preparation of callosal slices. The optic nerve is more robust and can withstand minor traumatic events without permanent injury. A low- Na^+ , high-sucrose cutting solution is not required for its dissection and 20 – 30 min is usually sufficient for optic nerves to stabilise before recording (compared to the 2 hours of stabilisation required in brain slices).

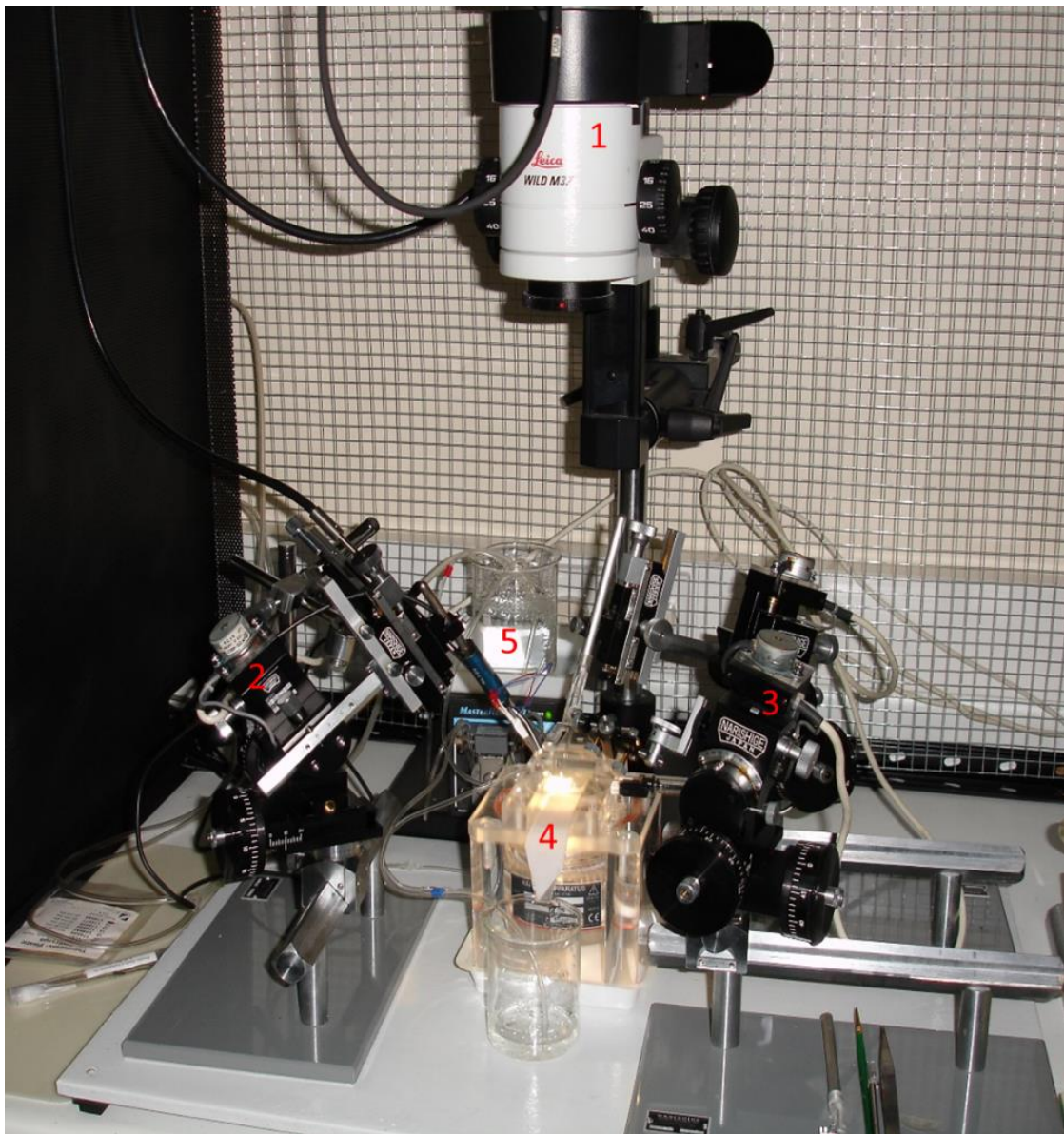


Figure 2.24. Electrophysiology rig used to record CAP from the optic nerve. The optic nerve was placed in the interphase chamber (4) and gently snug in the stimulating and recording electrodes visualised using the upright Leica Wild M3Z microscope. The electrodes were fixed to 2 manipulators (2 and 3), and the nerve was continuously perfused with aCSF (+/-) glucose.

We used modified suction electrodes (Stys *et al.*, 1991) to record from the optic nerve. We fabricated two L-shaped fused capillaries as the recording electrode (Fig. 2.25 – 1) and a single L-shaped capillary tube as the stimulating electrode (Fig. 2.25 – 2) and. A silver wire (LS 120493; Goodfellow) was threaded into the stimulating capillary tube (Fig. 2.25 – 2C) and another one was wrapped around the glass tip (Fig. 2.25 – 2D). Both wires were connected to the stimulus isolator unit (Fig. 2.25 – 2E). The two capillary tubes forming the recording electrode were taped together (Fig. 2.25 – 1), with a silver wire inserted in each, and connected to a head-stage (Fig. 2.25 – 1A and B) in series to an amplifier and 1401 plus data acquisition. The stimulus generator produced a current at the recording electrode between the two silver wires, which travelled through the optic nerve and was picked up from the capillary tube in which the nerve was inserted (Fig. 2.25 – G). The signal from the other capillary tube (Fig. 2.25 – H) was deducted from the latter (differential recording) to eliminate the background noise, thus ensuring that the signal was the actual summation of all the action potentials from the axons within the optic nerve.

From the *in vitro* experiments conducted on the optic nerve in interphase chambers it was very clear that the magnitude of the flow rate of the circulating media was critical in order to acquire a stable readout. A minimal increase in the flow rate caused a rise in the level of the circulating media with a dramatic reduction in signal amplitude. Since live imaging experiments require the tissue to be submerged beneath a column of media, such a combination of live imaging and electrophysiology experiments could not be permitted for the optic nerve preparation. With this in mind, we chose to use the acute brain slice as this allows for the perfusion of the slice across a thin column of perfusate without effecting the extracellular signal recording.

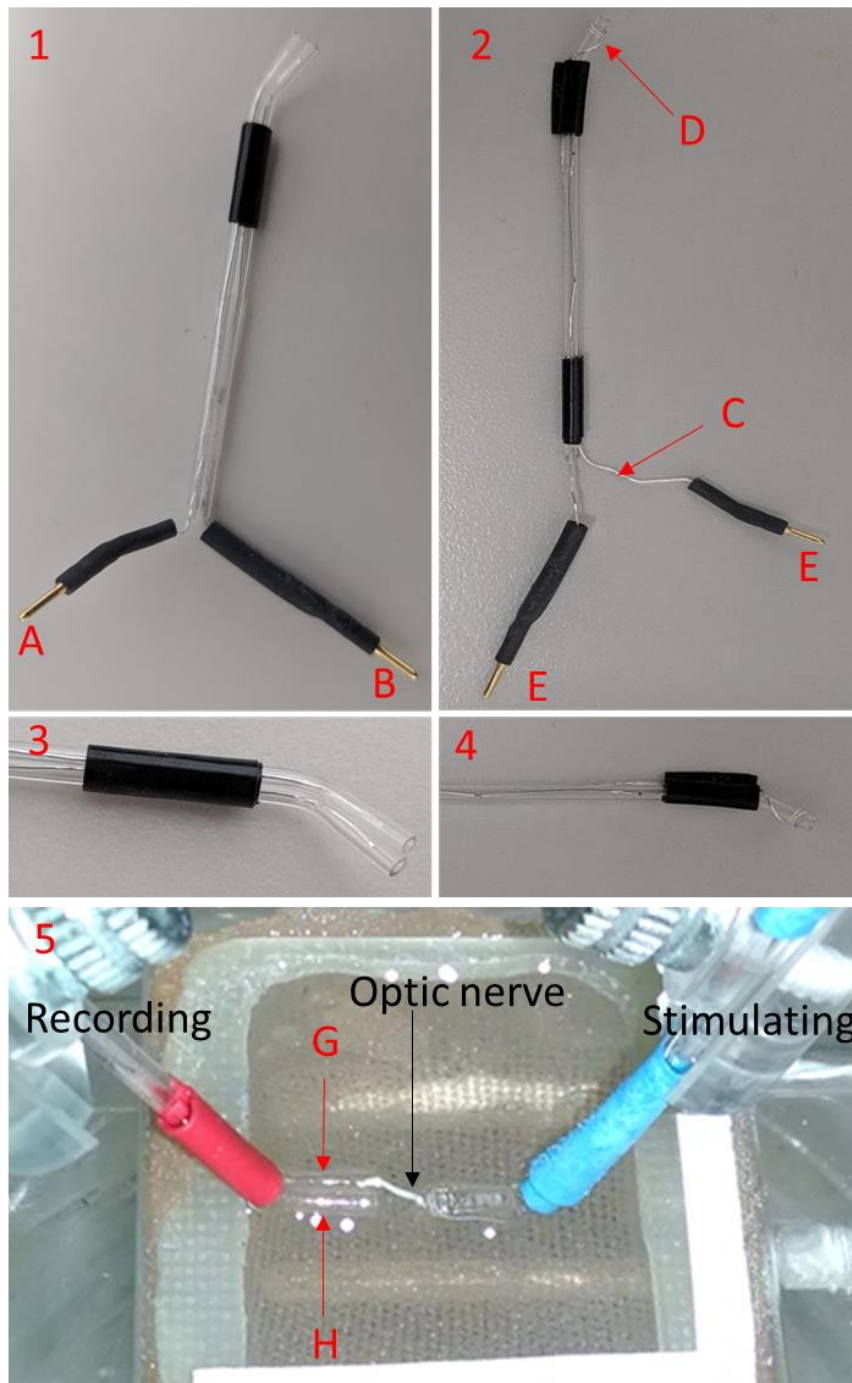


Figure 2.25. Electrodes used for CAP recording from the mouse optic nerve. 1 – double barrelled recording electrode (zoomed in 3); 2 – single barrelled stimulating electrode (zoomed in 4). [A-B] the silver wires of the recording electrode were connected to a head stage in line with an amplifier and data acquisition; [C-D] two silver wires of stimulating electrode, both of which connected to the stimulus isolator unit [E-F]; 5 – optic nerve inserted in the stimulating electrode and in one of the capillaries of the recording electrode. The signal recorded from the capillary tube H was deducted from that recorded from capillary tube G (differential recording).

2.3.14.2 Callosal brain slice electrophysiology

A stable recording from the callosal slices is quite challenging. Numerous studies utilised a metal bipolar stimulating electrode (with a tip distance in the range of 75-250 μm) and pulled recording glass electrodes filled with either 2.0 M NaCl or standard aCSF (Tekkök and Goldberg, 2001; Baker *et al.*, 2002; Reeves *et al.*, 2005). In our hands, these parameters did not give us the required CAP signal as the signal to noise ratio was very low.

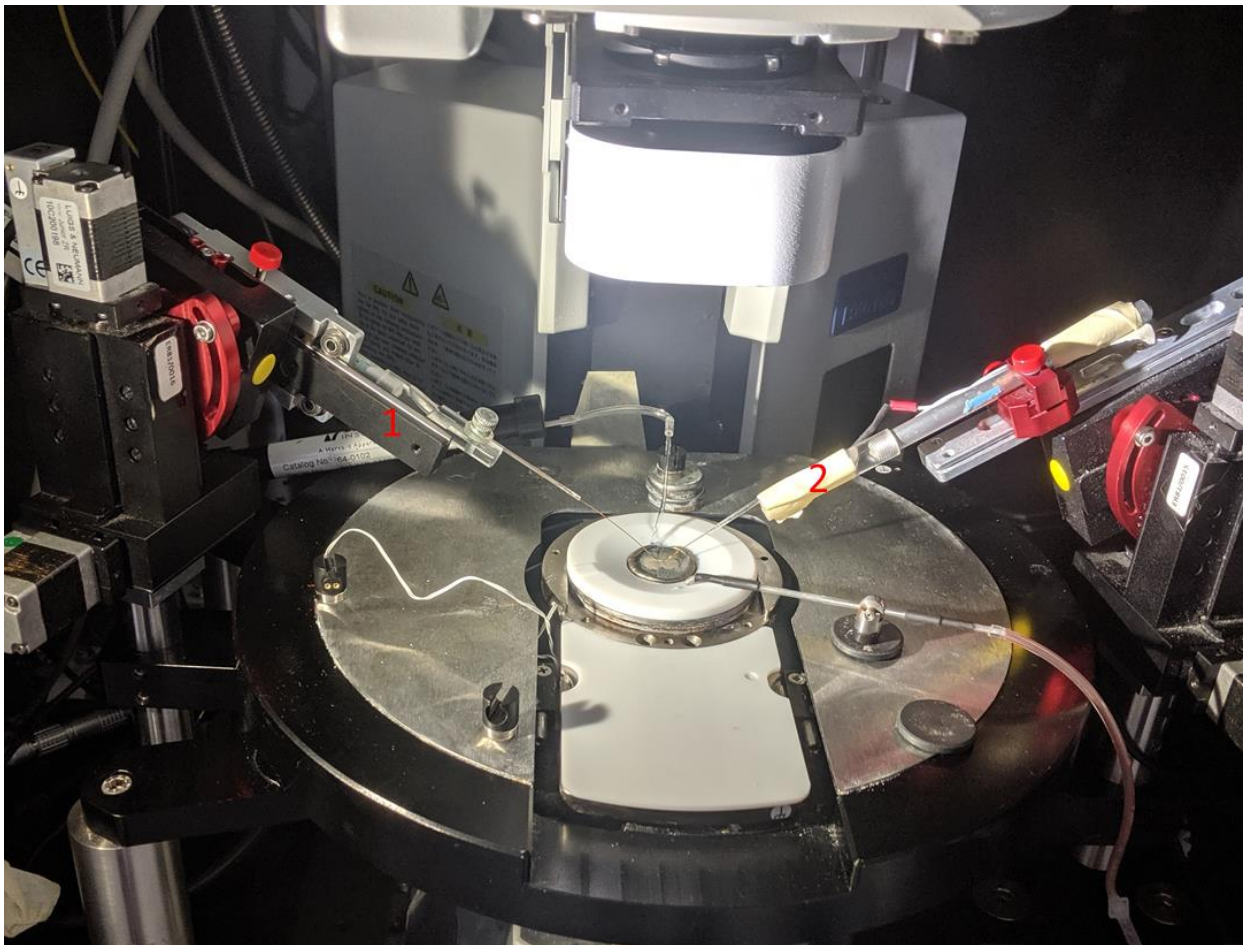


Figure 2.26. Electrophysiology rig used to record CAP from the callosal brain slice. The holding chamber and perfusion setup are similar to that used for live imaging. The recording (1) and stimulating (2) electrodes were connected to motorised manipulators and gently placed on top of the callosal slice.

A modification we made to these parameters documented in literature yielded reproducible results. We used 2 very fine stainless-steel rods (#100194; California Fine Wire Company) coated with an insulating material for both the stimulating and recording electrodes. For the stimulating electrodes (Fig 2.27 – 2), approximately 1mm of insulating material was removed from the tip (Fig 2.27 – red double-sided arrow), and the two tips were gently separated to approximately 500 μm – 1 mm apart (Fig 2.27 – blue double-sided arrow). These were placed on each side of the corpus callosum under low power magnification (top and bottom of one end) (Figure 2.28 – *Right*). As to the recording electrode (Fig 2.27 – 1), the insulating material was removed from a similar area to about 1 mm (Fig 2.27 – red double-sided arrow), with the two electrode tips separated by approximately 2mm – 3mm apart (Fig 2.27 – black double-sided arrow). One of the tips was placed directly on the corpus callosum and the other was kept at a distance and touching the grey matter (Figure 2.28 – *Left*). The stimulating electrode was connected to a stimulus isolator unit, and the recording electrode to a head-stage and in series to that an amplifier and 1401 plus data acquisition. This differential recording allowed for the output signal generated from the rod placed on the grey matter (Figure 2.8 B) to be subtracted from that obtained from the rod placed on the corpus callosum (Figure 2.8 A) and thus ensure that the evoked response was exclusive to the fibres crossing the corpus callosum across the two electrodes.

This setup enabled us to record stable evoke responses across the corpus callosum over time in the interphase chambers. These same parameters were also employed in the submersible chamber with satisfactory results as an increase in the column of water decreased the background noise which allowed for the increase in signal gain to ‘detect’ the smaller evoked responses.

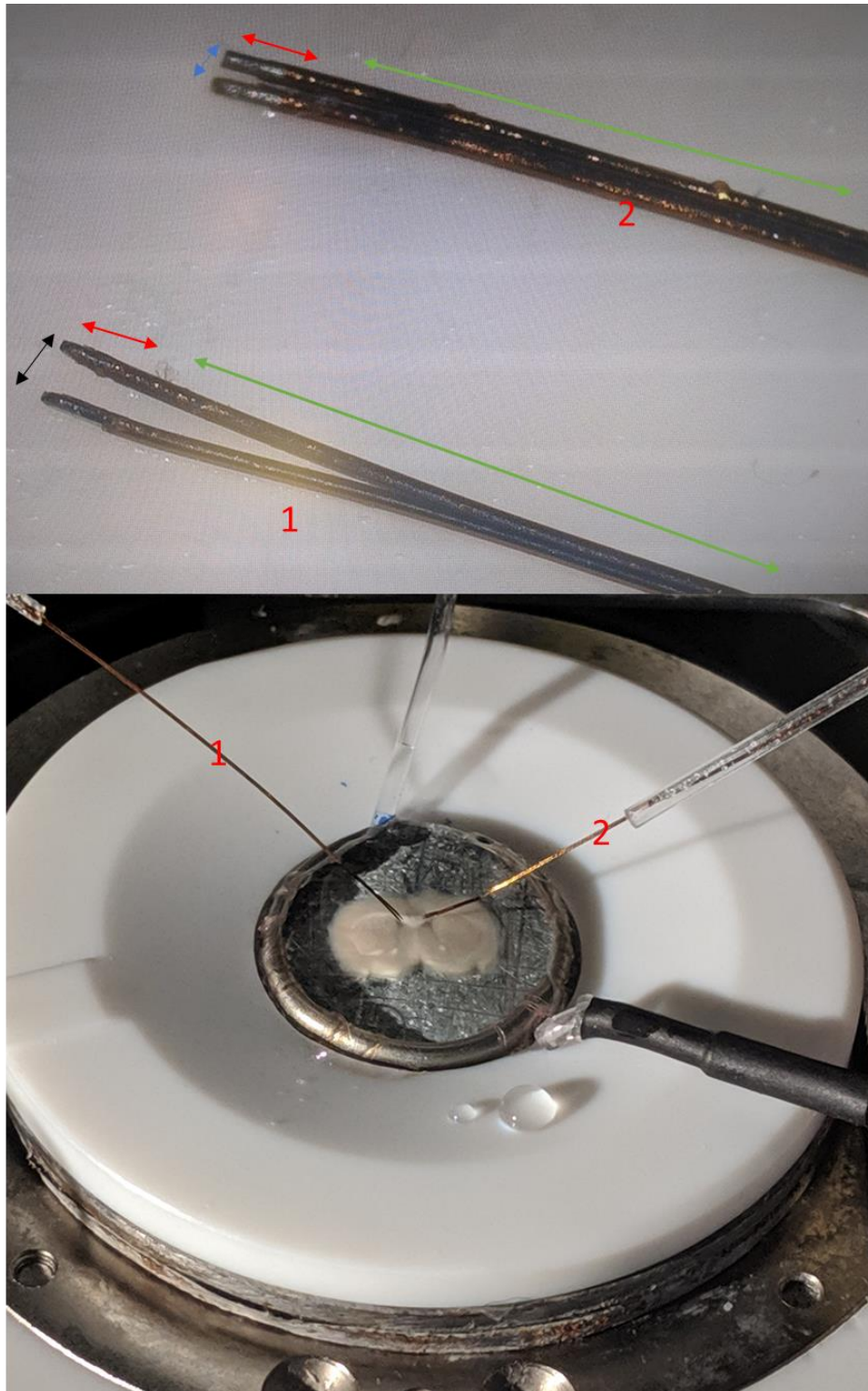


Figure 2.27. Electrodes used for CAP recording from the callosal brain slice. 1 – double barrelled recording electrode (zoomed in 3); 2 – single barrelled electrode (zoomed in 4). 5 – optic nerve inserted in both electrodes.

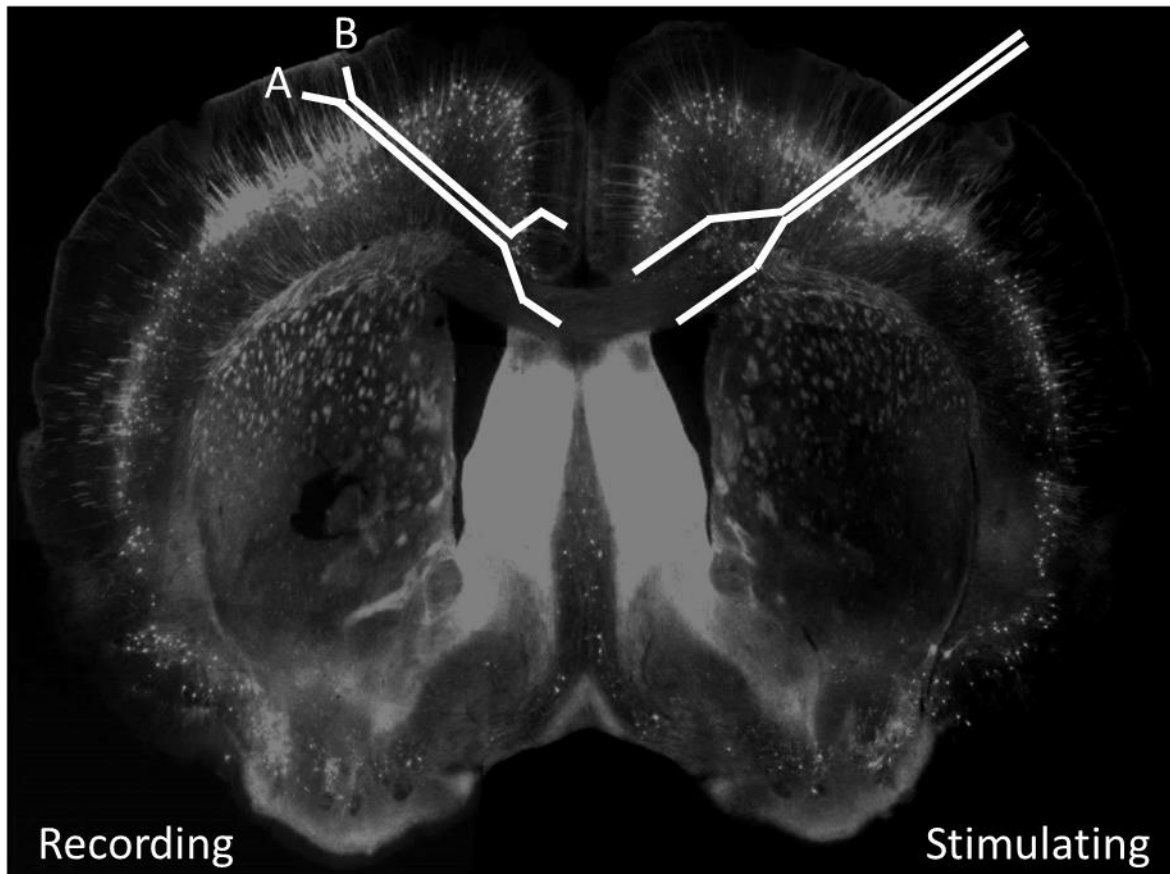


Figure 2.28. Distribution of the recording and stimulating electrodes for CAP recording from callosal fibres in the brain slice. Right: Two stainless steel electrodes placed on each hemisphere and along each end (top and bottom) of the corpus callosum. Left: One of the recording electrodes (A) placed along the midline of the corpus callosum and opposite the other hemisphere that contains the stimulating electrode at the other end of the corpus callosum. The differential electrode (B) is placed in the grey matter. The differential recording subtracts the signal obtained in B from A, to generate the evoked CAP response.

2.3.15 Recording of the compound action potential

After letting the brain slices rest for about 2 hours in the holding chamber, one of them was transferred to the submerged chamber. The flow rate was adjusted to about 3 ml/min, and the temperature was gradually increased to 37°C +/- 1°C. The electrodes were then gently lowered onto the brain slices until they were just touching the surface of the brain. The setup was left to rest for another 30 mins.

After the stabilisation phase, the pulse width and amplitude were gradually increased until an optimal signal was achieved. The position of the recording electrode was also changed in order to achieve the best sign to noise ratio. When an acceptable signal was achieved, a 125% supramaximal stimulus was delivered every 30 seconds. After a stable recording of at least 30 minutes, GD was initiated. This was done by perfusing the brain slice with aCSF devoid of glucose (replaced by sucrose to keep the osmolality constant). At the end of the period of GD, the brain slice was perfused again with glucose containing aCSF for another 2 hours.

2.3.16 Data analysis of compound action potential recording

Data was recorded on Signal 1.9 and saved for offline analysis. The area under the graph of each signal was recorded and referred to as CAP recording. The area under the CAP during stabilisation was averaged, and each time point was expressed as a percentage of the averaged baseline. One-way ANOVA followed by a Tuckey post-hoc test was done to compare the percentage CAP recovery following GD between different experimental protocols.

2.4 Results

2.4.1 Visualisation of axon structure with YFP-expressing callosal slices

In preliminary experiments we used conventional two-photon microscopy to visualise axon structure and the expression of YFP in 400 μm brain coronal slices in which the anatomical structure of the axonal tracts was clearly visible.

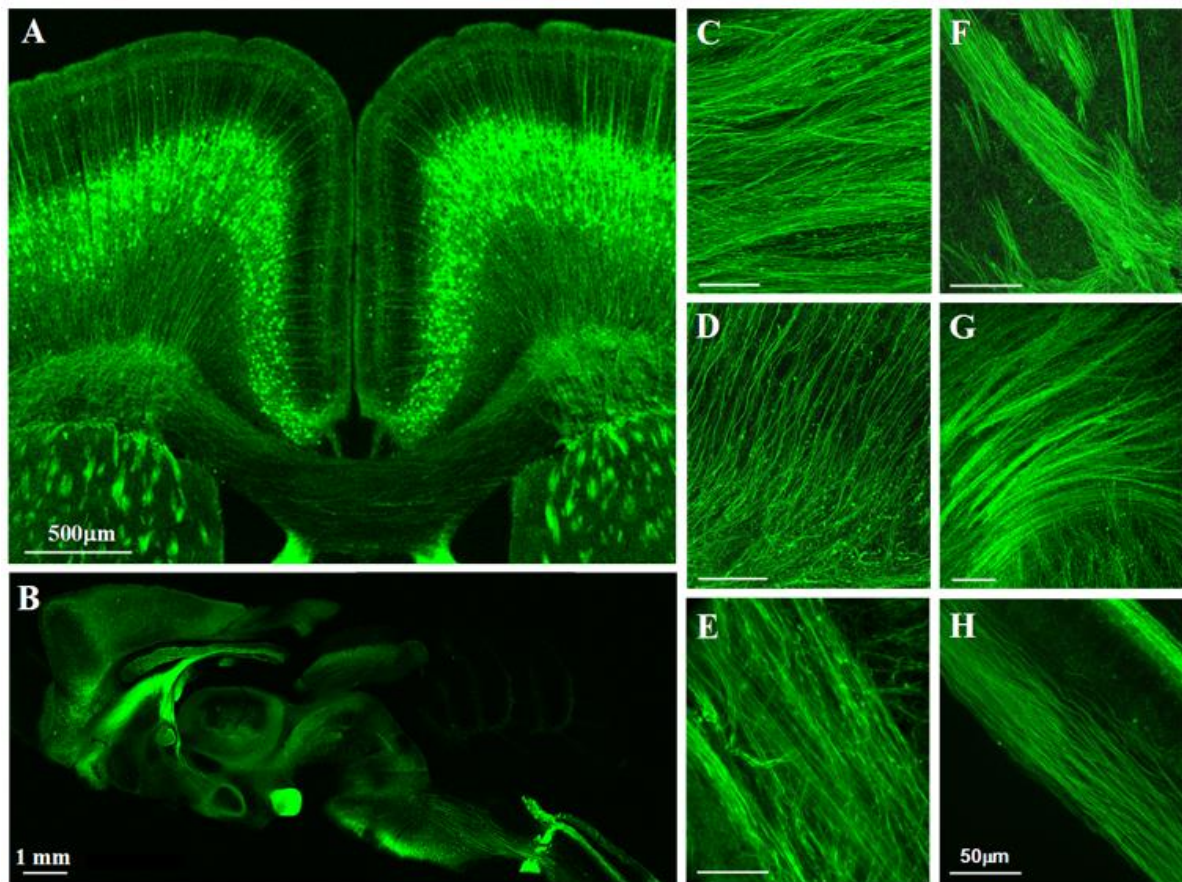


Figure 2.29. Visualization of axon morphology in transgenic mice (Thy1-YFP line H) with neuron-specific expression. Low magnification fluorescence micrographs of fixed brain sections in coronal (A) and sagittal (B) views show the expression and distribution of YFP-expressing axons. Note in A, the intense expression in cortical layer 5 neurons, with distinct axonal projections toward striatum and corpus callosum. C through H demonstrate the normal arrangement of fibre tracts with strong expression of YFP at higher magnification: (C) genu of corpus callosum, (D) cingulum, (E) external capsule, (F) striatum, (G) anterior commissure, (H) spinal cord.

Figure 2.30 shows a typical 400 μm thick YFP-H mouse brain coronal slice. A 4x lens was used to locate the middle of the corpus callosum (red box in Fig 2.30 A). This was replaced with a 25x lens to be able to get a higher magnification of individual groups of axons (Fig 2.30 B) and study in detail their morphology.

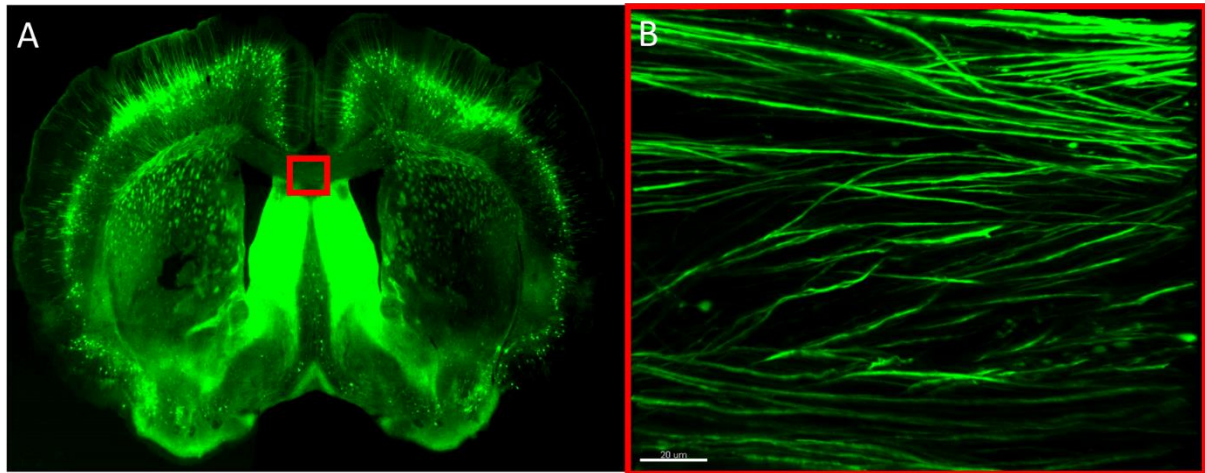


Figure 2.30. Coronal brain slice of YFP-H mouse. [A] Low power image of a YFP-H mouse brain coronal slice; red box – area of corpus callosum that was imaged. [B] High magnification of individual groups of axons in the corpus callosum showing healthy YFP-expressing axons after 2 hours of incubation. Scale bar: 20 μm

Live two-photon microscopy allowed us to image healthy appearing YFP-expressing axons restricted to a depth corresponding to within 50-80 μm below the surface. Within this depth, cutting damage in brain slice preparation is very limited. At greater depths, the fluorescence signal dropped off substantially. The decrease in the depth of detectable signal in white matter is thought to be due to the efficient light scattering properties of myelin. Cutting damage typically extended approximately 40 μm into the slice from the surface. The maximum depth of imaging reached for the callosal axons extended to 120 μm .

2.4.2 Progression of injury in YFP-expressing axons

A gradual change in the structure of the YFP-expressing axons was noticeable throughout the duration of our experiments. At the start of the experiment we made sure that most of the axons in the field of view were morphologically intact. Slices with a high number of injured axons were discarded.

Intact axons had linear profiles, with absence of focal swelling (Fig 2.31 A). The first sign of axonal injury was localised focal swelling (Fig 2. 31 B), followed by beading (Fig 2. 31 C) and fragmentation (Fig. 2. 31 D). An in-depth analysis of these injury hallmarks enabled us to extrapolate an axonal injury score for the duration of each experiment.

An interesting feature that was observed was that the smaller diameter axons were more vulnerable to injury than those with larger calibre. In fact, small diameter axons ($< 1\mu\text{m}$) showed earlier signs of injury after the insult (Figure 2.32). We followed the progression of injury of axons with a larger diameter ($> 2\ \mu\text{m}$), as these were easier to visualise. In experiments utilising interchangeable experimental protocols, we ascertained to compare axons of similar diameter to avoid bias.

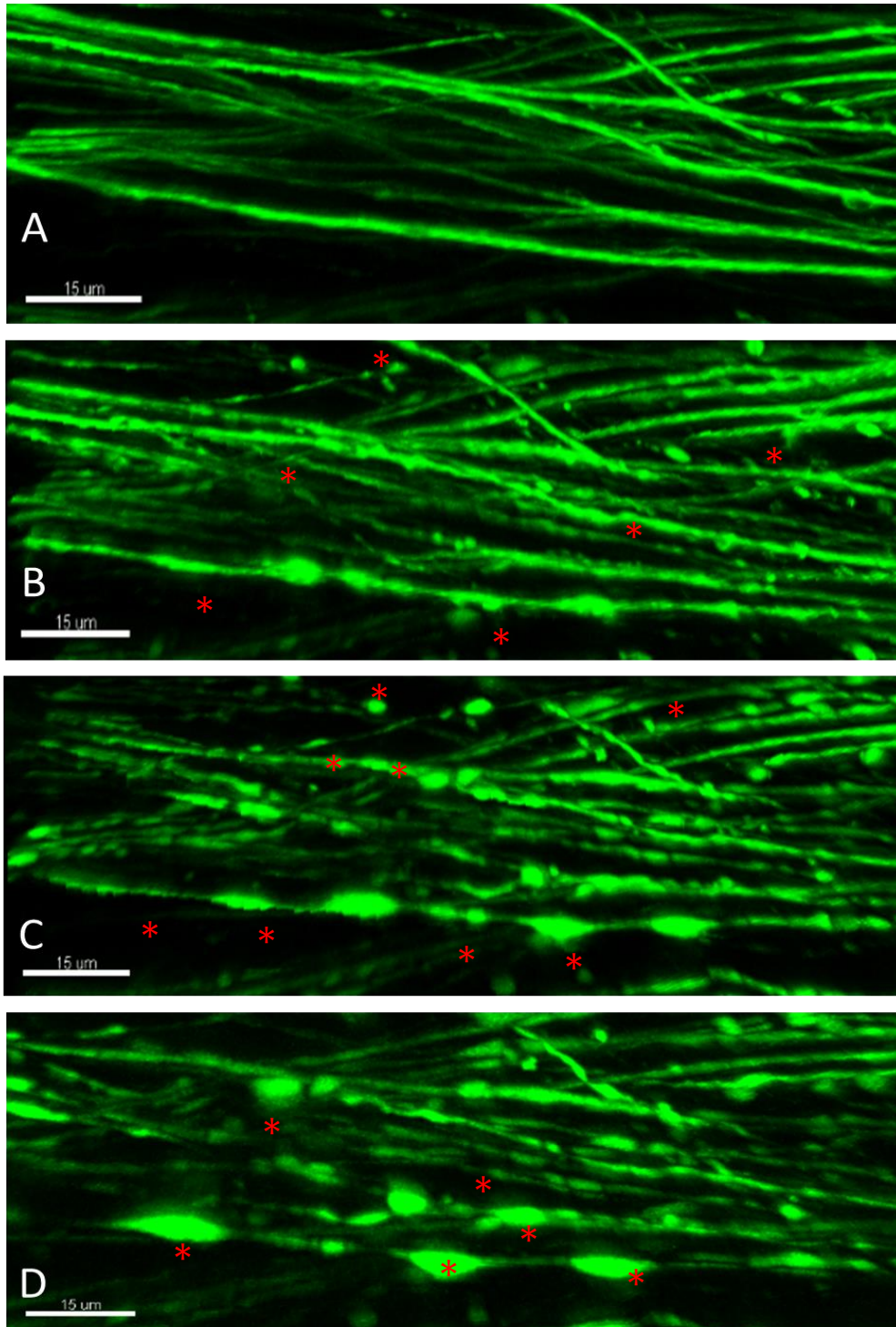


Figure 2.31. Progression of injury in YFP-expressing axons. (A) Intact axons show linear profiles with no evidence of structural injury. (B) Initial signs of axonal injury – formation of focal swelling (*). (C) Progression of axonal injury – axonal beading (*). (D) Terminal stage of axonal injury – fragmentation and axonal transection (*). Scale bar: 15 µm

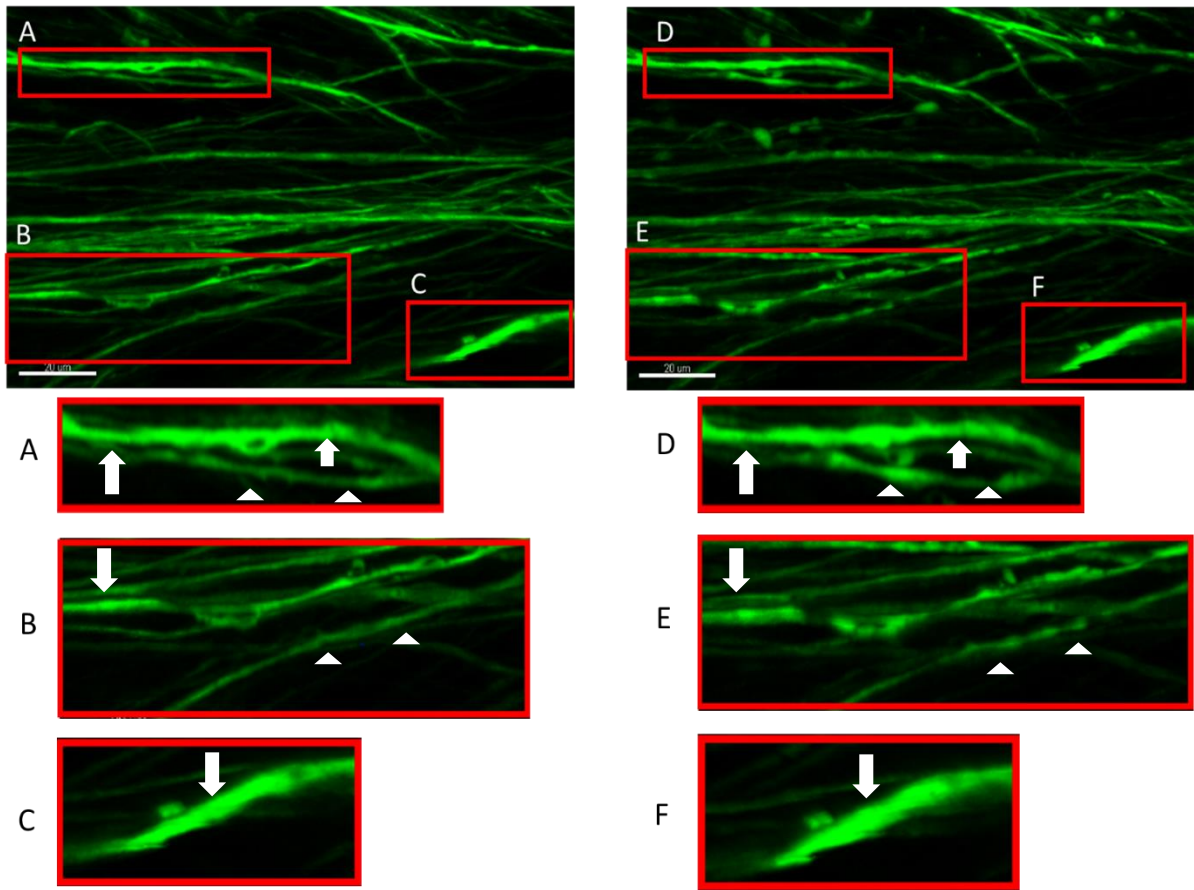


Figure 2.32. Small calibre axons are more vulnerable to injury by GD than the larger calibre axons. Left: Start of experiment – healthy axonal fibres. Right: The same axonal fibres following a mild insult exhibit some damage to axonal profiles. (A – F) high magnification of the insets above. Arrowheads point to healthy low calibre axons (A and B) and the commencement of focal swelling in the same axons following a mild insult (D and E). Arrows indicate healthy large calibre axons at the start of the experiment (A – C), with no evidence of focal injury after the insult (D – F). Scale bar: 20 μm .

2.4.3 Expression of YFP correspond to other common techniques commonly used to study axon integrity

In preliminary experiments we used conventional confocal fluorescence microscopy to compare changes in YFP-expressing axons with conventional immunocytochemistry for SMI 31 neurofilaments. This was later extended to also include assessment of axonal integrity through conventional light and electron microscopy.

The advantage of using transgenic mice with neuron-specific expression of the green fluorescent protein, YFP, under control of a thy1 promoter was the ease of visualisation of the morphology of individual axons. The usefulness of this model for assessment of axon morphology was shown in its close correspondence between other traditional methods commonly used to evaluate axon integrity. In control fixed tissue, YFP-expressing axons were easily visualised as bright and linear fluorescent fibres running across the corpus callosum. This allowed us to trace individual fibres over long distances with highly defined spatial resolution. Such result was compared to typical neurofilaments labelled by SMI-31 immunostaining which showed bright and linearly organised axonal fibres.

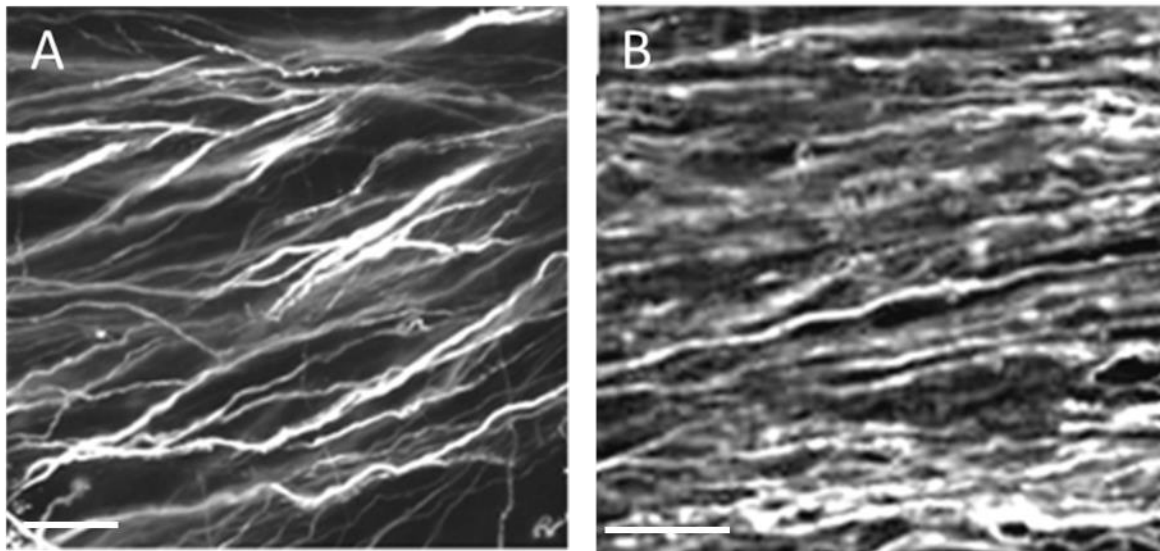


Figure 2.33. Comparison between YFP-expressing axons and SMI-31 immunostaining. (A) Confocal fluorescence of YFP-expressing axons; (B) immunofluorescence for SMI-31 recognition of phosphorylated neurofilaments. Scale bar: 10 μm

Light microscopic examination of the axons in the corpus callosum showed a heterogeneous array of small and medium-diameter axons with round or slightly oval profiles surrounded by compact myelin (Figure 2.34 A). At higher magnification through EM almost all axons above a certain diameter were observed to be myelinated and the thickness of the sheath generally corresponded to the calibre of the axon. The axoplasm was observed to be relatively lucent and granular. This was packed with a rich and organized network of microtubules and neurofilaments. Mitochondria appeared normal. Non-myelinated axons were typically of smaller calibre and observed to be present in groups of clusters between myelinated axons revealing a tightly compact and close association (Figure 2.34 B).

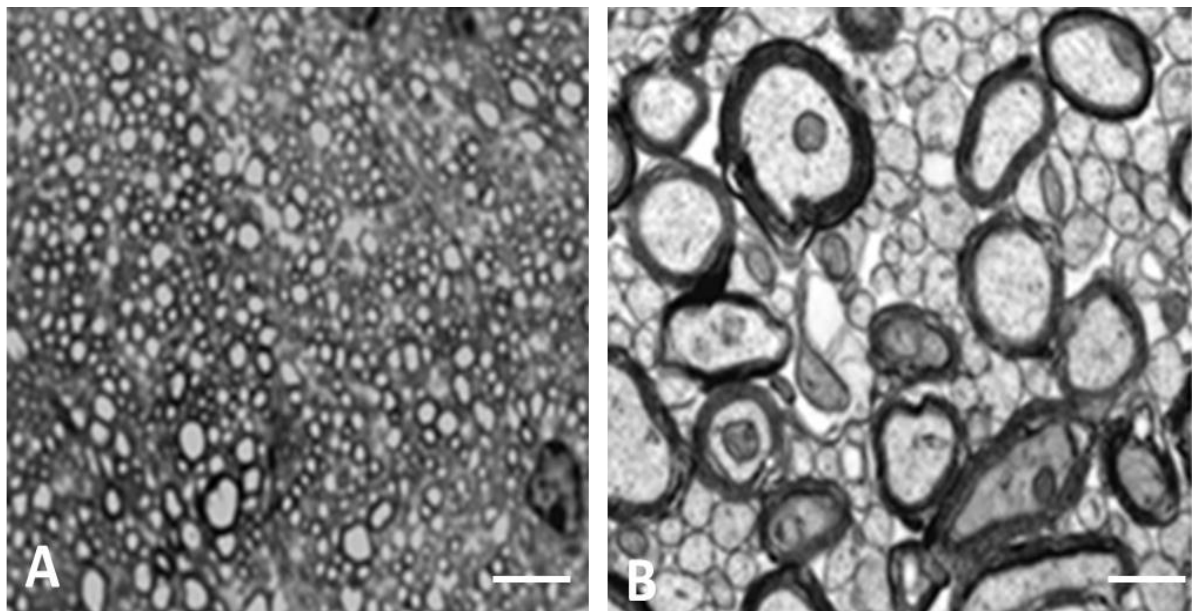


Figure 2.34. Brightfield and EM showing normal-appearing axonal ultrastructure including preserved myelin. (A) bright-field microscopy of semi-thin sections stained with toluidine blue, scale bar: 50µm; (B) ultra-thin section at the level of electron microscopy, scale bar: 2µm.

2.4.4 Axonal survival is dependent on the duration in glucose deprivation

After the 2-hr stabilisation period in the holding chamber, control slices were perfused with glucose-containing aCSF at 37°C for a period of 4 hr in the imaging chamber under the two-photon microscope. An image was acquired at every 1-hr interval to confirm the health status of the slices (Fig. 2.35 D). Experiments were only conducted on slices with healthy axonal profiles around the genu of the corpus callosum that were free from any signs of injury. The axonal injury score was calculated for each control slice and no significant difference in the injury score was found between each trial.

There was no evidence of axonal injury in slices during 15 (Fig. 2.35 A) and 30 (Fig. 2.35 B) min of GD, or during the 2-hr reperfusion with glucose containing aCSF. Focal swellings along the axons was observed by the end of 45 min of GD, which progressed to beading, fragmentation and axonal transection during reperfusion with glucose containing aCSF for up to 2 hr (Fig. 2.35 C). The axonal injury score was calculated for each experimental condition at each time point (Fig 2.36). A One-way-ANOVA followed by a Tuckey post hoc test was performed to compare the injury score between groups. The results are summarised in table 2.5.

	Start	GD	REP 1 hr	REP 2 hr
GD 15 min	0.26 ± 0.05	0.28 ± 0.06	0.29 ± 0.06	0.30 ± 0.04
GD 30 min	0.17 ± 0.06	0.26 ± 0.06	0.29 ± 0.06	0.32 ± 0.06
GD 45 min	0.23 ± 0.02	0.44 ± 0.10*	0.97 ± 0.13#	1.53 ± 0.11#
Controls	0.27 ± 0.05			

Table 2.5. Injury score of callosal slices exposed to variable lengths of GD in comparison to controls. Numbers are expressed as mean scores ($n = 3$) ± (SDV). There was no significant difference in injury scores between the control group and slices exposed to 15- and 30-min of GD for every time-point examined. A statistically significant difference in axonal injury score was found in group of callosal slices after exposure to 45 min of GD and after 1 hr and 2 hr of reperfusion, when compared to those groups that were only exposed to 15- and 30-min GD and the controls. (* $p = < 0.05$; # $p = < 0.001$)

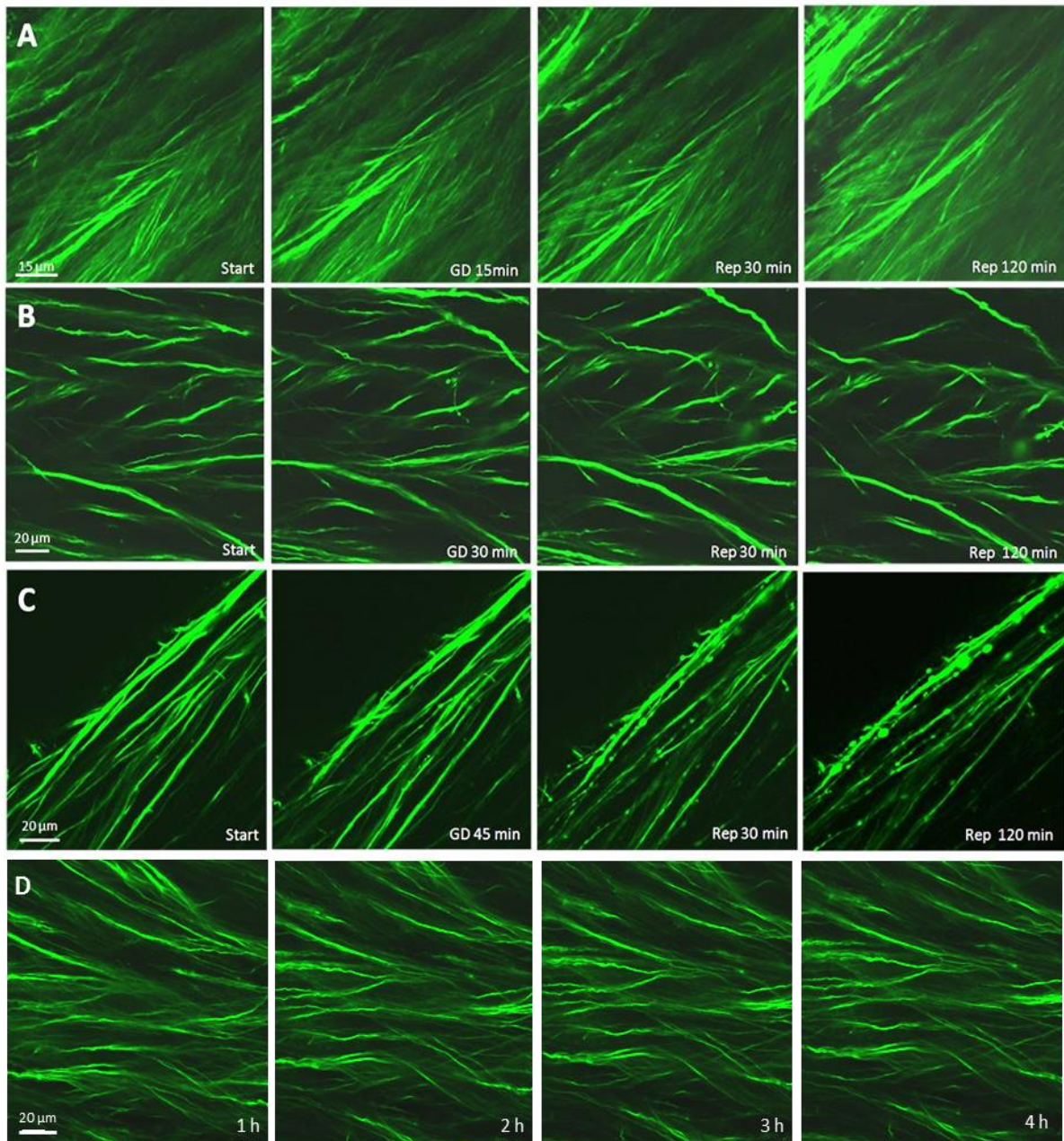


Figure 2.35. Sequential time frames that compare the integrity of axon profiles in c slices exposed to variable exposures of GD. There are no evident signs of axonal injury in slices exposed to 15 mins [A] and 30 min [B] of GD. There is focal swelling of axons at the end of 45 mins GD, which progressed to beading and fragmentation during the reperfusion phase [C]. There is complete preservation of healthy axon profiles in control slices kept in glucose-containing aCSF for 4 hours [D]. Scale bar: 20 μ m

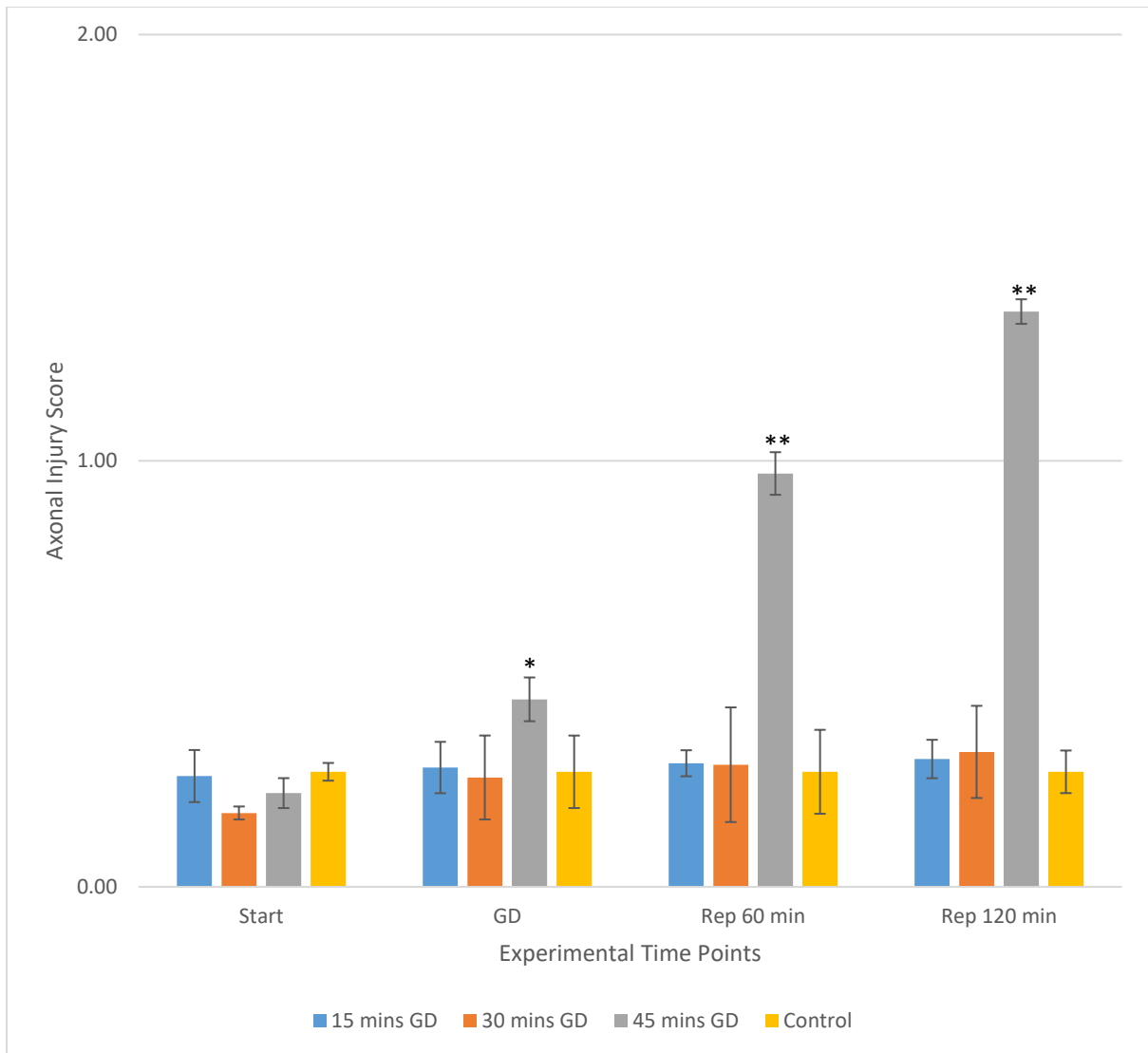


Figure 2.36. Comparison of axonal injury score between various extents in the duration of GD at different time points. There is no statistically significant difference between controls and those groups exposed to 15- and 30-min of GD. There was a statistically significant difference between slices exposed to 45 mins of GD to slices exposed to 15- and 30-min of GD and the controls. (* $p < 0.05$; ** $p < 0.001$)

2.4.5 Histopathological hallmarks of axonal injury in glucose deprivation

2.4.5.1 Pathological features of axonal injury from glucose deprivation

Live imaging enabled us to establish that reperfusion after 45 min of GD causes irreversible damage to axons. We then focused our efforts to look in some detail into the extent of white matter injury in terms of histopathological hallmarks of glucose deprivation in fixed slices that were equally exposed to GD.

In conformity with our previous findings, confocal images of fixed brain callosal sections from YFP mice exposed to 45 min of GD, showed the typical intact latent period of preserved axons seen immediately after the insult. Injury resolved abruptly during the first 30 min of reperfusion in single axons and this involved fragmentation of axons. By the end of 2 hr of reperfusion, there was extensive beading and fragmentation of the YFP axons. The linear organisation and continuity was largely lost and pronounced disconnection was evident. The reduction in the number of axons and the concomitant weak YFP signal was very pronounced. The relatively small calibre axons were first to be affected as seen by their earlier fragmentation (Fig 2.37 A).

SMI-31 immunostaining revealed the presence of axonal swellings, fragments of beaded axons and loss in linearity of axons in the corpus callosum by the end of the observation period. This suggests that phosphorylated epitopes of neurofilament sidearms are particularly sensitive to GD. The pattern of immunostaining was disrupted with patches of diffuse areas containing a dense core of disordered neurofilaments with some visible axonal beading and a generalised loss in fluorescence intensity. It is plausible to think that the misalignment of neurofilaments impairs axoplasmic transport resulting in swelling of the axon cylinder, clumping of proteins and axonal disconnection. Neurofilament immunofluorescence techniques demonstrated axon degeneration but did not resolve individual axon cylinders (possibly due in part to the large number of small, unmyelinated axons) (Fig 2.37 B).

Examination of toluidine-stained fixed slices by light microscopy of the slices exposed to 45 min of GD and 2 hr of reperfusion, showed extensive abnormally large axonal profiles with a darkened axoplasm and increased spacing between axons. Fewer glia was apparent, and those present were typically pale and swollen with dense clumping of the chromatin in the nucleus. There were considerable amounts of dark debris, presumably from degenerating glia and axons in the enlarged extracellular space (Fig 2.37 C). Consistent with the light microscopy observations, ultrastructural analysis revealed a direct correlation between SMI-31 immunoreactive head and bulb formations and the severe beading and fragmentation observed in YFP-expressing by the end of the observation time.

Under EM, axoplasmic, glial and some initial signs of myelin pathology was observed. In some but not all axons, the axoplasm appeared dark with swollen mitochondria. There were numerous collapsed axons with large abnormal periaxonal spaces. Some myelin pathology was also observed and was primarily associated with the larger calibre axons ($\geq 5\mu\text{m}$). Damaged myelin showed focal detachment and unwinding of the myelin sheath which in some instances appeared as whorls of unwinded myelin. Most of the larger-calibre axons appeared devoid of microtubules and neurofilaments or with reduced number, often aligned in a disorganised array. Peripheral pooling of what remained of the cytoskeleton elements was noticeable, especially in the more swollen and irregular-shaped axons. A conspicuous observation was the general absence of a large proportion of the small diameter unmyelinated axons that are typically arranged in clusters around the larger myelinated axons in normal tissue and those that were present, typically had swollen mitochondria. Vacuole formation within the axoplasm was almost always evident in the swollen and collapsed larger calibre axons. The vacuoles typically appeared as groups with a small diameter within the axoplasm or as one large empty vacuole (Fig. 2.37 D and Fig 2.38).

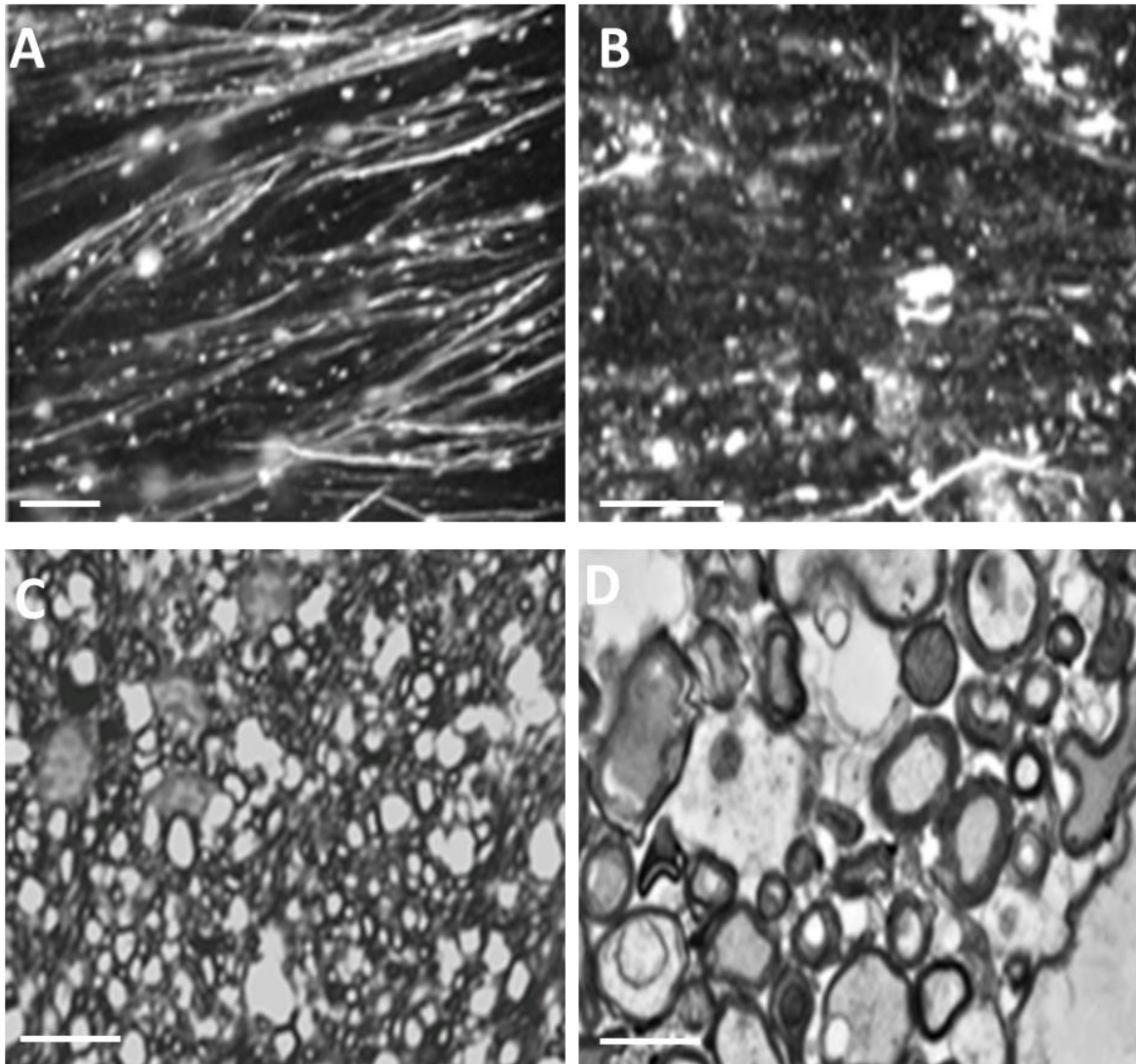


Figure 2.37. YFP fluorescence corresponds to other methods that evaluate axon integrity. Assessment of axon profiles in corpus callosum exposed to 45 min of GD. (A) Confocal fluorescence of YFP-expressing axons, scale bar: 10 μm ; (B) immunofluorescence for SMI-31 recognition of phosphorylated neurofilament, scale bar: 10 μm (C) bright-field microscopy of semi-thin sections stained with toluidine blue, scale bar: 50 μm ; (D) electron microscopy, scale bar: 2 μm .

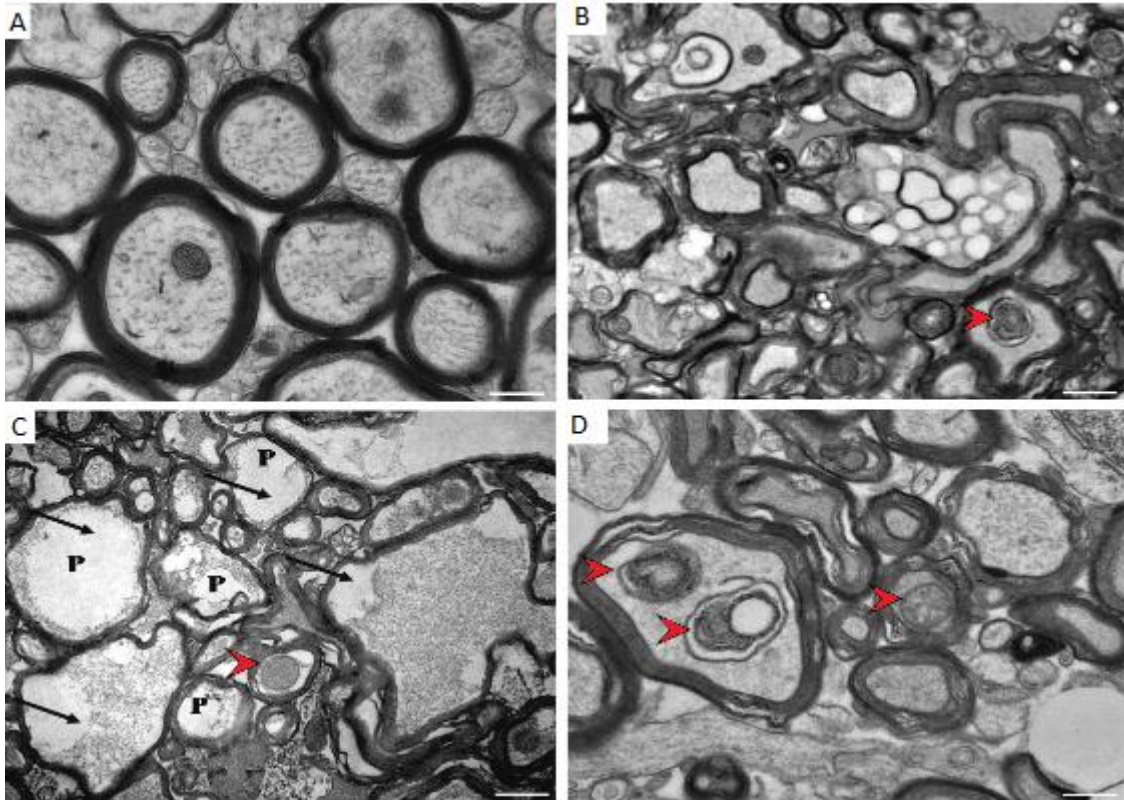


Figure 2.38. Transient GD in brain slices causes ultrastructural disruption of myelinated and unmyelinated axons in the corpus callosum. Electron micrographs (25,000 x) show corpus callosum axons in cross-section after (A) control perfusion, or (B-D) 45 min of GD followed by 2 hr reperfusion. (A) EM shows organisation of myelinated and unmyelinated fibres in the corpus callosum, with normal arrangement of cytoskeletal elements and mitochondria within the axoplasm. Ultrastructural disruption is evident in GD-treated white matter. (B) Swollen axons show degeneration of axonal microtubules and neurofilaments, with vacuoles interspersed in the axoplasm (arrows). The smaller unmyelinated axons are lost and the periaxonal space is enlarged. (C) Arrows indicate irregular-shaped and swollen axons with severe damage and lack of organisation of the cytoskeleton elements. The lucent periaxonal spaces between the axolemma and the inner myelin sheath are very prominent. In some axons there is extensive (P) peripheral pooling and clumping of microtubules and neurofilaments. A lucent space separates the axon from the myelin sheath. (D) Most myelin sheaths are preserved but there is occasional focal detachment and unravelling of myelin. Block arrows point to swollen mitochondria and distorted cristae. Scale bar; 2 μ m.

2.4.5.2 Pathological features of oligodendrocyte injury from glucose deprivation

In semi-thin sections from normal control tissue, oligodendrocytes were identified at the light microscope level as small cells ($\leq 10\mu\text{m}$ diameter) with a round, irregular or oval nucleus and no visible cytoplasm. Characterisation of these cells as inter-fascicular oligodendrocytes was easy, due to their different structural features from clear and dense neighbouring astrocytes, which are electron lucent and contain glycogen granules and fibrils.

Examination by EM showed that the nucleus occupied a prominent eccentric position within the cell and was surrounded in most cases at one pole by a thin rim of cytoplasm. The chromatin formed a prominent clumped pattern around the nucleus. At higher magnification, the rough endoplasmic reticulum, the golgi apparatus and the mitochondria are the prominent organelles within the cytoplasm. These organelles showed a high level of organisation. In all cases, the mitochondria showed no unusual features and had well-defined cristae arranged transversely. They generally appeared 'sunken' within the dense cytoplasm (Peters, 1991) (Fig. 2.39 B - C).

At the light microscopy level using conventional vital stains there was some difficulty to distinguish damaged or shrunken oligodendrocytes after GD. EM of ultra-thin sections from white matter revealed rapid morphologic changes in subcortical white matter oligodendrocytes in response to glucose deprivation after 2h of reperfusion. A great proportion of these cells had a swollen and round nucleus with marked condensation of the heterochromatin. At higher magnification, this was seen as compartmentalised chromatin bodies or as dispersed clumps throughout the nucleus. In some cases, the nuclear envelope was detached from the nucleus and formed extensive blebs or 'pockets' along its periphery. At the subcellular level a number of structural abnormalities were identified. These included the collapse of the golgi apparatus and the extensive swelling with loss of cristae of the mitochondria. A notable feature of pathology found in the greater part of these cells was the extensive mitochondrial swelling and the loss of cristae. In some but not all of the distended mitochondria some cristae were visible but with altered orientation and discontinuity (Fig. 2.39 B - C).

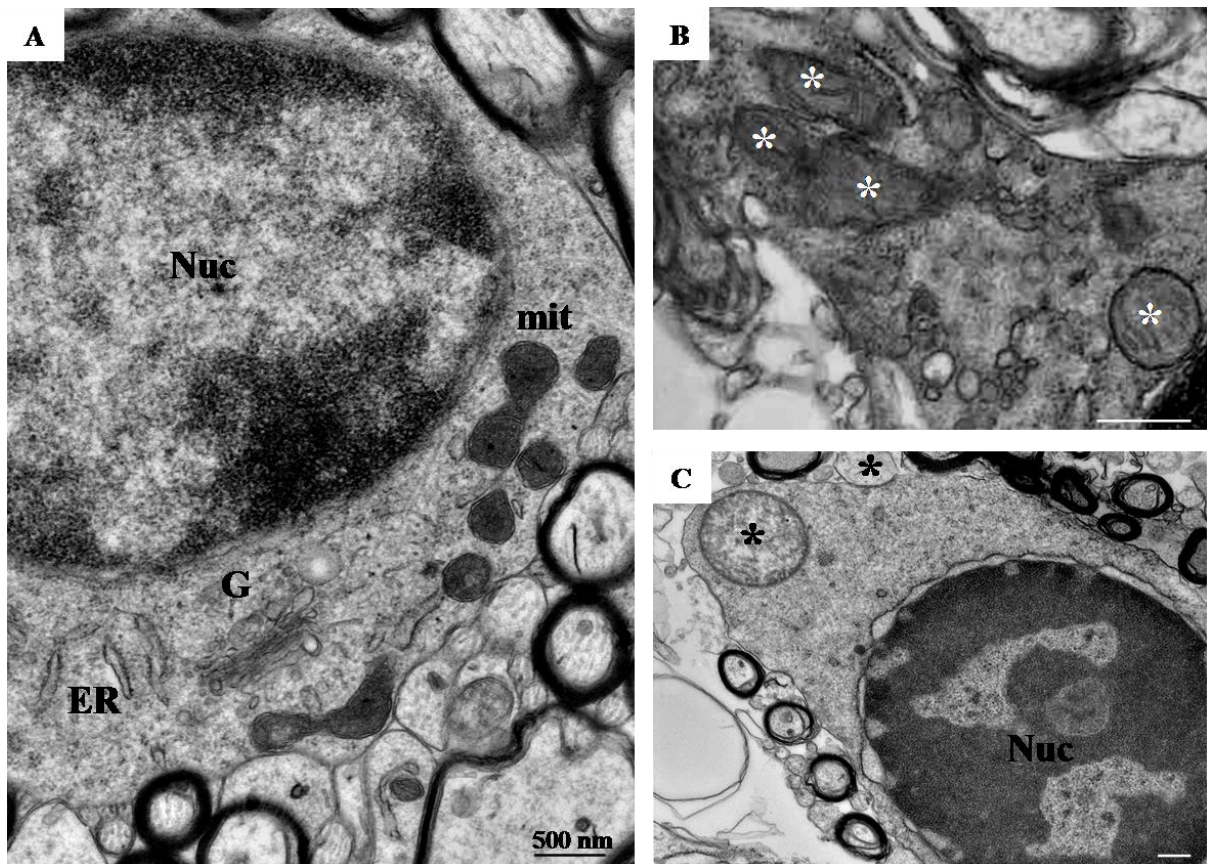


Figure 2.39. Oligodendrocyte pathology following GD. Representative electron micrographs from ultra-thin sagittal sections of brain slices at high magnification showing oligodendrocytes in normal tissue (A) and after exposure to 45 min GD followed by 2 hr reperfusion (B and C). (A) In normal oligodendrocytes there is an even distribution of chromatin within the nucleus (Nuc), and intact nuclear envelope. The cytoplasm contains a matrix of microtubules giving a granular appearance and is laced with normal appearing mitochondria (mit) occurring in groups. The short cisternae of the granular endoplasmic reticulum (ER) and the golgi apparatus (G) are recognizable. (B, C) In post-GD oligodendrocytes, mitochondria are swollen with loss or damage to the cristae (asterisks), dilated golgi apparatus, and vacuoles are present. In some oligodendrocytes, there is distension of the cistern of the nuclear envelope and dense chromatin clumping. Scale bars, 500 nm.

2.4.6 Compound action potential recordings from the optic nerve and callosal slice during normal physiology and following glucose deprivation

The CAP profile and shape recorded from the optic nerve was different from that obtained from the callosal slices and so were the electrophysiological parameters necessary to stimulate and generate a response. Table 2.6 summarises the parameters used for both setups.

	Brain Slice	Optic Nerve
Incubation	2 – 3 hours	20-30 mins
Stimulating electrode	Stainless steel: 500 μm – 1 mm tip separation; removal of 1mm of insulating material	Suction electrode (silver wire)
Recording electrode	Stainless steel: 2mm – 3mm tip separation; removal of 1mm of insulating material	Suction electrode (silver wire)
Stimulating Pulse Amplitude	1.5 – 3.5 mA	1.5 – 3.5 mA
Stimulating Pulse Width	20 – 50 μsec	20 – 50 μsec
Flow rate	3-4ml/min	3-4ml/min
Filtering	100 – 50000Hz	100 – 50000Hz
Action potential	0.5-1.5 mV	0.5-1.5 mV

Table 2.6. Parameters used for recording CAP from corpus callosum in brain slice in comparison to the optic nerve.

The recorded CAP signal from the *optic nerve* presented with the typical triphasic pattern. Each peak represents groups of axons with different extent in myelination, with the first peak representing the highly myelinated axons (fastest conduction), and the last peak by the least myelinated axons (slowest conduction). On the other hand, the CAP profile from the *corpus callosum* had the typical biphasic pattern. The average speed of the first peak was calculated to be in the order of 3.31 ± 0.19 m/sec ($n = 5$), whilst that for the second peak was 1.33 ± 0.25 m/sec ($n = 5$). This suggests that both peaks comprised of myelinated axons, with the first peak representing a population of axons with a higher degree of myelination, resulting in a faster conduction speed.

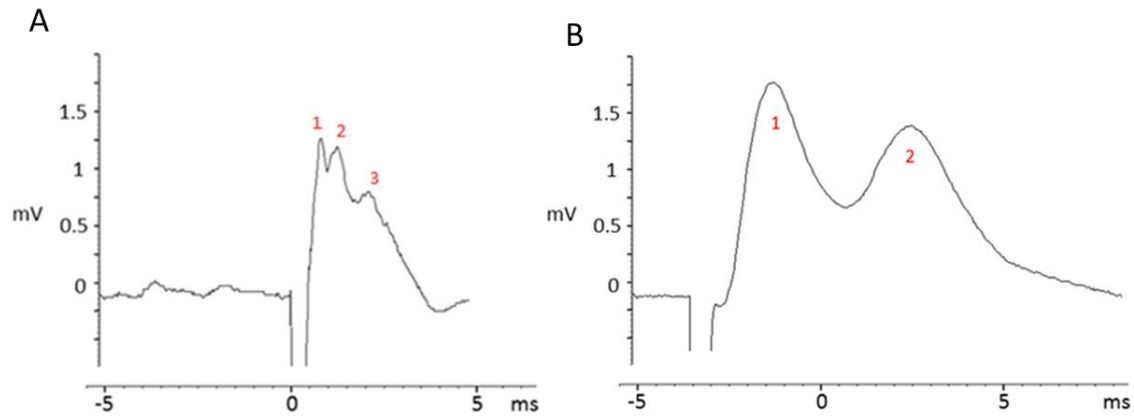


Figure 2.40. Typical CAP profiles derived from the optic nerve and callosal slice. [A] Three groups of axons each with different degrees of myelination produce 3 distinct peaks in the optic nerve with unequal conduction speeds. [B] Two distinct groups of myelinated axons produce a biphasic profile each with its distinct conduction speed in the callosal slice.

Exposure of the callosal slice to glucose deprivation caused a decremental and gradual loss in axonal conduction, with the heavily myelinated axons (responsible for the first peak of the recorded CAP), being more vulnerable to the insult than the less myelinated axons. Conduction was lost right after 15 min into GD in the heavily myelinated axons, whilst the less myelinated axons required at least 30 min of GD to lose their activity. We observed no recovery during reperfusion in the heavily myelinated axons, and limited recovery of the lesser myelinated ones.

An unpaired student t-Test assuming equal variance was conducted to compare the CAP recording between these two groups of axons during the period of GD and reperfusion with glucose containing aCSF. There is a statistically significant difference between the two groups ($p < 0.001$).

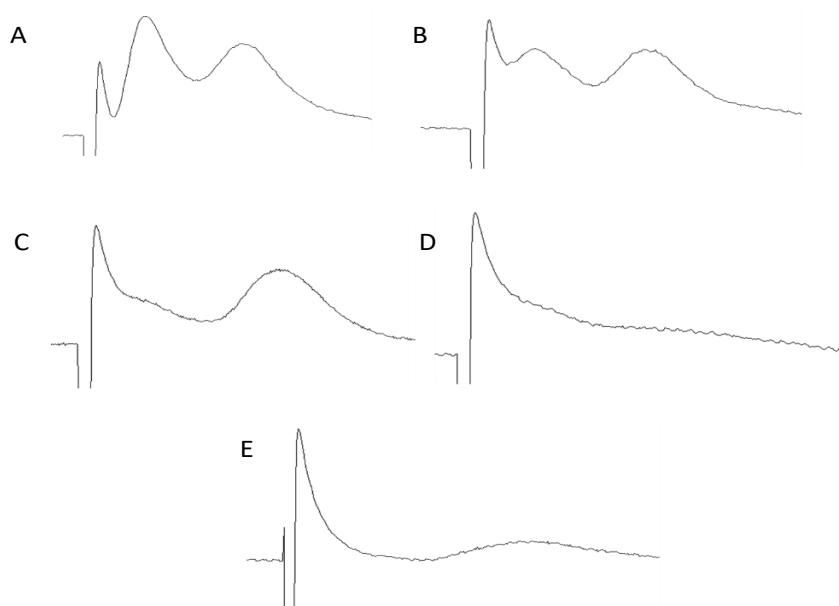
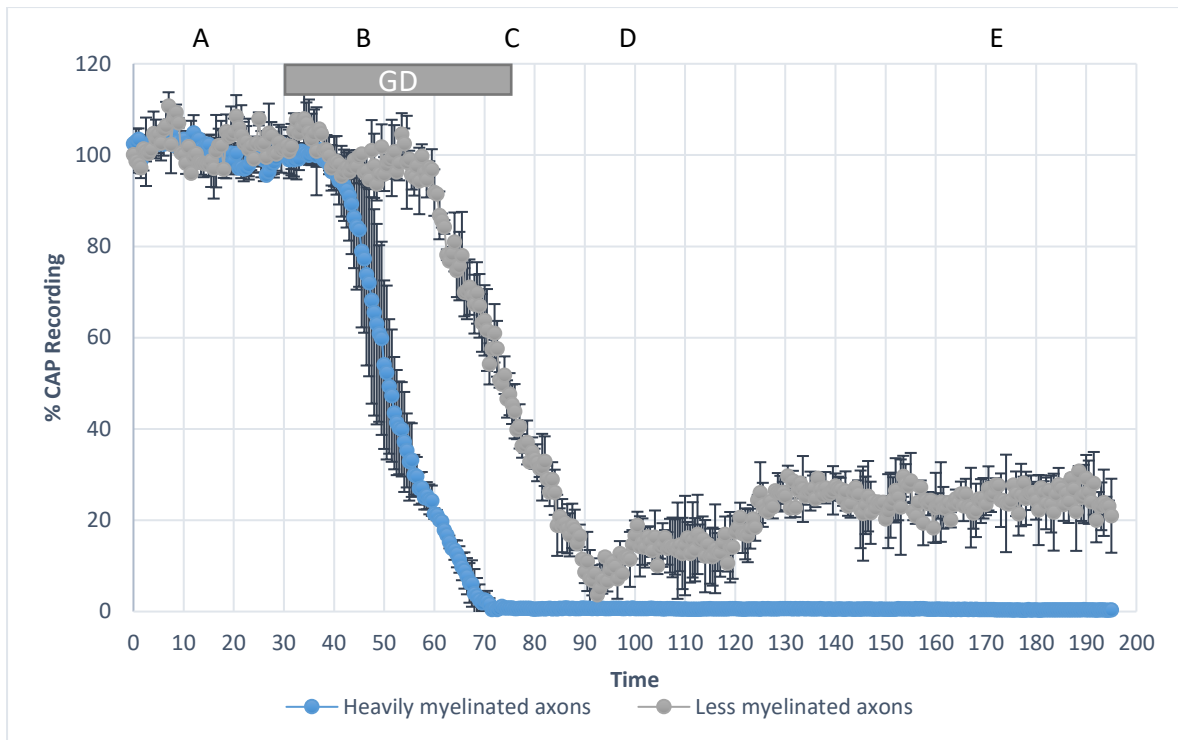


Figure 2.41. Heavily myelinated axons are more vulnerable to GD. *Upper graph:* There was complete loss of the first CAP peak after 15 mins of GD. The second successive peak was lost after 30-40 mins of GD. There was no recovery of the first peak during reperfusion. The second peak showed some partial recovery in CAP area (approximately 15-20 % of control) during reperfusion. Shaded area shows the duration of GD. *Lower Diagrams:* The CAP recorded at different stages of the experiment. Letters A-E correspond to different time-points that are annotated on the graph above. ($n=3$)

2.4.7 Loss of axonal conduction is dependent on the duration of glucose deprivation

A longer duration of GD results in a more severe insult and therefore in a more pronounced loss in axonal function. There was no loss of function following 15 mins GD with CAP recording remaining constant throughout the duration of the experiment. There was loss of conduction in about 40 % of the axon population in the corpus callosum during 30 min of GD. However, this loss was reversible, since minutes after the reintroduction of glucose, the amplitude of the CAP returned to normal level. Moreover, 45 min of GD resulted in loss in conduction in >80% of the axons present in the corpus callosum. Some axons showed evidence of recovery in the initial stages of reperfusion, but this was short-lived as the CAP then gradually declined into the reperfusion phase.

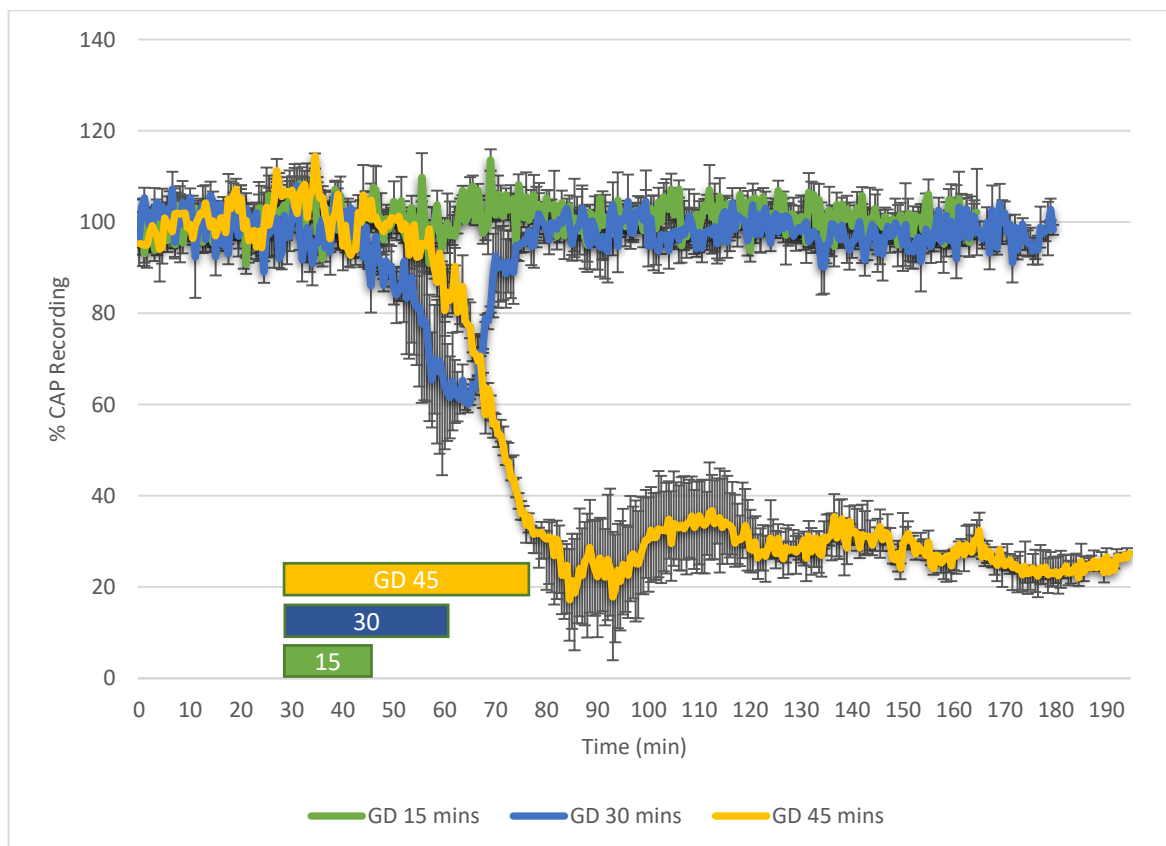


Figure 2.42. CAP recording from callosal slices exposed to variable extents in exposure to GD. There was no loss of conduction following 15 min GD. There was a partial loss of conduction in slices exposed to 30 min of GD, with a full recovery during reperfusion. A severe, irreversible loss of conduction was conspicuous after 45 min of GD with minimal recovery during reperfusion ($n=3$).

One-way ANOVA followed by Tukey's post hoc test shows a statistically significant difference ($p < 0.001$) in CAP recovery between slices exposed to 45 min of GD to those exposed to 15 and 30 min. There was no statistically significant difference between slices exposed to 15 and 30 min of GD.

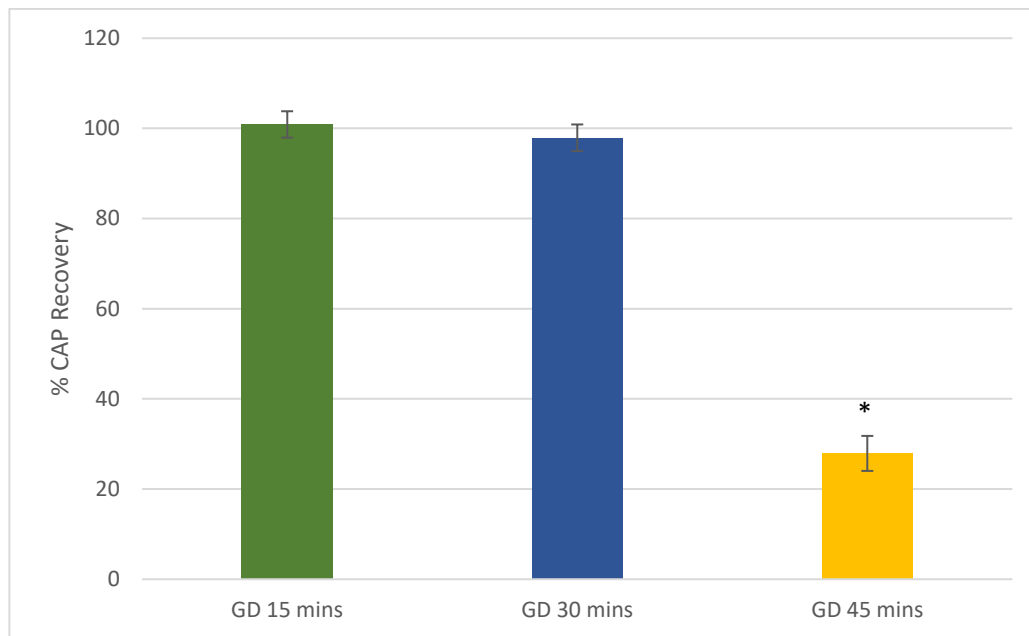


Figure 2.43. Percentage CAP recovery following variable lengths in exposure of GD. There is no statistically significant difference in CAP recovery between GD of 15 and 30 min. There is a statistically significant difference ($*p < 0.001$) in slices exposed to 45 min GD when compared to 15 and 30 min.

2.4.8 Loss of axonal conduction is dependent on the temperature

Lowering the bath temperature was protective as this attenuated the loss of axonal conduction during glucose deprivation. There was no loss in axonal conduction when slices were kept at RT (24°C). However, there was partial loss of CAP following 45 of GD at 33°C. Axonal conduction decreased at around 30 min of GD and this steady decline progressed early into reperfusion. Within 30 min of reperfusion conduction returned to 60% of baseline. As previously stated, 45 mins of GD at an operating temperature of 37°C resulted in almost a complete loss of axonal function with limited recovery during reperfusion.

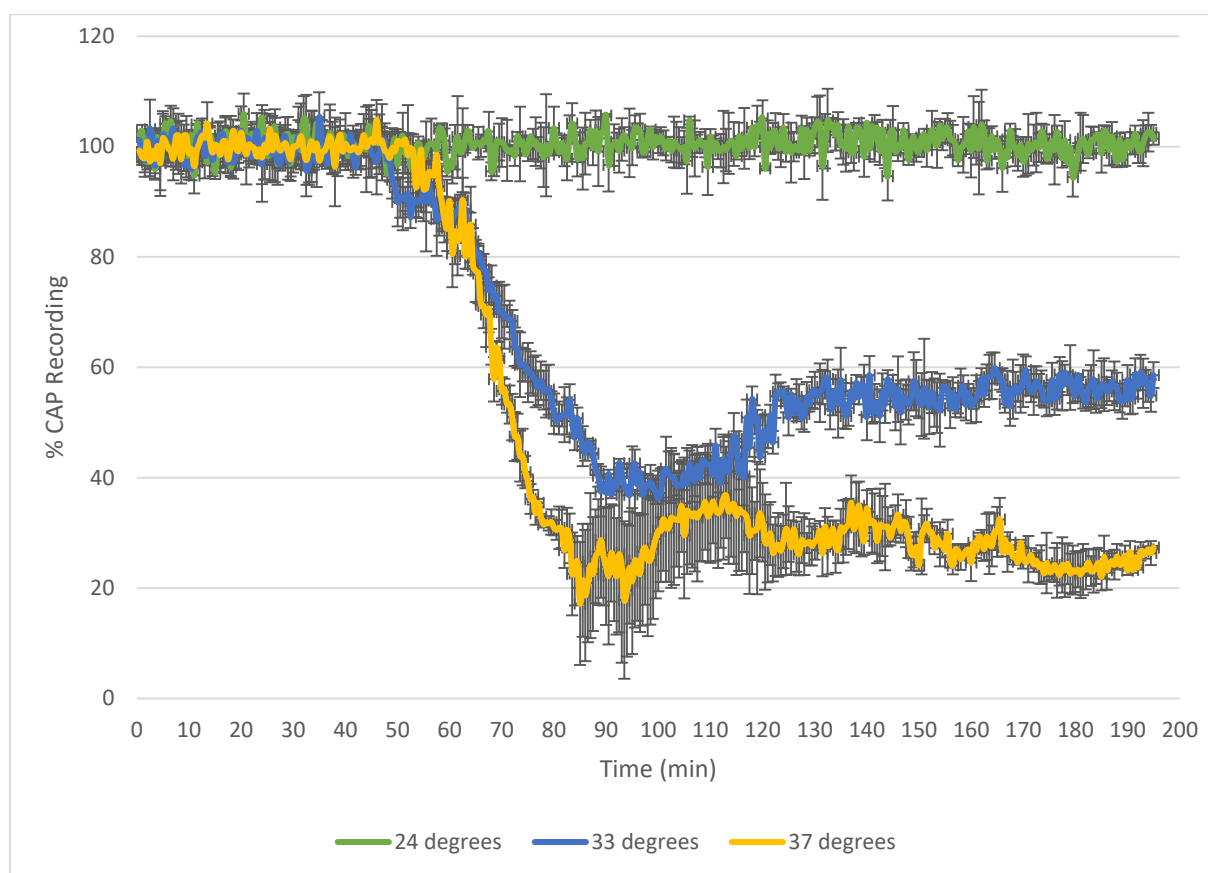


Figure 2.44. CAP recording from callosal slices exposed to GD maintained at different bath temperatures. There is no loss in conduction when glucose deprivation was initiated at room temperature. Callosal slices exposed to GD at 33°C showed partial loss in conduction with recovery of up to 60 % of baseline during reperfusion. Severe conduction loss was characteristic after 45 min of GD at 37°C with minimal recovery during reperfusion ($n=3$).

One-way ANOVA followed by Tukey's post hoc test found a statistically significant difference ($p < 0.001$) in CAP recovery between each experimental condition.

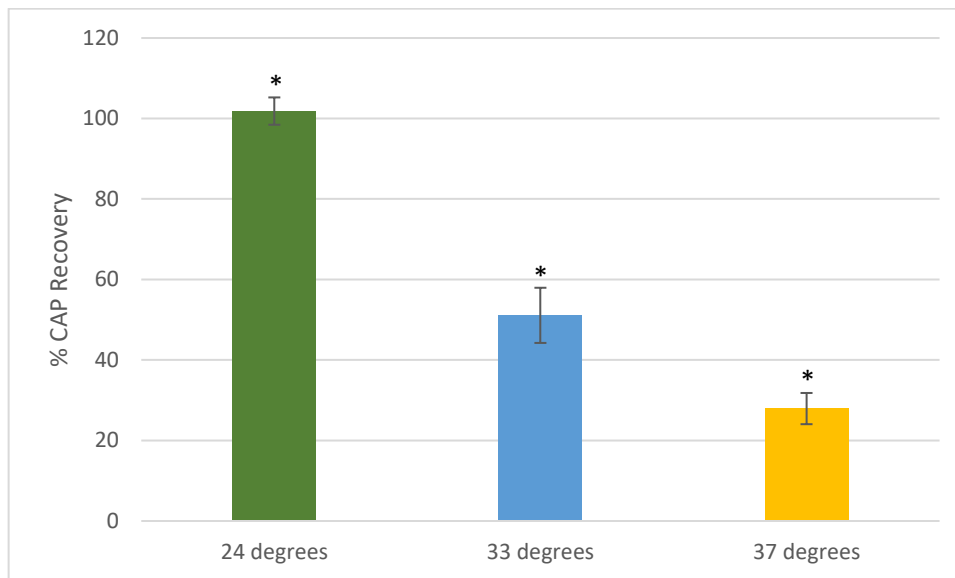


Figure 2.45. Percentage CAP recovery following 45 min of GD at different temperatures. Statistically significant ($*p < 0.001$) difference in CAP recovery between each experimental group.

2.5 Discussion

2.5.1 Acute callosal brain slices as the preferred model to study white matter injury

In this study, we explored two frequently used models to study white matter injury: the optic nerve and the callosal brain slice. The brain slice was chosen as the preparation of choice to characterise axonal injury during glucose deprivation. The main reason for this choice was due to its advantages when adapted under two-photon microscopy. The expression of YFP axons in the optic nerve is by far less widespread than that in the corpus callosum. The extremely high myelin density of the optic nerve limits adequate laser penetration and therefore limits the depth of imaging. Another advantage of the brain slice over the optic nerve is the ease of dye penetration. The thick and dense meningeal covering of the optic nerve limit the penetration of cellular markers and therefore the optic nerve presents a big challenge to obtain highly resolved images of particular significance. Finally, the axons of the adult optic nerve are all myelinated, whilst those present in the corpus callosum are made up of a mixture of myelinated and unmyelinated axons and which therefore represent an ideal and realistic environment.

Preparation of healthy slices was pivotal to this research and required extreme practice and dedication. To minimise slice injury during the cutting phase, we used the low Na^+ , high sucrose-containing aCSF, to limit the passive sodium influx with the subsequent water entry and cell swelling during the slice cutting (Aghajanian and Rasmussen, 1989). Other precautions to ensure healthy slices and successful experiments included the fresh preparation of the cutting solution and aCSF, precise pH adjustment, rapid mouse decapitation after deep anaesthesia, fast but gentle brain extraction in ice cold sucrose-containing aCSF and ideal frequency and speed settings of the vibratome when slicing brain tissue.

After cutting, the slices were left to recover in normal aCSF at RT for about 2 hr in the holding chamber. When slices were imaged immediately after the cutting, we regularly observed extensive swollen axons and beading, that recovered well during incubation. When slices are allowed to recover a spontaneous phenomenon occurs that reseals damaged axons through the controlled influx of calcium.

The main cause of the cutting injury is derived through Na^+ influx through inactivating voltage-gated sodium channels. The sodium overload causes swelling of the axons by osmotic uptake of water leading to depolarisation and activation of voltage gated calcium channels (VGCC) that further exacerbate this Ca^{2+} influx via reversal of the $\text{Na}^+/\text{Ca}^{2+}$ exchanger (Stys, 2005; Ribas and Lingor, 2016). Conversely, blocking Ca^{2+} influx and inhibiting calpain was shown to limit rapid axonal injury and improves recovery after traumatic injury (Williams *et al.*, 2014).

In our hands, cutting damage could be easily visualised in the first 20 – 40 μm below the surface of the slice, and this was irrespective of the time allowed for the slices to recover. This factor was generally the biggest drawback and challenge we experienced in experiments that required the topical application of specific intravital stains *in vivo*. The high density of the myelinating axons in the corpus callosum limited the penetration of these stains to the first 40 – 50 μm of slice tissue, which is the depth at which the cutting damage normally extends. We therefore maximised our slices preparation in an effort to improve dye penetration. This procedure was multifactorial and included several adjustments. These varied from increasing the dye loading concentration to increasing the incubation time and addition of detergents and surfactants to improve dye loading penetration.

2.5.2 YFP-expressing transgenic mice as a model to study axonal injury

In white matter, oligodendrocytes and axons comprise the functional unit of the myelinated axon. Two general approaches have been historically followed to identify axonal injury. The first one is to selectively identify the underlying myelin pathology by using specific vital stains such as luxol fast blue-periodic acid Schiff, Fluoromyelin, Nile Red etc. or to follow the traces of a silver complex from disrupted axolemma in axons, such as the Bielschowsky's silver stain (Wakita *et al.*, 1995; Schäbitz *et al.*, 2000). Assessment of pathology is then made through a graded scoring system based on morphologic changes in axons during pathology. A second commonly used approach is to identify the accumulation of β -APP that is normally transported by fast axoplasmic flow, or the loss in phosphorylated neurofilaments as assessed by SMI-31 immunoreactivity. Both immunocytochemical methods are based on a scoring system to grade the extent of axonal injury. Accumulation of β -APP in retraction bulbs is regarded as a very sensitive marker of ischaemic and traumatic axonal injury (Graham *et al.*, 2004) and has been previously documented in studies involving axonal injury in mammals after focal ischaemia (Valeriani *et al.*, 2000; Yam *et al.*, 1998).

However, these approaches do not provide detailed information on the white matter tracts that are primarily the main target of this type of injury. One main advantage in the use of YFP-expressing axons is that they can be readily visualised and traced over long distances. In addition, axonal damage manifested as beading, fragmentation or the loss of fluorescence can be easily used in a scoring system that is highly reproducible. Thus, YFP is a strong and specific vital marker for axons and provides a convenient method to observe axonal integrity over time. Because YFP is localised in neuronal cytoplasm, intrinsic morphological changes in the axoplasm due to various insults can be visualised in labelled axons by fluorescence microscopy techniques (Brendza *et al.*, 2003; Gillingwater *et al.*, 2002). Therefore, morphological changes over time (example, in the disintegration of axons) can provide very meaningful information as these events easily correlate with YFP signal changes of the fluorescent axons. Importantly, it has been shown that expression of YFP in neurons results in no apparent toxic effects (Feng *et al.*, 2000).

The pattern of axonal injury observed in our experiments was focal swelling, followed by beading and fragmentation, correlating well with previous literature (McCarren and Goldberg 2001; Alix *et al.* 2014). This pattern of injury enabled us to monitor the loss of structural integrity over time and generate a reproducible readout in the form of a graded scoring system. The earliest observable signature of axonal injury during glucose deprivation was the focal swelling, referred to as axonal spheroid formation (Cajal, 1928), and was first described by Waller (1851). As the injury matures this leads to beading, fragmentation, and ultimately axonal transection (Ferguson *et al.*, 1997; Trapp *et al.*, 1998). This cascade of injury is believed to be initiated by glutamate excitotoxicity through Ca^{2+} influx from the extracellular environment (Li and Stys, 2000; Ouardouz *et al.*, 2009a, b), together with Ca^{2+} released from the axoplasmic reticulum and store-operated channels (Stirling and Stys, 2010). The increase in intracellular Ca^{2+} activates the Ca^{2+} -dependent protease calpain, which leads to the local breakdown of the cytoskeleton (Kerschensteiner *et al.* 2005), thus resulting in spheroid formation.

In our model, we observed that YFP-expressing smaller calibre axons are more vulnerable to GD. We have previously reported that all YFP-expressing axons in the white matter are fully myelinated (Alix *et al.*, 2012), since the diameter of thinnest YFP-expressing axons is larger than the diameter of unmyelinated fibres present in the corpus callosum (Sturrock, 1980). In slices showing extensive axonal injury, the larger axons had a lower axonal injury score when compared to the small calibre axons. This finding correlates well with the EM data for glucose deprivation as presented in this study. We observed a typical absence of small calibre axons which were otherwise present in abundance in control slices and preferentially grouped around the larger calibre axons. We hypothesise that the larger calibre axons possess a relatively higher concentration of local substrates that serve as metabolic store that safeguard axons against longer periods of glucose deprivation. However, larger calibre axons are more heavily myelinated and have a faster conduction speed. Therefore, this result contrasted with a later finding in this study, wherein we reported that axons with faster conduction speeds are more vulnerable to injury than the slower, less myelinated and smaller axons. Further in-depth studies are therefore warranted to highlight how distinct and diverse sub-populations of axons in the corpus callosum differ with respect to vulnerability to glucose deprivation based on their structure and function.

2.5.3 Glucose deprivation equally injures axons and oligodendrocytes

In vivo imaging enabled us to follow the morphological changes that occur in YFP-expressing axons during glucose deprivation. Despite being an excellent tool to monitor changes in real time, the two-photon imaging lacks the spatial resolution of confocal and electron microscopy. To this end, we utilized an *in vitro* slice model perfused in an interphase chamber to better characterise the ultrastructural changes that occur during glucose deprivation. The damage we observed to oligodendrocytes and axons matches the well-established patterns of white matter injury (Pantoni *et al.*, 1996, Rosenberg, 1999; Valeriani, 2000).

The EM observations demonstrate that axons and oligodendrocytes are all targets of glucose deprivation in CNS white matter. After 45 minutes of glucose deprivation, the dissolution of the axonal cytoskeleton as shown by the loss of immunoreactivity for the heavily phosphorylated neurofilament proteins correlates well with the fragmented YFP-expressing axons. The dissolution of the cytoskeleton constitutes a major pathological change and is consistent with the Ca²⁺-mediated injury as demonstrated in other models of white matter injury (Johnson *et al.*, 2013; Ward *et al.*, 2014).

Extensive studies using rodent optic nerve preparations have shown that energy deprivation leads to axonal dysfunction by activation of voltage-dependent channels for Na⁺ and Ca²⁺, causing intra-axonal Ca²⁺ accumulation and activation of Ca²⁺-dependent disruptive pathways (Stys *et al.*, 2005; Waxman *et al.*, 1991). Consistent with other studies, the misalignment of neurofilaments is correlated with continued expansion of the disconnected axon cylinder. In this scenario, one can easily argue that misalignment of the neurofilaments impairs axoplasmic transport and axonal disconnection.

Many studies have reported the detection of apoptosis as a prominent feature in glucose deprived tissue (Yakovlev *et al.*, 1997; Ferrand-Drake *et al.*, 1999). Mitochondrial swelling has been recognised as an important component of axonal damage following an insult (Waxman *et al.*, 1991; Christman *et al.*, 1994; Rosenberg *et al.*, 1999; Maxwell *et al.*, 2003) and is thought to be initiated by Ca²⁺. It has been postulated that the mitochondria may attempt to sequester the massive influx of Ca²⁺ into the axon (Okonkwo *et al.*, 1999; Okonkwo and Povlishock, 1999; Büki *et al.*, 2000) only to be overwhelmed. This causes the Ca²⁺ to open the

mitochondrial permeability transition pore (Zoratti and Szabo, 1995), inducing a pathologic swelling of the mitochondria with the loss of function and energy failure. In addition, the axon cytoskeleton and mitochondria may become targets for the Ca^{2+} activated proteases, including calpains and caspases (Maxwell *et al.*, 1995; McCracken *et al.*, 1999; Pike *et al.*, 1998, Büki *et al.*, 1999). As in our present study, these sequential events are thought to culminate into focal swelling, beading, fragmentation and axonal transaction.

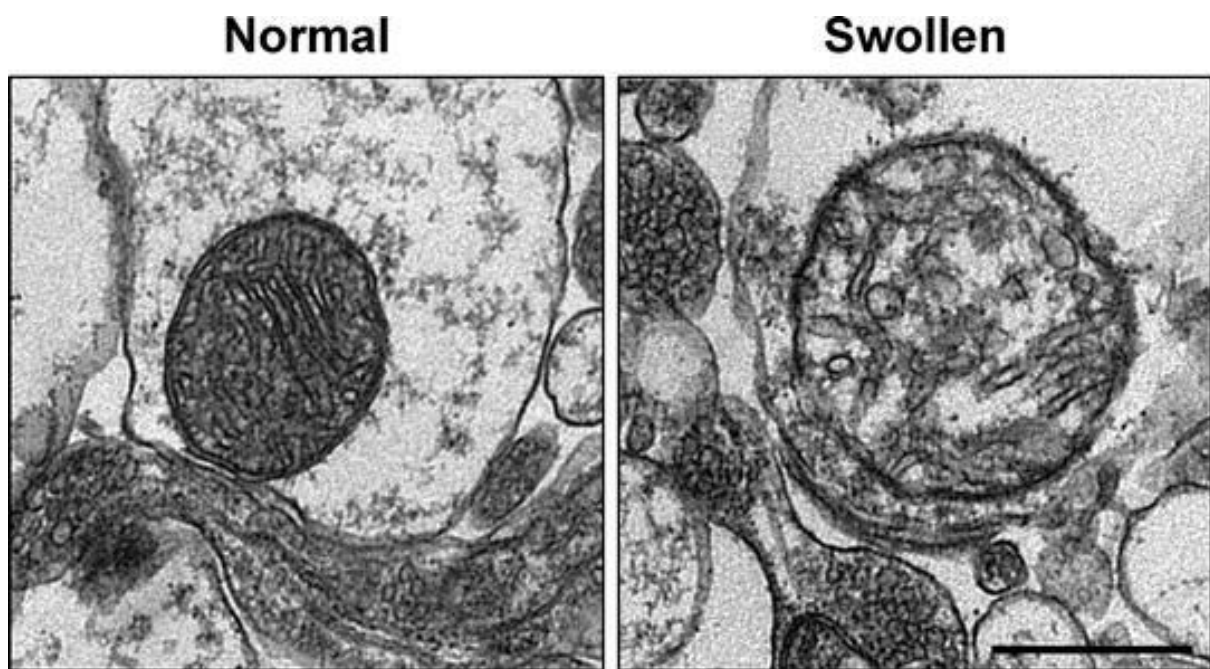


Figure 2.46. Electron microscopy comparing the normal and swollen appearance of a mitochondrion. The increase in intracellular Ca^{2+} is sequestered in the mitochondria, leading to an increase in the mitochondrial permeability transition pore, resulting in extensive swelling. (Reproduced from Arrázola and Inestrosa, 2015)

2.5.4 Glucose deprivation is a cause for the delay in structural injury to axons

During the initial phase of GD there is no apparent structural injury of axons in the callosal slices. This complements previous studies based on CAP recording from the rodent optic nerve (Ransom and Fern, 1997; Wender *et al.*, 2000; Brown *et al.*, 2001, 2003). The mechanism for this delayed injury is thought to be as a consequence of the reserve glycogen stores present in astrocytes (Ransom and Fern, 1997) or oligodendrocytes (Meyer *et al.*, 2018) that is converted to lactate and shuttled to neighbouring axons and glia, including the astrocytes. Chapter 3 will delve with these pathways and mechanisms in more detail.

Here we report that callosal axons possess sufficient energy reserves to withstand to up to 30 min of GD, since there were no signs of injury (axonal swelling, beading and fragmentation) during GD and up to 120min of reperfusion. The first signs of injury were evident by the end of 45 min of GD with focal swelling in a limited number of axons of small calibre axons. During the initial stage in reperfusion, we observed a brisk progression of injury which resolved from focal swelling to marked beading of axons. It has been shown that the re-introduction of glucose into a previously energy-deficient system is less beneficial to the survival of neurons than would be expected, and this manoeuvre might even worsen the outcome (Siesjö, 1992; Tasker *et al.*, 1992). It has also been suggested that re-introduction of glucose initiates the opening of the mitochondrial permeability transition pore and triggers the formation of reactive oxygen species (ROS) (Kristián T and Siesjö BK, 1996). Suh and colleagues (2007a, b) reported that hypoglycaemic injury is exacerbated if increasing levels of glucose are administered during reperfusion. This mechanism might suggest the cause for the complete disintegration and loss of fluorescence of the YFP axons that succumbed to the lethal 45 min of GD by the end of 2 hr of reperfusion in our experiments.

2.5.5 Loss of axonal function precedes the structural injury that is observed after glucose deprivation

CAP electrophysiology is a very useful tool to study white matter injury. It enables the assessment of the functional integrity of axons in normal physiology and in disease as the signal is recorded extracellularly from a large population of axons. In this study, we monitored the CAP both in the optic nerve and in callosal brain slices. In accordance with previous literature, we reported the characteristic triphasic signal in the optic nerve (Allen et al., 2006; Brown et al., 2003; Fern et al., 1998; Stys et al., 1998; Waxman et al., 1980), and a biphasic signal in the callosal brain slice (Reeves et al., 2005; Tekkök and Goldberg, 2001; Tekkök et al., 2005).

The live imaging experiments show that the earliest signs of axonal swelling occurred by the end of 45 min of GD, that mainly had an effect on the small calibre axons, leaving the large calibre axons intact. On the other hand, a reduction in amplitude of the CAP after 30 min of GD was very clear. The energy deficit resulting from the deprivation of glucose causes a decrease in the level of ATP and as a consequence there is a resultant increase in intracellular Na^+ due to failure of the energy-dependent Na^+/K^+ pump and further Na^+ influx through non-inactivating Na^+ channels and Na^+/K^+ inward rectifier channels (Stys, 2005). This leads to membrane depolarisation, which results in loss of axonal conduction and eventual conduction block because of high extracellular K^+ . A timely re-instatement of glucose that precedes the toxic build-up in intracellular Ca^{2+} would cause the membrane potential to recover and re-establish a normal CAP response as in the case when callosal slices were exposed to 30 min of GD.

On the other hand, a prolonged 45 min of GD causes a loss in CAP accompanied with axonal swelling and beading of axons. In this scenario, the increase in intracellular Na^+ , together with the membrane depolarisation causes reversal of the $\text{Na}^+/\text{Ca}^{2+}$ exchanger (Stys, 2005). This, together with release of Ca^{2+} from intracellular stores overloads the system and activates calpain and ROS. This culminates in severe axonal structural injury, initially with the formation of focal axonal swellings, and then progressing to beading and fragmentation (Kerschensteiner *et al.* 2005; Stirling and Stys, 2010).

2.5.6 Heavy myelinated axons are more vulnerable to glucose deprivation than the less myelinated axons.

In our electrophysiology experiments, the recorded signal was made up of two biphasic peaks separated in time and space, which represent two distinct populations of axons. In view of the difference in their conduction speed, we hypothesised that the first peak represented the myelinated axons, and the second peak those groups of axons which were unmyelinated. Unmyelinated axons require a much wider pulse width to be stimulated when compared to the fully myelinated ones (Fern *et al.*, 1998). In our setup, increasing the pulse width resulted in an increase in the amplitude of the first peak, concomitant with the loss of the second peak. A decrease in the pulse width gave the opposite response. This led us to hypothesise that the two peaks represented two completely different cohorts of axons.

However, after reviewing the literature, we realised that the second peak could not be representing the unmyelinated axons. We compared our signal to that obtained from the sciatic nerve (Potocnik *et al.*, 2006) and the optic nerve (Allen *et al.*, 2006). The sciatic nerve is made up of a mixture of myelinated and unmyelinated fibres (van Veen *et al.*, 1995), whilst all the fibres in the adult optic nerve are at this stage fully myelinated (Foster *et al.*, 1982). The sciatic nerve generates three peaks (Potocnik *et al.*, 2006). Typically, a large amplitude peak is closely followed by a much smaller second peak that is generated within 1 millisecond (ms) from the stimulus artefact (Figure 2.47 A). A third peak with a much smaller amplitude of about 20 – 30ms delay from the stimulus artefact completes the evoked response (Figure 2.47 B). This peak represents the slower, smaller, unmyelinated fibres (Schoonhoven and Stegeman, 1991). The signal obtained across the optic nerve is also composed of 3 peaks (Allen *et al.*, 2006). However, these peaks occur within 5ms of the stimulus artefact and the difference in amplitude is much smaller than that from the sciatic nerve (Figure 2.47 C). Our signal (Figure 2.47 D) was composed of two peaks within 5ms of the stimulus artefact and with almost identical amplitudes. We therefore concluded that in the callosal slice preparation, both peaks represent the myelinated fibres, albeit with different extents in myelination.

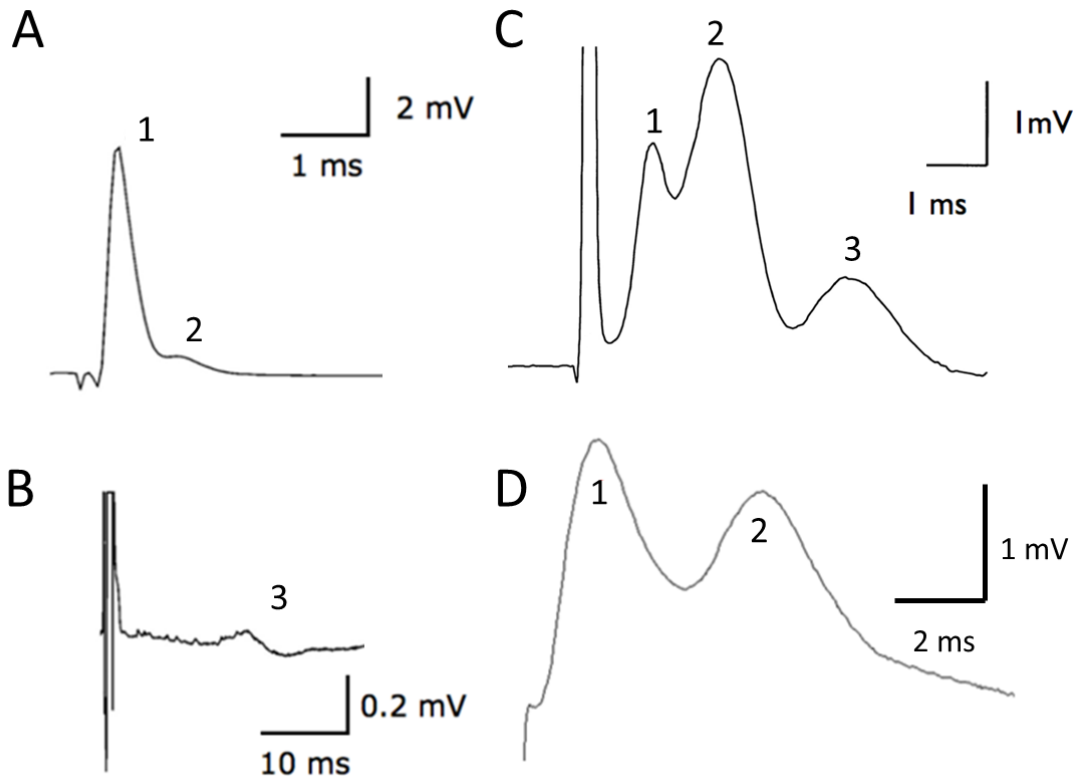


Figure 2.47. Representative trace recordings of the CAP profile from the sciatic nerve, optic nerve, and corpus callosum. [A-B] Recording from the sciatic nerve. Peaks 1 and 2 represent myelinated axons; peak 3 has a much smaller amplitude and is generated following a delay of 20-30ms and represents unmyelinated axons. [C] Recording from the optic nerve. Peaks 1, 2 and 3 represent axons with different degrees of myelination. [D] Recording from the corpus callosum. Peaks 1 and 2 represent axons with different degrees of myelination (adapted from: Potocnik *et al.*, 2006 – A and B; Allen *et al.*, 2006 – C).

To further proof that both peaks represented myelinated axons, we measured their conduction velocity. For the accurate measurement of the conduction speed we measured the delay from each peak when the distance between the two electrodes was increased by a predetermined amount. We determined that the conduction velocities of both peaks were both > 1 m/s, and therefore both peaks represented myelinated axons (Waxman, 1980).

In our study we observed that the first peak was lost at an earlier stage than the second. The first peak was normally lost right after 15 min of GD, with the second peak disappearing after 30 – 40 min of GD. During reperfusion, the recovery of the first peak was to a lesser extent than that of the second peak. Fast conducting fibres consist of larger calibre axons with a higher degree of myelination. We hypothesise that such axons have a much higher metabolic rate than the thinner less myelinated axons because of their higher energy demands to conduct fast transmission. It is therefore plausible to understand that this population of axons are the first to succumb to injury. This finding in a way contradicts what was observed during our live imaging experiments. Larger YFP callosal axons were more resistant to injury than the smaller calibre ones. One possible explanation is that YFP expression is only present in a subset of cortical neurons. It is therefore plausible to believe that in this case, we were unable to visualize the larger and more heavily myelinated fibres, which showed the earlier loss in conduction during glucose deprivation in the set of electrophysiological studies.

Harris and Attwell (2012), delved in some detail to shed some light on the energetics of white matter. They reported that during white matter development, the process of myelin formation by mature oligodendrocytes requires a considerable amount of energy. This energy expenditure is later repaid in terms of reduction of ATP utilisation secondary to the saltatory propagation of the action potential. However, the increase in energy consumption to synthesise the myelin for effective saltatory conduction outweighs the end result of the bioenergetic process of saltatory conduction. Thus, heavily myelinated axons consume more energy than the lesser myelinated axons (Harris and Attwell, 2012), which might be the reason to explain the early loss of CAP conduction in heavily myelinated axons following GD.

Chapter 3

Energy metabolism of white matter during glucose deprivation

3.1 Aims

Failure of the energy metabolism in white matter is a feature several neurodegenerative conditions (Matute and Ransom, 2012), Alzheimer's disease (Yao *et al.*, 2011), amyotrophic lateral sclerosis (Lee *et al.*, 2012a) and multiple sclerosis (Cambron *et al.*, 2012). An understanding of the dynamic changes in the metabolic status that occur in white matter during critical periods of glucose deprivation is very important in view of the selective vulnerability of white matter. In this section we explored the bioenergetic status of white matter during normal physiology along with periods of energy deprivation. *In vitro* and *in vivo* studies have amply explored the role of astrocytes in furnishing lactate to axons and neighbouring glia during periods heightened electrical activity and increased energy demand (Ransom and Fern 1997; Tekkök *et al.*, 2005; Brown *et al.*, 2005). The main three principle aims of this section are:

1. To explore the role of lactate released by astrocytes during periods of normal physiological function.
2. To determine whether lactate released by astrocytes is used by axons as an alternative energy substrate during periods of glucose deprivation.
3. To determine whether activation of β 2-adrenoreceptors protects axons during prolonged periods of glucose deprivation, and whether this mechanism involves the lactate shuttle.

3.2 Literature review

The human brain is responsible for a vast number of critical tasks. Although it comprises just 2 % of the total weight of a human being, it received 20 % of all the cardiac output (Sokoloff, 1960) and 25 % of plasma glucose (Raichle and Gusnard, 2002). The main energy metabolite used by the brain is glucose, and it requires a constant supply to maintain its normal function (Gruetter *et al.*, 1992; Chih and Roberts, 2003), since the central nervous system is extremely vulnerable to hypoglycaemia induced dysfunction and injury (Agardh and Rosen, 1983; Auer, 2004, Brown *et al.*, 2001, 2002).

Synapses account for most of the energy requirement in grey matter (Attwell and Laughlin, 2001; Howarth *et al.*, 2010). Contrary to previous belief, there synapses occur in white matter as well, both during development (Kukley *et al.*, 2007; Ziskin *et al.*, 2007; Káradóttir *et al.*, 2008) and after myelination is complete (Royeck *et al.*, 2010). However, these synapses consume less than 0.5% of the energy consumed by synapses in the grey matter (Harris and Attwell, 2012). The most energy consuming activity of white matter is reported to be the maintenance of the resting membrane potential: i.e. Na^+ efflux via the Na^+/K^+ pump (Siesjo, 1978; Attwell and Laughlin, 2001). This has been estimated to consume 40-50% of energy consumption in white matter (Whittam, 1962; Astrup *et al.*, 1981), since it is essential in action potential propagation and neurotransmitter release.

3.2.1 Brain energy metabolism

Under physiological conditions, brain activity is coupled to glucose and oxygen utilisation from the cerebral vasculature. These substrates are metabolised to produce energy and sustain normal function. Although glucose is the obligatory energy substrate in the brain, conditions such as fasting and uncontrolled diabetes subject the brain to utilise other blood-borne energy substrates, such as ketone bodies (Magistretti, 2008), while strenuous physical activity drives lactate production (van Hall *et al.*, 2009). Glucose enters the cell via specialised glucose transporters (GLUT); GLUT1 mediates glucose uptake from extracellular space into astrocytes, oligodendrocytes and microglia, while GLUT3 is responsible for neuronal glucose uptake (Simpson *et al.*, 2007). Upon entry, glucose undergoes phosphorylation by hexokinase (HK), producing glucose-6-phosphate (glucose-6P) in an energy-dependent reaction. Thereafter glucose-6P can undergo glycolysis, producing 2 molecules of pyruvate and 2 ATP molecules for every molecule of glucose.

In resting brain cells, pyruvate may be metabolised via the tricarboxylic acid (TCA) pathway or oxidative phosphorylation in the mitochondria resulting in the production of acetyl-CoA, CO₂, FADH and NADH. Under hypoxic conditions, pyruvate is rapidly reduced to lactate by lactate dehydrogenase (LDH), with concomitant oxidation of NADH, thereby regenerating NAD⁺. Lactate can also be produced under normoxia via aerobic glycolysis, also known as the Warburg effect (Warburg, 1956; Vaishnavi *et al.*, 2010).

3.2.2 Lactate as a metabolic substrate in the brain

The first observation which postulated that lactate was not merely a metabolism bi-product, but also an important alternative energy substrate was documented over five decades ago, when *in vitro* experiments conducted by McIlwain (1953) demonstrated that lactate and pyruvate could maintain brain tissue respiration as efficiently as glucose. This fuelled interest in brain metabolism and was superseded by several other studies, which sought to elucidate roles of other metabolites in supporting brain function. In a series of experiments, Schurr and colleagues demonstrated that synaptic function in the absence of glucose was sustained by lactate in rat hippocampal slices (Schurr *et al.*, 1988; Schurr and Rigor 1995). This was later confirmed by several other investigators (Stittsworth and Lanthorn, 1993; Bueno *et al.*, 1994; Izumi *et al.*, 1994). Schurr and colleagues (1997a, b) proposed that lactate not only serves as an alternative energy substrate, but it can support functional recovery post-hypoxia when given exogenously and is the obligatory aerobic energy substrate, being preferentially used over glucose (Schurr *et al.*, 1997a, b). This is postulated to occur since depletion of ATP levels during hypoxic events limit the brain's ability to produce energy via glucose phosphorylation, thereby driving lactate production as the only readily available precursor to pyruvate, allowing its entry into the TCA cycle to generate energy.

Astrocytes house the brain's only energy reserve, glycogen, which is utilised during energy deficit to produce lactate (Dienel *et al.*, 2007). Glycogenolysis reduces glucose consumption since lactate is being preferentially utilised as a metabolic substrate, thus levels of Glu6P are maintained to sustain feedback inhibition on HK. This mechanism represents a glucose-sparing effect, preserving glucose for critical cerebral functions (Dinuzzo *et al.*, 2012), further affirming the central, supportive role that astrocytes hold. During increased neuronal activity or low glucose conditions, the quicker, yet more inefficient process of glycolysis is favoured, with lactate being utilised preferentially over glucose in energy-demanding scenarios (Schurr *et al.*, 1988).

3.2.3 Metabolic interactions between astrocytes and neurons

Whenever glucose availability decreases, nerve cells turn to their only available energy store: glycogen. The presence of glycogen stores in the brain was first documented in the 1970s by electron microscopy (Koizumi and Shiraishi, 1970) and biochemical assay (Koizumi, 1974). Unlike other organs, in the brain glycogen is not homogeneously dispersed amongst the cell populations but is located exclusively in astrocytes (Cataldo and Broadwell, 1986). Its distribution mirrors the brain's energy demands. In particular it is concentrated in the fine astrocyte process that surrounds synapses (Calì *et al.*, 2016), and in those brain areas with the highest metabolic demand, including the hippocampus, striatum, cortex and cerebellar molecular layer (Oe *et al.*, 2016).

The high glycogen content in astrocytes forms the basis of the astrocyte-neuron lactate shuttle hypothesis (ANLS), first proposed by Pellerin and Magistretti (1994), postulating that energy delivery in the form of lactate supports active neuronal function and is provided via astrocytes (Pellerin and Magistretti, 2003, 2004; Bouzier *et al.*, 2003; Magistretti *et al.*, 1999; Magistretti and Pellerin, 1999). According to the hypothesis, glutamate released during neuronal activity is taken up by astrocytes that surround the synaptic complex. Glutamate is co-transported with Na^+ uptake, which stimulates activity of Na^+/K^+ ATPase to counteract a disrupted Na^+ gradient, in an energy-consuming manner. Glutamate undergoes active conversion to glutamine by glutamine synthase. This mechanism requires astrocytic conversion of its glycogen stores to glucose, or glucose uptake from the blood, which is then processed glycolytically to yield lactate. The resultant lactate is then exported into the extracellular space and shuttled via specialized monocarboxylate transporters (MCTs) (Halestrap, 2012) to nearby neurons, serving as a supplementary energetic substrate. Within neurons, lactate is converted to pyruvate via lactate dehydrogenase 1 (LDH1) and is processed oxidatively in the mitochondria, yielding ATP (Fig 3.1).

There are several factors that promote astrocytic glycogenolysis, thus increasing the availability of the energy substrate lactate to neurons, including vasoactive intestinal peptide, nor-adrenaline, adenosine, as well as K^+ (Hof *et al.*, 1988; Sorg and Magistretti, 1991).

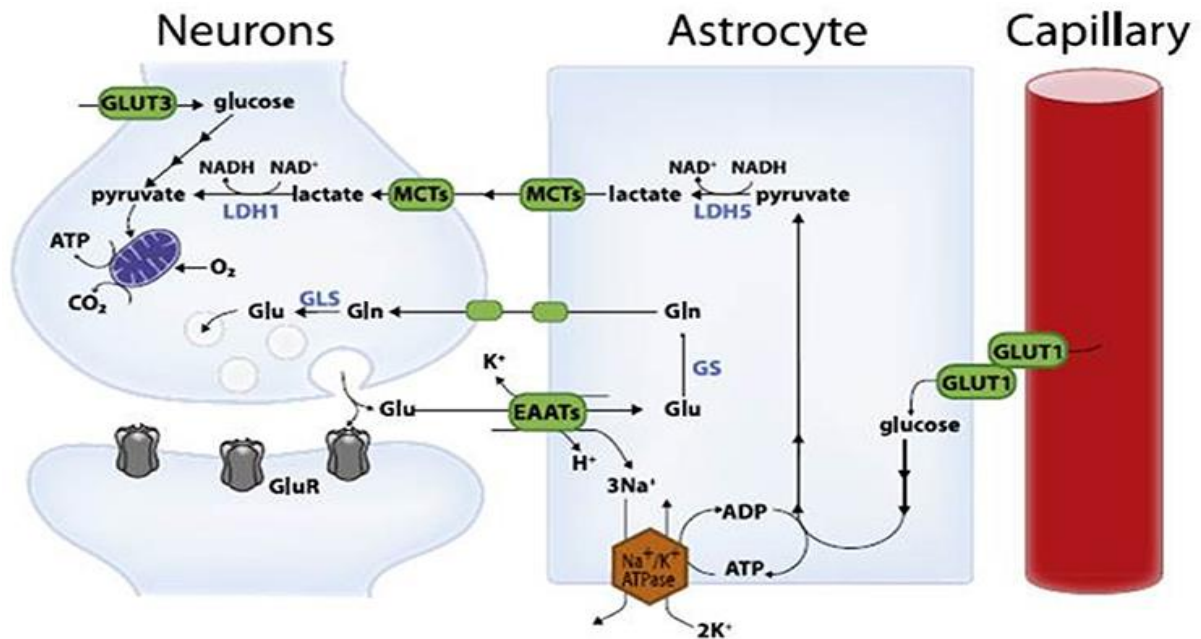


Figure 3.1. Schematic of the major pathways in the astrocyte-neuron lactate shuttle. Under physiological conditions, glucose uptake from the blood is mediated via glucose transporters GLUT1 in astrocytes, GLUT3 in neurons including axons and GLUT1/2 in oligodendrocytes, where it undergoes oxidative metabolism. Higher neuronal activity elicits an increase in glucose uptake, since activity and metabolism are tightly linked with a resultant release of axonal glutamate during action potentials. Removal of extracellular glutamate is affected by astrocytes via Na^+ -dependent glutamate transporters. The resultant surge in astrocytic intracellular Na^+ activates Na^+/K^+ ATPase, which necessitates ATP expenditure, and therefore drives astrocytic glucose uptake and mobilizes glycogen stores to produce lactate. Lactate is then shuttled via monocarboxylate transporter 4 (MCT4) to neighboring cells. In oligodendrocytes, it is taken up via MCT1 and subsequently oxidised. Within axons, lactate uptake is mediated via MCT2 to undergo oxidation and ATP production. (Reproduced from Mason, 2017).

A plethora of studies describe evidence supporting the ANLS hypothesis. Through experiments conducted on rat hippocampi, Suzuki and colleagues (2011) demonstrated that disruption of astrocytic MCTs interfered with long-term memory potentiation of synaptic strength; an effect that was restored by lactate, but not glucose application (Suzuki *et al.*, 2011). Disruption of the neuronal lactate transporter, MCT2, led to amnesia that was unaffected by neither lactate nor glucose supplementation, presenting a role for lactate transfer between astrocytes and neurons in memory formation. Accelerated blood glucose uptake was demonstrated in astrocytes upon intense neuronal activity triggered by whisker stimulation, which was otherwise normal in neurons under the same conditions (Chuquet *et*

al., 2010). This suggests that astrocytes play an important role in coupling glucose uptake to synaptic activity. Inhibition of α -cyano-4-hydroxycinnamate (4-CIN), a lactate transport inhibitor abrogated neuronal function in rat hippocampal slices even upon glucose supplementation (Schurr *et al.*, 1999).

Despite compelling evidence supporting the ANLS hypothesis, divergent theories concerning aspects of the ANLS have arisen, particularly because most assumptions of this hypothesis are based on *in vitro* studies. Using mathematical models of neurovascular coupling, Dinuzzo and colleagues examined the role of cerebral glycogen in response to brain stimulation (Dinuzzo *et al.*, 2010). The authors found that, rather than providing metabolic support in the form of lactate, astrocytic support was via indirect provision of glucose (Dinuzzo *et al.*, 2010), since glycogenolysis results in less astrocytic glucose uptake from the bloodstream, thereby allowing increased uptake into neurons. Kinetic properties of MCTs aided in the evaluation of glucose and lactate levels in response to neuronal stimulation and indicated diffusion of glucose, rather than lactate from basal lamina, across the interstitium, followed by uptake in neurons (Simpson *et al.*, 2007).

Application of mathematical models coupled with functional magnetic resonance spectroscopy (fMRS) allows for a reliable evaluation of compartmentalised metabolism in different cell types. This approach demonstrated that at normal glucose transport capacities, net lactate flow occurs from neuron to interstitium to astrocyte, in what the authors propose as a 'neuron-astrocyte lactate shuttle' or NALS (Mangia *et al.*, 2009). For the reverse to occur, that is, the astrocyte becomes the lactate exporter and neuron the importer, glucose transport capacity must be increased 12-fold, in disagreement with the ANLS hypothesis (Mangia *et al.*, 2009).

Despite conflicting results, it can still be argued that plasma lactate is an efficient metabolic substrate in the human brain and under certain conditions, may indeed be utilised preferentially by activated neurons.

3.2.4 Metabolic interactions between astrocytes and axons

Astrocytes play a key role in supporting axons during normal physiological function and under pathological conditions. However, whether the ANLSH can be applied to the interaction between astrocytes and axons has been largely controversial. The energy requirements to maintain physiologically active white matter tracts is substantial considering the extensive energy demand from axons and glial cells (Ransom and Orkand, 1996; Harris and Attwell, 2012). Delivery of energy substrates to axons is hindered by the fact that blood supply to white matter is considerably less than that of grey matter (Moody *et al.*, 1990), and by the myelin wrapped around axons, which hampers the entry of extracellular metabolite directly across and into axons (Nave, 2010a, b). This is somewhat compensated by the astrocyte processes contacting axons at nodes of Ranvier which could provide a route to transfer energy metabolites into axons (Pellerin *et al.*, 1998; Dringen *et al.*, 1993).

Astrocytes cannot release glucose. They can however convert it into lactate and provide it to axons. Baltan (2015) proposed three mechanisms in support of this theory. Astrocytes favour the transport of lactate into the extracellular space since the MCTs present on their membrane are MCT 1 and 4 (Poole *et al.*, 1996; Bröer *et al.*, 1997), and both have a low affinity to lactate, thus tend to export this substrate (Halestrap, 2012). On the other hand, MCT2 is the main monocarboxylate transporter present on axons (phil *et al.*, 2000). This has the highest affinity for lactate, with a preference towards active transport (Halestrap, 2012), making axons the ideal candidates to receive and metabolise lactate. LDH-1 promotes the production of pyruvate, whilst LDH-5 promotes lactate production (Cahn *et al.*, 1962). LDH-1 is found embedded within the axolemma in axons, whilst LDH-5 is found in astrocytes (Bittar *et al.*, 1996). Furthermore, the highest expression of glucose transporters is found on white matter astrocytes (Goursaud *et al.*, 2009). Astrocytic end-feet, rich in GLUT-1 type glucose transporters in turn abut against capillary walls in the brain and permit glucose uptake from the blood which is stimulated by glutamate receptor activation (Magistretti *et al.*, 1999).

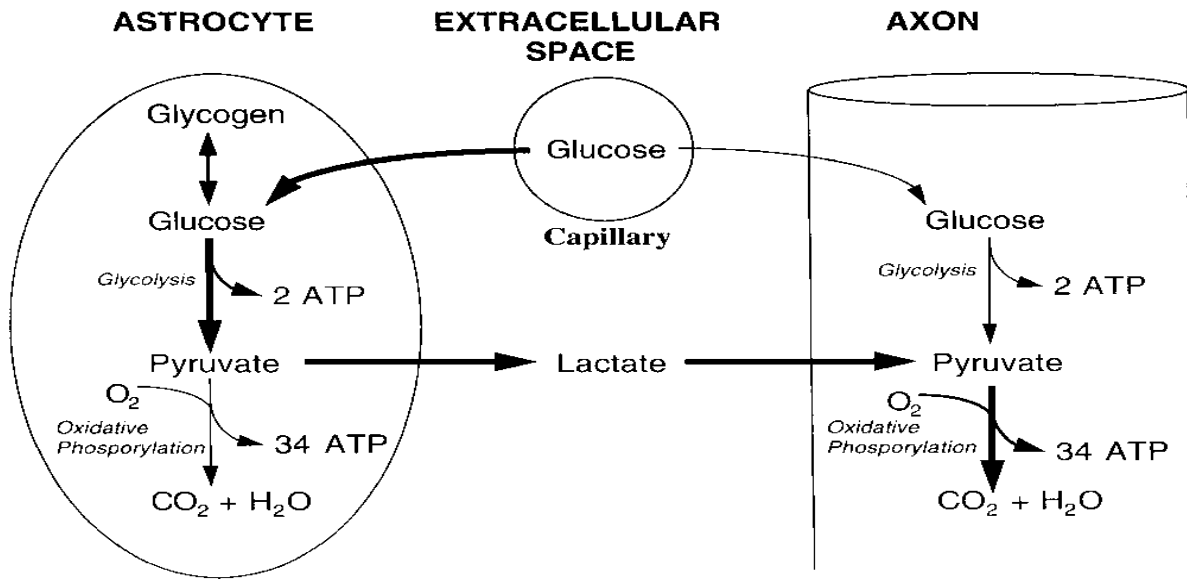
Experimental data suggests that the glycogen present in astrocytes is continuously being converted to lactate, which in turn is released into the extracellular space. This is taken up via the MCT-2 receptors present exclusively on axons and is metabolised aerobically to produce energy. This process is valuable in physiological conditions, during GD, and in response to an increase in neuronal activity (Ransom and Fern 1997; Tekkök *et al.*, 2005; Brown *et al.*, 2005).

Using the rodent optic nerve as a model of central white matter, Wender and colleagues (2000) reported that increasing the intracellular glycogen content during pre-treatment with a high-glucose load resulted in partial maintenance of axonal function during GD. On the other hand, decreasing glycogen content and inhibiting axonal lactate uptake exacerbated the GD-induced axonal injury.

Using the same model, in combination with electrophysiology and immunocytochemistry, Tekkök and colleagues (2005b) confirmed that lactate maintains functionally active axons during heightened periods of glucose deprivation. Blocking axonal lactate uptake by addition of D-lactate (a metabolically inert but transportable monocarboxylate) accelerated the decline in axonal function during GD. In addition, this study confirmed that MCT2 are predominantly found on axons and MCT1 on astrocytes, supporting the hypothesis that lactate is released from astrocytes and taken up by axons as an alternative energy source in times of high metabolic stress.

A more recent study on the rat optic nerve conducted by Chamber and colleagues (2014), provides further evidence in the association of lactate and axonal function during GD. Using a combination of electrophysiology and lactate biosensors, they reported a decrease in extracellular lactate minutes after the induction of GD, suggesting that lactate is consumed as the alternative energy source. Reperfusing with normal glucose containing aCSF, the same authors reported that the level of extracellular lactate returned to normal basal levels.

Normal Oxygen and Normal Glucose



Normal Oxygen and No Glucose

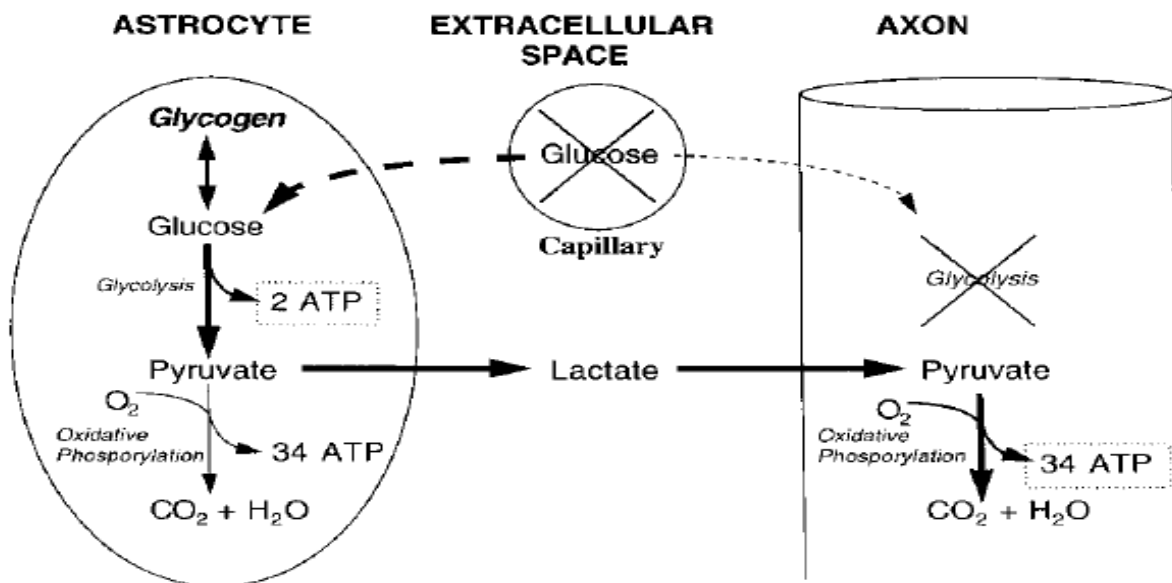


Figure 3.2. Proposed metabolic interactions occurring between astrocytes and axons. In the absence of blood glucose, the only source of energy substrate for the axon is lactate derived from glycogen stored in astrocytes. In the presence of oxygen, the lactate can be aerobically metabolized by axons to generate ATP (adapted from Ransom and Fern, 1997).

3.2.5 Metabolic interactions between oligodendrocytes and axons

Recent data supports the hypothesis that along with astrocytes, oligodendrocytes can also provide energy substrates to axons in times of stress. In fact, one particular study suggests that oligodendrocytes are instrumental in fuelling axonal activity (Morrison *et al.*, 2013). Other groups believe that a specialised and more specific lactate shuttle exists between oligodendrocytes and their myelinated axons (Fünfschilling *et al.*, 2012; Amaral *et al.*, 2013).

The intricate morphological connections between oligodendrocytes and axons facilitate the metabolic exchange between them. There are non-compacted regions of myelin that connect oligodendrocyte cell bodies to the periaxonal cytosolic space under the myelin sheath (Fünfschilling *et al.*, 2012). Under normal physiological conditions, delivery of energy substrates to the nodes of Ranvier is sufficient to maintain ATP production. However, when under metabolic stress, both oligodendrocytes and astrocytes supply axons with pyruvate/lactate as the need arises (Nave, 2010a, b; Fünfschilling *et al.*, 2012; Lee *et al.*, 2012a, b).

Studies on optic nerve explants exposed to GD provide evidence for axon-oligodendrocyte metabolic coupling (Fünfschilling *et al.*, 2012; Lee *et al.*, 2012a, b; Morrison *et al.*, 2013; Simons and Nave, 2015). In addition, abnormal metabolic support by oligodendrocytes is now accepted to underlie various diseases, ranging from amyotrophic lateral sclerosis to psychiatric diseases (Nave and Ehrenreich, 2014).

Lactate is considered to be the energy metabolite delivered by oligodendrocytes. Indeed, CAP can be evoked in white matter preparations (optic nerve, dorsal column and corpus callosum) and can persist for several hours but rapidly deteriorates under aglycaemic conditions. This failure can be effectively prevented by perfusion of L-lactate (Brown *et al.*, 2003). On the basis of these studies, it has been proposed that axons are at least partly energised by lactate (or pyruvate) provided by oligodendrocytes.

Saab *et al.*, (2016), demonstrated that NMDA receptors on oligodendrocytes play a key role in controlling the metabolic cooperation between oligodendrocytes and axons. In the optic nerve, NMDA receptor activation in response to glutamate release increases trafficking of glucose transporter GLUT1 to the oligodendrocyte membrane, thus sustaining glucose import to oligodendrocytes for glycolysis and downstream transfer of lactate to axons.

Although in literature one finds all this compelling evidence that lactate acts as an energy reserve during periods of GD, in a recent study, Meyer and colleagues (2018) challenged this notion. They reported that in the corpus callosum, lactate perfusion during periods of GD did not maintain axonal function. On the other hand, filling single oligodendrocytes with glucose, sustained axonal function during GD, supporting the hypothesis of the supportive role of oligodendrocytes to axons, but one which is mediated by glucose not lactate.

3.3 Methodology

In periods of increased energy demand or energy deprivation, astrocytes provide axons with an alternative energy substrate in the form of lactate to maintain normal physiological function (Ransom and Fern 1997; Tekkök *et al.*, 2005; Brown *et al.*, 2005). *In vitro* studies have shown that activation of β 2-adrenoreceptors stimulates the breakdown of glycogen in astrocyte, leading to the production of lactate (Hertz *et al.*, 2010). We wanted to test this hypothesis *in vivo*. In collaboration with Prof Jacques De Keyser from Vrije Universiteit Brussels, we tested this hypothesis through classical *in vivo* experiments and the findings were published as a manuscript in the journal, Neuroscience: (Laureys *et al.*, 2014).

Microdialysis probes were inserted into cerebellar white matter tracts to sample the extracellular concentrations of glucose, lactate, and glutamate following inhibition of axonal lactate uptake and the block of astrocytic glutamate uptake. Extracellular levels of glucose and lactate were also sampled through microdialysis following the addition of both agonists and antagonists of β 2-adrenoreceptors. In addition, we conducted a set of live-imaging experiments during which axonal lactate uptake was inhibited during a short period of GD; a β 2-adrenoreceptors agonist was added during prolonged GD; and a β 2-adrenoreceptors agonist was added again during a prolonged GD together with an axonal lactate uptake blocker. The drugs used in this section are summarised in Table 3.1.

Drug	Function	Concentration	Cat. No.
4-CIN	MCT2 Blocker ¹	0.1mM	28166-41-8
TBAO	EAAT blocker ²	250 μ M	4294-45-5
Clenbuterol	β 2-adrenoceptor agonist ³	20nM	21898-19-1
ICI-118,551	β 2-adrenoceptor antagonist ⁴	200nM	72795-01-8

Table 3.1. List of drugs used to study the potential role of lactate as an energy substrate during GD. All drugs were obtained from Sigma-Aldrich. Properties and usage of the drugs can be found: ¹(Erlichman *et al.* 2008; Wender *et al.* 2000; Pierre *et al.*, 2000); ²(Shimamoto *et al.*, 1998); ³(Zuurmond *et al.*, 1999; Izeboud *et al.*, 1999); ⁴(Hillman *et al.*, 2005)

3.3.1 In vivo microdialysis in white matter

Male C57bl/6 mice between 7 and 8 weeks of age (weighing 25–30 g), were anaesthetised with a mixture of xylazine/ketamine (10/100-mg/kg, IP) and mounted on a stereotaxic frame. An intracranial guide (CMA/ Microdialysis, Stockholm, Sweden) was implanted in the bilateral cerebellar white matter coordinates toward bregma were 5.7 mm posterior, 2.2 mm lateral and 2.3 mm ventral of the dura (Paxinos and Franklin, 2004). Immediately after surgery, guide cannula obturators were replaced by microdialysis probes (CMA7; membrane length: 1 mm theoretical cutoff: 6000 Da; CMA/Microdialysis, Solna, Sweden). Postoperative analgesia was ensured by ketoprofen (4 mg/kg, IP). Animals were allowed to recover from surgery overnight receiving laboratory chow and water ad libitum. Probe localisation was histologically verified post-mortem. Microdialysis probes were continuously perfused with aCSF at a flow-rate of 1 μ l/min (CMA/400 microdialysis pump, CMA/Microdialysis, Solna, Sweden). All experiments were performed on the day following surgery in non-anaesthetised freely moving mice. Tubings were flushed with 70% ethanol and rinsed with purified water before perfusion with aCSF to exclude any bacterial interference with the glucose/lactate levels. 1 μ l/min perfusion of the probes was started 2hr before the experiment to attain steady-state concentrations. Six dialysate samples (20 μ l) were collected at 20-min intervals to determine the basal concentrations. TBOA, 4-CIN, clenbuterol or ICI-118551 was dissolved in aCSF and added to the perfusion medium at the last 20-min baseline sample. Thereafter six 20-min samples were collected during compound administration. In a separate set of experiments ($n=5$) a control experiment was performed with a “sham” switch of syringes to exclude any effect of switching syringes on glucose, lactate and glutamate concentrations. A gradient liquid chromatographic method was used for the quantitative simultaneous determination of amino acids in dialysates as previously described (Van Hemelrijck *et al.*, 2005). All substances were identified and quantified by comparing retention times and peak areas with those of external standards. Microdialysate samples were analysed for glucose and lactate content using enzymatic lactate (607-100) and glucose (606-100) assay kits (Biovision, Mountainview, CA, USA) according to the manufacturers’ guideline. Fluorescence was measured at 460 nm using a microplate reader (Model 680 Bio-Rad, Hercules, CA, USA) and an excitation wavelength of 355 nm.

3.3.2 Live imaging experiments to determine role of lactate during glucose deprivation

To study the role of astrocytic lactate during glucose deprivation, we used the same experimental protocol used in chapter 2: live imaging of YFP-expressing axons with two-photon microscopy. Three different experimental paradigms were used.

	Duration of GD	Drug/s added
Paradigm 1	30 min	0.1mM of 4-CIN
Paradigm 2	45 min	20nM of Clenbuterol
Paradigm 3	45 min	20nM of Clenbuterol + 0.1mM of 4-CIN

Table 3.2. The experimental paradigms employed to study the potential role of astrocytic lactate during GD.

In the first paradigm, we studied the effects on axonal integrity when lactate uptake was deliberately blocked during a short period (30 mins) of glucose deprivation, during which usually no axonal injury occurs. In the second paradigm, we wanted to verify axonal viability when slices were subjected to β 2-adrenoreceptor stimulation during a more prolonged (45 min) exposure to glucose deprivation. Finally, in the third paradigm, we wanted to determine whether inhibition of lactate uptake by axons had any effect on the previous observation that β 2-adrenoreceptor activation served to preserve axon integrity during metabolic compromise.

Since 4-CIN necessitated dimethyl sulfoxide (DMSO) as a solvent, all solutions contained 0.01% DMSO. An additional control experiment of slices exposed to 30 min of GD in the presence of DMSO was performed to exclude any effect on axon integrity due to DMSO alone.

3.3.3 Statistical analysis

The average (with s.e.m.) of the 5 stable baseline dialysate levels for the animals included in the study are: 0.218 ± 0.016 mg/dl glucose, 0.036 ± 0.002 mg/dl lactate and 0.590 ± 0.046 μ M glutamate. Glutamate, glucose and lactate levels are expressed relative to the stable baseline levels, which were equated to 100% with s.e.m. A correction for changes induced by syringe exchange was performed by subtracting the % change in sham conditions for each time point. Statistical analysis between pharmacologically induced levels and baseline level was performed using a Friedman test followed by Dunn's multiple comparisons post hoc test. The basal area under the curve (AUC) was calculated as the sum of dialysate concentrations in the first six "basal" collections (20 min samples). AUC following drug was calculated as the sum of the dialysate concentrations in the six collections following the start of drug perfusion. AUC after drug administration was expressed as a percentage of basal AUC. Wilcoxon-signed rank test was used to compare basal and drug-induced AUC. Animals were excluded from analysis when contamination of the sample or technical problems rendered measurement impossible. Statistical analysis was performed with the InStat Prism statistical package (GraphPad Software, La Jolla, USA).

The statistical analysis used to compare axonal injury scores between conditions is the same one as described in chapter 2.

3.4 Results

3.4.1 Analysis of microdialysates after drug administration

The first set of results were obtained from the microdialysis experiments. For each experimental trial the probe localisation was histologically verified post-mortem (Refer to supplementary data.). Animals with aberrant probe location were excluded from the study.

To address the presence of functionally coupled glutamate–lactate metabolism in white matter we pharmacologically blocked both ends of the presumed glial–axonal shuttle. Inhibition of axonal lactate uptake by the MCT-2 blocker 4-CIN (0.1mM) resulted in an increased extracellular lactate concentration (Fig. 3.3 A), whereas extracellular glucose levels were not affected (Fig.3.3 B). Inhibition of axonal lactate uptake increased extracellular glutamate concentrations (Fig. 3.3 C). Inhibition of the astrocytic glutamate transporters by TBOA (200nM) led to the accumulation of extracellular glutamate (Fig. 3.3 C). TBOA also significantly diminished extracellular glucose levels (Fig. 2B) without influencing extracellular lactate concentration (Fig. 3.3 A).

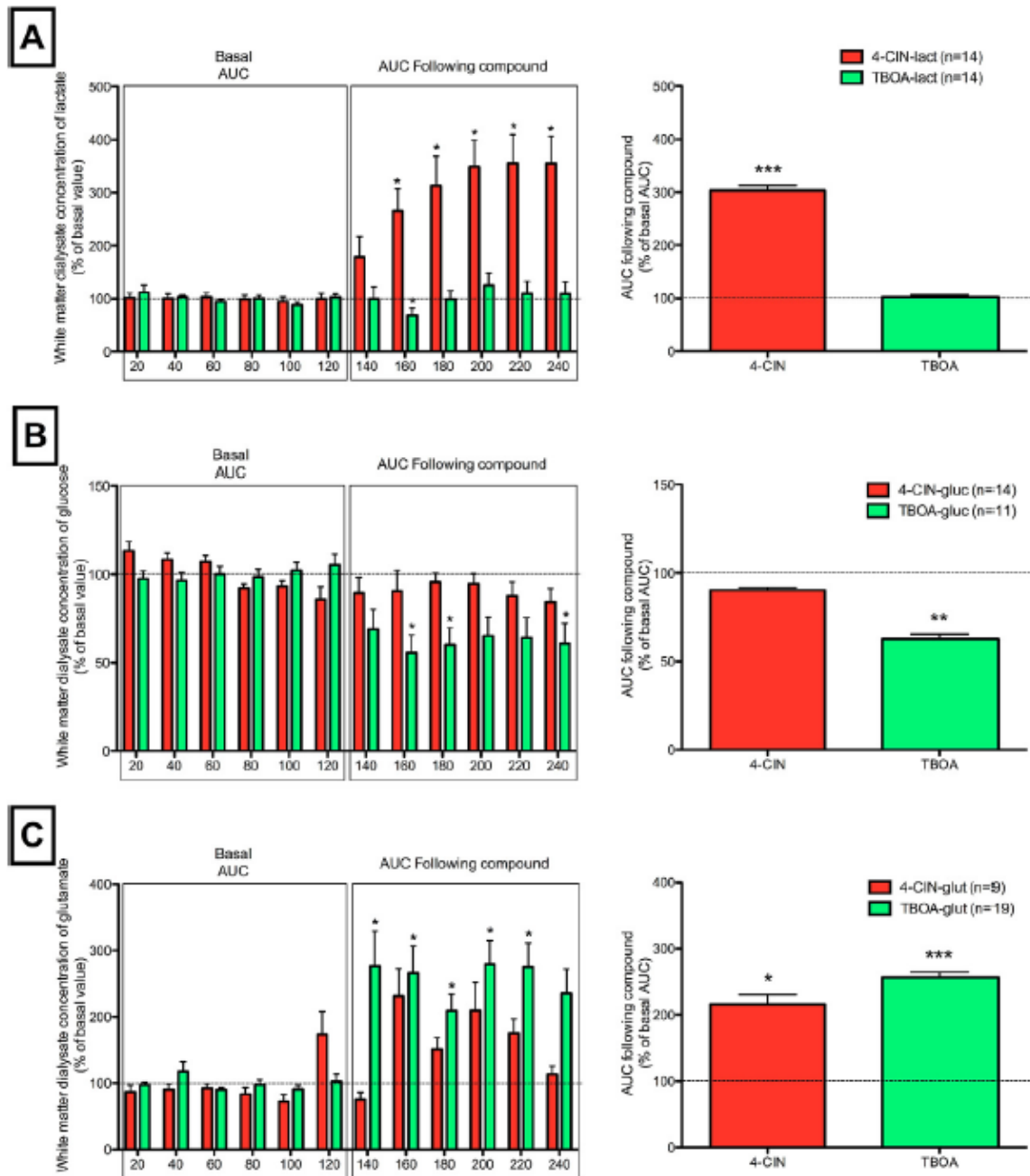


Figure 3.3. Microdialysate levels of glucose, lactate and glutamate following administration of 4-CIN and TBOA. Six dialysate samples were collected determine the basal concentrations expressed as 100%+s.e.m. Another 6 samples taken at 20 min interval after adding the drugs. Graphs show changes in extracellular (A) lactate, (B) glucose, and (C) glutamate concentration for 4-CIN (red bars) and TBOA (green bars). (* $p < 0.05$, ** $p < 0.005$, *** $p < 0.001$); n=as indicated in the figure (adapted from Laureys *et al.*, 2014).

3.4.2 The block in the uptake of lactate by axons during 30 min of glucose deprivation causes axonal injury

As previously reported in section 2.4.4, axons can withstand 30 min of GD without showing any outward signs in structural injury. Blocking the uptake of lactate after incubation with sucrose-containing aCSF containing 0.1mM of 4-CIN for 30 min, resulted in beading towards the end of the period of GD. Reperfusion with glucose-containing aCSF resulted in extensive damage accompanied by beading and fragmentation of axons.

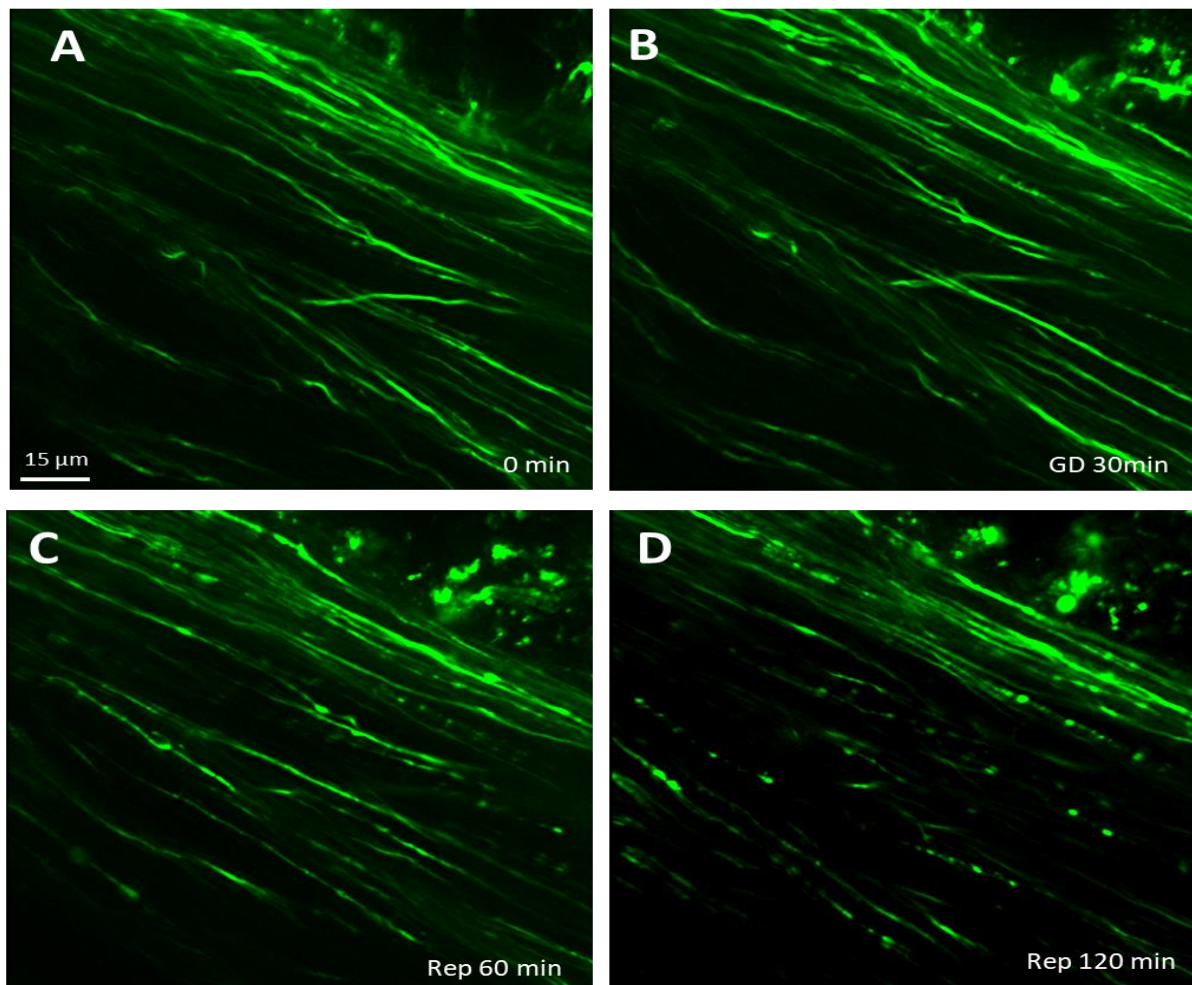


Figure 3.4. Sequential images of a callosal slice exposed to 30 min of GD in the presence of 4-CIN. Blocking axonal lactate uptake via 0.1mM 4-CIN caused axonal beading during 30 min of GD (B), and extensive beading and fragmentation was observed by 1 hr (C) and after 2 hr of GD (D) with reperfusion with glucose containing aCSF. Scale 15 μm

	At Start	Right after GD	Rep 1 hr	Rep 2 hr
GD 30 min + 4-CIN	0.17 ± 0.04	0.44 ± 0.05	1.00 ± 0.05	1.35 ± 0.03
GD 30 min	0.17 ± 0.06	0.26 ± 0.06	0.29 ± 0.03	0.32 ± 0.05
Controls	0.26 ± 0.06	0.26 ± 0.06	0.26 ± 0.06	0.26 ± 0.06

Table 3.3. Injury score of callosal axons exposed to 30 min of GD (+/-) 4-CIN and controls. Values are expressed as mean values ± standard deviation ($n=3$).

There was a statistically significant difference in axonal injury score in slices exposed to 30 min GD + 0.1.mM 4-CIN, when compared with controls and slices exposed only to 30 min of GD.

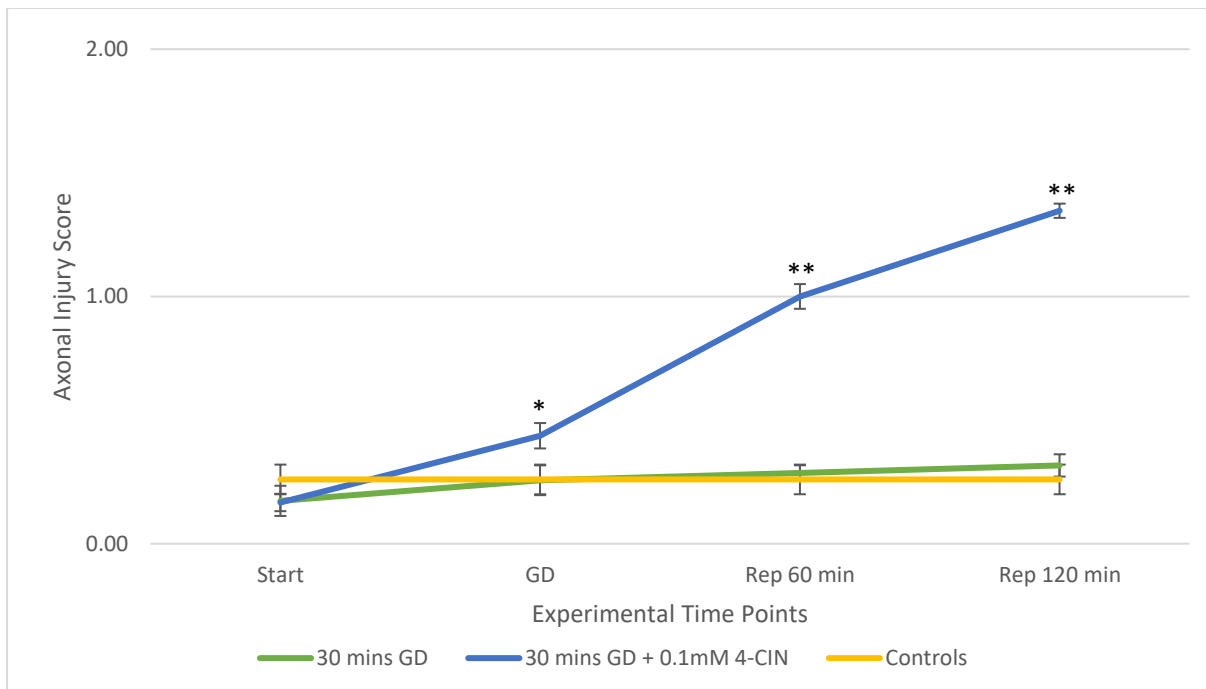


Figure 3.5. Injury score of callosal axons exposed to 30 min of GD (+/-) 4-CIN and controls. There is a statistically significant higher injury score in slices exposed to 30 min GD + 4-CIN when compared to those slices exposed to 30 min GD without the drug and controls (* $p < 0.05$, ** $p < 0.001$) ($n=3$).

No signs of axonal injury were reported in slices exposed to 30 min of GD in DMSO without the drug (4-CIN) followed by 2 hr reperfusion. Refer to supplementary data.

3.4.3 β 2-adrenergic stimulation protects axons during 45 min of glucose deprivation

As shown through our previous findings (section 2.4.4), callosal slices exposed to 45 min of GD resulted in severe structural injury following reperfusion with glucose-containing aCSF. Stimulation of the β 2-adrenergic receptors located on astrocytes through the addition of 20nM clenbuterol during a similar prolonged duration of GD, preserved axonal structure.

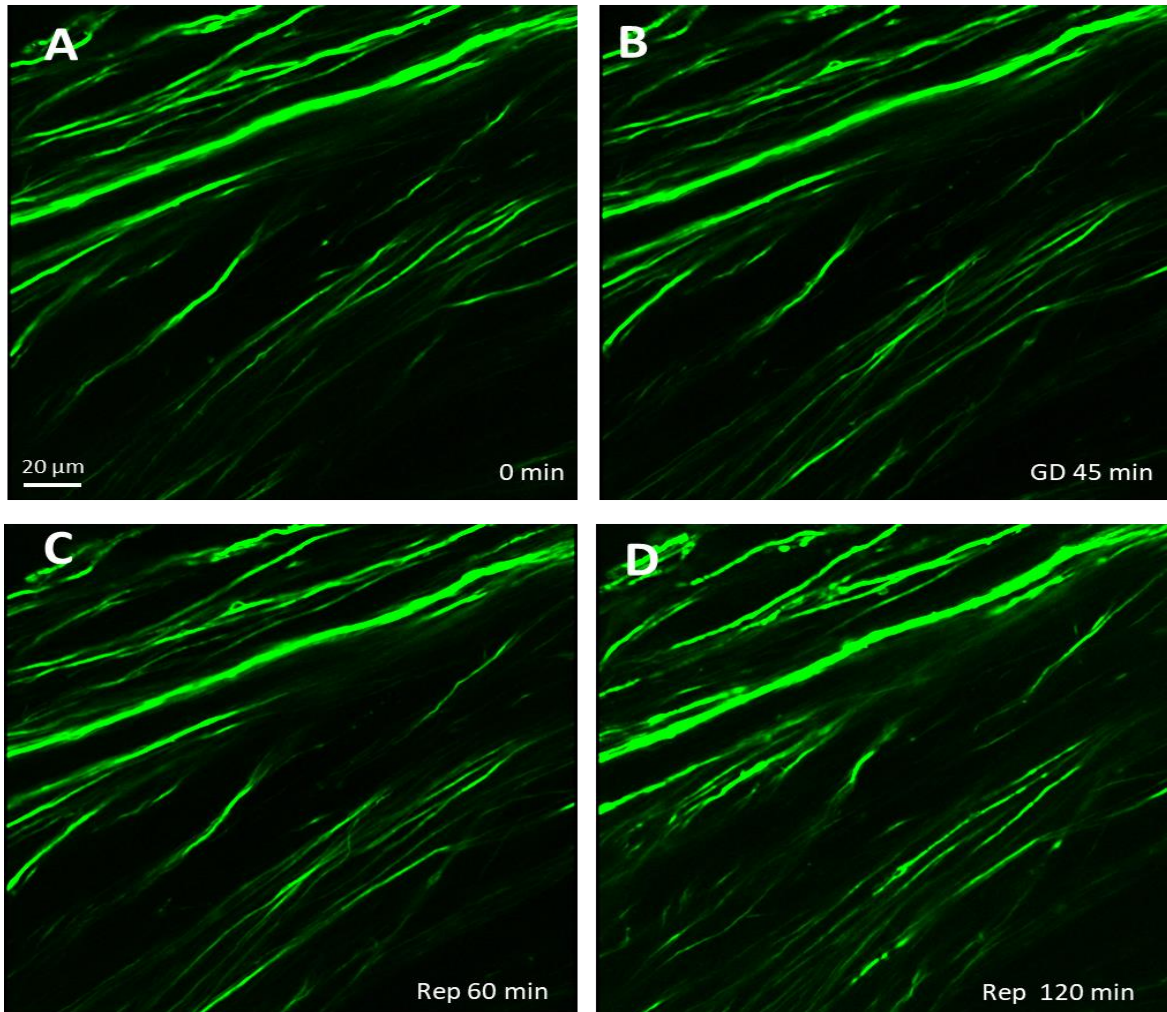


Figure 3.6. Sequential images of a callosal slice exposed to 45 min of GD in the presence of clenbuterol. β 2-adrenergic stimulation preserves axons after exposure to 45 min of GD. Addition of 20nM clenbuterol preserved axonal integrity at all stages of the observation period: at start (A) after 45 min of GD (B), at 1 hr of reperfusion (C) and at 2 hr of reperfusion. Scale 20 μ m

	Start	GD	Rep 1 hr	Rep 2 hr
GD 45 min + Clenbuterol	0.17 ± 0.02	0.23 ± 0.09	0.27 ± 0.09	0.33 ± 0.05
GD 45 min	0.22 ± 0.02	0.44 ± 0.10	1.00 ± 0.13	1.35 ± 0.11
Controls	0.26 ± 0.06	0.26 ± 0.06	0.26 ± 0.06	0.26 ± 0.06

Table 3.4. Injury score of callosal axons exposed to 45 min of GD (+/-) clenbuterol and controls. Values are expressed as averages ± standard deviation ($n=3$).

There was no statistically significant difference in axonal injury score between slices exposed to 45 mins GD + 20nM Clenbuterol and the controls in all the assayed time points. However, a statistically significant difference was found between slices exposed to 45 min GD (+/- drug), at all the assayed time points right after the start.

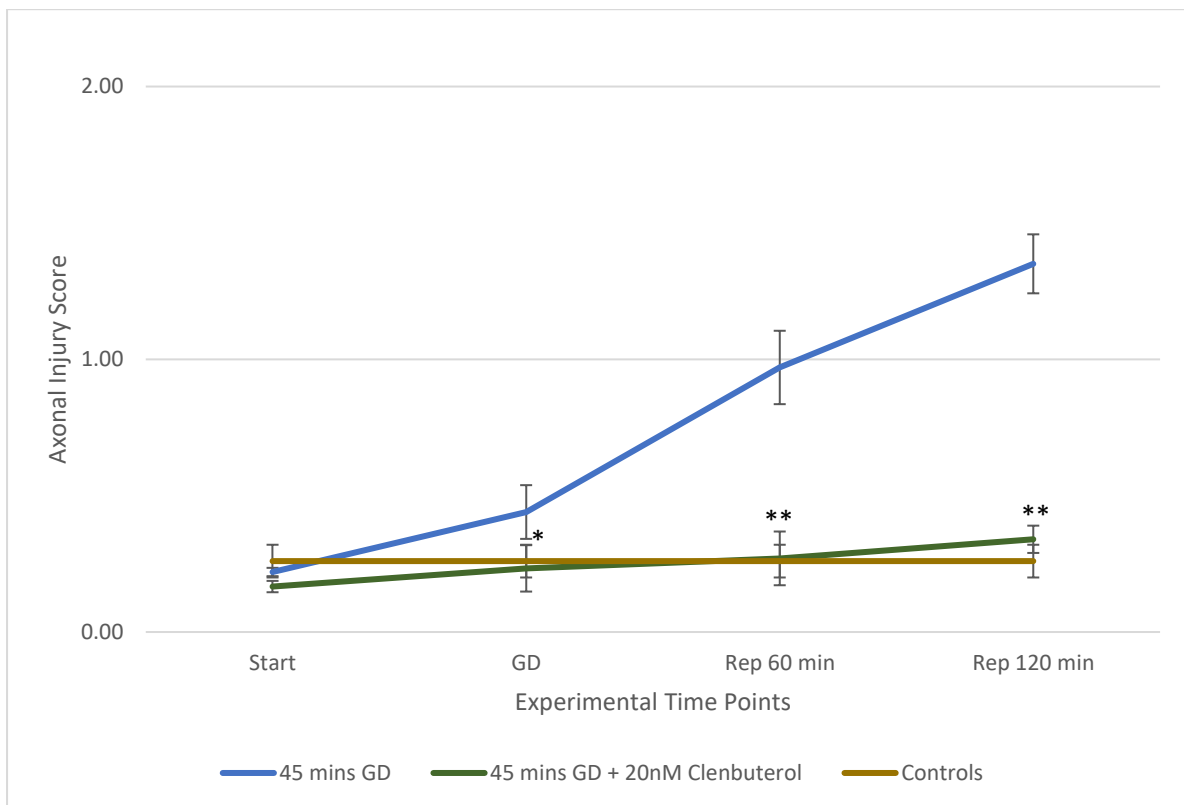


Figure 3.7. Injury score of callosal axons exposed to 45 min of GD (+/-) clenbuterol and controls. There was no difference in axonal injury score between control slices and slices exposed to 45 of GD with clenbuterol. A statistically significant higher injury score was evident in slices exposed to 45 min of GD without clenbuterol when compared to slices exposed to 45 min GD with clenbuterol treatment (* $p < 0.05$, ** $p < 0.001$) ($n=3$).

3.4.4 The block in the uptake of lactate by axons inhibits the protection of β 2-adrenergic stimulation during 45 min of glucose deprivation

The protective effect exerted by clenbuterol during 45 mins of GD was lost when callosal slices were exposed to 45 min of GD with the combined addition of 20nM Clenbuterol and 0.1mM 4-CIN. A loss in axonal structural integrity was observed after 45 mins of GD, and this was exacerbated during the reperfusion phase after restoration of the glucose-containing aCSF.

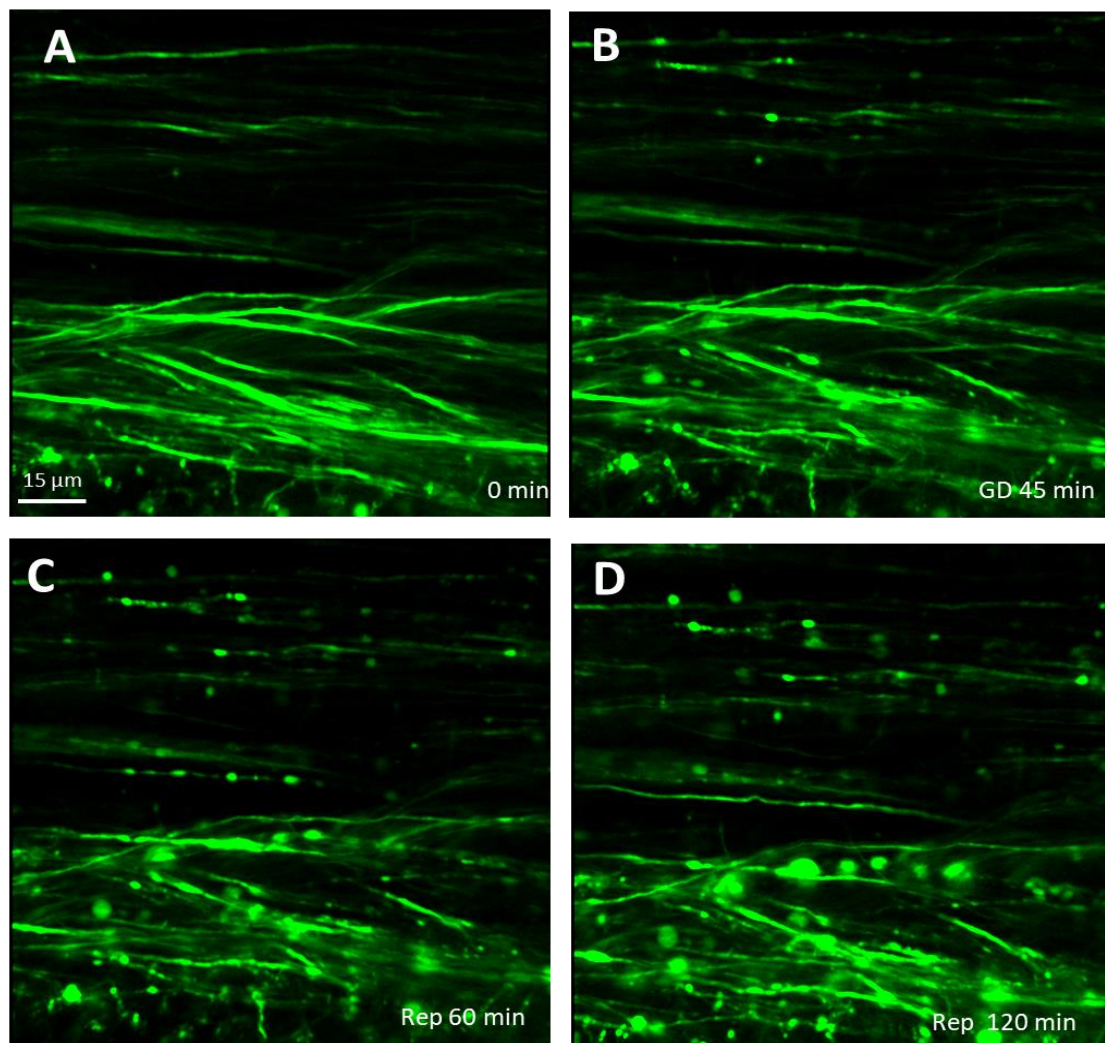


Figure 3.8. Sequential images of a callosal slice exposed to 45 min of GD in the presence of clenbuterol and 4-CIN. Blocking axonal uptake of lactate by 4-CIN causes extensive axonal injury after 45 min of GD despite β 2-adrenergic stimulation by the addition of clenbuterol. The addition of 0.1mM 4-CIN and 20nM Clenbuterol caused axonal beading at 45 min of GD (B), and fragmentation of axons by 1 hr into reperfusion (C) through 2 hr of reperfusion with glucose containing aCSF. Scale 15 μ m

	Start	GD	Rep 1 hr	Rep 2 hr
GD 45 min + Clenbuterol + 4-CIN	0.13 ± 0.06	0.64 ± 0.04	1.40 ± 0.04	1.55 ± 0.08
GD 45 min	0.22 ± 0.02	0.44 ± 0.10	1.00 ± 0.13	1.35 ± 0.11
Controls	0.26 ± 0.06	0.26 ± 0.06	10.26 ± 0.06	0.26 ± 0.06

Table 3.5. Injury score of callosal axons exposed to 45 min of GD (+/-) clenbuterol + 4-CIN and controls. Values are expressed as mean ± standard deviation ($n=3$).

There was a statistically significant difference in axonal injury score between callosal slices exposed to 45 mins of GD + 20nM Clenbuterol + 4-CIN and the control slices at all the assayed time points right after the start.

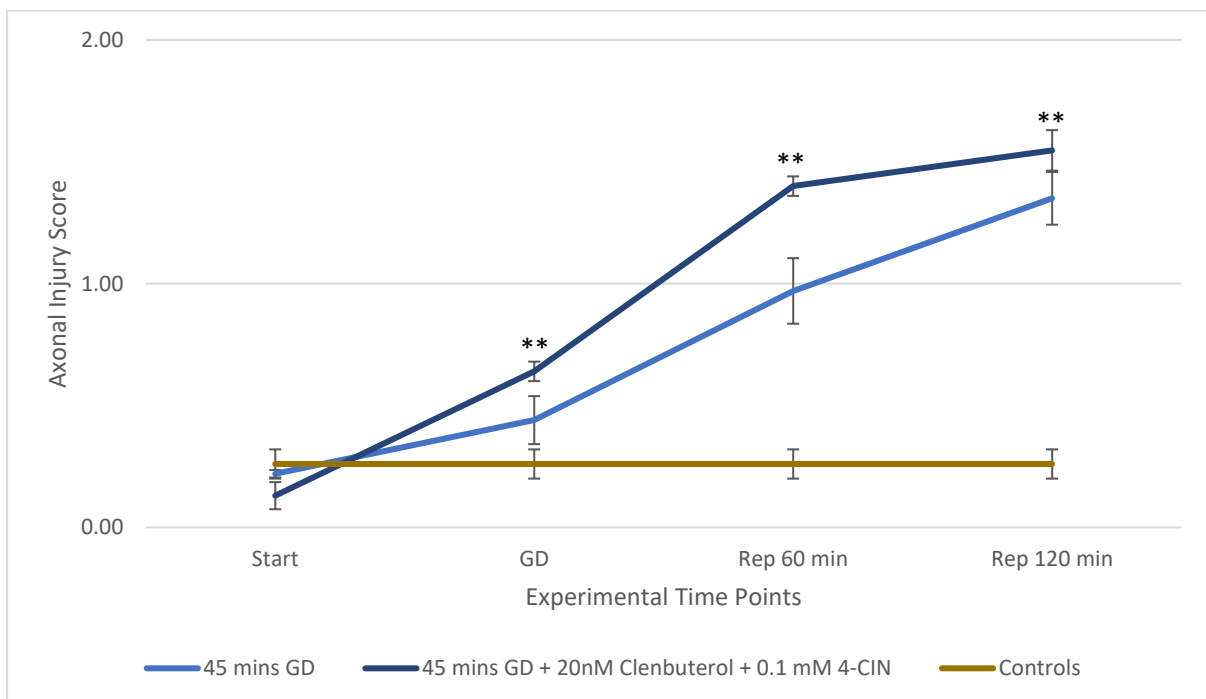


Figure 3.9. Injury score of callosal axons exposed to 45 min of GD (+/-) clenbuterol + 4-CIN and controls. There was a statistically significant higher injury score in slices exposed to 45 min of GD with the use of both drugs when compared with the control slices (** $p < 0.001$) ($n=3$).

3.4.5 β 2-adrenergic stimulation does not alter extracellular lactate and glucose concentration

A final set of microdialysis experiments were conducted to determine whether *in vivo* stimulation of β 2-adrenoreceptors exerted any effect on the extracellular levels of glucose and lactate. There was no change in the extracellular levels of either glucose (Fig 3.11 A) nor lactate (Fig 3.11 B) following the intracerebral injection of the β 2-antagonist ICI-118551 or β 2-agonist clenbuterol .

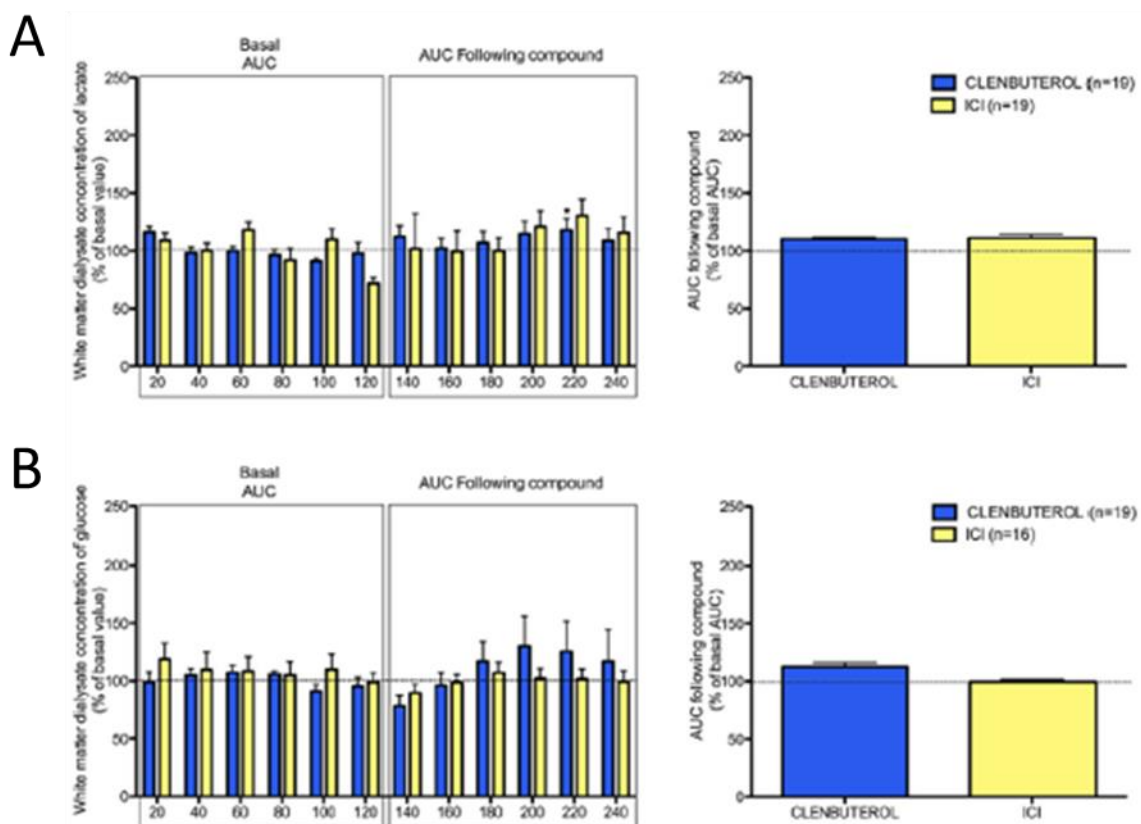


Figure 3.10. Microdialysis levels of glucose, lactate and glutamate following administration of Clenbuterol and ICI-118551. Six dialysate samples were collected determine the basal concentrations expressed as 100%+s.e.m. Another 6 samples taken at 20 min interval after adding the drugs. Graphs show changes in extracellular (D) lactate, and (B) glucose for Clenbuterol (blue bars) and ICI (yellow bars). (*p<0.05, **p<0.005, ***p<0.001); n=as indicated in the figure. (Adapted from Laureys *et al.*, 2014)

3.5 Discussion

Based on previous works (Ransom and Fern 1997; Wender *et al.*, 2000; Tekkök *et al.*, 2005b; Brown *et al.*, 2005; Fünfschilling *et al.*, 2012; Amaral *et al.*, 2013; Morrison *et al.*, 2013; Chamber *et al.*, 2014), we propose a working hypothesis on the of the supposed metabolic coupling mechanisms between axons and surrounding glial cells (Fig 3.11). Glucose is taken by astrocytes via GLUT1, a process facilitated by the close relationship of the astrocytes' end feet processes to blood vessels. During periods of low neuronal activity, glucose is converted to glycogen and stored in the astrocytes. In times of high energy demand, it is consumed in aerobic or anaerobic glycolysis. An increase in extracellular glutamate is picked up by astrocytes via GLT-1/GLAST, which is then converted to glutamine, a process requiring ATP. This conversion can then stimulate glycolysis of the intracellular glucose to produce lactate. MCT4, which is preferentially present on astrocytes, and has a low affinity for lactate, promotes lactate release in the extracellular space. Another source of extracellular lactate comes from oligodendrocytes, which release it via the MCT1 transporter. This extracellular lactate is then preferentially picked up via the high affinity MCT2 which is present on axons.

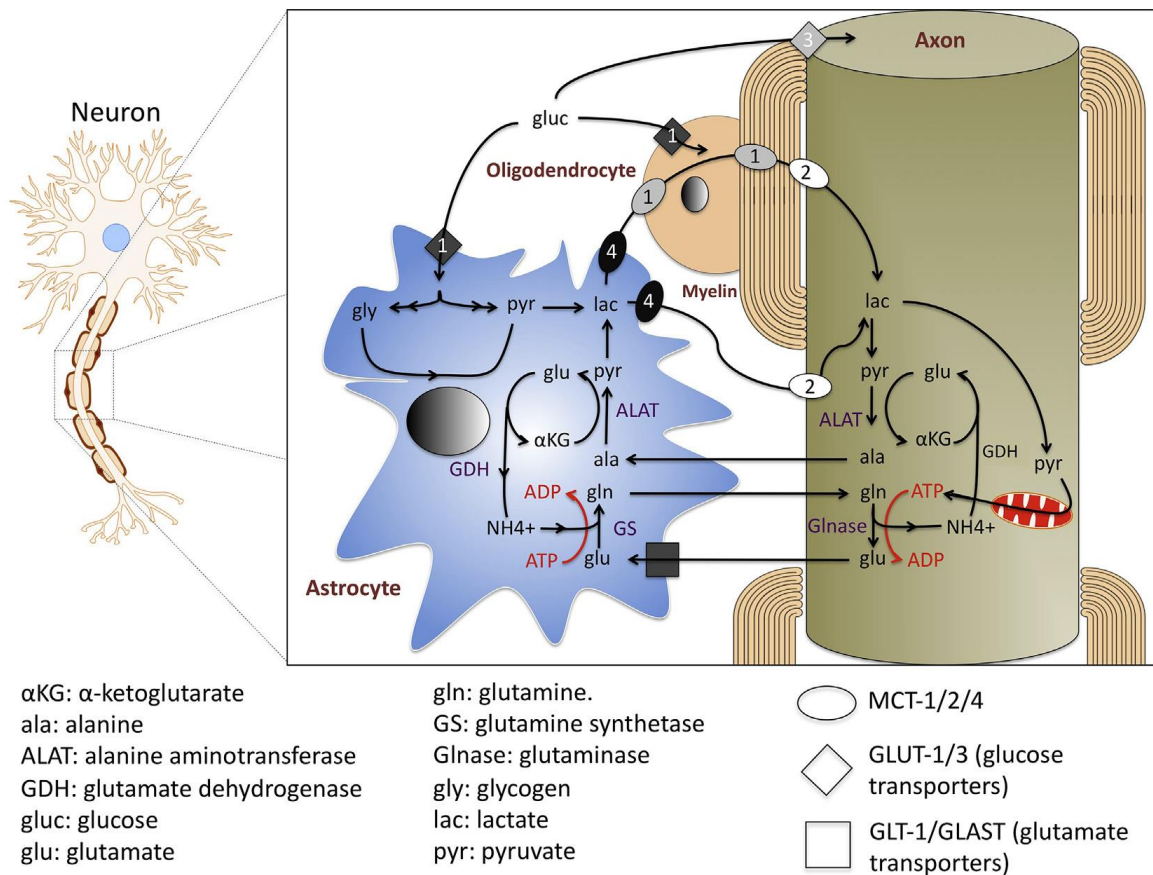


Figure 3.11. Summary of the lactate shuttle and the interconnected glutamate–glutamine cycle between astrocytes and axons. Glucose enters astrocytes from the extracellular space and at the endothelial blood–brain-barrier junction by GLUT-1 mediated transport. This glucose can be incorporated in glycogen or consumed in anaerobic glycolysis. Glycolytic processing of glucose is driven by the need for the ATP consumed by glutamate uptake and glutamine synthesis. The final product of this glycolysis, namely lactate, is released from astrocytes via MCT4. Oligodendrocytic MCT1-mediated transport releases lactate near the axons. Axons take up lactate for aerobic metabolism by means of their MCT2 transporters (reproduced from Laureys *et al.*, 2014).

3.5.1 The glucose-lactate shuttle in white matter during normal physiology

From the first set of microdialysis experiments, we established that blocking axonal lactate uptake results in an increase in extracellular lactate and glutamate. The increase in extracellular lactate during pharmacological blockade of axonal lactate uptake demonstrates the existence of a physiological glia–axonal lactate shuttle in white matter under basal conditions.

The increase in extracellular glutamate probably reflects inhibition of astrocytic lactate production (via astrocytic glycogenolysis) by feedback inhibition (Sotelo-Hitschfeld et al., 2012). *In vitro* data suggests that elevated inhibition of glycogenolysis elevates extracellular glutamate concentrations (Sickmann et al., 2009; Schousboe et al., 2010). Our *in vivo* data corroborate these findings, since we reported an elevation of extracellular glutamate following the addition of 4-CIN.

Functional glutamate reuptake by optic nerve axons has been demonstrated (Arranz et al., 2008) and may constitute a complementary mechanism of glutamate accumulation when axons are deprived of lactate influx.

Inversely inhibition of glutamate reuptake with TBOA decreased extracellular glucose levels compatible with enhanced glycolytic glucose consumption.

In summary, these data are in line with functional exchange machinery where glial cells produce lactate during the buffering process of extracellular glutamate, with lactate subsequently being transported to axons as energy source.

3.5.2 Lactate as a source of energy during glucose deprivation

Having established that axons utilise lactate during normoglycemia, we wanted to investigate the role of lactate consumption during glucose deprivation. In section 2.4.4, we reported that axons have enough energy reserve to withstand 30 min of GD. To determine whether during glucose deprivation, lactate can act as an alternative energy substrate, we conducted live imaging of the callosal slices exposed to 30 min of GD whilst blocking axonal lactate uptake (with 4-CIN). We observed that by the end of the 30 min of GD there was already considerably axonal focal swelling and beading. This exacerbated to increased beading, fragmentation, and axonal conduction at the end of the 2 hr of reperfusion with glucose containing aCSF. This suggests that lactate can act as an alternative energy substrate during glucose deprivation.

Our data confirmed previous findings based on electrophysiology and immunocytochemistry data on the rodent optic nerve, which reported that lactate is an essential energy substrate to white matter axons during both physiological and pathological conditions (Baltan, 2015, Ransom and Fern 1997; Tekkök *et al.*, 2005; Brown M *et al.*, 2005; Chamber *et al.* 2014).

3.5.3 Stimulation of astrocytic β 2-adrenergic receptors protects axons during glucose deprivation

In literature, there is evidence that glucose deprivation activates the β 2-adrenergic system, promoting glycolysis. A drop in glucose levels activates the neurons present in the Locus Coeruleus (Morilak *et al.*, 1987) resulting in a widespread increase of noradrenaline in the brain (Bengzon *et al.*, 1991). *In vitro* data suggests that activation of the β 2-adrenergic enhances astrocytic glycogenolysis (Hertz *et al.*, 2010). Although using the acute brain slice model has numerous advantages, it is devoid of the connection present in the live animal, and therefore has no noradrenergic input for the locus coeruleus projections. To circumvent this issue, we added clenbuterol, a β 2-adrenoceptor agonist.

We observed that clenbuterol extends axonal survival during glucose deprivation. Adding 10nM clenbuterol to 45 min of GD showed good preservation of axon integrity and complete neuroprotection that extended throughout the 2 hr of recirculation with glucose containing aCSF. We hypothesised that β 2-adrenergic stimulated astrocytic glycolysis, which in turn was transported via MCT2 into the axons and served as an additional energy substrate during the period of glucose deprivation. To determine whether it was the lactate that was offering the extra protection, we blocked the MCT2 transporter during the 45 min of GD with 4-CIN. Since the protective effect of β 2-adrenergic stimulation was lost, we further validated our hypothesis that the protective effect of β 2-adrenergic stimulation was mediated by an increase in lactate production.

The above findings were challenged by the results from the last set of microdialysis experiments. The addition of a β 2-adrenergic agonist and antagonist was added via the microdialysis probe. Neither drug had any effect on the extracellular levels of lactate and glucose. Therefore, the protective role we observed with clenbuterol in our experiments may be due to its anti-inflammatory, anti-oxidative and neurotrophic effects (Gleeson *et al.*, 2010), and not by enhanced astrocytic lactate production.

Chapter4

The central role of excitotoxicity to white mater following glucose deprivation

4.1 Aims

The spectrum of neurological deficits associated with hypoglycaemia suggests that the pathophysiology of the insult cannot be simply neuron starvation. Previous literature reports that glucose deprivation induced injury is mediated through a combination of ionic imbalances and excitotoxicity. In view of this, the main aims of this chapter are:

- i. To determine the exact role of AMPA/Kainate receptor overactivation on glia and study their downstream effect on axons.
- ii. To determine whether axonal injury following GD is Ca^{2+} dependent.
- iii. To establish whether the specific block of NMDA receptors located on oligodendrocytes protects axons during glucose deprivation.

4.2 Literature Review

Hypoglycaemic injury is mainly limited to the damage caused to the central nervous tissue, with other organs such as the heart, remaining mostly unaffected. Originally it was thought that this was due to the high metabolic rate of neurons coupled to their very low energy reserves, but ultimately the widespread effect of hypoglycaemia on brain injury cannot be simply attributed to neuron glucose starvation (Swanson, 2014). Magnetic resonance imaging studies of patients with hypoglycaemic brain injury show that white matter structures are affected as frequently and severely as grey matter despite energy demand in white matter being less than in grey matter (Ma, 2009; Johkura, 2012).

Hypoglycaemia was found to induce accumulation of excitatory amino acids, loss of ion homeostasis, inhibition of protein synthesis, intracellular calcium overload and alkalosis (Auer, 1986). Under normal conditions, glucose fuels the Krebs's cycle to generate ATP. During periods of hypoglycaemia, the decrease in acetate results in accumulation of oxaloacetate, leading to an increase in aspartate (Agardh *et al.*, 1978). The latter shifts to the extracellular space resulting in a 1600% increase above baseline levels (Sandberg *et al.*, 1985) and that is soon followed by a significant increase in glutamate (Sandberg *et al.*, 1986). The increase in these extracellular neurotransmitters results in selective neuronal necrosis, predominantly in the cerebral cortex, caudo-putamen and hippocampus (Auer and Siesjö, 1993).

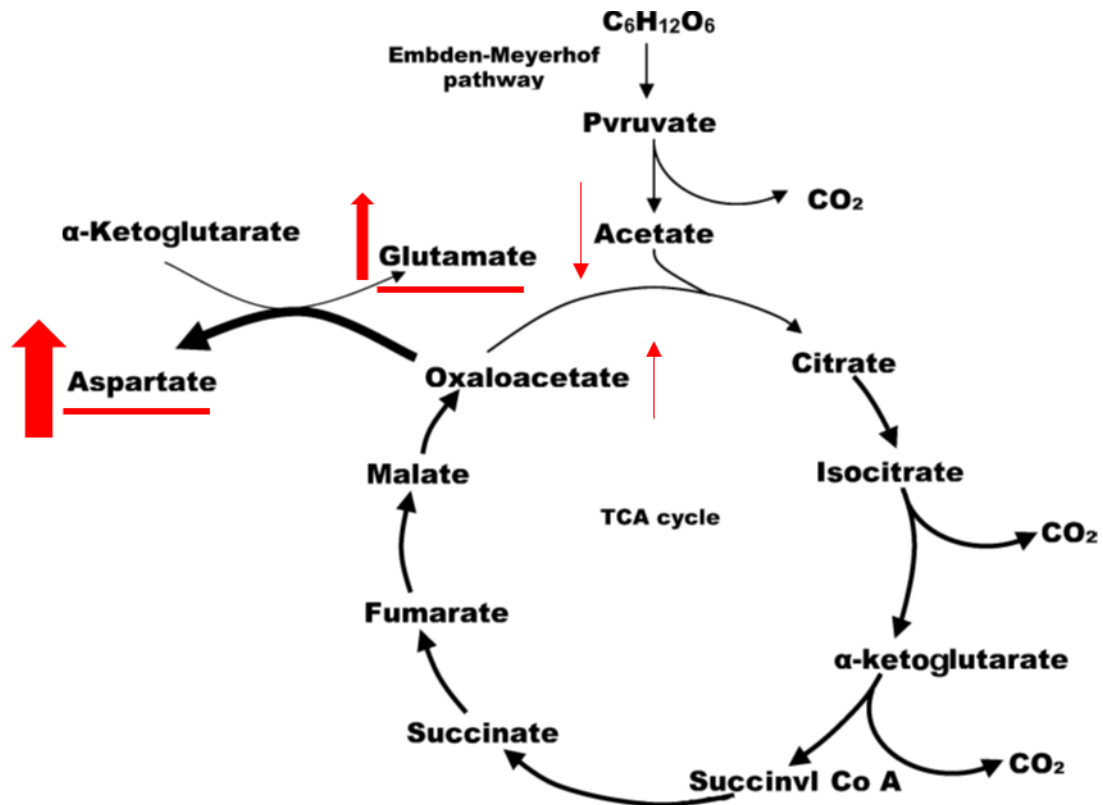


Figure 4.1. Alterations in the Embden-Meyerhof glycolysis and Tricarboxylic Acid Cycle that prevail during hypoglycaemia. The relative thickness of the arrows represents the quantitative flow of metabolites. A decrease in acetate results in an accumulation of oxaloacetate with a resultant increase in aspartate and glutamate (adapted from Auer, 2004).

As opposed to the acidosis that occurs during ischaemia, hypoglycaemia results in profound tissue alkalosis. This is due to an increase in ammonia and a decrease in lactate concentration. The increase in ammonia production follows cellular protein catabolism, and amino acid deamination, whilst lactate production is reduced due to a decreased glycolytic flux combined with lactate utilisation as an alternative energy source (Auer 2004).

4.2.1 Altered ionic flux contribute to axonal injury during glucose deprivation

Using the mouse optic nerve as a model of CNS white matter, Brown *et al.*, (2001) reported that GD-induced injury is Ca^{2+} dependent and involves the activation of L-type Ca^{2+} channels and the reversal of the $\text{Na}^+/\text{Ca}^{2+}$ exchanger. These two pathways result in a toxic Ca^{2+} overload, contributing to permanent loss of axonal excitability. The same group (Brown and Ransom, 2002) later reported that either a decrease or an increase in bath Ca^{2+} concentration during GD preserve the evoked CAP in the rat optic nerve. Ca^{2+} plays a critical role in the pathophysiology of white matter injury following an insult, and therefore it is easily comprehensible that GD in Ca^{2+} free aCSF would preserve axonal function. On the other hand, it seems that Ca^{2+} and other divalent cations have powerful biophysical effects on membrane potential and ion channel gating (Hille, 2001), such that higher extracellular concentrations have the net effect of decreasing excitability (Frankenhauser, 1957) and blocking the toxic Ca^{2+} influx as previously reported by Brown *et al.*, (2001).

4.2.2 Excitotoxicity contributes to axonal injury during glucose deprivation

Glutamate excitotoxicity plays a fundamental role in white matter injury during GD, and this comes by as no surprise considering that glutamate toxicity is implicated in so many acute and chronic disease states of the nervous system. Previous studies reported that blocking N-methyl-D-aspartate (NMDA) receptor activation (Wieloch, 1985) or blocking various downstream events in the cell death cascades triggered by excitotoxicity (Suh, 2007b) can limit the white matter injury caused by glucose deprivation.

The mechanism of white matter injury during GD may differ from that which occurs following ischaemia (Yang *et al.*, 2014). Glutamate excitotoxicity in white matter ischaemia is mainly mediated by the α -amino-3-hydroxy-5-methyl-4-isoxazolepropionic acid AMPA/Kainate receptors (McCarran and Goldberg, 2007; Tekkök *et al.*, 2007). On the other hand, Yang *et al.*, (2014) reported that during glucose deprivation, the loss in axonal function is mainly mediated by the activation of NMDA receptors. While it was reported that ischaemia causes uncontrolled glutamate efflux into the extracellular space, it was reported that glucose deprivation increases extracellular aspartate, which is a selective agonist at NMDA receptors. Another major difference between ischaemia and glucose deprivation is that the former produces acidosis, which blocks the redox group on NMDA receptors and therefore attenuates NMDA receptor-mediated neuronal injury (Lam *et al.*, 2013; Kaku *et al.* 1993), whereas glucose deprivation produces alkalinisation. The alkalinisation that occurs during GD may be due to the H⁺-regulated Ca²⁺ flux through NMDA receptors and the prevention of this change in pH may have had a role in preserving axonal function during hypoglycaemia (Yang *et al.*, 2014). Figures 4.2 – 4.4 compare white matter physiology under normal conditions to the pathophysiology occurring during ischaemia and glucose deprivation (Yang *et al.*, 2014).

A Normal

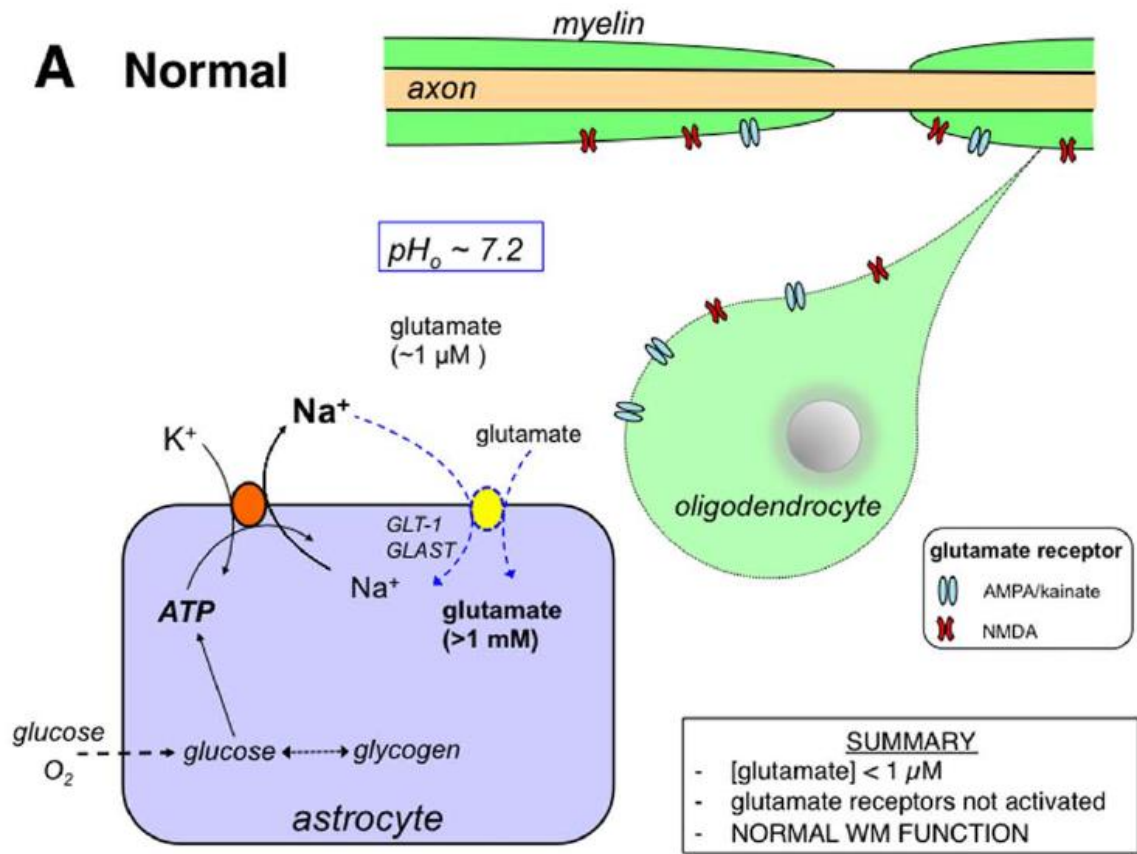


Figure 4.2. White matter under normal physiological conditions. Adequate levels of O₂ and glucose enable enough ATP production to maintain the activity of the Na⁺/K⁺ pump. This confers a normally functioning Na⁺-glutamate transporter in astrocytes, thus limiting the build-up of extracellular concentration of glutamate reaching neurotoxic levels. (Adapted from Yang *et al.*, 2014)

B Ischemia

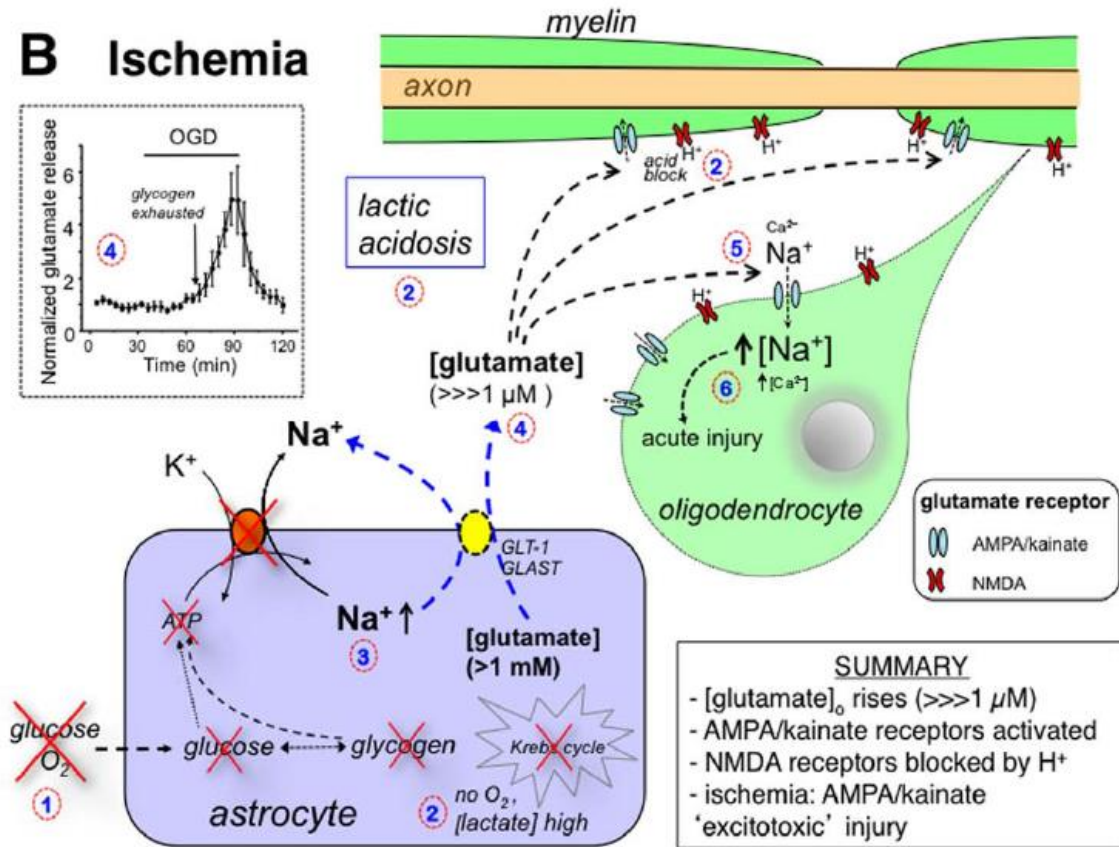


Figure 4.3. White matter during ischaemia. Under ischemic conditions, energy metabolism in astrocytes persists until glycogen is exhausted (1). Acidosis accompanies ischaemia and the high concentration of H⁺ inhibits NMDA receptors, thus limiting their role in the injury cascade (2). The decrease in ATP leads to failure of the Na⁺/K⁺ pump, thus increasing intracellular concentration of Na⁺ (3). This results in the reversal of the Na⁺-glutamate transporter, with consequent increase in extracellular glutamate (4). The rise in glutamate activates AMPA/kainate receptors on oligodendrocytes (5), causing an influx of Ca²⁺ and Na⁺, that trigger cell death cascades (6). (Adapted from Yang *et al.*, 2014)

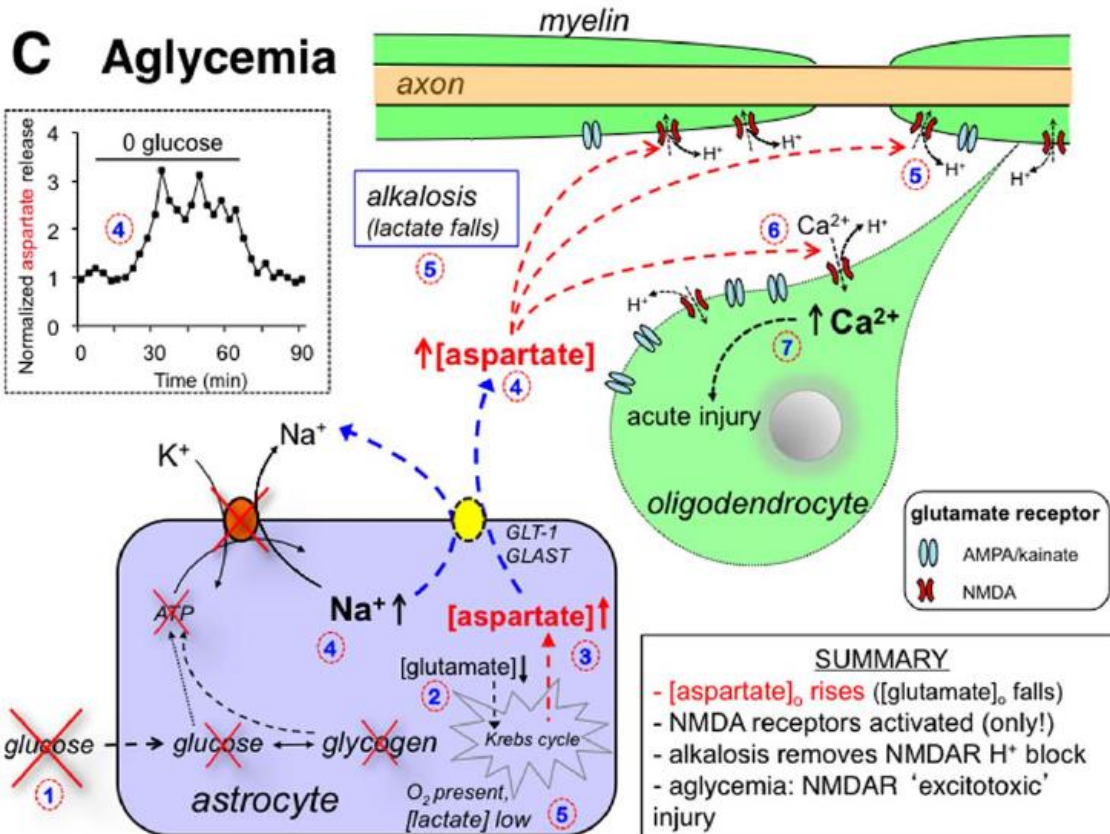


Figure 4.4. White matter during glucose deprivation. During energy deprivation that accompanies glucose deprivation, the availability of glucose is limited (1). Glutamate is utilized instead of glucose to fuel the TCA cycle, leading to a decrease in intracellular glutamate (2). Failure of the TCA cycle leads to accumulation of oxaloacetate with a dependent increase in aspartate (3). A decrease in ATP leads to failure of the Na⁺/K⁺ pump, and the reversal of the Na⁺-glutamate transporter. Since the level of intracellular glutamate is decreased (2), aspartate is transported in the extracellular space instead (4). The fall in extracellular lactate concentration is accompanied by an increase in pH, thereby modulating the NMDA receptor by interfering with its redox group (5). Aspartate, as an agonist to NMDA receptors activates them, leading to Ca²⁺ and Na⁺ influx (6), that trigger cell death cascades (7). (Adapted from Yang *et al.*, 2014)

4.2.3 General mechanisms of excitotoxicity in white matter

Every cell in the CNS that comprise ionotropic glutamate receptors is vulnerable to glutamate/aspartate mediated excitotoxic injury. Historically, excitotoxicity was associated with several neurodegenerative and psychiatric disorders affecting mainly the grey matter (Choi, 1988, 1994; Lipton and Rosenberg, 1994; Lee *et al.* 1999). However, several *in vitro* and *in vivo* experimental data suggest that white matter is also susceptible to excitotoxicity-induced injury (Matute *et al.* 1997; McDonald *et al.* 1998; Li and Stys, 2000).

Initial evidence of the role of AMPA/Kainate receptors to white matter injury came from cultured oligodendrocytes exposed to glutamate (Oka *et al.* 1993). Blocking AMPA/Kainate receptors during ischaemia in cell culture prevented oligodendrocyte death (McDonald *et al.*, 1998; Fern and Möller, 2000; Yoshioka *et al.*, 2000). This *in vitro* evidence was confirmed by *in vivo* data that showed that blocking AMPA/Kainate receptors protected cerebral white matter from hypoxia/ischaemia in the neonate (Follett *et al.*, 2001; Back *et al.*, 2007) and in the adult (Tekkök and Goldberg, 2001; Tekkök *et al.*, 2005a; McCarren and Goldberg, 2007) rodent brain. Other studies have also demonstrated that blocking these receptors is also protective in spinal cord in rats (Agrawal and Fehlings, 1997; Wrathall *et al.*, 1997). These receptors are located on the oligodendrocyte cell bodies, and the injury is either mediated through excitotoxicity via an increase in calcium influx following receptor activation (Sánchez-Gómez and Matute, 1999), or the reversal of the cystine–glutamate exchanger exposing the cell to ROS and oxidative stress as a result of the diminished synthesis of glutathione from cysteine (Oka *et al.*, 1993).

Traditionally, it was always assumed that excitotoxicity in white matter is only mediated via AMPA/Kainate receptors (Sheardown *et al.*, 1993; Volpe, 2001; Stys, 2004; Matute *et al.*, 2001; Dewar *et al.*, 2003) as proof of the presence of NMDA on oligodendrocytes was unavailable (Patneau *et al.*, 1994; Berger *et al.*, 1992). We now know that NMDA receptor subunits NR1, NR2A, NR2B, NR2C, NR2D and NR3A, are expressed on oligodendrocyte processes (Salter and Fern, 2005; Káradóttir *et al.*, 2005) and aggregate with the same density as those found in grey matter (Christensen *et al.*, 2016).

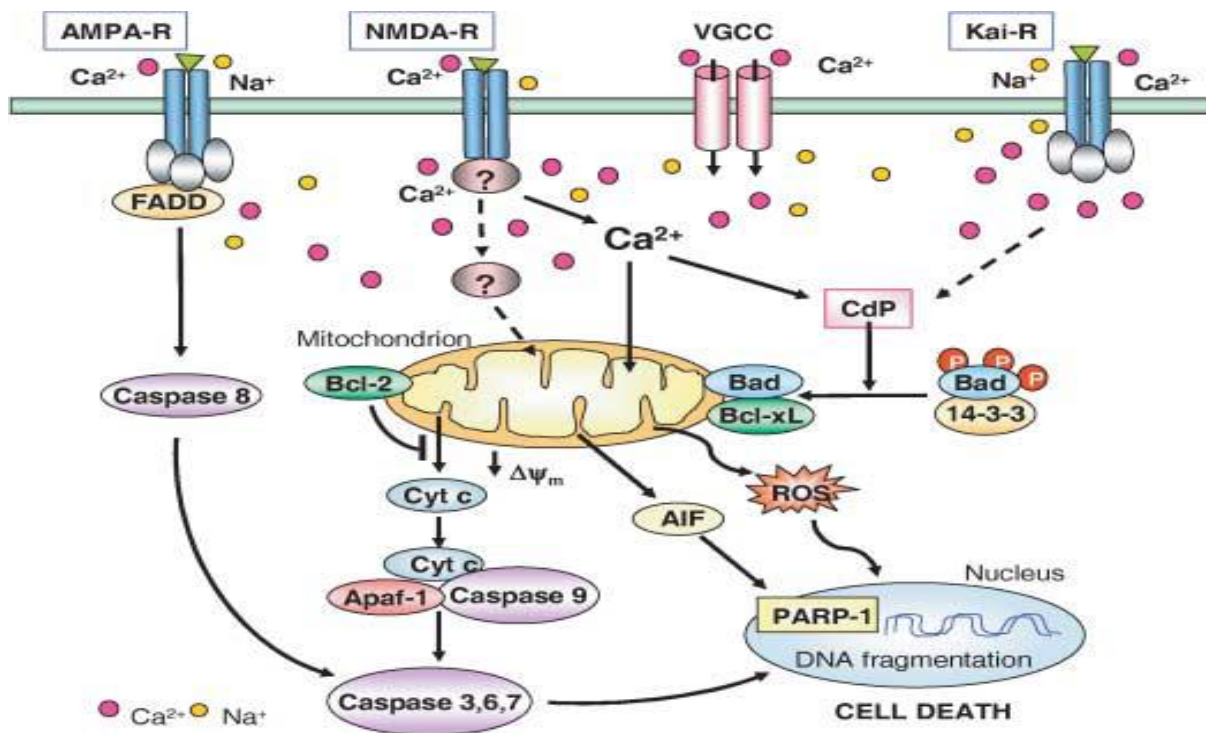


Figure 4.5. Proposed mechanism of oligodendrocyte injury mediated by AMPA/Kainate receptor activation. Activation of AMPA/Kainate receptors results in an influx of Na⁺ and Ca²⁺. This causes depolarisation and activates the voltage gated calcium channels (VGCC), which further increases the intracellular concentration of Ca²⁺. The Ca²⁺ overloads and poisons the electron transport chain in mitochondria and attenuates the mitochondrial membrane potential producing reactive oxygen species (ROS) and the downstream activation of caspases following the opening of the mitochondrial transition pore. (Adapted from Matute *et al.*, 2007)

Activation of these receptors was found to lead to a rapid Ca²⁺-dependent detachment and disintegration of oligodendroglial processes in the rodent optic nerve following ischaemia (Salter and Fern, 2005). Calcium imaging experiments in the spinal cord during ischaemia showed a robust build-up of Ca²⁺ accumulating within the myelin sheaths of oligodendrocytes. AMPA/Kainate receptor block limited the intracellular Ca²⁺ entry in the oligodendrocyte cell body but had no effect on the Ca²⁺ accumulating within the myelin processes. This Ca²⁺ overload was prevented from accumulating into the myelin when antagonists for NMDA receptors were added to the preparation (Micu *et al.*, 2006). The source of the extracellular build-up of glutamate responsible for the over activation of the NMDA receptors present in the myelin processes is believed to be from the reversal of the sodium-glutamate exchanger (Rossi *et al.*, 2000; Li *et al.*, 1999; Baltan *et al.*, 2008).

4.2.4 QNZ-46 block of the GluN2C/D subunits present on NMDA receptors protects axons and myelin from ischaemic injury

One way of modulating NMDA receptor function in experimental settings is by employing pharmacological interventions. MK-801 (or Dizocilpine or (5R,10S)-(+)-5-methyl-10,11-dihydro-5H-dibenzo[*a,d*]cyclohepten-5,10-imine) is a compound that acts as a non-competitive NMDA receptor antagonist not only in neurons, but also in oligodendrocytes (Li *et al.*, 2013). MK-801 binds inside the ion channel of the receptor at several of phencyclidine's (PCP) binding sites in a use- and voltage-dependent manner thus preventing the flow of ions, including Ca²⁺, through the channel. Thus, NMDA receptor antagonists have been extensively studied for use in treatment of diseases with excitotoxic components such as stroke, traumatic brain injury, and neurodegenerative diseases such as Huntington's, Alzheimer's, and amyotrophic lateral sclerosis (Gill *et al.*, 1987, 1992; Park *et al.*, 1988; Uematsu *et al.*, 1991; Nakanishi *et al.*, 1996; Abdel-Hamid *et al.*, 1997; Ma *et al.*, 1998; Arias *et al.*, 1999). NMDA receptor signalling in oligodendrocytes also plays a crucial role in their energy metabolism and regulates their differentiation and migration (Cao and Yao, 2013). Limiting NMDA overactivation has always been a much sought therapeutic target in the struggle to limit brain injury, although so far results from clinical trials have been far from satisfactory. To be clinically acceptable, a prospective drug should be able to allow normal physiological activity without presenting any adverse side effects. However, NMDA antagonists like MK-801 have largely failed to show safety in clinical trials, possibly due to inhibition of NMDA receptor function that is necessary for normal neuronal function. Since MK-801 is a particularly strong NMDA receptor antagonist, this drug is particularly likely to have psychotomimetic side effects and cause drowsiness leading to coma (Koroshetz and Moskowitz, 1996; Hickenbottom and Grotta, 1998; Lutsep and Clark, 1999; Rogawski, 2000; Palmer, 2001).

In a recent collaborative study with the University of Plymouth and that formed part of this thesis, we employed a novel NMDA receptor antagonist, 4-[6-Methoxy-2-[(1E)-2-(3-nitrophenyl)ethenyl]-4-oxo 3(4H)quinazoliny]benzoic acid (QNZ-46), which specifically binds to GluN2C/D-containing subunits on NMDA receptors that was found to curtail receptor function in a use-dependent manner (Doyle *et al.*, 2018). GluN2C/D-containing NMDA

receptors are generally extra-synaptic (Brickley *et al.*, 2003; Momiyama *et al.*, 1996; Harney *et al.*, 2008) and therefore this makes QNZ-46 an ideal candidate to block glutamate receptor-mediated currents without disturbing synaptic transmission (Mosley *et al.*, 2010; Hamilton *et al.*, 2016). Systemic pre-treatment (IP administration over 5 days) of the drug showed no signs of abnormal animal behaviour, toxicity or weight loss in mice. The drug readily enters the blood-brain barrier and strongly binds to NMDA receptors in the brain with a particular strong affinity to the myelinic NMDA receptors located in the white matter (Doyle *et al.*, 2018).

In this study, two-photon imaging confirmed that ischaemia causes vesicular release of glutamate from axons and this binds to activate specific GluN2C/D-containing NMDA receptors present on oligodendrocyte processes and myelin sheath. Blocking the calcium currents through these NMDA receptors demonstrated effective structural and functional protection to central white matter (Fig 4.6 – A) and improved functional recovery in a mouse model of middle cerebral artery occlusion (MCAO). The same level in efficacy was not achieved by block of the Transient Receptor Potential A1 channel (TRPA1) by A967076, an ion channel that mediates nociception through Ca²⁺ influx of sensory neurons (Fig 4.6 – A). We also show that prolonged pre-incubation of the mouse optic nerve with the classic NMDA antagonist (MK-801) increases the number of functional axons after ischemia in comparison to controls (Fig 4.6 – B).

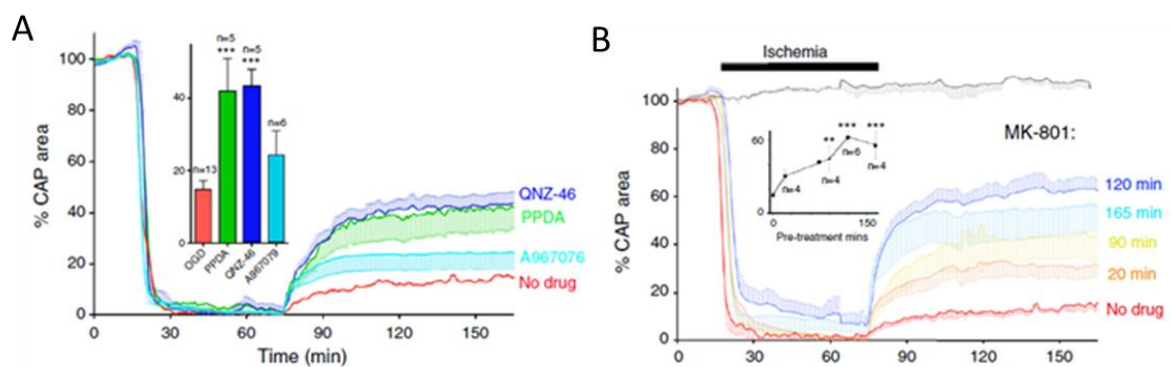


Figure 4.6. Myelin injury in the adult rat optic nerve is NMDA-receptor-mediated I. (A) Blocking specific GluN2C/D subunit with QNZ-46 and the anticonvulsant drug PPDA, were also protective. There was no protection by blocking TRPA1 channels with A967079. (B) Increasing the pre-treating time of the optic nerve to MK-801, increased the functional recovery of a greater number of axons after ischaemia. (Adapted from Doyle *et al.*, 2018)

Transgenic PLP-EGFP mice express an enhanced green fluorescent protein (EGFP) in oligodendrocytes, Schwann cells and the enteric glia of the gut and is therefore useful in visualising all stages of oligodendrocyte differentiation. In vehicle experiments, optic nerves from this mouse strain were pre-loaded with the myelin stain FluoroMyelin Red and exposed to 1 hr of ischaemia followed by 2 hr of reperfusion. In parallel experiments, pre-treatment of the optic nerves with QNZ-46 prevented the ischaemia-induced myelin injury as seen in the vehicle group (Figure 4.7).

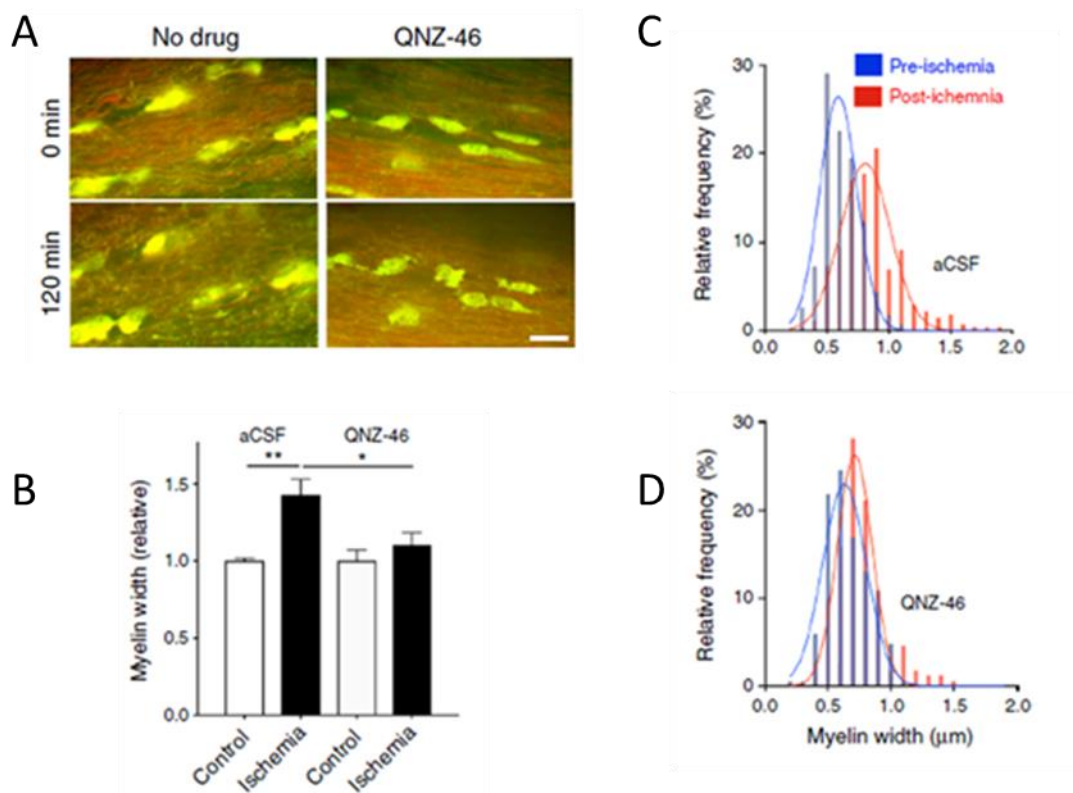


Figure 4.7. Myelin injury in the adult rat optic nerve is NMDA-receptor-mediated II. [A] Myelin structure is protected from ischemic damage by 120 min pre-treatment with QNZ-46, imaged via FM vital staining. [C-D] Ischemia evoked myelin swelling is prevented by 120 min QNZ-46 pre-treatment. (Adapted from Doyle *et al.*, 2018).

Ultrastructural analysis of the adult mouse optic nerve exposed to 60 min of OGD followed by 60 min reperfusion revealed myelin decompaction, especially the inner myelin layer, bubbling, and loss of myelin layers. Pre-incubation in QNZ-46 prevented the swelling of axons and preserved the g-ratio of axons. The normal G-ratio was not a consequence of the shrinkage of axons as there were no apparent changes in overall axon diameter when compared to axons from controls (Figure 4.8).

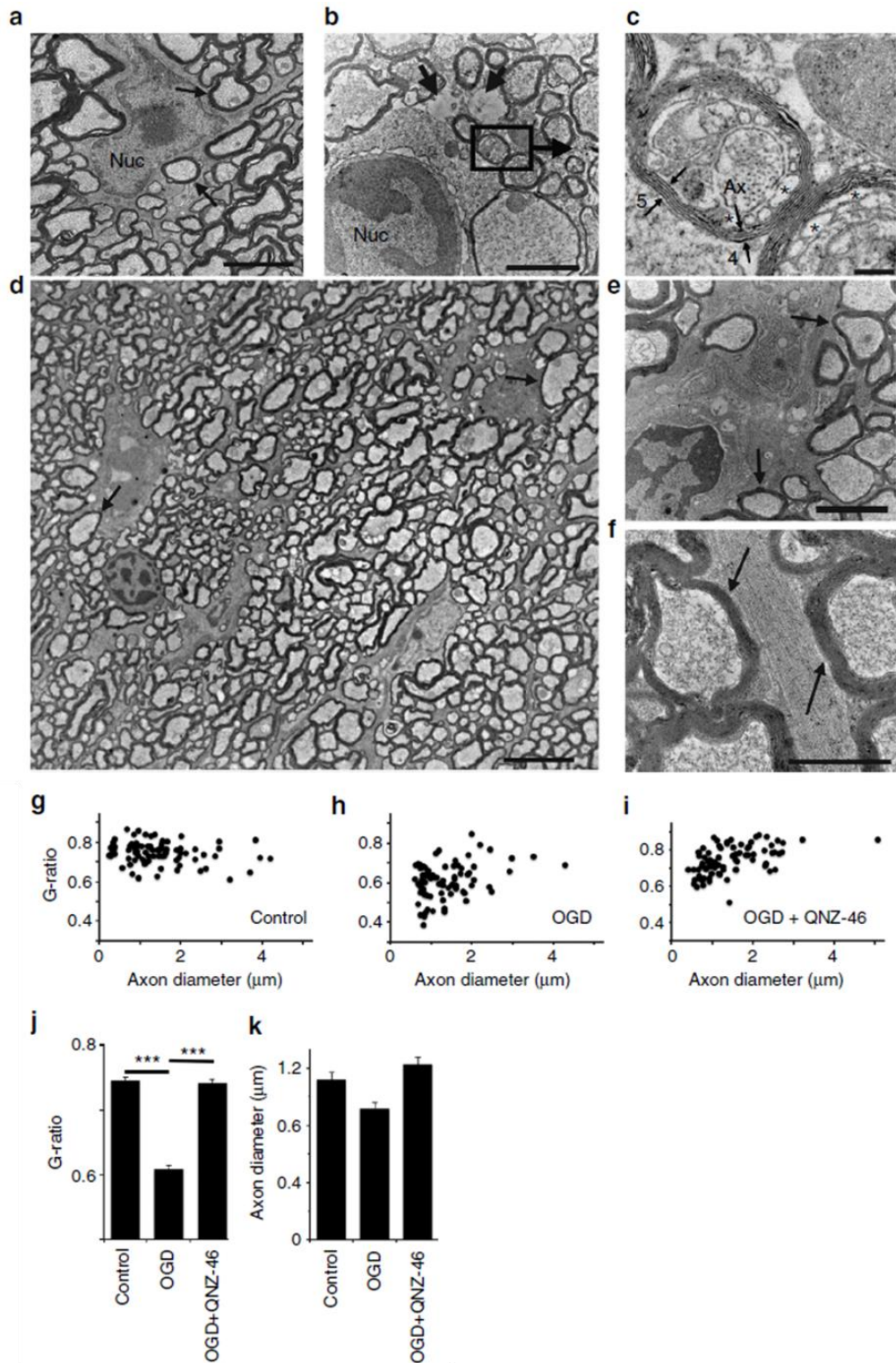


Figure 4.8. QNZ-46 mediated myelin protection in the adult mouse optic nerve. (A) Normal oligodendrocyte nucleus (Nuc) and myelinated axons (arrows) in control slices. Characteristic ischaemic injury to myelin (B) shown in high resolution (C). There is myelin decompaction, bubble formation, and loss of myelin layers. Preservation of both oligodendrocyte cell bodies (D-E) and processes (F) following pre-treatment with QNZ. (G-J) G-ratio of myelin thickness vs axon diameter. OGD induces axonal expansion, which is prevented by QNZ-46. There is no axonal shrinkage (K), confirming the protective role of QNZ-46 on myelin. (Adapted from Doyle *et al.*, 2018)

In a set of experiments involving 1 hr of MCAO in mice, pre-treatment for up to five days with IP of QNZ-46 caused smaller infarct volumes in mice when compared to the vehicle group. Moreover, there was excellent preservation of myelin and axons in the effected white matter as seen under light and fluorescence microscopy. Electron microscopical analysis confirmed the preserved ultrastructural cytoarchitecture within the core region of the ischemic focus and the improved functional outcome after the stroke (Doyle *et al.*, 2018).

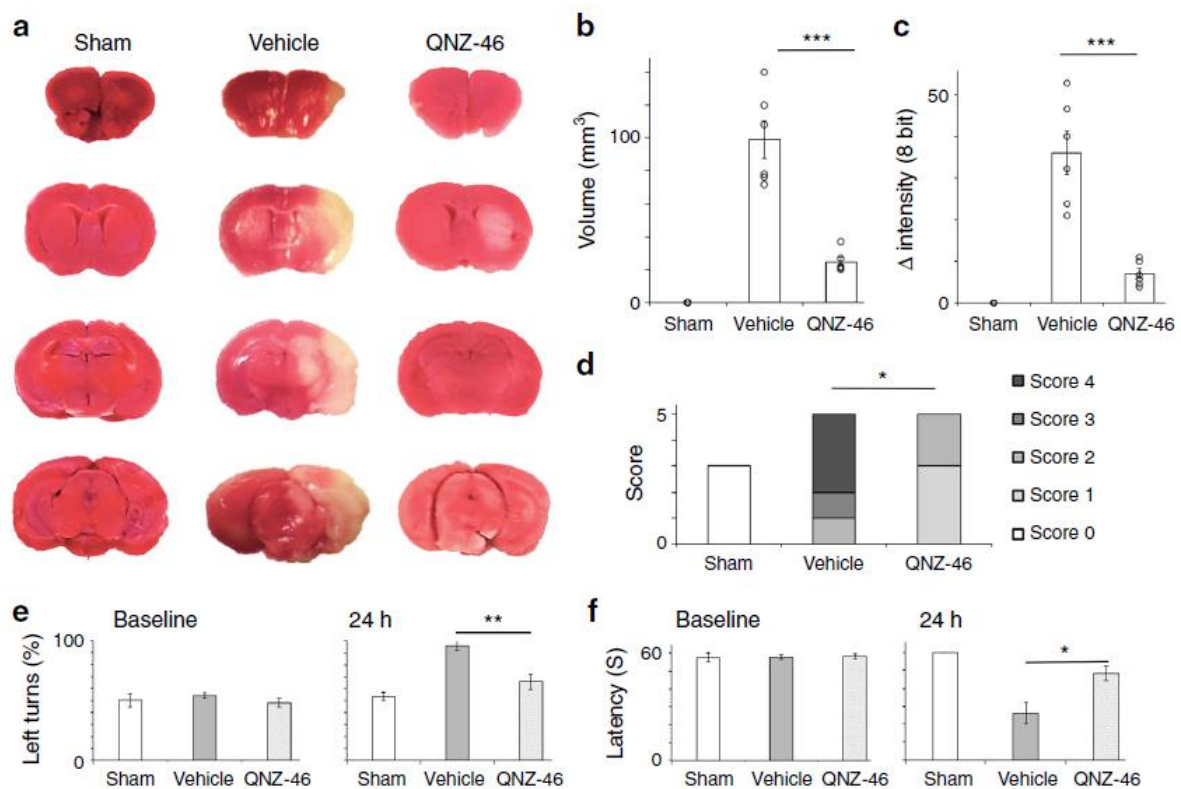


Figure 4.9. Systemic pre-treatment of mice with QNZ-46 protected both grey and white matter from ischaemic injury following MCAO I. [A-C] Reduction in infarct volume in QNZ-46-treated mice. [D-F] Improved functional recovery as assayed at 24 hours post-occlusion. (Adapted from Doyle *et al.*, 2018)

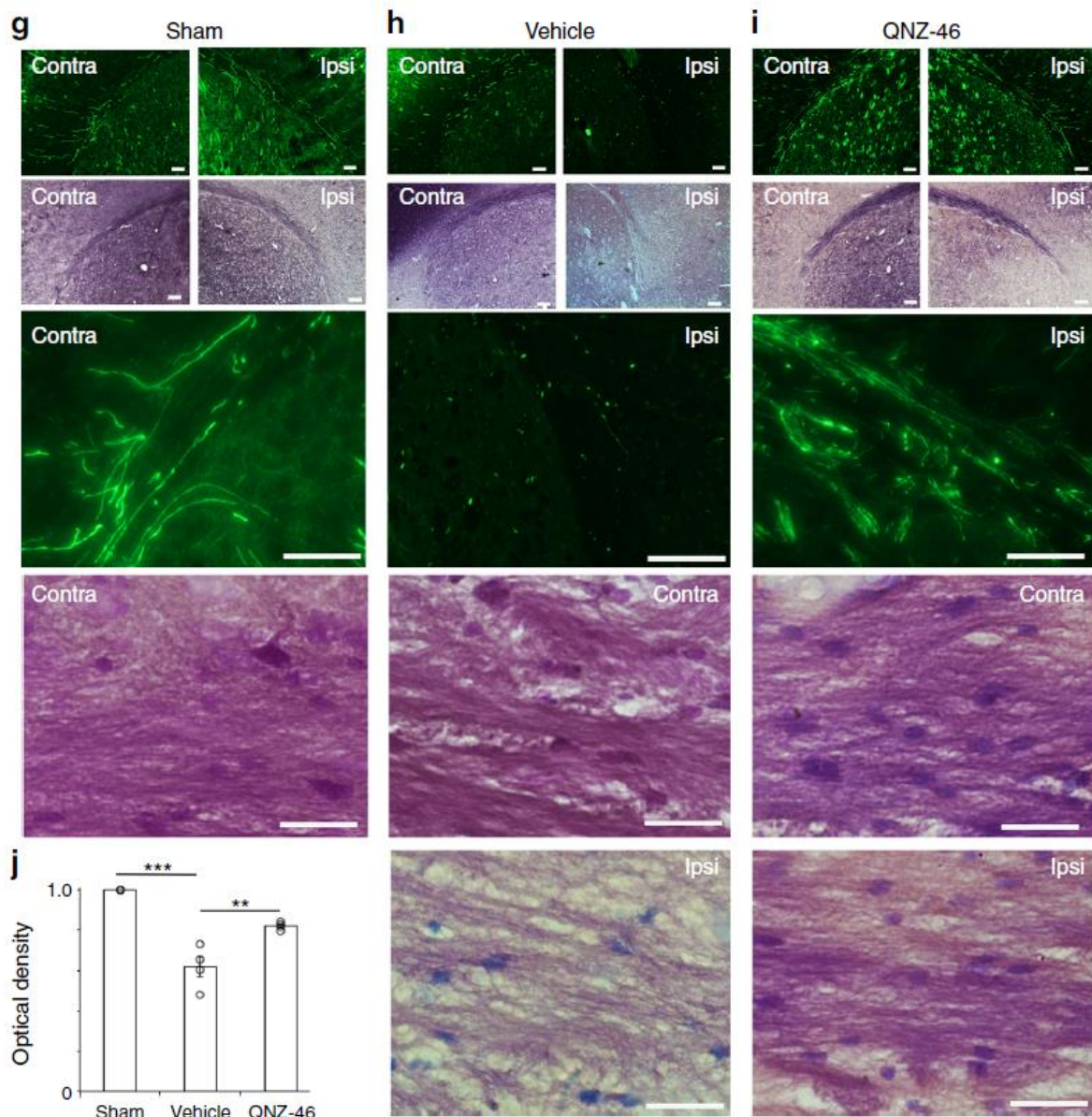


Figure 4.10. Systemic pre-treatment of mice with QNZ-46 protected both grey and white matter from ischaemic injury following MCAO II. [G-J] YFP axons (green) and luxol fast-blue/cresyl violet (blue/purple: myelin) expression in external capsule in both contralateral/ipsilateral hemisphere in sham (G) vehicle (H) and QNZ-46 pre-treated mice (I). Loss of YFP fluorescence, fragmentation of axons and the loss of myelin in ipsilateral hemisphere in vehicle (H). Maintenance of YFP fluorescence and myelin density on the ipsilateral hemisphere in the QNZ-46-treated mice. (Adapted from Doyle *et al.*, 2018)

4.3 Methodology

4.3.1 Pharmacological manipulation of antagonists to AMPA/Kainate receptors before and after glucose deprivation

White matter is vulnerable to excitotoxicity induced injury (Matute *et al.* 1997; McDonald *et al.* 1998; Li and Stys, 2000) and activation of the AMPA/Kainate receptors has been implicated in white matter injury during ischaemia (Tekkök and Goldberg, 2001; Tekkök *et al.*, 2005a; McCarren and Goldberg, 2007). Several AMPA/Kainate receptor antagonists have been developed, with the three classical ones being: 2,3-dihydroxy-6-nitro-7-sulfamoylbenzo(F)quinoxaline (NBQX) (Sheardown *et al.*, 1990), 6-(1H-imidazol-1-yl)-7-nitro-2,3(1H,4H)-quinoxalinedione hydrochloride (YM-90K) (Namba *et al.*, 1994) and [1,2,3,4-tetrahydro-7-morpholinyl-2,3-dioxo-6-(trifluoromethyl)quinoxalin-1-yl]methanephosphonate (ZK-700,775) (Turski *et al.*, 1998). All 3 antagonists have been shown to protect cerebral white matter from ischaemic injury (Buchan *et al.*, 1991; Gill *et al.* 1992, Sheardown *et al.* 1993, Shimizu-Sasamata *et al.*, 1996).

In this study, we wanted to evaluate the potential protective role of NBQX during glucose deprivation in the knowledge that glia in white matter are enriched with AMPA/KA receptors that may be activated during GD. We designed two different sets of live imaging experiments on YFP callosal slices maintained under two-photon microscopy. In these experiments we tested the effective temporal efficacy of drug treatment when administered before or after glucose deprivation. In the 'EARLY NBQX' group, 30µM NBQX was added to the aCSF throughout the period of GD and during reperfusion, while in the 'LATE NBQX' group, the same dose of drug was applied only on the onset and throughout reperfusion.

In a separate set of experiments that involved the maintenance of slices in interphase chambers, slices followed the same drug treatment protocol as above. In the process, slices were 'sampled' and immediately fixed at specific time-points (immediately after GD, after 1 hr and 2 hr of reperfusion) and prepared for EM to evaluate the ultrastructural changes in the white matter axons with drug exposure.

4.3.2 Quantification of axonal injury through electron microscopy

Quantification of the extent of axonal pathology as seen under EM was based on a modified procedure by *Garthwaite et al.* (1999). Since the cross-section of the callosal axons are not uniformly circular, their Feret (average) diameter was measured. In brief, for each section, the mean internal Feret diameter was calculated from four non-overlapping fields at 10,000X magnification, each within an area of 2000 μm^2 . The Feret diameter was taken as the mean of 36 diameters measured in 5° intervals. In normal mouse corpus callosum, the mean diameter of myelinated axons is 0.46 +/- 0.01 μm (Sturrock et al., 1980). Data was expressed as the mean proportion of axons with Feret internal diameter (i.e. myelin excluded) above 2.5 μm . TEM micrographs were captured at 10,000 magnification in each of 3 sections per condition. A total of 12 micrographs were obtained for each slice (3 animals/experimental group). Morphometric measurements from cross-sections of axons were processed using MetaMorph image analysis software (Universal Imaging, West Chester, PA). Glial cell bodies and their processes along with blood vessels were excluded from the analysis.

4.3.3 The effect of calcium on glucose deprivation

Previous literature based on the rodent optic nerve suggests that glucose deprivation induces activation of L-type Ca^{2+} channels and reverses the $\text{Na}^+/\text{Ca}^{2+}$ exchanger result in a toxic Ca^{2+} influx (Brown *et al.*, 2001). Overactivation of NMDA receptors during glucose deprivation also results in intense Ca^{2+} influx (Yang *et al.*, 2014). Thus, we wanted to evaluate the effect of exposing our central white matter model to glucose deprivation in a calcium free aCSF with the addition of the calcium chelator, glycol-bis(2-aminoethylether)-N,N,N',N'-tetraacetic acid (EGTA) (Caldwell, 1970).

After stabilisation, the brain slices were incubated for 30 min in Ca^{2+} free aCSF + 200 μM EGTA. They were then exposed to 45 min GD in Ca^{2+} free aCSF + 200 μM EGTA, followed by 2 hr of glucose and calcium containing standard aCSF. Throughout the duration of the experiment axonal structure and functions was continuously monitored by combined two-photon live-imaging and CAP recording.

4.3.4 Systemic administration of NMDA and AMPA antagonists to block key pathways that participate in white matter injury

We have previously shown (Doyle *et al.*, 2018) that QNZ-46 (Cat. No. 4801; Tocris) protects axons and myelin following ischaemia by blocking GluN2C/D-containing NMDA subunits present in oligodendrocyte processes and the myelin sheaths around axons. QNZ-46 crosses the blood brain barrier, accumulates predominantly in myelin and is non-toxic (Doyle *et al.*, 2018). We therefore wanted to extend the documented protective effect that this drug had on a stroke model and apply its use on a milder form of insult such as glucose deprivation.

In addition, we wanted to extend this white matter protection to oligodendrocytes by testing whether the combined addition of a novel AMPA receptor antagonist present on glia, is equally protective to both oligodendrocytes and axons after glucose deprivation. We used 3-(2-Chlorophenyl)-2-[2-[6-[(diethylamino)methyl]-2-pyridinyl]ethenyl]-6-fluoro-4(3H)-quinazolinone hydrochloride (CP-465,022) (Cat. No. 3932; Tocris), a very selective and potent non-competitive AMPA-specific receptor antagonist (Menniti *et al.*, 2000; Lazzaro *et al.*, 2002). As with the QNZ-46 drug, CP-465,022 readily crosses the blood-brain barrier and does not have any documented toxic side effects (Menniti *et al.*, 2003).

Both drugs were administered systemically via IP injection following a protocol as previously described (Doyle *et al.*, 2018). Briefly, equimolar concentrations (0.1mM) of QNZ-46 and CP-465,022 were combined or administered separately when dissolved in 20mM β -cyclodextrin (Sigma: C4767) in sterile PBS. The mice were weighed daily, and the dose adjusted to the animals' gross weight (2 mg/Kg QNZ-46; 1 mg/Kg QNZ-46 QNZ) on each of the five days of treatment. On the 5th day, the mice were sacrificed 4 hours after the last drug treatment and brain slices were prepared as previously described in chapter 2. After 2 hours stabilisation the slices were treated to 45 min of GD followed by 2 hr of reperfusion with glucose containing aCSF. In this set of experiments, combined electrophysiology and two-photon imaging were used to monitor axonal structure and function simultaneously in three separate cohorts of administered drugs. These included one group of mice ($n=3$) with treatment with QNZ-46, a second group ($n=3$) treated with CP-465,022 and a third group treated with both drugs ($n=3$).

QNZ-46 contains a quinazolinone backbone which confers its very distinctive fluorescent properties (Naleway *et al.*, 1994). Its presence in brain slices could be readily detected with fluorescence microscopy confirming that the drug penetration into the brain was successful. The antagonist was readily excited at 765nm with minimal (4 %) laser power and detected in the blue channel with a band pass (BP) of 420-465nm.

In a sub-set of these experiments, brain slices from mice injected with QNZ-46 were loaded with 10 μ M Nile Red (Cat. No. N1142; Invitrogen) for 10 min, followed by a 30 min washout. Nile Red is an oxazine fluorophore with a strong tendency to accumulate in lipid- and adipose-rich environments (Greenspan *et al.*, 1985). It is an ideal vital stain to myelin sheaths. It has been used to detect myelin injury following ischaemia (Chen *et al.*, 2013) and in multiple sclerosis (Poon *et al.*, 2018). In our experiments, we used it to try to co-localise it with QNZ-46.

4.4 Results

4.4.1 AMPA/Kainate receptor block protects axons and oligodendrocytes during glucose deprivation

As we reported in section 2.4.4, slices exposed to 45 min GD showed focal swelling and beading of axons in the early stages of reperfusion, which later progressed to axonal fragmentation and loss of fluorescence intensity by the end of the 2 hr of reperfusion. As expected, axon integrity was more robust when NBQX was added before the insult (Early NBQX) (Fig 4.11 C) rather than when this was added right after GD, during reperfusion (Late NBQX) (Fig 4.11 D).

Examination of thin sections by electron microscopy revealed that vacuolation was substantially less in those slices pre-treated with NBQX. The group treated with NBQX before the insult showed fewer swollen and collapsed axons and the extracellular space appeared normal except for a few areas with swollen axons. At higher magnification, fewer axons had signs of pathology in the myelin and most of the small-calibre unmyelinated axons were still visible. Although periaxonal spaces and swollen mitochondria were visible in some axons, they typically occurred in the larger calibre axons. The axoplasm appeared denser and more granular in the NBQX-treated group than in the group without treatment by the end of 2 hours of reperfusion. In both the early and late groups of NBQX treatment, the index of axonopathy was statistically significantly different than in the untreated group. There was however, no statistical difference between both groups tested. Because injury causes axonal swelling, the effect of injured axons was evaluated according to axon diameter. An important finding was the preservation of the small-calibre unmyelinated axons in the NBQX-treated group as opposed to that without treatment (Fig 4.12 – 4.13).

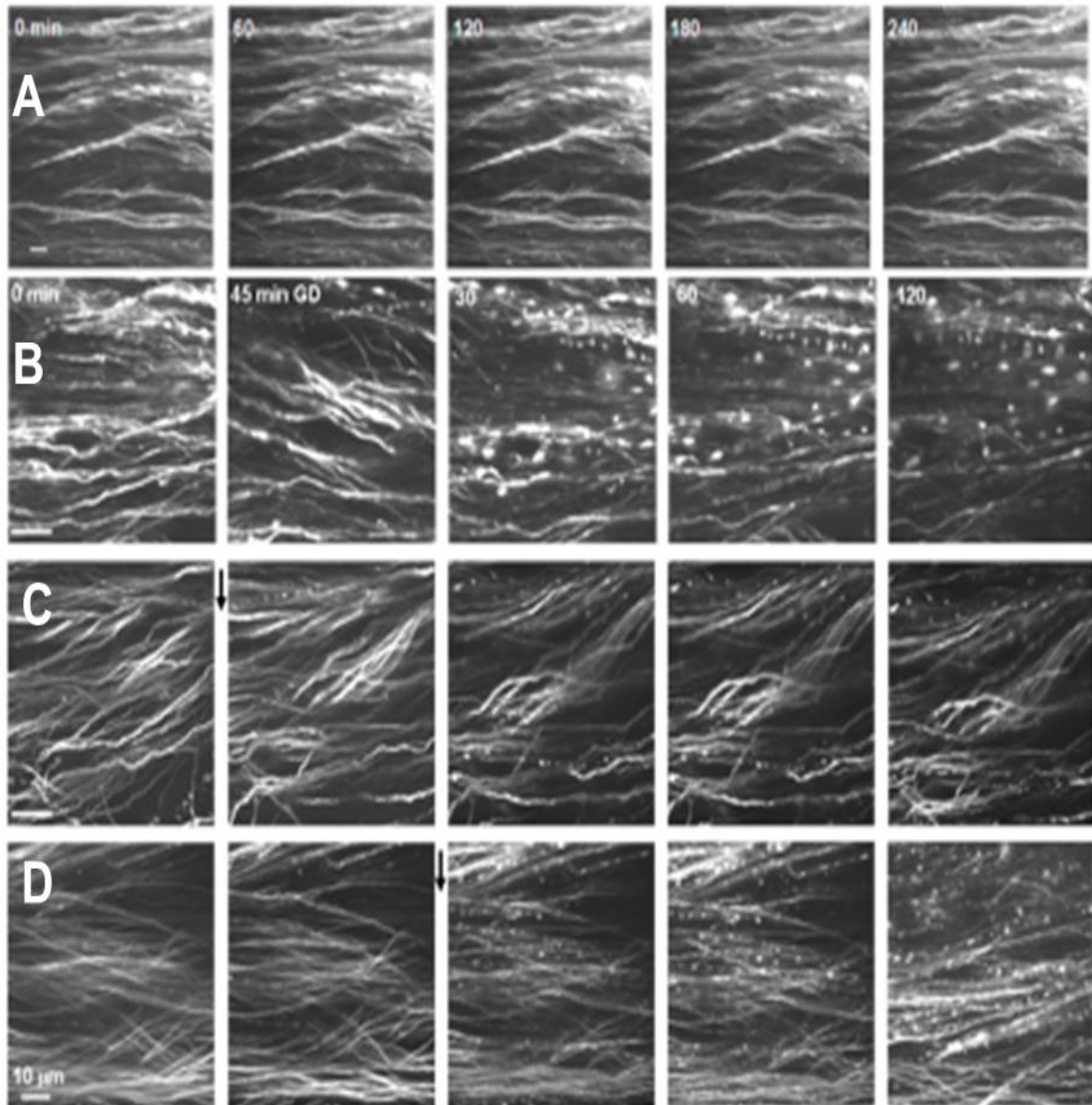


Figure 4.11. AMPA/KA receptor blockade attenuated axon injury following GD. (A) Control slice with normal aCSF perfusion shows well preserved morphology of YFP-expressing axons during repeated imaging over 4 hours. (B-D) NBQX administered before and after GD, substantially delays axonal injury and preserves axonal structure. (B) Exposure to transient OGD for 45 min caused delayed axonal injury, starting to develop 30 min after restoration of glucose perfusion. Extensive beading and fragmentation of axons was followed by loss of axon fluorescence after 2 hours of reperfusion. (C) Addition of NBQX (30 μ M) applied 30 min before and after the insult substantially preserved axon morphology and fluorescence. (D) Axonal beading and fragmentation were partially reduced even when NBQX was applied after the insult (arrows).

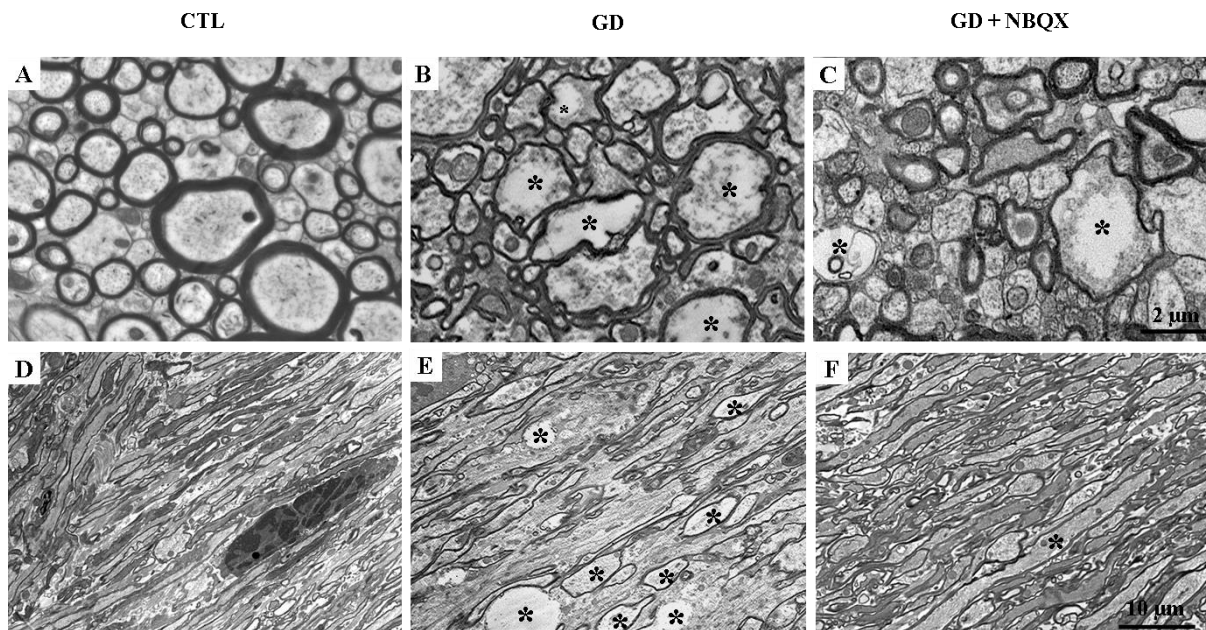


Figure 4.12. NBQX preserves axon structure following GD. Low magnification transmission electron micrographs in sagittal (top) and transverse (bottom) sections of corpus callosum to show the protection of axon profiles by NBQX. Slices were exposed to wash control conditions (A and D); 45 min glucose deprivation (B and E) or glucose deprivation + 30μM NBQX (C and F). Sections were fixed 2 hours later and prepared for EM. In the control slice, EM shows regular profiles of myelinated and unmyelinated axons. GD causes extensive distension of axon profiles and disruption of cellular organelles. Application of 30 μM NBQX during and after GD substantially reduces the injury, although some swollen axons are still visible (asterisks). Scale bars 2 μm (top), 10 μm (bottom).

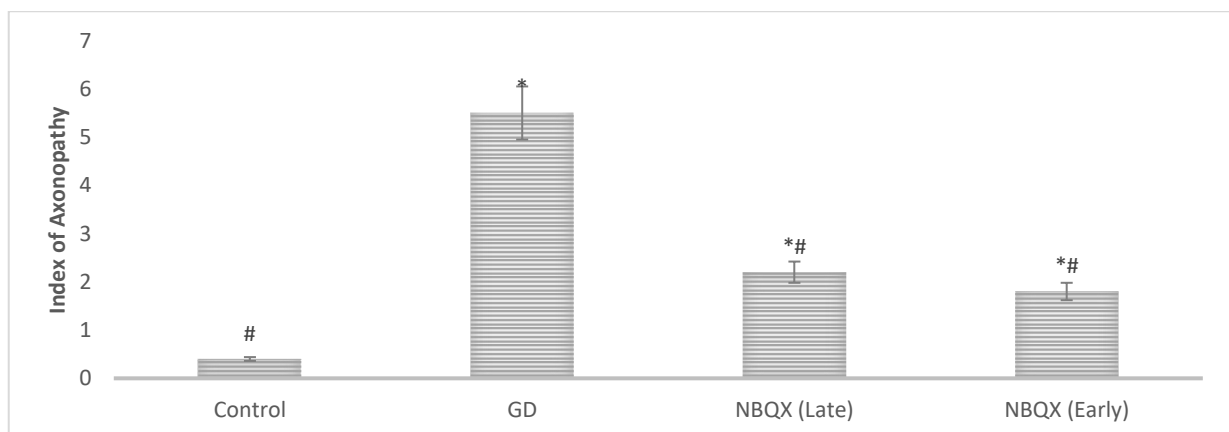


Figure 4.13. Quantitative assessment of axonal pathology from brain slices by EM. Compared with normoglycaemia (Control), GD-treated tissue shows significantly more pathology. Continuous application of 30μM NBQX before and after 45 min of GD significantly reduced axonal injury by the end of 2 hours of reperfusion. The index of axonopathy represents the number of axons with Feret diameter above 2.5 μm/2000μm². Values represent the mean ± SEM. *Significantly different from control. #Significantly different from GD, p < 0.001 is for the indicated comparisons.

In slices treated with NBQX, assessment by EM also revealed robust protection to oligodendrocytes. There were no morphological changes in oligodendrocyte cell body or nucleus to indicate injury. Within the nucleus there was normal distribution of the chromatin and the nucleus was not swollen. At higher magnification, the cytoplasm appeared to contain an array of normal mitochondria. Although some of the mitochondria looked swollen, these were few in numbers. Both the endoplasmic reticulum and golgi apparatus looked normal and well organized. Some vacuole formation was sometimes present in the cytoplasm of some of these cells.

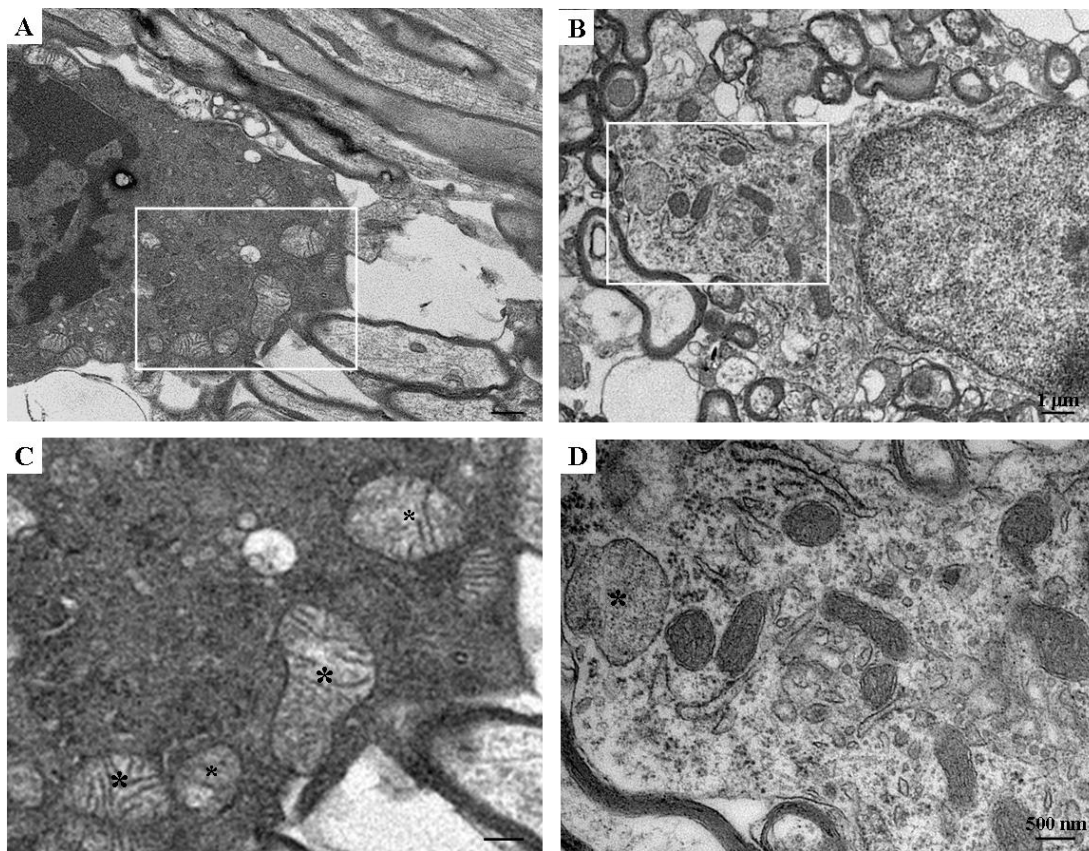


Figure 4.14. AMPA/KA receptor blockade following GD attenuates ultrastructural injury in oligodendrocytes. Representative electron micrographs from sagittal sections showing the protective effect of NBQX on oligodendrocytes when applied after the insult. Inset in A and B shows the magnified view in C and D respectively. A, Appearance of glial cell after GD. Glial cell body appears swollen and distended. There is lacunar enlargement of golgi apparatus, vacuole formation and swollen mitochondria. The increased extra-axonal spacing is considered indicative of axon and glial damage. B, Oligodendrocyte shows well preserved morphology of the organelles when NBQX was applied after GD. C, Vacuoles and swollen mitochondria are seen in injured glia after exposure to GD. Some of the cristae are broken and discontinuous. (D) Normal appearance of organelles in the cytoplasm. Only one mitochondrion in this view is abnormal. Asterisks denote damaged mitochondria.

4.4.2 Axonal injury during glucose deprivation is calcium-dependent

Following a 30 min equilibration period in Ca^{2+} free aCSF (with the addition of $200\mu\text{M}$ EGTA), callosal slices were transferred to an imaging chamber under two-photon microscopy for sequential live imaging. Slices were exposed to 45 min GD with the same composition of aCSF and then replaced by standard glucose and calcium containing aCSF during the 2 hr of reperfusion. Sequential image analysis at different time points revealed a statistically significant lower axonal injury score in slices incubated in a Ca^{2+} - free media as opposed to those that were supplemented with Ca^{2+} during the course of the experiment.

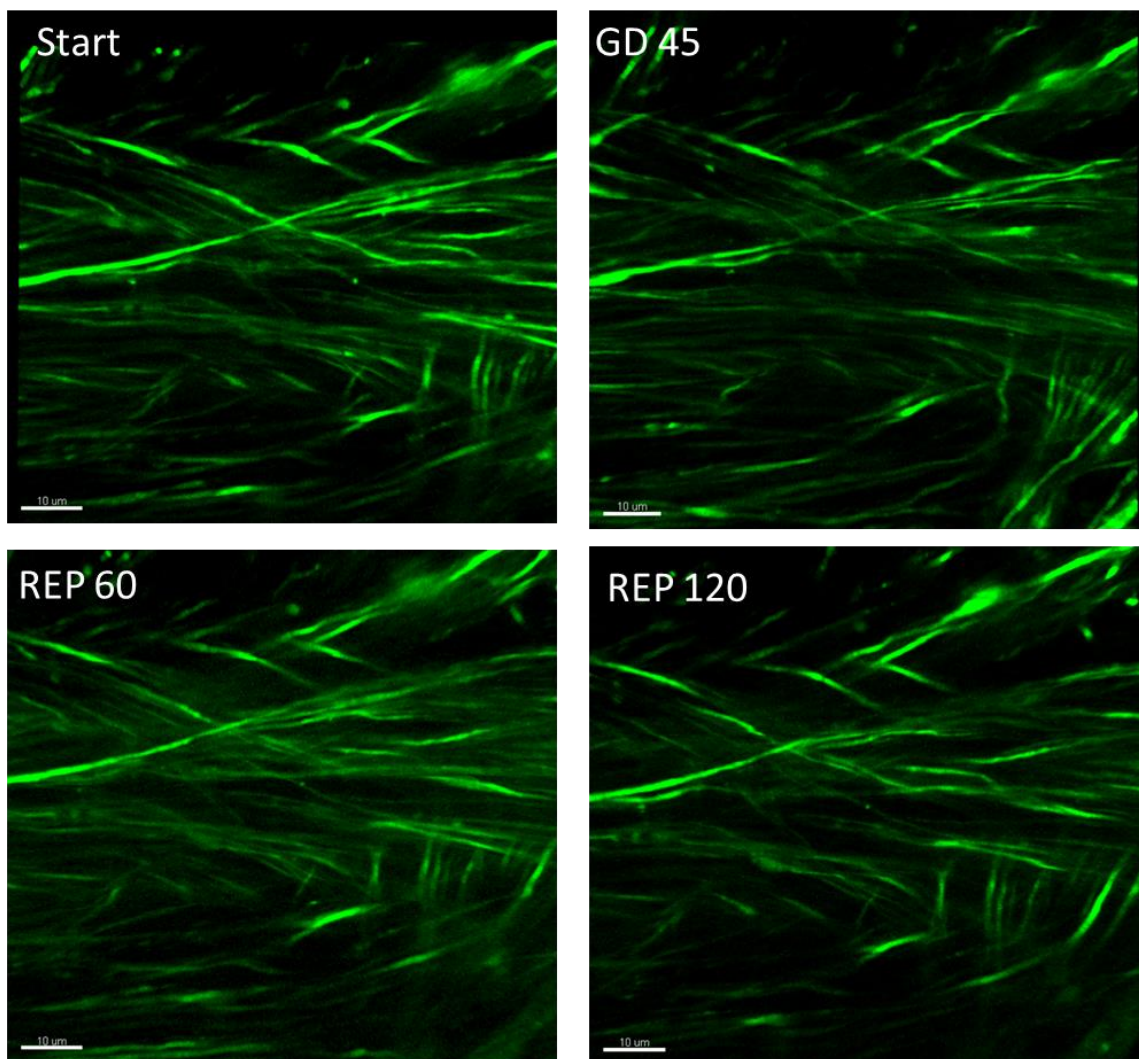


Figure 4.15. Sequential images from a callosal slice exposed to 45 min of GD in a Ca^{2+} -free environment. Preservation of axonal structural integrity in slices exposed to glucose deprivation in a Ca^{2+} -free environment. There was no focal swelling, beading and fragmentation, that occurs during the reperfusion phase following 45 min of GD in a Ca^{2+} -containing medium. Scale bar: $20\mu\text{m}$

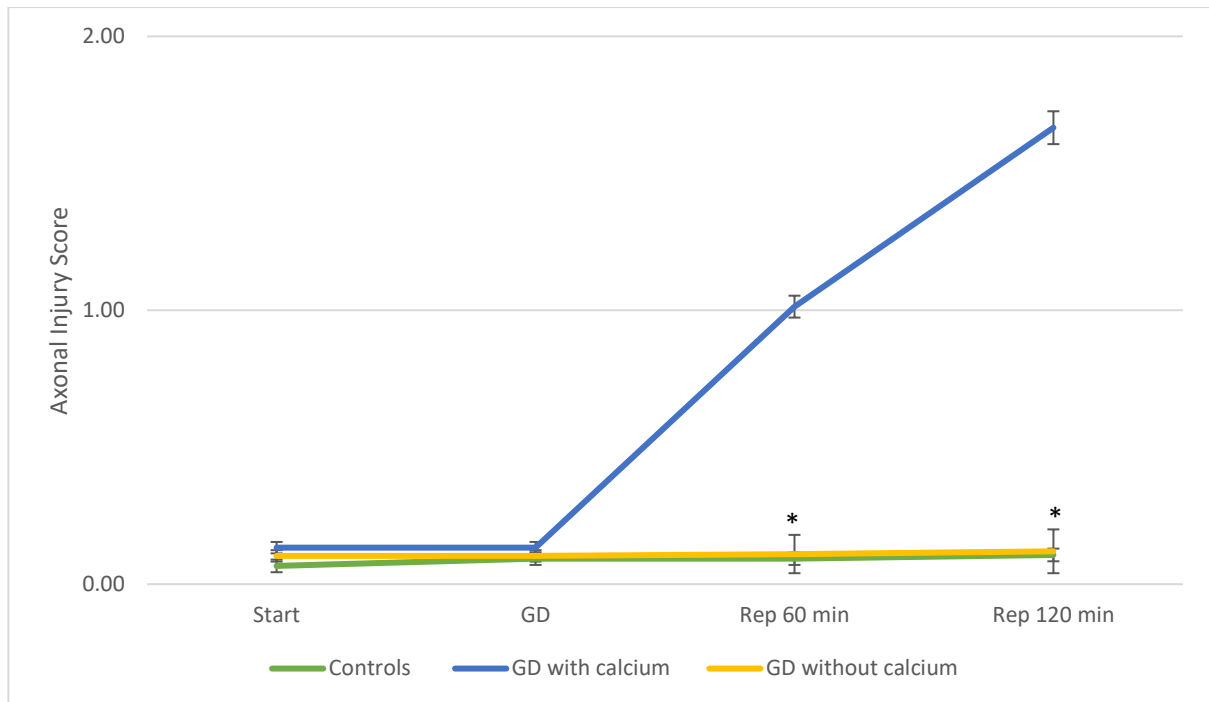


Figure 4.16. Injury score of callosal axons exposed to 45 min of GD in a calcium-free environment. Axons are not injured by glucose deprivation in a calcium-free environment and the injury score is maintained at baseline levels. There is a statistically significant difference (* $p < 0.001$) in injury between slices exposed to glucose deprivation in the absence of Ca^{2+} when compared to glucose deprivation in the presence of Ca^{2+} . There is no difference in the axonal injury score between glucose deprivation in the absence of Ca^{2+} and control slices maintained under normoglycaemia in standard aCSF ($n=3$).

Electrophysiological recordings of the CAP across the corpus callosum showed a similar trend in the decline in electrical activity into 30 min of GD in both groups of slices exposed to GD in the presence or absence of Ca^{2+} . As previously reported in section 2.4.7 and in agreement with other studies (Brown *et al.*, 2001), there was no recovery in CAP in slices exposed to GD in the presence of Ca^{2+} in contrast to the complete recovery of those slices maintained in Ca^{2+} -free medium when reperfusion was restored.

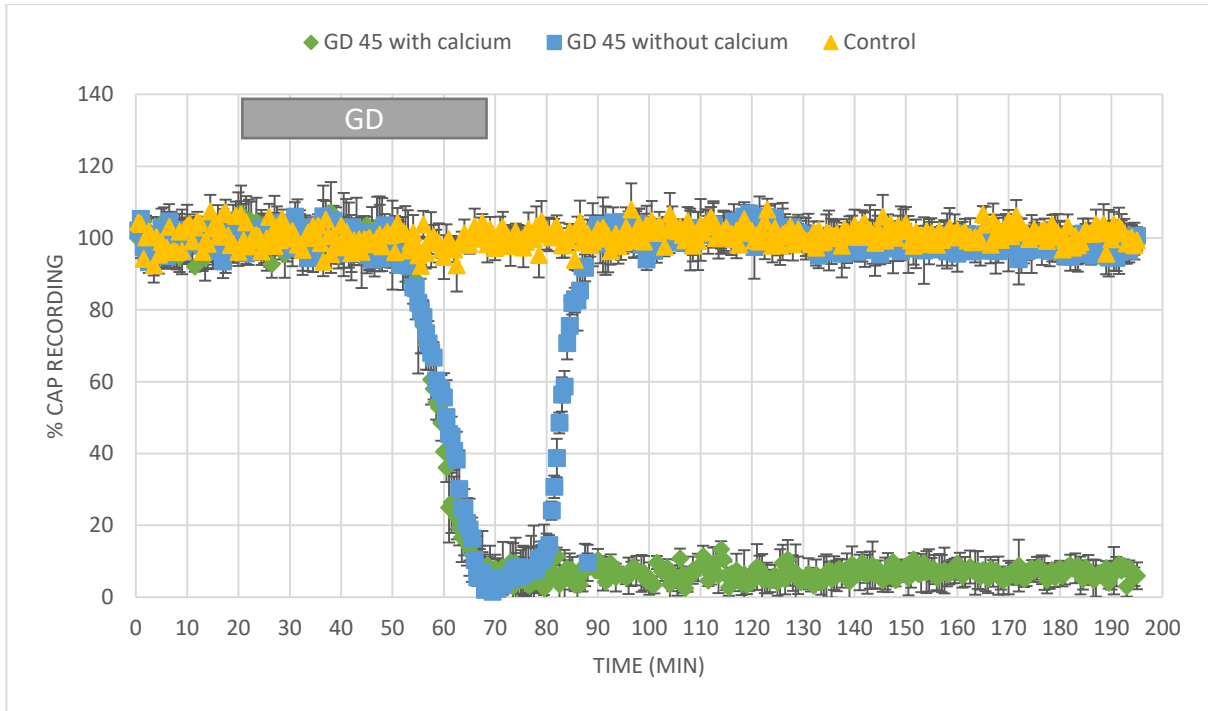


Figure 4.17. CAP recording from callosal slices exposed to 45 min of GD (+/-) Ca^{2+} and controls. Complete recovery of axonal function after glucose deprivation in a Ca^{2+} - free environment I. There is a loss of the % CAP during 45 min of GD both in the presence and absence of Ca^{2+} . Recovery in the % CAP only occurred in those slices that were maintained in a Ca^{2+} - free environment throughout the experiment.

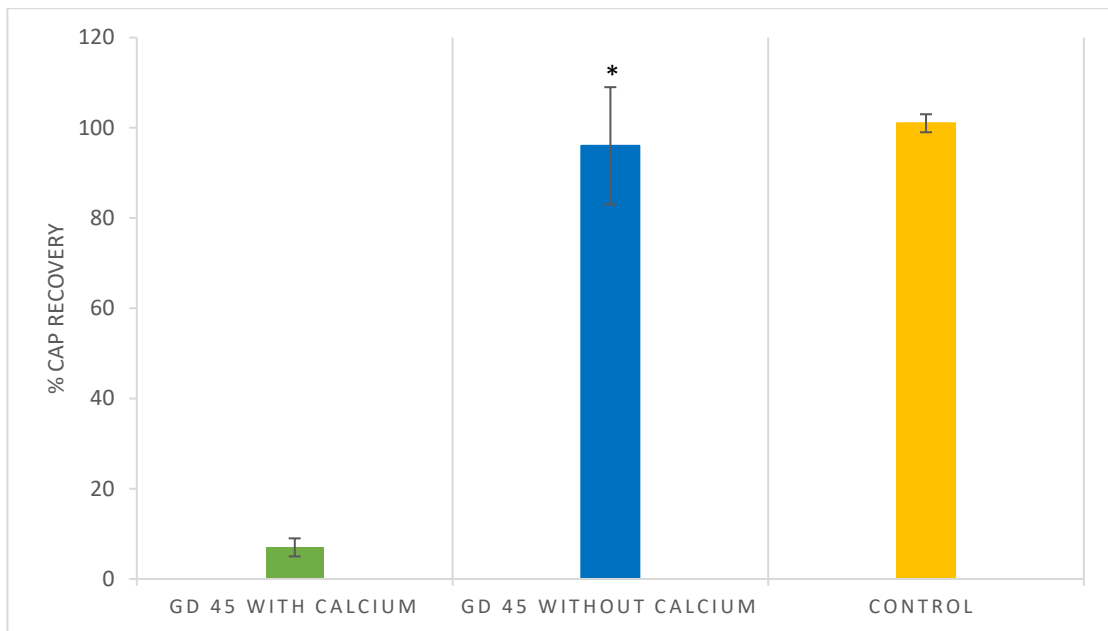


Figure 4.18. Percentage CAP recovery of callosal slices exposed to 45 min of GD (+/-) Ca^{2+} and controls. There is a statistically significant difference (* $p < 0.001$) in the % CAP recovery amongst slices exposed to GD in the absence of Ca^{2+} to those slices maintained in the presence of Ca^{2+} . The GD group maintained in the absence of Ca^{2+} and the control slices maintained under normoglycaemia recovered to the same level.

4.4.3 The preferential localization of QNZ-46 in myelin is key to neuroprotection

Following systemic administration (IP) 4 h min prior to the killing, vital QNZ-46 fluorescence was preferentially distributed in white matter demonstrating brain penetration and myelin retention since the tissue was dissected into QNZ-46 free aCSF for imaging. Slices were co-loaded with Nile Red, a vital stain which stains myelin. We observed co-staining between QNZ-46 and Nile Red in the myelin sheaths.

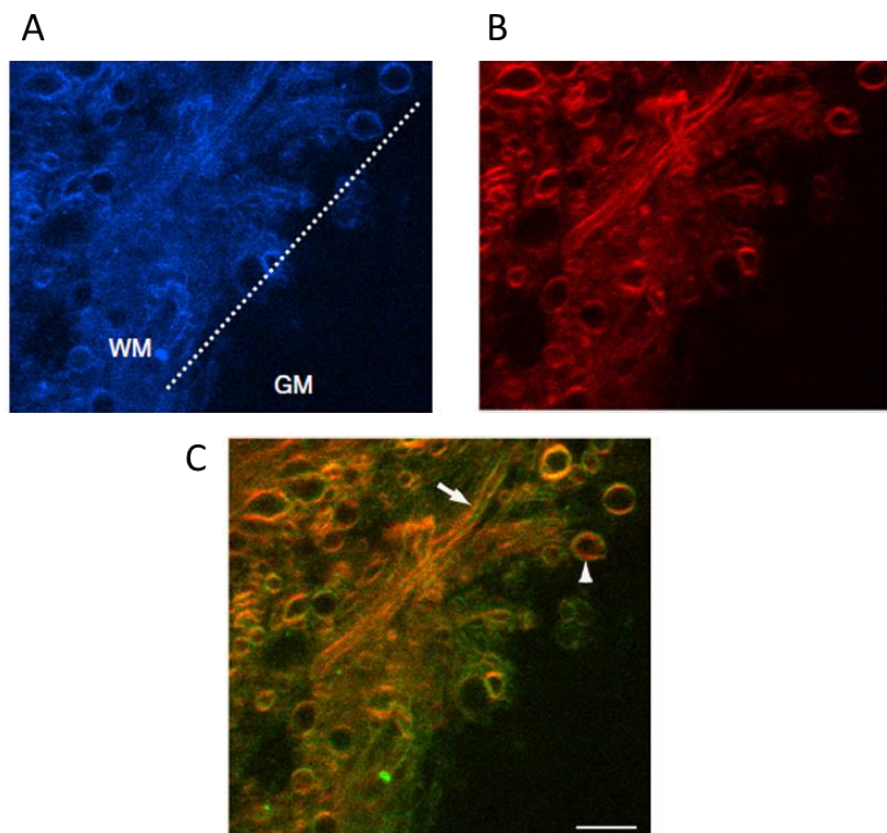


Figure 4.19. QNZ-46/FM co-staining in brain slice following systemic QNZ-46 injection at 4 hr before sacrifice. Differential staining between white and grey matter of QNZ-46 [A] and Nile Red [B]. [C] Double staining of QNZ and Nile Red around linear profiles (arrows) and rounded swollen axons (arrow heads) (adapted from Doyle *et al.*, 2018).

4.4.4 The combined AMPA and NMDA receptor block protect axons following glucose deprivation

Callosal slices from mice injected with the vehicle (β -cyclodextrin + DMSO) for 5 consecutive days, were incubated for 4 hours at 37°C. Other slices from the same group of mice were exposed to 45 min of GD and 2 hr of reperfusion with glucose-containing aCSF. This was done to determine whether the vehicle exerts any negative or toxic effect on axons. Combined two-photon imaging and CAP recording from these slices, showed no sign of axonal injury and CAP was maintained throughout the course of the 4-hour incubation period in glucose-containing aCSF. On the other hand, there was severe structural axonal injury and loss of conduction in slices exposed to 45 min GD. There was no statistically significant difference in the % CAP recovery, or axonal injury score between controls (\pm vehicle), and those slices exposed to 45 min of GD (\pm vehicle). Refer to supplementary data.

When QNZ-46 and CP-465,022 were administered separately, they presented an almost identical pattern of neuroprotection to callosal axons exposed to glucose deprivation. In both cases, there was only some focal swelling and very mild beading present by the end of the imaging session. This was in stark contrast to those slices from mice injected with vehicle. A statistically significant lower axonal injury score was found in the drug treated groups in comparison to the vehicle by the end of the experiment. In mice treated separately with either QNZ-46 or CP-465,022, CAP recording showed a trend towards a decline to around 50 % of baseline towards the end of glucose deprivation. Reperfusion with glucose-containing aCSF showed a gradual recovery of function that capped to around 80% of the baseline in both cases. A statistically significant difference in the % CAP recovery between the drug treated groups and vehicle is evident. This protective effect that each of these drugs exerted when applied in single, was augmented when both drugs were co-administered simultaneously. In the drug combination group, intact axons were observed along 45 mins of glucose deprivation and throughout the 2hr period of reperfusion. This observation was confirmed electrophysiologically by the preservation of the CAP amplitude that was recorded in the same slices during the imaging session. A statistically significant difference in axonal injury score obtained through imaging along with a significant difference in % CAP recovery during electrophysiology was present between the combined drug-treated group and that treated singly.

	Start	GD	Rep 1 hr	Rep 2 hr
Controls + Vehicle	0.07 ± 0.02	0.09 ± 0.02	0.09 ± 0.02	0.11 ± 0.02
GD + Vehicle	0.13 ± 0.02	0.13 ± 0.02	1.01 ± 0.10	1.67 ± 0.06
GD + QNZ	0.10 ± 0.02	0.10 ± 0.02	0.49 ± 0.09	0.62 ± 0.06
GD + CP	0.10 ± 0.02	0.10 ± 0.02	0.51 ± 0.02	0.64 ± 0.04
GD + CP + QNZ	0.07 ± 0.02	0.09 ± 0.02	0.11 ± 0.02	0.13 ± 0.05

Table 4.1. Comparison of the axonal injury scores at different experimental time-points between different experimental protocols. Values expressed at means ± standard deviation (QNZ – QNZ-46; CP – CP-465,022).

		Start	GD 45 min	REP 1 hr	REP 2 hr
Control + Vehicle	GD + Vehicle	X	X	p < 0.001	p < 0.001
	GD + QNZ	X	X	p < 0.001	p < 0.001
	GD + CP	X	X	p < 0.001	p < 0.001
	GD + QNZ + CP	X	X	X	X
GD + Vehicle	GD + QNZ	X	X	p < 0.001	p < 0.001
	GD + CP	X	X	p < 0.001	p < 0.001
	GD + QNZ + CP	X	X	p < 0.001	p < 0.001
GD + QNZ	GD + CP	X	X	X	X
GD + QNZ + CP	GD + QNZ	X	X	p < 0.05	p < 0.001
	GD + CP	X	X	p < 0.05	p < 0.001

Table 4.2. One-way ANOVA followed by Tukey’s post hoc test for multiple comparisons between groups. X – no statistically significant difference between groups.

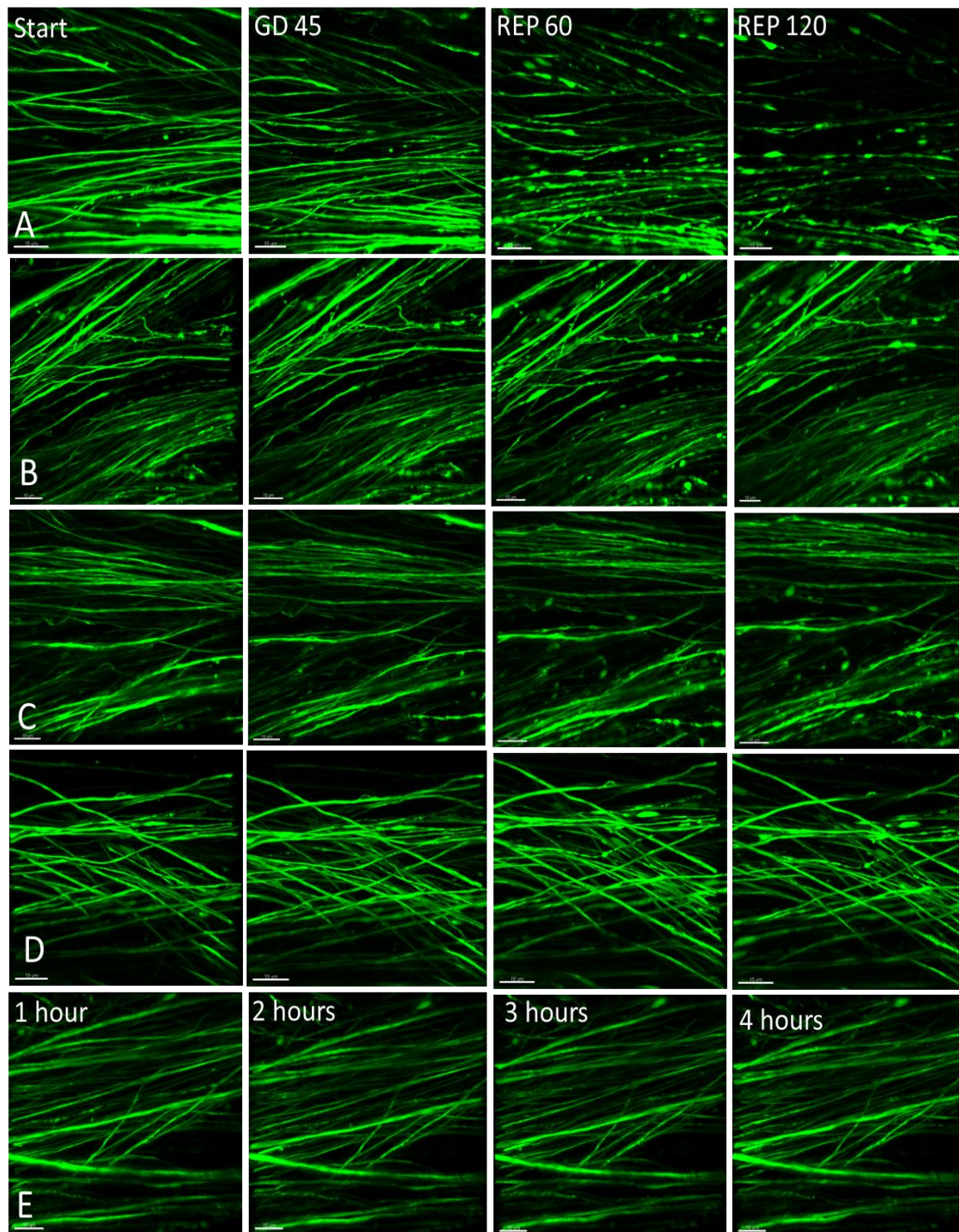


Figure 4.20. QNZ-46 and CP-465,022 protect axons following glucose deprivation. [A] Focal swelling was evident during the early phase of reperfusion and progressed to beading and fragmentation through the 2 hr of reperfusion in the vehicle treated group. Axonal injury was limited to some focal swelling with minimal focal beading during the reperfusion phase in mice injected with QNZ-46 [B] and with CP-465,022 [C]. [D] No signs of axonal injury were observed in those mice treated in combination with both drugs. [E] Control slices. Scale bar: 15 μ m

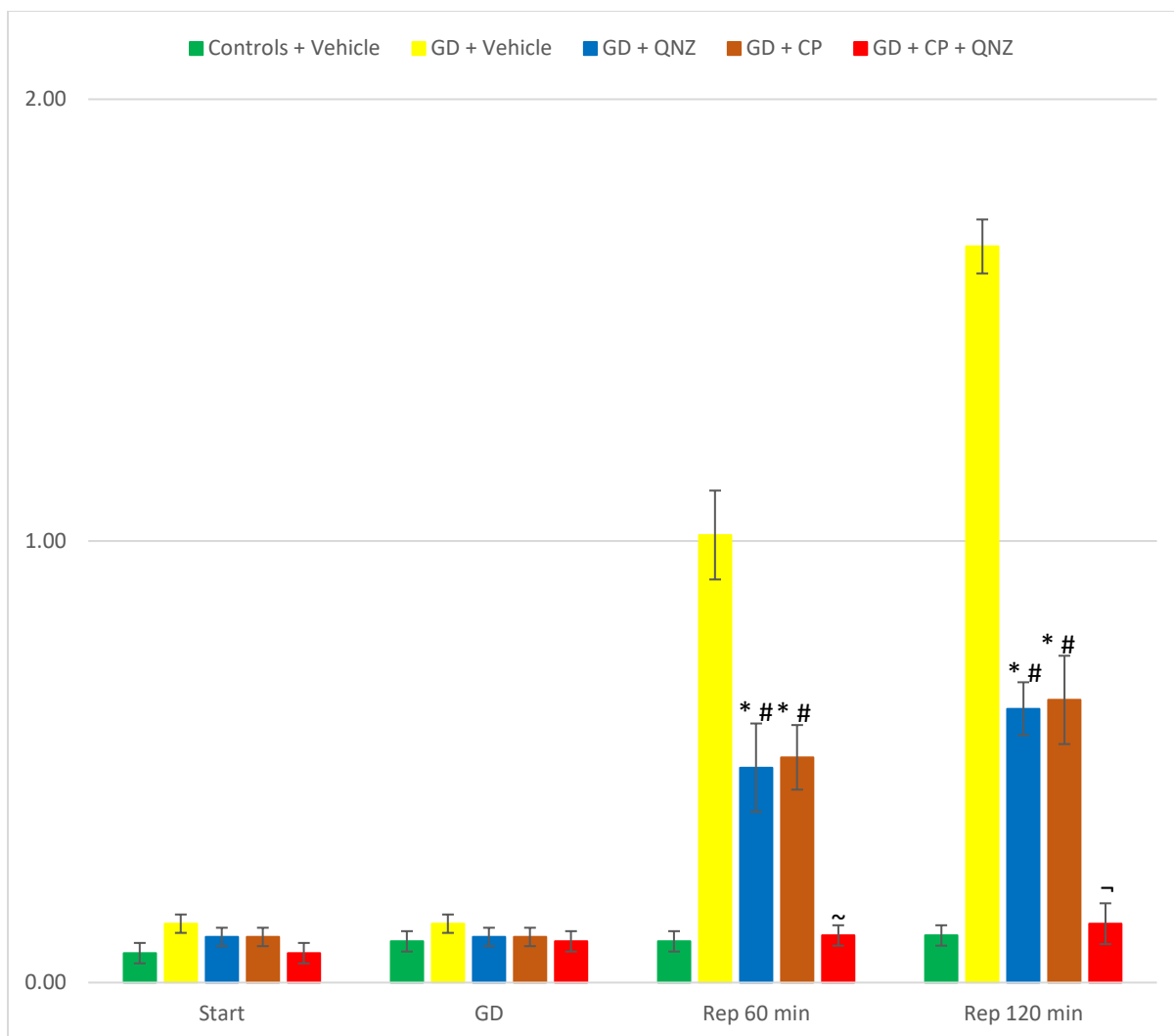


Figure 4.21. Addition of QNZ-46 and CP-465,022 attenuates the axonal injury score during the reperfusion. There is no statistically significant difference between the experimental conditions at the start of the experiment and immediately after GD in all groups * $p < 0.001$: statistically significant higher axonal injury score at 60- and 120-min reperfusion in slices from mice treated with QNZ-46 and CP-465,022 when compared to controls # $p < 0.001$: statistically significant lower axonal injury score at 60- and 120-min reperfusion in slices from mice treated with CP-465,022 when compared to vehicle-treated mice. No statistically significant difference was found between slices from mice treated with both drugs and controls throughout the observation period. A statistically significant lower injury score is seen between slices from mice injected singly with either QNZ-46 or CP-465,022 when compared to slices from mice injected with both drugs at 1hr- ($\sim p < 0.5$) and 2 hr reperfusion ($\sim p < 0.01$), ($n=3$).

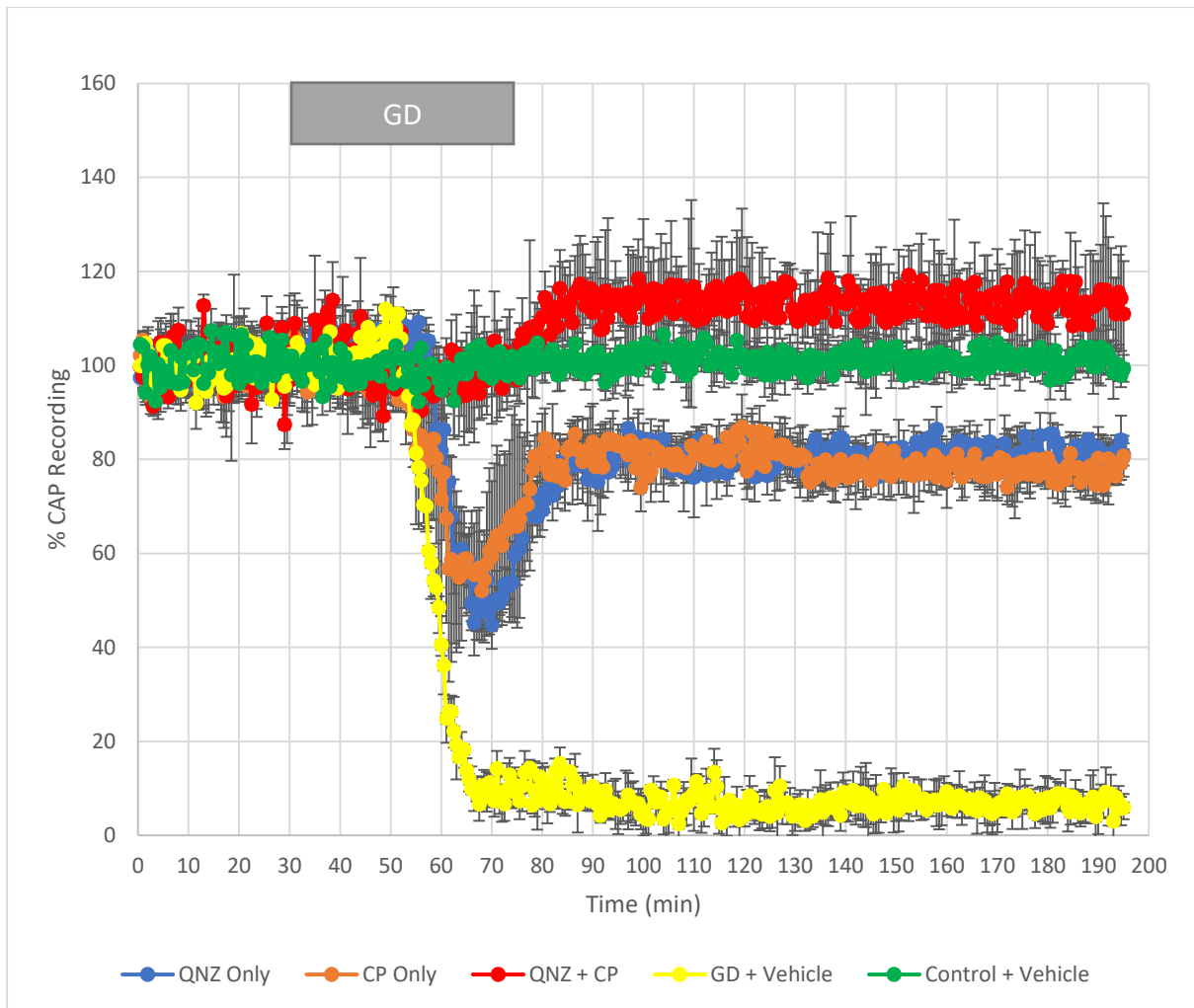


Figure 4.22. Combination therapy with QNZ-46 and CP-465,022 maintains electrical excitability during GD I. There is some partial loss in CAP amplitude during GD that accompanies the partial recovery in the reperfusion phase in slices from mice treated in single with QNZ-46 (blue) and CP-465,022 (orange). There is no change in CAP amplitude throughout either GD or reperfusion in slices from mice treated with both drugs (red). The vehicle-treated group shows loss of function that failed to recover (yellow) and the control group of normoglycaemia showed a stable profile in CAP recording (green) typical of healthy axons.

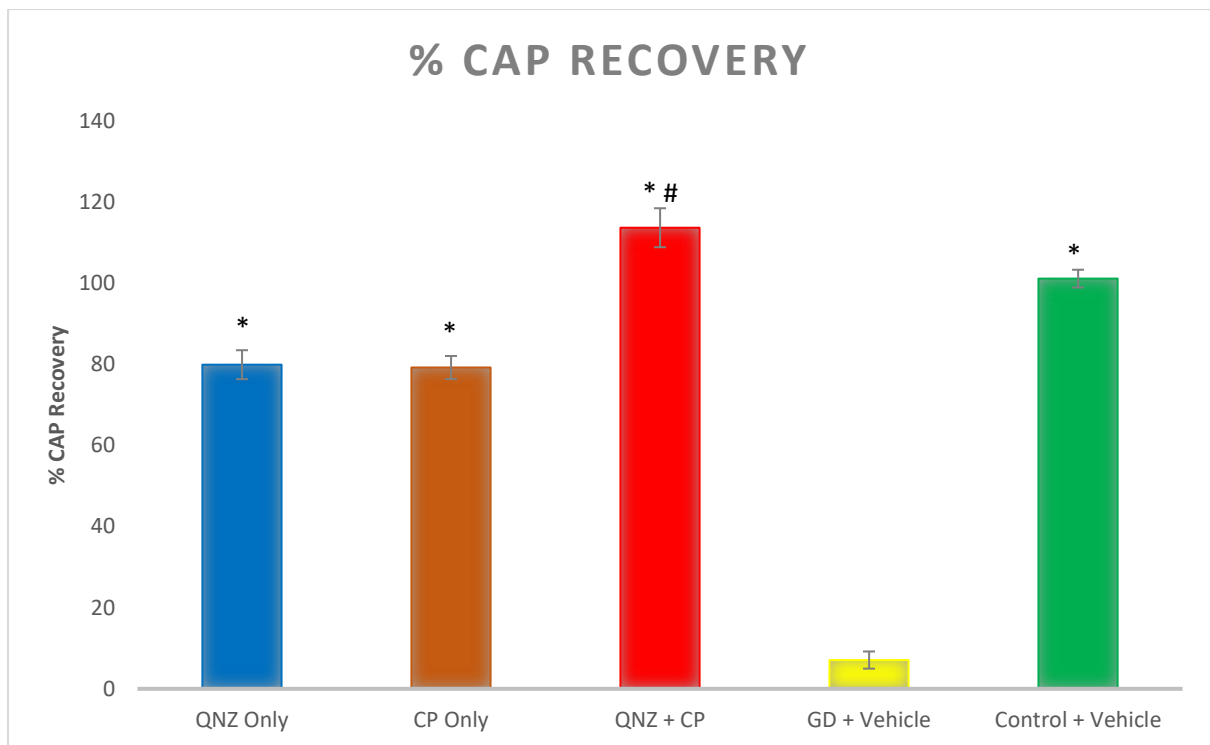


Figure 4.23. Combination therapy with QNZ-46 and CP-465,022 maintains axonal conduction integrity during GD II. * $p < 0.001$: By the end of each condition, there was a statistically significant difference in % CAP recovery by the end of reperfusion between (i) controls (ii) mice treated with either QNZ-46 or CP-465,022 (iii) mice treated in combination with QNZ-46 and CP-465,022, and the (iv) vehicle treated mice. # $p < 0.001$: following 45 min GD, there was a statistically significant difference in % CAP recovery during reperfusion between slices from mice treated simultaneously with both drugs, and slices from mice treated singly with either QNZ-46 or CP-465,022 ($n=3$).

4.5 Discussion

4.5.1 Block of AMPA/Kainate receptors with NBQX protects axons and glia from injury

The dogma that injury secondary to the over-activation of glutamate receptors is limited to CNS grey matter has long been refuted. There is abundant data suggesting that white matter is also susceptible to excitotoxicity (Matute *et al.* 1997; McDonald *et al.* 1998; Li and Stys, 2000) and that blocking AMPA/Kainate protects white matter from various insults (Follett *et al.*, 2001; Tekkök and Goldberg, 2001; Tekkök *et al.*, 2005a; McCarren and Goldberg, 2007; Agrawal and Fehlings, 1997; Wrathall *et al.*, 1997).

Our results implicate a direct role for AMPA/kainate receptors in aglycaemic injury to central white matter elements, including axons and oligodendrocytes. Pharmacological blockade of AMPA/kainate receptors was effective when administered before or after GD, suggestive of the persistent activation of AMPA/Kainate receptors by extracellular release of the excitatory neurotransmitter, glutamate. NBQX administered before the course of GD blocked AMPA/Kainate receptors and protected axons and oligodendrocytes. However, there was partial protection afforded to axons and oligodendrocytes when NBQX was administered late (after GD), suggesting that mechanisms independent of AMPA/Kainate receptors are likely to contribute to the GD-induced toxicity.

Activation of AMPA/Kainate receptors mediate oligodendrocyte injury by increasing the influx of Ca^{2+} through reversal of the Na^+/Ca^{2+} exchanger (Sánchez-Gómez and Matute, 1999), and by increasing the cell's vulnerability through oxidative stress as a result of the reversal of the glutamate-cystine exchanger at high extracellular glutamate concentrations (Oka *et al.*, 1993). Our EM data confirms that blocking AMPA/Kainate receptors during glucose deprivation prevents morphological changes in oligodendrocytes cell body and nucleus. Further ultrastructural details from EM show normal appearing nuclei and mitochondria with cristae, together with well organised and normal appearance of the endoplasmic reticulum and golgi apparatus.

In separate complementary experiments with treatment with NBQX, there was a clear protection to oligodendrocytes and only a small number of axons showed signs of pathology when compared to the untreated group. Moreover, the myelin sheaths appeared intact and importantly, most of the small-calibre unmyelinated axons remained preserved. This may suggest that blocking AMPA/KA receptors on oligodendrocytes protects not only these cells but preserves also the axon along with its myelin sheath.

An interesting finding was that most small-calibre and unmyelinated axons were left intact in slices treated with NBQX. Unmyelinated axons are not directly in contact with the oligodendrocyte cell bodies and therefore the protection of the latter via NBQX should have no effect on the unmyelinated axons. One possible explanation could be that injured oligodendrocytes release their toxic cytoplasmic contents including ROS (Tekkök and Goldberg, 2001), that damage neighbouring axons, glia and blood vessels that contribute to the propagation of the initial insult. Protecting oligodendrocytes by blocking the overactivity of AMPA/KA receptors might be a good strategy to preserve the integrity of neighbouring support cells and nerve fibres in the long term.

4.5.2 The combined block of GluN2C/D subunits on NMDA receptors and AMPA receptors protects oligodendrocytes and axons following glucose deprivation

The increase in intracellular calcium has long been implicated to be deleterious to the central nervous system (Young, 1992; Orrenius and Nicotera, 1994), and is not surprising that it mediates glucose deprivation induced injury both to grey and white matter. Hippocampal slices exposed to glucose deprivation resulted in an increase in intracellular calcium in pyramidal cells (Takata and Okada, 1995; Takata *et al.*, 1995), and GD induced conduction block in the rodent optic nerve which was completely prevented when the GD was performed in a calcium-free environment (Brown *et al.*, 2001).

Excitotoxicity is believed to play a crucial role in white matter injury during GD (Wieloch, 1985; Suh, 2007b; Yang *et al.*, 2014), and it is mainly mediated by an increase in intracellular Ca^{2+} (Sánchez-Gómez and Matute, 1999; Salter and Fern, 2005). AMPA receptors present on the oligodendrocyte's somas (Steinhäuser and Gallo, 1996; García-Barcina and Matute, 1998) are slightly different from those present in grey matter. They lack the GluA2 subunit (Matute, 1999), thus making them permeable to Ca^{2+} (Wright and Vissel, 2012) unlike the oligodendrocytes present in grey matter (Burnashev, 1996). This rise in intracellular Ca^{2+} accumulates in the mitochondria, leading to mitochondrial membrane depolarisation that leads to the production of ROS and the release of proapoptotic factors such as caspases-3 and 8 (Verkhatsky *et al.*, 1998; Sánchez-Gómez *et al.*, 2003; Matute, 2006). In addition, activation of NMDA receptors expressed on oligodendrocytes' processes generates membrane depolarisation and a rise in cytosolic Ca^{2+} triggering myelin disintegration (Salter and Fern, 2005; Bakiri *et al.*, 2009). These processes are made up of a much smaller intracellular volume when compared to the oligodendrocyte soma. Thus, even a relatively small influx of Na^+ and Ca^{2+} from the channel pore of this type of receptor would be sufficient to elicit a profound increase in intracellular anion species that injure these fragile myelinating processes (Káradóttir *et al.*, 2005).

We first confirmed the central role played by calcium in this deleterious cascade of events by exposing slices to glucose deprivation in a Ca^{2+} -free environment. We observed a complete preservation of axonal structure with full recovery of axonal conduction upon reperfusion. This in itself serves as ample proof of previous studies that emphasise on the central role of Ca^{2+} during glucose deprivation and as a direct cause of axonal injury.

The next step was to identify pharmacological avenues to block contributing factors that cause injury to white matter. Since aglycaemic injury is thought to be preferentially mediated via NMDA receptor overactivation (Yang *et al.*, 2014), we hypothesised that the addition of QNZ-46, the same drug used in our previously published data (Doyle *et al.*, 2018), might also afford protection to axons during a milder form of injury than ischemia per se. Our results confirmed that QNZ-46 is not toxic to mice and that the drug easily crosses the blood brain barrier because of its lipophilic nature that accumulates preferentially in myelin. Mice treated with QNZ-46 showed a statistically significant lesser degree of structural and functional injury of their white matter axons during glucose deprivation when compared with vehicle-untreated mice.

In view of these results, we hypothesised that blocking NMDA receptors on the oligodendrocytes' processes and in the myelin sheath in addition to the block of their transmembrane AMPA receptors located on their soma, we then should expect an additional cumulative protective effect. We have already shown that blocking AMPA/Kainate receptors with NBQX protected both axons and oligodendrocytes during glucose deprivation. To separately block AMPA receptors located on the oligodendrocyte cell body (Steinhäuser and Gallo, 1996; García-Barcina and Matute, 1998), we chose the novel and very selective non-competitive AMPA-specific receptor antagonist, CP-465,022 (Menniti *et al.*, 2000; Lazzaro *et al.*, 2002). The protective effect of this drug on glucose deprivation was practically similar to that observed with QNZ-46 alone. This was confirmed by imaging that showed excellent preservation of axon integrity and through electrophysiological recordings of function through conduction studies. All in all, this merely suggests that AMPA receptors located on oligodendrocytes participate in mediating axonal injury during glucose deprivation and are likely to be a potential therapeutic target for white matter.

The axonal protection against GD provided by each drug individually was amplified when the two drugs were administered in combination. Our results therefore confirm that overactivation of both NMDA receptors on the oligodendrocyte's processes and AMPA receptors on the oligodendrocytes' somas play a crucial part in the excitotoxicity induced axonal injury that evolves during glucose deprivation. Since overactivation of AMPA and NMDA receptors on the oligodendrocytes results in cell death which lead to myelin destruction and secondary axonal injury (Tekkök and Goldberg, 2001; Matute, 2011), blocking both receptors simultaneously by these two drugs offers an ideal therapeutic strategy to treat against aglycaemic injury, and any other brain insult which damages oligodendrocyte and/or myelin directly.

Chapter 5

Nitric oxide and glucose deprivation induced axonal injury

5.1 Aims

Excitotoxicity plays an important role in axonal injury as a result of glucose deprivation. In the previous section we showed that the block of specific NMDA receptors on myelin processes and AMPA receptors on oligodendrocytes cell bodies is highly protective against glucose deprivation. Nitric Oxide (NO) is a free radical that acts as a neurotransmitter and a neurotoxin depending on the site of production and its concentration. One of the proposed sequence of events in the cascade that occurs during axonal injury during ischemia is the elevation in the levels of NO (Stys, 2005). Therefore, the main aims of this chapter are:

- i. To determine the working concentration of NO required to induce irreversible conduction block in axons.
- ii. To establish whether this concentration of NO that causes conduction block is also effective to cause structural injury in axons.
- iii. To capture the presence of NO in white matter during glucose deprivation using specific fluorescent dyes.
- iv. To monitor the level of NO during glucose deprivation.
- v. To establish whether blocking NO production protects axons during glucose deprivation.

5.2 Literature Review

5.2.1 A dual role of nitric oxide in the brain

NO is a free radical that can act both as a signalling molecule and a neurotoxin. Since glutamate mediated excitotoxicity is an important mediator of brain injury (Choi, 1994), and activation of NMDA receptors generates NO in a Ca^{2+} -dependent manner (Garthwaite *et al.*, 1988), NO is hypothesised to be involved in various mechanisms of brain injury.

The role that NO plays in the mechanisms of brain injury has been the source of much debate. Due to its complex biological characteristics, NO can either be detrimental or beneficial to the injured brain. There are many advocates of the dual role NO can play in brain physiology and pathophysiology. This dual role is summarised in Figures 5.1, 5.2 (Iadecola, 1997).

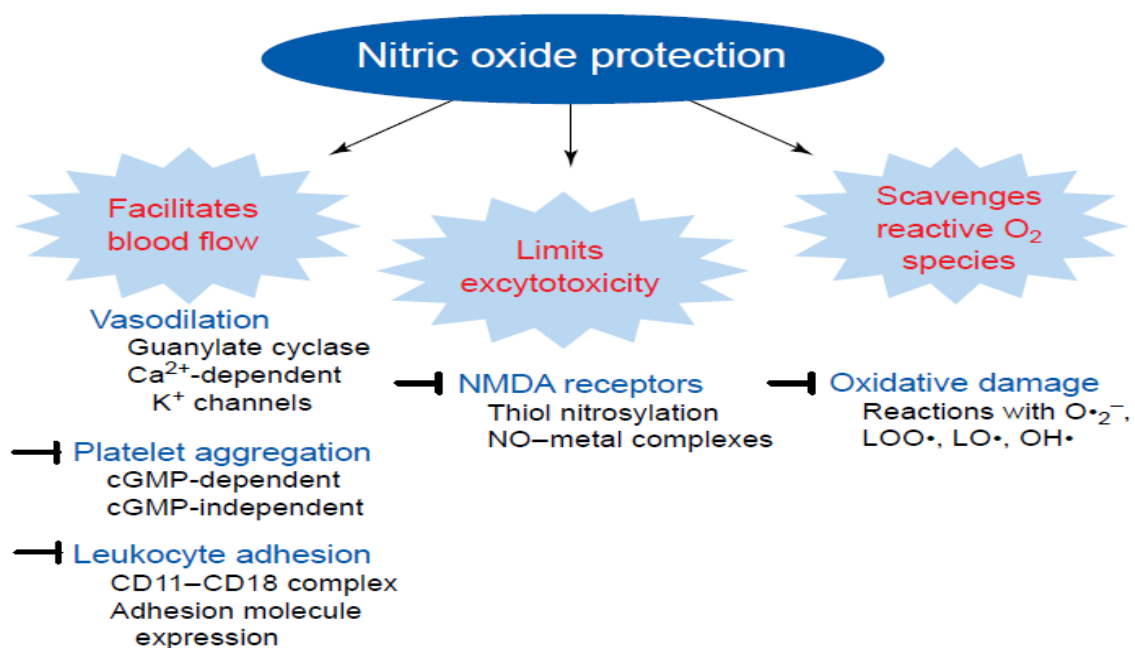


Figure 5.1. Potential protective mechanisms of NO during brain injury (reproduced from Iadecola, 1997).

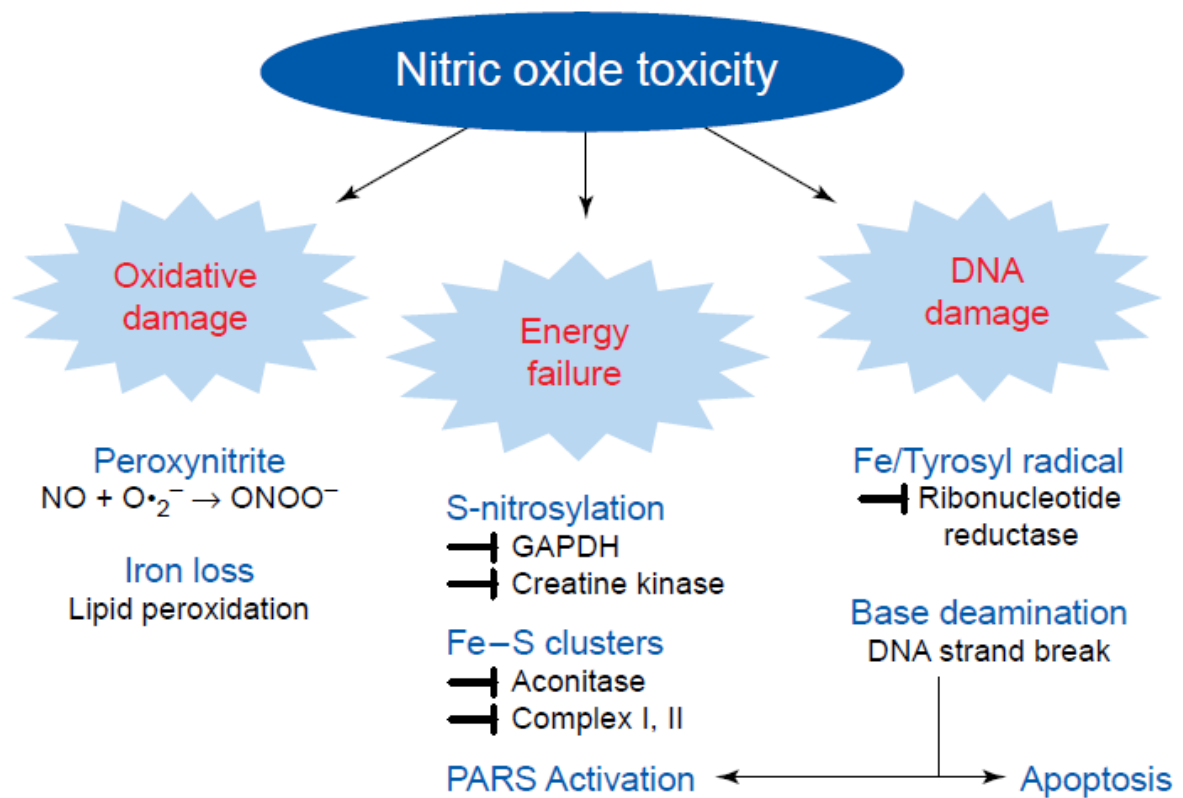


Figure 5.2. Potential destructive mechanisms of NO during brain injury (reproduced from Iadecola, 1997)

5.2.2 Production of nitric oxide in the brain

NO is synthesised from the oxidation of L-arginine by the enzyme nitric oxide synthase (NOS) (Marletta, 1994). There are three isoforms of NOS: neuronal NOS (nNOS or type I); inducible NOS (iNOS or type II); and endothelial NOS (eNOS or type III), (Griffith and Stuehr, 1995).

The eNOS and nNOS isoforms are constitutively expressed. iNOS is not normally expressed but its production can be induced by immunological stimuli or neuronal damage. eNOS and nNOS are known as calmodulin and calcium dependent. They can only synthesise NO when the intracellular Ca^{2+} concentration is elevated, and calmodulin is bound to the enzyme. iNOS produces NO continuously and independently of intracellular Ca^{2+} (Nathan and Xie, 1994).

eNOS and nNOS produce NO in small and highly regulated bursts, suited for the molecular messenger function of NO (Garthwaite and Boulton, 1994). On the contrary, iNOS produces large amounts of NO over long periods, which makes it responsible for the neurotoxicity caused by NO (Gross and Wolin, 1995). Moreover, both eNOS and nNOS are equally involved in the pathophysiological role of NO. In most pathological states, intracellular Ca^{2+} concentration remains persistently elevated, and therefore eNOS and nNOS become continuously active and can produce potentially toxic amounts of NO (Iadecola, 1995a).

5.2.3 Nitric oxide causes conduction block in axons

The addition of NO to both peripheral and central white matter tracts have been reported to induce axonal conduction block. Tibial nerves exposed to NO rapidly suffered loss of conduction, followed by Wallerian degeneration. This neurotoxic effect was hypothesized to be primarily due to energy restriction by inhibition of mitochondrial respiration (Alvarez *et al.*, 2008).

In the literature we find three main factors that determine the degree of axonal conduction block: concentration of NO; frequency of stimulation; and degree of myelination. As expected, the NO-induced conduction block is dose-dependent. Spinal nerve roots exhibited a reversible conduction block when exposed to low NO concentration ($< 7 \mu\text{M}$), and an irreversible one with higher NO concentrations ($> 13 \mu\text{M}$). This block was prevented by partially blocking Na^+ channels, and the Na^+/Ca^+ exchanger (Kapoor *et al.*, 2003). Axons in the spinal cord showed a similar response to NO. The rapid reduction in CAP amplitude following NO administration was also dose-dependent (Ashki *et al.*, 2006). The NO-induced conduction block is also dependent on the frequency of nerve stimulation. Nerves stimulated with low frequency showed reversible NO conduction block, whilst those stimulated at high frequency exhibited irreversible conduction block despite having been exposed to the same concentration of NO. The fibres which suffered irreversible block, showed morphological changes consistent with acute Wallerian degeneration (Smith *et al.*, 2001). There is contrasting evidence on the relationship between the amount of myelination and the degree of NO induced conduction block. Redford *et al.*, (1997) reported that demyelinated and early remyelinated axons are particularly sensitive to block by NO, even at low NO concentrations, like those found at sites of inflammation. On the contrary, Shrager and Youngman (2017), found that in multiple models of peripheral and central white matter, myelinated fibres were preferentially reversibly blocked by concentrations of NO like those encountered in inflammatory lesions. The pattern of NO induced loss of axonal conduction was very similar to that induced by tetrodotoxin. It was therefore hypothesised that NO likely interacts with axonal Na^+ channels through an intermediate that is associated with myelin.

5.2.4 Nitric oxide is a cause of white matter injury

Several studies have evaluated the potential negative effect of NO to white matter components. A benchmark paper was published by Garthwaite and colleagues in 2002. They exposed the rat optic nerve to a variety of NO donors at various concentrations and over variable periods to study the ultrastructural alterations caused by NO to different white matter components. They reported that axons are the most vulnerable, followed by oligodendrocytes and astrocytes. The main structural feature of axonal injury was persistent swelling. Astrocytes and oligodendrocytes survived insults that clearly induced axonopathy, which suggests that NO caused axonal injury that is not secondary to glial damage. They also compared the pattern in the structural and functional injury caused during anoxia and ischaemia. They hypothesised that NO competes with O₂ to bind with cytochrome *c* oxidase (complex IV) thus inhibiting the respiratory chain (Brown, 1999; Heales *et al.*, 1999). This leads to a decrease in the levels of ATP, failure of the Na⁺/K⁺ pump, Na⁺ influx and depolarisation. Terminal depolarisation represents the basis of the conduction block that is observed on addition of the NO donors. Glial cells were more resistant to the respiratory chain inhibition caused by NO and a plausible explanation could be that they contain less Na⁺ channels than axons, use alternative pathways for ATP generation, and have larger levels of anti-oxidants (Heales *et al.*, 1999). Moreover, longer exposure to NO has been shown to cause severe injury (Merrill *et al.*, 1993; Mitrovic *et al.*, 1994), presumably due to the formation of peroxynitrite and eventual death as a result of oxidative stress (Garthwaite *et al.*, 2002). Elevated levels of NO have been reported to cause oligodendrocyte degeneration, and S-nitrosation of a proteolipid protein responsible for intraperiod myelin stabilisation, essential for proper myelination (Bizzozero *et al.*, 2004).

5.2.5 Putative role of nitric oxide during glucose deprivation

The role of NO in brain ischaemia has been well documented in the literature (Malinski *et al.*, 1993; Zhang *et al.*, 1995; Huk *et al.*, 1998; Yong *et al.*, 2005; Yang *et al.* 2008; Corsani *et al.*, 2008; ArunaDevi *et al.*, 2010). It plays a crucial role both in the acute phase of ischaemic damage and in the delayed events contributing to its evolution (Iadecola *et al.*, 1997). The levels of NO in the brain increase to micromolar levels within 20 min following MCAO (Malinski *et al.*, 1993). This sharp rise in NO could be inhibited by glutamate-receptor antagonists, indicating that the increased NO thus produced is initiated by glutamate (Lin *et al.*, 1996). The immediate rise in the level of NO could be explained due to the rapid increase in activity of both neuronal and endothelial NOS (within minutes) following induction of ischaemia (Kader *et al.*, 1993; Iadecola *et al.*, 1995a; Nagafuji *et al.*, 1994). The increase in activity of inducible NOS is delayed, with a surge that occurs 6 – 12 hours after injury (Iadecola *et al.*, 1995b; Iadecola *et al.*, 1996).

Despite abundant evidence on the pathophysiology of NO during ischaemia, the role of NO in glucose deprivation is not clear. As in ischaemia, glucose deprivation causes excitotoxicity (Yang *et al.*, 2014), and NO has been shown to mediate glutamate neurotoxicity in neuronal cultures (Dawson *et al.*, 1991). We therefore hypothesised that NO plays can potentially also contribute to cause brain injury following glucose deprivation. To our knowledge, the only reference that reported an increase in NO during glucose deprivation was that by Kojima and colleagues (2001a), and the increase was only documented in the grey matter. The same authors reported an increase in NO in the CA1 region of the hippocampus during GD, which was blocked by L-NAME (a non-specific NOS inhibitor) and which gradually decreased at reperfusion.

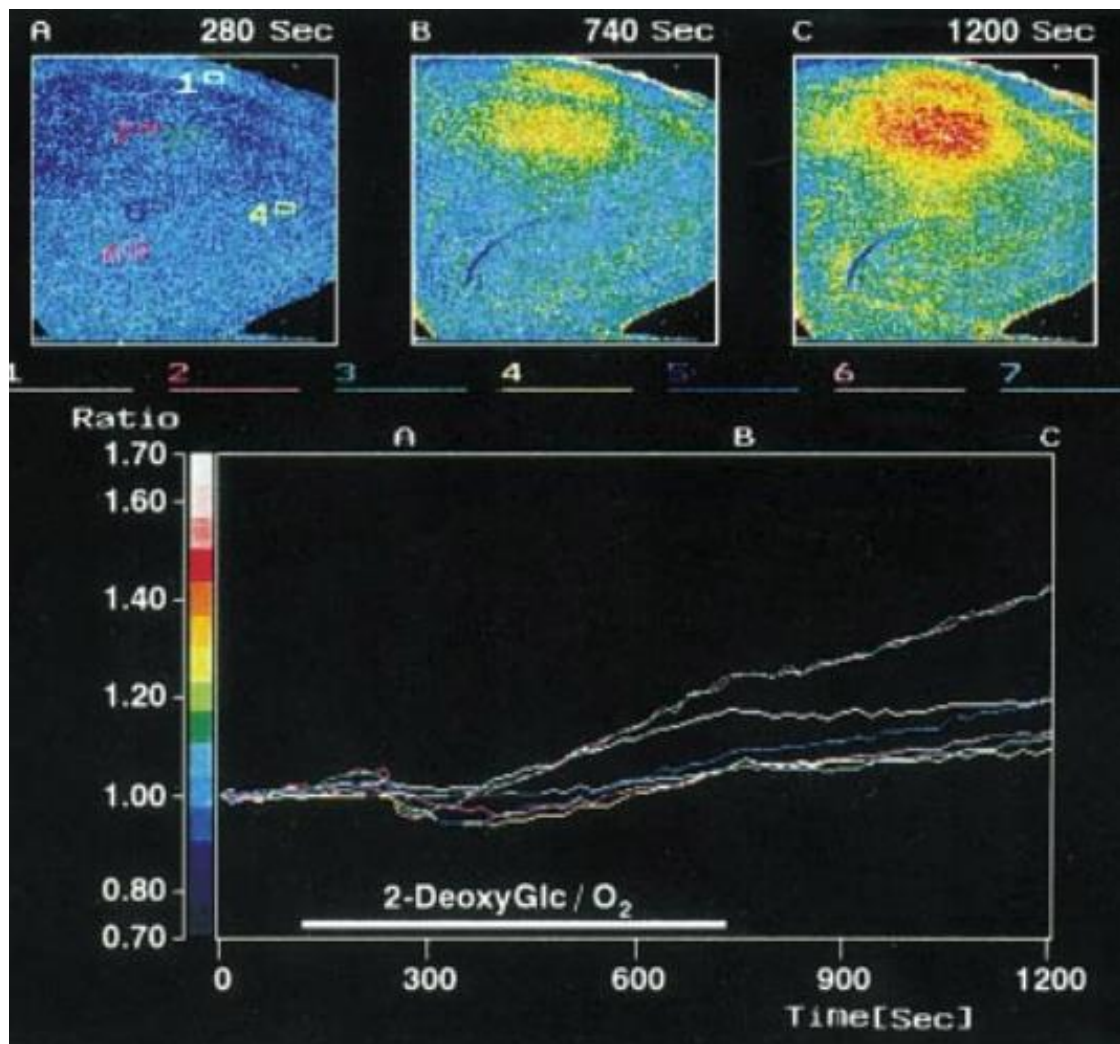


Figure 5.3. Changes in the fluorescence response in rat hippocampal slices with elevation in NO during GD. Slices were loaded in NO sensitive fluorescent dye DAF-FM DA. A - C: an increase in the fluorescence of NO in the CA1 region of the hippocampus; coloured lines in the charts shows the average intensities of the corresponding areas (Reproduced from Kojima *et al.*, 2001a).

5.3 Methodology

5.3.1 Application of nitric oxide donor to callosal slices

NO is a volatile gas with a very short half-life in aqueous solution. Therefore, compounds that spontaneously release NO over time are used to study the effect of NO on the brain. From the NO donors that are available for the purpose of research, we chose 2,2'-(2-Hydroxy-2-nitrosohydrazinylidene)bis-ethanamine (DETA NONOate) (Cat. No. 6077; Tocris). The main advantage of this donor is the long half-life of about 20 hours (Garthwaite *et al.* 2002). This is advantageous as it permits a stable release of NO throughout the duration of most experiments. It has been used to study the injury caused by NO in the sciatic nerve (Alvarez *et al.*, 2008), optic nerve (Garthwaite *et al.* 2002), and the spinal cord nerve roots (Smith *et al.*, 2001).

To our knowledge there is no literature available as to the working concentrations of DETA NONOate on brain slices. To this end, we performed several dose-response experiments to determine the correct dose that provokes conduction block in callosal axons.

The callosal brain slices were prepared for combined live-imaging and electrophysiology under two-photon microscopy as described in chapter 2. After stabilisation for 2 hours in a holding chamber, the callosal slices were transferred to the imaging chamber of the submersible type. After optimising the output signal, slices were stimulated for 30 mins to achieve a baseline recording. 1 mM of DETA NONOate was added to the perfusate every 30 mins. Axonal conduction and monitoring of the YFP-expressing axons were monitored simultaneously throughout the duration of the experiment to follow the integrity of the preparation over time.

5.3.2 Detection of nitric oxide in white matter using fluorescent dyes

To detect NO in our preparation, we worked on protocols that utilise NO-sensitive dyes that detect and quantify low concentrations of NO that work as fluorescent reporters in vivo. There are 3 main types of such reagents that can be used for this technique: diaminoaromatic fluorescent compounds (DAFCs) such as diaminofluorescein (DAF), diaminorhodamine (DAR), and diaminoanthraquinone (DAQ), copper-based compounds, and fluorescence resonance energy transfer (FRET)-based NO indicators (Hong *et al.*, 2009). We chose two of these agents, that detect intracellular levels of NO: Diaminofluorescein-FM diacetate (DAF-FM DA) (Cat. No. D23842; Invitrogen) and Diaminorhodamine-4M-AM (DAR-4M AM) (Cat. No. sc-221530; Santa Cruz Biotechnology). These particular NO-sensing dyes are cell permeable and non-fluorescent until they enter cells where they are hydrolysed by esterases and react with NO to form a fluorescent benzotriazole complex. The specificity of these dyes lies in the fact that they do not react with the common scavengers of NO that form the common by-products that include, nitrates, nitrites or peroxynitrite (Miller and Chang, 2007). The properties of these two drugs is summarised in the table below.

	DAF-FM DA	DAR-4M AM
Site of action	Intracellular – released by esterases	Intracellular – released by esterases
Fluorescence quantum yield on detection of NO	160	840
Dependence on pH	No	No
Detection limit	~3 nM	~10 nM
Photosensitivity	Significantly photostable	Sensitive to light

Table 5.1. Comparison between the properties of DAF-FM DA and DAR-4M AM. (Summarised data obtained from: Kojima *et al.*, 1998, 1999, 2001b).

DAF-FM has been used to detect levels of NO in isolated porcine coronary artery, cell cultures of rat bladder, smooth muscles (Itoh *et al.*, 2000), cultured astrocytes (Li *et al.*, 2003), primary neural cell cultures (Tjalkens *et al.*, 2011), and neurons from rat slice cultures (Kovács *et al.*, 2009). DAR-4M AM has been used to detect levels of NO in myocytes (Chang *et al.*, 2008), osteocytes (Vatsa *et al.*, 2006), macrophages (Jo *et al.*, 2016), colonic epithelial cells (MacEachern *et al.*, 2011), endothelial cells (Kikuchi *et al.*, 2008), and neurons (Imura *et al.*, 2005).

After 2-hour stabilisation in a holding chamber, a brain slice was transferred to the imaging chamber filled with oxygenated and circulating aCSF. The protocol for dye loading was similar to both dyes. 10µM of the dye was dissolved in 2ml aCSF and directly loaded in the imaging chamber that contained the slice. This solution was continuously bubbled with 95%O₂/5%CO₂, and the temperature gradually increased to 33°C. Slices were left incubating in the dye for 60 mins at 33°C with the pump circulating the aCSF switched off. A needle attached to a cylinder of carbogen was inserted close to the slice in the imaging chamber that served to oxygenate the preparation. Since both dyes are light sensitive, this procedure was carried out under low light levels. After the incubation period, the slice was washed off for 30 min with circulating aCSF and the temperature gradually increased to 37°C.

	DAF-FM DA	DAR-4M AM
Excitation	765 nm	850 nm
Emission	515nm – 560nm	565nm – 605nm

Table 5.2. Excitation and emission wavelengths employed for the detection of DAF-FM DA and DAR-4M AM under two-photon microscopy.

The appropriate laser and detection channel were selected according to the dye being used. The laser settings were adjusted for low power, sufficient to distinguish a signal at the detector to limit photobleaching. The laser power and the detector gain were kept constant throughout the duration of each experiment.

The emission signal for DAF-FM DA occurs at a wavelength of 515nm (green) and overlaps the emission spectra for YFP. For this reason, the YFP mice were not suitable as the background fluorescent from the YFP would influence the experimental outcome. For this reason, the non-fluorescent CD-1 mice were chosen for those experiments that involved the use of DAF-FM DA. In some experiments, we made use of Nile Red (Cat. No. N1142; Invitrogen) to demarcate the myelin sheaths across the corpus callosum and determine whether the source of NO from DAF-FM DA arises from the white matter.

The emission signal for DAR-4M AM occurs at a wavelength of 575nm (red), which can be easily separated from the YFP signal. For this reason, YFP mice were chosen for those experiments that involved the use of DAR-4M AM. In some experiments, brain slices from CD-1 mice were also loaded with DAR-4M AM and exposed to GD, in order to determine whether any background fluorescence derived from YFP interferes and contributes to a change in signal intensity despite its presence in a separate channel.

5.3.3 Quantitative analysis of signal intensity changes from the nitric oxide sensitive dyes

After a 30 min washout of the dye, an area within the genu of the corpus callosum was selected for imaging. The size of this region was kept constant for each experiment to minimise any potential bias between experiments.

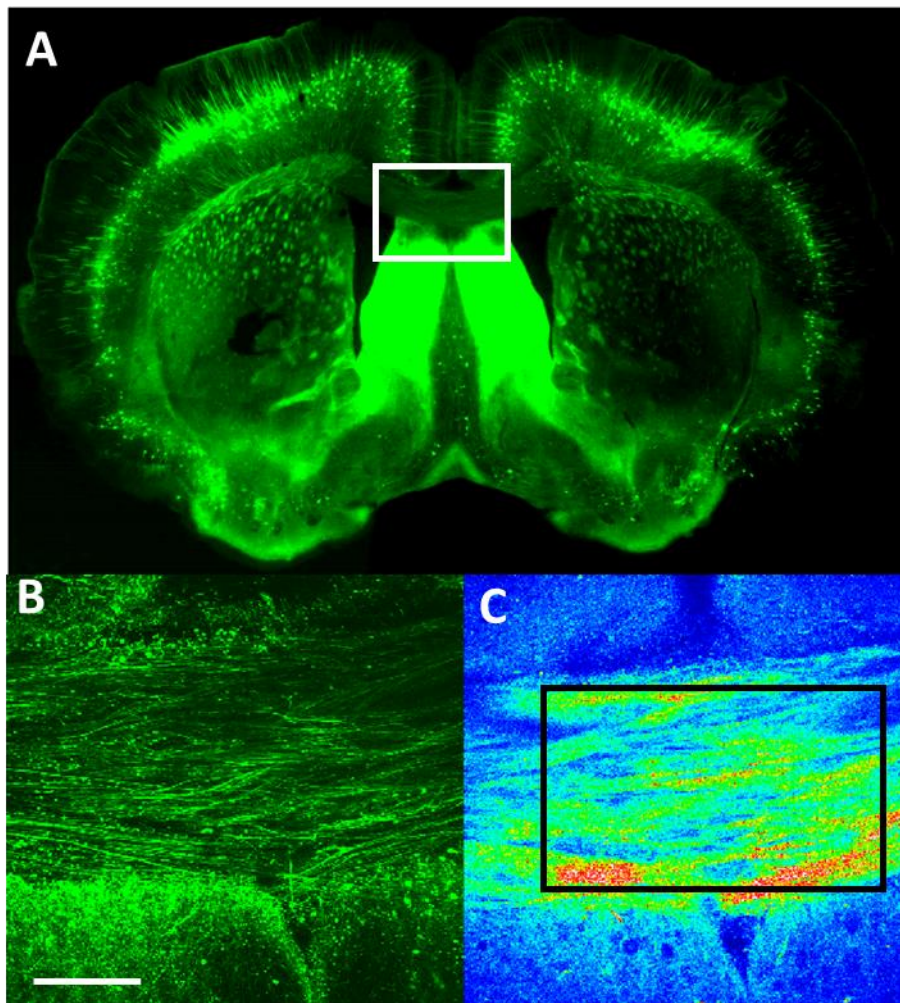


Figure 5.4. Localisation of the ROI to monitor changes in fluorescence of NO-sensitive dyes during GD. [A] YFP coronal brain slices; white box is shown at a higher magnification in B and C. [B] The selected area that was used for the visualization of NO-sensitive dyes across YFP axons at the genu of the corpus callosum [C] Same brain region after dye loading with DAR-4M AM. Images were observed in pseudo-colour so that any change in signal intensity is more discernible. Black box delineates the size of a typical ROI. Scale bar: 50 μm .

A Z-stack (40 – 50 μ m) within the region of interest (ROI) was taken using the least laser and detector gain settings. These settings were kept the same through all stages of the experiment. Stacked images were taken at the start of the experiment and sequentially at 10, 20, 30, and 45 min of GD and at 30 min and 60 min of reperfusion with glucose containing aCSF. Z-stacks obtained from different experimental time points were saved for offline analysis. During the analysis of data, images from the first 15 – 20 μ m of the stack were discarded to eliminate the cutting surface that typically concentrates much of the NO-sensitive dye in damaged axons. The images were analysed for changes in signal intensity using Olympus FluoView V100 software. For all the images, a single ROI selected over the whole frame was chosen, and the value of the signal intensity for each slice within a single stack was obtained. The intensity at each level of the stack was averaged to obtain a single value for each representative time point. The signal intensity at the start of the experiment was normalized to '0' and the image intensity at each time point calculated as a percentage increase/decrease as from the start of the experiment. All signal intensity data were expressed as means \pm standard deviation. Statistical significance was determined by one-way ANOVA followed by a Tuckey post hoc test.

5.3.4 Addition of nitric oxide synthase inhibitors to slices exposed to glucose deprivation

Here we explore whether a detectable increase in NO is released during glucose deprivation. To this end slices were exposed to N^G-Nitro-L-arginine methyl ester (L-NAME) (Cat. No. 0665/100; Tocris) during the course of GD. L-NAME is a non-specific NOS inhibitor (Knowles and Moncada, 1994; Pfeiffer *et al.*, 1996) and has been previously reported to block NO production during glucose deprivation in grey matter (Kojima *et al.*, 2001a).

Following the 2-hour stabilisation period in the holding chamber, the slice was transferred to the imaging chamber and prepared for combined live imaging and CAP recording. After locating a suitable area across the corpus callosum, CAP recording was initiated and once a stable baseline was obtained the slice was left to incubate for 30 mins in 100 μ M of L-NAME in aCSF. The slice was exposed to 45 min of glucose deprivation in the presence of L-NAME and allowed to reperfuse for up to 2hrs in glucose containing aCSF in the absence of L-NAME. Axonal conduction, together with the integrity of the YFP-expressing axons was monitored simultaneously throughout the duration of the experiment as described in chapter 2.

5.4 Results

5.4.1 Exposure of callosal axons to donors of nitric oxide cause irreversible conduction block but no structural injury

To determine the dose of NO donor required to elicit conduction block, slices were exposed to a step-wise incremental dose of DETA NONOate in the order of 1 mM addition every 30 min. There was no change in axonal conduction following the addition of the first two aliquots in quick succession (up to 2mM). With the addition of another two aliquots there was a marked 20% loss in conduction with every dose. With the fifth dose (5mM), a rapid decline in signal strength was observed within 10 mins of drug application that lead to an irreversible block in conduction.

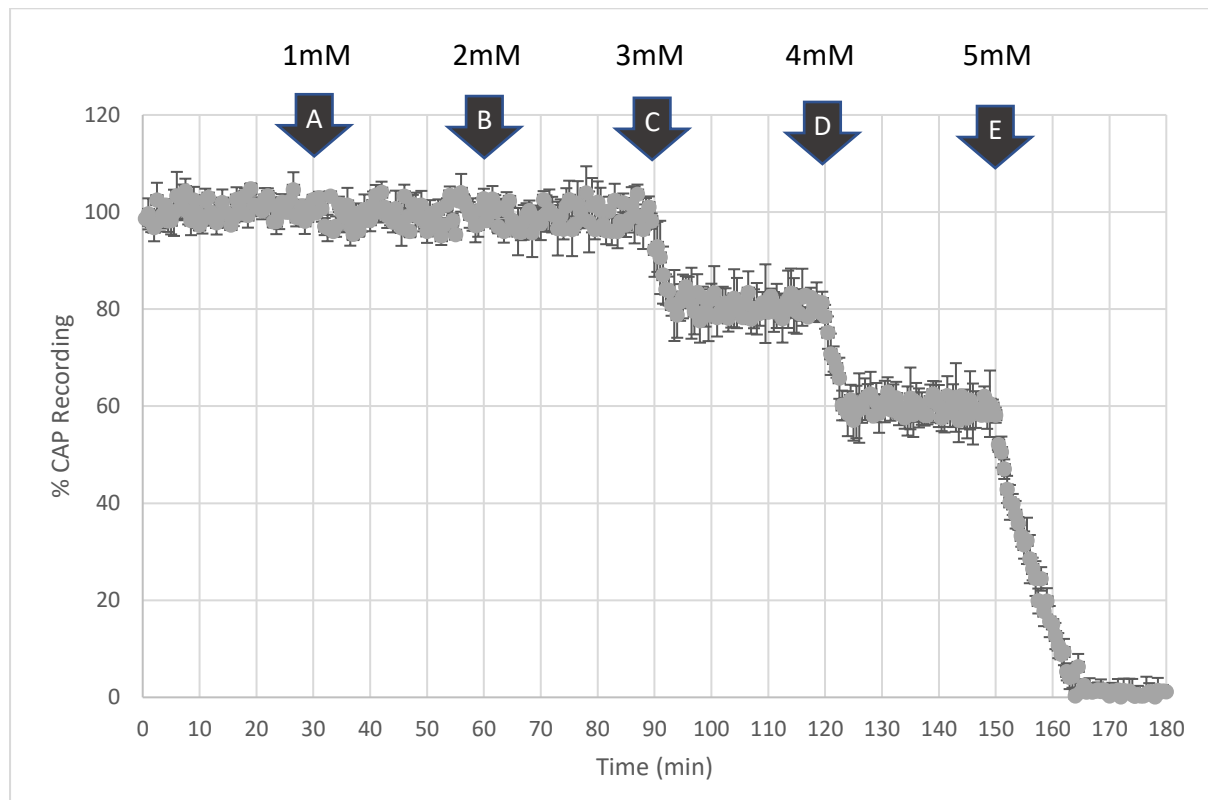


Figure 5.5. Dose-dependent conduction block with addition of DETA NONOate. There is no loss in the CAP after addition of the first two aliquots (2mM) of NO donor (A and B). There is a 20% reduction in CAP area after the third (C) and fourth dose equivalent to 4mM (D). There is a complete block in conduction block after addition of the fifth dose, that corresponds to 5mM (E) ($n=3$).

After 30 min, the drug was washed out, but there was no recovery of axonal conduction.

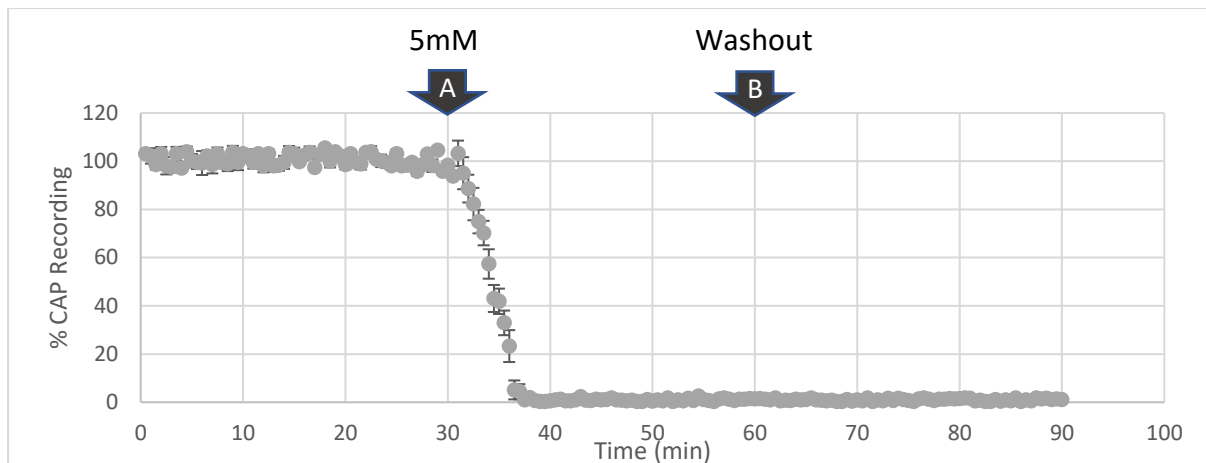


Figure 5.6. CAP recording following addition of DETA NONOate. There is a rapid loss in the CAP with 5 mM of NO donor (A), without any recovery during the washout period (B). ($n=3$)

During the combined live-imaging and electrophysiology experiments, we monitored the structural integrity of the YFP axons under two-photon microscopy for the duration that the slices were exposed to the donor. Despite the rapid and irreversible conduction block, we saw no signs of axonal injury during the 30 min exposure to the drug in all experiments conducted.

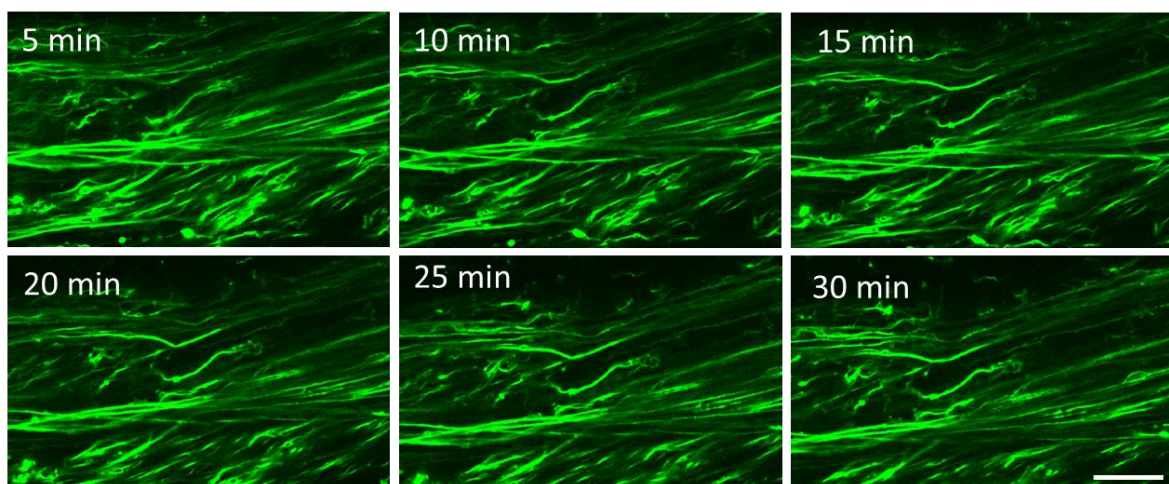


Figure 5.7. Live imaging of YFP axons following application of DETA NONOate. There is clear evidence of intact integrity of axons within the field of view when the slice was incubated in 5mM DETA NONOate for up to 30 mins. Images were taken every 5 min. Scale bar: 15 μ m

In separate experiments, we questioned the possibility as to whether NO might be the cause of injury, only to occur at a more delayed stage. For this reason, brain slices were exposed to 5 mM DETA NONOate for 2 and 3 hrs respectively in the glucose-containing aCSF. In both instances, we did not observe any form of injury. There was only some focal swelling in a few axons and no evidence of beading and fragmentation. There was no statistically significant difference in the axon scoring between controls and slices exposed to the NO donor.

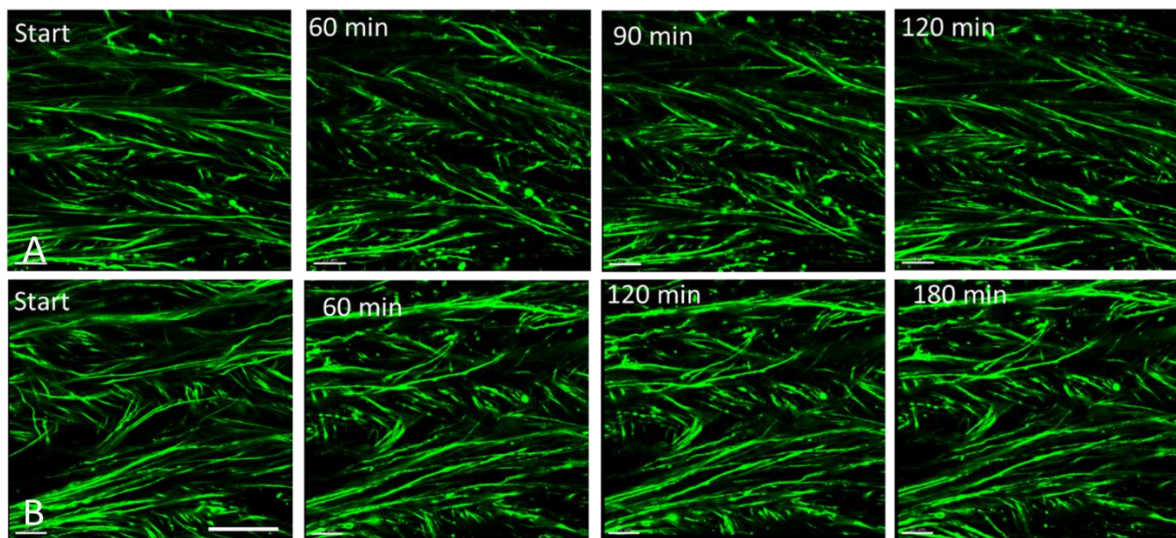


Figure 5.8. Sequential images of callosal slices during prolonged exposure to DETA NONOate. Minimal focal swelling in few of the axons throughout the 2-hour (A) and 3-hour (B) observation period, with drug exposure. Scale bar: 20 μ m.

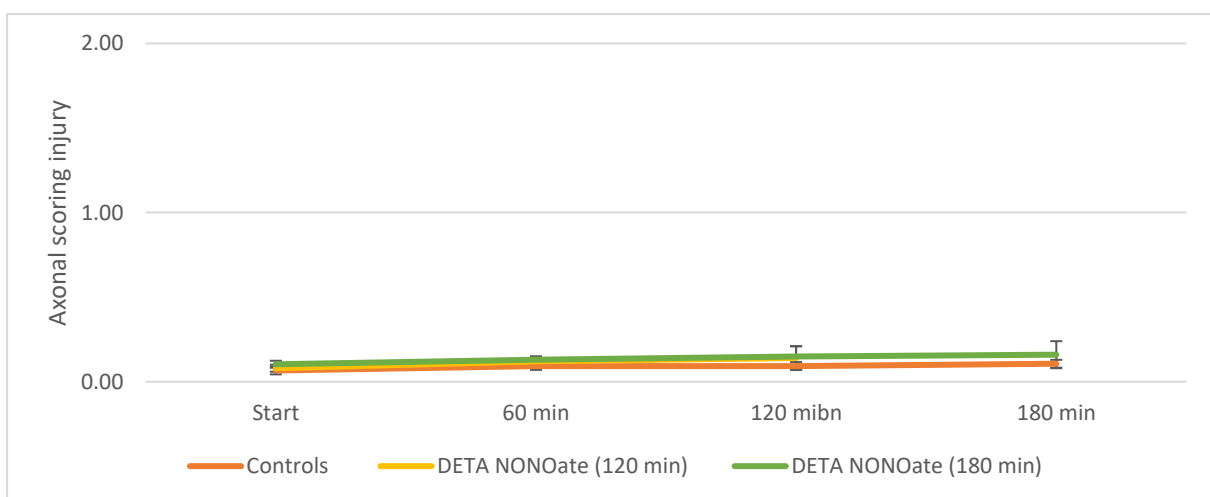


Figure 5.9. Axonal injury score in slices exposed to DETA NONOate for 2 and 3 hrs against control slices held in aCSF. There is an insignificant change in axonal injury score in slices exposed to the NO donor, and this was not statistically significant ($n=3$).

5.4.2 Nitric oxide is localised in glia, the axoplasm and myelin

Brain slices were loaded with either 10 μ M DAR-4M AM or 10 μ M DAF-FM DA for 60 min at 33 $^{\circ}$ C, followed by a 30 min washout during which the temperature was gently raised to 37 $^{\circ}$ C. From a stacked image taken at the surface, down to the typical limits of tissue-dye penetration, we estimated that the typical depth of dye loading of these dyes was in the order of around 40 - 60 μ m below the surface. In the white matter, the dye was clearly present in glial cells, the myelin sheath and the axoplasm of some axons.

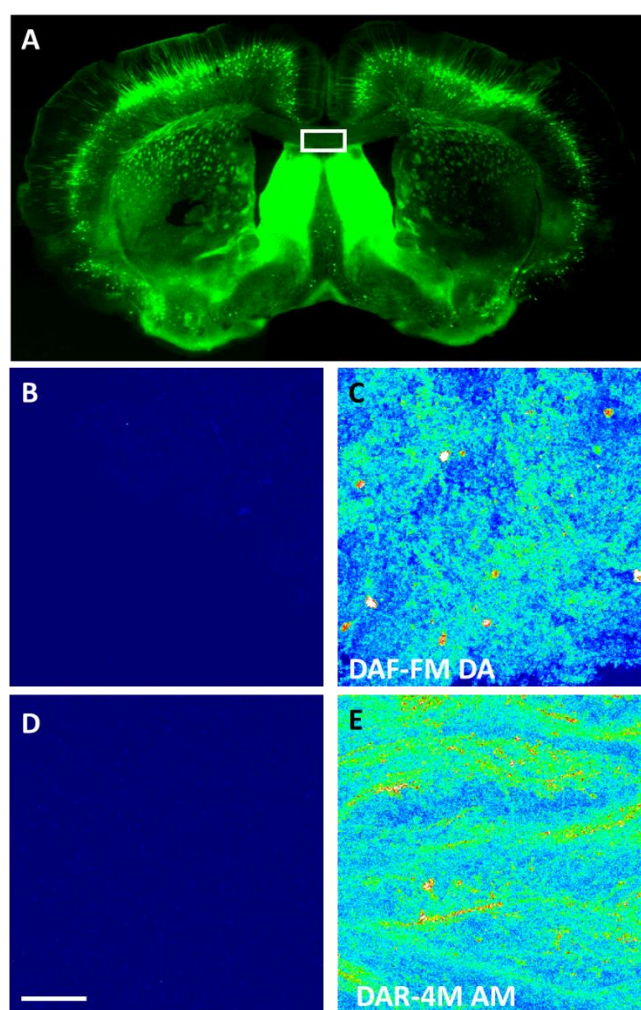


Figure 5.10. Brain slice from a CD-1 mouse loaded with 10 μ M DAF-FM DA or 10 μ M DAR-4M AM. [A] A low power image of a YFP coronal brain slice; white box is the imaging area within the corpus callosum, enlarged in B – E. CD-1 mouse corpus callosum before dye loading [B and D] and after loading with 10 μ M DAF-FM DA and [C] 10 μ M DAR-4M AM [E]. [B, C] Excitation: 765nm; Emission BP: 515nm – 560nm. [D, E] Excitation: 850nm; Emission BP: 565nm – 605nm. Scale bar: 30 μ m.

Slices from YFP mice were also loaded with 10 μ M DAR-4M AM and there was excellent separation from both channels. Of note was that for some reason, the DAR-4M AM had a very strong affinity to the myelin and glial staining was not recognisable as with the case of DAF-FM DA.

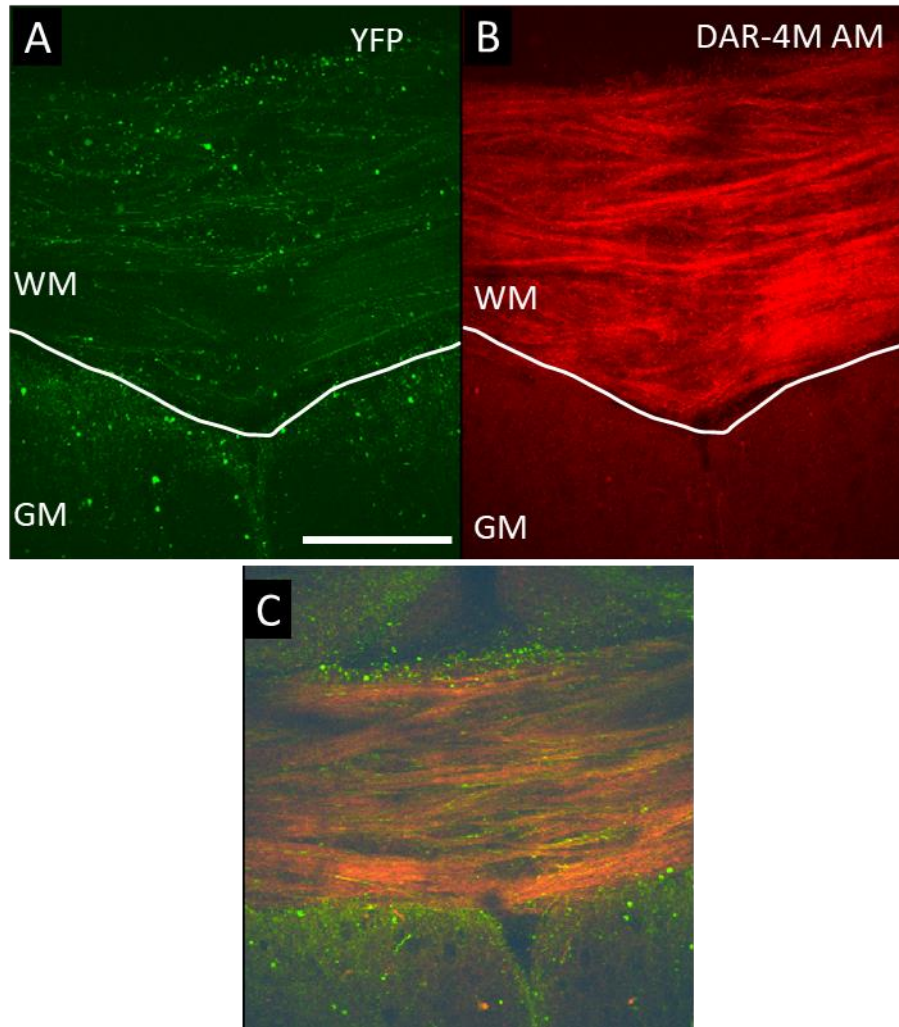


Figure 5.11. Low magnification view of callosal slice from a YFP mouse after incubation in 10 μ M DAR-4M AM. YFP slice loaded with 10 μ M DAR-4M AM and both channels were excited at 850 nm. The DAR-4M AM was preferentially present within the white matter, showing a strong affinity to the myelin [A] YFP emission BP: 515nm – 560nm [B] DAR-4M AM emission at BP: 565nm – 605nm. [C] Merged image of A and B. WM – white matter; GM – grey matter. Scale bar: 50 μ m.

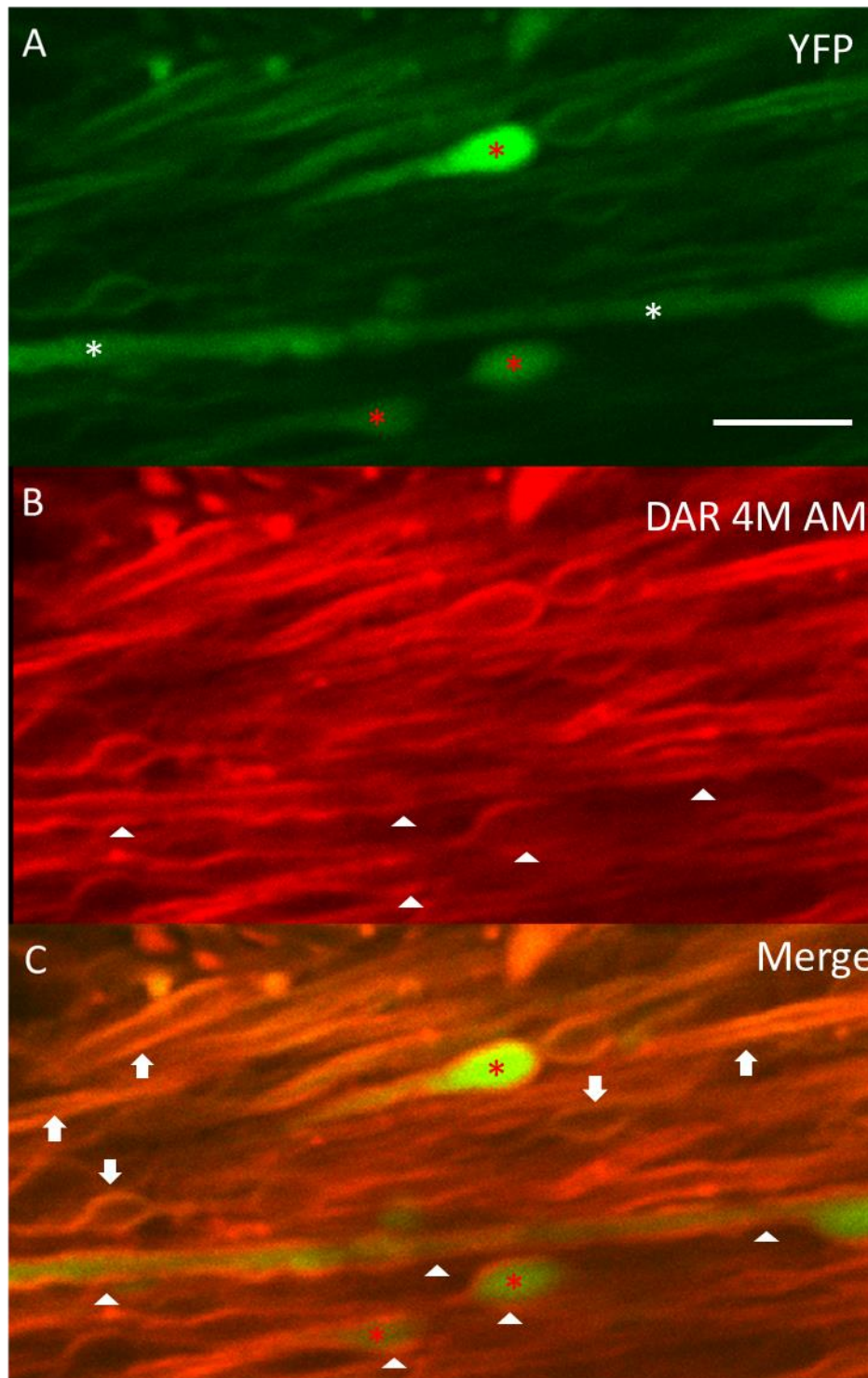


Figure 5.12. High magnification view of callosal slice from a YFP mouse after incubation in 10µM DAR-4M AM. YFP slice loaded with 10µM DAR-4M AM and excited at 850 nm. DAR-4M AM is seen localised in myelin surrounding linear axon profiles (white *) and beaded axonal spheres (red *) (arrowheads), and in myelin surrounding non-YFP expressing axons (arrows). [A] YFP emission BP: 515nm – 560nm; [B] DAR-4M AM emission BP: 565nm – 605nm. [C] merged images. Scale bar: 5 µm.

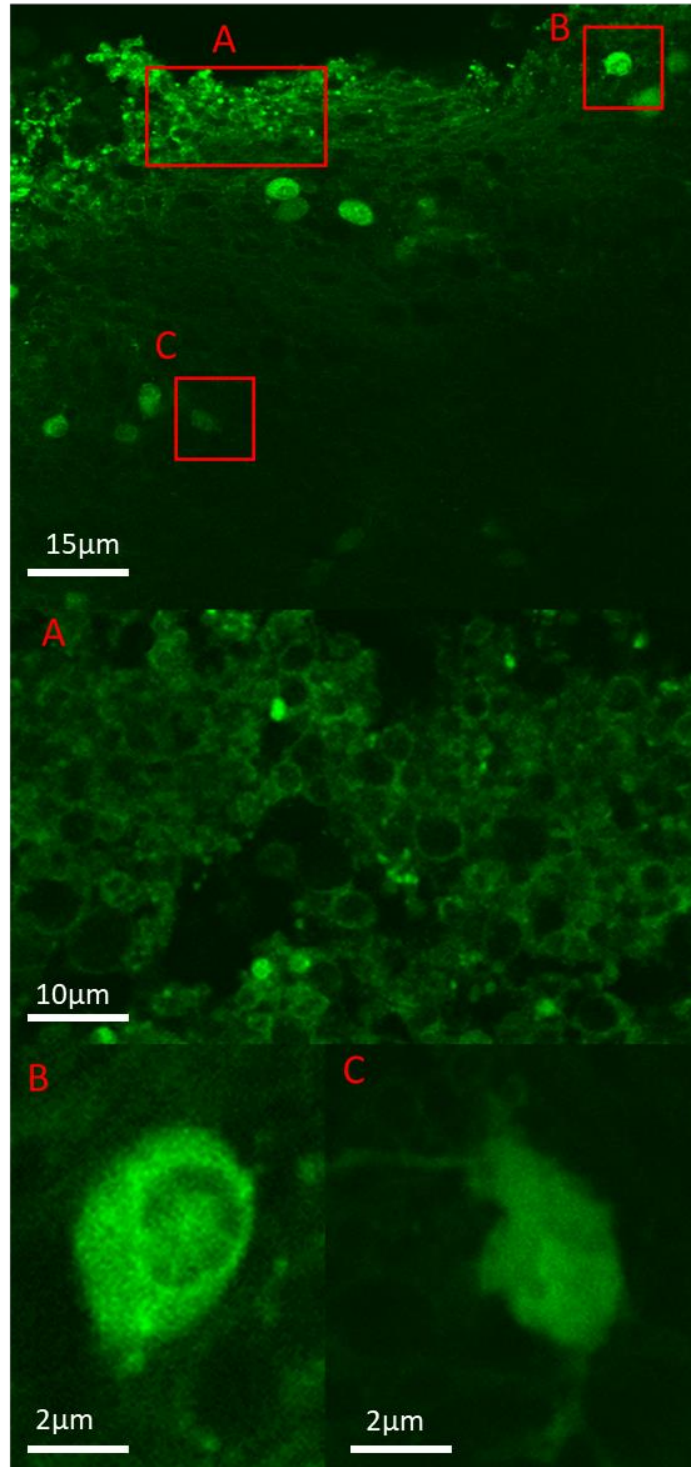


Figure 5.13. High magnification view of callosal slice from a CD-1 mouse after incubation in 10µM DAF-FM DA. *Above:* A low power view of the corpus callosum labelled with DAF-FM DA at the surface of the slice. *Below:* Higher magnification of the insets above. [A] DAF-FM concentrated in the myelin around severely beaded axons located at the surface of the slice. [B – C] The dye is strongly concentrated within the cytoplasm of what looks like an injured oligodendrocyte with a characteristic swollen nucleus and oval cytoplasm [B] Typical appearance of a fibrillary astrocyte [C]. Excitation: 765nm; Emission BP: 515nm–560nm.

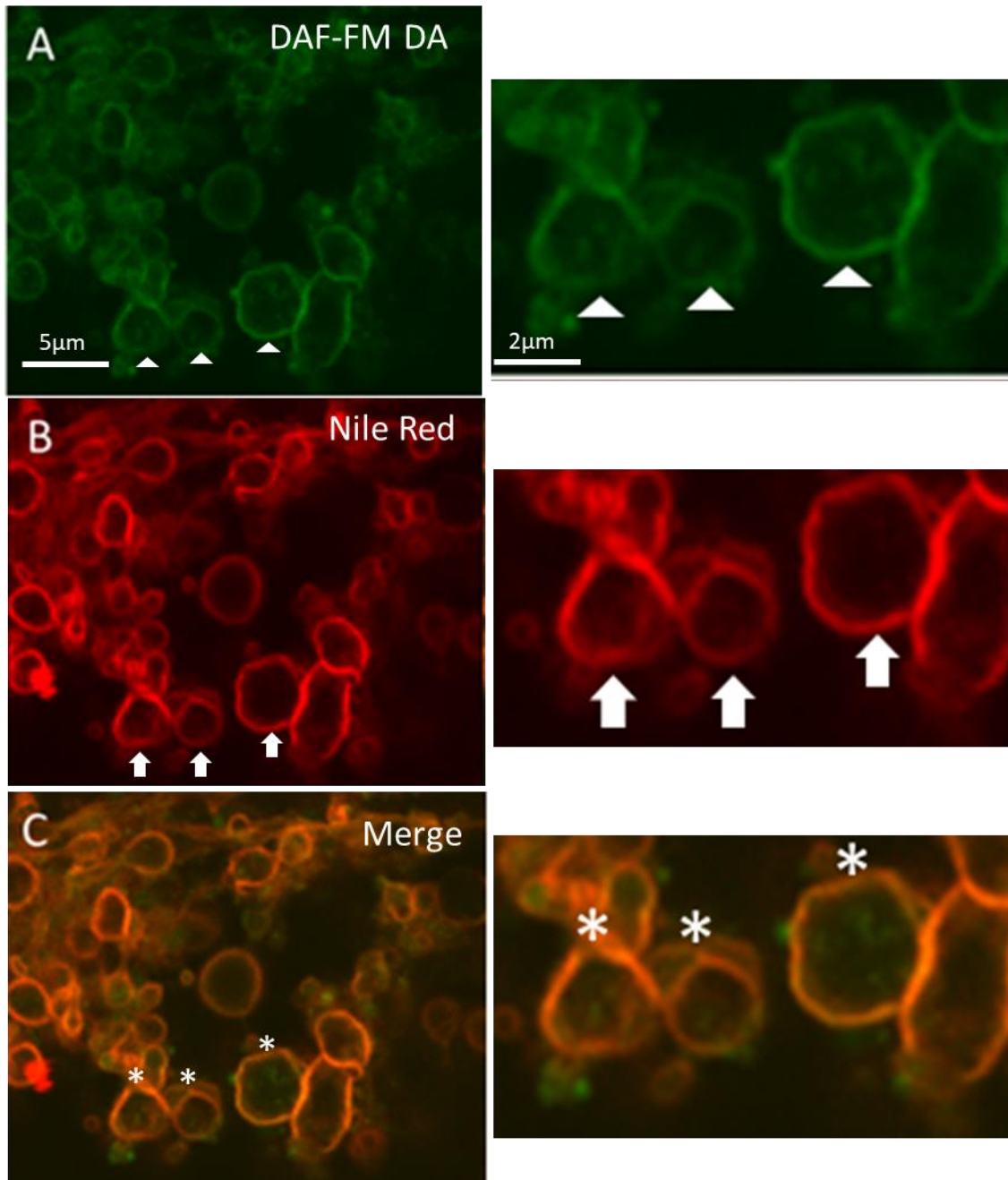


Figure 5.14 High magnification view of callosal slice from a CD-1 mouse after incubation in 10µM DAF-FM DA supplemented with 10 µM Nile Red. Both the DAF-FM DA (green) [A] and Nile Red (red)[B] stained the myelin around the beaded axons on the surface of the slice. [C] co-localisation of DAF-FM and Nile Red within myelin confirms that the DAF-FM-NO adduct is confined within the myelin (orange *). Since Nile red specifically binds to lipids, there is no red staining within the axoplasm in B (arrows). The green DAF-FM DA is present within the beaded axons in A (arrowheads), suggesting that NO is present to some extent in the axoplasm and enriched within the myelin. [A] Excitation: 765nm; Emission BP: 515nm – 560nm; [B] Excitation: 850nm; Emission BP: 565nm – 605nm. DAF – DAF-FM DA; NR – Nile Red

5.4.3 Increased levels of nitric oxide occur during the initial phase of glucose deprivation

Slices from CD-1 mice were loaded with either 10 μ M DAF-FM DA or 10 μ M DAR-4M AM and exposed to 2 hr of glucose-containing aCSF to monitor any changes in the level of signal intensity over time in control experiments. Stacked images were taken at the start of the experiment and sequentially at 10, 20, 30, 45, 75 and 105 min, that match with the chosen time-points in experiments concerning GD. We observed a gradual decline in the DAR-4M AM signal over time suggesting possible dye washout and/or photobleaching. There was no change in signal intensity in the DAF-FM DA loaded slices.

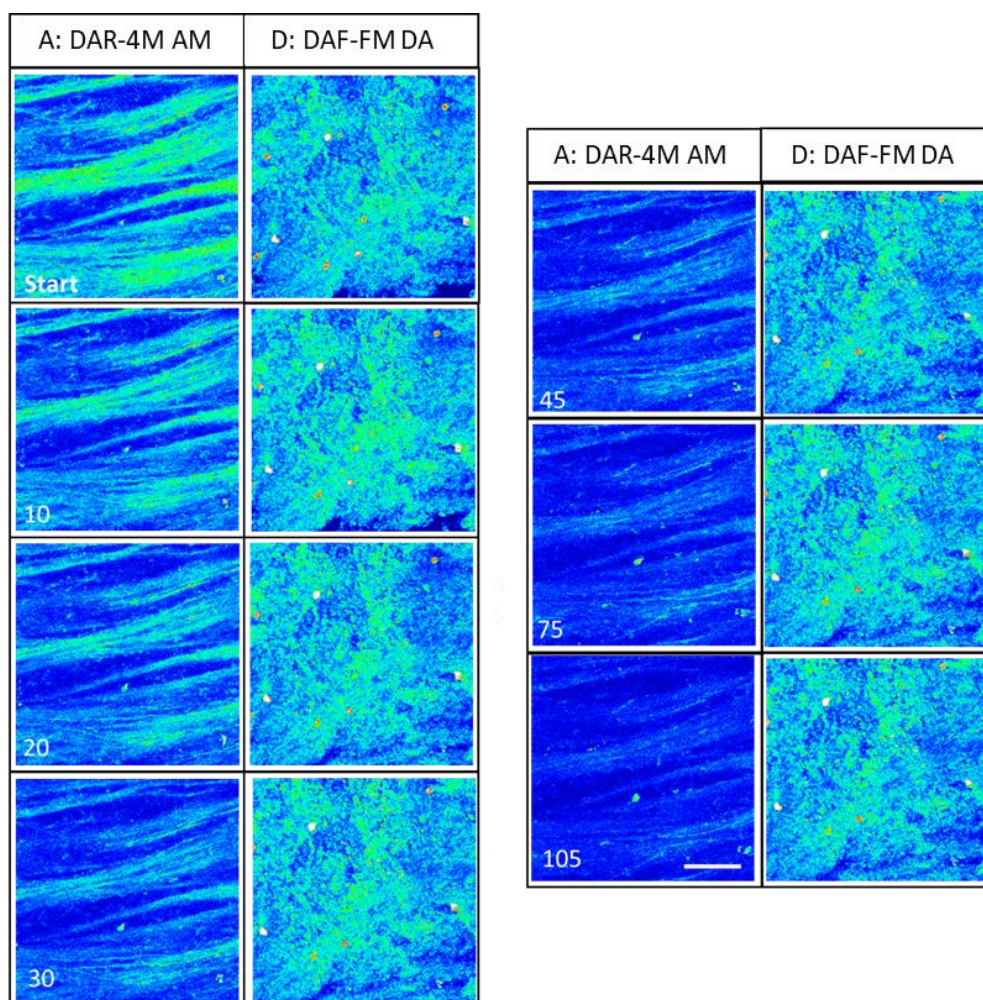


Figure 5.14. Sequential time frames show a side-by-side comparison of the change in signal intensity over time in DAR-4M AM and DAF-FM DA loaded slices that were perfused for 2 hr in glucose containing aCSF. Gradual decline in signal intensity over time in DAR-4M AM loaded slice (A) Stable dye signal intensity over time in the DAF-FM DA loaded slice (B). [A] Excitation: 850nm; Emission BP: 565nm–605nm; [B] Excitation: 765nm; Emission BP: 515nm–560nm. Scale bar: 30 μ m

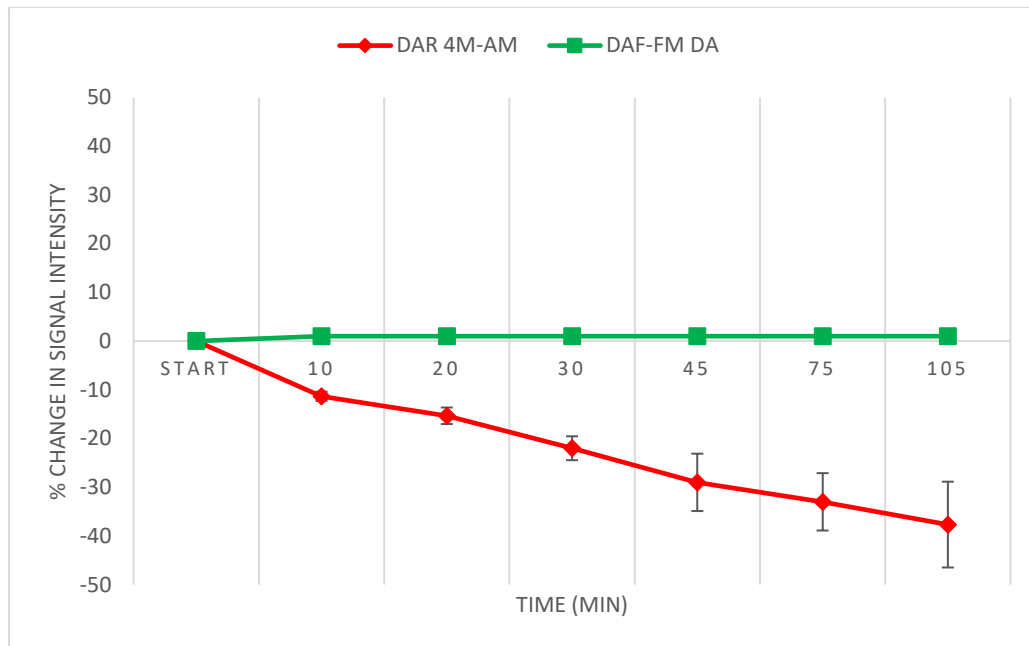


Figure 5.15. Side-by-side comparison of the percentage change in signal intensity from the start of the recording period in DAR-4M AM and DAF-FM DA pre-treated slices kept for 2 hr in glucose containing aCSF. Slices loaded with DAR 4M AM exhibited a gradual decline in signal intensity over the 2-hour of imaging, showing a 40% decrease in signal intensity from the start. There is no change in signal intensity in the DAF-FM DA loaded slice. ($n=3$)

In separate experiments, brain slices from CD-1 mice were incubated in 10 μ M DAR-4M AM and exposed to 45 min of GD, followed by 60 min of reperfusion. Stacked images were taken at the start of the experiment and sequentially at 10, 20, 30, and 45 min of GD and at 30 min and 60 min of reperfusion with glucose containing aCSF. A gradual increase in signal intensity was observed during the first 20 min of glucose deprivation and this was followed by a gradual decrease over the 25 mins that was required for completion of the GD. The decline in signal intensity persisted steadily throughout the 1hr of reperfusion (Fig 5.16). An unpaired student t-Test assuming equal variance was conducted to compare the signal intensity at each time-point between controls and those slices exposed to glucose deprivation. There was a statistically significant difference in signal intensity at each timepoint from 10 min onwards.

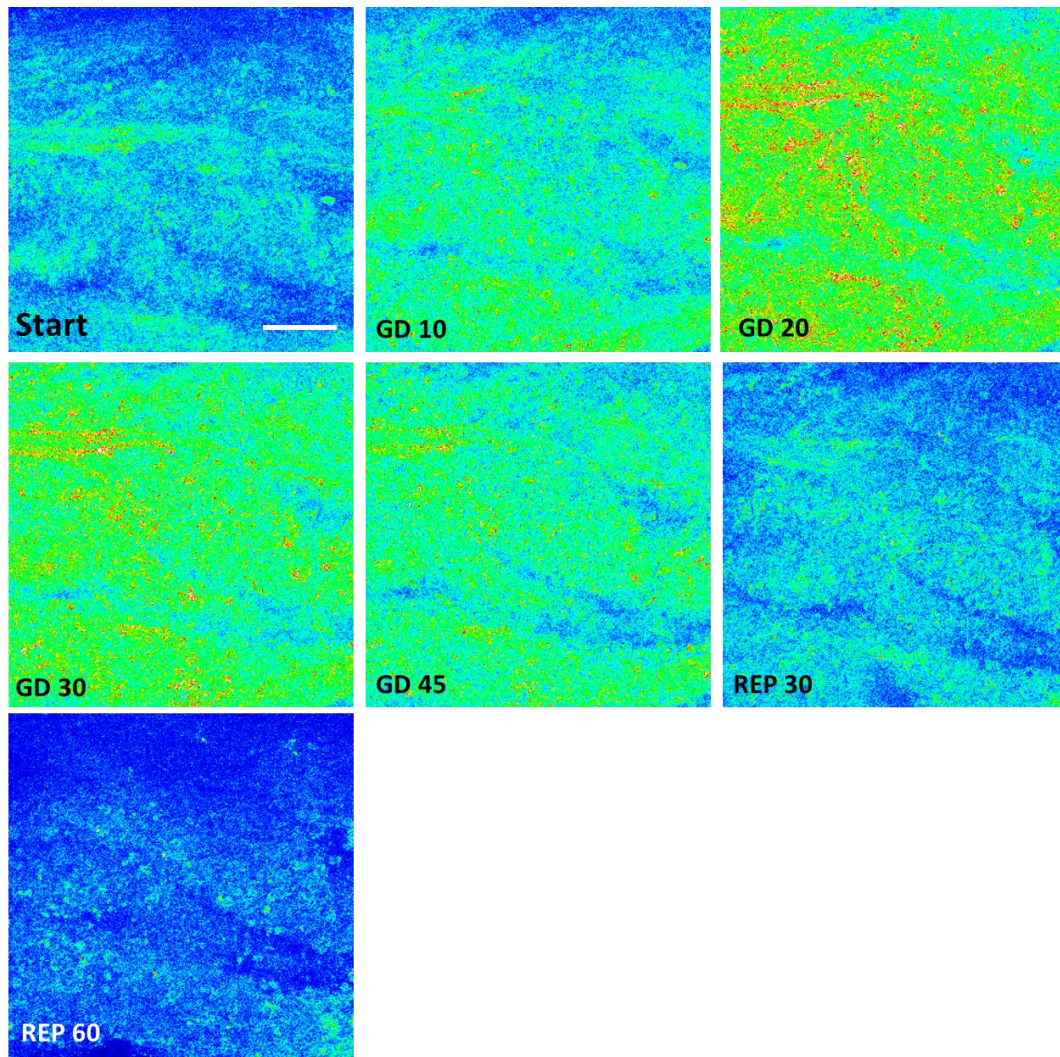


Figure 5.16. Signal intensity in slice loaded with DAR-4M AM and exposed to 45 min GD and 1 hr reperfusion. There is an increase in signal intensity of the DAR-4M AM during the first 20 min of GD, followed by a gradual steady decline that persisted into the phase of reperfusion. Excitation: 850nm; Emission BP: 565nm–605nm. Scale bar: 30 μ m

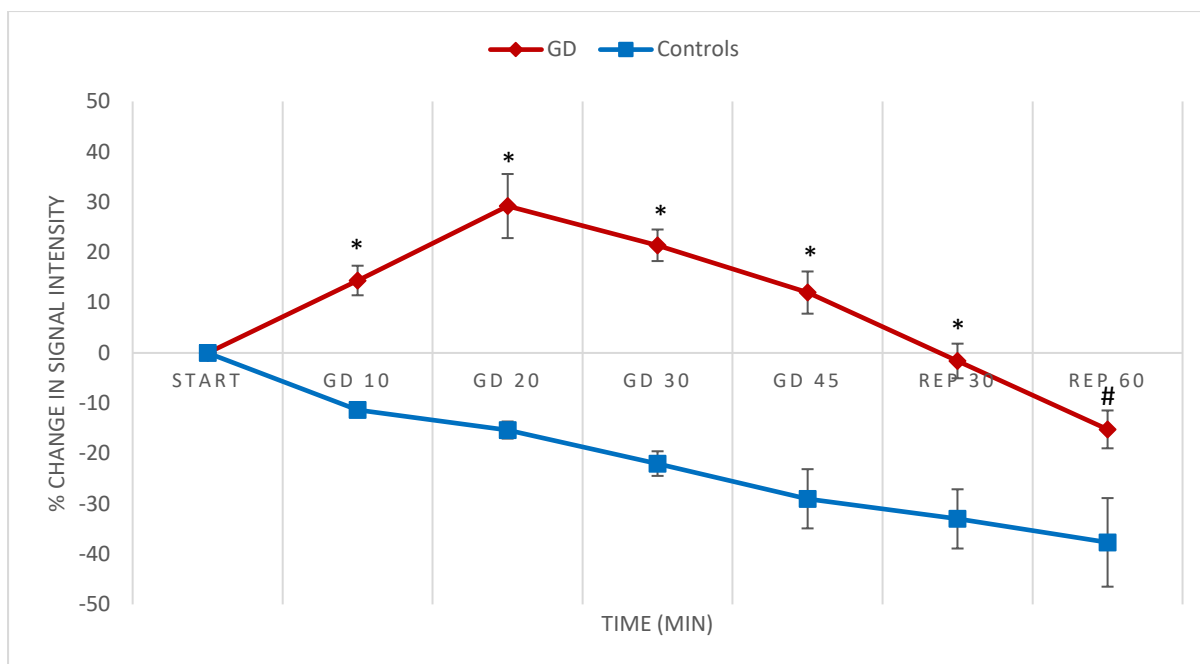


Figure 5.17. Side-by-side comparison of the change in signal intensity over time in DAR-4M AM control slices against those slices there were exposed to GD. There is a statistically significant difference in the signal intensity pattern starting immediately from the start to 20 mins of GD when compared to controls. (* $p < 0.001$; # $p < 0.05$). ($n=5$)

When these same experiments were repeated in slices incubated in DAF-FM DA, we observed inconsistent results. In some instances, we observed a similar increase in signal intensity at the onset of GD, that was followed by a steady and gradual decline. However, in the vast majority of these experiments, there was no discernible change in signal intensity of any significance. We could not figure out the reason behind this inconsistency, even though we made sure to maintain strict experimental procedures. Therefore, the observation that levels in NO increase at the initial phase of GD is based entirely from the former experiments obtained from the DAR-4M AM. The temporal profile in signal intensity for each experiment with these NO-sensing dyes has been included as supplementary material.

5.4.4 The block in nitric oxide attenuates the injury caused to axons following glucose deprivation

Slices pre-treated for 30 min with 100 μM of the non-specific NOS inhibitor L-NAME were exposed to 45 min of GD with the same inhibitor and this was followed by 2 hr of reperfusion with glucose containing aCSF without the drug. Focal swelling of select axons with some beading but with no transection or loss in confluence was evident by the end of the observation period (Fig 5.18). A statistically significant lower axonal injury score was seen in YFP slices treated with L-NAME when compared with slices exposed to glucose deprivation without the drug (Fig 5.19).

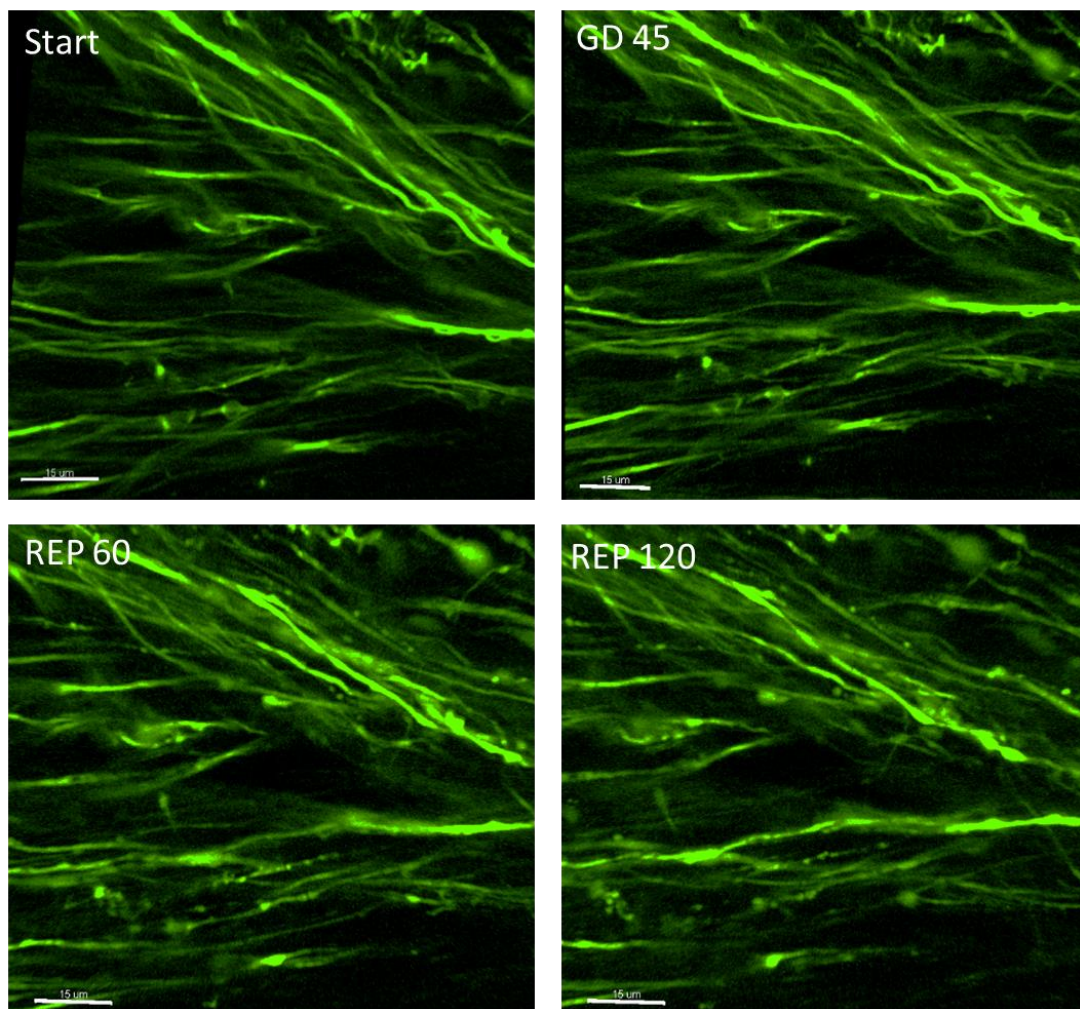


Figure 5.18. Sequential images of a YFP slice treated with L-NAME and exposed to 45 min of GD followed by 2 hr of reperfusion. L-NAME partially maintains axonal structural integrity during glucose deprivation. Focal swelling formed during the reperfusion phase progressed to some beading in axons. There was no axonal fragmentation or transection. Scale bar: 20 μm

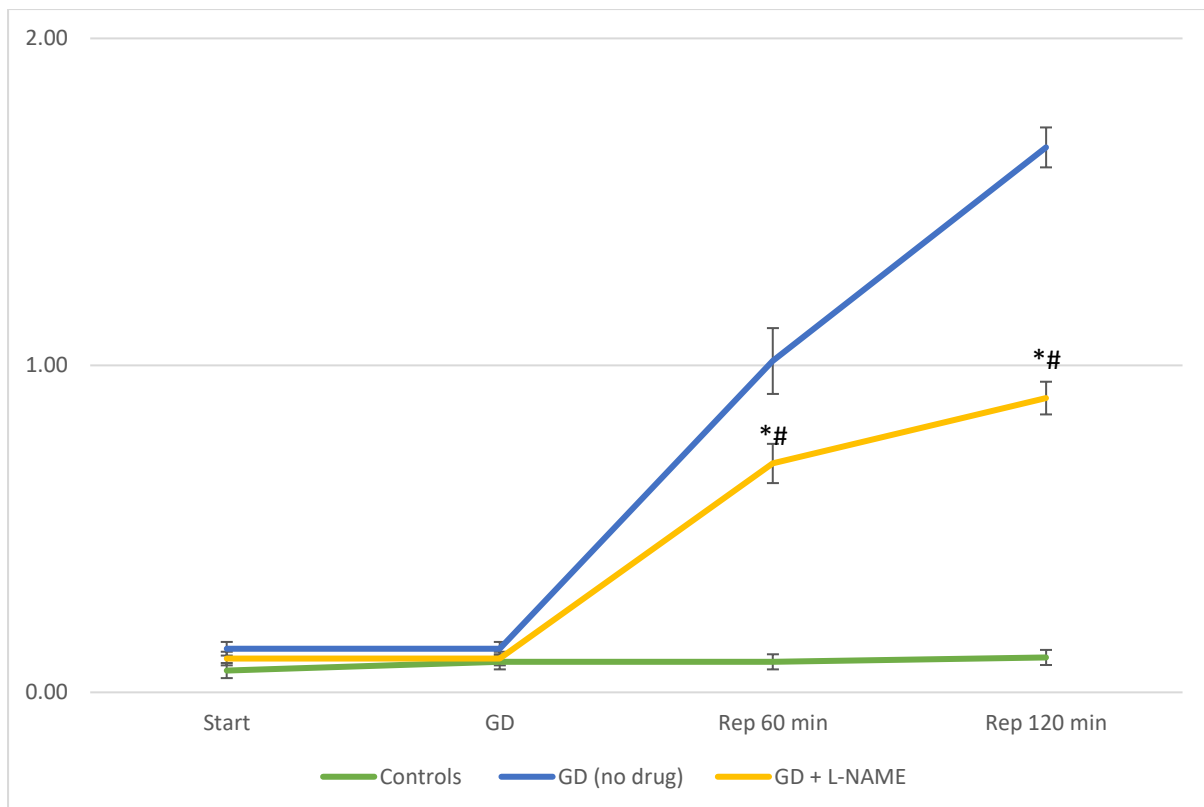


Figure 5.19. Axonal injury score in YFP slices exposed to GD (+/-) L-NAME and controls. L-NAME treated slices exposed to 45 min GD show a statistically significant (* $p < 0.001$) lower axonal injury score when compared with untreated slices. A statistically significant increase (# $p < 0.001$) in axonal injury score is seen between L-NAME treated slices and controls. ($n = 3$)

As to electrophysiological recordings performed during the course of imaging, we observed a slight delay in the loss of CAP during glucose deprivation in slices that were previously treated with L-100 μM NAME. The conduction recovered to about 40 % of baseline during reperfusion with glucose containing aCSF without the drug.

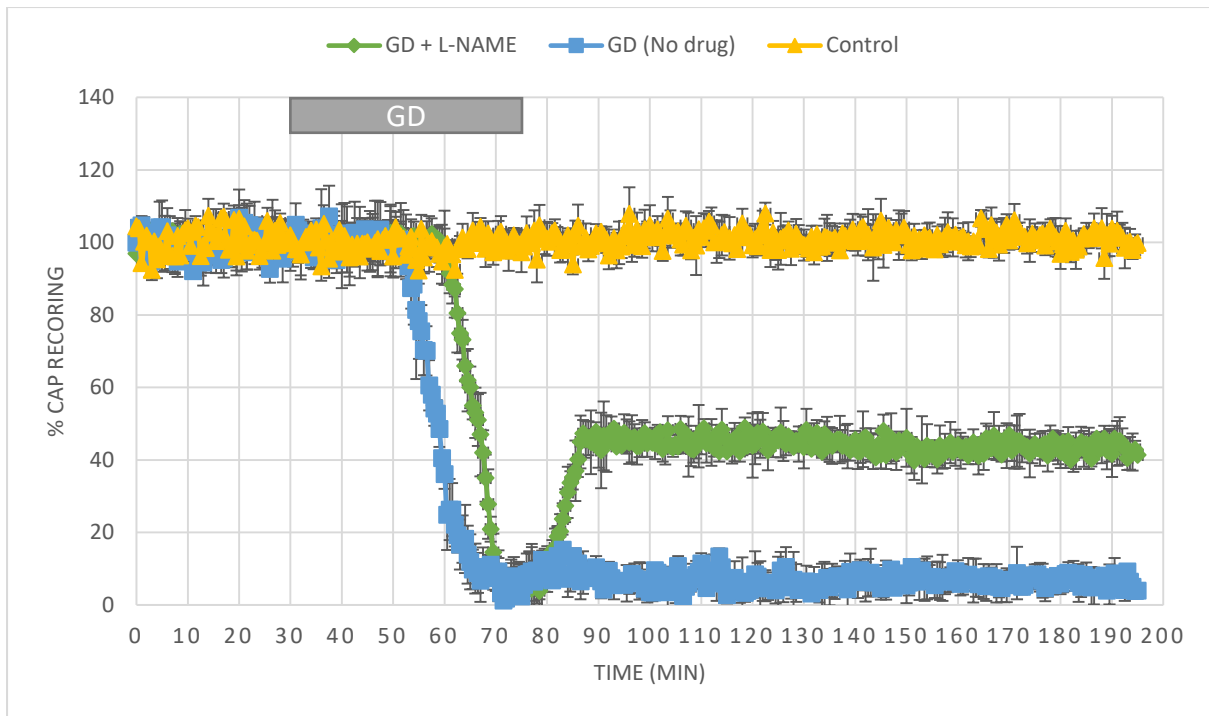


Figure 5.20. CAP recording from slices exposed to GD (+/-) L-NAME and controls. There is a delay in the loss of CAP during exposure to GD in L-NAME treated slices, that recovered to about 40 % in the reperfusion phase without the drug. ($n = 3$)

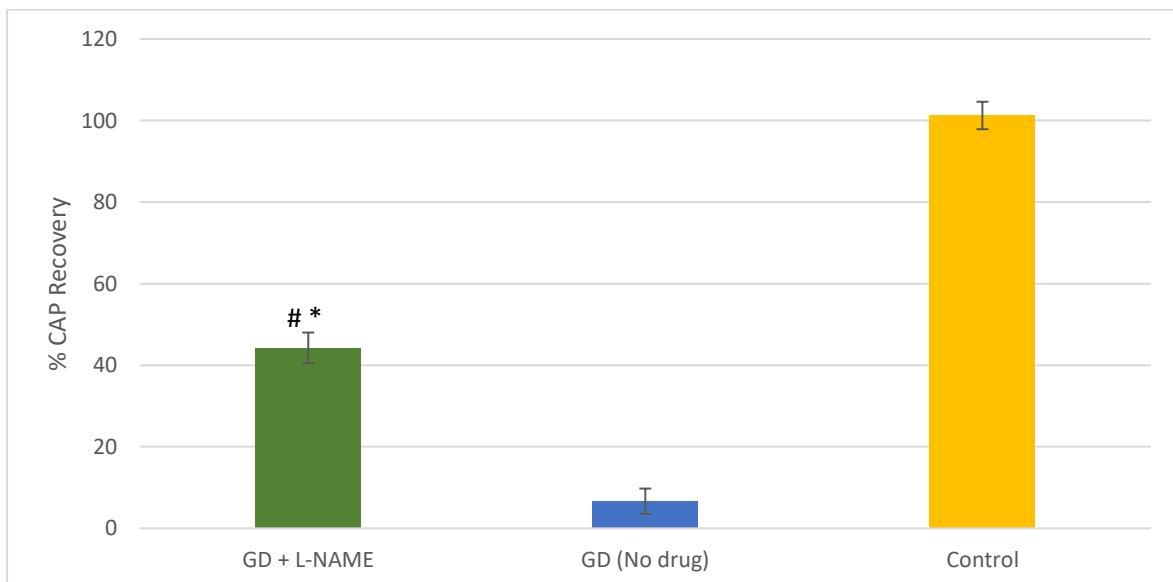


Figure 5.21. Percentage CAP recovery from slices exposed to GD (+/-) L-NAME and controls. There is a statistically significant difference in percentage CAP recovery in L-NAME treated slices when compared with untreated slices ($*p < 0.001$) and controls ($\# p < 0.001$) ($n = 3$).

5.5 Discussion

5.5.1 Incubation of callosal slices with the NO donor DETA NONOate, causes irreversible conduction block but no structural injury

There is substantial evidence in the literature that exposure of central (optic nerve) and peripheral (spinal nerve root) white matter to NO causes conduction block in these elements (Shrager *et al.*, 1998; Kapoor *et al.*, 2003; Ashki *et al.* 2006; Smith *et al.*, 2001; Shrager and Youngman, 2017). Our results confirm these previous findings and we reaffirm that this block is dose-dependent (Kapoor *et al.*, 2003; Ashki *et al.* 2006). There was no loss of CAP after administration of 2 mM of the NO donor, DETA NONOate. A partial block in conduction was observed at 4 mM, and this was irreversible with 5 mM of DETA NONOate. Alvarez *et al.*, (2008) report that the addition of 5mM DETA NONOate in aqueous media, yields a stable level of NO of around 5 μ M. This concentration is of the same order of NO that was found to occur in inflammatory lesions within the central nervous system (Brown *et al.*, 1995; Shibuki and Okada, 1991; Malinsky *et al.*, 1993; Hooper *et al.*, 1995). Our results therefore confirm that the working concentration of NO used in our experiments was of sufficient magnitude to cause axonal conduction block in pathological states.

In this study exposure to low micromolar levels of NO caused a very rapid and irreversible block in electrical conduction but no apparent signs of structural injury in callosal axons. Similarly, when slices were exposed to the same level of NO, there was still no injury to the axons over the course of 3 hrs. Results from experiments obtained from spinal nerve roots (Kapoor *et al.*, 2003) suggests that this conduction block is caused through the overload of Na^+ through voltage-gated Na^+ channels and that as a consequence causes reversal of $\text{Na}^+/\text{Ca}^{2+}$ exchanger with an overload in Ca^{2+} and membrane depolarisation. Since the conduction block the NO donor was irreversible despite the washout, other factors may also be involved. NO competes with O_2 to bind with cytochrome *c* oxidase (complex IV) thus inhibiting the respiratory chain to cause an increase in ROS that poisons the electron transport chain and produces peroxynitrite that disintegrates membranes (Brown, 1999; Heales *et al.*, 1999).

The absence of structural injury in our model, might be to some extent explained by the observations made by Garthwaite and colleagues (2002) wherein they reported that axonal structural injury is time-dependent and delayed. Incubation of the rodent optic nerve with 1mM S-Nitroso-N-acetylpenicillamine (SNAP) for 4 hr produced moderate axonal swelling, whereas a 6-h exposure produced major swelling. In addition, examining the optic nerve 2 hr after a 4-hr exposure to 1mM sodium nitroprusside (SNP) revealed unaffected axons, whereas examining it 19 hr after the insult resulted in maximal axonopathy (Garthwaite *et al.*, 2002).

5.5.2 Glucose deprivation increases nitric oxide production

We have experienced numerous challenges in trying to detect NO in live brain tissue. NO is a very volatile gas with an extremely short half-life that exists in extremely low concentrations in the brain and is rapidly scavenged to form nitrates and nitrites. A hypothetical ideal sensor should be highly specific to NO with a high spatial and temporal sensitivity to NO. Malinski and Taha (1992) were the first to determine directly the levels of NO occurring in single cells through a fabricated porphyrinic microsensor. A year later, the same group measured the amount of NO released in the rat brain after transient middle cerebral artery occlusion (Malinski *et al.*, 1993). Nowadays several microsensors are commercially available to detect numerous substances, including NO. Being the gold standard for the detection of NO, we had previously expended much of our energy to work with nafion-coated and NO sensitive electrodes from WPI, but with inconsistent and erratic results. As an alternative to our failed results with microsensors, we worked on protocols that utilise NO-sensitive dyes that detect and quantify low concentrations of NO. Our findings suggest that these dyes are very lipophilic, as they preferentially localise within the myelin sheaths, and this was especially for the DAR-4M AM. DAF-FM DA was also highly concentrated within the cell bodies of oligodendrocytes and what looked like an astrocyte in one case. Future work would require immunocytochemical analysis of the particular glial type that responded through an elevation in NO.

Induction of MCAO in rats resulted in elevated NO levels at around 15 min from the onset of ischaemia, followed by a gradual decline (Malinski *et al.*, 1993 Kader *et al.*, 1993) possibly due to depleted substrate availability (Malinski *et al.*, 1993). Although triggered by a different insult (GD) and occurring in a different brain region (white instead of grey matter), our results match perfectly these findings. To the best of our knowledge this is the first time increased NO levels have been documented during glucose deprivation in white matter. Furthermore, in our model, the peak in NO levels (20/25 min) just preceded the glucose deprivation induced CAP decline (25/30) we observed in our previous experiments. Any correlation between the two events is only hypothetical, since we have insufficient proof that they are directly related.

5.5.3 Nitric oxide contributes to axonal injury following glucose deprivation

We have established that injury following GD is calcium-dependent (section 4.4.2) and in part mediated via NMDA and AMPA receptors excitotoxicity (section 4.4.4). NMDA receptors are organised into multiprotein signalling complexes within the postsynaptic density (PSD), and a prominent organising protein is PSD-95 (McEwen *et al.*, 1999), which couples the NMDA receptor to intracellular proteins and signalling enzymes (Falkenstein *et al.*, 2000). Through a PDZ domain (PDZ2), PSD-95 binds the COOH-terminus to the NR2 subunit of the NMDA receptor as well as to nNOS (McEwen *et al.*, 1999; Falkenstein *et al.*, 2000, Aarts, 2002). This binding couples NMDA receptor activity to the production of NO that mediates NMDA receptor-dependent excitotoxicity (Kousteni *et al.*, 2001). Increased NO is believed to react with superoxide (O_2^-) to form peroxynitrite ($ONOO^-$), which is cytotoxic (Cui *et al.*, 2007).

In view of the fundamental link between excitatory neurotransmitters and NO, we hypothesised that the elevated level of NO we detected (section 5.4.3) might be involved in GD-induced axonal injury. L-NAME is a non-specific NOS inhibitor, which was found to decrease the levels of NO following both ischaemia (Margail *et al.*, 1997; Wei *et al.*, 1994) and glucose deprivation (Kojima *et al.*, 2001a). Addition of 100 μ M L-NAME during GD resulted in partial protection of callosal axons in terms of structure and function. This suggests that elevated levels of NO contribute to some extent to axonal injury during glucose deprivation. To the best of our knowledge this is the first time that NO has been implicated in the pathophysiology of axonal injury following GD.

Chapter 6

Conclusion

Failure of white matter energy metabolism plays a major role in several neurological disorders. Hypoglycaemia is the limiting factor in the glycaemic management of diabetes, and it has potentially devastating effects on the brain. Many patients suffering from diabetes average two episodes of acute hypoglycaemia per week, and 2% to 4% of diabetes-related deaths are attributed to hypoglycaemia. Once plasma glucose falls below 3 mmol/L, higher cortical function begins to deteriorate. In an acute setting, lowering levels of glucose result in impaired cognitive function, confusion, seizures, and coma. Chronic exposure of the brain to low levels of glucose results in neuronal necrosis, cerebral oedema, and a multitude of neurological deficits.

Historically, most of the neuroscience research focused on cerebral grey matter, as it was believed that injury to white matter is not as common. Long thought to be passive tissue, white matter affects learning and brain functions, modulating the distribution of action potentials, acting as a relay and coordinating communication between different brain regions. Through the improved resolution of powerful neuroimaging modalities, we now appreciate more than ever that the human brain consists of almost 50% of white matter, and that in most neurological disorders both white and grey matter regions are equally effected. Some of the most common disorders exclusively affect the white matter, so a better understanding of the underlying pathological mechanisms that occur in white matter is very much needed. In this study, we aimed to characterise the hallmarks of aglycaemic injury in the white matter and propose relevant pharmacological avenues for treatment to limit this unique and important form of injury.

The optic nerve and callosal brain slice are two frequently used models to study white matter. We chose the latter model because of its wider applicability for imaging under two-photon microscopy, as well as being more representative of central white matter since unlike the optic nerve, it is equally composed of myelinated and unmyelinated axons. To help us track the morphological changes in the axoplasm that occur in real-time, we used transgenic YFP-

expressing mice. YFP is a strong and specific vital marker for axons and localised in the neuronal cytoplasm. We found a good correlation between the pattern of axonal injury visible in YFP axons with other well-established methods to study axon structure. These include SMI-31 labelling of phosphorylated neurofilaments under fluorescence microscopy and the use of brightfield and EM techniques. Another aspect of this study involved monitoring axonal function over time (CAP conduction) in tandem with live imaging under two-photon microscopy. Near infra-red laser used in two-photon excitation suffers from significantly less absorption in biological specimens than UV or blue-green light, making the technique ideal to image thick and dense specimens such as the central white matter. The gradual loss in intensity of excitation light from scattering is also reduced, as scattering decreases with decreasing excitation frequency. By recording the evoked electrical impulses across the corpus callosum, we were able to assess in real time the health status and the level of function of the axons at all stages of the experiments conducted. To the best of our knowledge this is the first time that combined live imaging and electrophysiology of evoked potential (CAP) were performed simultaneously in brain slices to study white matter injury *in vivo*.

The electrophysiological experiments allowed the monitoring and assessment of the typical biphasic signal across the corpus callosum. These peaks represent two very distinct and diverse populations of axons. We observed that the faster, myelinated axons are more vulnerable to aglycaemic injury than those of a lesser extent, possibly due to their higher metabolic demand as a result of their higher degree of myelination and energy requirement. In our preparation, we were unable to detect the electrical signature arising from unmyelinated axons. To our knowledge, data from central white matter in the literature is solely based on the central role of myelinated axons. Here we report that axons with different degrees of myelination behave differently, so it is reasonable to assume that unmyelinated axons possess different vulnerabilities and might react differently when treated pharmacologically. Therefore, a study of the electrical properties of these diverse groups of axons is clearly warranted. A clearer understanding of their properties and characteristics would undoubtedly help increase our understanding of their diverse role in normal brain function and their impact in white matter disease.

In our combined imaging and electrophysiological study, axonal conduction was lost well before any recognisable signs in axonal injury. CAP recording started to decline after 30 min of GD, with the first signs of focal swelling commencing at 45 min of GD. The initial decline in ATP (Mergenthaler *et al.*, 2013, Bosche *et al.*, 2013 and Sunwoldt *et al.*, 2017.) results into failure of the Na⁺/K⁺ pump leading to membrane depolarisation and loss of action potential. The timely re-instatement of glucose, ahead of the toxic build-up of intracellular Ca²⁺, is crucial for the recovery of the membrane potential and re-establishment of electrical conduction. This same manoeuvre prevented the disruption of the cytoskeletal elements that is normally observed after prolonged GD.

From results that were published in Neuroscience (Laureys *et al.*, 2014), in collaboration with Prof Jacques De Keyser from Vrije Universiteit Brussels, we showed that central callosal axons continuously utilise lactate as their main energy substrate under normal physiological conditions. Mouse white matter axons import lactate through the MCT-2 (Tekkok *et al.*, 2005) to fuel their needs. Using *in vivo* microdialysis from mouse cerebellar white matter we demonstrate continuous axonal lactate uptake and glial–axonal metabolic coupling of glutamate/lactate exchange. The pharmacological administration of 4-CIN to block the uptake of lactate over the course of 30 min of GD that normally is of insufficient time to cause injury, resulted in irreversible axonal damage. These experiments suggest that the provision of lactate is required for the maintenance of central axons.

Hypoglycaemia activates Locus Coeruleus neurons (Morilak *et al.*, 1987) leading to increased noradrenaline release throughout the brain (Benzon *et al.*, 1991). Noradrenaline can enhance astrocytic glycogenolysis by β 2-adrenergic activation as previously described *in vitro* (Hertz *et al.*, 2010). Callosal slices are deprived of noradrenergic input from locus coeruleus projections necessitating pharmacological stimulation. β 2-adrenergic stimulation with clenbuterol indeed sustained axonal survival during GD in our imaging experiments. Moreover, this effect was found to be ineffective by the addition of 4-CIN, which blocks axonal lactate uptake. Since the protective effect of clenbuterol and the negative effect of 4-CIN might represent independent effects we investigated the role of β 2-adrenergic stimulation and inhibition from extracellular levels of glucose and lactate sampled *in vivo*. Neither stimulation nor inhibition led to significant changes in extracellular glucose or lactate

concentrations suggesting that alternative mechanisms may exist to convey β 2-adrenergic axonal protection during GD.

Aglycaemia mediates its damage to white matter by excitotoxicity and overloads cells with Ca^{2+} through receptor channels that permit Ca^{2+} entry. Yang *et al.*, (2014) report a massive increase in extracellular aspartate, which preferentially over-activates NMDA receptors located on oligodendrocytes in the mouse optic nerve following GD. These receptors were found to be concentrated in myelin and oligodendrocyte processes (Káradóttir *et al.*, 2005, Micu *et al.*, 2006) and overactivation of the GluN2C/D subunits were reported to mediate the bulk of pathological Ca^{2+} influx into the myelin sheath of adult optic axons following ischaemia (Micu *et al.*, 2006). This rise in Ca^{2+} activates calpain-1 and phospholipase C present in the myelin (Hinman *et al.*, 2004), promoting the degradation of key structural components. This suggests that these receptors may have an important role in diseases preferentially affecting myelin and thus offer an ideal therapeutic target against similar conditions.













Based on these findings we had previously reported (Doyle *et al.* 2018) that QNZ-46, a selective GluN2C/D NMDA subunit blocker protects axons and myelin following ischaemia. The main advantages of this use-dependent drug are that it crosses the blood brain barrier when administered systemically, is non-toxic and is intrinsically fluorescent. This makes it an ideal candidate for potential future therapeutic intervention in white matter disorders. In this study, mice treated with QNZ-46 exhibited relatively preserved axons and electrical conduction was maintained even after exposure to GD, confirming its protective role.

Yang *et al.*, 2014, argue that AMPA receptors on oligodendrocytes are not directly involved in aglycaemic injury in the mouse optic nerve. They show that aglycaemia causes an extracellular increase in aspartate and this neurotransmitter has no affinity to AMPA receptors. However, our data by far contradicts this hypothesis. We report that the addition of the AMPA/Kainate receptor antagonist, NBQX, protects both axons and oligodendrocytes when administered before or after GD. Live-imaging experiments showed preserved YFP axons in slices treated with NBQX throughout the course of GD and reperfusion. Ultrastructural data derived from EM, further corroborated this finding. We show normal appearing nuclei, mitochondria with intact cristae, and normal appearing endoplasmic reticulum and golgi in oligodendrocytes along with intact axons.

To further validate the results obtained with NBQX, we selected CP-465,022, a more selective and potent non-competitive AMPA-specific receptor antagonist. Similar to what we observed with QNZ-46, CP-465,022 partially protected axonal structure and electrical conduction during GD. In a study conducted by Sandberg and colleagues (1985), GD induced a massive efflux of aspartate into the extracellular space that was accompanied with a significant increase in extracellular glutamate (Sandberg *et al.*, 1986). Glutamate is sourced from the vesicular release from the axoplasm and augmented from the reversal of the Na⁺/glutamate exchanger from astrocytes. It is plausible that this effect may underlie the cause for the excitotoxicity that is responsible from excessive AMPA receptor excitation.

We show that the protection mediated by QNZ-46 and CP-465,022 when applied in single was further amplified when administered together. This is in support that aglycaemic injury is mediated by overactivation of NMDA receptors located on oligodendrocyte processes and within the axon myelin sheaths (Doyle *et al.* 2018, Micu *et al.*, 2006), and through AMPA receptors located on oligodendrocytes soma. To the best of our knowledge, this is the first study to show that a combined block of NMDA and AMPA receptors protects central axons during aglycaemia.

Several previous studies (Tekkök and Goldberg, 2001, Salter and Fern 2005, Káradóttir *et al.*, 2005, Micu *et al.*, 2006, Matute, 2007 and Yang *et al.*, 2014), explored the role played by the GluN2C/D subunits containing NMDA receptors and AMPA receptors during white matter injury in various preparations. Based on their studies and further supported by this work, we now propose a further mechanistic perspective of aglycaemic injury in white matter (Figure 6.1).

	GluN2C/D NMDA receptors		Na ⁺ /Glutamate transporter		GLT-1/GLAST		Glutamate		Ca ²⁺		QNZ-46
	AMPA receptors		Na ⁺ /K ⁺ Pump		VGCC		Aspartate		Na ⁺		CP-465,022

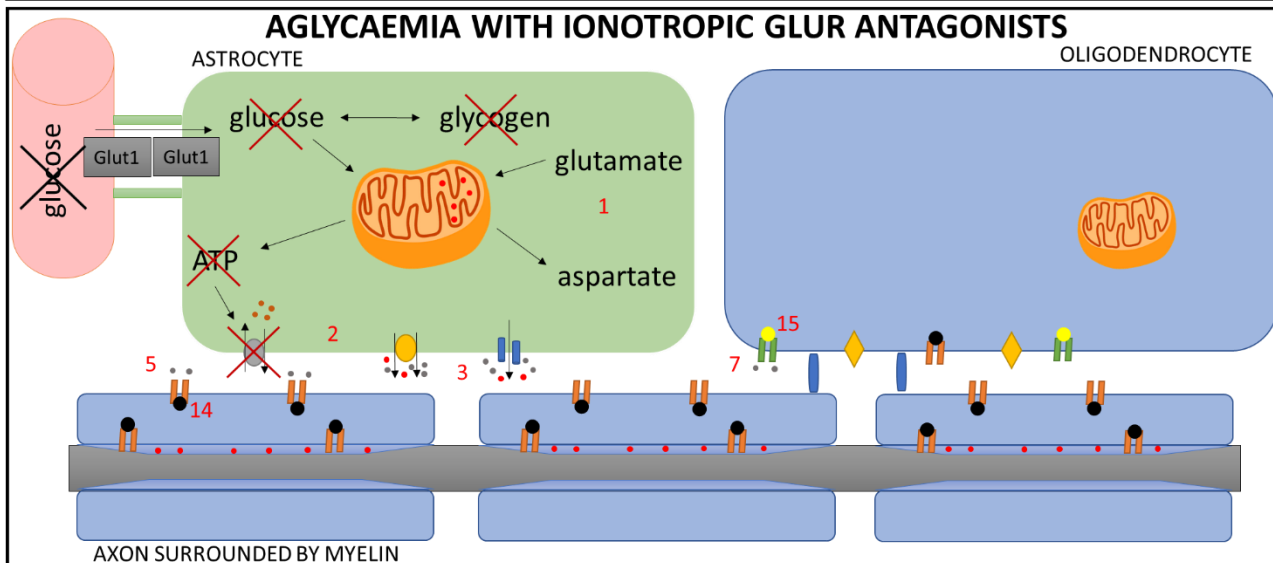
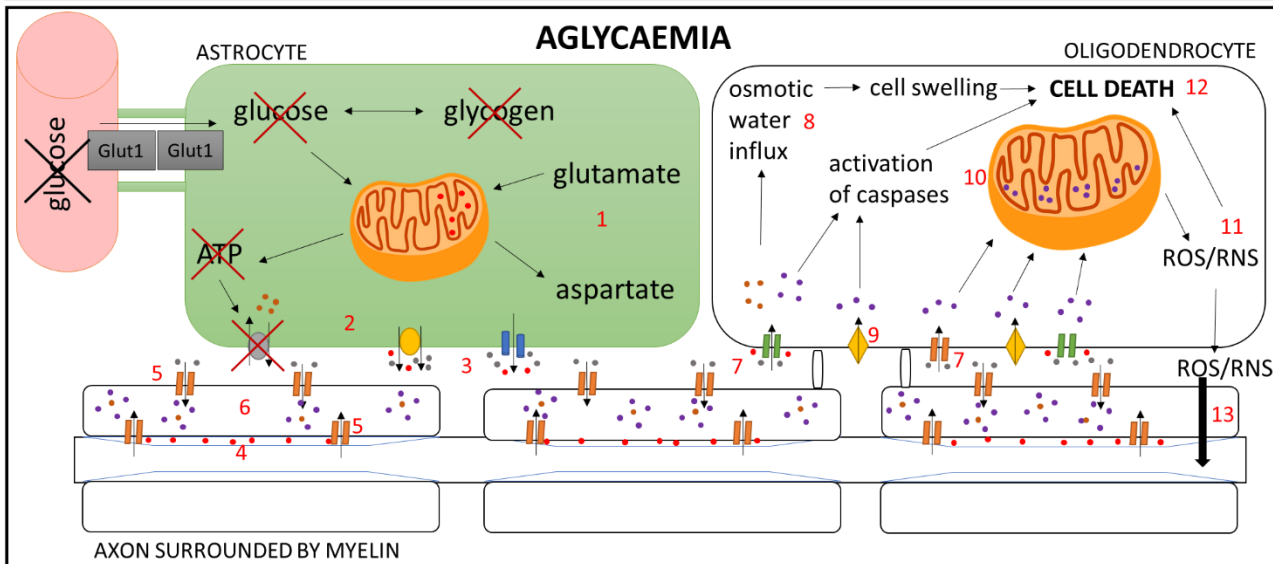
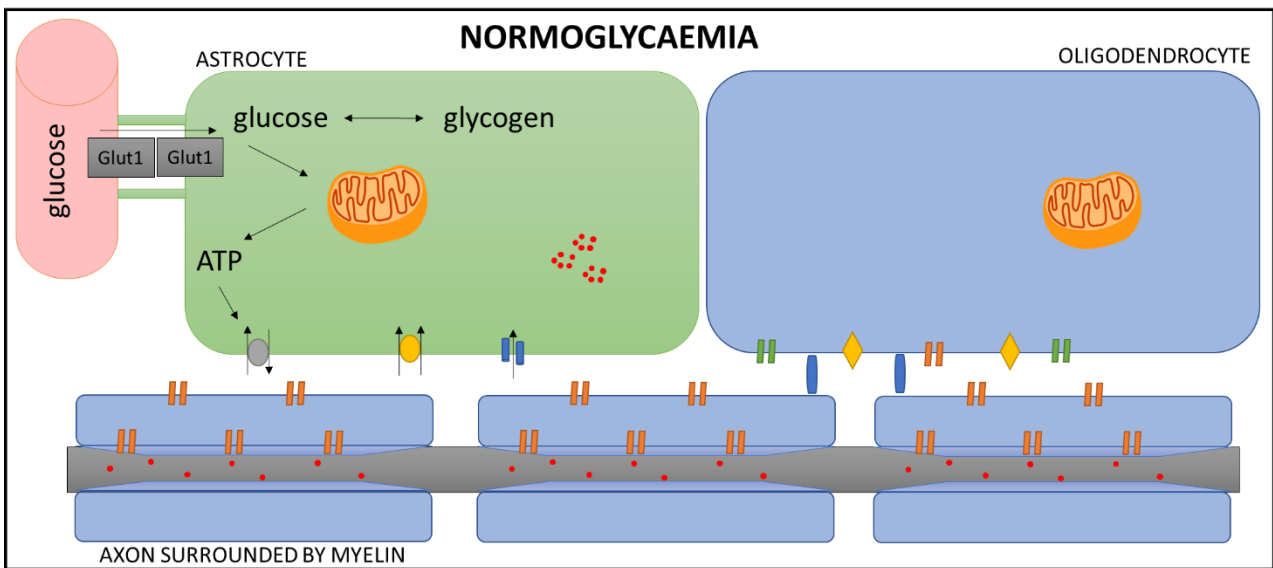


Figure 6.1. The proposed protective mechanisms mediated by QNZ-46 and CP-465,022 to counteract aglycaemic axonal injury. Adequate levels glucose enable enough ATP production to maintain the activity of the Na⁺/K⁺ pump. This confers a normally functioning Na⁺-glutamate transporter in astrocytes, thus limiting the build-up of extracellular concentration of glutamate. A decrease in the supply of glucose causes astrocytes to utilise glutamate to fuel the Krebs's cycle resulting in an increase of aspartate (1). The decline in ATP causes failure of the Na⁺/K⁺ pumps, reversing the Na⁺/glutamate transporter (2). The aspartate and to a lesser degree glutamate, are transported to the extracellular space via the reversed Na⁺/glutamate transporter and GLT1/GLAST (3). The rise in extracellular aspartate and glutamate, together with the glutamate that accumulates within the periaxonal space from depolarized axons (4) leads to overactivation of NMDA receptors present on the myelin and oligodendrocyte processes (5) culminating in a deleterious influx of Ca²⁺ and Na⁺ that damages myelin causing secondary axonal injury and loss of conduction (6). The elevated extracellular levels of aspartate/glutamate are responsible for the over-activation of AMPA and NMDA receptors present on oligodendrocyte soma (7). Na⁺ entry results in osmotic influx of water that accompanies cellular swelling (8). The resultant membrane depolarisation activates VGCC (9) and causes an increased Ca²⁺ flux through calcium permeable AMPA receptors (which lack GLuR2A subunit) that poisons mitochondria (10). This results in mitochondrial swelling and increased ROS/RNS production (11). Cellular swelling, ROS/RNS, and Ca²⁺ activated caspases cause oligodendrocyte death (12). ROS/RNS are released in the extracellular space, and further exacerbate the injury by damaging neighbouring glia and axons (13). QNZ-46 strongly attaches to the interaxonal myelinic GluN2C/D NMDA subunits, which it blocks, preventing the deleterious Ca²⁺ entry and preserves the integrity of myelin and axons (14). CP-465,022 binds to AMPA receptors present on the oligodendrocytes' soma, thus preventing secondary injury to propagate to neighbouring axons.

During normoglycaemia there is sufficient energy substrate present in the astrocyte to produce ATP and maintain the activity of the Na⁺/K⁺ pump. This confers a normally functioning Na⁺-glutamate transporter, thus limiting the extracellular build-up of glutamate. Once the glycogen stores are depleted glutamate is used instead of glucose to fuel the Krebs's cycle leading to an over-accumulation of aspartate. A further decline in ATP leads to failure of the Na⁺/K⁺ pump and the reversal of the Na⁺-glutamate transporter. This leads to a massive efflux of aspartate and to a lesser degree of glutamate into the extracellular space via the reversed Na⁺/glutamate transporter and through the Glutamate-Aspartate Transporter (GLAST).

In our recent work (Doyle *et al.*, 2018), we report that ischaemia in mice causes vesicular glutamate release from within the axoplasm that is partially trapped within the peri-axonal space. This source of glutamate is then free to over-activate NMDA receptors present within

the myelin sheaths, causing disintegration and conduction failure. Based on this fresh evidence, we hypothesise that the lack of energy that is crux to aglycaemia, can also contribute to the build-up of glutamate into the peri-axonal space and that is free to injure the myelin. In the process, both glutamate and aspartate activate the GluN2C/D subunits on NMDA receptors located on the oligodendrocyte processes (Salter and Fern, 2005; Micu *et al.*, 2006), mature myelin sheaths (Micu *et al.*, 2006) and inter-nodal axolemma (Ourdouz *et al.*, 2009) resulting in a toxic influx of Ca^{2+} , and to a lesser degree of Na^{+} . The Ca^{2+} overload leads to proteolytic digestion of the axon cylinder and Na^{+} influx eventually contributes to axon swelling, myelin detachment and myelin disintegration. In addition, the uncontrolled influx of Ca^{2+} through NMDA receptors activates nNOS that leads to the production of NO that eventually generates RNS.

The increase in extracellular aspartate and glutamate concentration also results in over-activation of the AMPA/KA (lacking the GluR2A) and NMDA receptors located on the oligodendrocytes soma causing cellular swelling through channels that are permeable to both Ca^{2+} and Na^{+} . Therefore, overactivation of AMPA and VGCC are responsible to the toxic build-up of Ca^{2+} into oligodendrocytes. This increase in Ca^{2+} is sequestered into the mitochondria, leading to the formation of the mitochondrial permeability transition pore, with extensive swelling and production of reactive oxygen and nitrogen species (ROS/RNS). Membrane disintegration from caspases and free radical production further contribute to oligodendrocyte death. Released free radicals can further exacerbate the injury as they diffuse in the extracellular space causing secondary injury to the lipid membranes and myelin of neighbouring glia and axons.

QNZ-46 readily permeates into the myelin since it is lipophilic and strongly attaches to the myelinic GluN2C/D NMDA subunits, which it blocks. This prevented the deleterious Ca^{2+} influx and preserved the integrity of the myelin and axons as seen through imaging and from CAP recording. CP-465,022, preserved the electrical activity to the same level and maintained a stable CAP profile throughout. Since CP-465,022 binds only to AMPA receptors, which are absent from axons but present on glia, then it is clear that the drug protected oligodendrocytes and this prevented secondary injury to propagate to neighbouring axons.

We have established that aglycaemic injury is calcium-dependent and in part mediated via NMDA and AMPA receptors excitotoxicity. Ca^{2+} activates nNOS, which is associated with the NMDA NR2 subunit through PSD-95. Thus, the high Ca^{2+} /calmodulin concentrations reached in close proximity to the NMDA receptor after channel opening can activate nNOS increasing NO production (Aarts, 2002). We therefore hypothesise that NO might be involved in the pathophysiology of aglycaemia. Through a series of electrophysiological experiments, we first determined that low micromolar levels of NO (typical to the levels present in inflammatory lesions in the brain), was sufficient to confer irreversible conduction block with no significant structural axonal injury. Evidence from the optic nerve (Garthwaite *et al.*, 2002) suggests, that prolonged exposure to NO is required to elicit a delayed form of structural injury to axons. In separate imaging experiments, we show that NO increases during aglycaemia and this occurs within the first 20 min of the insult, followed by a gradual decline. These live imaging experiments were very challenging and with some variable results, but the pattern clearly mimics the rise in NO as seen during ischaemia in the classical study conducted by Malinski using porphyrinic NO electrodes in the rat brain (Malinski *et al.*, 1993). To the best of our knowledge this is the first instance that levels of NO were detected or imaged during aglycaemia in white matter. The peak of the increase of NO preceded the decline in axonal conduction as recorded electrophysiologically. Although the temporal profile of the two events may be well correlated, there is insufficient proof to state that the loss in axon conduction is a result of the increased level of NO.

Inhibiting NOS catalytic activity decreases NMDA mediated excitotoxicity in grey matter during ischaemia (Choi, 1994; Dawson *et al.*, 1996). We have previously shown (Doyle *et al.*, 2018) and further strengthened through this work, that the selective excitotoxic block of the GluN2C/D on NMDA receptors is key to the preservation of axons and myelin during GD. This represents a key pathway that can be therapeutically exploited in excitotoxic disorders. NMDA receptor overactivation during ischaemia in grey matter has been shown to be linked to an increased activity of NO in rats (Aarts, 2002). Thus, we hypothesise that the protection afforded to white matter axons with QNZ-46 is in part due to the suppression in NO activity by the block in the Ca^{2+} -mediated NMDA receptor-dependent excitotoxicity (Fig. 6.2). In support of this theory, addition of a non-specific NOS inhibitor (L-NAME) to slices pre-treated with L-NAME showed partial preservation of axons after GD and a statistically significant low

axonal injury score. Similarly, an equally statistically significant higher percentage in recovery of the CAP was found in the treated slices against the controls.

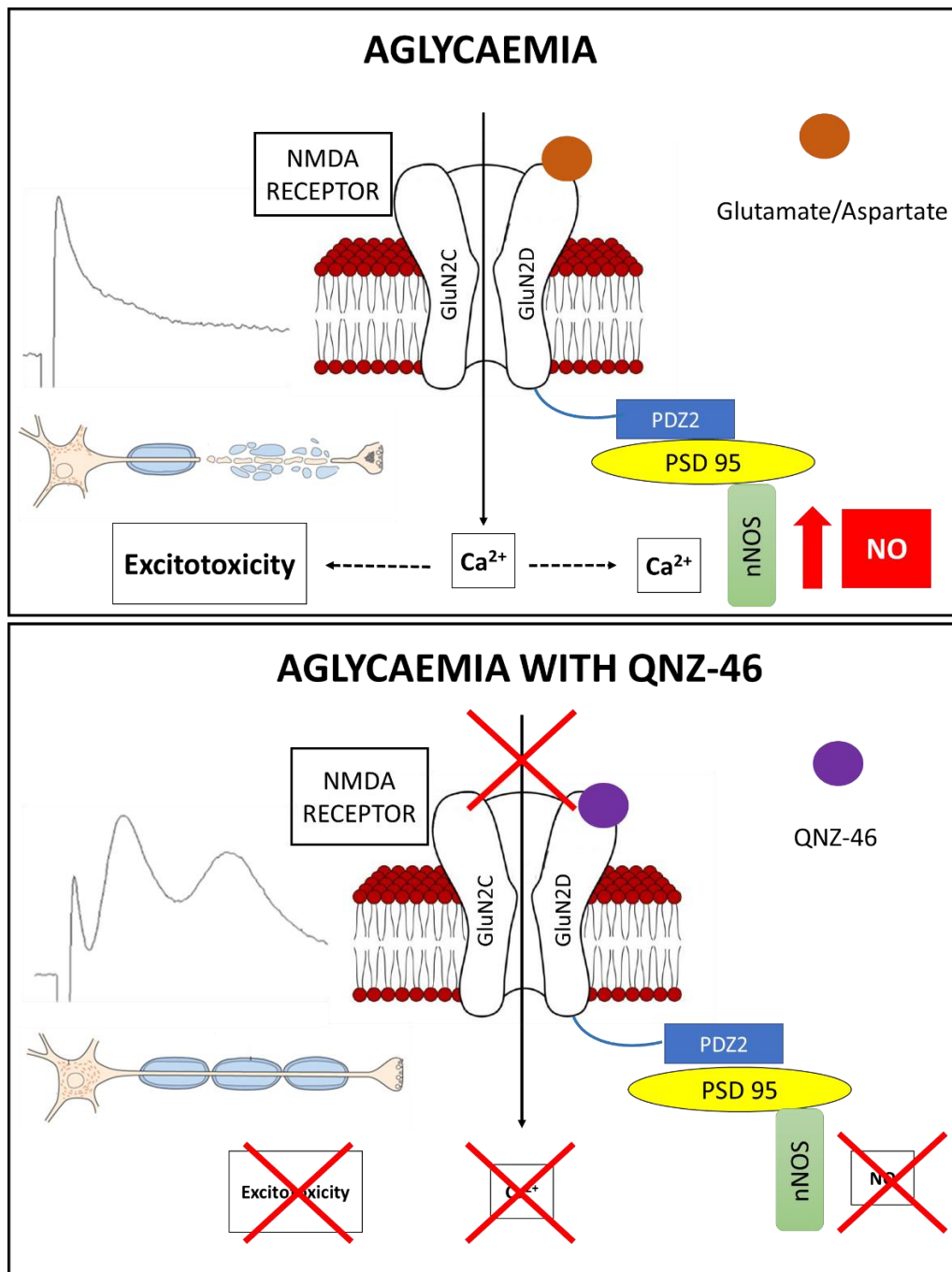


Figure 6.2. A hypothetical schematic showing how QNZ-46 suppresses NO formation following GD. GD causes the increased release of extracellular levels of aspartate/glutamate that over-activate NMDA receptors. This results in a toxic Ca^{2+} influx which readily promotes the Ca^{2+} -dependent NOS, leading to increased NO production, including $ONOO^-$. The subsequent loss in axonal conduction is followed by structural axonal injury. QNZ-46 inhibits the GluN2C/D subunits of the NMDA receptors, preventing the influx of Ca^{2+} , thus averting the deleterious cascade of events that follows.

The main limitation of the present study can be understood from both a clinical and experimental perspective. In these types of experiments, investigators can easily devise the exact experimental conditions to conduct aglycaemia. However, the level of hypoglycaemia in humans is variable and depends on age, sex, metabolic status, disease etc. Therefore, there are several confounding factors that are involved in order to produce experimental hypoglycaemia, and this can only be achieved arbitrarily. In humans, aglycaemia usually accompanies anoxia during severe episodes of brain ischaemia following occlusion of a major artery. Moreover, aglycaemia is a more severe form of insult than hypoglycaemia, and therefore the pathophysiology of aglycaemia can be safely translated to include instances of hypoglycaemic injury that normally occurs in humans.

In conclusion, this study provides an overview of the hallmarks of aglycaemic injury in white matter that was studied by a combination of techniques that included in main, electrophysiology, imaging and pharmacology. Establishing a reproducible model for combined imaging and electrophysiology is highly intricate and very challenging because the hardware is extremely complex, and the procedures employed are specialised and very delicate. However, we think that through this study we may have uncovered some important mechanisms of injury and tested several avenues of pharmacological significance. Administration of lactate during hypoglycaemia will undoubtedly provide a neurometabolic substrate that will extend the critical time-window to limit injury to the brains' white matter. The pharmacological properties of QNZ-46 makes it an exciting prime candidate for future therapeutic intervention against disorders that principally affect myelin. We also report for the first time that this drug treatment conferred robust protection to axon fibres during GD, and this finding is very promising for future studies. The systemic combined treatment *in vivo* in mice with CP-465,022 strengthened this neuroprotection as seen in the preserved axonal structural integrity and conduction following GD. Finally, lowering levels of NO using a specific NOS inhibitor proved to be protective against GD. Such a pharmacological strategy might extend the protection to other white matter diseases including neurometabolic disorders.

Future direction

We aim to further investigate the combined protective mechanism afforded by the systemic administration of QNZ-46 and CP-465,022 and provide further evidence of the role of NO following GD. Briefly the main next steps will involve:

- i. To determine whether the protective effect on axons during GD by QNZ-46, is directly exerted through maintenance of the myelin sheaths. This will be performed with the aid of a series of live-imaging experiments (which we have already commenced) using Nile Red (a fluorescent, lipophilic stain for myelin) together with assessment of ultrastructure using EM.
- ii. To conclude whether the protective effect of CP-465,022 to axons is mediated through oligodendrocyte viability. Live-imaging experiments using PLP-EGFP transgenic mice with bath application of propidium iodide (identifies damaged nuclei in cells) will be used. Antibodies for caspase-3,6,9, anti-AIF etc. can identify apoptotic cells from brain slices. This will be supplemented by ultrastructural analysis using EM.
- iii. To confirm the indirect presence of NO following GD. In a series of slice experiments, we would like to detect the immunocytochemical presence of the by-product of NO, nitrotyrosine. NO causes tyrosine nitration of structural proteins and this substrate can be therefore used as indirect evidence of the presence of NO. Moreover, NO can also bind to superoxide to produce the highly reactive peroxynitrite (ONOO^-). We intend to use edaravone as a free radical scavenger to ascertain that axonal conduction block is mediated by NO and not by peroxynitrite.
- iv. To perform a set of live imaging experiments with slices loaded with DAR-4M AM to determine whether the increase in NO as observed in our study can be directly blocked with QNZ-46 during GD.

References

1. Aarts M, Liu Y, Liu L, Besshoh S, Arundine M, Gurd JW, Wang YT, Salter MW, Tymianski M. Treatment of ischemic brain damage by perturbing NMDA receptor- PSD-95 protein interactions. *Science*. 2002 Oct 25;298(5594):846-50.
2. Abdel-Hamid KM, Tymianski M. Mechanisms and effects of intracellular calcium buffering on neuronal survival in organotypic hippocampal cultures exposed to anoxia/aglycemia or to excitotoxins. *J Neurosci*. 1997 May 15;17(10):3538-53.
3. ADVANCE Collaborative Group, Patel A, MacMahon S, Chalmers J, Neal B, Billot L, Woodward M, Marre M, Cooper M, Glasziou P, Grobbee D, Hamet P, Harrap S, Heller S, Liu L, Mancia G, Mogensen CE, Pan C, Intensive blood glucose control and vascular outcomes in patients with type 2 diabetes. *N Engl J Med*. 2008 Jun 12;358(24):2560-72
4. Agardh CD, Folbergrova J, and Siesjö BK. Cerebral metabolic changes in profound insulin-induced hypoglycemia, and in the recovery period following glucose administration. *J. Neurochem*. 1978; 31:1135–1142
5. Agardh CD, Rosen I. Neurophysiological recovery after hypoglycemic coma in the rat: correlation with cerebral metabolism. *J Cereb Blood Flow Metab* 1983;3:78–85.
6. Aghajanian GK, Rasmussen K. Intracellular studies in the facial nucleus illustrating a simple new method for obtaining viable motoneurons in adult rat brain slices. *Synapse*. 1989;3(4):331-8.
7. Agrawal SK, Fehlings MG. Role of NMDA and non-NMDA ionotropic glutamate receptors in traumatic spinal cord axonal injury. *Neurosci*. 1997 Feb 1;17(3):1055-63.
8. Akram K, Pedersen-Bjergaard U, Carstensen B, Borch-Johnsen K, Thorsteinnsson B. Frequency and risk factors of severe hypoglycaemia in insulin-treated Type 2 diabetes: a cross-sectional survey. *Diabet Med*. 2006 Jul;23(7):750-6.
9. Albayram S, Ozer H, Gokdemir S, Gulsen F, Kiziltan G, Kocer N, *et al.*, Reversible reduction of apparent diffusion coefficient values in bilateral internal capsules in transient hypoglycemia-induced hemiparesis. *AJNR Am J Neuroradiol* 2006;27(8):1760-2.
10. Alix JJ, Zammit C, Riddle A, Meshul CK, Back SA, Valentino M, Fern R. Central axons preparing to myelinate are highly sensitive to ischemic injury. *Ann Neurol*. 2012 Dec;72(6):936-51.

11. Allen L, Anderson S, Wender R, Meakin P, Ransom BR, Ray DE, Brown AM. Fructose supports energy metabolism of some, but not all, axons in adult mouse optic nerve. *J Neurophysiol*. 2006 Mar;95(3):1917-25.
12. Allicar MP, Megas F, Houzard S, Baroux A, Thai F, Augendre-Ferrante B. Frequency and costs of hospital stays for hypoglycemia in France in 1995 [In French] *Presse Med*. 2000;29:657–61.
13. Alvarez S, Moldovan M, Krarup C. Acute energy restriction triggers Wallerian degeneration in mouse. *Exp Neurol*. 2008 Jul;212(1):166-78.
14. Amaral AI, Meisingset TW, Kotter MR, Sonnewald U. Metabolic aspects of neuron-oligodendrocyte-astrocyte interactions. *Front Endocrinol (Lausanne)*. 2013; 4:54.
15. Ames A 3rd. CNS energy metabolism as related to function. *Brain Res Brain Res Rev*. 2000 Nov;34(1-2):42-68.
16. Anderson JM, Milner RD, Strich SJ. Effects of neonatal hypoglycemia on the nervous system: a pathological study. *J Neurol Neurosurg Psychiatry* 1967;95:295–310.
17. Andresen M, Gazmuri JT, Marín A, Regueira T, Rovegno M. Therapeutic hypothermia for acute brain injuries. *Scand J Trauma Resusc Emerg Med*. 2015 Jun 5;23:42.
18. Aoki T, Sato T, Hasegawa K, Ishizaki R, Saiki M. Reversible hyperintensity lesion on diffusion-weighted MRI in hypoglycemic coma. *Neurology*. 2004;63:392–393.
19. Arabi YM, Tamim HM, Rishu AH. Hypoglycemia with intensive insulin therapy in critically ill patients: predisposing factors and association with mortality. *Crit Care Med*. 2009;37:2536–2544.
20. Arias RL, Tasse JR, Bowlby MR. Neuroprotective interaction effects of NMDA and AMPA receptor antagonists in an in vitro model of cerebral ischemia. *Brain Res*. 1999 Jan 23;816(2):299-308.
21. Arky RA. Hypoglycemia associated with liver disease and ethanol. *Endocrinol Metab Clin North Am* 1989;18:75–90.
22. Arranz AM, Hussein A, Alix JJ, Pérez-Cerdá F, Allcock N, Matute C, Fern R. Functional glutamate transport in rodent optic nerve axons and glia. *Glia*. 2008 Sep;56(12):1353-67.
23. Arrázola MS, Inestrosa NC. Monitoring mitochondrial membranes permeability in live neurons and mitochondrial swelling through electron microscopy analysis. *Methods Mol Biol*. 2015;1254:87-97

24. ArunaDevi R1 Ramteke VD, Kumar S, Shukla MK, Jaganathan S, Kumar D, Sharma AK, Tandan SK. Neuroprotective effect of s-methylisothiourea in transient focal cerebral ischemia in rat. *Nitric Oxide*. 2010 Jan 1;22(1):1-10.
25. Ashki N, Hayes KC, Shi R. Nitric oxide reversibly impairs axonal conduction in Guinea pig spinal cord. *J Neurotrauma*. 2006 Dec;23(12):1779-93.
26. Astrup J, Sørensen PM, Sørensen HR. Oxygen and glucose consumption related to Na⁺-K⁺ transport in canine brain. *Stroke*. 1981 Nov-Dec;12(6):726-30.
27. Åsvold BO, Sand T, Hestad K, Bjørgaas MR. Cognitive function in type 1 diabetic adults with early exposure to severe hypoglycemia: a 16-year follow-up study. *Diabetes Care*. 2010 Sep;33(9):1945-7.
28. Attwell D, Laughlin SB. An energy budget for signaling in the grey matter of the brain. *J Cereb Blood Flow Metab*. 2001 Oct;21(10):1133-45.
29. Auer R, Kalimo H, Olsson Y, Wieloch T. The dentate gyrus in hypoglycemia: pathology implicating excitotoxin-mediated neuronal necrosis. *Acta Neuropathol*. 1985;67(3-4):279-88.
30. Auer RN, Hugh J, Cosgrove E, Curry B. Neuropathologic findings in three cases of profound hypoglycemia. *Clin Neuropathol*. 1989 Mar-Apr;8(2):63-8.
31. Auer RN, Siesjö BK. Hypoglycaemia: brain neurochemistry and neuropathology. *Baillieres Clin Endocrinol Metab* 1993;7(3):611-25.
32. Auer RN, Wieloch T, Olsson Y, Siesjö BK. The distribution of hypoglycemic brain damage. *Acta Neuropathol*. 1984;64(3):177-91.
33. Auer RN. Hypoglycemic brain damage. *Metab Brain Dis* 2004;19: 169–175
34. Auer RN. Progress review: hypoglycemic brain damage. *Stroke*. 1986 Jul-Aug;17(4):699-708.
35. Back SA, Craig A, Kayton RJ, Luo NL, Meshul CK, Allcock N, Fern R. Hypoxia-ischemia preferentially triggers glutamate depletion from oligodendroglia and axons in perinatal cerebral white matter. *J Cereb Blood Flow Metab*. 2007 Feb;27(2):334-47.
36. Baena RC, Busto R, Dietrich WD, Globus MY, Ginsberg MD. Hyperthermia delayed by 24 hours aggravates neuronal damage in rat hippocampus following global ischemia. *Neurology*. 1997 Mar;48(3):768-73.

37. Baker AJ, Phan N, Moulton RJ, Fehlings MG, Yucel Y, Zhao M, Liu E, Tian GF. Attenuation of the electrophysiological function of the corpus callosum after fluid percussion injury in the rat. *J Neurotrauma*. 2002 May;19(5):587-99.
38. Baker M, Bostock H, Grafe P, Martius P. Function and distribution of three types of rectifying channel in rat spinal root myelinated axons. *J Physiol*. 1987 Feb;383:45-67.
39. Bakiri Y, Burzomato V, Frugier G, Hamilton NB, Káradóttir R, Attwell D. Glutamatergic signaling in the brain's white matter. *Neuroscience*. 2009 Jan 12;158(1):266-74.
40. Baltan S, Besancon EF, Mbow B, Ye Z, Hamner MA, Ransom BR. White matter vulnerability to ischemic injury increases with age because of enhanced excitotoxicity. *J Neurosci*. 2008 Feb 6;28(6):1479-89.
41. Baltan S. Can lactate serve as an energy substrate for axons in good times and in bad, in sickness and in health? *Metab Brain Dis*. 2015 Feb;30(1):25-30.
42. Banker BQ. The neuropathological effects of anoxia and hypoglycemia in the newborn. *Dev Med Child Neurol* 1967;9:544–50.
43. Bareyre FM, Kerschensteiner M, Misgeld T, Sanes JR. Transgenic labeling of the corticospinal tract for monitoring axonal responses to spinal cord injury. *Nat Med*. 2005 Dec;11(12):1355-60.
44. Barkovich AJ, Ali FA, Rowley HA, Bass N. Imaging patterns of neonatal hypoglycemia. *AJNR Am J Neuroradiol*. 1998 Mar;19(3):523-8.
45. Beirowski B, Berek L, Adalbert R, Wagner D, Grumme DS, Addicks K, Ribchester RR, Coleman MP. Quantitative and qualitative analysis of Wallerian degeneration using restricted axonal labelling in YFP-H mice. *J Neurosci Methods*. 2004 Mar 15;134(1):23-35.
46. Bengzon J, Brundin P, Kalén P, Kokaia M, Lindvall O. Host regulation of noradrenaline release from grafts of seizure-suppressant locus coeruleus neurons. *Exp Neurol*. 1991 Jan;111(1):49-54.
47. Berger T, Walz W, Schnitzer J, Kettenmann H. GABA- and glutamate-activated currents in glial cells of the mouse corpus callosum slice. *J Neurosci Res*. 1992 Jan;31(1):21-7.
48. Bergner DW, Goldberger JJ. Diabetes mellitus and sudden cardiac death: what are the data? *Cardiol J*. 2010;17:117–129.
49. Berz JP, Orlander JD. Prolonged cerebellar ataxia: an unusual complication of hypoglycemia. *J Gen Intern Med*. 2008 Jan;23(1):103-5. Epub 2007 Nov 14.

50. Biessels GJ, Kappelle AC, Bravenboer B, Erkelens DW, Gispen WH. Cerebral function in diabetes mellitus. *Diabetologia*. 1994 Jul;37(7):643-50.
51. Bittar PG, Charnay Y, Pellerin L, Bouras C, Magistretti PJ. Selective distribution of lactate dehydrogenase isoenzymes in neurons and astrocytes of human brain. *J Cereb Blood Flow Metab*. 1996; 16:1079–1089.
52. Bizzozero OA, DeJesus G, Howard TA. Exposure of rat optic nerves to nitric oxide causes protein S-nitrosation and myelin decompaction. *Neurochem Res*. 2004 Sep;29(9):1675-85.
53. Blasetti A, Chiuri RM, Tocco AM, Di Giulio C, Mattei PA, Ballone E, *et al.*, The effect of recurrent severe hypoglycemia on cognitive performance in children with type 1 diabetes: a meta-analysis. *J Child Neurol*. 2011;26:1383–1391.
54. Boeve BF, Bell DG, Noseworthy JH. Bilateral temporal lobe MRI changes in uncomplicated hypoglycemic coma. *Can J Neurol Sci*. 1995;22:56–58.
55. Bosche B, Schäfer M, Graf R, Härtel FV, Schäfer U, Noll T. Lithium prevents early cytosolic calcium increase and secondary injurious calcium overload in glycolytically inhibited endothelial cells. *Biochem Biophys Res Commun*. 2013 May 3;434(2):268-72.
56. Bostock H, Grafe P. Activity-dependent excitability changes in normal and demyelinated rat spinal root axons. *J Physiol*. 1985 Aug;365:239-57.
57. Böttcher J, Kunze A, Kurrat C, Schmidt P, Hagemann G, Witte OW, *et al.*, Localized reversible reduction of apparent diffusion coefficient in transient hypoglycemia induced hemiparesis. *Stroke* 2005;36(3):e20-2.
58. Bouzier-Sore AK, Voisin P, Canioni P, Magistretti PJ, Pellerin L. Lactate is a preferential oxidative energy substrate over glucose for neurons in culture. *J Cereb Blood Flow Metab*. 2003 Nov;23(11):1298-306.
59. Brendza RP, O'Brien C, Simmons K, McKeel DW, Bales KR, Paul SM, Olney JW, Sanes JR, Holtzman DM. PDAPP; YFP double transgenic mice: a tool to study amyloid-beta associated changes in axonal, dendritic, and synaptic structures. *J Comp Neurol*. 2003 Feb 17;456(4):375-83.
60. Brickley SG, Misra C, Mok MH, Mishina M, Cull-Candy SG. NR2B and NR2D subunits coassemble in cerebellar Golgi cells to form a distinct NMDA receptor subtype restricted to extrasynaptic sites. *J Neurosci*. 2003 Jun 15;23(12):4958-66.

61. Brown AM and Ransom BR. Neuroprotective effects of increased extracellular Ca²⁺ during hypoglycaemia in white matter. *J Neurophysiol.* 2002 Sep;88(3):1302-7.
62. Brown AM, Baltan Tekkök S, Ransom BR. Energy transfer from astrocytes to axons: the role of CNS glycogen. *Neurochem Int.* 2004 Sep;45(4):529-36.
63. Brown AM, Sickmann HM, Fosgerau K, Lund TM, Schousboe A, Waagepetersen HS, Ransom BR. Astrocyte glycogen metabolism is required for neural activity during hypoglycaemia or intense stimulation in mouse white matter. *Neurosci Res.* 2005 Jan 1-15;79(1-2):74-80.
64. Brown AM, Tekkök SB, Ransom BR. Glycogen regulation and functional role in mouse white matter. *J Physiol.* 2003 Jun 1;549(Pt 2):501-12.
65. Brown AM, Tekkök SB, Ransom BR. Hypoglycemia and white matter: pathophysiology of axon injury and role of glycogen. *Diabetes Nutr Metab.* 2002 Oct;15(5):290-3
66. Brown AM, Wender R, Ransom BR. Ionic mechanisms of aglycemic axon injury in mammalian central white matter. *J Cereb Blood Flow Metab* 2001;21:385–395.
67. Brown AM, Westenbroek RE, Catterall WA, Ransom BR. Axonal L-type Ca²⁺ channels and anoxic injury in rat CNS white matter. *J Neurophysiol.* 2001 Feb;85(2):900-11.
68. Brown GC, Bolanos JP, Heales SJ, Clark JB. Nitric oxide produced by activated astrocytes rapidly and reversibly inhibits cellular respiration. *Neurosci Lett* 1995;193:201–204
69. Brown GC. Nitric oxide and mitochondrial respiration. *Biochim Biophys Acta.* 1999 May 5;1411(2-3):351-69.
70. Buchan AM, Xue D, Huang ZG, Smith KH, Lesiuk H. Delayed AMPA receptor blockade reduces cerebral infarction induced by focal ischemia. *Neuroreport.* 1991 Aug;2(8):473-6.
71. Bueno D, Azzolin IR, Perry MLS. Ontogenic study of glucose and lactate utilisation by rat cerebellum slices. *Med Sci Res.* 1994; 22:631-632.
72. Büki A, Okonkwo DO, Wang KK, Povlishock JT. Cytochrome c release and caspase activation in traumatic axonal injury. *J Neurosci.* 2000 Apr 15;20(8):2825-34.
73. Büki A, Siman R, Trojanowski JQ, Povlishock JT. The role of calpain-mediated spectrin proteolysis in traumatically induced axonal injury. *J Neuropathol Exp Neurol.* 1999 Apr;58(4):365-75.
74. Burnashev N. Calcium permeability of glutamate-gated channels in the central nervous system. *Curr Opin Neurobiol.* 1996 Jun;6(3):311-7.

75. Buskila Y, Abu-Ghanem Y, Levi Y, Moran A, Grauer E, Amitai Y. Enhanced astrocytic nitric oxide production and neuronal modifications in the neocortex of a NOS2 mutant mouse. *PLoS One*. 2007 Sep 5;2(9):e843.
76. Buskila Y, Amitai Y. Astrocytic iNOS-dependent enhancement of synaptic release in mouse neocortex. *J Neurophysiol*. 2010 Mar;103(3):1322-8.
77. Butt AM, Ransom BR. Morphology of astrocytes and oligodendrocytes during development in the intact rat optic nerve. *J Comp Neurol*. 1993 Dec 1;338(1):141-58.
78. Butt AM, Pugh M, Hubbard P, James G. Functions of optic nerve glia: axoglial signalling in physiology and pathology. *Eye (Lond)*. 2004 Nov;18(11):1110-21.
79. Cahn RD, Zwilling E, Kaplan NO, Levine L. Nature and Development of Lactic Dehydrogenases: The two major types of this enzyme form molecular hybrids which change in makeup during development. *Science*. 1962 Jun 15;136(3520):962-9.
80. Cajal, S. Degeneration & regeneration of the nervous system. New York; Harper Press (1928).
81. Cakmakci H, Usal C, Karabay N, Kovanlikaya A. Transient neonatal hypoglycemia: cranial US and MRI findings. *Eur Radiol*. 2001;11(12):2585-8. Epub 2001 Jan 25.
82. Caldwell P.C. Calcium Chelation and Buffers. In: Cuthbert A.W. (eds) *A Symposium on Calcium and Cellular Function*. (1970) Biological Council (The Co-ordinating Committee for Symposia on Drug Action). Palgrave Macmillan, London. p10-16
83. Cali C, Baghabra J, Boges DJ, Holst GR1, Kreshuk A, Hamprecht FA, Srinivasan M, Lehväslaiho H1, Magistretti PJ. Three-dimensional immersive virtual reality for studying cellular compartments in 3D models from EM preparations of neural tissues. *J Comp Neurol*. 2016 Jan 1;524(1):23-38.
84. Cambron M, D'Haeseleer M, Laureys G, Clinckers R, Debruyne J, De Keyser J. White-matter astrocytes, axonal energy metabolism, and axonal degeneration in multiple sclerosis. *J Cereb Blood Flow Metab*. 2012 Mar;32(3):413-24
85. Cao N, Yao ZX. Oligodendrocyte N-methyl-D-aspartate receptor signaling: insights into its functions. *Mol Neurobiol*. 2013 Apr;47(2):845-56.
86. Caraballo RH, Sakr D, Mozzi M, Guerrero A, Adi JN, Cersosimo RO, et al. Symptomatic occipital lobe epilepsy following neonatal hypoglycemia. *Pediatr Neurol* 2004;31:24–9.

87. Carley LR, Raymond SA. Comparison of the after-effects of impulse conduction on threshold at nodes of Ranvier along single frog sciatic axons. *J Physiol.* 1987 May;386:503-27.
88. Carter LM, Starkey ML, Akrimi SF, Davies M, McMahon SB, Bradbury EJ. The yellow fluorescent protein (YFP-H) mouse reveals neuroprotection as a novel mechanism underlying chondroitinase ABC-mediated repair after spinal cord injury. *J Neurosci.* 2008 Dec 24;28(52):14107-20.
89. Cataldo AM, Broadwell RD. Cytochemical identification of cerebral glycogen and glucose-6-phosphatase activity under normal and experimental conditions. II. Choroid plexus and ependymal epithelia, endothelia and pericytes. *J Neurocytol* (1986) 15: 511.
90. Chalmers J, Risk MTA, Kean DM, Grant R, Ashworth B, Campbell IW. Severe amnesia after hypoglycemia: clinical, psychometric, and magnetic resonance imaging correlations. *Diabetes Care.* 1991;14:922–925.
91. Chambers TW, Daly TP, Hockley A, Brown AM. Contribution of glycogen in supporting axon conduction in the peripheral and central nervous systems: the role of lactate. *Front Neurosci.* 2014 Nov 25;8:378.
92. Chang KC, Barth AS, Sasano T, Kizana E, Kashiwakura Y, Zhang Y, Foster DB, Marbán E. CAPON modulates cardiac repolarization via neuronal nitric oxide synthase signaling in the heart. *Proc Natl Acad Sci U S A.* 2008 Mar 18;105(11):4477-82.
93. Chen Y, Yi Q, Liu G, Shen X, Xuan L, Tian Y. Cerebral white matter injury and damage to myelin sheath following whole-brain ischemia. *Brain Res.* 2013 Feb 7;1495:11-7.
94. Chih CP, Roberts EL Jr. Energy substrates for neurons during neural activity: a critical review of the astrocyte-neuron lactate shuttle hypothesis. *J Cereb Blood Flow Metab.* 2003 Nov;23(11):1263-81.
95. Cho SJ, Minn YK, Kwon KH. Severe hypoglycemia and vulnerability of the brain. *Arch Neurol.* 2006;63:138.
96. Choi DW. Calcium: still center-stage in hypoxic-ischemic neuronal death. *Trends Neurosci.* 1995 Feb;18(2):58-60.
97. Choi DW. Glutamate neurotoxicity and diseases of the nervous system. *Neuron.* 1988 Oct;1(8):623-34.
98. Choi DW. Glutamate receptors and the induction of excitotoxic neuronal death. *Prog Brain Res.* 1994;100:47-51.

99. Christensen PC, Samadi-Bahrami Z2, Pavlov V2, Stys PK3, Moore GRW2. Ionotropic glutamate receptor expression in human white matter. *Neurosci Lett*. 2016 Sep 6;630:1-8.
100. Christman CW, Grady MS, Walker SA, Holloway KL, Povlishock JT. Ultrastructural studies of diffuse axonal injury in humans. *J Neurotrauma*. 1994 Apr;11(2):173-86.
101. Chugani HT. A critical period of brain development: studies of cerebral glucose utilization with PET. *Prev Med*. 1998 Mar-Apr;27(2):184-8.
102. Chuquet J, Quilichini P, Nimchinsky EA, Buzsaki G. Predominant enhancement of glucose uptake in astrocytes versus neurons during activation of the somatosensory cortex. *J Neurosci*. 2010; 30:15298-15303.
103. Colbert CM. Preparation of cortical brain slices for electrophysiological recording. *Methods Mol Biol*. 2006;337:117-25.
104. Collingridge GL. The brain slice preparation: a tribute to the pioneer Henry McIlwain. *J Neurosci Methods*. 1995 Jun;59(1):5-9.
105. Control Group, Turnbull FM, Abraira C, Anderson RJ, Byington RP, Chalmers JP, Duckworth WC, Evans GW, Gerstein HC, Holman RR, Moritz TE, Neal BC, Ninomiya T, Patel AA, Paul SK, Travert F, Woodward M. Intensive glucose control and macrovascular outcomes in type 2 diabetes. *Diabetologia*. 2009 Nov;52(11):2288-98.
106. Corsani L, Bizzoco E, Pedata F, Gianfriddo M, Fausone-Pellegrini MS, Vannucchi MG. Inducible nitric oxide synthase appears and is co-expressed with the neuronal isoform in interneurons of the rat hippocampus after transient ischemia induced by middle cerebral artery occlusion. *Exp Neurol*. 2008 Jun;211(2):433-40.
107. Cryer PE, Davis SN, Shamon H. Hypoglycemia in diabetes. *Diabetes Care*. 2003 Jun;26(6):1902-12.
108. Cryer PE. Diverse causes of hypoglycemia-associated autonomic failure in diabetes. *N Engl J Med*. 2004;350:2272-2279.
109. Cryer PE. Hypoglycemia, functional brain failure, and brain death. *J Clin Invest*. 2007 Apr;117(4):868-70.
110. Cui H, Hayashi A, Sun HS, Belmares MP, Cobey C, Phan T, Schweizer J, Salter MW, Wang YT, Tasker RA, Garman D, Rabinowitz J, Lu PS, Tymianski M. PDZ protein interactions underlying NMDA receptor-mediated excitotoxicity and neuroprotection by PSD-95 inhibitors. *J Neurosci*. 2007 Sep 12;27(37):9901-15.

111. Cummins KL, Perkel DH, Dorfman LJ. Nerve fiber conduction-velocity distributions. I. Estimation based on the single-fiber and compound action potentials. *Electroencephalogr Clin Neurophysiol.* 1979 Jun;46(6):634-46.
112. Dave KR, Pileggi A, Raval AP. Recurrent hypoglycemia increases oxygen glucose deprivation-induced damage in hippocampal organotypic slices. *Neurosci Lett.* 2011b May 27;496(1):25-9.
113. Dave KR, Tamariz J, Desai KM, Brand FJ, Liu A, Saul I, Bhattacharya SK, Pileggi A. Recurrent hypoglycemia exacerbates cerebral ischemic damage in streptozotocin-induced diabetic rats. *Stroke.* 2011a May;42(5):1404-11.
114. Davis EA, Jones TW. Hypoglycemia in children with diabetes: incidence, counterregulation and cognitive dysfunction. *J Pediatr Endocrinol Metab* 1998;11(suppl 1):177–182.
115. Del Rey A, Roggero E, Randolph A, Mahuad C, McCann S, Rettori V, Besedovsky HO. IL-1 resets glucose homeostasis at central levels. *Proc Natl Acad Sci U S A.* 2006 Oct 24;103(43):16039-44.
116. Dewar D, Underhill SM, Goldberg MP. Oligodendrocytes and ischemic brain injury. *J Cereb Blood Flow Metab.* 2003 Mar;23(3):263-74.
117. Diabetes Control and Complications Trial Research Group, Nathan DM, Genuth S, Lachin J, Cleary P, Crofford O, Davis M, Rand L, Siebert C, Poulter N, Rodgers A, Williams B, Bompont S, de Galan BE, Joshi R, Travert F. The effect of intensive treatment of diabetes on the development and progression of long-term complications in insulin-dependent diabetes mellitus. *N Engl J Med.* 1993 Sep 30;329(14):977-86.
118. Diaz J, Antoine J, Azad N. A case of hypoglycemia, lactic acidosis, and hematologic malignancy. *Endocr Pract.* 2010;16:241–243.
119. Dienel GA, Ball KK, Cruz NF. A glycogen phosphorylase inhibitor selectively enhances local rates of glucose utilization in brain during sensory stimulation of conscious rats: implications for glycogen turnover. *J Neurochem.* 2007; 102:466-478.
120. DiNuzzo M, Mangia S, Maraviglia B, Giove F. Glycogenolysis in astrocytes supports blood-borne glucose channeling not glycogen-derived lactate shuttling to neurons: evidence from mathematical modeling. *J Cereb Blood Flow Metab.* 2010; 30:1895-1904.
121. DiNuzzo M, Mangia S, Maraviglia B, Giove F. The role of astrocytic glycogen in supporting the energetics of neuronal activity. *Neurochem Res.* 2012; 37:2432-2438.

122. Dolinak D, Smith C, Graham DI. Hypoglycaemia is a cause of axonal injury. *Neuropathol Appl Neurobiol.* 2000 Oct;26(5):448-53.
123. Dong CJ, Hare WA. Contribution to ischemic injury of rat optic nerves by intracellular sodium overload. *Doc Ophthalmol.* 2005 Jan;110(1):15-23.
124. Doyle S, Hansen DB, Vella J, Bond P, Harper G, Zammit C, Valentino M2 Fern R. Vesicular glutamate release from central axons contributes to myelin damage. *Nat Commun.* 2018 Mar 12;9(1):1032. doi: 10.1038/s41467-018-03427-1.
125. Dringen R, Gebhardt R, Hamprecht B. Glycogen in astrocytes: possible function as lactate supply for neighboring cells. *Brain Res.* 1993; 623:208–214.
126. Edwards A, Wyatt J, and Thoresen M. Treatment of hypoxic-ischaemic brain damage by moderate hypothermia. *Arch Dis Child Fetal Neonatal Ed.* 1998 Mar; 78(2): F85–F88.
127. Emery B. Regulation of oligodendrocyte differentiation and myelination. *Science.* 2010 Nov 5;330(6005):779-82.
128. Erlichman JS, Hewitt A, Damon TL, Hart M, Kurasz J, Li A, Leiter JC. Inhibition of monocarboxylate transporter 2 in the retrotrapezoid nucleus in rats: a test of the astrocyte-neuron lactate-shuttle hypothesis. *J Neurosci.* 2008 May 7;28(19):4888-96.
129. European Medicines Agencies. Guideline on clinical investigation of medicinal products in the treatment or prevention of diabetes mellitus. 2012. Available at: http://www.ema.europa.eu/docs/en_GB/document_library/Scientific_guideline/2012/06/WC500129256.pdf
130. Falciglia M, Freyberg RW, Almenoff PL, D'Alessio DA, Render ML. Alessio DA, Render ML. Hyperglycemia-related mortality in critically ill patients varies with admission diagnosis. *Crit Care Med.* 2009;37:3001–3009.
131. Falkenstein E, Tillmann HC, Christ M, Feuring M, Wehling M. Multiple actions of steroid hormones--a focus on rapid, nongenomic effects. *Pharmacol Rev.* 2000 Dec;52(4):513-56.
132. Feldman-Billard S, Massin P, Meas T, Guillausseau PJ, Héron E. Hypoglycemia-induced blood pressure elevation in patients with diabetes. *Arch Intern Med.* 2010;170:829–831.
133. Feng G, Mellor RH, Bernstein M, Keller-Peck C, Nguyen QT, Wallace M, Nerbonne JM, Lichtman JW, Sanes JR. Imaging neuronal subsets in transgenic mice expressing multiple spectral variants of GFP. *Neuron.* 2000 Oct;28(1):41-51.

134. Ferguson B, Matyszak MK, Esiri MM, Perry VH. Axonal damage in acute multiple sclerosis lesions. *Brain*. 1997 Mar;120 (Pt 3):393-9.
135. Ferguson SC, Blane A, Perros P, McCrimmon RJ, Best JJK, Wardlaw J, *et al.*, Cognitive ability and brain structure in type 1 diabetes: relation to microangiopathy and preceding severe hypoglycemia. *Diabetes*. 2003;52:149–156.
136. Fern R, Davis P, Waxman SG, Ransom BR. Axon conduction and survival in CNS white matter during energy deprivation: a developmental study. *J Neurophysiol*. 1998 Jan;79(1):95-105.
137. Fern R, Möller T. Rapid ischemic cell death in immature oligodendrocytes: a fatal glutamate release feedback loop. *J Neurosci*. 2000 Jan 1;20(1):34-42.
138. Fern R, Ransom BR, Waxman SG. Voltage-gated calcium channels in CNS white matter: role in anoxic injury. *J Neurophysiol*. 1995 Jul;74(1):369-77.
139. Ferrand-Drake M, Friberg H, Wieloch T. Mitochondrial permeability transition induced DNA-fragmentation in the rat hippocampus following hypoglycemia. *Neuroscience*. 1999;90(4):1325-38.
140. Filan PM, Inder TE, Cameron FJ, Kean MJ, Hunt RW. Neonatal hypoglycemia and occipital cerebral injury. *J Pediatr* 2006;148:552–5.
141. Finelli PF. Diffusion-weighted MR in hypoglycemic coma. *Neurology* 2001;57(5):933.
142. Follett PL, Rosenberg PA, Volpe JJ, Jensen FE. NBQX attenuates excitotoxic injury in developing white matter. *J Neurosci*. 2000 Dec 15;20(24):9235-41.
143. Foster RE, Connors BW, Waxman SG. Rat optic nerve: electrophysiological, pharmacological and anatomical studies during development. *Brain Res*. 1982 Mar;255(3):371-86.
144. Frankenhaeuser B. The effect of calcium on the myelinated nerve fibre *J Physiol*. 1957 Jul 11; 137(2): 245–260.
145. Fujioka M, Okuchi K, Hiramatsu KI, Sakaki T, Sakaguchi S, Ishii Y. Specific changes in human brain after hypoglycemic injury. *Stroke* 1997;28:584–587.
146. Fulton BP, Walton K. Electrophysiological properties of neonatal rat motoneurons studied in vitro. *J Physiol*. 1986 Jan;370:651-78.
147. Fünfschilling U, Supplie LM, Mahad D, Boretius S, Saab AS, Edgar J, Brinkmann BG, Kassmann CM, Tzvetanova ID, Möbius W, Diaz F, Meijer D, Suter U, Hamprecht B, Sereda

- MW, Moraes CT, Frahm J, Goebbels S, Nave KA. Glycolytic oligodendrocytes maintain myelin and long-term axonal integrity. *Nature*. 2012 Apr 29;485(7399):517-21.
148. García-Barcina JM, Matute C. AMPA-selective glutamate receptor subunits in glial cells of the adult bovine white matter. *Brain Res Mol Brain Res*. 1998 Jan;53(1-2):270-6.
149. Garthwaite G, Brown G, Batchelor AM, Goodwin DA, Garthwaite J. Mechanisms of ischaemic damage to central white matter axons: a quantitative histological analysis using rat optic nerve. *Neuroscience*. 1999;94(4):1219-30.
150. Garthwaite G, Goodwin DA, Batchelor AM, Leeming K, Garthwaite J. Nitric oxide toxicity in CNS white matter: an in vitro study using rat optic nerve. *Neuroscience*. 2002;109(1):145-55.
151. Garthwaite J, Boulton CL. Nitric oxide signaling in the central nervous system. *Annu Rev Physiol*. 1995;57:683-706.
152. Garthwaite J, Charles SL, Chess-Williams R. Endothelium-derived relaxing factor release on activation of NMDA receptors suggests role as intercellular messenger in the brain. *Nature*. 1988 Nov 24;336(6197):385-8.
153. Geddes J, Schopman JE, Zammitt NN, Frier BM. Prevalence of impaired awareness of hypoglycaemia in adults with Type 1 diabetes. *Diabet Med*. 2008;25:501–504.
154. Gerhart DZ, Enerson BE, Zhdankina OY, Leino RL, Drewes LR. Expression of monocarboxylate transporter MCT1 by brain endothelium and glia in adult and suckling rats. *Am J Physiol*. 1997 Jul;273(1 Pt 1):E207-13.
155. Ghajar JB, Plum F, Duffy TE. Cerebral oxidative metabolism and blood flow during acute hypoglycemia and recovery in unanesthetized rats. *J Neurochem*. 1982 Feb;38(2):397-409.
156. Gill GV, Woodward A, Casson IF, Weston PJ. Cardiac arrhythmia and nocturnal hypoglycaemia in type 1 diabetes--the 'dead in bed' syndrome revisited. *Diabetologia*. 2009;52:42–45.
157. Gill R, Foster AC, Woodruff GN. Systemic administration of MK-801 protects against ischemia-induced hippocampal neurodegeneration in the gerbil. *J Neurosci*. 1987 Oct;7(10):3343-9.
158. Gill R, Nordholm L, Lodge D. The neuroprotective actions of 2,3-dihydroxy-6-nitro-7-sulfamoyl-benzo(F)quinoxaline (NBQX) in a rat focal ischaemia model. *Brain Res*. 1992 May 15;580(1-2):35-43.

159. Gillingwater TH, Thomson D, Mack TG, Soffin EM, Mattison RJ, Coleman MP, Ribchester RR. Age-dependent synapse withdrawal at axotomised neuromuscular junctions in Wld(s) mutant and Ube4b/Nmnat transgenic mice. *J Physiol*. 2002 Sep 15;543(Pt 3):739-55.
160. Gleeson LC, Ryan KJ, Griffin EW, Connor TJ, Harkin A. The β 2-adrenoceptor agonist clenbuterol elicits neuroprotective, anti-inflammatory and neurotrophic actions in the kainic acid model of excitotoxicity. *Brain Behav Immun*. 2010 Nov;24(8):1354-61.
161. Gogitidze Joy N, Hedrington MS, Briscoe VJ, Tate DB, Ertl AC, Davis SN. Effects of acute hypoglycemia on inflammatory and pro-atherothrombotic biomarkers in individuals with type 1 diabetes and healthy individuals. *Diabetes Care*. 2010;33:1529–1535.
162. Goldberg MP, Ransom BR. New light on white matter. *Stroke*. 2003 Feb;34(2):330-2.
163. Goursaud S, Kozlova EN, Maloteaux JM, and Hermans E. Cultured astrocytes derived from corpus callosum or cortical grey matter show distinct glutamate handling properties. *J Neurochem*. 2009; 108:1442-1452.
164. Graham DI, Smith C, Reichard R, Leclercq PD, Gentleman SM. Trials and tribulations of using beta-amyloid precursor protein immunohistochemistry to evaluate traumatic brain injury in adults. *Forensic Sci Int*. 2004 Dec 16;146(2-3):89-96.
165. Greenspan P, Mayer EP, Fowler SD. Nile red: a selective fluorescent stain for intracellular lipid droplets. *J Cell Biol*. 1985 Mar;100(3):965-73.
166. Greer JE, McGinn MJ, Povlishock JT. Diffuse traumatic axonal injury in the mouse induces atrophy, c-Jun activation, and axonal outgrowth in the axotomized neuronal population. *J Neurosci*. 2011 Mar 30;31(13):5089-105.
167. Griffith OW, Stuehr DJ. Nitric oxide synthases: properties and catalytic mechanism. *Annu Rev Physiol*. 1995;57:707-36.
168. Gross SS, Wolin MS. Nitric oxide: pathophysiological mechanisms. *Annu Rev Physiol*. 1995;57:737-69.
169. Gruetter R. Glycogen: the forgotten cerebral energy store. *J Neurosci Res*. 2003 Oct 15;74(2):179-83.
170. Gupta DK, Singla R, Kale SS, Sharma BS. Intracerebral hypoglycemia and its clinical relevance as a prognostic indicator in severe traumatic brain injury: A cerebral microdialysis study from India. *Neurol India*. 2016 Mar-Apr;64(2):259-64.

171. Halestrap AP. The monocarboxylate transporter family--Structure and functional characterization. *IUBMB Life*. 2012 Jan;64(1):1-9.
172. Hamilton NB, Kolodziejczyk K, Kougioumtzidou E, Attwell D. Proton-gated Ca(2+)-permeable TRP channels damage myelin in conditions mimicking ischaemia. *Nature*. 2016 Jan 28;529(7587):523-7.
173. Hansen KB, Traynelis SF. Structural and mechanistic determinants of a novel site for noncompetitive inhibition of GluN2D-containing NMDA receptors. *J Neurosci*. 2011 Mar 9;31(10):3650-61.
174. Harney SC, Jane DE, Anwyl R. Extrasynaptic NR2D-containing NMDARs are recruited to the synapse during LTP of NMDAR-EPSCs. *J Neurosci*. 2008 Nov 5;28(45):11685-94. doi: 10.1523/JNEUROSCI.3035-08.2008.
175. Harris JJ, Attwell D. The energetics of CNS white matter. *J Neurosci*. 2012 Jan 4;32(1):356-71.
176. Heales SJ, Bolaños JP, Stewart VC, Brookes PS, Land JM, Clark JB. Nitric oxide, mitochondria and neurological disease. *Biochim Biophys Acta*. 1999 Feb 9;1410(2):215-28.
177. Hershey T, Bhargava N, Sadler M, White NH, Craft S. Conventional versus intensive diabetes therapy in children with type 1 diabetes: effects on memory and motor speed. *Diabetes Care*. 1999 Aug;22(8):1318-24.
178. Hershey T, Perantie DC, Warren SL, Zimmerman EC, Sadler M, White NH. Frequency and timing of severe hypoglycemia affects spatial memory in children with type 1 diabetes. *Diabetes Care*. 2005;28:2372-2377.
179. Hertz L, Lovatt D, Goldman SA, Nedergaard M. Adrenoceptors in brain: cellular gene expression and effects on astrocytic metabolism and [Ca(2+)]_i. *Neurochem Int*. 2010 Nov;57(4):411-20.
180. Hickenbottom SL, Grotta J. Neuroprotective therapy. *Semin Neurol*. 1998;18(4):485-92.
181. Hille B, Woodhull AM, Shapiro BI. Negative surface charge near sodium channels of nerve: divalent ions, monovalent ions, and pH. *Philos Trans R Soc Lond B Biol Sci*. 1975 Jun 10;270(908):301-18.
182. Hillman KL, Doze VA, Porter JE. Functional characterization of the beta-adrenergic receptor subtypes expressed by CA1 pyramidal cells in the rat hippocampus. *J Pharmacol Exp Ther*. 2005 Aug;314(2):561-7.

183. Hof PR, Pascale E, Magistretti PJ. K⁺ at concentrations reached in the extracellular space during neuronal activity promotes a Ca²⁺-dependent glycogen hydrolysis in mouse cerebral cortex. *J Neurosci*. 1988 Jun;8(6):1922-8.
184. Holemans X, Dupuis M, Misson N, Vanderijst JF. Reversible amnesia in a Type 1 diabetic patient and bilateral hippocampal lesions on magnetic resonance imaging (MRI) *Diabet Med*. 2001;18:761–763.
185. Holstein A, Plaschke A, Egberts EH. Incidence and costs of severe hypoglycemia. *Diabetes Care*. 2002;25:2109–10.
186. Holstein A, Plaschke A, Hammer C, Egberts EH. Characteristics and time course of severe glimepiride- versus glibenclamide-induced hypoglycaemia. *Eur J Clin Pharmacol*. 2003;59:91–97.
187. Hong H, Sun J, Cai W. Multimodality imaging of nitric oxide and nitric oxide synthases. *Free Radic Biol Med*. 2009 Sep 15;47(6):684-98.
188. Hooper DC, Ohnishi ST, Kean R, et al. Local nitric oxide production in viral and autoimmune diseases of the central nervous system. *Proc Natl Acad Sci USA* 1995;92: 5312–5316.
189. Howarth C, Peppiatt-Wildman CM, Attwell D. The energy use associated with neural computation in the cerebellum. *J Cereb Blood Flow Metab*. 2010 Feb;30(2):403-14.
190. Huang Z, Sjöholm A. Ethanol acutely stimulates islet blood flow, amplifies insulin secretion, and induces hypoglycemia via nitric oxide and vagally mediated mechanisms. *Endocrinology*. 2008;149:232–236.
191. Huk I, Brovkovich V, Nanobash Vili J, Weigel G, Neumayer C, Partyka L, Patton S, Malinski T. Bioflavonoid quercetin scavenges superoxide and increases nitric oxide concentration in ischaemia-reperfusion injury: an experimental study. *Br J Surg*. 1998 Aug;85(8):1080-5.
192. Hyllienmark L, Maltez J, Dandenell A, Ludvigsson J, Brismar T. EEG abnormalities with and without relation to severe hypoglycaemia in adolescents with type 1 diabetes. *Diabetologia*. 2005 Mar;48(3):412-9. Epub 2005 Mar 1.
193. Iadecola C, Xu X, Zhang F, el-Fakahany EE, Ross ME. Marked induction of calcium-independent nitric oxide synthase activity after focal cerebral ischemia. *J Cereb Blood Flow Metab*. 1995a Jan;15(1):52-9.

194. Iadecola C, Zhang F, Casey R, Clark HB, Ross ME. Inducible nitric oxide synthase gene expression in vascular cells after transient focal cerebral ischemia. *Stroke*. 1996 Aug;27(8):1373-80.
195. Iadecola C, Zhang F, Xu S, Casey R, Ross ME. Inducible nitric oxide synthase gene expression in brain following cerebral ischemia. *J Cereb Blood Flow Metab*. 1995b May;15(3):378-84.
196. Iadecola C. Bright and dark sides of nitric oxide in ischemic brain injury. *Trends Neurosci*. 1997 Mar;20(3):132-9.
197. Ichai C, Preiser JC Société Française d'Anesthésie-Réanimation; Société de Réanimation de langue Française; Experts group. International recommendations for glucose control in adult non diabetic critically ill patients. *Crit Care*. 2010;14:R166
198. Imura T, Kanatani S, Fukuda S, Miyamoto Y, Hisatsune T. Layer-specific production of nitric oxide during cortical circuit formation in postnatal mouse brain. *Cereb Cortex*. 2005 Mar;15(3):332-40.
199. Itoh Y, Ma FH, Hoshi H, Oka M, Noda K, Ukai Y, Kojima H, Nagano T, Toda N. Determination and bioimaging method for nitric oxide in biological specimens by diaminofluorescein fluorometry. *Anal Biochem*. 2000 Dec 15;287(2):203-9.
200. Izeboud CA, Monshouwer M, van Miert AS, Witkamp RF. The beta-adrenoceptor agonist clenbuterol is a potent inhibitor of the LPS-induced production of TNF-alpha and IL-6 in vitro and in vivo. *Inflamm Res*. 1999 Sep;48(9):497-502.
201. Jo J, Tatsutomi M and Tabata Y. Visualization of nitric oxide-producing macrophages with a polymer micelle-based fluorescent probe. *Front. Bioeng. Biotechnol*. 2016 Conference Abstract: 10th World Biomaterials Congress.
202. Johkura K, Nakae Y, Kudo Y, Yoshida TN, Kuroiwa Y. Early diffusion MR imaging findings and short-term outcome in comatose patients with hypoglycemia. *AJNR Am J Neuroradiol*. 2012 May;33(5):904-9.
203. Johnson VE, Stewart W, Smith DH. Axonal pathology in traumatic brain injury. *Exp Neurol*. 2013 Aug;246:35-43.
204. Jonsson L, Bolinder B, Lundkvist J. Cost of hypoglycemia in patients with type 2 diabetes in Sweden. *Value Health*. 2006;9:193–8.
205. Jung SL, Kim BS, Lee KS, Yoon KH, Byun JY. Magnetic resonance imaging and diffusion-weighted imaging changes after hypoglycemic coma. *J Neuroimaging*. 2005;15:193–196.

206. Kader A, Frazzini VI, Solomon RA, Trifiletti RR. Nitric oxide production during focal cerebral ischemia in rats. *Stroke*. 1993 Nov;24(11):1709-16.
207. Kaku DA, Giffard RG, Choi DW. Neuroprotective effects of glutamate antagonists and extracellular acidity. *Science*. 1993 Jun 4;260(5113):1516-8.
208. Kalimo II, Auer RN, Siesjö BK. The temporal evolution of hypoglycemic brain damage. *Acta Neuropathol* 1985;67:37–50.
209. Kalra S, Mukherjee JJ, Venkataraman S, Bantwal G, Shaikh S, Saboo B, Das AK, Ramachandran A. Hypoglycemia: The neglected complication. *Indian J Endocrinol Metab*. 2013 Sep;17(5):819-34.
210. Kapoor R, Davies M, Blaker PA, Hall SM, Smith KJ. Blockers of sodium and calcium entry protect axons from nitric oxide-mediated degeneration. *Ann Neurol*. 2003 Feb;53(2):174-80.
211. Kapoor R, Davies M, Smith KJ. Temporary axonal conduction block and axonal loss in inflammatory neurological disease. A potential role for nitric oxide? *Ann N Y Acad Sci*. 1999;893:304-8.
212. Káradóttir R, Cavelier P, Bergersen LH, Attwell D. NMDA receptors are expressed in oligodendrocytes and activated in ischaemia. *Nature*. 2005 Dec 22;438(7071):1162-6.
213. Káradóttir R, Hamilton NB, Bakiri Y, Attwell D. Spiking and nonspiking classes of oligodendrocyte precursor glia in CNS white matter. *Nat Neurosci*. 2008 Apr;11(4):450-6.
214. Kedia N. Treatment of severe diabetic hypoglycemia with glucagon: an underutilized therapeutic approach. *Diabetes Metab Syndr Obes*. 2011;4:337-46.
215. Kelesidis T, Canseco E. Levofloxacin-induced hypoglycemia: a rare but life-threatening side effect of a widely used antibiotic. *Am J Med*. 2009;122:e3–e4.
216. Kelesidis T, Canseco E. Quinolone-induced hypoglycemia: a life-threatening but potentially reversible side effect. *Am J Med*. 2010;123:e5–e6.
217. Keller BC, Nussensveig D, Dowell JE. Diffuse large B-cell lymphoma in a hepatitis C virus-infected patient presenting with lactic acidosis and hypoglycemia. *Am J Med Sci*. 2010;339:202–204.
218. Kerschensteiner M, Schwab ME, Lichtman JW, Misgeld T. In vivo imaging of axonal degeneration and regeneration in the injured spinal cord. *Nat Med*. 2005 May;11(5):572-7. 0.

219. Khurana S, Li WK. Baptisms of fire or death knells for acute-slice physiology in the age of 'omics' and light? *Rev Neurosci*. 2013;24(5):527-36.
220. Kikuchi M, Shirasaki H, Himi T. Platelet-activating factor (PAF) increases NO production in human endothelial cells-real-time monitoring by DAR-4M AM. *Prostaglandins Leukot Essent Fatty Acids*. 2008 Apr-May;78(4-5):305-9.
221. Kim JH, Choi JY, Koh SB, Lee Y. Reversible splenial abnormality in hypoglycemic encephalopathy. *Neuroradiology*. 2007;49:217-222.
222. Kim JH, Koh SB. Extensive white matter injury in hypoglycemic coma. *Neurology*. 2007 Mar 27;68(13):1074.
223. Kim JT, Oh TJ, Lee YA, Bae JH, Kim HJ, Jung HS, Cho YM, Park KS, Lim S, Jang HC, Lee HK. Increasing trend in the number of severe hypoglycemia patients in Korea. *Diabetes Metab J*. 2011 Apr;35(2):166-72.
224. Kinnala A, Rikalainen H, Lapinleimu H, Parkkola R, Kormanen M, Kero P. Cerebral magnetic resonance imaging and ultrasonography findings after neonatal hypoglycemia. *Pediatrics*. 1999 Apr;103(4 Pt 1):724-9.
225. Kirchhoff BA, Lugar HM, Smith SE, Meyer EJ, Perantie DC, Kolody BC, Koller JM, Arbelaez AM, Shimony JS, Hershey T. Hypoglycaemia-induced changes in regional brain volume and memory function. *Diabet Med*. 2013 Apr;30(4):e151-6.
226. Knowles RG, Moncada S. Nitric oxide synthases in mammals. *Biochem J*. 1994 Mar 1;298 (Pt 2):249-58.
227. Kocsis JD, Gordon TR, Waxman SG. Mammalian optic nerve fibers display two pharmacologically distinct potassium channels. *Brain Res*. 1986 Sep 24;383(1-2):357-61.
228. Kodl CT, Franc DT, Rao JP, Anderson FS, Thomas W, Mueller BA, *et al.*, Diffusion tensor imaging identifies deficits in white matter microstructure in subjects with type 1 diabetes that correlate with reduced neurocognitive function. *Diabetes*. 2008;57:3083-3089
229. Koizumi J, Shiraishi H. Ultrastructural appearance of glycogen in the hypothalamus of the rabbit following chlorpromazine administration. *Exp Brain Res*. 1970;10(3):276-82.
230. Koizumi J. Glycogen in the central nervous system. *Prog Histochem Cytochem*. 1974;6(4):1-37.

231. Kojima H, Hirata M, Kudo Y, Kikuchi K, Nagano T. Visualization of oxygen-concentration-dependent production of nitric oxide in rat hippocampal slices during aglycemia. *J Neurochem.* 2001a Mar;76(5):1404-10.
232. Kojima H, Hirotsu M, Nakatsubo N, Kikuchi K, Urano Y, Higuchi T, Hirata Y, Nagano T. Bioimaging of nitric oxide with fluorescent indicators based on the rhodamine chromophore. *Anal Chem.* 2001b May 1;73(9):1967-73
233. Kojima H, Nakatsubo N, Kikuchi K, Kawahara S, Kirino Y, Nagoshi H, Hirata Y, Nagano T. Detection and imaging of nitric oxide with novel fluorescent indicators: diaminofluoresceins. *Anal Chem.* 1998 Jul 1;70(13):2446-53.
234. Kojima H, Urano Y, Kikuchi K, Higuchi T, Hirata Y, Nagano T. Fluorescent Indicators for Imaging Nitric Oxide Production. *Angew Chem Int Ed Engl.* 1999 Nov 2;38(21):3209-3212.
235. Koroshetz WJ, Moskowitz MA. Emerging treatments for stroke in humans. *Trends Pharmacol Sci.* 1996 Jun;17(6):227-33.
236. Kousteni S, Bellido T, Plotkin LI, O'Brien CA, Bodenner DL, Han L, Han K, DiGregorio GB, Katzenellenbogen JA, Katzenellenbogen BS, Roberson PK, Weinstein RS, Jilka RL, Manolagas SC. Nongenotropic, sex-nonspecific signaling through the estrogen or androgen receptors: dissociation from transcriptional activity. *Cell.* 2001 Mar 9;104(5):719-30.
237. Kovács R, Rabanus A, Otáhal J, Patzak A, Kardos J, Albus K, Heinemann U, Kann O. Endogenous nitric oxide is a key promoting factor for initiation of seizure-like events in hippocampal and entorhinal cortex slices. *J Neurosci.* 2009 Jul 1;29(26):8565-77.
238. Kristián T, Siesjö BK. Calcium-related damage in ischemia. *Life Sci.* 1996;59(5-6):357-67.
239. Kukley M, Capetillo-Zarate E, Dietrich D. Vesicular glutamate release from axons in white matter. *Nat Neurosci.* 2007 Mar;10(3):311-20.
240. Laing SP, Swerdlow AJ, Slater SD, Botha JL, Burden AC, Waugh NR, et al. The British Diabetic Association Cohort Study, II: cause-specific mortality in patients with insulin-treated diabetes mellitus. *Diabet Med.* 1999;16:466–471.
241. Lam TI, Brennan-Minnella AM, Won SJ, Shen Y, Hefner C, Shi Y, Sun D, Swanson RA. Intracellular pH reduction prevents excitotoxic and ischemic neuronal death by inhibiting NADPH oxidase. *Proc Natl Acad Sci U S A.* 2013 Nov 12;110(46):E4362-8.

242. Lau CI, Wang HC, Hsu WC. Hypoglycemic encephalopathy as the initial presentation of hepatic tumor: a case report. *Neurologist*. 2010;16:206–207.
243. Laureys G, Valentino M, Demol F, Zammit C, Muscat R, Cambron M, Kooijman R, De Keyser J. β_2 -adrenergic receptors protect axons during energetic stress but do not influence basal glio-axonal lactate shuttling in mouse white matter. *Neuroscience*. 2014 Sep 26;277:367-74.
244. Lazzaro JT, Paternain AV, Lerma J, Chenard BL, Ewing FE, Huang J-H, Welch WM, Ganong AH, Menniti FS. CP-465,022 is a potent and selective noncompetitive AMPA receptor antagonist. *Neuropharmacology*. 2002;42:143–153.
245. Lee JM, Zipfel GJ, Choi DW. The changing landscape of ischaemic brain injury mechanisms. *Nature*. 1999 Jun 24;399(6738 Suppl):A7-14.
246. Lee S, Leach MK, Redmond SA, Chong SY, Mellon SH, Tuck SJ, Feng ZQ, Corey JM, Chan JR. A culture system to study oligodendrocyte myelination processes using engineered nanofibers. *Nature Methods*. 2012b; 9:917–922.
247. Lee Y, Morrison BM, Li Y, Lengacher S, Farah MH, Hoffman PN, Liu Y, Tsingalia A, Jin L, Zhang PW, Pellerin L, Magistretti PJ, Rothstein JD. Oligodendroglia metabolically support axons and contribute to neurodegeneration. *Nature*. 2012a Jul 26;487(7408):443-8.
248. Leese GP, Wang J, Broomhall J, Kelly P, Marsden A, Morrison W, Frier BM, Morris AD; DARTS/MEMO Collaboration. Frequency of severe hypoglycemia requiring emergency treatment in type 1 and type 2 diabetes: a population-based study of health service resource use. *Diabetes Care*. 2003 Apr;26(4):1176-80.
249. Levi AD, Green BA, Wang MY, Dietrich WD, Brindle T, Vanni S, Casella G, Elhammady G, Jagid J. Clinical application of modest hypothermia after spinal cord injury. *J Neurotrauma*. 2009 Mar;26(3):407-15.
250. Lewis SR, Evans DJ, Butler AR, Schofield-Robinson OJ, Alderson P. Hypothermia for traumatic brain injury. *Cochrane Database Syst Rev*. 2017 Sep 21;9:CD001048.
251. Li C, Xiao L, Liu X, Yang W, Shen W, Hu C, Yang G, He C. A functional role of NMDA receptor in regulating the differentiation of oligodendrocyte precursor cells and remyelination. *Glia*. 2013 May;61(5):732-49.
252. Li N, Sul JY, Haydon PG. A calcium-induced calcium influx factor, nitric oxide, modulates the refilling of calcium stores in astrocytes. *J Neurosci*. 2003 Nov 12;23(32):10302-10.

253. Li S, Mealing GA, Morley P, Stys PK. Novel injury mechanism in anoxia and trauma of spinal cord white matter: glutamate release via reverse Na⁺-dependent glutamate transport. *J. Soc. Neurosci.* 1999 19; RC16.
254. Li S, Stys PK. Mechanisms of ionotropic glutamate receptor-mediated excitotoxicity in isolated spinal cord white matter. *J Neurosci.* 2000 Feb 1;20(3):1190-8.
255. Lin SZ, Chiou AL, Wang Y. Ketamine antagonizes nitric oxide release from cerebral cortex after middle cerebral artery ligation in rats. *Stroke.* 1996 Apr;27(4):747-52.
256. Lin YY, Hsu CW, Sheu WH, Chu SJ, Wu CP, Tsai SH. Risk factors for recurrent hypoglycemia in hospitalized diabetic patients admitted for severe hypoglycemia. *Yonsei Med J.* 2010;51:367–374.
257. Lincoln NB, Faleiro RM, Kelly C, *et al.*, Effect of long-term glycemic control on cognitive function. *Diabetes Care* 1996;19:656–658.
258. Lipton SA, Rosenberg PA. Excitatory amino acids as a final common pathway for neurologic disorders. *N Engl J Med.* 1994 Mar 3;330(9):613-22.
259. Lou LF, Zhang J. Current Status of Diagnosis and Treatment in Hypoglycemic Encephalopathy. *Yi Xue Zong Shu* 2010;16:2008-10.
260. Lundkvist J, Berne C, Bolinder B, Jonsson L. The economic and quality of life impact of hypoglycemia. *Eur J Health Econ.* 2005;6:197–202.
261. Lutsep HL, Clark WM. Neuroprotection in acute ischaemic stroke. Current status and future potential. *Drugs R D.* 1999 Jan;1(1):3-8.
262. Ma J, Endres M, Moskowitz MA. Synergistic effects of caspase inhibitors and MK-801 in brain injury after transient focal cerebral ischaemia in mice. *Br J Pharmacol.* 1998 Jun;124(4):756-62.
263. Ma JH, Kim YJ, Yoo WJ, Ihn YK, Kim JY, Song HH, Kim BS. MR imaging of hypoglycemic encephalopathy: lesion distribution and prognosis prediction by diffusion-weighted imaging. *Neuroradiology.* 2009 Oct;51(10):641-9.
264. MacEachern SJ, Patel BA, McKay DM, Sharkey KA. Nitric oxide regulation of colonic epithelial ion transport: a novel role for enteric glia in the myenteric plexus. *J Physiol.* 2011 Jul 1;589(Pt 13):3333-48.
265. Maeshima S, Ozaki F, Masuo O, Yamaga H, Okita R, Moriwaki H. Memory impairment and spatial disorientation following a left retrosplenial lesion. *J Clin Neurosci.* 2001;8:450–451.

266. Magistretti PJ, Pellerin L, Rothman DL, Shulman RG. Energy on demand. *Science*. 1999 Jan 22;283(5401):496-7.
267. Magistretti PJ, Pellerin L. Cellular mechanisms of brain energy metabolism and their relevance to functional brain imaging. *Philos Trans R Soc Lond B Biol Sci*. 1999 Jul 29;354(1387):1155-63.
268. Magistretti PJ. 2008. Brain energy metabolism. In *Fundamental Neuroscience*. (Squire L.R., Berg D., Bloom F.E., du Lac S., Ghosh A., and Spitzer N.C., eds.) pp. 271-293. Academic Press, San Diego Ca.
269. Malinski T, Bailey F, Zhang ZG, Chopp M. Nitric oxide measured by a porphyrinic microsensor in rat brain after transient middle cerebral artery occlusion. *J Cereb Blood Flow Metab*. 1993 May;13(3):355-8.
270. Malinski T, Taha Z. Nitric oxide release from a single cell measured in situ by a porphyrinic-based microsensor. *Nature*. 1992 Aug 20;358(6388):676-8.
271. Malloy P, Correia S, Stebbins G, Laidlaw DH. Neuroimaging of white matter in aging and dementia. *Clin Neuropsychol*. 2007 Jan;21(1):73-109.
272. Mangia S, Simpson IA, Vannucci SJ, Carruthers A. The in vivo neuron-to-astrocyte lactate shuttle in human brain: evidence from modeling of measured lactate levels during visual stimulation. *J Neurochem*. 2009; 109:55-62.
273. Marcoux FW, Morawetz RB, Crowell RM, DeGirolami U, Halsey JH Jr. Differential regional vulnerability in transient focal cerebral ischemia. *Stroke*. 1982 May-Jun;13(3):339-46.
274. Margail I, Allix M, Boulu RG, Plotkine M. Dose- and time-dependence of L-NAME neuroprotection in transient focal cerebral ischaemia in rats. *Br J Pharmacol*. 1997 Jan;120(1):160-3.
275. Margulescu AD, Sisu RC, Cinteza M, Vinereanu D. Noncardiogenic acute pulmonary edema due to severe hypoglycemia--an old but ignored cause. *Am J Emerg Med*. 2008;26:839.e3-839.e6.
276. Marik PE, Preiser JC. Toward understanding tight glycemic control in the ICU: a systematic review and metaanalysis. *Chest*. 2010;137:544-551.
277. Marion CM, Radomski KL, Cramer NP, Galdzicki Z, Armstrong RC. Experimental Traumatic Brain Injury Identifies Distinct Early and Late Phase Axonal Conduction Deficits of White Matter Pathophysiology, and Reveals Intervening Recovery. *J Neurosci*. 2018 Oct 10;38(41):8723-8736.

278. Marletta MA. Nitric oxide synthase: aspects concerning structure and catalysis. *Cell*. 1994 Sep 23;78(6):927-30.
279. Mason S. Lactate Shuttles in Neuroenergetics—Homeostasis, Allostasis and Beyond *Front Neurosci*. 2017; 11: 43.
280. Matsumura M, Nakashima A, Tofuku Y. Electrolyte disorders following massive insulin overdose in a patient with type 2 diabetes. *Intern Med*. 2000;39:55–57.
281. Matute C, Alberdi E, Domercq M, Pérez-Cerdá F, Pérez-Samartín A, Sánchez-Gómez MV. The link between excitotoxic oligodendroglial death and demyelinating diseases. *Trends Neurosci*. 2001 Apr;24(4):224-30.
282. Matute C, Alberdi E, Domercq M, Sánchez-Gómez MV, Pérez-Samartín A, Rodríguez-Antigüedad A, Pérez-Cerdá F. Excitotoxic damage to white matter. *J Anat*. 2007 Jun;210(6):693-702. Epub 2007 May 15.
283. Matute C, Domercq M, Fogarty DJ, Pascual de Zulueta M, Sánchez-Gómez MV. On how altered glutamate homeostasis may contribute to demyelinating diseases of the CNS. *Adv Exp Med Biol*. 1999;468:97-107.
284. Matute C, Domercq M, Sánchez-Gómez MV. Glutamate-mediated glial injury: mechanisms and clinical importance. *Glia*. 2006 Jan 15;53(2):212-24.
285. Matute C, Ransom BR. Roles of white matter in central nervous system pathophysiology. *ASN Neuro*. 2012 Mar 22;4(2).
286. Matute C, Sánchez-Gómez MV, Martínez-Millán L, Miledi R. Glutamate receptor-mediated toxicity in optic nerve oligodendrocytes. *Proc Natl Acad Sci U S A*. 1997 Aug 5;94(16):8830-5.
287. Matute C. Glutamate and ATP signalling in white matter pathology. *J Anat*. 2011 Jul;219(1):53-64.
288. Maxwell WL, Domleo A, McColl G, Jafari SS, Graham DI. Post-acute alterations in the axonal cytoskeleton after traumatic axonal injury. *J Neurotrauma*. 2003 Feb;20(2):151-68.
289. Maxwell WL, McCreath BJ, Graham DI, Gennarelli TA. Cytochemical evidence for redistribution of membrane pump calcium-ATPase and ecto-Ca-ATPase activity, and calcium influx in myelinated nerve fibres of the optic nerve after stretch injury. *J Neurocytol*. 1995 Dec;24(12):925-42.

290. McCarran WJ, Goldberg MP. White matter axon vulnerability to AMPA/kainate receptor-mediated ischemic injury is developmentally regulated. *J Neurosci*. 2007 Apr 11;27(15):4220-9.
291. McCracken E, Hunter AJ, Patel S, Graham DI, Dewar D. Calpain activation and cytoskeletal protein breakdown in the corpus callosum of head-injured patients. *J Neurotrauma*. 1999 Sep;16(9):749-61.
292. McDonald JW, Althomsons SP, Hyrc KL, Choi DW, Goldberg MP. Oligodendrocytes from forebrain are highly vulnerable to AMPA/kainate receptor-mediated excitotoxicity. *Nat Med*. 1998 Mar;4(3):291-7.
293. McEwen BS, Alves SE. Estrogen actions in the central nervous system. *Endocr Rev*. 1999 Jun;20(3):279-307.
294. McIlwain H, Buchel L, Cheshire JD. The inorganic phosphate and phosphocreatine of Brain especially during metabolism in vitro. *Biochem J*. 1951 Jan;48(1):12-20.
295. McIlwain H. Substances which support respiration and metabolic response to electrical impulses in human cerebral tissues. *J Neurol Neurosurg Psychiatry* 1953; 16:257-266.
296. Meakin PJ, Fowler MJ, Rathbone AJ, Allen LM, Ransom BR, Ray DE, Brown AM. Fructose metabolism in the adult mouse optic nerve, a central white matter tract. *J Cereb Blood Flow Metab*. 2007 Jan;27(1):86-99.
297. Menni F, de Lonlay P, Sevin C, Touati G, Peigné C, Barbier V, Nihoul-Fékété C, Saudubray JM, Robert JJ. Neurologic outcomes of 90 neonates and infants with persistent hyperinsulinemic hypoglycemia. *Pediatrics*. 2001 Mar;107(3):476-9.
298. Menniti FS, Buchan AM, Chenard BL, Critchett DJ, Ganong AH, Guanowsky V, Seymour PA, Welch WM. CP-465,022, a selective noncompetitive AMPA receptor antagonist, blocks AMPA receptors but is not neuroprotective in vivo. *Stroke*. 2003 Jan;34(1):171-6.
299. Menniti FS, Chenard BL, Collins MB, Ducat MF, Elliott ML, Ewing FE, Huang JI, Kelly KA, Lazzaro JT, Pagnozzi MJ, Weeks JL, Welch WM, White WF. Characterization of the binding site for a novel class of noncompetitive alpha-amino-3-hydroxy-5-methyl-4-isoxazolepropionic acid receptor antagonists. *Mol Pharmacol*. 2000;58:131
300. Mergenthaler P, Lindauer U, Dienel GA, Meisel A. Sugar for the brain: the role of glucose in physiological and pathological brain function. *Trends Neurosci*. 2013 Oct;36(10):587-97.

301. Meyer N, Richter N, Fan Z, Siemonsmeier G, Pivneva T, Jordan P, Steinhäuser C, Semtner M1, Nolte C, Kettenmann H. Oligodendrocytes in the Mouse Corpus Callosum Maintain Axonal Function by Delivery of Glucose. *Cell Rep*. 2018 Feb 27;22(9):2383-2394.
302. Michenfelder JD, Milde JH. The relationship among canine brain temperature, metabolism, and function during hypothermia. *Anesthesiology*. 1991 Jul;75(1):130-6.
303. Micu I, Jiang Q, Coderre E, Ridsdale A, Zhang L, Woulfe J, Yin X, Trapp BD, McRory JE, Rehak R, Zamponi GW, Wang W, Stys PK. NMDA receptors mediate calcium accumulation in myelin during chemical ischaemia. *Nature*. 2006 Feb 23;439(7079):988-92.
304. Miller EW, Chang CJ. Fluorescent probes for nitric oxide and hydrogen peroxide in cell signaling. *Curr Opin Chem Biol*. 2007 Dec;11(6):620-5.
305. Mishriki YY. Hypoglycemia-induced neurogenic-type pulmonary edema: an underrecognized association. *Endocr Pract*. 2004;10:429–431.
306. Momiyama A, Feldmeyer D, Cull-Candy SG. Identification of a native low-conductance NMDA channel with reduced sensitivity to Mg²⁺ in rat central neurones. *J Physiol*. 1996 Jul 15;494 (Pt 2):479-92.
307. Moody DM, Bell MA, Challa VR. Features of the cerebral vascular pattern that predict vulnerability to perfusion or oxygenation deficiency: an anatomic study. *American J of Neuroradiol*. 1990; 11:431–439.
308. Morilak DA, Fornal CA, Jacobs BL. Effects of physiological manipulations on locus coeruleus neuronal activity in freely moving cats. III. Glucoregulatory challenge. *Brain Res*. 1987 Sep 29;422(1):32-9.
309. Morrison BM, Lee Y, Rothstein JD. Oligodendroglia: metabolic supporters of axons. *Trends Cell Biol*. 2013 Dec;23(12):644-51
310. Mosley CA, Acker TM, Hansen KB, Mullasseril P, Andersen KT, Le P, Vellano KM, Bräuner-Osborne H, Liotta DC, Traynelis SF. Quinazolin-4-one Derivatives: A Novel Class of Noncompetitive NR2C/D Subunit-Selective N-Methyl-d-aspartate Receptor Antagonists. *J. Med. Chem*. 2010 53;5476–5490
311. Murakami Y, Yamashita Y, Matsuishi T, Utsunomiya H, Okudera T, Hashimoto T. Cranial MRI of neurologically impaired children suffering from neonatal hypoglycaemia. *Pediatr Radiol*. 1999 Jan;29(1):23-7.

312. Murakmi Y, Yamashita Y, Matsuishi T, Utsunomiya T, Okudera T, Hashimoto T. Cranial MRI of neurologically impaired children suffering from neonatal hypoglycemia. *Pediatr radiol* 1999;29:23–7.
313. Musen G, Lyoo IK, Sparks CR, Weinger K, Hwang J, Ryan CM, *et al.*, Effects of type 1 diabetes on gray matter density as measured by voxel-based morphometry. *Diabetes*. 2006;55:326–333.
314. Nagafuji T, Sugiyama M, Matsui T. Temporal profiles of Ca²⁺/calmodulin-dependent and -independent nitric oxide synthase activity in the rat brain microvessels following cerebral ischemia. *Acta Neurochir Suppl (Wien)*. 1994;60:285-8.
315. Nakanishi H, Kawachi A, Okada M, Fujiwara M, Yamamoto K. Protective effect of MK-801 on the anoxia-aglycemia induced damage in the fluorocitrate-treated hippocampal slice of the rat. *Brain Res*. 1996 Sep 2;732(1-2):232-6.
316. Namba T, Morimoto K, Sato K, Yamada N, Kuroda S. Antiepileptogenic and anticonvulsant effects of NBQX, a selective AMPA receptor antagonist, in the rat kindling model of epilepsy. *Brain Res*. 1994 Feb 28;638(1-2):36-44.
317. Nathan C, Xie QW. Regulation of biosynthesis of nitric oxide. *J Biol Chem*. 1994 May 13;269(19):13725-8.
318. Nave KA, Ehrenreich H. Myelination and oligodendrocyte functions in psychiatric diseases. *JAMA Psychiatry*. 2014; 71:582–584.
319. Nave KA. Myelination and support of axonal integrity by glia. *Nature*. 2010a; 468:244–252.
320. Nave KA. Myelination and the trophic support of long axons. *Nature Reviews Neuroscience*. 2010b; 11:275–283.
321. Negishi M, Shimomura K, Proks P, Mori M, Shimomura Y. Mechanism of disopyramide-induced hypoglycaemia in a patient with Type 2 diabetes. *Diabet Med*. 2009;26:76–78.
322. Neumiller JJ, Setter SM, Gates BJ, Sonnett TE, Dobbins EK, Campbell K. Pharmacological management of glycemic control in the geriatric patient with type 2 diabetes mellitus. *Consult Pharm*. 2009;24:45–63.
323. Northam EA, Rankins D, Lin A, Wellard RM, Pell GS, Finch SJ, Werther GA, Cameron FJ. Central nervous system function in youth with type 1 diabetes 12 years after disease onset. *Diabetes Care*. 2009 Mar;32(3):445-50. doi: 10.2337/dc08-1657. Epub 2009 Jan 16.

324. Nuñez ML, Penela MM, da Costa JC. Differences in the dynamics of frontal sharp transients in normal and hypoglycemic newborns. *Clin Neurophysiol.* 2000 Feb;111(2):305-10.
325. Oe Y, Baba O, Ashida H, Nakamura KC, Hirase H. Glycogen distribution in the microwave-fixed mouse brain reveals heterogeneous astrocytic patterns. *Glia.* 2016 Sep;64(9):1532-45.
326. Oka A, Belliveau MJ, Rosenberg PA, Volpe JJ. Vulnerability of oligodendroglia to glutamate: pharmacology, mechanisms, and prevention. *J Neurosci.* 1993 Apr;13(4):1441-53.
327. Okonkwo DO, Büki A, Siman R, Povlishock JT. Cyclosporin A limits calcium-induced axonal damage following traumatic brain injury. *Neuroreport.* 1999 Feb 5;10(2):353-8.
328. Okonkwo DO, Povlishock JT. An intrathecal bolus of cyclosporin A before injury preserves mitochondrial integrity and attenuates axonal disruption in traumatic brain injury. *J Cereb Blood Flow Metab.* 1999 Apr;19(4):443-51.
329. Orrenius S, Nicotera P. The calcium ion and cell death. *J Neural Transm Suppl.* 1994; 43:1-11.
330. Ouardouz M, Coderre E, Basak A, Chen A, Zamponi GW, Hameed S, Rehak R, Yin X, Trapp BD, Stys PK. Glutamate receptors on myelinated spinal cord axons: I. GluR6 kainate receptors. *Ann Neurol.* 2009a Feb;65(2):151-9.
331. Ouardouz M, Coderre E, Zamponi GW, Hameed S, Yin X, Trapp BD, Stys PK. Glutamate receptors on myelinated spinal cord axons: II. AMPA and GluR5 receptors. *Ann Neurol.* 2009b Feb;65(2):160-6.
332. Palmer GC. Neuroprotection by NMDA receptor antagonists in a variety of neuropathologies. *Curr Drug Targets.* 2001 Sep;2(3):241-71.
333. Pan WH, Cedres LB, Liu K, Dyer A, Schoenberger JA, Shekelle RB, Stamler R, Smith D, Collette P, Stamler J. Relationship of clinical diabetes and asymptomatic hyperglycemia to risk of coronary heart disease mortality in men and women. *Am J Epidemiol.* 1986 Mar;123(3):504-16.
334. Pantoni L, Garcia JH, Gutierrez JA. Cerebral white matter is highly vulnerable to ischemia. *Stroke.* 1996 Sep;27(9):1641-6; discussion 1647.
335. Park CK, Nehls DG, Graham DI, Teasdale GM, McCulloch J. The glutamate antagonist MK-801 reduces focal ischemic brain damage in the rat. *Ann Neurol.* 1988 Oct;24(4):543-51.

336. Patneau DK, Wright PW, Winters C, Mayer ML, Gallo V. Glial cells of the oligodendrocyte lineage express both kainate- and AMPA-preferring subtypes of glutamate receptor. *Neuron*. 1994 Feb;12(2):357-71.
337. Pedersen-Bjergaard U, Pramming S, Heller SR, Wallace TM, Rasmussen AK, Jørgensen HV, et al. Severe hypoglycaemia in 1076 adult patients with type 1 diabetes: Influence of risk markers and selection. *Diabetes Metab Res Rev*. 2004;20:479–86.
338. Pellerin L, Magistretti PJ. Glutamate uptake into astrocytes stimulates aerobic glycolysis: a mechanism coupling neuronal activity to glucose utilization. *Proc Natl Acad Sci U S A*. 1994 Oct 25;91(22):10625-9.
339. Pellerin L, Magistretti PJ. How to balance the brain energy budget while spending glucose differently. *J Physiol*. 2003 Jan 15;546(Pt 2):325.
340. Pellerin L, Magistretti PJ. Neuroscience. Let there be (NADH) light. *Science*. 2004 Jul 2;305(5680):50-2.
341. Pellerin L, Pellegrini G, Bittar PG, Charnay Y, Bouras C, Martin JL, Stella N, Magistretti PJ. Evidence supporting the existence of an activity-dependent astrocyte- neuron lactate shuttle. *Dev Neurosci*. 1998; 20:291–299.
342. Pfeiffer S, Leopold E, Schmidt K, Brunner F, Mayer B. Inhibition of nitric oxide synthesis by NG-nitro-L-arginine methyl ester (L-NAME): requirement for bioactivation to the free acid, NG-nitro-L-arginine. *Br J Pharmacol*. 1996 Jul;118(6):1433-40.
343. Philp NJ, Yoon H, Lombardi L. Mouse MCT3 gene is expressed preferentially in retinal pigment and choroid plexus epithelia. *Am J Physiol Cell Physiol*. 2001 May;280(5):C1319-26.
344. Pierre K, Pellerin L, Debernardi R, Riederer BM, Magistretti PJ. Cell-specific localization of monocarboxylate transporters, MCT1 and MCT2, in the adult mouse brain revealed by double immunohistochemical labeling and confocal microscopy. *Neuroscience*. 2000;100(3):617-27.
345. Pierre K, Pellerin L. Monocarboxylate transporters in the central nervous system: distribution, regulation and function. *J Neurochem*. 2005 Jul;94(1):1-14.
346. Pike BR, Zhao X, Newcomb JK, Posmantur RM, Wang KK, Hayes RL. Regional calpain and caspase-3 proteolysis of alpha-spectrin after traumatic brain injury. *Neuroreport*. 1998 Aug 3;9(11):2437-42.

347. Poole RC, Sansom CE, Halestrap AP. Studies of the membrane topology of the rat erythrocyte H⁺/lactate cotransporter (MCT1). *Biochem J.* 1996; 320:817–824.
348. Poon KWC, Brideau C, Klaver R, Schenk GJ, Geurts JJ, Stys PK. Lipid biochemical changes detected in normal appearing white matter of chronic multiple sclerosis by spectral coherent Raman imaging. *Chem Sci.* 2018 Jan 2;9(6):1586-1595.
349. Potocnik I, Tomsic M, Sketelj J, Bajrovic FF. Articaine is more effective than lidocaine or mepivacaine in rat sensory nerve conduction block in vitro. *J Dent Res.* 2006 Feb;85(2):162-6.
350. Pramming S, Thorsteinsson B, Bendtson I, Binder C. Symptomatic hypoglycaemia in 411 type 1 diabetic patients. *Diabet Med.* 1991;8:217–22.
351. Raff MC and Miller RH. Glial cell development in the rat optic nerve. *Trends in Neurosciences.* 1984; 7, pp.469–472
352. Raichle ME, Gusnard DA. Appraising the brain's energy budget. *Proc Natl Acad Sci U S A.* 2002 Aug 6;99(16):10237-9.
353. Ransom BR, Fern R. Does astrocytic glycogen benefit axon function and survival in CNS white matter during glucose deprivation? *Glia.* 1997 Sep;21(1):134-41.
354. Ransom BR, Orkand RK. Glial-neuronal interactions in non-synaptic areas of the brain: studies in the optic nerve. *Trends Neurosci.* 1996 Aug;19(8):352-8.
355. Razavi Nematollahi L, Kitabchi AE, Stentz FB, Wan JY, Larijani BA, Tehrani MM, Gozashti MH, Omidfar K, Taheri E. Proinflammatory cytokines in response to insulin-induced hypoglycemic stress in healthy subjects. *Metabolism.* 2009 Apr;58(4):443-8.
356. Redford EJ, Kapoor R, Smith KJ. Nitric oxide donors reversibly block axonal conduction: demyelinated axons are especially susceptible. *Brain.* 1997 Dec;120 (Pt 12):2149-57.
357. Reeves TM, Phillips LL, Povlishock JT. Myelinated and unmyelinated axons of the corpus callosum differ in vulnerability and functional recovery following traumatic brain injury. *Exp Neurol.* 2005 Nov;196(1):126-37.
358. Ribas VT, Lingor P. Calcium channel inhibition-mediated axonal stabilization improves axonal regeneration after optic nerve crush. *Neural Regen Res.* 2016 Aug;11(8):1245-6
359. Richardson JT. Cognitive function in diabetes mellitus. *Neurosci Biobehav Rev.* 1990 Winter;14(4):385-8.

360. Rogawski MA. Low affinity channel blocking (uncompetitive) NMDA receptor antagonists as therapeutic agents--toward an understanding of their favorable tolerability. *Amino Acids*. 2000;19(1):133-49.
361. Rosenberg LJ, Teng YD, Wrathall JR. 2,3-Dihydroxy-6-nitro-7-sulfamoylbenzo(f)quinoxaline reduces glial loss and acute white matter pathology after experimental spinal cord contusion. *J Neurosci*. 1999 Jan 1;19(1):464-75.
362. Rossi DJ, Oshima T, Attwell D. Glutamate release in severe brain ischaemia is mainly by reversed uptake. *Nature*. 2000 Jan 20;403(6767):316-21.
363. Royeck M, Nishiyama A, Dietrich D. Persistence of neuronal transmitter release onto oligodendrocyte precursor cells during progressive myelination in the mouse optic tract. *Soc Neurosci Abstr*. 2010;36:554-11
364. Saab AS, Tzvetavona ID, Trevisiol A, Baltan S, Dibaj P, Kusch K, Möbius W, Goetze B, Jahn HM, Huang W, Steffens H, Schomburg ED, Pérez-Samartín A, Pérez-Cerdá F, Bakhtiari DO, Matute C, Löwel S, Griesinger CO, Hirrlinger J, Kirchhoff F, Nave KA. Oligodendroglial NMDA Receptors Regulate Glucose Import and Axonal Energy Metabolism. *Neuron*. 2016 Jul 6;91(1):119-32.
365. Salter MG, Fern R. NMDA receptors are expressed in developing oligodendrocyte processes and mediate injury. *Nature*. 2005 Dec 22;438(7071):1167-71.
366. Sánchez-Gómez MV, Alberdi E, Ibarretxe G, Torre I, Matute C. Caspase-dependent and caspase-independent oligodendrocyte death mediated by AMPA and kainate receptors. *J Neurosci*. 2003 Oct 22;23(29):9519-28.
367. Sánchez-Gómez MV, Matute C. AMPA and kainate receptors each mediate excitotoxicity in oligodendroglial cultures. *Neurobiol Dis*. 1999 Dec;6(6):475-85.
368. Sandberg M, Butcher SP, Hagberg H. Extracellular overflow of neuroactive amino acids during severe insulin-induced hypoglycemia: in vivo dialysis of the rat hippocampus. *J Neurochem*. 1986 Jul;47(1):178-84.
369. Sandberg M, Nyström B, Hamberger A. Metabolically derived aspartate--elevated extracellular levels in vivo in Iodoacetate poisoning. *J Neurosci Res*. 1985;13(4):489-95.
370. Saraya A, Yokokura M, Gono T, Seino S. Effects of fluoroquinolones on insulin secretion and beta-cell ATP-sensitive K⁺ channels. *Eur J Pharmacol*. 2004;497:111-117.

371. Schäbitz WR, Li F, Fisher M. The N-methyl-D-aspartate antagonist CNS 1102 protects cerebral gray and white matter from ischemic injury following temporary focal ischemia in rats. *Stroke*. 2000 Jul;31(7):1709-14.
372. Schoonhoven R, Stegeman DF. Models and analysis of compound nerve action potentials. *Crit Rev Biomed Eng*. 1991;19(1):47-111.
373. Schurr AC, Miller JJ, Payne RS, Rigor BM. An increase in lactate output by brain tissue serves to meet the energy needs of glutamate-activated neurons. *J Neurosci*. 1999; 19:34-39.
374. Schurr AC, Payne RS, Miller JJ, Rigor BM. Brain lactate is an obligatory aerobic substrate for functional recovery after hypoxia: further in vitro validation. *J Neurochem*. 1997b; 69:423-426.
375. Schurr AC, Payne RS, Miller JJ, Rigor BM. Brain lactate, not glucose, fuels the recovery of synaptic function from hypoxia upon reoxygenation: an in vitro study. *Brain Res*. 1997a; 744:105-11.
376. Schurr AC, Rigor BM. 1995. The pharmacology of excitotoxins and energy deprivation in hippocampal slices. In *Brain Slices in Basic and Clinical Research* (Schurr A., and Rigor B.M., eds.), pp 221-241. CRC Press, Boca Raton.
377. Schurr AC, West CA and Rigor BM. Lactate-supported synaptic function in the rat hippocampal slice preparation. *Science*. 1988; 240:1326-1328.
378. Shaefi S, Mittel AM, Hyam JA, Boone MD, Chen CC, Kasper EM. Hypothermia for severe traumatic brain injury in adults: Recent lessons from randomized controlled trials. *Surg Neurol Int*. 2016 Nov 28;7:103.
379. Sheardown MJ, Nielsen EO, Hansen AJ, Jacobsen P, Honoré T. 2,3-Dihydroxy-6-nitro-7-sulfamoyl-benzo(F)quinoxaline: a neuroprotectant for cerebral ischemia. *Science*. 1990 Feb 2;247(4942):571-4.
380. Sheardown MJ, Suzdak PD, Nordholm L. AMPA, but not NMDA, receptor antagonism is neuroprotective in gerbil global ischaemia, even when delayed 24 h. *Eur J Pharmacol*. 1993 Jun 4;236(3):347-53.
381. Shibuki K, Okada D. Endogenous nitric oxide release required for long-term synaptic depression in the cerebellum. *Nature* 1991;349:326–328.

382. Shimamoto K, Lebrun B, Yasuda-Kamatani Y, Sakaitani M, Shigeri Y, Yumoto N, Nakajima T. DL-threo-beta-benzyloxyaspartate, a potent blocker of excitatory amino acid transporters. *Mol Pharmacol*. 1998 Feb;53(2):195-201.
383. Shimizu-Sasamata M, Kawasaki-Yatsugi S, Okada M, Sakamoto S, Yatsugi S, Togami J, Hatanaka K, Ohmori J, Koshiya K, Usuda S, Murase K. YM90K: pharmacological characterization as a selective and potent alpha-amino-3-hydroxy-5-methylisoxazole-4-propionate/kainate receptor antagonist. *J Pharmacol Exp Ther*. 1996 Jan;276(1):84-92.
384. Shirayama H, Ohshiro Y, Kinjo Y, Taira S, Teruya I, Nakachi K, *et al.*, Acute brain injury in hypoglycaemia-induced hemiplegia. *Diabet Med* 2004;21(6):623-4.
385. Shorr RI, Ray WA, Daugherty JR, Griffin MR. Incidence and risk factors for serious hypoglycemia in older persons using insulin or sulfonylureas. *Arch Intern Med*. 1997 Aug 11-25;157(15):1681-6.
386. Shrager P, Custer AW, Kazarinova K, Rasband MN, Mattson D. Nerve conduction block by nitric oxide that is mediated by the axonal environment. *J Neurophysiol*. 1998 Feb;79(2):529-36.
387. Shrager P, Youngman M. Preferential conduction block of myelinated axons by nitric oxide. *J Neurosci Res*. 2017 Jul;95(7):1402-1414
388. Siesjö BK, editor. *Brain energy metabolism*. New York: Wiley; 1978.
389. Siesjö BK. Hypoglycemia, brain metabolism, and brain damage. *Diabetes Metab Rev*. 1988 Mar;4(2):113-44.
390. Siesjö BK. Pathophysiology and treatment of focal cerebral ischemia. Part I: Pathophysiology. *J Neurosurg*. 1992 Aug;77(2):169-84.
391. Simons M, Nave KA. Oligodendrocytes: Myelination and Axonal Support. *Cold Spring Harb Perspect Biol*. 2015 Jun 22;8(1):a020479.
392. Simpson IA, Carruthers A, Vannucci SJ. Supply and demand in cerebral energy metabolism: the role of nutrient transporters. *J Cereb Blood Flow Metab*. 2007; 27:1766-1791.
393. Smith KJ, Kapoor R, Hall SM, Davies M. Electrically active axons degenerate when exposed to nitric oxide. *Ann Neurol*. 2001 Apr;49(4):470-6.
394. Sokoloff L. The metabolism of the central nervous system in vivo. In: Field J, Magoun H, Hall V, editors. *Handbook of physiology*. Washington D.C.: American Physiological Society; 1960. pp. 1843–1864.

395. Sommerfield AJ, Wilkinson IB, Webb DJ, Frier BM. Vessel wall stiffness in type 1 diabetes and the central hemodynamic effects of acute hypoglycemia. *Am J Physiol Endocrinol Metab.* 2007 Nov;293(5):E1274-9.
396. Sorg O, Magistretti PJ. Characterization of the glycogenolysis elicited by vasoactive intestinal peptide, noradrenaline and adenosine in primary cultures of mouse cerebral cortical astrocytes. *Brain Res.* 1991 Nov 1;563(1-2):227-33.
397. Sorg O, Magistretti PJ. Characterization of the glycogenolysis elicited by vasoactive intestinal peptide, noradrenaline and adenosine in primary cultures of mouse cerebral cortical astrocytes. *Brain Res.* 1991 Nov 1;563(1-2):227-33.
398. Sorlini M, Benini F, Cravarezza P, Romanelli G. Hypoglycemia, an atypical early sign of hepatocellular carcinoma. *J Gastrointest Cancer.* 2010;41:209–211.
399. Sotelo-Hitschfeld T, Fernández-Moncada I, Barros LF. Acute feedback control of astrocytic glycolysis by lactate. *Glia.* 2012 Apr;60(4):674-80.
400. Steinhäuser C, Gallo V. News on glutamate receptors in glial cells. *Trends Neurosci.* 1996 Aug;19(8):339-45.
401. Stirling DP, Stys PK. Mechanisms of axonal injury: internodal nanocomplexes and calcium deregulation. *Trends Mol Med.* 2010 Apr;16(4):160-70.
402. Stittsworth JD, Lanthorn TH. Lactate mimics only some effects of D-glucose on epileptic depolarization and long-term synaptic failure. *Brain Res.* 1993; 630: 21-27.
403. Sturrock, R. R. Myelination of the mouse corpus callosum. *Neuropathol. Appl. Neurobiol.* (1980).6, 415–420
404. Stys PK, Ransom BR, Waxman SG, Davis PK. Role of extracellular calcium in anoxic injury of mammalian central white matter. *Proc Natl Acad Sci U S A.* 1990 Jun;87(11):4212-6.
405. Stys PK, Ransom BR, Waxman SG. Compound action potential of nerve recorded by suction electrode: a theoretical and experimental analysis. *Brain Res.* 1991 Apr 12;546(1):18-32.
406. Stys PK, Waxman SG, Ransom BR. Ionic mechanisms of anoxic injury in mammalian CNS white matter: role of Na⁺ channels and Na⁽⁺⁾-Ca²⁺ exchanger. *J Neurosci.* 1992a Feb;12(2):430-9.
407. Stys PK. Anoxic and ischemic injury of myelinated axons in CNS white matter: from mechanistic concepts to therapeutics. *J Cereb Blood Flow Metab.* 1998 Jan;18(1):2-25.

408. Stys PK. General mechanisms of axonal damage and its prevention. *Neurol Sci.* 2005 Jun 15;233(1-2):3-13.
409. Stys PK. White matter injury mechanisms. *Curr Mol Med.* 2004 Mar;4(2):113-30.
410. Stys PK1, Waxman SG, Ransom BR. Effects of temperature on evoked electrical activity and anoxic injury in CNS white matter. *J Cereb Blood Flow Metab.* 1992b Nov;12(6):977-86.
411. Su J, Wang L. Research advances in neonatal hypoglycemic brain injury. *Transl Pediatr.* 2012 Oct;1(2):108-15.
412. Suh SW, Frederickson CJ, Danscher G. Neurotoxic zinc translocation into hippocampal neurons is inhibited by hypothermia and is aggravated by hyperthermia after traumatic brain injury in rats. *J Cereb Blood Flow Metab.* 2006 Feb;26(2):161-9.
413. Suh SW, Gum ET, Hamby AM, Chan PH, Swanson RA. Hypoglycemic neuronal death is triggered by glucose reperfusion and activation of neuronal NADPH oxidase. *J Clin Invest.* 2007a Apr;117(4):910-8.
414. Suh SW, Hamby AM, Swanson RA. Hypoglycemia, brain energetics, and hypoglycemic neuronal death. *Glia.* 2007b Sep;55(12):1280-6.
415. Sünwoldt J, Bosche B, Meisel A, Mergenthaler P. Neuronal Culture Microenvironments Determine Preferences in Bioenergetic Pathway Use. *Front Mol Neurosci.* 2017 Sep 29;10:305.
416. Suzuki A, Stern SA, Bozdagi O, Huntley GW, Walker RH, Magistretti PJ, Alberini CM. Astrocyte-neuron lactate transport is required for long-term memory formation. *Cell* 2011; 44:810-823hall
417. Suzuki A, Stern SA, Bozdagi O, Huntley GW, Walker RH, Magistretti PJ, Alberini CM. Astrocyte-neuron lactate transport is required for long-term memory formation. *Cell* 2011; 44:810-823
418. Swanson, RA. Glucose, Acid, and Aspartate: Friends and Foes of the Axon. *Ann Neurol.* 2014 Apr; 75(4): 490–491.
419. Taguchi Y, Kamiyama H, Kubo M, Horie Y. Internal capsule and splenial lesions in hypoglycemic hemiparesis. *Intern Med.* 2011;50:533–534.
420. Takata T, Hirai H, Shigemoto T, Okada Y. The release of glutamate and accumulation of intracellular calcium in the guinea pig hippocampal slices during glucose deprivation. *Neurosci Lett.* 1995 Apr 7;189(1):21-4.

421. Takata T, Okada Y. Effects of deprivation of oxygen or glucose on the neural activity in the guinea pig hippocampal slice--intracellular recording study of pyramidal neurons. *Brain Res.* 1995 Jun 12;683(1):109-16.
422. Talos DM, Fishman RE, Park H, Folkerth RD, Follett PL, Volpe JJ, Jensen FE. Developmental regulation of alpha-amino-3-hydroxy-5-methyl-4-isoxazole-propionic acid receptor subunit expression in forebrain and relationship to regional susceptibility to hypoxic/ischemic injury. I. Rodent cerebral white matter and cortex. *J Comp Neurol.* 2006a Jul 1;497(1):42-60.
423. Talos DM, Follett PL, Folkerth RD, Fishman RE, Trachtenberg FL, Volpe JJ, Jensen FE. Developmental regulation of alpha-amino-3-hydroxy-5-methyl-4-isoxazole-propionic acid receptor subunit expression in forebrain and relationship to regional susceptibility to hypoxic/ischemic injury. II. Human cerebral white matter and cortex. *J Comp Neurol.* 2006b Jul 1;497(1):61-77.
424. Talos DM, Follett PL, Folkerth RD, Fishman RE, Trachtenberg FL, Volpe JJ, Jensen FE. Developmental regulation of alpha-amino-3-hydroxy-5-methyl-4-isoxazole-propionic acid receptor subunit expression in forebrain and relationship to regional susceptibility to hypoxic/ischemic injury. II. Human cerebral white matter and cortex. *J Comp Neurol.* 2006 Jul 1;497(1):61-77.
425. Talos DM, Follett PL, Folkerth RD, Fishman RE, Trachtenberg FL, Volpe JJ, Jensen FE. Developmental regulation of alpha-amino-3-hydroxy-5-methyl-4-isoxazole-propionic acid receptor subunit expression in forebrain and relationship to regional susceptibility to hypoxic/ischemic injury. II. Human cerebral white matter and cortex. *J Comp Neurol.* 2006 Jul 1;497(1):61-77.
426. Tasker RC, Coyle JT, Vornov JJ. The regional vulnerability to hypoglycemia-induced neurotoxicity in organotypic hippocampal culture: protection by early tetrodotoxin or delayed MK-801. *J Neurosci.* 1992 Nov;12(11):4298-308.
427. Tekkök SB, Brown AM, Westenbroek R, Pellerin L, Ransom BR. Transfer of glycogen-derived lactate from astrocytes to axons via specific monocarboxylate transporters supports mouse optic nerve activity. *J Neurosci Res.* 2005b Sep 1;81(5):644-52.
428. Tekkök SB, Faddis BT, Goldberg MP. AMPA/kainate receptors mediate axonal morphological disruption in hypoxic white matter. *Neurosci Lett.* 2005a Jul 15;382(3):275-9.

429. Tekkök SB, Goldberg MP. Ampa/kainate receptor activation mediates hypoxic oligodendrocyte death and axonal injury in cerebral white matter. *J Neurosci*. 2001 Jun 15;21(12):4237-48.
430. Tekkök SB, Ye Z, Ransom BR. Excitotoxic mechanisms of ischemic injury in myelinated white matter. *J Cereb Blood Flow Metab*. 2007 Sep;27(9):1540-52.
431. ter Braak EW, Appelman AM, van de Laak M, Stolk RP, van Haeften TW, Erkelens DW. Clinical characteristics of type 1 diabetic patients with and without severe hypoglycemia. *Diabetes Care*. 2000;23:1467–71.
432. Tjalkens RB, Carbone DL, Wu G. Detection of nitric oxide formation in primary neural cells and tissues. *Methods Mol Biol*. 2011; 758:267-77
433. Tofade TS, Liles EA. Intentional overdose with insulin glargine and insulin aspart. *Pharmacotherapy*. 2004;24:1412–1418.
434. Traill Z, Squier M, Anslow P. Brain imaging in neonatal hypoglycaemia. *Arch Dis Child Fetal Neonatal Ed*. 1998 Sep;79(2):F145-7.
435. Trapp BD, Peterson J, Ransohoff RM, Rudick R, Mörk S, Bö L. Axonal transection in the lesions of multiple sclerosis. *N Engl J Med*. 1998 Jan 29;338(5):278-85.
436. Tsalikian E, Mauras N, Beck RW, Tamborlane WV, Janz KF, Chase HP, et al. Impact of exercise on overnight glycemic control in children with type 1 diabetes mellitus. *J Pediatr*. 2005;147:528–534.
437. Turski L, Huth A, Sheardown M, McDonald F, Neuhaus R, Schneider HH, Dirnagl U, Wiegand F, Jacobsen P, Ottow E. ZK200775: a phosphonate quinoxalinedione AMPA antagonist for neuroprotection in stroke and trauma. *Proc Natl Acad Sci U S A*. 1998 Sep 1;95(18):10960-5.
438. Uchida D, Ohigashi S, Hikita S, Kitamura N, Motoyoshi M, Tatsuno I. Acute pulmonary edema caused by hypoglycemia due to insulin overdose. *Intern Med*. 2004;43:1056–1059.
439. Uematsu D, Araki N, Greenberg JH, Sladky J, Reivich M. Combined therapy with MK-801 and nimodipine for protection of ischemic brain damage. *Neurology*. 1991 Jan;41(1):88-94.
440. Uematsu D, Greenberg JH, Reivich M, Karp A. Cytosolic free calcium, NAD/NADH redox state and hemodynamic changes in the cat cortex during severe hypoglycemia. *J Cereb Blood Flow Metab*. 1989 Apr;9(2):149-55.

441. UK Hypoglycaemia Study Group. Risk of hypoglycaemia in types 1 and 2 diabetes: effects of treatment modalities and their duration. *Diabetologia*. 2007 Jun;50(6):1140-7.
442. Underhill SM, Goldberg MP. Hypoxic injury of isolated axons is independent of ionotropic glutamate receptors. *Neurobiol Dis*. 2007 Feb;25(2):284-90.
443. Vaishnavi SN, Vlassenko AG, Rundle MM, Snyder AZ, Mintun MA, Raichle ME. Regional aerobic glycolysis in the human brain. *Proc Natl Acad Sci USA* 2010; 107:17757-17762.
444. Valeriani V, Dewar D, McCulloch J. Quantitative assessment of ischemic pathology in axons, oligodendrocytes, and neurons: attenuation of damage after transient ischemia. *J Cereb Blood Flow Metab*. 2000 May;20(5):765-71.
445. van Hall G, Stromstad M, Rasmussen P, Jans O, Zaar M, Gam C, Quistorff B, Secher NH, Nielsen HB. Blood lactate is an important energy source for the human brain. *J Cereb Blood Flow Metab*. 2009; 29:1121-1129.
446. van Veen BK, Schellens RL, Stegeman DF, Schoonhoven R, Gabreëls-Festen AA. Conduction velocity distributions compared to fiber size distributions in normal human sural nerve. *Muscle Nerve*. 1995 Oct;18(10):1121-7.
447. Vatsa A, Mizuno D, Smit TH, Schmidt CF, MacKintosh FC, Klein-Nulend J. Bio imaging of intracellular NO production in single bone cells after mechanical stimulation. *J Bone Miner Res*. 2006 Nov;21(11):1722-8.
448. Verkhratsky A, Orkand RK, Kettenmann H. Glial calcium: homeostasis and signaling function. *Physiol Rev*. 1998 Jan;78(1):99-141.
449. Volpe J. Hypoglycemia and brain injury. In: *Neurology of the newborn*. Philadelphia: Saunders; 2001. p. 97–520.
450. Wakita H, Tomimoto H, Akiguchi I, Kimura J. Protective effect of cyclosporin A on white matter changes in the rat brain after chronic cerebral hypoperfusion. *Stroke*. 1995 Aug;26(8):1415-22.
451. Waller A. Experiments on the Section of the Glosso-Pharyngeal and Hypoglossal Nerves of the Frog, and Observations of the Alterations Produced Thereby in the Structure of Their Primitive Fibres. *Edinb Med Surg J*. 1851 Oct 1;76(189):369-376.
452. Warburg O. On the origin of cancer cells. *Science* 1956; 123: 309-314
453. Ward RE, Huang W, Kostusiak M, Pallier PN, Michael-Titus AT, Priestley JV. A characterization of white matter pathology following spinal cord compression injury in the rat. *Neuroscience*. 2014 Feb 28;260:227-39.

454. Waxman SG, Bangalore L. Electrophysiologic consequences of myelination. In: Robert AL, John WG, Hans L, Klaus-Armin N, Robert M, Bruce DT (eds) Myelin biology and disorders. Academic, San Diego. 2004;pp 117–141
455. Waxman SG, Ransom BR, Stys PK. Non-synaptic mechanisms of Ca(2+)-mediated injury in CNS white matter. Trends Neurosci. 1991 Oct;14(10):461-8.
456. Waxman SG. Determinants of conduction velocity in myelinated nerve fibers. Muscle Nerve. 1980 Mar-Apr;3(2):141-50.
457. Wei HM, Chi OZ, Liu X, Sinha AK, Weiss HR. Nitric oxide synthase inhibition alters cerebral blood flow and oxygen balance in focal cerebral ischemia in rats. Stroke. 1994 Feb;25(2):445-9; discussion 449-50.
458. Wender R, Brown AM, Fern R, Swanson RA, Farrell K, Ransom BR. Astrocytic glycogen influences axon function and survival during glucose deprivation in central white matter. J Neurosci. 2000 Sep 15;20(18):6804-10.
459. Whitmer RA, Karter AJ, Yaffe K, Quesenberry CP Jr, Selby JV. Hypoglycemic episodes and risk of dementia in older patients with type 2 diabetes mellitus. JAMA. 2009 Apr 15;301(15):1565-72.
460. Whittam R. The dependence of the respiration of brain cortex on active cation transport. Biochem J. 1962 Jan;82:205-12.
461. Wieloch T. Hypoglycemia-induced neuronal damage prevented by an N-methyl-D-aspartate antagonist. Science. 1985 Nov 8;230(4726):681-3.
462. Williams PR, Marincu BN, Sorbara CD, Mahler CF, Schumacher AM, Griesbeck O, Kerschensteiner M, Misgeld T. A recoverable state of axon injury persists for hours after spinal cord contusion in vivo. Nat Commun. 2014 Dec 16;5:5683.
463. Workgroup on Hypoglycemia, American Diabetes Association. Defining and reporting hypoglycemia in diabetes: a report from the American Diabetes Association Workgroup on Hypoglycemia. Diabetes Care. 2005 May;28(5):1245-9.
464. Wrathall JR, Teng YD, Marriott R. Delayed antagonism of AMPA/kainate receptors reduces long-term functional deficits resulting from spinal cord trauma. Exp Neurol. 1997 Jun;145(2 Pt 1):565-73.
465. Wright A, Vissel B. The essential role of AMPA receptor GluR2 subunit RNA editing in the normal and diseased brain. Front Mol Neurosci. 2012 Apr 11;5:34.

466. Yakovlev AG, Knoblach SM, Fan L, Fox GB, Goodnight R, Faden AI. Activation of CPP32-like caspases contributes to neuronal apoptosis and neurological dysfunction after traumatic brain injury. *J Neurosci*. 1997 Oct 1;17(19):7415-24.
467. Yalnizoglu D, Halioglu G. Neurological outcome in patients with MRI pattern of damage typical for neonatal hypoglycemia. *Brain Dev* 2007;29:285–92.
468. Yam PS, Dewar D, McCulloch J. Axonal injury caused by focal cerebral ischemia in the rat. *J Neurotrauma*. 1998 Jun;15(6):441-50.
469. Yamamoto C, McIlwain H. Electrical activities in thin sections from the mammalian brain maintained in chemically-defined media in vitro. *J Neurochem*. 1966 Dec;13(12):1333-43.
470. Yang X, Hamner MA, Brown AM, Evans RD, Ye ZC, Chen S, Ransom BR. Novel hypoglycemic injury mechanism: N-methyl-D-aspartate receptor-mediated white matter damage. *Ann Neurol*. 2014 Apr;75(4):492-507.
471. Yang Y, Ke-Zhou L, Ning GM, Wang ML, Zheng XX. Dynamics of nitric oxide and peroxynitrite during global brain ischemia/reperfusion in rat hippocampus: NO-sensor measurement and modeling study. *Neurochem Res*. 2008 Jan;33(1):73-80. Epub 2007 Aug 4.
472. Yao J, Rettberg JR, Klosinski LP, Cadenas E, Brinton RD. Shift in brain metabolism in late onset Alzheimer's disease: implications for biomarkers and therapeutic interventions. *Mol Aspects Med*. 2011 Aug;32(4-6):247-57.
473. Yong Y, Gang-Min N, Zhuo-Hui G, Xiao-Xiang Z. Modeling the diffusion of nitric oxide produced by neuronal cells in brain ischemia. *Conf Proc IEEE Eng Med Biol Soc*. 2005;7:7321-4.
474. Yoshioka A, Yamaya Y, Saiki S, Kanemoto M, Hirose G, Beesley J, Pleasure D. Non-N-methyl-D-aspartate glutamate receptors mediate oxygen--glucose deprivation-induced oligodendroglial injury. *Brain Res*. 2000 Jan 31;854(1-2):207-15.
475. Young W. Role of calcium in central nervous system injuries. *J Neurotrauma*. 1992 Mar;9 Suppl 1:S9-25.
476. Yue SJ, Wang MJ, Wang QH, Yu XH, Yang YJ. Congenital hyperinsulinism: a difficult and complicated case study. *Zhongguo Dang Dai Er Ke Za Zhi*. 2006 Oct;8(5):391-4.

477. Zammitt NN, Geddes J, Warren RE, Marioni R, Ashby JP, Frier BM. Serum angiotensin-converting enzyme and frequency of severe hypoglycaemia in Type 1 diabetes: Does a relationship exist? *Diabet Med.* 2007;24:1449–54.
478. Zhang K, Sejnowski TJ. A universal scaling law between gray matter and white matter of cerebral cortex. *Proc Natl Acad Sci U S A.* 2000 May 9;97(10):5621-6.
479. Zhang ZG, Chopp M, Bailey F, Malinski T. Nitric oxide changes in the rat brain after transient middle cerebral artery occlusion. *J Neurol Sci.* 1995 Jan;128(1):22-7.
480. Ziskin JL, Nishiyama A, Rubio M, Fukaya M, Bergles DE. Vesicular release of glutamate from unmyelinated axons in white matter. *Nat Neurosci.* 2007 Mar;10(3):321-30.
481. Zoratti M, Szabò I. The mitochondrial permeability transition. *Biochim Biophys Acta.* 1995 Jul 17;1241(2):139-76.
482. Zuurmond HM, Hessling J, Blüml K, Lohse M, Ijzerman AP. Study of interaction between agonists and asn293 in helix VI of human beta(2)-adrenergic receptor. *Mol Pharmacol.* 1999 Nov;56(5):909-16.

Supplementary material

8.1 Probe localisation in microdialysis experiments

An intracranial guide (CMA/Microdialysis, Stockholm, Sweden) was implanted in the bilateral cerebellar white matter (coordinates toward bregma were 5.7 mm posterior, 2.2 mm lateral and 2.3 mm ventral of the dura (Paxinos and Franklin, 2004)). Probe localisation was histologically verified post-mortem (Fig. 9.1) and animals with aberrant probe location were excluded from the study.

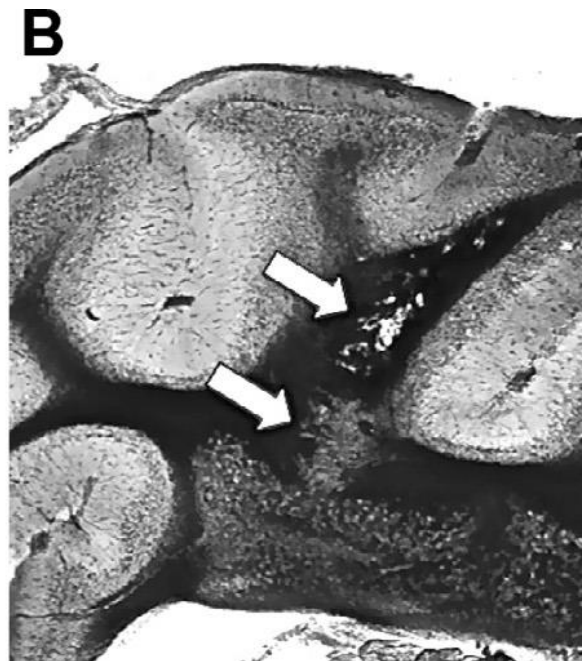


Figure 8.1. Representative image showing the site of insertion of the microdialysis probe. Arrows are indicating the tract of the probe. (Adapted from Laureys *et al.*, 2014)

8.2 Concentration of DMSO used is not toxic to YFP axons

There were no signs of axonal injury in slices exposed to 30 min of GD in DMSO, suggesting that the concentration of DMSO used to dissolve 4-CIN was did not exert any deleterious effect on callosal axons, and that the injury observed in section 3.4.2 was due to the 4-CIN induced axonal lactate uptake, and not DMSO.

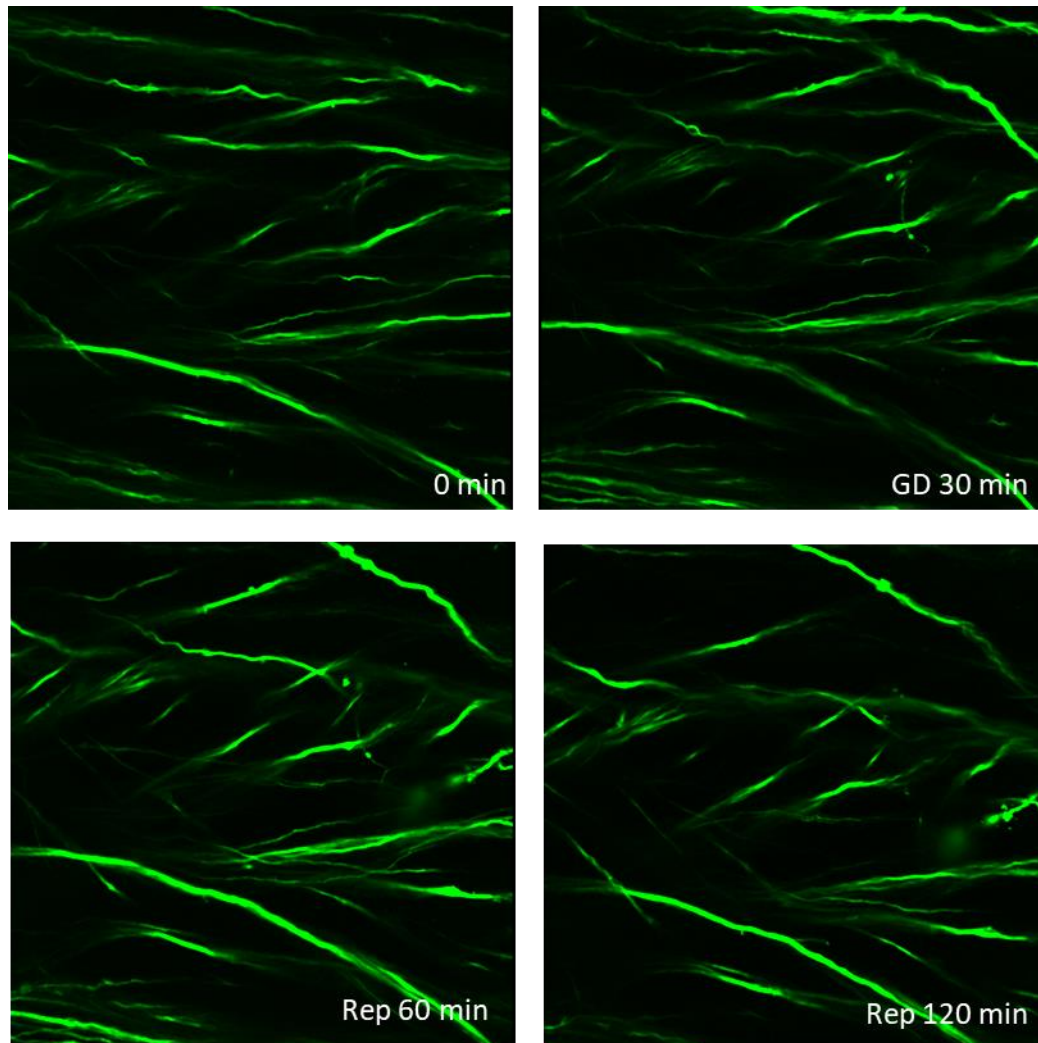


Figure 8.2. Sequential images of YFP axons exposed to 30 min GD in DMSO. There is no axonal injury in slices exposed to 30 mins of GD with DMSO and 2 hr reperfusion.

8.3 Vehicle injected mice exhibited normal physiology and pathology

Callosal slices from mice injected with the vehicle (β -cyclodextrin + DMSO) for 5 consecutive days, were incubated for 4 hours at 37°C. Other slices from the same group of mice were exposed to 45 min of GD and 2 hr of reperfusion with glucose-containing aCSF. Combined two-photon imaging and CAP recording from these slices, showed no sign of axonal injury and CAP was maintained throughout the course of the 4-hour incubation period in glucose-containing aCSF. On the other hand, there was severe structural axonal injury and loss of conduction in slices exposed to 45 min GD.

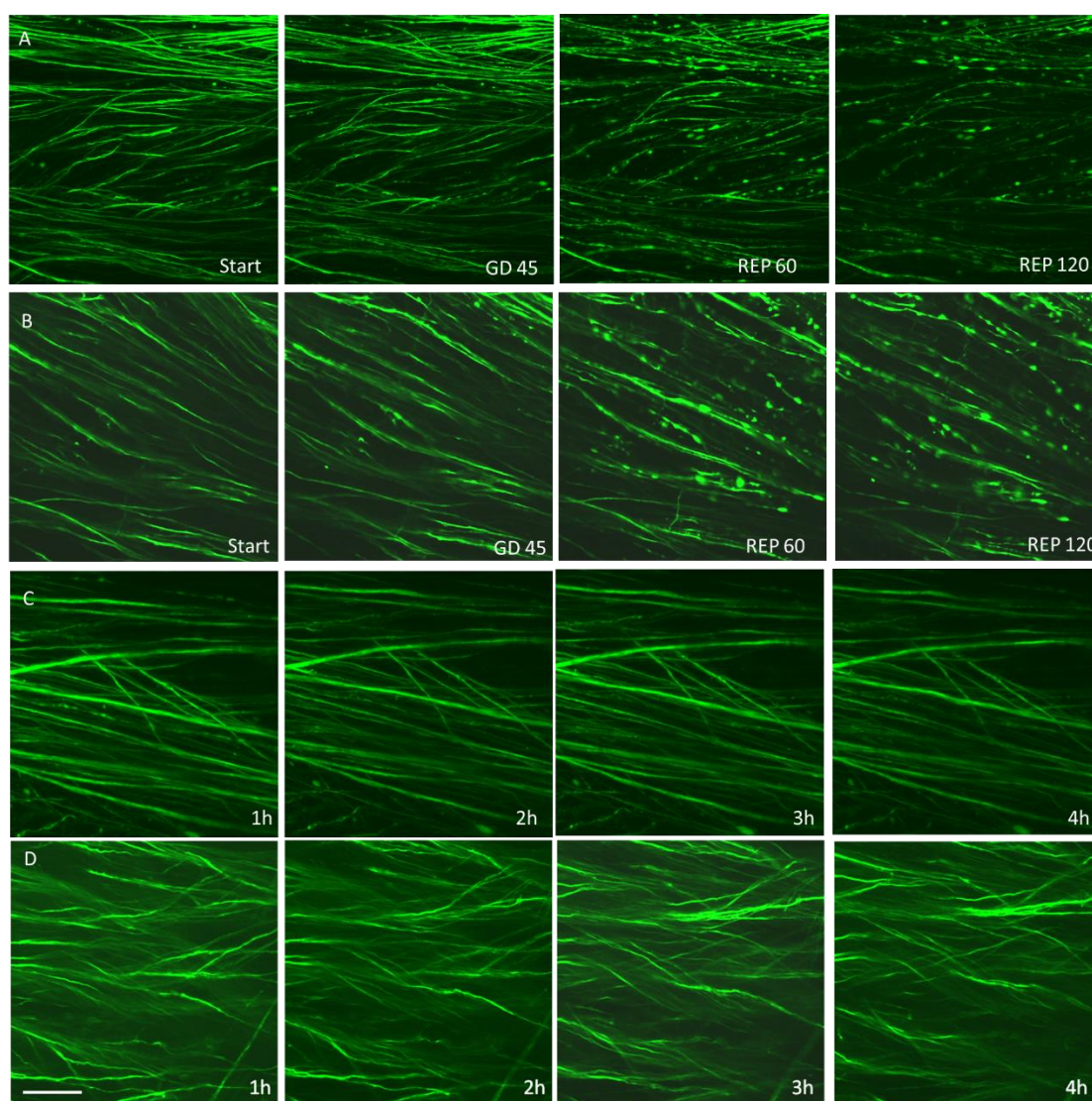


Figure 8.3. Sequential images of slices exposed to 45 min GD (+/-) and controls. Axonal beading and fragmentation during reperfusion in slices subjected to glucose deprivation with (A) and without (B) the vehicle. Normal axon morphology in slices exposed to 4 hours of glucose containing aCSF with (C) and without (D) the vehicle. Scale bar 20 μ m

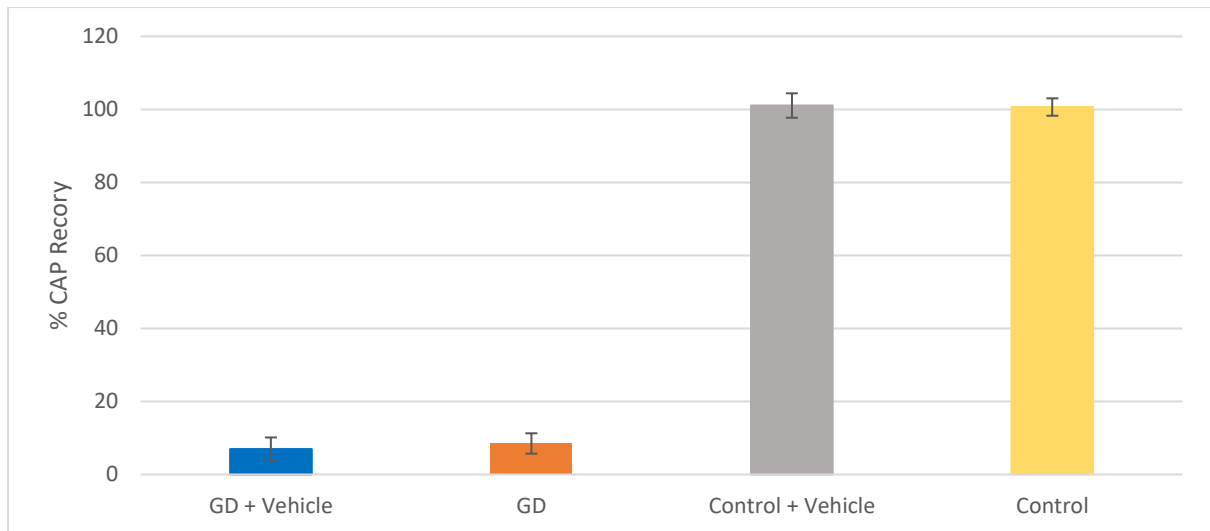


Figure 8.4. Percentage CAP recovery in slices exposed to 45 min GD and controls (+/-) the vehicle. There was no statistically significant difference in CAP recovery between control slices and slices exposed to 45 min of GD (+/-) vehicle.

8.4 Signal intensities of NO fluorescent dyes during glucose deprivation

We observed a consistent increase in the signal intensity during the initial phase of glucose deprivation from DAR-4M AM loaded slices in all 5 experimental runs (Table 9.1). On the contrary, out of the 6 experimental runs with slices loaded with DAF-FM DA, there was a mild increase in the signal in only 2 cases (Table 9.2).

	Start	GD 10	GD 20	GD 30	GD 45	REP 30	REP 60
<i>n</i> = 1	0	19	40	25	13	4	-14
<i>n</i> = 2	0	15	21	18	11	0	-9
<i>n</i> = 3	0	10	25	18	6	-2	-15
<i>n</i> = 4	0	13	30	25	19	-4	-18
<i>n</i> = 5	0	15	30	21	11	-6	-20
<i>Average</i>	0	14	29.2	21	12	-1.6	-15.2
<i>ST DEV</i>	<i>0</i>	<i>2.9</i>	<i>6.4</i>	<i>3.1</i>	<i>1.2</i>	<i>3.4</i>	<i>3.8</i>

Table 8.1. Percentage change from start in the signal intensity DAR-4M AM at different experimental time points

	Start	GD 10	GD 20	GD 30	GD 45	REP 30	REP 60
<i>n</i> = 1	0	6	11	9	8	5	1
<i>n</i> = 2	0	1	-1	1	0	-1	-2
<i>n</i> = 3	0	6	10	5	4	4	3
<i>n</i> = 4	0	1	1	-1	-1	-1	1
<i>n</i> = 5	0	1	1	2	1	1	1
<i>n</i> = 6	0	-1	1	-1	0	0	0
<i>Average</i>	0	2.3	3.6	3.5	2.62	1.5	0.3
<i>ST DEV</i>	0	2.7	4.6	4.8	3.8	2.6	1.1

Table 8.2. Percentage change from start in the signal intensity of DAF-FM DA at different experimental time points

The validity of the results obtained from the DAF-FM DA experiments were challenged by the fact that using one-way ANOVA followed by Tukey's post hoc test, there was a statistically significant difference ($p < 0.05$) between the 6 trials conducted. On the contrary, there was no statistically significant difference between the individual experimental runs concerning the DAR-4M AM loaded slices, highlighting the legitimacy of these results.

Taking into consideration all trials involving the slices loaded with DAF-FM DA, there was no statistically significant difference in signal intensity at any experimental time points between controls and slices exposed to glucose deprivation.

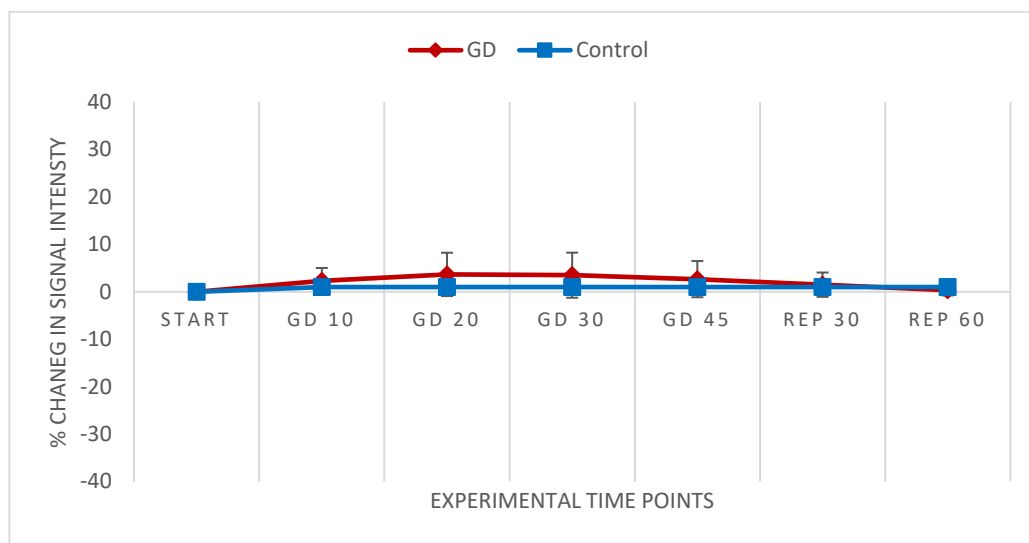


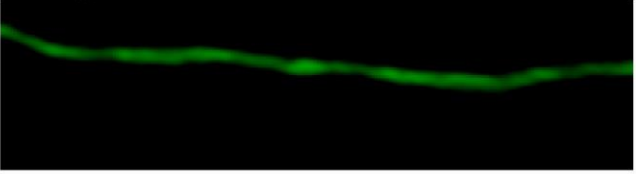
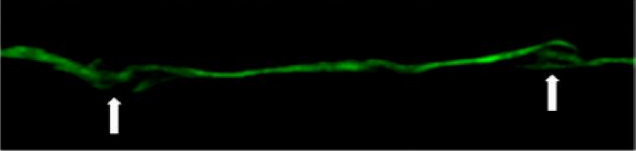
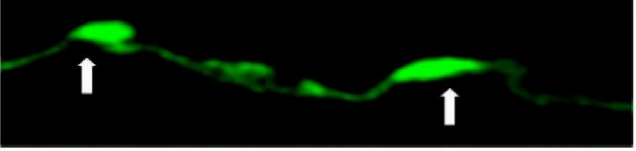
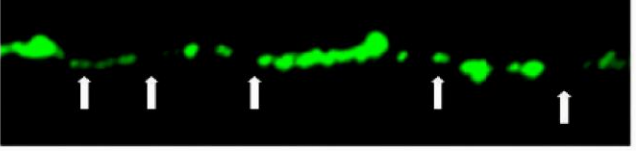
Figure 8.5. Percentage change in signal intensity in slices incubated in DAF-FM DA and exposed to 45 min of GD and controls. Comparison of the percentage change from start of the DAF-FM DA signal intensity between controls and slices exposed to glucose deprivation. No statistically significant difference in signal intensity between DAF-FM DA loaded control slices and similar slices exposed to 45 min GD. (n=6)

Publications

Alix JJ, Zammit C, Riddle A, Meshul CK, Back SA, Valentino M, Fern R. Central axons preparing to myelinate are highly sensitive [corrected] to ischemic injury. *Ann Neurol*. 2012 Dec;72(6):936-51. [*supplementary material*]

Laureys G, Valentino M, Demol F, Zammit C, Muscat R, Cambron M, Kooijman R, De Keyser J. β_2 -adrenergic receptors protect axons during energetic stress but do not influence basal glio-axonal lactate shuttling in mouse white matter. *Neuroscience*. 2014 Sep 26;277:367-74.

Doyle S, Hansen DB, Vella J, Bond P, Harper G, Zammit C, Valentino M, Fern R. Vesicular glutamate release from central axons contributes to myelin damage. *Nat Commun*. 2018 Mar 12;9(1):1032.

Score	Extent of injury	Example
0	No injury	
1	Focal swelling	
2	Beading	
3	Fragmentation	

Supplemental Figure 3

Examples of injury scoring in THY-1/GFP-M mice.

β_2 -ADRENERGIC RECEPTORS PROTECT AXONS DURING ENERGETIC STRESS BUT DO NOT INFLUENCE BASAL GLIO-AXONAL LACTATE SHUTTLING IN MOUSE WHITE MATTER

G. LAUREYS,^{a,*†} M. VALENTINO,^{b,†} F. DEMOL,^a
C. ZAMMIT,^c R. MUSCAT,^b M. CAMBRON,^a
R. KOIJMAN^{d,‡} AND J. DE KEYSER^{a,e,‡}

^a Department of Neurology, University Hospital Brussels, Center for Neurosciences, Vrije Universiteit Brussel, Laarbeeklaan 101, 1090 Brussels, Belgium

^b Department of Physiology and Biochemistry, Faculty of Medicine & Surgery, University of Malta, Msida MSD 2080, Malta

^c Department of Anatomy, Faculty of Medicine & Surgery, University of Malta, Msida MSD 2080, Malta

^d Experimental Pharmacology, Center for Neurosciences, Vrije Universiteit Brussel, Laarbeeklaan 103, 1090 Brussels, Belgium

^e Department of Neurology, University Medical Center Groningen, Groningen, The Netherlands

Abstract—*In vitro* studies have demonstrated that β_2 -adrenergic receptor activation stimulates glycogen degradation in astrocytes, generating lactate as a potential energy source for neurons. Using *in vivo* microdialysis in mouse cerebellar white matter we demonstrate continuous axonal lactate uptake and glial–axonal metabolic coupling of glutamate/lactate exchange. However, this physiological lactate production was not influenced by activation (clenbuterol) or blocking (ICI 118551) of β_2 -adrenergic receptors. In two-photon imaging experiments on *ex vivo* mouse corpus callosum subjected to aglycemia, β_2 -adrenergic activation rescued axons, whereas inhibition of axonal lactate uptake by α -cyano-4-hydroxycinnamic acid (4-CIN) was associated with severe axonal loss. Our results suggest that axonal protective effects of glial β_2 -adrenergic receptor activation are not mediated by enhanced lactate production.
© 2014 IBRO. Published by Elsevier Ltd. All rights reserved.

Key words: glucose, lactate, glutamate, white matter, axons, β_2 -adrenergic receptors.

INTRODUCTION

Recent data suggest that chronic failure of white matter energy metabolism plays a role in several

neurodegenerative diseases (Matute and Ransom, 2012) such as Alzheimer's disease (Yao et al., 2011), amyotrophic lateral sclerosis (Lee et al., 2012) and multiple sclerosis (Cambron et al., 2012).

Brain neuro-energetics is a major area of scientific debate with opposing opinions on how electro-active neurons and their surrounding “supportive” glial cells thrive or fail by exchange of glucose versus lactate as primary energetic substrates. Pellerin and Magistretti introduced the astrocyte–neuron lactate shuttle hypothesis (ANLSH) (Pellerin and Magistretti, 1994) in which synaptic glutamate-release is balanced by astrocytic re-uptake and conversion to glutamine. This process is supposed to be driven by astrocytic glycolysis that generates lactate, subsequently taken up by active neurons to fuel their energetic demands. However, with regard to synapses in gray matter there are experimental data both in favor (Sampol et al., 2013) and against (Hall et al., 2012) the ANLSH hypothesis. Applicability of the ANLSH to the white matter setting however remains largely unexplored and most data are derived from *ex vivo* studies in rodent optic nerve suggesting a role for glycogen-derived lactate as an energy source for axons (Wender et al., 2000; Tekkok et al., 2005). Most of the glycogen of the central nervous system white matter resides in astrocytes (Wender et al., 2000) and is converted to lactate which is released into the extracellular space. Axons in mouse white matter take-up lactate through the monocarboxylate transporter (MCT)-2 (Tekkok et al., 2005), and metabolize it aerobically to energy. More recent *ex vivo* data demonstrates that lactate imported via MCT-1 transporters can rescue oligodendrocytes and prevent demyelination under low glucose conditions (Rinholm et al., 2011). Subsequently, Lee et al. demonstrated how oligodendrocytes provide axons with lactate, critical to their survival, via the same MCT-1 transporter (Lee et al., 2012). These data point to glial cell-derived lactate as a critical factor for axonal energy metabolism and survival in white matter. A summary of the supposed metabolic coupling mechanisms between axons and surrounding glial cells is illustrated in Fig. 1.

In vitro studies revealed that astrocytic glycogenolysis is under noradrenergic control, and that activation of astrocytic β_2 -adrenergic receptors induces glycogenolysis and increases Na^+ , K^+ -ATPase activity (Hertz et al., 2010). Little is known about these regulatory mechanisms in white matter *in vivo*, and we are aware of only one study showing that noradrenaline pretreatment

*Corresponding author. Tel: +32-2-477-64-10.

E-mail address: laureysg@hotmail.com (G. Laureys).

† Share first authorship.

‡ Share senior authorship.

Abbreviations: aCSF, artificial cerebrospinal fluid; ANLSH, astrocyte–neuron lactate shuttle hypothesis; AUC, area under the curve; 4-CIN, α -cyano-4-hydroxycinnamic acid; DMSO, dimethyl sulfoxide; MCT, monocarboxylate transporter; TBOA, DL-threo- β -benzyloxyaspartic acid; YFP, yellow fluorescent protein.

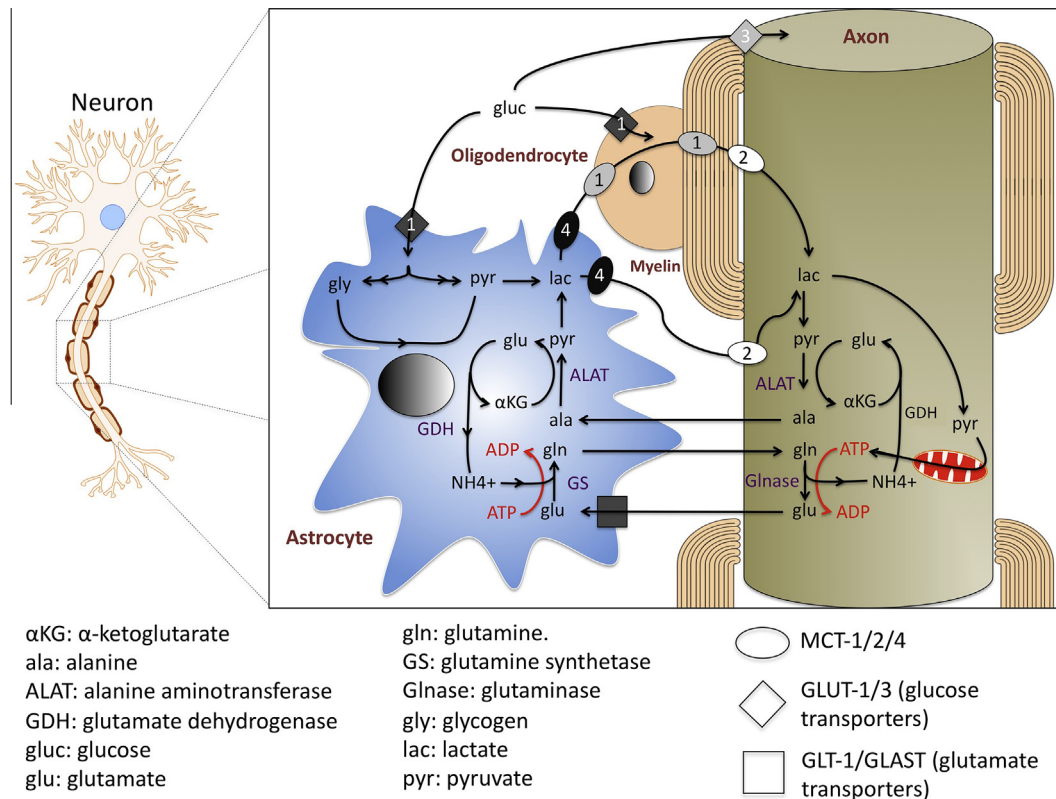


Fig. 1. Summary of the lactate shuttle and the interconnected glutamate–glutamine and alanine cycle between astrocytes and axons. Glucose enters astrocytes from the EC space and at the endothelial blood–brain–barrier junction by GLUT-1 mediated transport. This glucose can be incorporated in glycogen or consumed in anaerobic glycolysis. Glycolytic processing of glucose is driven by the need for the ATP consumed by glutamate uptake and glutamine synthesis. The final product of this glycolysis, namely lactate, is released from astrocytes via MCT4. Oligodendrocytic MCT1-mediated transport releases lactate near the axons. Axons take up lactate for aerobic metabolism by means of their MCT2 transporters. This process is partly accompanied by the exchange of alanine, which is generated in the axons from lactate via ALAT.

reduces glycogen content in isolated mouse optic nerve (Wender et al., 2000).

In the present study we explored the *in vivo* existence of astro-axonal coupling of lactate and glutamate metabolism and the potential influence of β_2 -adrenergic receptors in this process during axonal damage as a result of oxygen/glucose deprivation.

EXPERIMENTAL PROCEDURES

Chemicals and reagents

Aqueous solutions were made from purified water (Seralpur pro 90 CN, Belgolabo, Overijse, Belgium) and filtered through a 0.2- μ m-membrane filter. The perfusion fluid for microdialysis consisted of artificial cerebrospinal fluid (aCSF) (147 mM NaCl, 3 mM KCl, 1 mM MgCl₂·6H₂O, 1.2 mM CaCl₂·6H₂O, 200 μ M ascorbate, 352 mM NaH₂PO₄·H₂O, pH 7.4). ICI-118551 (200 nM), clenbuterol-hydrochloride (200 nM), DL-threo- β -benzyloxyaspartic acid (TBOA) (250 μ M) and α -cyano-4-hydroxycinnamic acid (4-CIN) (1 mM) (all from Sigma–Aldrich, St. Louis, MO, USA) were dissolved in aCSF and administered via the microdialysis probe. Selective *in situ* concentrations for each compound were determined using published affinity constants, and concentrations applied in the perfusion medium were

calculated based on a microdialysis probe recovery of 10%. The 10% correction factor considers approximate recovery for small molecules considering the used flow-rate and type of microdialysis probe (Grubb et al., 2002). For the two-photon imaging experiments the selective concentrations were applied without using the correction factor. The selectivity of 4-CIN for MCT-2 renders the interaction with energetic substrate uptake at the stipulated dose in astrocytes unlikely. Interaction with mitochondrial pyruvate uptake is improbable at the stipulated dose as previously determined (Erichman et al., 2008; Newman et al., 2011).

Surgery

Protocols were in accordance with national guidelines and regulations on animal experiments and approved by the Ethics Committee on Animal Experiments of the Vrije Universiteit Brussel, Belgium and the Ethics Committee of the University of Malta. Male C57Bl/6 mice (Charles Rivers, France) between 7 and 8 weeks of age (weighing 25–30 g), were anesthetized with a mixture of xylazine/ketamine (10/100-mg/kg, i.p.) and mounted on a stereotaxic frame. An intracranial guide (CMA/Microdialysis, Stockholm, Sweden) was implanted in the bilateral cerebellar white matter (coordinates toward bregma were 5.7 mm posterior, 2.2 mm lateral and

2.3 mm ventral of the dura (Paxinos and Franklin, 2004)). Immediately after surgery, guide cannula obturators were replaced by microdialysis probes (CMA7; membrane length: 1 mm theoretical cutoff: 6000 Da; CMA/Microdialysis, Solna, Sweden). Postoperative analgesia was ensured by ketoprofen (4 mg/kg, i.p.). Animals were allowed to recover from surgery overnight receiving laboratory chow and water *ad libitum*. Probe localization was histologically verified postmortem (Fig. 4B). Animals with aberrant probe location were excluded from the study.

Intracerebral microdialysis

Microdialysis probes were continuously perfused with aCSF at a flow-rate of 1 μ l/min (CMA/400 microdialysis pump, CMA/Microdialysis, Solna, Sweden). All experiments were performed on the day following surgery in non-anesthetized freely moving mice. Tubings were flushed with 70% ethanol and rinsed with purified water before perfusion with aCSF to exclude any bacterial interference with the glucose/lactate levels. 1 μ l/min perfusion of the probes was started 2 h before the experiment to attain steady-state concentrations. Six dialysate samples (20 μ l) were collected at 20-min intervals to determine the basal concentrations. TBOA, 4-CIN, clenbuterol or ICI-118551 was added to the perfusion medium at the last 20-min baseline sample. Thereafter six 20-min samples were collected during compound administration. In a separate set of experiments ($n = 5$) a control experiment was performed with a “sham” switch of syringes to exclude any effect of switching syringes on glucose, lactate and glutamate concentrations.

Liquid chromatographic assays

We used a gradient liquid chromatographic method for the quantitative simultaneous determination of amino-acids in dialysates as previously described (Van Hemelrijck et al., 2005). All substances were identified and quantified by comparing retention times and peak areas with those of external standards.

Enzymatic colorimetric assays

Microdialysate samples were analyzed for glucose and lactate content using enzymatic lactate (607-100) and glucose (606-100) assay kits (Biovision, Mountainview, CA, USA) according to the manufacturers' guideline. Fluorescence was measured at 460 nm using a microplate reader (Model 680 Bio-Rad, Hercules, CA, USA) and an excitation wavelength of 355 nm.

Preparation of fresh slices for imaging of corpus callosum axons

Adult 12–20-week-old mice weighing 25–27 g with a C57BL6/J genetic background were used in experiments. To enhance the visualization of axon morphology, we used transgenic mice with neuron-specific expression of yellow fluorescent protein (YFP), under control of the thy1 promoter (Feng et al., 2000). We selected a mouse transgenic line (Line H), which

expressed YFP in a subset of cortical neurons that project axons across the corpus callosum. After deep halothane anesthesia and decapitation, the cranium was opened and the brain rapidly removed and placed in chilled and oxygenated (95% O₂/5% CO₂) aCSF buffer supplemented with 75 mM sucrose. This hyperosmolar slicing solution prevents brain edema and is rich in magnesium and low in sodium and calcium, consisting of (mM) 234 sucrose, 11 glucose, 24 NaHCO₃, 2.5 KCl, 1.25 NaH₂PO₄, 10 MgSO₄ and 0.5 CaCl₂. After removing the cerebellum and brainstem, the entire brain was mounted on the ice-cold platform of a Vibratome 1000 vibroslicer (Technical Products, St. Louis, MO) covered in modified ice-cold aCSF. The brain was oriented to cut coronal slices (400 μ m thick) from the genu of the corpus callosum through the caudal extent of the hippocampus. Immediately after sectioning, slices were transferred to a Haas-type interface brain slice chamber (Harvard Apparatus, South Natick, MA) and allowed to recover at room temperature in oxygenated (95% O₂/5% CO₂) aCSF for 1 h at a flow rate of 3.5 ml/min aCSF was composed of (mM) 126 NaCl, 3.5 KCl, 1.3 MgCl₂, 2 CaCl₂, 1.2 NaH₂PO₄, 25 NaHCO₃, 10 glucose, 0.43 L-lactate, pH 7.4. The osmolality (~300 mOsm) was checked with a micro-osmometer (Precision Systems, Natick, MA).

Two-photon imaging of brain slices

A brain slice was then transferred to a submerged minichamber (0.5 ml) with a coverglass bottom (Warner Instrument Corporation, Hamden, CT) mounted on an upright BX50W1 Olympus Multiphoton microscope (Olympus, Tokyo, Japan) and perfused with room temperature oxygenated (95% O₂/5% CO₂) aCSF at a flow rate of approximately 3.5 ml/min. Final temperature control (33 \pm 1 $^{\circ}$ C) was maintained using an in-line heater (Warner Instrument Corporation, Hamden, CT) equipped with a feedback thermistor placed in the chamber and the temperature raised gradually over 1 h. Slices were continually perfused with oxygenated buffer during imaging by means of a gravity flow perfusion system and vacuum aspiration within the imaging chamber. Glucose deprivation was initiated by replacing glucose in normal oxygenated aCSF with 10 mM sucrose for a period of 15, 30 or 45 min and imaging was continued through 120 min of reperfusion with substitution to glucose-containing aCSF. In alternate experiments, aCSF in the aglycemic phase was supplemented with 0.1 mM 4-CIN (stock solution dissolved in 0.1 N NaOH), 20 nM clenbuterol or a combination of both drugs. Since 4-CIN necessitated dimethyl sulfoxide (DMSO) as a solvent, all solutions contained 0.01% DMSO. Control experiments for 15, 30 and 45 min hypoglycemia in the absence of DMSO excluded any effect on axon integrity due to DMSO alone. Control slices maintained in oxygenated superfusion medium at 33 \pm 1 $^{\circ}$ C demonstrated intact linear axonal morphology for at least 5 h after preparation (Fig. 4A). YFP-labeled axons were visualized with a 920-nm laser line (7% laser power) using a water-based 25 \times

Olympus XLPLN25xWMP objective (NA 1.05, WD 2.0, IR-corrected).

Image processing

Image acquisition was performed using the Olympus FluoView software. Single-focal-plane images were collected at 30-min intervals or, more frequently, stacks of five optical sections at an incremental z-step of 1 μm apart. Subsequently, all z-stacks of images were projected along the z-axis to recreate two-dimensional representations of the three-dimensional structures within the imaged tissue. Post-acquisition images were only adjusted for brightness, contrast and background noise by using ImageJ. For brightness and contrast adjustments the depth of pixel intensities that spanned the entire 8-bit range (0–255) was readjusted for display optimization. The two-photon experiments were performed in triplicate for confirmation of reproducibility.

Scoring of axonal injury

Axon damage was quantified by visual scoring as previously described (Tekkok and Goldberg, 2001; McCarran and Goldberg, 2007). Images were divided into a 5×5 grid, and each grid box was scored by a blinded observer for the presence of axon damage using the following system: 0, no damage; 1, axon swelling and/or beading; 2, axon fragmentation. The total score for a single section (0–50) was divided by the number of grid boxes to give a mean damage score (0–2). Damage scores from three different experiments were averaged and recorded for each condition.

Statistical analysis

The average (with s.e.m.) of the 5 stable baseline dialysate levels for the animals included in the study are: 0.218 ± 0.016 mg/dl glucose, 0.036 ± 0.002 mg/dl lactate and 0.590 ± 0.046 μM glutamate. Glutamate, glucose and lactate levels are expressed relative to the stable baseline levels, which were equated to 100% with s.e.m. A correction for changes induced by syringe exchange was performed by subtracting the % change in sham conditions for each time point. Statistical analysis between pharmacologically induced levels and baseline level was performed using a Friedman test followed by Dunn's multiple comparisons post hoc test. The basal area under the curve (AUC) was calculated as the sum of dialysate concentrations in the first six "basal" collections (20 min samples). AUC following drug was calculated as the sum of the dialysate concentrations in the six collections following the start of drug perfusion. AUC after drug administration was expressed as a percentage of basal AUC. Wilcoxon-signed rank test was used to compare basal and drug-induced AUC. Animals were excluded from analysis when contamination of the sample or technical problems rendered measurement impossible. Statistical analysis was performed with the InStat Prism statistical package (GraphPad Software, La Jolla, USA). Axonal injury data are expressed as mean \pm s.e.m., statistical significance

versus controls was determined by a one-way ANOVA. p values are reported in the figure.

RESULTS

Exploration of metabolic shuttling in white matter

To address the presence of functionally coupled glutamate–lactate metabolism in white matter our first step was to pharmacologically block both ends of the presumed glial–axonal shuttle. Inhibition of axonal lactate uptake by the MCT-2 blocker 4-CIN resulted in an increased extracellular lactate concentration (Fig. 2A), whereas extracellular glucose levels were not affected (Fig. 2B). Inhibition of axonal lactate uptake increased extracellular glutamate concentrations (Fig. 2C). Inhibition of the astrocytic glutamate transporters by TBOA led to the accumulation of EC glutamate (Fig. 2C). TBOA also significantly diminished extracellular glucose levels (Fig. 2B) without influencing extracellular lactate concentration (Fig. 2A).

To evaluate the impact of astrocytic lactate production on axonal survival we performed a series of two-photon sequential imaging experiments. The effects of aglycemia on morphological damage of axons have not yet been described. Following aglycemia applied for up to 30 min, axonal structures were maintained throughout the complete recovery phase of 120 min of recirculation with glucose-containing aCSF (Fig. 3A). Forty-five minutes of glucose deprivation caused few immediate changes, but resulted in gradual axonal beading and fragmentation during reperfusion (Fig. 3B). To investigate if glycogen-derived lactate served as the protective factor during aglycemia, 4-CIN was supplemented to corpus callosum slices undergoing 30 min of aglycemia. Toward the end of the aglycemic period axonal beading was observed (Fig. 3C), followed by extensive damage during reperfusion as compared to the 30 min of aglycemia without 4-CIN (Fig. 3A).

Role of β_2 -adrenergic receptors in axonal neuroprotection and basal lactate production

The mean axonal injury scores for the various conditions are shown in Fig. 3. No statistically significant difference was observed in the axonal injury score throughout the duration of control experiments [$F(14, 350) = 0.385$, $p = 0.979$]. Control slices maintained in oxygenated superfusion medium demonstrated intact linear axonal morphology for at least 5 h after preparation (Fig. 4A). When compared with control slices, 30 min of GD did not result in any significant axonal injury while 45 min of GD did ($p < 0.001$). Addition of 0.1 mM 4-CIN during 30 min of GD resulted in considerable axonal damage, with these slices scoring a statistically significant ($p < 0.001$) higher axonal injury than control slices and slices following 30 min of GD without the drug. Addition of 20 nM clenbuterol offered protection to slices during 45 min of GD, with no statistically significant difference in axonal injury score between such slices and controls. This protection was lost when axonal lactate uptake was blocked by co-administration of 0.1 mM 4-CIN during

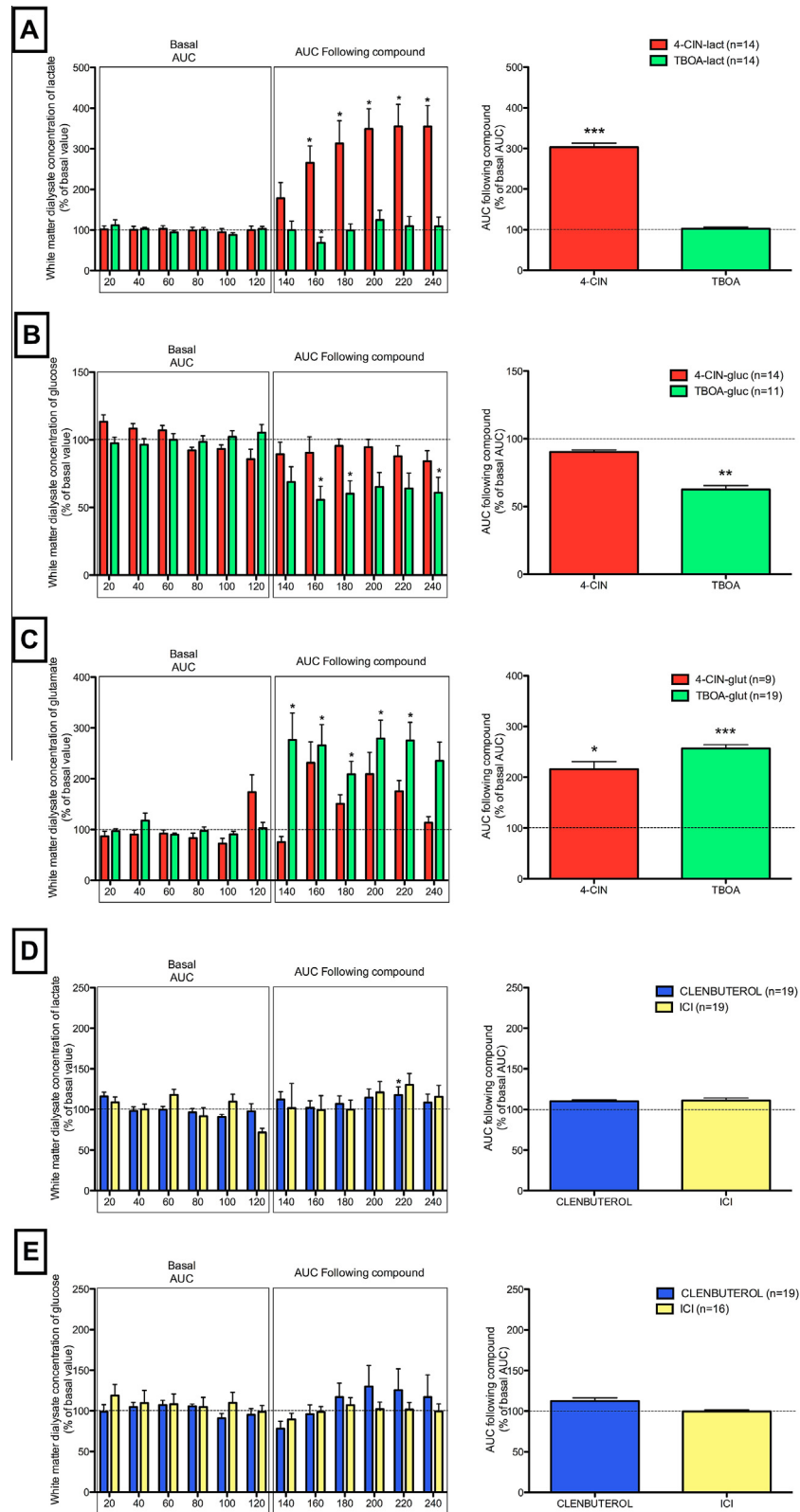


Fig. 2. Microdialysis experiments: six dialysate samples (20 μ l) were collected at 20-min intervals to determine the basal concentrations expressed as 100% + s.e.m. 4-CIN, TBOA, clenbuterol or ICI was added to the perfusion medium at the last 20-min baseline sample and thereafter six 20-min samples were collected during compound administration. Changes in EC (A) lactate, (B) glucose and (C) glutamate concentration are illustrated for 4-CIN (red bars) and TBOA (green bars), changes in EC (D) lactate and (E) glucose concentration for clenbuterol (blue bars) and ICI (yellow bars). Statistical analysis between pharmacologically-induced and baseline levels was performed using a Friedman test followed by Dunn's multiple comparisons posthoc test ($p < 0.05$). The area under the curve (AUC) was also calculated as the sum of the 2-h baseline concentrations and compared with the sum of the 2-h concentrations after compound administration using the Wilcoxon signed rank test ($*p < 0.05$, $**p < 0.005$, $***p < 0.001$), $n =$ as indicated in the figure. (For interpretation of the references to color in this figure legend, the reader is referred to the web version of this article.)

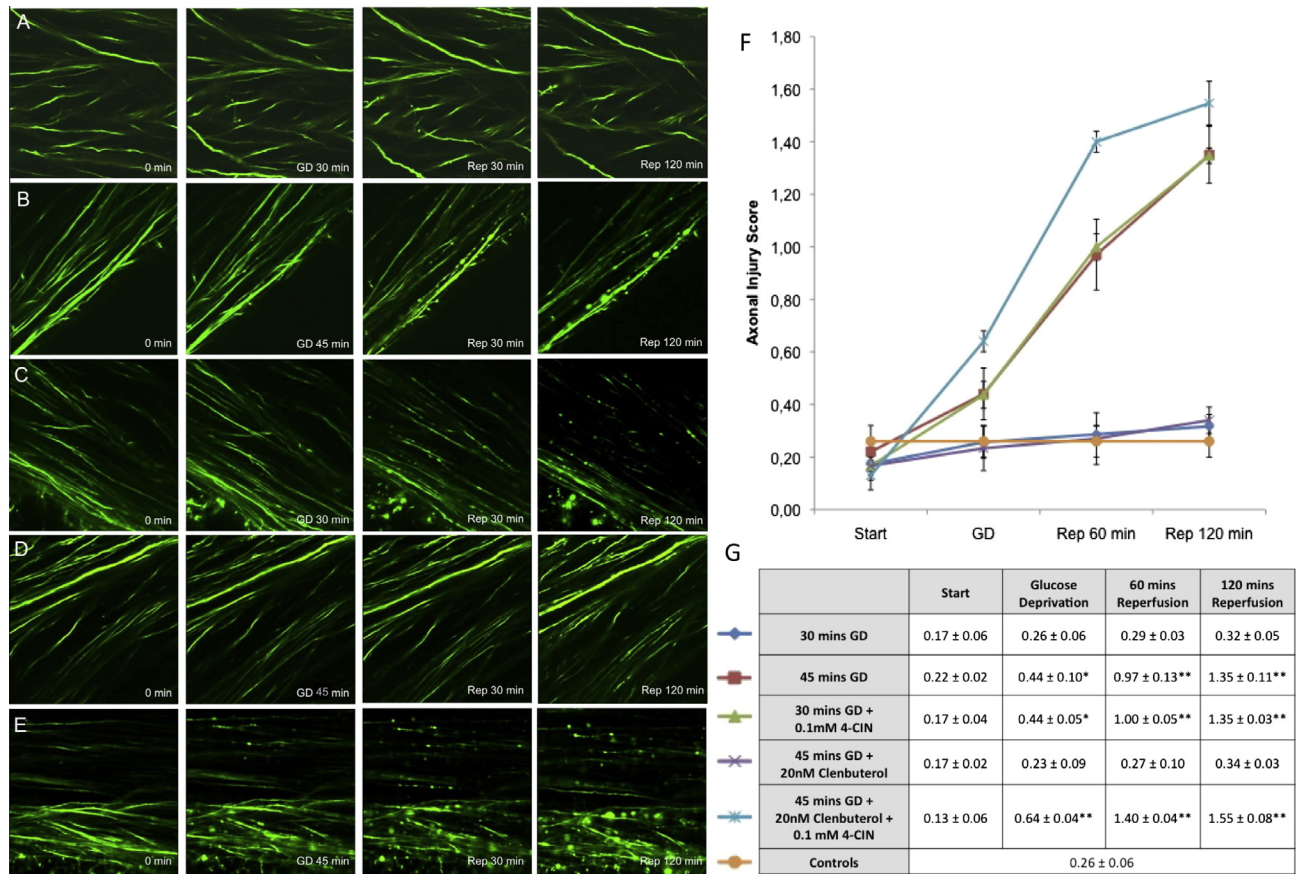


Fig. 3. Two-photon experiments: (A)–(E) shows representative images of the 2-photon imaging experiments. In (F) the mean axonal injury scores + s.e.m. are plotted for the different conditions. For clarity table (G) summarizes the mean scores ($n = 3$) ± (SDV), scores significantly different from control are marked: * $p < 0.05$; ** $p < 0.001$. Transient GD (30 min (A), \blacktriangleleft) did not result in axonal injury but a more prolonged duration (45 min (B), \blacktriangleleft) did. Addition of 0.1 mM 4-CIN resulted in axonal injury even during transient (30 min) GD (C), \blacktriangleleft , while 20 nM Clenbuterol was protective during prolonged (45 min) GD (D), \blacktriangleleft . This protection was lost when 0.1 mM 4-CIN was added to 20 nM Clenbuterol during prolonged (45 min) GD (E), \blacktriangleleft . (For interpretation of the references to color in this figure legend, the reader is referred to the web version of this article.)

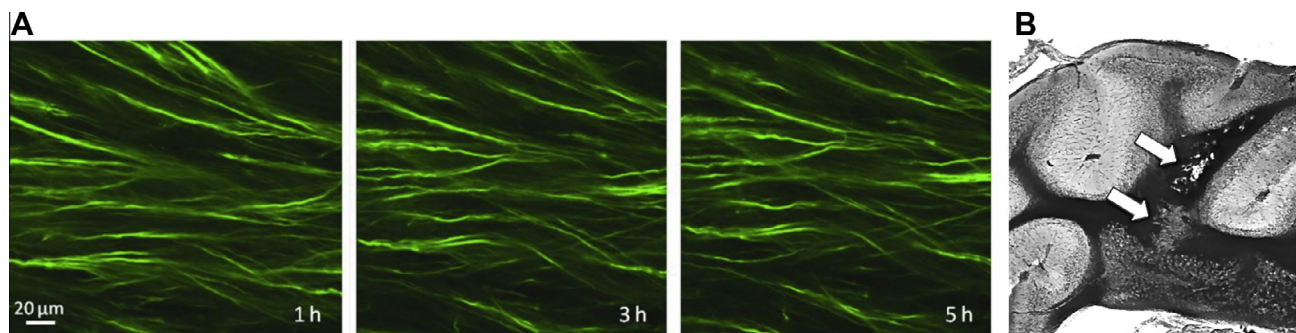


Fig. 4. Control slices maintained in oxygenated superfusion medium showed intact linear axonal morphology for at least 5 h after preparation (A). A representative picture of probe localization, arrows indicate the tract of the probe (B).

45 min GD, with slices now showing a statistically significant ($p < 0.001$) difference in axonal injury score when compared with control slices. Although axonal damage was clearly visible, fluorescence was relatively preserved (for comparison see Fig. 3C illustrating loss of fluorescence with administration of 4CIN only), suggesting that clenbuterol still exerted protective effects independent of a possible lactate-mediated effect blocked by 4CIN. *In vivo* intracerebellar administration

of the selective β_2 -antagonist ICI-118551 or β_2 -agonist clenbuterol did not significantly change extracellular lactate or glucose concentrations (Fig. 2D, E).

DISCUSSION

The increase in extracellular lactate during pharmacological blockade of axonal lactate uptake demonstrates the existence of a physiological

glia–axonal lactate shuttle in white matter under basal conditions. Inhibition of glycogenolysis elevates extracellular glutamate concentrations *in vitro* (Sickmann et al., 2009; Schousboe et al., 2010). Our data demonstrate an *in vivo* counterpart during 4-CIN administration since the increase in extracellular glutamate probably reflects inhibition of astrocytic lactate production by feedback inhibition (Sotelo-Hitschfeld et al., 2012). Functional glutamate reuptake by optic nerve axons has been demonstrated (Arranz et al., 2008) and may constitute a complementary mechanism of glutamate accumulation when axons are deprived of lactate influx. Inversely inhibition of glutamate reuptake with TBOA decreased extracellular glucose levels compatible with enhanced glycolytic glucose consumption. In summary, these data are in line with functional exchange machinery where glial cells produce lactate during the buffering process of extracellular glutamate, with lactate subsequently being transported to axons as energy source. In our sequential two-photon imaging experiments we found a time window of 30 min of aglycemia before axonal damage occurred following reperfusion with glucose. These findings confirm a morphological counterpart to the previously described 30-min protective glycogen-buffer in *ex vivo* experiments of rodent optic-nerve electrophysiology (Wender et al., 2000). When we blocked axonal lactate uptake during 30 min of aglycemia damage occurred, confirming that lactate supports axonal energetic needs.

Hypoglycemia activates Locus Coeruleus neurons (Morilak et al., 1987) leading to increased noradrenaline release throughout the brain (Bengzon et al., 1991). Noradrenaline can enhance astrocytic glycogenolysis by β_2 -adrenergic activation as previously described *in vitro* (Hertz et al., 2010). Therefore, we suggested β_2 -adrenergic stimulation would provide glycogenolytic support of axons in our model. Callosal slices are deprived of noradrenergic input from locus coeruleus projections necessitating pharmacological stimulation. β_2 -adrenergic stimulation with clenbuterol indeed sustained axonal survival during aglycemia in our two-photon experiments (Fig. 3D). Moreover this effect was found to be counteracted by the addition of 4-CIN (Fig. 3E). Since the protective effect of clenbuterol and the deleterious effect of 4-CIN might represent independent effects we investigated the role of β_2 -adrenergic stimulation and inhibition on *in vivo* extracellular levels of glucose and lactate. Neither stimulation nor inhibition led to significant changes in extracellular glucose or lactate concentrations suggesting alternative mechanisms convey β_2 -adrenergic axonal protection during aglycemia.

CONCLUSION

We showed that β_2 -adrenergic receptors exert axonal protective effects under aglycemic conditions. Although our data support the existence of a functional glutamate–lactate exchange system between white matter glia and axons, β_2 -adrenergic receptors did not affect this system. Therefore, we postulate that protection of axons during energetic stress by the β_2 -adrenergic receptor agonist clenbuterol may occur

through previously described anti-inflammatory, anti-oxidative and neurotrophic effects of clenbuterol (Gleeson et al., 2010), and not by enhanced astrocytic lactate production.

DISCLOSURE/CONFLICT OF INTEREST

The authors declare no conflict of interest.

Acknowledgments—The authors acknowledge the excellent technical assistance of A. De Smet. This work was supported by an FWO (Fonds Wetenschappelijk Onderzoek) - Vlaanderen grant (G.A.100.11.N.10) and in part by a Research Grant from the University of Malta (MDSIN09-12). We kindly thank the Charcot foundation Belgium and the Willy Gepts fund for their additional financial support. Melissa Cambron is a research fellow with the FWO Vlaanderen. The transgenic YFP-H mice were a kind gift from Prof Jochen Herms, Institut für Neuropathologie, Ludwig-Maximilians-Universität, München, Germany.

REFERENCES

- Arranz AM, Hussein A, Alix JJ, Perez-Cerda F, Allcock N, Matute C, Fern R (2008) Functional glutamate transport in rodent optic nerve axons and glia. *Glia* 56:1353–1367.
- Bengzon J, Brundin P, Kalen P, Kokaia M, Lindvall O (1991) Host regulation of noradrenaline release from grafts of seizure-suppressant locus coeruleus neurons. *Exp Neurol* 111:49–54.
- Cambron M, D'Haeseleer M, Laureys G, Clinckers R, Debruyne J, De Keyser J (2012) White-matter astrocytes, axonal energy metabolism, and axonal degeneration in multiple sclerosis. *J Cereb Blood Flow Metab*.
- Erlichman JS, Hewitt A, Damon TL, Hart M, Kurasz J, Li A, Leiter JC (2008) Inhibition of monocarboxylate transporter 2 in the retrotrapezoid nucleus in rats: a test of the astrocyte–neuron lactate–shuttle hypothesis. *J Neurosci* 28:4888–4896.
- Feng G, Mellor RH, Bernstein M, Keller-Peck C, Nguyen QT, Wallace M, Nerbonne JM, Lichtman JW, Sanes JR (2000) Imaging neuronal subsets in transgenic mice expressing multiple spectral variants of GFP. *Neuron* 28:41–51.
- Gleeson LC, Ryan KJ, Griffin EW, Connor TJ, Harkin A (2010) The beta2-adrenoceptor agonist clenbuterol elicits neuroprotective, anti-inflammatory and neurotrophic actions in the kainic acid model of excitotoxicity. *Brain Behav Immun* 24:1354–1361.
- Grubb BR, Chadburn JL, Boucher RC (2002) *In vivo* microdialysis for determination of nasal liquid ion composition. *Am J Physiol Cell Physiol* 282:C1423–C1431.
- Hall CN, Klein-Flugge MC, Howarth C, Atwell D (2012) Oxidative phosphorylation, not glycolysis, powers presynaptic and postsynaptic mechanisms underlying brain information processing. *J Neurosci* 32:8940–8951.
- Hertz L, Lovatt D, Goldman SA, Nedergaard M (2010) Adrenoceptors in brain: cellular gene expression and effects on astrocytic metabolism and $[Ca^{2+}]_i$. *Neurochem Int* 57:411–420.
- Lee Y, Morrison BM, Li Y, Lengacher S, Farah MH, Hoffman PN, Liu Y, Tsingalia A, Jin L, Zhang PW, Pellerin L, Magistretti PJ, Rothstein JD (2012) Oligodendroglia metabolically support axons and contribute to neurodegeneration. *Nature* 487:443–448.
- Matute C, Ransom BR (2012) Roles of white matter in central nervous system pathophysiology. *ASN Neuro* 4.
- McCarran WJ, Goldberg MP (2007) White matter axon vulnerability to AMPA/kainate receptor-mediated ischemic injury is developmentally regulated. *J Neurosci* 27:4220–4229.
- Morilak DA, Fornal CA, Jacobs BL (1987) Effects of physiological manipulations on locus coeruleus neuronal activity in freely moving cats. III. Glucoregulatory challenge. *Brain Res* 422:32–39.

- Newman LA, Korol DL, Gold PE (2011) Lactate produced by glycogenolysis in astrocytes regulates memory processing. *PLoS One* 6:e28427.
- Paxinos G, Franklin KPJ (2004) The mouse brain in stereotaxic coordinates. Elsevier.
- Pellerin L, Magistretti PJ (1994) Glutamate uptake into astrocytes stimulates aerobic glycolysis: a mechanism coupling neuronal activity to glucose utilization. *Proc Natl Acad Sci USA* 91:10625–10629.
- Rinholm JE, Hamilton NB, Kessaris N, Richardson WD, Bergersen LH, Attwell D (2011) Regulation of oligodendrocyte development and myelination by glucose and lactate. *J Neurosci* 31:538–548.
- Sampol D, Ostrofet E, Jobin ML, Raffard G, Sanchez S, Bouchaud V, Franconi JM, Bonvento G, Bouzier-Sore AK (2013) Glucose and lactate metabolism in the awake and stimulated rat: a ¹³C-NMR study. *Front Neuroenergetics* 5:5.
- Schousboe A, Sickmann HM, Walls AB, Bak LK, Waagepetersen HS (2010) Functional importance of the astrocytic glycogen-shunt and glycolysis for maintenance of an intact intra/extracellular glutamate gradient. *Neurotox Res* 18:94–99.
- Sickmann HM, Walls AB, Schousboe A, Bouman SD, Waagepetersen HS (2009) Functional significance of brain glycogen in sustaining glutamatergic neurotransmission. *J Neurochem* 109(Suppl. 1):80–86.
- Sotelo-Hitschfeld T, Fernandez-Moncada I, Barros LF (2012) Acute feedback control of astrocytic glycolysis by lactate. *Glia* 60:674–680.
- Tekkok SB, Brown AM, Westenbroek R, Pellerin L, Ransom BR (2005) Transfer of glycogen-derived lactate from astrocytes to axons via specific monocarboxylate transporters supports mouse optic nerve activity. *J Neurosci Res* 81:644–652.
- Tekkok SB, Goldberg MP (2001) Ampa/kainate receptor activation mediates hypoxic oligodendrocyte death and axonal injury in cerebral white matter. *J Neurosci* 21:4237–4248.
- Van Hemelrijck A, Sarre S, Smolders I, Michotte Y (2005) Determination of amino acids associated with cerebral ischaemia in rat brain microdialysates using narrowbore liquid chromatography and fluorescence detection. *J Neurosci Methods* 144:63–71.
- Wender R, Brown AM, Fern R, Swanson RA, Farrell K, Ransom BR (2000) Astrocytic glycogen influences axon function and survival during glucose deprivation in central white matter. *J Neurosci* 20:6804–6810.
- Yao J, Rettberg JR, Klosinski LP, Cadenas E, Brinton RD (2011) Shift in brain metabolism in late onset Alzheimer's disease: implications for biomarkers and therapeutic interventions. *Mol Aspects Med* 32:247–257.


(Accepted 16 July 2014)
(Available online 24 July 2014)

ARTICLE

DOI: 10.1038/s41467-018-03427-1

OPEN

Vesicular glutamate release from central axons contributes to myelin damage

Sean Doyle¹, Daniel Bloch Hansen¹, Jasmine Vella², Peter Bond¹, Glenn Harper¹, Christian Zammit², Mario Valentino² & Robert Fern ¹

The axon myelin sheath is prone to injury associated with *N*-methyl-D-aspartate (NMDA)-type glutamate receptor activation but the source of glutamate in this context is unknown. Myelin damage results in permanent action potential loss and severe functional deficit in the white matter of the CNS, for example in ischemic stroke. Here, we show that in rats and mice, ischemic conditions trigger activation of myelinic NMDA receptors incorporating GluN2C/D subunits following release of axonal vesicular glutamate into the peri-axonal space under the myelin sheath. Glial sources of glutamate such as reverse transport did not contribute significantly to this phenomenon. We demonstrate selective myelin uptake and retention of a GluN2C/D NMDA receptor negative allosteric modulator that shields myelin from ischemic injury. The findings potentially support a rational approach toward a low-impact prophylactic therapy to protect patients at risk of stroke and other forms of excitotoxic injury.

¹University of Plymouth, Plymouth PL6 8BY, UK. ²University of Malta, Msida MSF 2080, Malta. Correspondence and requests for materials should be addressed to R.F. (email: Robert.fern@plymouth.ac.uk)

Myelin is an insulating, low-capacitance layer that wraps around the axon cylinder and is essential for fast action potential conduction. Myelin injury is fundamental to the functional loss of the white matter of the CNS experienced in multiple sclerosis, trauma, and stroke^{1–3}. Surprisingly, *N*-methyl-D-aspartate (NMDA)-type glutamate receptor (GluR) expression levels in myelin are comparable to those at neuronal synapses^{4–6}, are found in humans⁶, and confer an elevated injury sensitivity under conditions of high extracellular glutamate^{4,5,7,8}. The established view is that the glutamate release responsible for over-activation of myelinic NMDA GluRs under pathological conditions occurs via reverse glutamate uptake^{9–11}. However, extracellular glutamate concentration has not previously been directly recorded within white matter while recent reports highlight vesicular release as an alternative potential source of white matter glutamate^{12–14}. Under ischemic conditions, axonal vesicular glutamate release will empty directly onto the myelin sheath and may be trapped within the peri-axonal space between the axolemma and the internal myelin surface. The spatial characteristics of axon vesicular glutamate release may therefore be particularly relevant to myelin pathology. Myelinic NMDA receptors incorporate GluN2 C and D subunits and should be sensitive to selective negative allosteric modulators. GluN2C/D-containing NMDA receptors are generally extra-synaptic while negative allosteric modulators exhibit use-dependent properties. These features suggest that a putative myelinic NMDA receptor/axo-vesicular glutamate pathway may be particularly amenable to therapeutic intervention with clinical potential.

Results

Vesicular glutamate release in white matter is primarily axonal.

Vesicular docking in white matter was examined via live two-photon confocal imaging of fluorescent FM4-64¹⁵ in corpus callosum axons of adult Thy-1/YFP mice. Low magnification images revealed extensive axonal FM4-64 loading, with individual axons reliably imaged at higher magnification (Fig. 1a–d). A similar approach using GFAP-GFP mice revealed fibrous white matter astrocytes with low levels of FM4-64 staining compared to neighboring axons (Fig. 1e, f; Supplementary Fig. 1d, e). FM4-64 de-staining (vesicular docking) was evoked by 50 mM K^+ perfusion, producing rapid docking in corpus callosum axons (significant within 60 s), but not in astrocytes (Fig. 1g). The $[K^+]$ used to evoke this response is comparable to that recorded during brain ischemia¹⁶, and produced axon depolarization sufficient to reversibly block excitability (Supplementary Fig. 1a–c). To our knowledge, this is the first direct comparison of vesicular fusion within different cellular components in white matter, and it reveals extensive fusion in axons compared to their companion astrocytes and is consistent with earlier observation of vesicular release from axons¹⁵. We have shown previously that YFP(+) axons in this model are myelinated¹⁷ and the diameter of YFP(+) axon in the current study had a range considerably higher than the upper limit for non-myelinated axons in mouse corpus callosum¹⁸ (Supplementary Fig. 1f). As there was no evidence of localized de-staining along YFP(+) axons imaged in long-section (L-S), the majority of vesicular fusion in these axons must occur under the myelin sheath and empty into the periaxonal space. This mechanism was also triggered by ischemic conditions where significant axonal release was found after 15 min (Fig. 1h).

The glutamate concentration in the extracellular space ($[glutamate]_e$) increased by $13.0 \pm 3.6 \mu M$ during perfusion with 50 mM $[K^+]$ (Fig. 1i–k), a rise that was not inhibited by glutamate transport inhibition (200 μM TBOA) but was significantly reduced by inhibition of vesicular glutamate loading (50 nM bafilomycin; Fig. 1i–k). Note, axonal glutamate

transporters are localized primarily to the node of Ranvier rather than the internodal region¹⁹ and TBOA is likely to access axonal transport sites relatively quickly. In the adult corpus callosum, TBOA evoked a $1.3 \pm 0.4 \mu M$ peak increase in resting $[glutamate]_e$ indicating ongoing glutamate regulation in white matter via glutamate transport under physiological conditions (Supplementary Fig. 2).

FM4-64 axon imaging reported uniform vesicle fusion along axons with no focal sites of fusion that might indicate local glutamate release at nodes of Ranvier; vesicular glutamate release must therefore empty largely into the periaxonal space under the myelin sheath which covers 99% of the axon cylinder. Consistent with this, an established DiOC₆(3)/X-rhod-1 confocal imaging protocol⁸ reported elevated $[Ca^{2+}]_i$ in the cytoplasmic compartment of the myelin sheath following depolarization with 50 mM K^+ (Fig. 2a, b). Myelin X-rhod-1 loading is largely peri-axonal^{5,8} and the myelinic K^+ -evoked $[Ca^{2+}]_i$ rise was prevented by pre-incubation with bafilomycin, indicating myelin calcium influx following vesicular glutamate release from axons. Ultrastructural analysis of long-section (L-S) rodent optic nerve (RON) axons revealed regions of 20–50 nm axoplasmic vesicle clusters within the internodal zones (Fig. 2c arrows); vesicles were not clustered within nodal regions and were not observed in glial processes aligned adjacent to myelinated axons. RONs exposed to 30 min of oxygen–glucose deprivation (OGD) prior to fixation contained significantly fewer internodal axoplasmic vesicles (Fig. 2d, f, g), and in these nerves the vesicles were found at the sub-myelinic axolemma occasionally caught in the act of membrane docking/fusion (Fig. 2d, e). As in control nerves, such vesicles were absent from glial processes neighboring the myelin (e.g., Fig. 2d). The ultrastructural and X-rhod-1 imaging data confirm internodal axoplasmic vesicle-axolemma docking, which will release glutamate into the periaxonal space beneath the myelin sheath and may lead to early focal myelin damage. Axon cylinders were largely unaffected after 30 min of OGD and retained normal microtubules, a feature of healthy axons (Fig. 2d, white arrows). Early signs of myelin damage were evident at sites where axoplasmic vesicles were present and included localized splitting and bubbling of the lamina (Fig. 2d, e*).

White matter ischemic glutamate release is primarily vesicular.

The corpus callosum sits adjacent to gray matter structures such as the cortex (Fig. 1a) that have extensive glutamatergic input. To avoid the potential for spillover from gray matter synapses, we examined $[glutamate]_e$ in isolated RON, a white matter structure with no neuronal synapses or neighboring gray matter. Resting $[glutamate]_e$ was $8.9 \pm 1.4 \mu M$ in adult rat RON, higher than the 1.3–4.5 μM range recorded in other white matter preparations (Supplementary Fig. 2a). Glutamate biosensor electrodes were found to be anoxia-sensitive (Supplementary Fig. 3) and ischemia was therefore modeled using combined aglycemia/oxidative phosphorylation block, producing a 22.4–27.5 μM glutamate rise (Fig. 3a, b). Block of glutamate transport (TBOA or zero- Na^+) did not significantly reduce the ischemic glutamate increase, but release was both Ca^{2+} - and voltage-gated Ca^{2+} channel (100 μM diltiazem)-dependent as predicted for vesicular release (Fig. 3a, b). Recording from adult RON required a long period of stabilization following sensor insertion (Supplementary Fig. 4c), and ischemic $[glutamate]_e$ was more extensively examined in juvenile rat RON, which stabilized more quickly. At this age, ischemia evoked a $5.6 \pm 0.8 \mu M$ $[glutamate]_e$ rise that was not significantly affected by block of glutamate transport (TBOA, or zero- Na^+), swelling-mediated glutamate release (5 mM furosemide), cysteine-glutamate antiport (250 μM SAS), P2X7-, pannexin- and connexin-channels (100 μM CBX), or swelling-operated channels

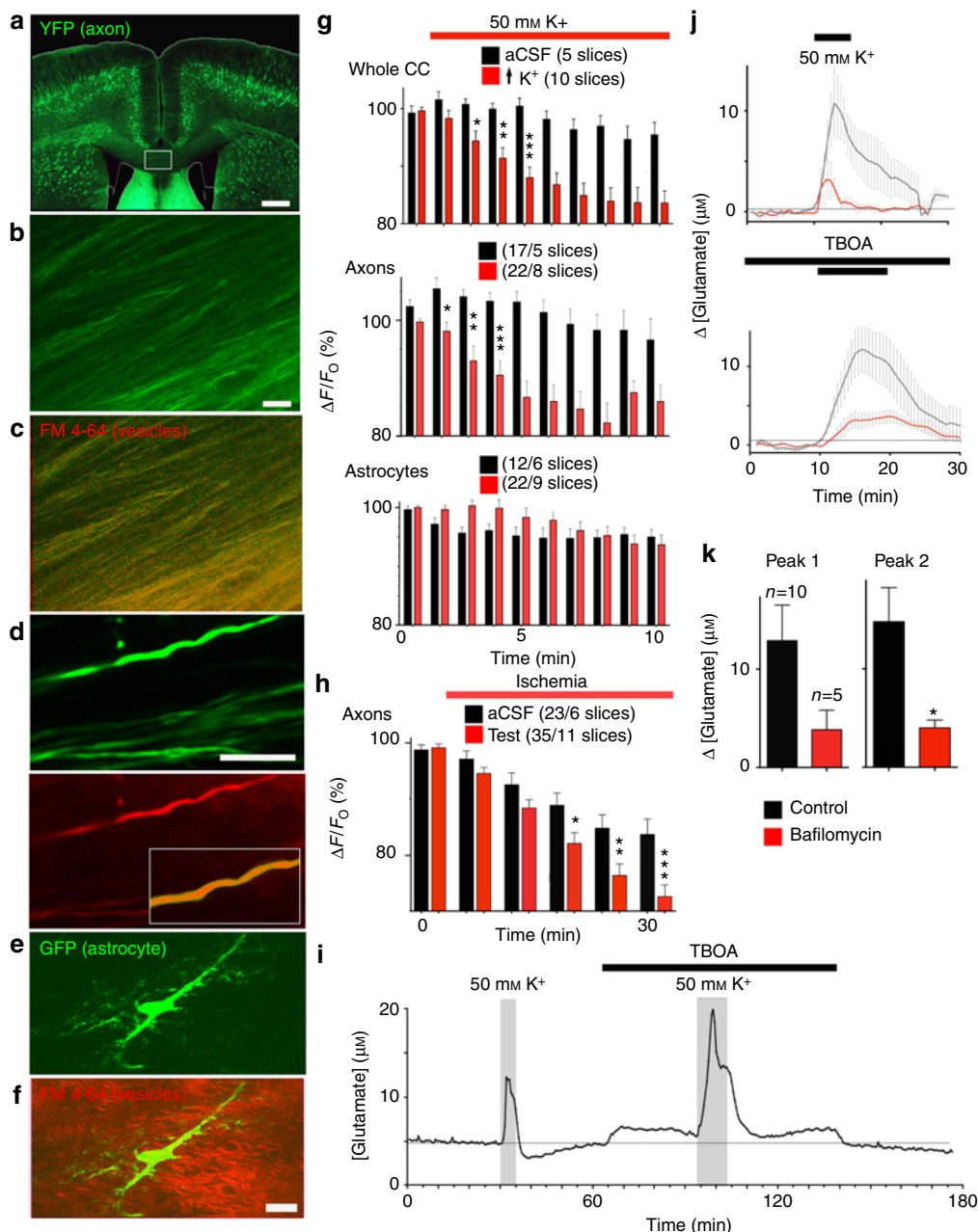


Fig. 1 Axons are the principle site of white matter vesicular fusion. **a** Thy-1-YFP expression in adult coronal section (box: corpus callosum). **b, c** YFP(+) corpus callosum axons (**b**) and FM4-64 vesicles (**c** overlaid red). **d** Single axons (overlaid at higher gain in the box). **e, f** Corpus callosum astrocyte (**e**) in adult GFAP-GFP mouse and FM4-64 staining (**f** overlaid red). **g** K⁺-evoked FM4-64 de-staining in whole corpus callosum, axons, and astrocytes. **h** Corpus callosum axon FM4-64 de-staining in aCSF and during ischemia. **i** K⁺-evoked [glutamate]_e release is not inhibited by TBOA. **j** Both the first (top) and second (bottom) 50 mM K⁺-evoked glutamate rise is reduced by bafilomycin (50 nM, red trace). **k** Data summary shown on the bottom. Scale = 1 mm (**a**), 10 μm (**b, d, f**). Stars indicate the first mean to reach significance. Grouped analysis ANOVA; correct for multiple comparisons using the Holm–Šidák method. *P* values: **g** top *0.016, **0.001, ***0.0000; **g** middle *0.038, **0.002, ***0.0004; **h** *0.021, **0.009, ***0.0013. Unpaired *t*-test *P* values: **k** Peak 1 ns 0.1119; Peak 2 *0.048

(100 μM NPPB) (Fig. 3c, d). Glutamate release was Ca²⁺-dependent and was significantly reduced by blockers of vesicular glutamate release (50 nM bafilomycin or 500 nM rose bengal; Fig. 3e, f), confirming the significance of vesicular release to ischemic [glutamate]_e elevation in white matter.

NMDA receptors mediate acute myelin injury during ischemia. Drug penetration into the peri-axonal space is known to be slow. For example, diffusion from the node of Ranvier into the peri-

nodal space that is contiguous with the periaxonal space takes several hours²⁰. Drugs may also access the peri-axonal space directly through the myelin sheath if they are lipid soluble, e.g. the NMDA blocker MK-801 that associates/dissociates with synaptic lipid membrane with a time constant (τ) of ~4 min²¹, indicating $\tau = 56$ min for penetration through the sheath of a typical mature RON axon. Prior studies have shown that short periods of NMDA-receptor block fail to protect adult white matter from ischemic injury^{11,22}, and we also found no protection following a 20 min pre-treatment period with MK-801 (Fig. 4b). However,

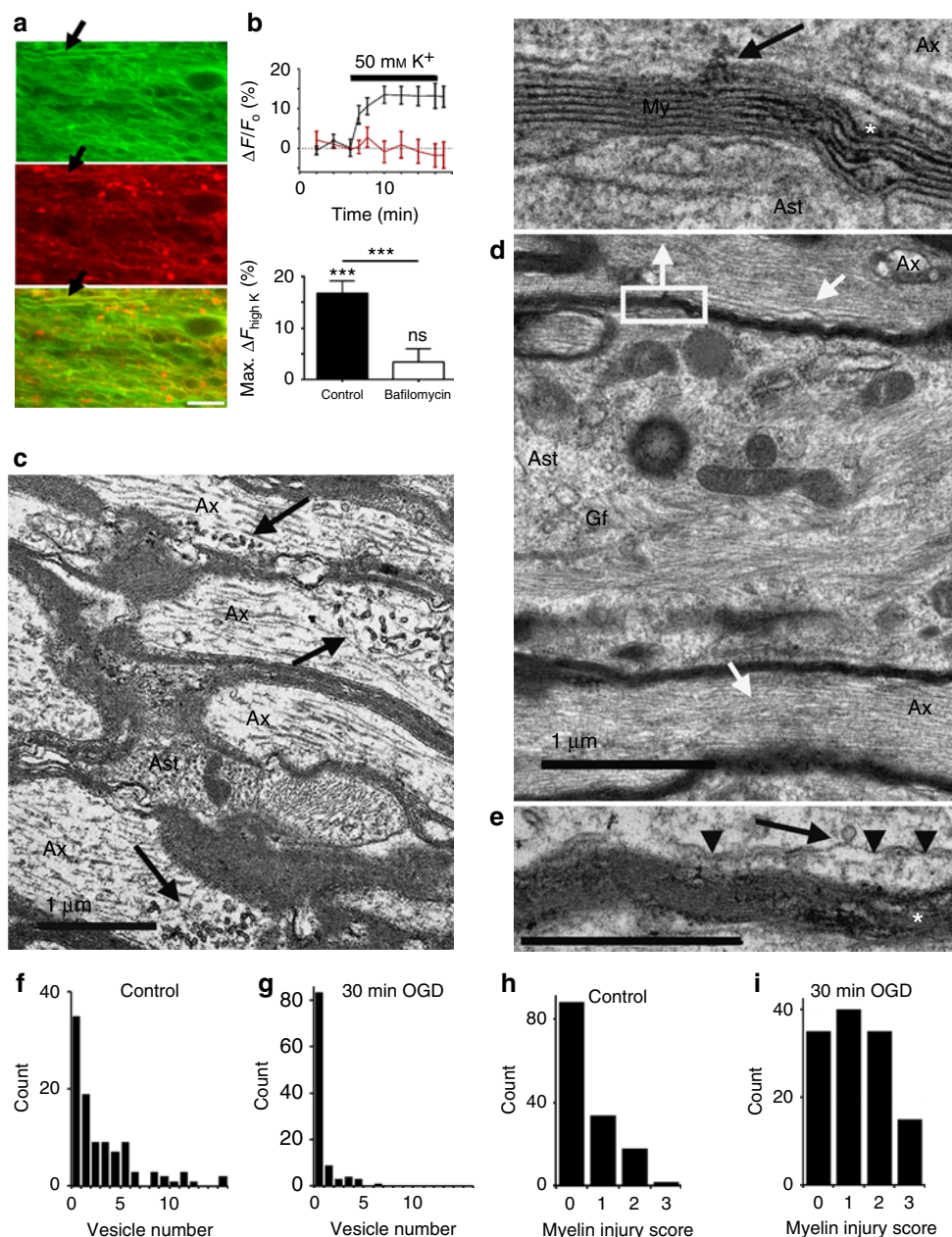


Fig. 2 Vesicular release under the myelin. **a** Myelin loaded with DiOC₆ (green) and the Ca²⁺-indicator X-rhod-1 (red) in adult mouse RON. Note the loading into myelin profiles (e.g., arrow). **b** Top: X-rhod-1 intensity (relative to initial mean) is elevated following depolarization with 50 mM K⁺ (black line) consistent with activation of NMDA receptors in the myelin, an effect blocked by pre-treatment with the vesicular loading blocker bafilomycin (red line). **b** Bottom: data summary. Asterisks on the error bars indicate $P = 0.0000$ significance vs., the initial fluorescence mean; on the bar they indicate $P = 0.0000$ significance vs., the two conditions. $n = 5$ mice in each protocol, 1–3 slices/mouse, ANOVA with Holm–Šidák post test. Bar = 8 μm . **c** 20–50 nm vesicles are present in clusters in the sub-myelinic axoplasm (e.g., arrows) (Ax = axons; Ast = astrocyte process containing glial filaments; bar = 1 μm). **d** Sub-myelinic vesicles are less common in RONs fixed after 30 min of OGD and can be seen juxtaposed on the axolemma (black arrow). White boxed area shown at higher magnification above. Note the absence of vesicles in the astrocyte process identified by the presence of glial filaments (Gf), and the retention of microtubules in myelinated axons (white arrows). Bar = 1 μm . **e** A single vesicle (black arrow) docked with the axolemma (arrow heads) beneath the myelin following OGD. Note the presence of focal myelin injuries in both (**d**) and (**e**) (white asterisks). Bar = 500 nm. **f, g** The distribution of vesicle clusters in axon profiles by number of vesicles in control and 30 min OGD RONs (per field of view). Note the large number of axons with zero vesicles following OGD (scales differ). **h, i** Focal myelin injury scores are shifted to higher values in myelin regions adjacent to axoplasmic vesicles post OGD compared to control RONs

MK-801 protection increased with pre-treatment time with maximal protection of >400% after 120 min pre-treatment (Fig. 4a, b). Myelinic NMDA GluRs contain the GluN2C/D subunit^{4,5,7} and we tested 120 min pre-treatment with the GluN2C/D-specific antagonists PPDA (50 μM) and QNZ-46 (50

μM)²³, which also significantly increased recovery from ischemia (Fig. 4c). TRPA1 receptor block (10 μM A967076) has recently been shown to be protective against ischemic injury in oligodendrocyte processes and myelin sheaths²⁴, but did not provide functional white matter protection in our model of acute ischemic

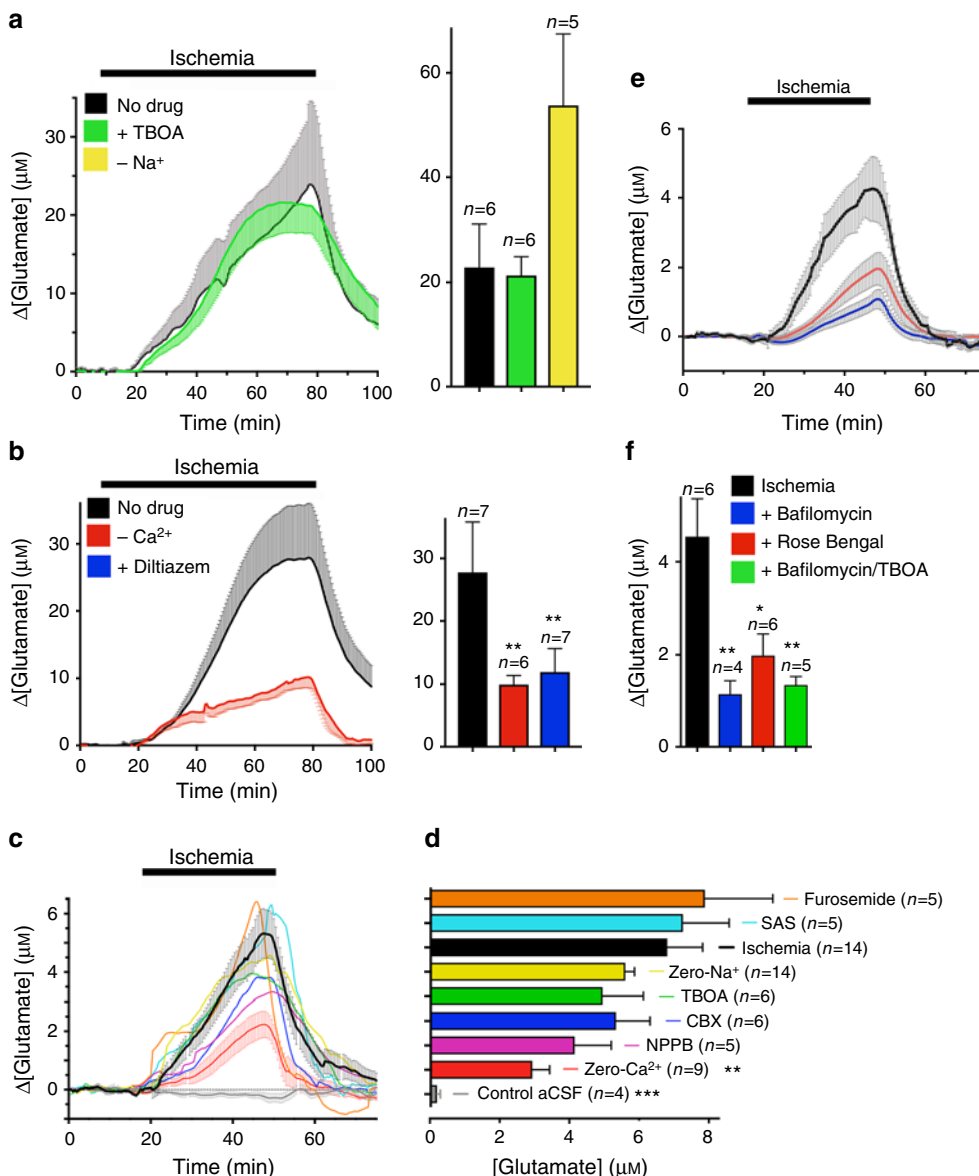


Fig. 3 White matter ischemic glutamate release is primarily vesicular. **a** Ischemia-evoked $[\text{glutamate}]_e$ elevation in adult rat RON is Na⁺-independent/TBOA-insensitive. **b** The ischemic $[\text{glutamate}]_e$ rise is Ca²⁺-dependent (ANOVA with Holm–Šidák post test: $P = 0.012$) and diltiazem-sensitive ($P = 0.010$). **c, d** In juvenile rat RON, the ischemic $[\text{glutamate}]_e$ elevation ($P = 0.001$ vs., control aCSF) is Ca²⁺-dependent ($P = 0.009$ vs., ischemia)/Na⁺-independent and resistant to inhibitors of non-vesicular glutamate release pathways. **e, f** Ischemic $[\text{glutamate}]_e$ elevation in juvenile RON is significantly inhibited by blockers of vesicular glutamate loading bafilomycin ($P = 0.004$); rose bengal ($P = 0.013$) and combined bafilomycin + TBOA ($P = 0.004$)

injury (Fig. 4c). Previous studies of oligodendrocyte injury have often relied on live imaging of the cells cytoplasmic domain^{5,7,24}. Simultaneous live imaging of the myelinic and cytoplasmic domains of oligodendrocytes revealed that they are largely distinct (Fig. 4d) and that morphological and structural changes in oligodendrocyte processes imaged via fluorescence label expression do not reflect myelin pathology. Dual domain imaging during ischemia showed the myelin decompaction predicted by prior ultrastructural studies (Fig. 4e, f), with ongoing disruption of cell processes/somata swelling. Myelin thickness increased from $0.67 \mu\text{m} \pm 0.02$ to $0.90 \mu\text{m} \pm 0.07$ after 60 min ischemia + 60 min recovery, an effect that was prevented by 120 min pre-treatment with QNZ-46 (Fig. 4e, f). Ultrastructural analysis revealed extensive myelin decompaction and bubbling following the standard OGD protocol, in addition to disruption of glial

processes and soma (Fig. 5a–c). Bubbling of the inner myelin layer was particularly evident following OGD (Fig. 5c) and involved regions where the inner myelin layer detached from the remaining compact myelin and formed a series of bubbles. Myelin bubbling was accompanied by a reduction in the number of myelin layers (Fig. 5c small arrows). Axon cylinders in these regions (Fig. 3c Ax) often retained microtubule profiles and a clearly contiguous axolemma separating the cylinder from the myelin bubbles. The myelin protection recently reported following TRPA1 block did not extend to structures defined as axoplasmic vesicles²⁴, which appear to have similar features to the myelin bubbles we here identify under the remaining compact myelin sheath. 120 min pre-treatment with QNZ-46 almost entirely prevented these structural changes (Fig. 5d–f). Quantitative analysis of myelin decompaction via G-ratio analysis of

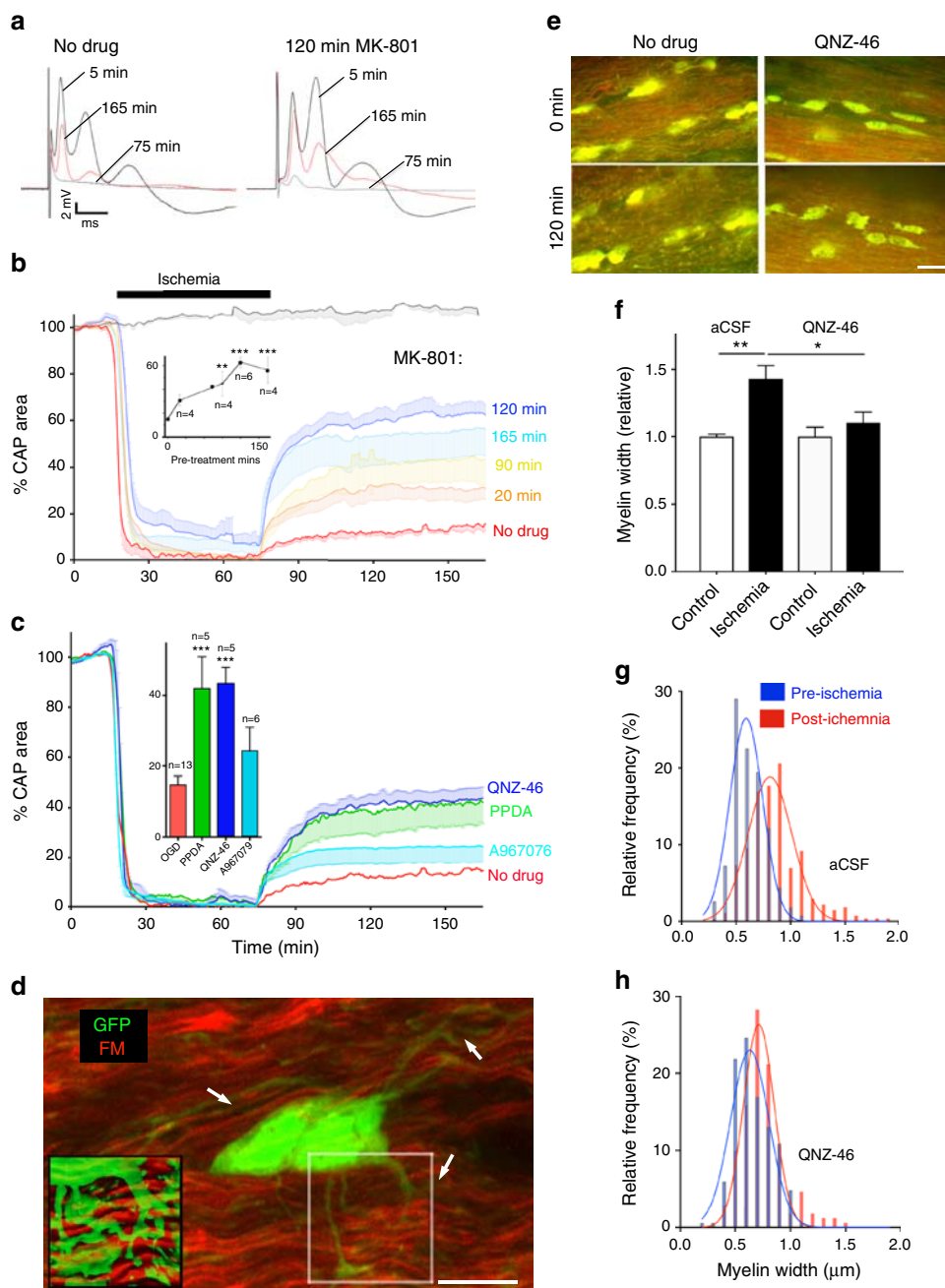


Fig. 4 Myelin injury is NMDA-receptor-mediated. **a** CAP recordings from adult rat RON showing elevated functional recovery from ischemia following 120 min MK-801 pre-treatment. **b** Ischemia-evoked loss and recovery of function following different periods of MK-801 pre-treatment (insert: data summary). ANOVA with Holm–Šidák post test. *P* values: 90 min **0.002; 120 min ***0.0001; 165 min ***0.0000. **c** 120 min pre-treatment with selective NMDA receptor GluN2C/D blockers QNZ-46 (*P* = 0.0013) or PPDA (*P* = 0.0009), or the TRPA1 blocker A967076. **d** Oligodendrocyte cytoplasmic domain (PLP-GFP mouse, arrows) is distinct from the myelin domain (FM: fluoromyelin red) in live adult mouse RON. Highlighted square shown in insert as rendered stack. **e** Myelin structure is protected from ischemic damage by 120 min pre-treatment with QNZ-46, imaged via FM vital staining. **f–h** Ischemia evoked myelin swelling (*P* = 0.000 in aCSF) is prevented by 120 min QNZ-46 pre-treatment (*P* = 0.047 vs. aCSF). Scale = 10 μ m

axon cross-section (X-S) confirmed the myelin protecting properties of the drug (Fig. 5g–k). GluR-mediated myelin loss during OGD was confirmed in the RON by diminished intensity of the established myelin stain FluoroMyelin Red (FM) (Fig. 5l).

QNZ-46 is a 4-oxo-3(4H)quinazolinyl derivative containing the trans-stilbene pharmacophore²³ and has the lipophilicity common to fluorescent myelin stains²⁵, although with reduced aromaticity in the A ring (Supplementary Fig. 5a). The structure

also contains the quinazolinone backbone known to exhibit strong fluorescence²⁶ and the drug therefore has the structural components of a fluorescent myelin stain. QNZ-46 had a peak emission at 450 nm in a lipid environment (Supplementary Fig. 5b), allowing drug uptake to be monitored in real time. QNZ-46 loaded into adult rat RON from the bath over 120 min and was retained following wash-out (Fig. 6a). After 120 min of bath loading into brain slices, vital QNZ-46 fluorescence was localized

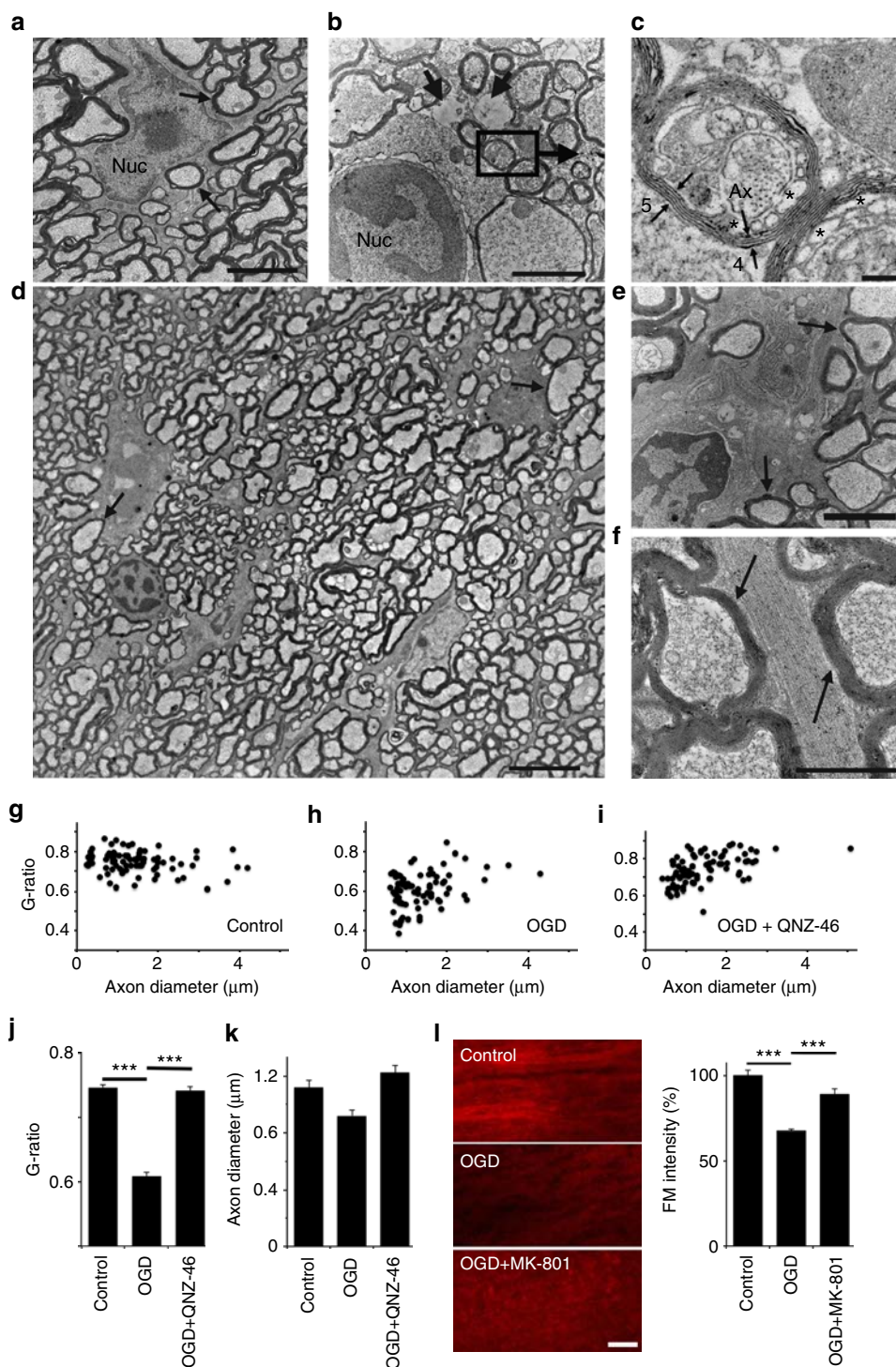


Fig. 5 Myelin protection in adult mouse RON. **a** Oligodendrocyte (Nuc = nucleus) and myelinated axons (e.g., arrows) in control RON have a normal healthy structure. **b, c** Following OGD there is glial disruption including nuclear condensation and process degeneration (e.g., short arrows) with myelin disruption in the axon population. Note that the inner myelin layers are often separated and may form bubbles. For example in **(c)** (higher power image of the boxed area in **(b)**) where a region of myelin on the left side of the axon has five layers (small arrows) and no bubbles but the inner layer has four layers with a series of bubble profiles on the right side (e.g., *). Note retention of microtubules within the axon profile (Ax). **d-f** Uniform protection of myelin structure (e.g., arrows) throughout RONs fixed after OGD + QNZ-46. Note that glial cell soma (**d, e**) and processes (**f**) also retain normal structure in this protocol. **g-j** Myelin thickness assessed as G-ratio under the three conditions, showing myelin expansion following OGD (ANOVA with Holm–Šidák post test; $P = 0.0001$) and prevention of this effect by perfusion with QNZ-46 ($P = 0.0007$). **j, k** Mean data showing the changes in G-ratio under these conditions (**j**); which are not accounted for by significant axonal shrinking (**k**). **l** Myelin stained with fluoroMyelin (FM) under these conditions (left) and (right) the mean FM intensity decline evoked by OGD ($P = 0.00027$), which is prevented by MK801 ($P = 0.00062$). Bar **a, b, e, f** = 1 μm; **d** = 5 μm; **c, l** = 100 nm

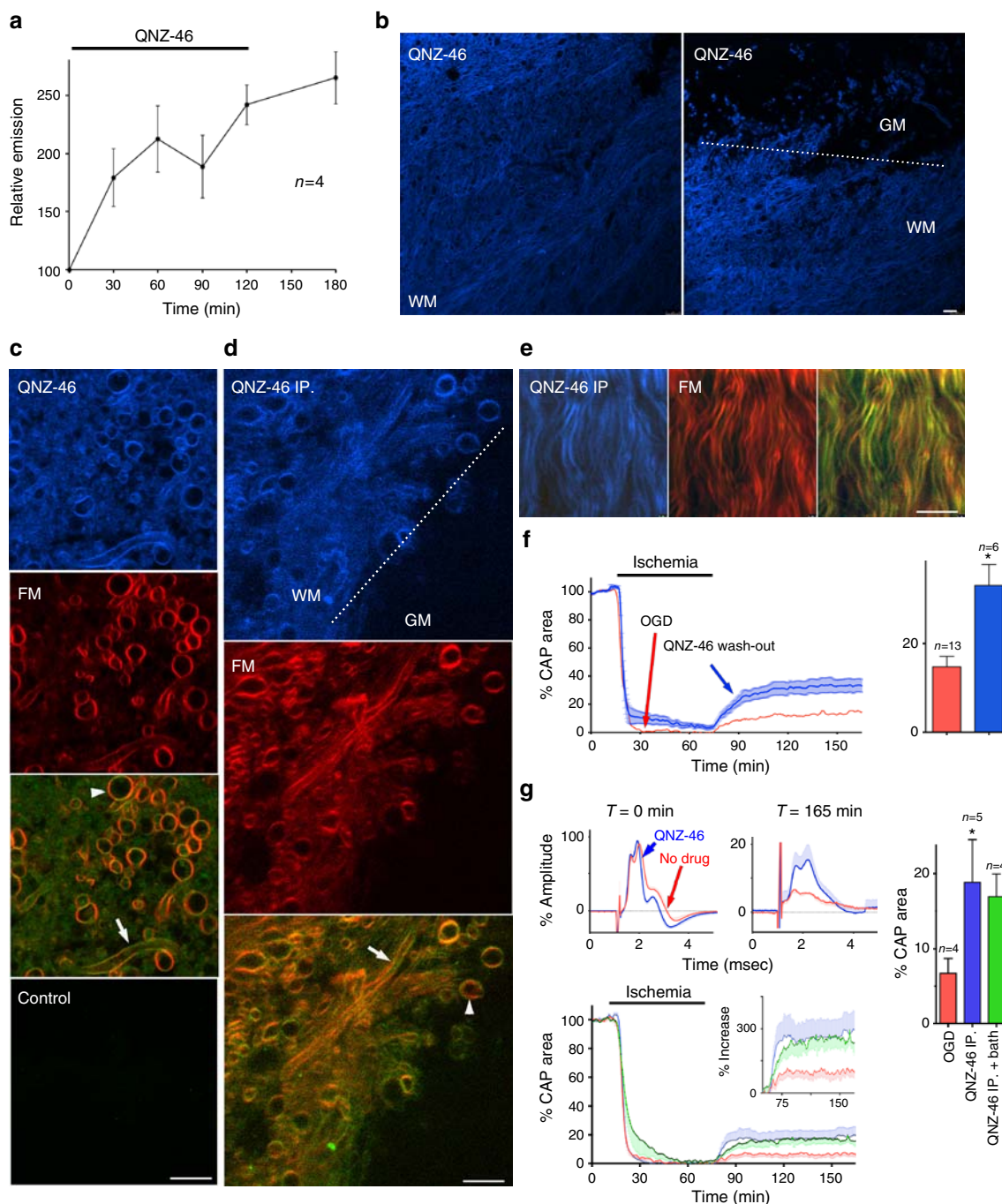


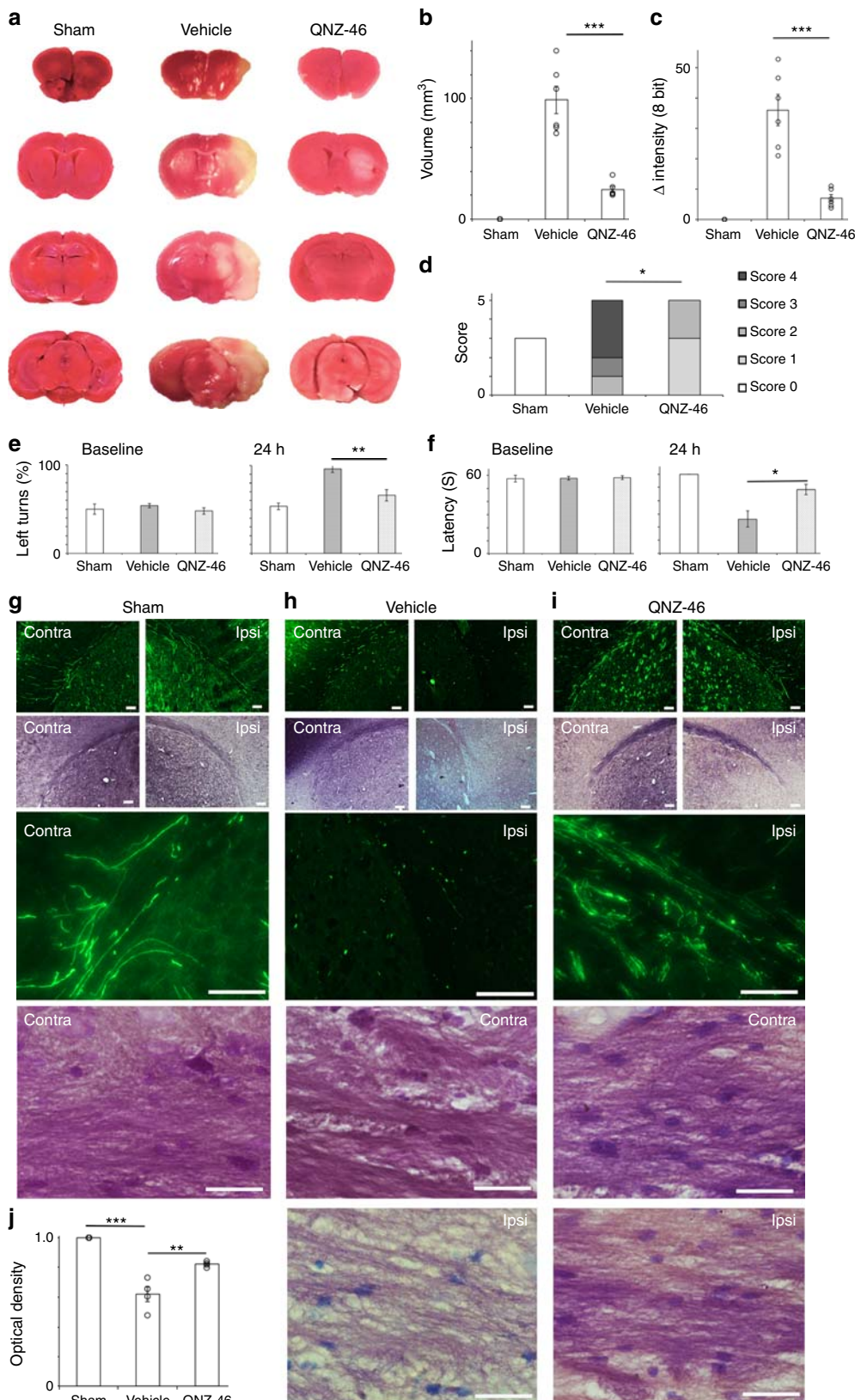
Fig. 6 QNZ-46 is absorbed by myelin. **a** QNZ-46 emission shows accumulation and retention in adult rat RON. **b** Confocal imaging of vital QNZ-46 fluorescence (120 min treatment) in adult corpus callosum (left) and the white matter–gray matter border (right). **c** Vital QNZ-46/FM co-staining of myelinated axon profiles. **d, e** Vital QNZ-46/FM co-staining in brain slice (**d**) and RON (**e**) following systemic QNZ-46 injection 4 h pre-sacrifice. **f** 60 min QNZ-46 pre-treatment + 60 min wash-out is functionally protective of adult rat RON (ANOVA with Holm–Šidák post test; $P = 0.037$). **g** Systemic QNZ-46 pre-treatment is functionally protective of mouse RON perfused with aCSF (blue, $P = 0.047$), and is not significantly different when QNZ-46 is included in the bath (green). Note, proportional recovery was similar to that found in Fig. 3c (insert). Merged images recolored for clarity. Scale bars = 5 μm

to myelin axon profiles, was low in gray matter regions, and co-localized with FM (Fig. 6b, c). Following i.p. injection (20 mg/kg in 50/50 DMSO/ β -cyclodextrin 240 min prior to the killing, based on known CNS action of a similar compound²⁷), vital QNZ-46 fluorescence had a similar distribution in mouse brain slices to that produced by bath loading (Fig. 6d, e), demonstrating brain penetration and myelin retention (tissue was dissected into QNZ-46 free aCSF for imaging).

QNZ-46 is an allosteric modulator of GluN2C/D-containing NMDA GluRs with use-dependent features^{23,28}. It is the most selective inhibitor of GluN2C/D-containing GluR currently identified with a >50-fold IC₅₀ differential over GluN2A/B-containing receptors. In silico modeling indicates drugability, although with a high polar surface area (Supplementary Fig. 5c). The myelin partitioning and trapping evident in Fig. 6a–e suggests QNZ-46 may provide myelin protection following

removal from the extracellular space. Indeed, 60 min pre-treatment followed by 60 min of wash-out significantly elevated functional recovery in the adult rat RON (Fig. 6f). No similar effect was found with the non-NMDA glutamate receptor blocker NBQX, an anti-excitotoxic drug thought to act at the

oligodendrocyte cell body⁷ (Supplementary Fig. 6). Systemic i.p. injection of QNZ-46 followed by 240 min recovery, dissection and 60 min bath perfusion with aCSF also increased compound action potential (CAP) recovery in adult mouse RON from $6.8 \pm 1.9\%$ to $18.9 \pm 5.6\%$, representing a >270% increase compared to vehicle-



treated control (Fig. 6g). This effect was not potentiated by the presence of QNZ-46 in the bath, suggesting that systemic QNZ-46 pre-treatment and myelin trapping results in maximal protection (Fig. 6g). The efficacy of QNZ-46 trapped within myelin may suggest drug interaction with an NMDA receptor site within the lipid lamella/oligodendrocyte cell membrane. Alternatively, myelin may act as a reservoir that gradually releases QNZ-46 to act at extra- or intra-cellular sites on the receptor. In either case, our data suggest that incorporation of myelin-targeted elements such as trans-stilbene may enhance the effectiveness of myelin treatments generally.

Although crossing the blood–brain barrier and segregating into myelin, systemic pre-treatment with QNZ-46 produced no apparent behavioral effects or acute toxicity. A 120 min single dose pre-treatment protocol was tested in a standard 60 min transient middle cerebral artery occlusion (tMCAO) model of stroke. Brain lesions assessed 24 h post-reperfusion in vehicle treated wild-type mice included extensive damage to white matter structures such as the external capsule and gray matter regions such as the overlying motor cortex. Drug treatment greatly reduced lesion volume and improved the performance in behavioral tests compared to vehicle-treated controls (Fig. 7a–e).

External capsule axon integrity assessed via YFP expression in Thy-1-YFP mice was lost within the lesion site in the vehicle cohort, but was largely preserved in the QNZ-46 treated cohort (Fig. 7g–j). Myelin integrity was protected to a similar extent (Fig. 7g–j).

A second series of tMCAO data was generated with mice perfusion fixed after the 24 h recovery for ultrastructural analysis. Lesion reduction following QNZ-46 pre-treatment was replicated in these experiments (lesion volume vehicle = $119.4 \pm 8.9 \text{ mm}^3$, QNZ-46 = $38.9 \pm 7.0 \text{ mm}^3$; $P < 0.0001$). Neuronal somata, neuropil, and white matter structure was well preserved in the external capsule-motor cortex border region of the contralateral hemisphere (Fig. 8c). Widespread cellular breakdown was apparent in the comparable vehicle-treated ipsilateral region (Fig. 8d, e), including necrotic cell death, neuropil degeneration, and universal myelin destruction in both white matter tracts and gray matter axons (Supplementary Fig. 7). In mice pre-treated with QNZ-46, all cellular elements were relatively preserved (Fig. 8f–h; Supplementary Fig. 7), with myelinated axons having no signs of myelin splitting or bubbling. Largely uninjured neuronal somata, neuropil, and glial somata were apparent throughout the region, although astrocyte processes (some containing glial filaments) were swollen and damaged (Fig. 8g, white arrows). Quantitative assessment of somata injury (which will include both neurons and glia since they cannot be reliably distinguished post vehicle-treated injury) showed QNZ-46 protection in the ipsilateral hemisphere of both white matter and gray matter areas, with no significant difference in somata damage between contra- and ipsilateral sides in white matter (Fig. 8i). Myelin expansion (G-ratio, not measured in ipsilateral white matter due to the extent of damage) was not present in the ipsilateral white matter of QNZ-46-treated mice. It is apparent from these in vivo experiments that a single dose pre-treatment with QNZ-46 protected both gray matter and white matter

structures to deliver a high level of structural and functional neuroprotection.

Discussion

The results highlight the significance of vesicular glutamate release from axons and demonstrate the involvement of this phenomenon in ischemia-evoked myelin damage. Earlier reports have documented reverse glutamate release under ischemic conditions in the CA1 region of the neonatal hippocampus⁹, adult spinal cord¹⁰, and mouse optic nerve¹¹. To our knowledge, the current report is the first to directly measure extracellular glutamate in white matter and while glutamate transport was found to be significant for homeostatic regulation of the neurotransmitter, we found no evidence for significant ischemic release via this mechanism. Ischemic glutamate release pathways in the white matter of the brain are likely to differ from those operating in gray matter areas such as the hippocampus CA1, while earlier white matter studies have generally examined secondary effects of reverse glutamate transport block and this may account for the discrepancy between earlier findings and the current results.

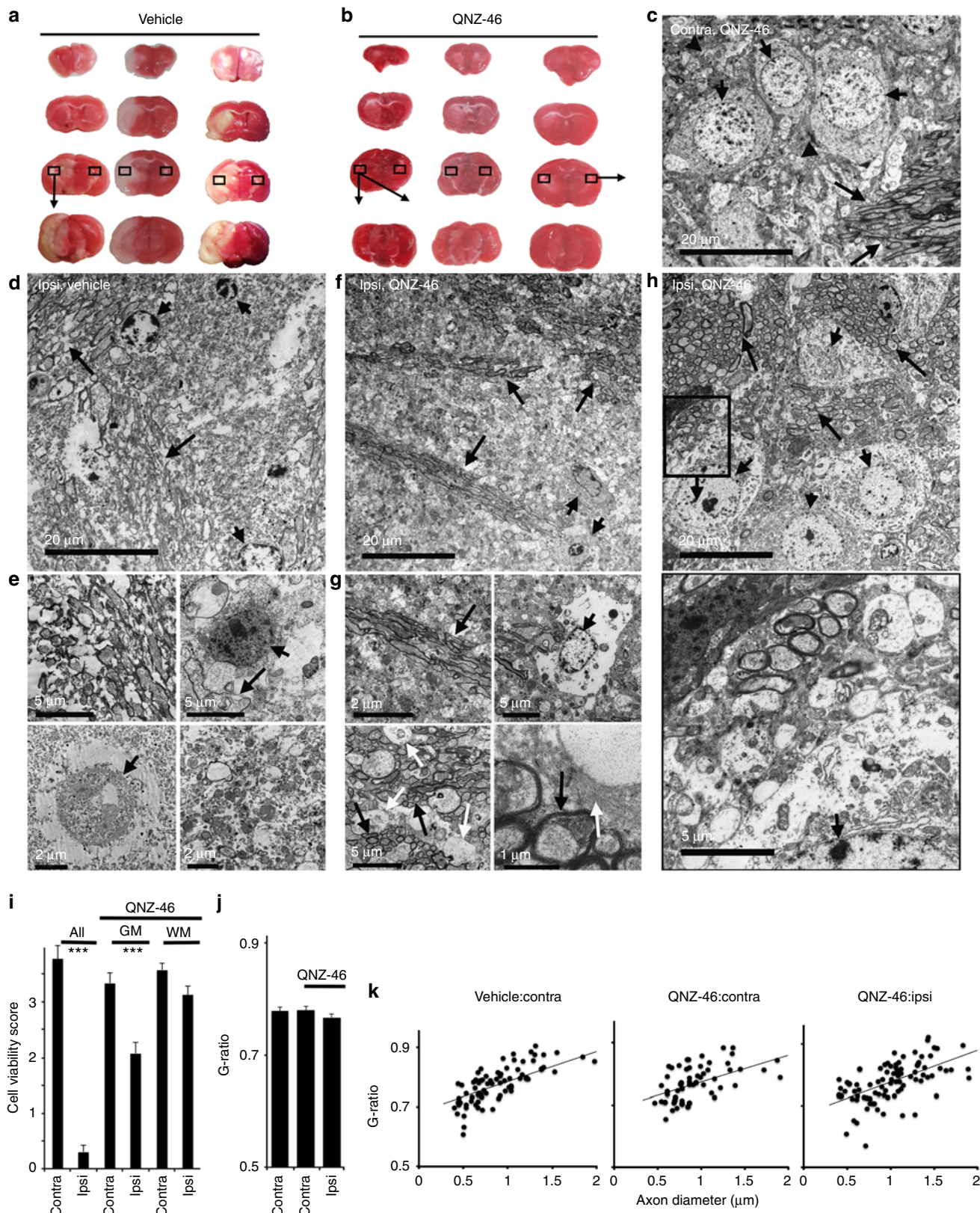
Approximately 95% of clinical strokes involve white matter, which accounts for ~49% of stroke total mean infarct volume²⁹. Stroke in the territory of penetrating arteries preferentially target white matter and accounts for ~25% of stroke cases, representing the second leading cause of dementia^{3,30}. White matter stroke features rapid myelin damage³¹ and remyelination failure in white matter lesions significantly contributes to functional loss^{3,30}. The mechanisms underlying myelin injury in these acute ischemic lesions have high clinical relevance and may share common features with other forms of myelin damage, for example those operating in multiple sclerosis and CNS trauma^{32,33}. We have shown that acute ischemic myelin injury results from vesicular glutamate release from axons, leading to cytotoxic over-activation of GluN2C/D-containing myelinic NMDA GluRs preventable by the selective negative allosteric modulator QNZ-46 (Supplementary Fig. 8). QNZ-46 has high selectivity for GluN2C/D-containing GluRs, shows novel myelin accumulation and retention, is brain accessible, and has the basic features of a clinically useful drug, suggesting outstanding clinical potential against excitotoxic myelin injury. QNZ-46 exhibits persistent CNS protection, elevating injury tolerance after the drug is removed from the extracellular space, and has clinical potential for treatment of prevalent neurological disorders involving myelin damage in particular in patients at risk of ischemic injuries such as stroke.

While the neuroprotective effect of broad-spectrum NMDA GluR blockers is well established, these drugs have failed to translate into clinical practice. The reasons for this are complex and involve unacceptable side effects and the short therapeutic window that follows stroke onset. This second problem may be insurmountable; the FAST-MAG trial achieved paramedic delivery of the NMDA receptor blocker Mg^{2+} within 45 min of stroke symptom onset but failed to improve outcomes³⁴. Negative allosteric modulators such as QNZ-46 exhibit use-dependent block predisposing them to target pathological over-activation of

Fig. 7 A single QNZ-46 pre-treatment produces high levels of white matter and gray matter neuro-protection. **a–c** Brain lesion volume 24 h post-tMCAO. **d–f** Functional recovery prior to the killing. Drug treatment significantly improved the outcome in all measures. ANOVA with Holm–Šidák post test. P values: **b** ***0.0000; **c** **0.000; **e** *0.004; **f** *0.011. Mann–Whitney test; **d** * <0.05 . **g–j** YFP expression (green) and luxol fast-blue/cresyl violet (blue/purple: myelin) in Thy-1-YFP mice. **g** YFP(+) axons project within the external capsule which is extensively myelinated in contralateral (Contra) and ipsilateral (Ipsi) hemispheres in sham-operated mice. Higher power micrographs are shown at the bottom. **h** Mice treated with vehicle show disruption and loss of axonal YFP that extends to both hemispheres and loss of myelin within the ipsilateral white matter. **i** Drug-treated mice retain YFP(+) axons and myelin staining in both hemispheres. **j** Myelin stain density is significantly reduced in the vehicle-treated group (**0.0002), and preserved by QNZ-46 pre-treatment (**0.005). Scale bars = 100 μm

receptors over normal physiological receptor function^{23,24}. The physiological functions of oligodendrocyte NMDA GluRs includes regulation of GLUT-1 expression²² and axo-glial myelin³⁵. Constitutive targeted ablation of the obligatory Nr1 subunit in oligodendrocytes leads to a switch in the mechanism regulating

myelination and a downregulation of GLUT-1 that is associated with gradual structural compromise; these effects may be avoided by this class of drug. In the adult CNS, GluN2C/D subunits are primarily incorporated into extra-synaptic NMDA receptors³⁶⁻³⁸, and are expressed at lower levels in gray matter regions than are



other NMDA GluR subunits^{39,40}, two additional factors that will limit the side-effects of drug treatment. Stroke incidence is well correlated with age, prior transient ischemic attack, hypertension, and prior stroke⁴¹. Our findings suggest that prophylactic treatment in patients at risk of stroke may offer an alternative strategy for clinical intervention that avoids the therapeutic window. The extent of the structural and functional neuroprotection offered by QNZ-46 is surprising; in particular the effect in gray matter where neuron somata and neuropil were protected against ischemic injury *in vivo*. Targeting of extra-synaptic NMDA receptors has shown promise for a wide range of neurological conditions including dementia⁴², and QNZ-46 may protect gray matter in a similar fashion. The combined protective effect in both categories of CNS tissue adds to the clinical potential of the drug.

Methods

Animals and reagents. All animal procedures conformed to local ethical standards and ARRIVE guidelines. UK home office and Maltese national regulations were followed as appropriate. For RON experiments, nerves were dissected from juvenile (P8–12) or adult (P90–120) Wistar rats, adult (P80–110) PLP-GFP or C57 wild-type mice. Acute coronal vibratome-cut sections were cut in oxygenated, ice-cold cutting solution (in mM): NaCl, 92; KCl, 2.5; NaH₂PO₄, 1.2; MgSO₄, 2; CaCl₂, 2; NaHCO₃, 30; glucose, 25; Hepes, 20; Na Pyruvate, 3; Thiourea, 2; Na Ascorbate, 5; pH, 7.4. Experiments were performed in artificial cerebrospinal fluid (aCSF), composition (in mM): NaCl, 126; KCl, 3; NaH₂PO₄, 2; MgSO₄, 2; CaCl₂, 2; NaHCO₃, 26; glucose, 10; pH, 7.45, bubbled with 5% CO₂/95% O₂ and kept at 37 °C. KCl (47 mM) was added to aCSF (NaCl replacement) for “High K⁺” experiments. For zero-Ca²⁺ aCSF, CaCl₂ was omitted, and 50 μM EGTA was added. For zero-Na⁺ aCSF, Na⁺ was replaced with NMDG. Oxygen-glucose deprivation was used as the model of ischemia for CAP and confocal imaging experiments: aCSF was replaced by a glucose-free aCSF (+10 mM sucrose to maintain osmolality) saturated with 95% N₂/5% CO₂. The chamber atmosphere was switched to 5% CO₂/95% N₂ during OGD perfusion. Osmolarity of solutions was measured and adjusted as required. NBQX was purchased from Tocris (UK), PPDA and QNZ-46 from either Tocris or Abcam (UK), bafilomycin from Viva Bioscience (UK); all other reagents were from Sigma (UK) including carbenoxolone (CBX), 5-nitro-2-(3-phenyl-propylamino)benzoic acid (NPPB), sulfasalazine (SAS) and three-beta-benzoyloxyaspartate (TBOA).

In vivo treatment for in vitro recording. Adult C57 mice were injected i.p. with 200 μl of 50% DMSO solution containing 1 mM β-cyclodextrin +20 mg/kg QNZ-46, or a vehicle control without the QNZ-46. Injections were performed blind by animal house staff and mice were left for 240 min on a warming pad. Other than mild sedation in both groups attributed to the DMSO, the animals showed no signs of distress or aberrant behavior. RON or brain slices were collected as above, in solutions that did not contain QNZ-46.

Electrophysiology. RON CAPs were evoked and recorded with glass electrodes and the rectified area used to determine changes in conduction. CAPs were evoked via square-wave constant current pulses (Iso stim A320, WPI), amplified (Cyber Amp 320, Axon Instruments), subtracted from a parallel differential electrode, filtered (low pass: 800–10,000 Hz), digitized (1401 mini, Cambridge Electronic Design) and displayed on a PC running Signal software (Cambridge Electronic Design). Non-recoverable CAP loss from the RON indicates irreversible failure of axon function. Glutamate microelectrode biosensors (Sarissa Biomedical, Coventry,

UK), amplified via a Duo-Stat ME-200+ potentiostat (Sycopel International, London, UK), were used to record glutamate concentration. Signals were differential to a null electrode and both active and null electrodes were gradually inserted into brain slice or RON, in the latter case through a small incision in the nerve sheath. An Ag/AgCl reference electrode was introduced into the bath. Sensors were calibrated in the chamber at the end of each experiment. Values from the null, sensor, and sensor-minus-null outputs were recorded at 0.5 Hz and subsequently converted into glutamate concentration (Supplementary Fig. 4). Recorded glutamate was high following electrode placement, presumably due to localized tissue damage (Supplementary Fig. 4), and declined to a low stable concentration over a 120–180 min (neonatal RON), 300–420 min (adult RON) or 180–240 min (slices) rest period before experiments were initiated. Nerves may have been pre-treated with 50 μM BAPTA-AM for zero-Ca²⁺ experiments (no difference was detected and data were pooled). Corpus callosum glutamate sensor experiments were conducted on 400 μm sections from adult Wistar rats, adult (P80–110) THY-1/YFP (Line H), GFAP-GFP or C57 wild-type mice. Slices were gradually warmed to 37 °C over ~60 min and rested for 120 min prior to use. Unless otherwise stated, preparations were maintained in an oxygenated (1.5 l/min) interface perfusion chamber (Harvard Apparatus Inc.) and continuously superfused (0.6–1 ml/min) with aCSF. Due to the oxygen-sensitivity of the glutamate biosensors, chemical anoxia (1 nM rotenone for neonates/25 μM antimycin-a for adults) + aglycemia was used as the model of ischemia for [glutamate]_e recordings.

Two-photon confocal imaging. After deep isoflurane anesthesia and decapitation, the brain was rapidly removed into chilled aCSF supplemented with 75 mM sucrose and vibratome sectioned into coronal slices (400 μm thick) from the genu of the corpus callosum through the caudal extent of the hippocampus. Immediately after sectioning, slices were transferred to a Haas-type interface brain slice chamber (Harvard Apparatus, South Natick, MA) and allowed to recover at room temperature in aCSF for 60 min. Slices were transferred to a mini submerged chamber (0.5 ml) with a coverglass bottom (Warner Instrument Corporation, Hamden, CT) mounted on an upright BX50W1 Olympus Multiphoton microscope (Olympus, Tokyo, Japan) and perfused with room temperature aCSF at 3.5 ml/min. Final temperature control (37 ± 1 °C) was maintained using an in-line heater (Warner Instrument Corporation, Hamden, CT) equipped with a feedback thermistor placed in the chamber and the temperature raised gradually over 60 min. The multiphoton system housed Keplerian beam expanders with IR introduction light paths. A mode-locked MaiTai HP DeepSee laser system (Spectra-Physics) with a tuneable Ti: sapphire oscillator (690–1040 nm) was used as the excitation light source (pulse width < 100 fs; pulse repetition rate 80 Mhz) and controlled through an acousto-optical-modulator. The Group Velocity Dispersion was electronically compensated by a prism-coupled pre-chirper and the beam diameter adjusted by a Kepler telescope. Image acquisition was performed using the Olympus Fluoview software.

Vesicular imaging was conducted on brain slices from transgenic animals using FM4-64. Corpus callosum slices were initially superfused with aCSF + 10 μM FM4-64 for 10 min. Slices were then subjected to a 50 mM K⁺ aCSF + 10 μM FM4-64 for 5 min, and subsequently returned to aCSF + 10 μM FM4-64 for a further 20 min. Next, slices were washed in aCSF (without FM4-64) for 15 min and a suitable region of the corpus callosum was identified. Finally, slices were exposed to 50 mM K⁺ aCSF for 10 min (or ischemia for 30 min) to promote vesicular fusion/FM4-64 unloading. Images were acquired every 10 s following laser excitation at 890 nm and collected using standard red and green filter settings. Mean pixel intensity within YFP(+) axons or GFP(+) astrocytes was determined using Olympus Fluoview software, with the regions of interest determined by the green profile of axons/glia. Fluorescent emission scans during excitation at 405 nm were conducted using 10 nm bin width and the lambda-scan function, with 10 mM QNZ-46 in DMSO diluted 50:50 in immersion oil.

Fig. 8 Structural protection following systemic QNZ-46 pre-treatment. **a, b** Brain lesions in vehicle- and QNZ-46-treated mice subject to the standard MCAO protocol. Boxed areas (external capsule-motor cortex border) were examined via TEM. **c** Cortical neuronal somata (nuclei indicated by short arrows), neuropil (arrow heads), and myelinated axons (long arrows) in contralateral QNZ-46-treated mice appeared normal with no unusual features. **d, e** Ipsilateral vehicle-treated external capsule-motor cortex border showed wide-scale cellular destruction and loss of structure including disrupted myelinated axon tracts (arrows **d, e** top left) and necrotic neuronal soma (arrow heads **d, e** bottom left). White matter glial cell soma and process were also necrotic (**e**, top right, short arrow) and occasional distorted myelin profiles were apparent (**e**, top right, arrow). Cell processes in the neuropil were generally disrupted with free-floating mitochondria present (**e**, bottom right). **f–h** Ipsilateral QNZ-46-treated external capsule-motor cortex border showed almost normal structural features in both white matter and gray matter areas. Myelinated axon tracts showed no myelin damage (**f, g** top left, **h** arrows) and both neuronal and glial soma (**f, g** top right, **h** short arrows) appeared largely intact. Glial processes were often swollen (**g**, bottom left and right white arrows) and in many cases could be identified as astrocytic containing glial filaments (**g**, bottom right, white arrow). Neuronal, neuropil, and myelinated axon profiles are shown at higher gain in the expanded boxed area in **h** (lower panel). **i** Cell viability was severely compromised (ANOVA with Holm–Šidák post test; ****P* = 0.0000) in ipsilateral vehicle-treated mice (where white matter and gray matter, neuron and glia could not always be distinguished and are grouped together). QNZ-46 pre-treatment significantly improved cell viability in both white matter and gray matter (****P* = 0.0000 vs. untreated ipsilateral injury), with no significant difference between ipsi- and contralateral cells in white matter regions. **j–k** G-ratio was not significantly different in ipsi- and contralateral white matter axons in QNZ-46 pre-treated mice. Note axon disruption precluded the measurement of G-ratio in ipsilateral vehicle-treated white matter

Single-photon imaging. Live imaging of NMDA-receptor-mediated myelin injury: PLP-GFAP RONS were exposed to FluoroMyelin Red (5%; 100 min, 5 °C in cutting solution) with or without drug, prior to dye wash-out and mounting in a temperature-controlled perfusion chamber (Warner Instruments, Hamden, CT, USA). RONS were superfused at 2 ml/min with aCSF with or without drug and imaged in a single plane on an inverted Nikon TE2000-U microscope. Imaging was achieved via spinning disk confocal imaging (Crest-Optics, X-light) and collected via MetaMorph software (Molecular Devices). FluoroMyelin Red and GFP were consecutively imaged following excitation of both at 488 nm using a 650 ± 50 nm BP filter (Thorlabs, Newton, New Jersey, USA) and a standard GFP filter set (Chroma Technology Corporation, Bellows Falls, VT, USA), respectively. RONS were imaged 20 min prior to switching to a 60-min period of OGD and then switched back for 60 min of recovery. Myelin decompaction was assessed using intensity line-plots drawn perpendicular to the longitudinal axis of individual myelin sheaths using ImageJ (NIH). Pre-OGD myelin sheath width was not significantly different in control and treated preparations and the data were pooled. Single-photon, laser scanning confocal images of QNZ-46 bath-loaded adult mouse ON and 200 µm coronal brain sections (P90–120) Wistar rats, (P80–110) PLP-GFP or C57 mice and brain sections from QNZ-46-injected mice, were collected using a Leica TCS SP8 microscope, using loading protocol and settings for GFP and FluoroMyelin Red comparable to those used for spinning disk above. QNZ-46 was imaged following excitation at 405 nm using filter settings standard for DAPI emission. Wide-field QNZ-46 imaging was performed using an Olympus epi-fluorescence microscope and a standard DAPI filter set; emission was quantified from the whole nerve section using ImageJ.

Measurement of myelinic vesicular-mediated Ca²⁺ increase: brain sections were prepared from adult (p100-p160) CD1 WT mice and dye loaded at room temperature (22 °C) for 2 h in the presence or absence of bafilomycin in continuously bubbled aCSF (5% CO₂/95% O₂) containing 10 µM X-Rhod-1 AM and 1 µM DiOC6⁸. Subsequently, sections were maintained in DiOC6-containing aCSF with or without bafilomycin until imaging. Dye-loaded sections were placed in a perfusion chamber and continuously superfused at 1 ml/min with bubbled aCSF or high-K aCSF (50 mM K⁺, see above). Single-photon laser scanning confocal images of corpus callosum myelinated axons were collected using a Leica TCS SP8 microscope at 37 °C. Excitation/emission wavelengths was 488/492–560 nm for DiOC6 and 561/585–655 nm for X-Rhod-1. Polygonal ROIs of DiOC6 and X-Rhod-1 dual-loaded axons were selected to exclude adjacent X-Rhod-1-loaded cell bodies. X-Rhod-1 intensity was normalized to the pre-high-K signal and data from individual mice were averaged for a single *n* (1–3 slices per mouse).

Transient middle cerebral artery occlusion. Eleven male Thy1-YFP and 15 C57 wild-type mice weighing 25–30 g were analgesized with buprenorphine (0.03 mg/kg b.w. i.p.) 2 h before surgery and subsequently anesthetized with isoflurane (3% initial, 1.0–1.5% maintenance) and 60% NO in O₂. Animals were maintained normothermic (37 ± 0.5 °C) by means of a servo controlled heating blanket (Harvard Apparatus, Holliston, MA) with rectal temperature monitoring. Pulse oximetry (Spo2), heart rate, and respiratory rate were monitored continuously (STARR Life Sciences Corp., Allison Park, PA), along with systemic blood pressure via a Kent CODA[®] Standard tail-cuff blood pressure system (Kent Scientific Corporation, Torrington, USA). A fiber-optic probe (VP10M200ST, Moor Instruments Ltd, Axminster, UK) was affixed to the skull over the middle cerebral artery for measurement of regional cerebral blood flow using a moorVMS-LDF Laser Doppler System. Under microscope, the left common carotid, internal carotid, and external carotid arteries were exposed through a midline neck incision. The proximal portions of the left common carotid and the external carotid arteries were ligated and a 6–0 silicon-coated nylon suture (60SPRePK5-21910, Doccol Corporation, Massachusetts, USA) introduced into the internal carotid artery to occlude the middle cerebral artery at its origin. Mice were allowed to recover from anesthesia in a warm recovery cage throughout the duration of occlusion. After 60 min, reperfusion was obtained by withdrawal of the suture. Middle cerebral artery occlusion was confirmed by a sudden drop in relative cerebral blood flow to approximately 85% less than baseline measurement. Animals were subsequently administered buprenorphine for analgesia and placed in a recovery cage for 2 h before returning to their home cages with free access to food and water. Plasma glucose concentration was measured before tMCAO, 5 min and 24 h after reperfusion. Sham-treated animals received all surgical procedures but the filament was not inserted into the MCA. For animals pretreated with either QNZ-46 or vehicle (50:50;DMSO/β-cyclodextrin), the active drug or carrier was administered intraperitoneally 120 min before tMCAO.

Clinical evaluation. Body weight (g) was recorded prior to surgery and at 24 h for sham-, vehicle- and drug-treated groups. While a slight weight increase was observed in sham controls, experimental groups demonstrated weight loss after 24 h. Ischemia-induced weight loss was attenuated in drug-treated mice compared to vehicle group, although this was not significant (vehicle vs. drug-treated group: 5.30 ± 0.38 g vs. 4.58 ± 0.33 g).

Modified Bederson score. Neurological performance⁴³ was assessed by two independent and blinded investigators 24 h post tMCAO according to the

following scoring system: 0, no neurological deficit; 1, forelimb flexion; 2, decreased resistance to lateral push; 3, unidirectional circling; 4, longitudinal spinning; 5, no movement.

Corner test. The corner test detects abnormalities of sensory and motor function including vibrissae, forelimb and hindlimb use, and postural motor function⁴⁴. The apparatus consisted of two cardboard boards each with a dimension of 30 × 20 × 1 cm³. The edges of the two boards were attached at a 30° angle with a small opening along the joint to encourage entry into the corner. The mouse was made to enter between the two boards facing the corner. As the animal progressed into the corner, both sides of the vibrissae were stimulated together and the mouse reared forward and upward, and then back to face the open end of the boards. The direction towards which the mouse turned was recorded for a total of ten trials per animal. Recordings were performed at baseline (prior to surgery) and again at 24 h reperfusion.

Wire hanging test. Motor function was evaluated using a wire hanging test for grip strength, balance, and endurance. This test is based on the latency of a mouse to fall off a metal wire upon exhaustion. The apparatus consisted of a 2-mm-thick metallic wire stretched between two poles held 50 cm above the ground, with a pillow in between to prevent injury upon falling. The mouse's hindlimbs were covered with adhesive tape to prevent the animal from using all four paws. The mouse was trained to suspend its body by holding on to the wire. Pre-training was performed for 2 consecutive days before and on surgery day, prior to obtaining baseline values. The mouse was suspended for short intervals (10–20 s) for several trials and then returned to its cage. If the mouse fell before the end of the trial, it was immediately returned and allowed to grasp the wire. Mice were only returned to their home cage once training was completed. Experimental recordings were taken at baseline (prior to surgery) and again at 24 h reperfusion. Suspension time was measured for three trials per session with a maximum of 60 s per trial and a 30-s recovery period in between.

Infarct volume. Lesion volume was assessed 24 h post-MCAO following neurological assessment. Brains were removed, sectioned at 2 mm using a brain matrix and incubated in 2% 2,3,5-triphenyltetrazolium chloride (TTC; Sigma-Aldrich) in saline for 20 min at 37 °C. Four slices per mouse were imaged and processed for infarct volume evaluation by blinded manual area tracing using digital imaging and image analysis software (ImageJ). For each section, the unstained area was defined as the ischemic lesion while red-stained areas delineated viable tissue⁴⁵. Direct infarct volume was calculated by linear trapezoidal extrapolation (Cavalieri principle); for each brain sample, volume of infarction was calculated by integrating the area of damage at each stereotactic level and the slice thickness. An indirect/corrected infarct volume was then calculated to compensate for the space-occupying effect of brain edema. For each brain, an edema index was calculated by dividing the sum of ipsilateral hemisphere volumes by the sum of contralateral hemisphere volumes. The actual infarct volume adjusted for edema was then determined by dividing the direct infarct volume by the edema index⁴⁵.

Tissue processing and histological assessment. Thy-1-YFP mice subject to sham-, vehicle- and drug-treated tMCAO were killed (ketamine/xylazine), transcardially perfused (4% paraformaldehyde in PBS) and the brains were removed, post-fixed (24 h at 4 °C), cryopreserved (30% sucrose for 72 h at 4 °C), embedded (low-melting point agarose, Sigma-Aldrich, A0576), and chilled. Free-floating 20 µm coronal sections (compresso VF-300, Precisionary Instruments Inc., San Jose, California) were mounted onto gelatin-coated slides and YFP-imaged (EVOS Auto FL, ThermoFischer Scientific) using the appropriate green (496/518) filter set. The sections were immediately subsequently stained with 0.1% luxolfast blue (LFB, Solvent Blue 38, Sigma-Aldrich)/0.25% cresyl violet (Sigma-Aldrich) and myelin-imaged bright field. The mean optical density (OD) of the LFB stain was used as a measure of myelin integrity⁴⁶. For each section, two ×20 and five ×60 non-overlapping images from homologous ipsilateral and contralateral external capsule were acquired and processed for OD using ImageJ software. OD calibration was carried out such that pixel values, usually in gray level units, were in OD. Each image was converted to 8-bit and the ROI was outlined manually. Any incidental border region of the cortex was excluded from analysis. OD was measured from ipsilateral and corresponding contralateral hemispheres and expressed as a ratio.

Electron microscopy. For brain sections: 24 h following the standard tMCAO protocol mice were anesthetized and transcardially perfused for 5 min with cold 4% PFA in 0.1 M Sørensen's solution. The brain was then removed, sectioned at 2 mm using a brain matrix and incubated in 2% TTC for 20 min and assessed for lesion volume as above. Sections were then immersion-fixed in 2.5% glutaraldehyde/0.1 M Sørensen's overnight and stored in Sørensen's solution. The external capsule-motor cortex border region from both hemispheres was excised prior to post-fixation (1% osmium tetroxide), serially dehydration and epoxy infiltration. Ultrathin coronal sections (50–70 nm) were counterstained with uranyl acetate and lead citrate prior to blind examination using a Jeol 100CX electron microscope. Micrographs were analyzed for axon G-ratio by hand tracing (ImageJ, NIH) the external and internal myelin profile of all X-S axons within a micrograph and converting the area to

idealized circles. Somata viability was assessed using a basic scoring system where one point was awarded for each of: (a) an intact cell membrane; (b) the presence of undamaged organelles such as mitochondria; (c) a normal nuclear morphology; and (d) the presence of clear cytoplasm. The external capsule-motor cortex border region of three vehicle-treated and three QNZ-46-treated mice were analyzed.

For RON: following either 30 min OGD (for long-sectioning: L-S) or 60 min OGD + 60 min recovery (for cross-sectioning: X-S), adult mouse nerves were immersion-fixed in 4% PFA in Sørensen's for 5 min followed by 2.5% glutaraldehyde/0.1 M Sørensen's overnight and storage in Sørensen's. A minimum of four grid-sections in each of a minimum of three nerves were analyzed blind by hand including the tracing of axons and myelin profiles (X-S), axoplasmic vesicle counting (L-S) and focal myelin damage (L-S). G-ratio in X-S was calculated as above; vesicle counting was performed in L-S to allow vesicles to be distinguished from microtubules. Focal myelin injury was scored: 0 = normal compact myelin; 1 = one layer of myelin splitting; 2 = myelin bubbling involving multiple lamella; 3 = complete myelin breakdown.

Statistics. Data are mean \pm SEM, significance determined by *t*test or ANOVA with Holm–Šidák post hoc test as appropriate; Mann–Whitney *U* test was performed for nonparametric variables (Modified Bederson Score). CAP and biosensor recordings were stable over long periods of control recording and glutamate receptor antagonists had no effect under control conditions (Supplementary Fig. 6). For long periods of drug pre-treatment, control experiments were performed with the identical protocols to allow direct comparison. **P* = <0.05 (rounded three decimal places), ***P* = <0.01 (rounded three decimal places), ****P* = <0.001 (rounded four decimal places). Sample sizes for experimental groups are based on power calculations using established variability. Data from all completed experiments are included and no outliers were excluded. Two animals subjected to tMCAO died post-operatively and were not counted. Sham and test tMCAO trials were alternated and the experimenters were blinded to the contents of the injection; the micrographs generated from these experiments were analyzed blind (REF) and only unblinded once analysis was complete. All test experiments were intercalated with the relevant controls and where possible trials were conducted blind, including all in vivo treatments.

Data availability. All relevant data are available from the authors upon request.

Received: 24 January 2017 Accepted: 13 February 2018

Published online: 12 March 2018

References

- Fern, R. F., Matute, C. & Stys, P. K. White matter injury: ischemic and nonischemic. *Glia* **62**, 1780–1789 (2014).
- Macrez, R., Stys, P. K., Vivien, D., Lipton, S. A. & Docagne, F. Mechanisms of glutamate toxicity in multiple sclerosis: biomarker and therapeutic opportunities. *Lancet Neurol.* **15**, 1089–1102 (2016).
- Iadecola, C. The pathobiology of vascular dementia. *Neuron* **80**, 844–866 (2013).
- Karadottir, R., Cavalier, P., Bergersen, L. H. & Attwell, D. NMDA receptors are expressed in oligodendrocytes and activated in ischaemia. *Nature* **438**, 1162–1166 (2005).
- Micu, I. et al. NMDA receptors mediate calcium accumulation in myelin during chemical ischaemia. *Nature* **439**, 988–992 (2006).
- Christensen, P. C., Samadi-Bahrami, Z., Pavlov, V., Stys, P. K. & Moore, G. R. W. Ionotropic glutamate receptor expression in human white matter. *Neurosci. Lett.* **630**, 1–8 (2016).
- Salter, M. G. & Fern, R. NMDA receptors are expressed in developing oligodendrocyte processes and mediate injury. *Nature* **438**, 1167–1171 (2005).
- Micu, I. et al. Real-time measurement of free Ca²⁺ changes in CNS myelin by two-photon microscopy. *Nat. Med.* **13**, 874–879 (2007).
- Rossi, D. J., Oshima, T. & Attwell, D. Glutamate release in severe brain ischaemia is mainly by reversed uptake. *Nature* **403**, 316–321 (2000).
- Li, S., Mealing, G. A., Morley, P. & Stys, P. K. Novel injury mechanism in anoxia and trauma of spinal cord white matter: glutamate release via reverse Na⁺-dependent glutamate transport. *J. Neurosci.: Off. J. Soc. Neurosci.* **19**, RC16 (1999).
- Baltan, S. et al. White matter vulnerability to ischemic injury increases with age because of enhanced excitotoxicity. *J. Neurosci.: Off. J. Soc. Neurosci.* **28**, 1479–1489 (2008).
- Micu, I. et al. The molecular physiology of the axo-myelinic synapse. *Exp. Neurol.* **276**, 41–50 (2016).
- Spitzer, S., Volbracht, K., Lundgaard, I. & Karadottir, R. T. Glutamate signalling: a multifaceted modulator of oligodendrocyte lineage cells in health and disease. *Neuropharmacology* **110**, 574–585 (2016).
- Fields, R. D. A new mechanism of nervous system plasticity: activity-dependent myelination. *Nat. Rev. Neurosci.* **16**, 756–767 (2015).
- Kukley, M., Capetillo-Zarate, E. & Dietrich, D. Vesicular glutamate release from axons in white matter. *Nat. Neurosci.* **10**, 311–320 (2007).
- Gido, G., Kristian, T. & Siesjö, B. K. Extracellular potassium in a neocortical core area after transient focal ischemia. *Stroke; J. Cereb. Circ.* **28**, 206–210 (1997).
- Alix, J. J. et al. Central axons preparing to myelinate are highly sensitive to ischemic injury. *Ann. Neurol.* **72**, 936–951 (2012).
- Sturrock, R. R. Myelination of the mouse corpus callosum. *Neuropathol. Appl. Neurobiol.* **6**, 415–420 (1980).
- Arranz, A. M. et al. Functional glutamate transport in rodent optic nerve axons and glia. *Glia* **56**, 1353–1367 (2008).
- Guo, J. et al. Abnormal junctions and permeability of myelin in PMP22-deficient nerves. *Ann. Neurol.* **75**, 255–265 (2014).
- Moring, J., Niego, L. A., Ganley, L. M., Trumbore, M. W. & Herbette, L. G. Interaction of the NMDA receptor noncompetitive antagonist MK-801 with model and native membranes. *Biophys. J.* **67**, 2376–2386 (1994).
- Saab, A. S. et al. Oligodendroglial NMDA receptors regulate glucose import and axonal energy metabolism. *Neuron* **91**, 119–132 (2016).
- Mosley, C. A. et al. Quinazolin-4-one derivatives: a novel class of noncompetitive NR2C/D subunit-selective N-Methyl-D-aspartate receptor antagonists. *J. Med. Chem.* **53**, 5476–5490 (2010).
- Hamilton, N. B., Kolodziejczyk, K., Kougioumtzidou, E. & Attwell, D. Proton-gated Ca(2+)-permeable TRP channels damage myelin in conditions mimicking ischaemia. *Nature* **529**, 523–527 (2016).
- Wang, C. N. et al. In situ fluorescence imaging of myelination. *J. Histochem. Cytochem.* **58**, 611–621 (2010).
- Naleway, J. J. et al. Synthesis and use of new fluorogenic precipitating substrates. *Tetrahedron Lett.* **35**, 8569–8572 (1994).
- Lozovaya, N. et al. Selective suppression of excessive GluN2C expression rescues early epilepsy in a tuberous sclerosis murine model. *Nat. Commun.* **5**, 4563 (2014).
- Hansen, K. B. & Traynelis, S. F. Structural and mechanistic determinants of a novel site for noncompetitive inhibition of GluN2D-containing NMDA receptors. *J. Neurosci.: Off. J. Soc. Neurosci.* **31**, 3650–3661 (2011).
- Wang, Y. et al. White matter injury in ischemic stroke. *Progress Neurobiol.* **141**, 45–60 (2016).
- Sozmen, E. G. et al. Nogo receptor blockade overcomes remyelination failure after white matter stroke and stimulates functional recovery in aged mice. *Proc. Natl. Acad. Sci. USA* **113**, E8453–E8462 (2016).
- Pantoni, L., Gracia, J. H. & Gutierrez, J. A. Cerebral white matter is highly vulnerable to ischemia. *Stroke; J. Cereb. Circ.* **27**, 1641–1646 (1996). discussion 1647.
- Romanelli, E. et al. Myelinosome formation represents an early stage of oligodendrocyte damage in multiple sclerosis and its animal model. *Nat. Commun.* **7**, 13275 (2016).
- Mierzwa, A. J., Marion, C. M., Sullivan, G. M., McDaniel, D. P. & Armstrong, R. C. Components of myelin damage and repair in the progression of white matter pathology after mild traumatic brain injury. *J. Neuropathol. Exp. Neurol.* **74**, 218–232 (2015).
- Chamorro, A., Dirnagl, U., Urra, X. & Planas, A. M. Neuroprotection in acute stroke: targeting excitotoxicity, oxidative and nitrosative stress, and inflammation. *Lancet Neurol.* **15**, 869–881 (2016).
- Lundgaard, I. et al. Neuregulin and BDNF induce a switch to NMDA receptor-dependent myelination by oligodendrocytes. *PLoS Biol.* **11**, e1001743 (2013).
- Brickley, S. G., Misra, C., Mok, M. H., Mishina, M. & Cull-Candy, S. G. N. R. 2B and NR2D subunits coassemble in cerebellar Golgi cells to form a distinct NMDA receptor subtype restricted to extrasynaptic sites. *J. Neurosci.: Off. J. Soc. Neurosci.* **23**, 4958–4966 (2003).
- Momiyama, A., Feldmeyer, D. & Cull-Candy, S. G. Identification of a native low-conductance NMDA channel with reduced sensitivity to Mg²⁺ in rat central neurones. *J. Physiol.* **494**(Pt 2), 479–492 (1996).
- Harney, S. C., Jane, D. E. & Anwyl, R. Extrasynaptic NR2D-containing NMDARs are recruited to the synapse during LTP of NMDAR-EPSCs. *J. Neurosci.: Off. J. Soc. Neurosci.* **28**, 11685–11694 (2008).
- Monyer, H., Burnashev, N., Laurie, D. J., Sakmann, B. & Seeburg, P. H. Developmental and regional expression in the rat brain and functional properties of four NMDA receptors. *Neuron* **12**, 529–540 (1994).
- Akazawa, C., Shigemoto, R., Bessho, Y., Nakanishi, S. & Mizuno, N. Differential expression of five N-methyl-D-aspartate receptor subunit mRNAs in the cerebellum of developing and adult rats. *J. Comp. Neurol.* **347**, 150–160 (1994).
- Mohan, K. M. et al. Risk and cumulative risk of stroke recurrence: a systematic review and meta-analysis. *Stroke; J. Cereb. Circ.* **42**, 1489–1494 (2011).
- Bading, H. Therapeutic targeting of the pathological triad of extrasynaptic NMDA receptor signaling in neurodegenerations. *J. Exp. Med.* **214**, 569–578 (2017).

43. Bederson, J. B. et al. Rat middle cerebral artery occlusion: evaluation of the model and development of a neurologic examination. *Stroke; J. Cereb. Circ.* **17**, 472–476 (1986).
44. Zhang, L. et al. A test for detecting long-term sensorimotor dysfunction in the mouse after focal cerebral ischemia. *J. Neurosci. Methods* **117**, 207–214 (2002).
45. Yanamoto, H., Hong, S. C., Soleau, S., Kassell, N. F. & Lee, K. S. Mild postischemic hypothermia limits cerebral injury following transient focal ischemia in rat neocortex. *Brain Res.* **718**, 207–211 (1996).
46. Chan, P. H. The *N*-methyl-d-aspartate antagonist CNS 1102 protects cerebral gray and white matter from ischemic injury following temporary focal ischemia in rats - Editorial Comment. *Stroke; J. Cereb. Circ.* **31**, 1714–1714 (2000).

Acknowledgements

We thank Robert Zammit for assistance with the multi-photon confocal imaging and Waldemar Woznica for assistance with IP injections performed at Plymouth. This work was supported by BBSRC (J016969/1), by the University of Plymouth and by the Alfred Mizzi Foundation, Malta.

Author contributions

S.D. performed and analyzed all CAP, biosensor and two-photon microscopy recordings; D.B.H. performed and analyzed the laser-scanning and spinning disk confocal imaging; J.V. conducted the tMCAO protocol; P.B. and G.H. prepared the EM sections; M.V. supervised and contributed to the two-photon imaging and the tMCAO experiments; C. Z. contributed to two-photon imaging; R.F. supervised the project, developed the theory of a myelin shield, analyzed the EM, and wrote the manuscript.

Additional information

Supplementary Information accompanies this paper at <https://doi.org/10.1038/s41467-018-03427-1>.

Competing interests: The authors declare no competing interests.

Reprints and permission information is available online at <http://npg.nature.com/reprintsandpermissions/>

Publisher's note: Springer Nature remains neutral with regard to jurisdictional claims in published maps and institutional affiliations.



Open Access This article is licensed under a Creative Commons Attribution 4.0 International License, which permits use, sharing, adaptation, distribution and reproduction in any medium or format, as long as you give appropriate credit to the original author(s) and the source, provide a link to the Creative Commons license, and indicate if changes were made. The images or other third party material in this article are included in the article's Creative Commons license, unless indicated otherwise in a credit line to the material. If material is not included in the article's Creative Commons license and your intended use is not permitted by statutory regulation or exceeds the permitted use, you will need to obtain permission directly from the copyright holder. To view a copy of this license, visit <http://creativecommons.org/licenses/by/4.0/>.

© The Author(s) 2018